IMAGING OF THE SUDBURY STRUCTURE, ONTARIO, CANADA, USING THE SEISMIC REFLECTION AND REFRACTION METHOD

BY

LINGXIU JIAO

焦 灵 秀

A thesis
Submitted to the Faculty of Graduate Studies
in Partial Fulfillment of the Requirements
for the Degree of

DOCTOR OF PHILOSOPHY

Department of Geological Sciences
University of Manitoba
Winnipeg, Manitoba

THE UNIVERSITY OF MANITOBA

FACULTY OF GRADUATE STUDIES

*****

COPYRIGHT PERMISSION PAGE

Imaging of the Sudbury Structure, Ontario, Canada, using the Seismic Reflection and Refraction Method

BY

Lingxiu Jiao

A Thesis/Practicum submitted to the Faculty of Graduate Studies of The University of Manitoba in partial fulfillment of the requirements of the degree

of

Doctor of Philosophy

Abstract

The Sudbury Structure in Ontario, Canada, has been extensively investigated since its discovery more than a hundred years ago. The genesis of the structure has been an object of controversy since its discovery. In this thesis, the 1992 Lithoprobe Abitibi-Grenville Transect high-resolution seismic wide-angle reflection and refraction data from the Sudbury subtransect (profiles AB and XY) are processed and modeled to provide geophysical constraints on addressing the controversy. Information on the subsurface structure of the crust and upper mantle will allow better understanding of the Sudbury Structure's geological evolution.

Cerveny's ray tracing algorithm was employed to model the complicated crustal structure along profile AB. The RAYINVR ray tracing inversion algorithm was used to obtain the relatively simple crustal structure along profile XY. A 3-D ray tracing algorithm based on the Fletcher Reeves conjugate gradient technique was developed to model the fan-shot data. A 3-D weighted backprojection tomographic method was used to reconstruct the 3-D velocity image of the Sudbury and surrounding area.

The modeling results using the seismic data have revealed a lenticular higher velocity body under the Sudbury Basin. The high-velocity body extends from 4 to 9 km depth and its velocity is approximately 6.31-6.4 km/s. Along profile XY the body dips toward northwest whereas along profile AB it dips slightly toward southeast. The lenticular high-velocity body was also imaged on the 3-D tomographic modeling. Comparison of the modeled velocities and the velocities measured from rock samples

indicates that the high-velocity body is associated with the norite of the Sudbury Igneous Complex. According to both 2-D and 3-D ray tracing modeling results, interpretation of the seismic data indicates that there is neither an apparent central uplift in the crust and upper mantle, nor an igneous "feeding-root" in the lower crust beneath the basin. The seismic refraction study has, therefore, confirmed most geological and meteorite impact model constraints; however, the high-velocity body imaged in this research requires further petrological and high-resolution seismic investigation in 3-D.

Acknowledgments

I would like to thank my advisor, Dr. W. Moon, for his invaluable supervision and encouragement during the thesis research.

I would also like to thank Dr. I. Ferguson for kindly and patiently reviewing my thesis, and providing helpful comments and constructive advice. I thank Professors B. Southern and D. Hall for serving on my committee.

I wish to thank the external examiner, Dr. K. Vasudevan of the University of Calgary, for his useful review. Dr. Vasudevan also kindly provided computer facilities of the Lithoprobe Seismic Processing Facilities for me to work on thesis revisions while in Calgary.

I wish to express my sincere appreciation to Dr. L. Ayres for his useful reviews of the thesis, his detailed comments regarding Chapter 2, and his editing of the manuscript's English. I also wish to extend my appreciation to D. Leverington and J. Selway for kindly assisting in the editing of the English in the manuscript. I thank Dr. R. Maier of the Lithoprobe Seismic Processing Facility, University of Calgary, for his timely help and his assistance in editing the manuscript's English. I greatly appreciate the various innovative ideas that were proposed by Dr. W. Kinsner (University of Manitoba) regarding fractal techniques. I thank my colleagues D. Leverington and J. Ristau for their help during my Ph. D. study.

I thank Lithoprobe for providing me with the seismic data used in the thesis study. I would also like to express my thanks to Dr. C. Zelt for kindly providing a copy of his

RAYINVR software package. Dr. J. Hole generously provided a copy of his 3-D tomographic computer codes for this study. I have greatly benefited from the use of the Generic Mapping Tools programs, provided by Drs. P. Wessel and W. Smith, for creating partial seismic figures.

I would like to express many thanks to my husband, Fanle for his love, great support, and understanding, and for taking care of our children while I was busy with my thesis studies. I thanks all my family members, especially my parents (Haiqin and Shuling) for their support and encouragement.

Table of Contents

Abstract i

Acknowledgments iii

Table of Contents v

Figure List x

Table List xxix

Table of Symbols and Abbreviations xxxi

1 Introduction 1

1.1 Study Area, Geological Background and Hypotheses 1

1.2 Objectives of the Research 4

2 Geology of the Sudbury Area and Hypotheses for the Origin of the Sudbury Structure 9

2.1 General Geology 9

2.1.1 Regional Geological Setting 11

2.2 Sudbury Structure 16

2.2.1 Sudbury Igneous Complex 17

2.2.2 Whitewater Group of the Sudbury Basin 18

2.2.3 Breccias 21

2.3 Tectonic History 22

2.4 Hypotheses on the Origin of the Sudbury Structure 25

2.4.1 Hypothesis on Internal Volcanic Origin 26

2.4.2 Hypothesis on Meteorite Impact Origin 29

3 Review of Previous Geophysical Studies **36**

3.1 Seismic Studies 36

3.1.1 Seismic Reflection 37

3.1.2 Seismic Refraction 42

3.1.3 Borehole and VSP 42

3.2 Other Geophysical Studies 46

3.2.1 Potential Field Studies 47

3.2.2 Electromagnetic and Other Surveys 54

3.2.3 Remote Sensing 56

4 Seismic Refraction Survey **59**

4.1 Instruments 61

4.1.1 The Geological Ssurvey of Canada's PRS1 61

4.2 Seismic Survey 64

4.2.1 Survey Parameters 65

4.2.2 Shooting and Recording 65

4.2.3 Data Processing 66

5 Modeling of In-line Data (Profile AB) **68**

5.1 Cerveny Ray Tracing Algorithm 68

5.1.1 Basic Principles in Ray Theory 69

5.1.2 Source Functions 71

5.1.3 Determination of Ray Path, Traveltime and Amplitude 73

5.2 Modeling of In-line Profile AB 79

5.2.1 Reflectors Suggested by Previous Seismic Studies 80
5.2.2 Seismic Refraction Data Processing and Displaying 86
5.2.3 Seismic Phase Analysis 88
5.2.4 Modeling Procedure 103
5.3 Summary 123
6 Modeling of In-line Data (Profile XY) **125**
6.1 RAYINVR Ray Tracing Inversion Algorithm 125
6.1.1 Model Parameterization 126
6.1.2 Ray Tracing (Forward Modeling) 128
6.1.3 Inversion 130
6.2 Modeling of In-line Profile XY 134
6.2.1 Seismic Phase Analysis 134
6.2.2 Modeling Procedure 144
6.3 Summary 167
7 Fan-shot Data Modeling **170**
7.1 3-D Modeling Method 170
7.1.1 Fletcher Reeves Ray Tracing 170
7.1.2 Inversion 179
7.2 Modeling of the Sudbury Data 182
7.2.1 Fan Shot Data Processing and Displaying 182
7.2.2 Seismic Phase Analysis and Picking 182
7.2.3 Modeling Procedure 200
7.3 Summary 227

8 3-D Seismic Tomography **230**

8.1 Algorithm 230

8.1.1 Finite-difference Forward Modeling 231

8.1.2 Backprojection Tomographic Inversion 235

8.2 3-D Seismic Tomographic Imaging of the Sudbury Structure 238

8.2.1 Model Parameterization 239

8.2.2 3-D Tomographic Modeling 241

8.3 Summary 266

9 Discussion and Model of the Sudbury Structure **268**

9.1 Interpretation and Discussion of the Results 268

9.1.1 2-D Modeling 268

9.1.2 3-D Modeling 273

9.1.3 Discussions of Other Studies Conducted during this Thesis Work 277

9.2 Model of the Sudbury Structure 279

9.2.1 Impact Model 279

9.2.2 Development of Geological Sequences 280

10 Conclusions **285**

References **289**

Appendix A Variance Fractal Dimension Technique of Detecting Seismic phases **310**

Appendix B Length Fractal Dimension Technique of Detecting Seismic phases **311**

B.1 Length Fractal Dimension 311

B.2 Application to Seismic Reflection Data 313

Appendix C Potential Field Data Processing and Anomalies **319**

C.1 Processing Steps 319

C.2 Preliminary Interpretation 324

Appendix D Remote Sensing Data and GIS Applications **329**

D.1 Preliminary Processing of Radar Image 329

D.2 Speckle Noise Reduction 330

D.3 GIS Displaying 335

Figure List

Figure 2.1 Location of the Sudbury Structure relative to the regional tectonic elements of North America (Modified from http://www.science.ubc.ca/~eoswr/slideshow/accounts/lithoprobe/slidefiles/earth1.html) [accessed on June 10, 2000]. The Sudbury Structure is in the circled area. 10

Figure 2.2 General geology map of the Sudbury area (Modified from Card et al., 1984; Green et al., 1988; Ketchum et al., 1998; Meldrum et al., 1997). 12

Figure 2.3 Simplified geological map of the Sudbury basin structure (After Miao, 1995). 16

Figure 2.4 Schematic lithologic column of the Sudbury Structure (Modified from Deutsch, 1994; Naldrett and Hewins, 1984). 19

Figure 2.5 Development sequence of an endogenic model proposed by Muir (1984). A_1: earlier stage; A_2 and A_3: later stages; A_4: post-Sudbury event stage (see the text for details). 28

Figure 2.6 Development sequence of the exogenic meteorite impact model proposed by Grieve (1994). a, b, c and d represent the formation of the original crater and the Sudbury Igneous Complex in minutes after a meteorite stuck Sudbury. e and f indicate the Formation of the Onaping Formation as a fall-back debris. g represents the current deformed structure. 34

Figure 3.1 Locations of the seismic reflection profiles and sample images (Modified from Clowes, 1997). 38

Figure 3.2 Migrated seismic image of line 41. A, B, C, D, E, F, Q, P, R, S, Es and Ds are seismic reflectors. CF: Creighton Fault; FLF: Fairbank Lake Fault; VLF: Vermilion Lake Fault; CCF: Cameron Creek Fault (After Milkereit et al., 1992). 39

Figure 3.3 Seismic reflection image and geological interpretation of reprocessed seismic data. LFLF: Little Fairbank Lake Fault; SLF: Skill Lake Fault; FLF: Fairbank Lake Fault; CLF: Cameron Lake Fault; CCF: Cameron Creek Fault (After Wu. et al., 1995). 40

Figure 3.4 Seismic images of lines42 and 41. AA', R_1R_1', R_2R_2', 1 and 2 are reflection interfaces revealed on line 42 (After Miao, 1995). 41

Figure 3.5 2-D tomographic velocity model. a: final velocity model of line AB; b: velocity anomaly of line AB; c: velocity uncertainty of line AB; d: final velocity model of line XY; e: velocity anomaly of line XY (After Winardhi and Mereu, 1997). 43

Figure 3.6 Borehole geophysical data in Sudbury. Density, P- and S- wave velocities, derived Poisson's ratio and synthetic seismogram for a 30-140 Hz source are indicated in **a**. G: Granophyre; TZ: Quartz Gabbro; N: Norite; F: Footwall Complex. **b** shows not only density, P- and S- wave velocities, Poisson's ratio radioelements (**a** after Milkereit et al., 1994; **b** after White et al., 1994b).

..... 44

Figure 3.7 Corridor-stacked VSP section and seismic reflection image (After Miao, 1995). 46

Figure 3.8 Bouguer gravity anomaly map in the Sudbury Area. EE' is the gravity profile of Gupta et al.'s model A and whereas NS is the profile of the new 2.5 gravity model. Interpretations corresponding to these two profiles are indicated in Figure 3.9 a and 3.9b respectively. Anomalies A, B, D, H, K. M and X are referred to the text. (After McGrath and Broome, 1994). 48

Figure 3.9a Geological interpretation of gravity model A (After Gupta et al., 1984). 50

Figure 3.9b The 2.5-D gravity model proposed by McGrath and Broome (1994). MF: Murray Fault; Gr: Granophyre; Ow: Onwatin; Ch: Chelmsford. 51

Figure 3.10 Total field magnetic anomalies (a) and magnetic model (b). C-O: Chelmsford and Onwatin; O: Onaping: G: Granophyre; N: Norite; LGC: Levack Gneiss Complex; CG: Cartier Granite. D: Electromagnetic survey profile (After Hearst et al., 1994). 53

Figure 3.11 Resistivity versus depth profile interpreted from UTEM survey. The dipping lines are reflectors indicated on the seismic image shown in Figure 3.2. Es, Ds, P, Q, and R corresponds to reflectors pointed out in Figure 3.2 (CF: Creighton Fault; FLF; Fairbank Lake Fault.) (After Boerner et al., 1994). 55

Figure 3.12 Remote sensing images overlain by geophysical and radioelement data. **a.** VLF (very low frequency) electromagnetic image. Lines are geological formation boundaries. **b.** composite radio-elements image with geological formation boundaries. **c.** integration of airborne SAR (synthetic aperture radar) C-

HH overlain by vertical magnetic gradient data (**a** and **b** after Singh et al., 1993; **c** after Singhroy et al., 1993). 58

Figure 4.1 Source and receiver locations for the 1992 Lithoprobe high-resolution wide-angle reflection and refraction seismic survey (After Moon and Jiao, 1998). 60

Figure 4.2 Main components of the PRS1(After Asudeh et al., 1992). M: mass; MUX: multiplexer system control bus; TCXO: temperature compensated crystal oscillator. 63

Figure 5.1 A ray coordinate System. X: point coordinate at which a ray intersects an interface; τ : time; γ_1 and γ_2 : ray parameters. 72

Figure 5.2 Location map of profile J of the GLIMPCE seismic experiment across Lake Huron (After Epili and Mereu, 1991). 81

Figure 5.3 Reflection section (**a**) and its interpretation (**b**) along profile J in the eastern part of the GLIMPCE experiment crossing the Grenville Front in Lake Huron (After Clowes et al., 1992). 82

Figure 5.4 2-D seismic refraction section with shingle-like events (**a**) and interpreted velocity model (**b**) (After Epili and Mereu., 1991). 83

Figure 5.5 Location map of Abitibi-Grenville Lithoprobe line 15 (After Kellett et al., 1993). 84

Figure 5.6 Geological section interpreted by a combination of seismic reflection data of line 15 and geological information (Kellett et al., 1993). 85

Figure 5.7 Velocity structures along profiles AB (**a**) and XY (**b**) from the 1992 Lithoprobe seismic refraction survey across Sudbury (After Miao, 1995). 87

Figure 5.8 Wide-angle seismic reflection and refraction section for in-line ab0. 89

Figure 5.9 Wide-angle seismic reflection and refraction section for in-line ab1. 90

Figure 5.10 Wide-angle seismic reflection and refraction section for in-line ab2. 91

Figure 5.11 Wide-angle seismic reflection and refraction section for in-line ab3. 92

Figure 5.12 Wide-angle seismic reflection and refraction section for in-line ab4. 93

Figure 5.13 Wide-angle seismic reflection and refraction section for in-line ab6. 94

Figure 5.14 Wide-angle seismic reflection and refraction section for in-line ab7. 95

Figure 5.15 Wide-angle seismic reflection and refraction section for in-line ab8. 96

Figure 5.16 Wide-angle seismic reflection and refraction section for in-line ab9. 97

Figure 5.17 Wide-angle seismic reflection and refraction section for in-line ab10. 98

Figure 5.18 Initial velocity model along profile AB obtained by forward modeling. Solid lines represent the structural boundaries. 105

Figure 5.19 Wide-angle seismic reflection and refraction section for in-line ab0. **a**: seismic section; **b**: ray path; **c**: synthetic seismogram. ⊖–⊖ : calculated travel-time. 107

Figure 5.20 Wide-angle seismic reflection and refraction section for in-line ab1. **a**: seismic section; **b**: ray path; **c**: synthetic seismogram. ⊖–⊖ : calculated trav-eltime. 108

Figure 5.21 Wide-angle seismic reflection and refraction section for in-line ab2. **a**: seismic section; **b**: ray path; **c**: synthetic seismogram. ⊖–⊖ : calculated travel-time. 109

Figure 5.22 Wide-angle seismic reflection and refraction section for in-line ab3. **a**: seismic section; **b**: ray path; **c**: synthetic seismogram. ⊖–⊖ : calculated travel-time. 110

Figure 5.23 Wide-angle seismic reflection and refraction section for in-line ab4. **a**: seismic section; **b**: ray path; **c**: synthetic seismogram. ⊖–⊖ : calculated travel-time. 111

Figure 5.24 Wide-angle seismic reflection and refraction section for in-line ab6. **a**: seismic section; **b**: ray path. **c**: synthetic seismogram. ⊖–⊖ : calculated travel-time. 112

Figure 5.25 Wide-angle seismic reflection and refraction section for in-line ab7. **a**: seismic section; **b**: ray path; **c**: synthetic seismogram. ⊖–⊖ : calculated travel-time. 113

Figure 5.26 Wide-angle seismic reflection and refraction section for in-line ab8. **a**: seismic section; **b**: ray path; **c**: synthetic seismogram. ⊖–⊖ : calculated traveltime. 114

Figure 5.27 Wide-angle seismic reflection and refraction section for in-line ab9. **a**: seismic section; **b**: ray path; **c**: synthetic seismogram. ⊖–⊖ : calculated traveltime. 115

Figure 5.28 Wide-angle seismic reflection and refraction section for in-line ab10. **a**: seismic section; **b**: ray path; **c**: synthetic seismogram. ⊖–⊖ : calculated traveltime. 116

Figure 5.29 Velocity structure along profile AB obtained by forward modeling. Solid lines represent the structural boundaries. 122

Figure 6.1 Example of model parameterization. - - - : layer interfaces and layer blocks; ■ : interface block boundary points; ● : velocity nodes. 126

Figure 6.2 The velocity and interface parameterization in a trapezoid boundary block. 127

Figure 6.3 Take-off angles for turning (**a**), reflection (**b**), and refraction (**c**) waves (After Zelt and Smith, 1992). 129

Figure 6.4 Wide-angle seismic reflection and refraction section of shot xy0 for in-line XY. 135

Figure 6.5 Wide-angle seismic reflection and refraction section of shot xy1 for in-line XY. 136

Figure 6.6 Wide-angle seismic reflection and refraction section of shot xy2 for in-line XY. 137

Figure 6.7 Wide-angle seismic reflection and refraction section of shot xy4 for in-line XY. 138

Figure 6.8 Wide-angle seismic reflection and refraction section of shot xy5 for in-line XY. 139

Figure 6.9 Model parameterization of profile XY. Solid lines denote the interface boundaries. Dash lines represent the velocity boundaries. Open circles represent the interface boundaries node and filled squares represent velocity nodes. 145

Figure 6.10 In-line seismic section for xy0. **a**: seismic section with picked traveltimes; **b**: ray path ($\mathbf{b_1}$) and observed and calculated traveltimes ($\mathbf{b_2}$); **c**: synthetic seismogram. The solid line in **a** represents the picked traveltimes. 148

Figure 6.11 In-line seismic section for xy1. **a**: seismic section with picked traveltimes; **b**: ray path ($\mathbf{b_1}$) and observed and calculated traveltimes ($\mathbf{b_2}$); **c**: synthetic seismogram. The solid line in **a** represents the picked traveltimes. 149

Figure 6.12 In-line seismic section for xy2. **a**: seismic section with picked traveltimes; **b**: ray path ($\mathbf{b_1}$) and observed and calculated traveltimes ($\mathbf{b_2}$); **c**: synthetic seismogram. The solid line in **a** represents the picked traveltimes. 150

Figure 6.13 In-line seismic section for xy4. **a**: seismic section with picked traveltimes; **b**: ray path ($\mathbf{b_1}$) and observed and calculated traveltimes ($\mathbf{b_2}$); **c**: synthetic seismogram. The solid line in **a** represents the picked traveltimes. 151

Figure 6.14 In-line seismic section for xy5. **a**: seismic section with picked traveltimes; **b**: ray path ($\mathbf{b_1}$) and observed and calculated traveltimes ($\mathbf{b_2}$); **c**: synthetic seismogram. The solid line in **a** represents the picked traveltimes. 152

Figure 6.15 Ray paths for turning Pg waves (**a**), head wave refractions (**b**) and turning wave propagating through the first layer and the upper second layer (**c**). sp indicates shot points. 153

Figure 6.16 A selective plot of ray paths of Pr (**a**), PcP and Pc (**b**), and PmP and Pn (**c**) phases. 158

Figure 6.17 The seismic velocity structure modeled using the RAYINVR ray tracing forward and inverse modeling algorithm along profile XY. The solid line represents the geological interface boundaries. 162

Figure 7.1 A sketch of the fan shot survey pattern in a plane view. ⌒: receiving line; * : shot point; ab0: shot number; — : line linking shot of ab0 and receiver along profile XY; — : line linking shot xy0 and receiver along the southern part of the cross point of profile AB; — : line linking shot xy5 and a receiver along the southern part of the cross point of profile AB. 171

Figure 7.2 Schematic drawing of the model parameterization. Planes are defined by equation 7.1. v_i denote the constant velocities between two adjacent layers; i represents the layer index; ✦: shot point; ▲: receiver point; o : unlabeled coordinate point;● : labelled coordinate point. Three ray paths are drawn in the diagram which are refraction at the first interface, the reflected wave at the mth interface, and the refraction at the mth interface. 174

Figure 7.3 Flow chart for the Fletcher Reeves conjugate gradient method. n represents a maximum iteration number allowed. After iterations n, if the termination criterion is not satisfied, the calculation procedure is restarted by using a new initial value X^0 which equals X^{k+1} obtained from the previous iteration. If an iteration number is less than the maximum and the termination criterion is not satisfied, the conjugfate coefficent will be modified and a new iteration is required. 180

Figure 7.4 Locations of four quadrants separated by two seismic survey lines AB and XY. 183

Figure 7.5 Fan-shot seismic section ab0. 184

Figure 7.6 Fan-shot seismic section ab1. 185

Figure 7.7 Fan-shot seismic section ab2. 186

Figure 7.8 Fan-shot seismic section ab3. 187

Figure 7.9 Fan-shot seismic section ab4. 188

Figure 7.10 Fan-shot seismic section ab6. 189

Figure 7.11 Fan-shot seismic section ab7. 190

Figure 7.12 Fan-shot seismic section ab8. 191

Figure 7.13 Fan-shot seismic section ab9. 192

Figure 7.14 Fan-shot seismic section ab10. 193

Figure 7.15 Fan-shot seismic section xy0. 194

Figure 7.16 Fan-shot seismic section xy1. 195

Figure 7.17 Fan-shot seismic section xy2. 196

Figure 7.18 Fan-shot seismic section xy4. 197

Figure 7.19 Fan-shot seismic section xy5. 198

Figure7.20 Fan-shot seismic section ab0. **a:** traveltime section used for inversion modeling; **b**: the observed and calculated traveltime curves. ⊙⊙ : picked traveltimes; I-I: picked traveltime with error bars; •—•: calculated traveltime. 206

Figure7.21 Fan-shot seismic section ab1. **a:** traveltime section used for inversion modeling; **b**: the observed and calculated traveltime curves. ⊙⊙ : picked traveltimes; I-I: picked traveltime with error bars; •—•: calculated traveltime. 207

Figure7.22 Fan-shot seismic section ab2. **a:** traveltime section used for inversion modeling; **b**: the observed and calculated traveltime curves. ⊙⊙ : picked traveltimes; I-I: picked traveltime with error bars; •—•: calculated traveltime. 208

Figure7.23 Fan-shot seismic section ab3. **a:** traveltime section used for inversion modeling; **b**: the observed and calculated traveltime curves. ⊙⊙ : picked traveltimes; I-I: picked traveltime with error bars; •—•: calculated traveltime. 209

Figure7.24 Fan-shot seismic section ab4. **a:** traveltime section used for inversion modeling; **b**: the observed and calculated traveltime curves. ⊙⊙ : picked traveltimes; I-I: picked traveltime with error bars; •—•: calculated traveltime. 210

Figure7.25 Fan-shot seismic section ab6. **a:** traveltime section used for inversion modeling; **b**: the observed and calculated traveltime curves. ⊙⊙ : picked traveltimes; I-I: picked traveltime with error bars; •—• : calculated traveltime. 211

Figure7.26 Fan-shot seismic section ab7. **a:** traveltime section used for inversion modeling; **b**: the observed and calculated traveltime curves. ⊙⊙ : picked traveltimes; I-I: picked traveltime with error bars; •—• : calculated traveltime. 212

Figure7.27 Fan-shot seismic section ab8. **a:** traveltime section used for inversion modeling; **b**: the observed and calculated traveltime curves. ⚬⚬: picked traveltimes; I-I: picked traveltime with error bars; •••: calculated traveltime. 213

Figure7.28 Fan-shot seismic section ab9. **a:** traveltime section used for inversion modeling; **b**: the observed and calculated traveltime curves. ⚬⚬ : picked traveltimes; I-I: picked traveltime with error bars; ••• : calculated traveltime. 214

Figure7.29 Fan-shot seismic section ab10. **a:** traveltime section used for inversion modeling; **b**: the observed and calculated traveltime curves. ⚬⚬ : picked traveltimes; I-I picked traveltime with error bars; •••: calculated traveltime. 215

Figure7.30 Fan-shot seismic section xy0. **a:** traveltime section used for inversion modeling; **b**: the observed and calculated traveltime curves. ⚬⚬: picked traveltimes; I-I: picked traveltime with error bars; ••• : calculated traveltime. 216

Figure7.31 Fan-shot seismic section xy1. **a:** traveltime section used for inversion modeling; **b**: the observed and calculated traveltime curves. ⚬⚬ : picked traveltimes; I-I: picked traveltime with error bars; •••: calculated traveltime. 217

Figure7.32 Fan-shot seismic section xy2. **a:** traveltime section used for inversion modeling; **b**: the observed and calculated traveltime curves. ⚬⚬ : picked traveltimes; I-I: picked traveltime with error bars; ••• : calculated traveltime. 218

Figure7.33 Fan-shot seismic section xy4. **a:** traveltime section used for inversion modeling; **b**: the observed and calculated traveltime curves. ⚬⚬ : picked traveltimes; I-I: picked traveltime with error bars; ••• : calculated traveltime. 219

Figure7.34 Fan-shot seismic section xy5. **a:** traveltime section used for inversion modeling; **b**: the observed and calculated traveltime curves. ⚬⚬ : picked traveltimes; I-I: picked traveltime with error bars; ⚬—⚬ : calculated traveltime. 220

Figure 7.35 Crustal thickness map obtained by using the 3-D ray tracing inversion. ____: thickness location; numbers in km: crustal thickness. 224

Figure 8.1 A cubic cell for scheme A. ● :known traveltimes points; ● : calculated traveltime point. 232

Figure 8.2 Two cubic cells for scheme B. ● : known traveltime points; ◎ : unknown traveltime points; ● : calculated traveltime point. 233

Figure 8.3 Two cubic cells for scheme C. ● :known traveltime points; ◎ : unknown traveltime points; ● : calculated traveltime point. 233

Figure 8.4 Errors expected for the three schemes for a uniform medium at the range of 10 grid points (After Vidale, 1990). 234

Figure 8.5 Tomographic imaging area indicated by the thick framed line. Dashed lines represent the velocity imaging profiles; characters and numbers beside dashed lines denote velocity imaging profiles. 240

Figure 8.6 Seismic tomographic velocity image of profile WE1 (**a** in a grey scale and b in a color scale) and corresponding ray coverage (**c** in a grey scale and **d** in a HSV color scale generated in Khoros (Release 2.02). 245

Figure 8.7 Seismic tomographic velocity image of profile WE2 (**a** in a grey scale and b in a color scale) and corresponding ray coverage (**c** in a grey scale and **d** in a HSV color scale generated in Khoros (Release 2.02). 247

Figure 8.8 Seismic tomographic velocity image of profile WE3 (**a** in a grey scale and b in a color scale) and corresponding ray coverage (**c** in a grey scale and **d** in a HSV color scale generated in Khoros (Release 2.02). 248

Figure 8.9 Seismic tomographic velocity image of profile WE4 (**a** in a grey scale and b in a color scale) and corresponding ray coverage (**c** in a grey scale and **d** in a HSV color scale generated in Khoros (Release 2.02). 250

Figure 8.10 Seismic tomographic velocity image of profile WE5 (**a** in a grey scale and b in a color scale) and corresponding ray coverage (**c** in a grey scale and **d** in a HSV color scale generated in Khoros (Release 2.02). 251

Figure 8.11 Seismic tomographic velocity image of profile NS1 (**a** in a grey scale and b in a color scale) and corresponding ray coverage (**c** in a grey scale and **d** in a HSV color scale generated in Khoros (Release 2.02). 252

Figure 8.12 Seismic tomographic velocity image of profile NS2 (**a** in a grey scale and b in a color scale) and corresponding ray coverage (**c** in a grey scale and **d** in a HSV color scale generated in Khoros (Release 2.02). 253

Figure 8.13 Seismic tomographic velocity image of profile NS3 (**a** in a grey scale and b in a color scale) and corresponding ray coverage (**c** in a grey scale and **d** in a HSV color scale generated in Khoros (Release 2.02). 254

Figure 8.14 Seismic tomographic velocity image of profile NS4 (**a** in a grey scale and b in a color scale) and corresponding ray coverage (**c** in a grey scale and **d** in a HSV color scale generated in Khoros (Release 2.02). 255

Figure 8.15 Seismic tomographic velocity image of profile NS5 (**a** in a grey scale and b in a color scale) and corresponding ray coverage (**c** in a grey scale and **d** in a HSV color scale generated in Khoros (Release 2.02). 256

Figure 8.16 Seismic tomographic velocity image of profile NS6 (**a** in a grey scale and b in a color scale) and corresponding ray coverage (**c** in a grey scale and **d** in a HSV color scale generated in Khoros (Release 2.02). 257

Figure 8.17 Seismic velocity images of the depth slice at 2 km deep (**a**, **b**) and corresponding ray coverage (**c**, **d**). **d** shows ray coverage in a HSV color scale generated in Khoros (Release 2.02). 260

Figure 8.18 Seismic velocity images of the depth slice at 5 km deep (**a**, **b**) and corresponding ray coverage (**c**, **d**). **d** shows ray coverage in a HSV color scale generated in Khoros (Release 2.02). 262

Figure 8.19 Seismic velocity images of the depth slice at 10 km deep (**a**, **b**) and corresponding ray coverage (**c**, **d**). **d** shows ray coverage in a HSV color scale generated in Khoros (Release 2.02). 264

Figure 9.1 Relation of the depth and diagram for fresh, unfolded lunar craters (After Melosh, 1989). 280

Figure 9.2 Relation of depth and diameter of large complex terrestrial craters: 1. El'gygytgyn,Russia; 2. Haughton, Canada; 3. Ries, Germany; 4. West Clearwater Lake, Canada; 5. Siljian, Sweden; 6. Manicouagan, Canada; 7. Vredefort, South Africa (Based on Pilkington and Grieve, 1992; Rondot, 1994). 281

Figure 9.3 Schematic cartoon of the development sequences of the Sudbury impact structure: (a) Impact cratering, vaporizing and melting (Based on Grieve et al.,

1991);(b) Formations of melting sheet and the Sudbury Breccia and Footwall Breccia (After Avermann et al., 1994 and Miao, et al., 1995); (c) Final stage of the impact cratering and emplacement of the melting sheet; (d) Formation of the sediments, thrusting and erosion; (e) The present Sudbury structure after strong northwest-southeast compressive deformation and subsequent erosion during the Penokean and Grenville orogenies. 283

Figure 9.4 The enlarged present Sudbury structure after strong northwest-southeast deformation and erosion during the Penokean and Grenville orogenies. Due to the poor data resolution, uncertainty in the mid-crustal velocity boundary beneath the Sudbury data resolution, uncertainty in the mid-crustal velocity boundary beneath the Sudbury. 284

Figure A.1 1-D digital time series signal B_j.

Figure A.2 A noise separation increment diagram and its trajectory generation.

Figure A.3 Logarithmic plot of the variance of the amplitude increment (b_s) v.s. time increment (s) for signal and noise.

Figure A.4 Variance fractal dimension trajectories for a synthetic seismic signal with 36, 48, 64 and 128 samples window sizes.

Figure A.5 Variance fractal dimension trajectories with 48 samples window size and 1,4,8 and 12-sampling intervals window interval.

Figure A.6 Variance fractal dimension trajectory for the Pg seismic signal from the fan-shot **ab**2 data.

Figure A.7 Variance fractal dimension trajectory for the Pn seismic signal from the in-line **ab**10 data. **a**: trace 4; **b**: trace 35.

Figure A.8 Variance fractal dimension trajectory for the ground roll seismic signal from the in-line **ab2** data.

Figure A.9 Variance fractal dimension trajectory for the PmP seismic signal from the fan-shot **ab2** data. **a**: trace 26; **b**: trace 28. The upper and lower trajectories in **a** were computed using the sample window sizes of 48 and 128 respectively. The upper and lower trajectories in **b** were computed using the sample window sizes of 48 and 128 respectively.

Figure A.10 The improved variance fractal dimension trajectory for the seismic refraction signal from the fan-shot **ab2** data. The upper trajectory was computed from the original data and the lower trajectory was computed with added random noise.

Figure A.11 The variance fractal dimension trajectories for the seismic reflection signal (trace 40 of the shot gather 516 of line 40-1). The upper trajectory was computed from the original data and the lower trajectory was computed with added random noise.

Figure A.12 Variance fractal dimension trajectories for the seismic reflection signals from traces 151 to 160 of the shot gather 516 of line 40-1. **a**: traces 151 to 160; **b**: variance fractal dimension trajectories for the traces 151 to 160. Dots represent the first arrivals picked by the technique.

Figure B.1 Length fractal dimension curves or trajectories for demo data (from ITA INSIGHT software package). 314

Figure B.2 Length fractal dimension curves or trajectories for demo data (from ITA INSIGHT software package). 315

Figure B.3 Length fractal dimension curves for high resolution seismic reflection data (line in the Sudbury area). 316

Figure B.4 Travel Time pick for seismic reflection data (line 40) from Lithoprobe Sudbury survey. Dots: picked first arrival times. 318

Figure C.1 Geological setting in the Sudbury study area and the potential field data coverage. 320

Figure C.2 **a**: Bouguer gravity anomaly in Sudbury; **b**: shaded relief Bouguer gravity anomaly image in the Sudbury area; **c**: low-pass residual shaded relief gravity anomaly image in the Sudbury area; **d**:5 km up-continuation Bouguer gravity anomaly in the Sudbury area. 322

Figure C.3 **a**: Total field aeromagnetic anomaly map in the Sudbury area; **b**: shaded relief aeromagnetic anomaly image at a sun angle of elevation 45° and azimuth 45°; **c**: shaded relief aeromagnetic anomaly image at a sun angle of elevation 45° and azimuth 45°; **d**: second derivative aeromagnetic anomaly image. 323

Figure C.4 **a**: shaded relief 5 km upward continuation aeromagnetic anomaly image Figure C.4 **a**: shaded relief 5 km upward continuation aeromagnetic anomaly image 5 km upward continuation aeromagnetic anomaly image at a sun angle of elevation 45° and azimuth 134°; **c**: shaded relief 5 km upward continuation aeromagnetic anomaly image at a sun angle of elevation 45° and azimuth 219°; **d**: shaded relief 5 km upward continuation aeromagnetic anomaly image at a sun angle of elevation 45° and azimuth 267°. 325

Figure C.5 Lunar Copernicus crater. 328

Figure D.1 Original radar image in Sudbury (1996) with 21 control points for geo-reference. Red crosses and numbers represent the control point.Yellow framed area is enlarged in Figure D.2. 332

Figure D.2 Original radar image without filtering. The area is indicated by yellow frame in Figure D.1. 333

Figure D.3 The radar image filterd by 7 x 7 Forest filter. The area corresponds to the region in Figure D.2. 334

Figure D.4 The Forest (7 x 7) filtered radar image in Sudbury with geographic correction. 336

Figure D.5 The filtered radarsat image overlain by the geological boundaries and seismic survey locations marked by the red triangles. 337

Table List

Table 2.1 Major tectonic events and rock units in the Sudbury area 23

Table 3.1 Seismic (P-wave) velocities of rocks in the Sudbury area 45

Table 4.1 Design parameters of the PRS1 recording system (After Asudeh et al., 1992) 62

Table 4.2 Refraction survey geometry, timing system and data recording instrument parameters (After Asudeh et al., 1992) 67

Table 6.1 Number of arrival time picks and uncertainties for line XY 144

Table 6.2 RMS traveltime residual and χ^2 in the inversion of the seismic refraction data of profile XY 154

Table 6.3 Model resolution of main parameters 165

Table 7.1 Number of phases picked for inversion 201

Table 7.2 Initial model parameters 202

Table 7.3 RMS traveltime residuals and χ^2 for fan shot data inversion modeling 205

Table 7.4 Results of inversion in the Northwest (quadrant 1) 221

Table 7.5 Results of inversion in the Northeast (quadrant 2) 223

Table 7.6 Results of inversion in the Southeast (quadrant 3) 226

Table 7.7 Results of inversion in the Southwest (quadrant 4) 228

Table 8.1 First arrival picking information for each shot 242

Table 8.2 RMS traveltime residuals of the modeling 243

Table D.1 UTM Coordinates of the control points (C.P.) and the corresponding pixel positions in the RADARSAT image 331

Table of Symbols and Abbreviations

Symbol	Definition and Explanation
ρ	density in the medium
$\boldsymbol{U}$	particle displacement vector
t	traveltime
∇	gradient operator
∂^2 / ∂^2	the second partial derivative operator
Σ	summation operator
F_k, F'_k	source signal functions, the derivatives of the F_k
f_k, g_k	a pair of Hilbert transform used in deriving a source signal function
$\int$	integration operator
$\boldsymbol{N}, \boldsymbol{M}, \boldsymbol{L}$	dynamic variables used in amplitude coefficient fundamental equations
λ	Lamé parameter
μ	shear modulus
τ	time function
U_k	amplitude coefficients of ray series
ξ	variable representing time or special coordinates (x, y, z)
t, n, b	unit tangent vector, unit normal vector and unit binormal vector respectively
P, S	P wave and S wave
τ, γ_1, γ_2	ray coordinates
J	Jacobian of the transforms from the Cartesian coordinate system into the ray coordinate system
f_M	primary frequency of a harmonious source signal carrier
$\gamma, \nu, t_0,$	parameters of the source time function
θ	phase angle
α, β	velocities for P wave and S wave respectively
$\boldsymbol{p}$	slowness vector
v	velocity
φ	angle between the positive x-axis and the line projected by a ray on the horizontal x-y plane which is in the range of 0 to 2π
δ	angle between the positive z-axis and a ray, which is in the range of 0 to π
$\boldsymbol{U}^{\perp}_k$	amplitude coefficients contributed by S wave
T	torsion of a ray curve
A	amplitude of source signal

M	a point at the coordinate of (x, y, z, τ)
$U_\xi(M)$	amplitude components along ζ axis
V	source parameter related to the velocity and density
g	source direction
Q	product of the coefficients of reflection or transmission reflectivity
q_ξ	appropriate ray transform coefficient
L	geometric expression which is related to J
$\Delta\chi$	distance between two points
$J_\perp$	equals to 1 for a line source, and $\|\chi\|$ for a point source
v_1, v_2, v_3, v_4	velocities at four corners of a trapezoid
s_1, b_1, s_2, b_2	parameters of line functions at the upper and lower interfaces with index 1 and 2 respectively
dz/dx	derivative of depth with respect to distance
v_x, v_z	partial derivatives of velocity with respect to distance and depth respectively
t_k	traveltimes recorded at the kth receiver at the surface
$l_{i,k}$	path lengths of a ray penetrating through the ith velocity node upward to the kth receiver
t	observed traveltime vector
t_0	calculated traveltime vector
M	true model parameter vector
M_0	calculated model parameter vector
A	partial derivative matrix including the elements of the partial derivatives of traveltimes with respect to model parameters
Δt	traveltime residual vector
ΔM	vector of the model parameter estimation adjustment
D	a damping parameter
C_t	variance diagonal matrix of the estimated data
C_m	variance diagonal matrix of the estimated model
σ_i, σ_j	estimated uncertainties of the ith traveltime measurement and a priori estimation of the uncertainty of the jth model parameter respectively
R	model resolution matrix
I	identity matrix
C	standard error matrix
χ^2	normalized chi-squared parameter
a_i, b_i, c_i, d_i	coefficients of the ith plane's equation
$x_{i,j}$, $y_{i,j}$, $z_{i,j}$	coordinates of intersection points on the ith interface; j equals to 1 for a down-going ray and 2 for an up-going ray
$r_{i,j}$	ray path between two intersected points
R	parameter indicating reflection wave and refraction wave

m	number of interfaces
$\varsigma_{m,i}$	coordinates x and y, i =1,2.
X	vector containing the intersected points' coordinates of a ray
c	computed traveltime
X^*	coordinate vector which is the specific point regarded as the origin of the coordinate system
b	downhill gradient of the traveltime
X^k	coordinate vector at kth iteration
P^k	local downhill gradient at kth iteration
λ^k	scalar minimizing the traveltime
β^k	conjugate coefficient at kth iteration
T_l	observed traveltime at the lth receiver
g^*	estimate of model parameters
t_l	computed traveltime on the basis of the estimated model
ΔT	traveltime residual vector
ΔG	model parameter adjustment vector
A'	partial derivative matrix with respect to the model parameters
$s(x, y, z)$	slowness as a function of (x, y, z)
t_i	traveltimes at the ith point
h	the grid spacing in each cube
r	a position vector
$u(r)$	slowness
$l[u(r)]$	the integral ray path
$\delta u(r)$	slowness perturbation
δt	traveltime residual
$m(r)$	model parameter function
$g_i(r)$	kernels of integration of the linear transformation equation in 3-D tomography
$h_j(r)$	basic function used in tomographic study
α_j	parameters in the jth cell
Γ_{ij}	integration of the products of basic function and kernels along the ray path
l_j	total lengths of the jth ray path
K	number of rays penetrating the neighboring cells around a grid point
$w_k(r)$	length of the portion of the kth ray
B_j	amplitude of a signal at the jth sample
s	s-units scales
b_{js}	increment of the signal amplitude over s-scaled time increment
σ^2_{fs}	sample variance
σ^2	variance for the whole population of the signal

$\sigma^2_{fs'}$	unbiased estimation of the variance
n_1	number of samples in a given window
$Var(b_s)$	variance over s-unit time scales
δt	time increments
H	Hurst exponent
X_s	logarithmic s-unit scales
Y_s	logarithmic variances
S	slope of X_s versus Y_s
E	Euclidean dimension
D_σ	variance fractal dimension
d	slope of the regression line of length versus scales
D_l	length fractal dimension

Abbreviations	**Definition and Explanation**
RAYINVR	Ray tracing inversion algorithm
3-D, 3D	three dimensions
GIS	Geographic Information System
Ga	one thousand megayears
VSP	vertical seismic profiling
ERS-1	Earth Resource Satellite launched by the European Space Agency
SAR	synthetic aperture radar
UTEM	University of Toronto EM system
C-HH	C-band HH polarized wave
GSC	Geological Survey of Canada
USGS	United States Geological Survey
PRS1	portable refraction seismograph type 1
PRS4	portable refraction seismograph type 4
GPS	global position system
GEOS	Geocentric Earth Orbiting Satellite
sps	samples per second
s	seconds
Pg	P wave traveling through the upper crust
Pn	P wave refracted at the Moho interface
Pc	P wave refracted at the interface between the upper and lower crust
PmP	P wave reflected at the Moho interface
PcP	P wave reflected at the interface between the upper and lower crust
Pr	a strong reflection coherent in a limited number of traces responsible for reflections off small-scale structural interfaces such as structural boundaries and faults with high reflectivity

SEGY	one of the data formats suggested by Society of Exploration Geophysicists
GLIMPCE	Great Lake International Multidisciplinary Program on Crustal Evolution
S/N	signal to noise ratio
GMT	Geographical Mapping Tools (a software package)
RMS	root mean square
VFD	variance fractal dimension
AGT	Abitibi-Grenville Transect (a Lithoprobe transect)
PCI	an image processing software
UTM	Universal Transverse Mercator projection

Chapter 1

Introduction

Over geological time, a large number of space objects have impacted terrestrial planets and created impact structures. The geological structure of Sudbury has two interpretations: one is an endogenic origin and the other is an exogenic meteorite impact origin. This chapter briefly outlines the Sudbury study area and the controversial issues associated with the origin of the Sudbury Structure. The chapter then describes the research objectives of this thesis. This research is aimed at providing important constraints for the geophysical parameters in the Sudbury area and obtaining a geophysical interpretation of the much debated Sudbury geological structure.

1.1 Study Area, Geological Background and Hypotheses

The Sudbury study area is located in south-central Ontario, Canada. The Sudbury Structure itself, approximately 60 km north of Lake Huron, is at the center of the study area and is the main target of this thesis research. The Sudbury Structure lies at the junction of three geological provinces in the Canadian Shield: the Archean Superior Province, Proterozoic Southern Province and Paleoproterozoic Grenville Province. The current Sudbury structure has a distorted elliptical shape with a NE-trend. The Sudbury Structure is "a collective term" (Giblin, 1984) which includes the Sudbury Basin filled

with young sedimentary rocks, the Sudbury Igneous Complex surrounding the basin, and brecciated basement rocks of the Superior and Southern provinces which surround the Sudbury Igneous Complex. The Levack Gneiss Complex is located to the north of the North Range of the Sudbury Igneous Complex.

The Sudbury Structure is a well-known tectonic feature not only because it hosts one of the world's largest Ni-Cu deposits, but also because it is a unique geological feature of enigmatic origin and evolutionary processes. A considerable amount of geological study spanning over one hundred years has shaped our understanding of the main features of the Sudbury geology such as the shape of the structure and the nature of mineral deposits. Despite the large amount of research conducted in the past, new problems and controversies have arisen due to the geological complexity of the structure. Generally, the central issues have been focused on three topics: (1) the origin of the Sudbury Structure; (2) the shape and origin of the Sudbury Igneous Complex; and (3) the formations of the Sudbury Breccia and Onaping Formation of the Whitewater series sediments in the Sudbury Basin overlying the Sudbury Igneous Complex (Giblin, 1984).

There are two main hypotheses for the formation of the Sudbury Structure: a) the structure has an endogenic origin; and b) the structure is a product of a meterorite impact event. The Sudbury geology is uniquely related to its regional setting in many aspects. For example, the Sudbury brecciation country rocks and mineral deposits have similar features to those of volcanic structures. These similarities convince many geoscientists of a volcanic site in Sudbury. Before the 1960's, the volcanic origin was dominantly believed by geoscientists. After the 1970's, a few scientists still proposed an internal volcanic origin for the Sudbury Structure. Card and Hutchinson (1972) suggested that the

mineral deposits in Sudbury were "generated during successive stages in the prolonged evolution of a major Proterozoic volcanic-sedimentary complex". Muir (1984) proposed an endogenic volcanic model, related to a mantle hot spot. Although most geological features of the structure can be explained by endogenic processes, the precise mechanism explaining the observed shocked metamorphic effects associated with these processes remains to be developed (French, 1990).

In 1964, Dietz first proposed that the Sudbury Structure may have evolved from a meteorite impact structure resulting from an event during the Precambrian. His proposal was based on the discovery of shatter cones, which challenged the early volcanic formation hypothesis. Shatter cones are small cones ranging from a few cm to 2 m long, formed on tensional release surfaces in rocks and are products of high-velocity impact shock metamorphism (Robertson and Grieve, 1975). Following the discovery of shatter cones, petrographic evidence of various shock metamorphic effects was presented by French (1967) which strengthened the meteorite impact hypothesis. From the 1970's to the 1990's, a number of detailed studies of the geology, geochemistry and geophysics of the Sudbury Igneous Complex and Onaping Formation favoring the meteorite impact origin of the Sudbury Structure were published (French, 1972; Morrison, 1984; Peredery and Morrison, 1984; Faggart and Basu, 1985; Grieve, 1990, Avermann, 1994, Deutsch, 1994; Boerner et al., 1994; Golightly, 1994; Ames et al., 1998, Avermann, 1999; Dickin et al., 1999). Although a vast amount of geological and geochemical evidence supports the meteorite impact hypothesis, further investigation of the deep structure is still needed to fully understand key issues related to the genesis of the Sudbury Structure and the true nature of the Sudbury Structure, Sudbury Igneous Complex and Onaping Formation.

1.2 Objectives of the Research

The past hundred years of Sudbury geological studies have focused on the investigation of the surface and near-surface features. The origin of the Sudbury Structure and its deformation history cannot be clearly understood without information on the 3-D geometry at greater depths. Geophysical methods can indirectly probe and reveal the physical characteristics of the Earth from the surface to great depths by providing images of crustal structure. They can give invaluable insights on the origin and nature of the Sudbury Structure, leading towards a full understanding of its structural evolution. In studies of crustal structures, the seismic method provides a higher resolution than other geophysical methods such as gravity, magnetics, magnetotelluric sounding and electromagnetics. Since the 1980's, high-resolution geophysical surveys have been carried out by Lithoprobe through regional transects in the Sudbury area. Sudbury seismic reflection data were collected during the Lithoprobe Abitibi-Grenville Transect seismic survey in 1990 to investigate in detail the shallow subsurface structures (Clowes, 1997).

Interpretations of high-resolution geophysical data from past studies, including seismic reflection and potential field surveys, explain the current non-circular shape of the Sudbury Structure. However, the detailed processes involved in the formation of the present-day Sudbury structure and the origin of the Sudbury Igneous Complex cannot be fully understood without knowledge of the 3-D crustal and upper mantle structures and the geological relationship between the Sudbury region and the adjacent areas. The volcanic formation hypothesis implies that there is a magma root zone or "feeding root"

deep in the crust and upper mantle. Alternatively, an impact structure has no "structural roots". Therefore, verification of whether there is a "feeding root" in the lower crust and upper mantle beneath the Sudbury Structure can constrain the origins of the Sudbury Structure, Sudbury Igneous Complex and Onaping Formation. Thus, a large-scale high-resolution seismic refraction experiment was planned and carried out during the 1992 Lithoprobe Abitibi-Grenville Transect seismic experiment in order to image the three-dimensional deep geometry of the crust and upper mantle in the vicinity of the Sudbury Structure (Clowes, 1989; Irving et al., 1993). Two approximately perpendicular profiles were designed over the structure: 1) profile AB extending approximately 265 km from northwest to southeast, traversing the Abitibi subprovince of the Superior Province, the Sudbury Structure, Grenville Front Tectonic Zone and the Britt Domain in the Grenville Province; and 2) profile XY extending approximately 165 km from southwest to northeast, crossing the Huronian Supergroup in the Southern Province and the Sudbury Structure. Receivers not only recorded signals from in-line shooting but also recorded signals from off-line shooting (or fan shooting).

In this thesis research, the primary research objective is to put geophysical constraints on the formation and nature of the Sudbury Structure, Sudbury Igneous Complex and Onaping Formation by processing, modeling and interpreting high-resolution seismic wide-angle reflection and refraction data from the 1992 Lithoprobe seismic experiment. To achieve this goal, the following five basic research objectives were established:

1. processing and modeling of in-line seismic reflection and refraction sections to explore the crustal and upper mantle velocity structures in the Sudbury region and adjacent areas;

2. developing a 3-D seismic ray-tracing forward modeling algorithm and applying the damped least-squares inversion technique to model the crustal structure using fan-shot data;
3. imaging the 3-D crustal velocity structure by using the 3-D weighted backprojection seismic tomographic method;
4. interpreting the seismic data by using supplementary information from results of gravity and aeromagnetic data, and discussing the evolution of the Sudbury Structure;
5. developing computer-based seismic phase detection techniques for distinguishing seismic phases from background noise.

This dissertation is ordered as follows:

Chapter 1 describes the geology of the study area. The controversial scientific issues identified in the history of its geological study are also briefly addressed. Finally, the objectives of this research are summarized.

Chapter 2 reviews the regional geological setting in the Sudbury area, tectonic history and the Sudbury Structure. It also discusses the hypotheses on the genesis and natures of the Sudbury Structure, Sudbury Igneous Complex and Onaping Formation in more detail. Models of the formation of the Sudbury Structure and Sudbury Igneous Complex are also described in this chapter.

Chapter 3 includes a review of previous geophysical studies which mainly includes modeling results and interpretations of seismic reflection data, gravity, magnetics, magnetotelluric sounding, electromagnetics, paleomagnetics, borehole, and remote sensing data in the study area. A seismic refraction study in the area adjacent to this study is also reviewed.

Chapter 4 includes an overview of the 1992 Lithoprobe high-resolution seismic wide-angle reflection and refraction experiment. It also describes the survey geometry, recording parameters and recording instruments.

Chapters 5 focuses on the Cerveny ray tracing forward modeling algorithm and modeling of the reflection and refraction seismic data along profile AB. It also briefly discusses the pre-processing of the high-resolution seismic refraction data by using the IT&A INSIGHT 5.1.1 seismic processing software package.

Chapter 6 includes the forward and inverse modeling results obtained using the RAYINVR ray tracing inversion algorithm provided by Zelt and Smith (1992) for modeling the seismic data along profile XY. The first section describes the method and the second describes the seismic velocity structure obtained along profile XY.

Chapter 7 discusses fan-shot data modeling, including the development of a ray tracing traveltime modeling algorithm on the basis of the Fletcher Reeves conjugate gradient method (Cai, 1982; Press et al., 1989) in multi-dimensional space. It includes a discussion of the velocity structure in the vicinity of the Sudbury Structure obtained using this modeling technique.

Chapter 8 outlines the application of the 3-D seismic tomographic technique to the Sudbury region after a description of the basic principle of the weighted back-projection seismic tomographic algorithm (Hole, 1992). 3-D seismic tomographic images modeled on the basis of first arrivals are discussed in order to provide valuable information on the velocity structure of the subsurface.

Chapter 9 synthesizes the results from the modeling and interpretation of the seismic reflection and refraction data. The geological model of the Sudbury Structure is

developed based on the interpretation of the 1992 Lithoprobe Abitibi-Grenville Transect seismic wide-angle reflection and refraction data. Considerations of the previous geological, geochemical and geophysical results on the evolution and deformation of the Sudbury Structure, Sudbury Igneous Complex and Onaping Formation are included with the seismic data to produce a modified geological model for the formation of the Sudbury Structure.

Chapter 10 contains the final summary, conclusions, and suggestions for future research.

There are four appendices in the thesis. Appendix A describes the variance fractal dimension trajectory technique for the detection of seismic phases from background noise in seismic data. Appendix B describes the length fractal dimension approach for distinguishing the first break from the high-resolution seismic reflection data. Appendix C briefly discusses the processing procedures applied to geophysical potential field data to define regional structure features. Appendix D includes the processing of the Sudbury radar image using Geographic Information System (GIS) software packages.

Chapter 2

Geology of the Sudbury Area and Hypotheses for the Origin of the Sudbury Structure

2.1 General Geology

The Sudbury study area is at the junction of three Precambrian geological provinces of the Canadian Shield: the Archean Superior Province, the Proterozoic Southern Province and the Proterozoic Grenville Province (Figure 2.1). On the basis of U-Pb dating of zircon collected from the Sudbury Igneous Complex the Sudbury Structure is believed to have formed at ~1.85 Ga (Krogh et al., 1984). As discussed in Chapter 1, the genesis and nature of the Sudbury Structure, Sudbury Igneous Complex and Onaping Formation have been studied and debated for more than one hundred years, partly because of the nickel deposits hosted in the Sudbury Structure, and the enigmatic and unique geological features. Although numerous authors have proposed various evidence in favor of a meteorite impact origin of the Sudbury Structure, there are still controversies about the origin and nature of the Sudbury Structure, Sudbury Igneous Complex and Onaping Formation.

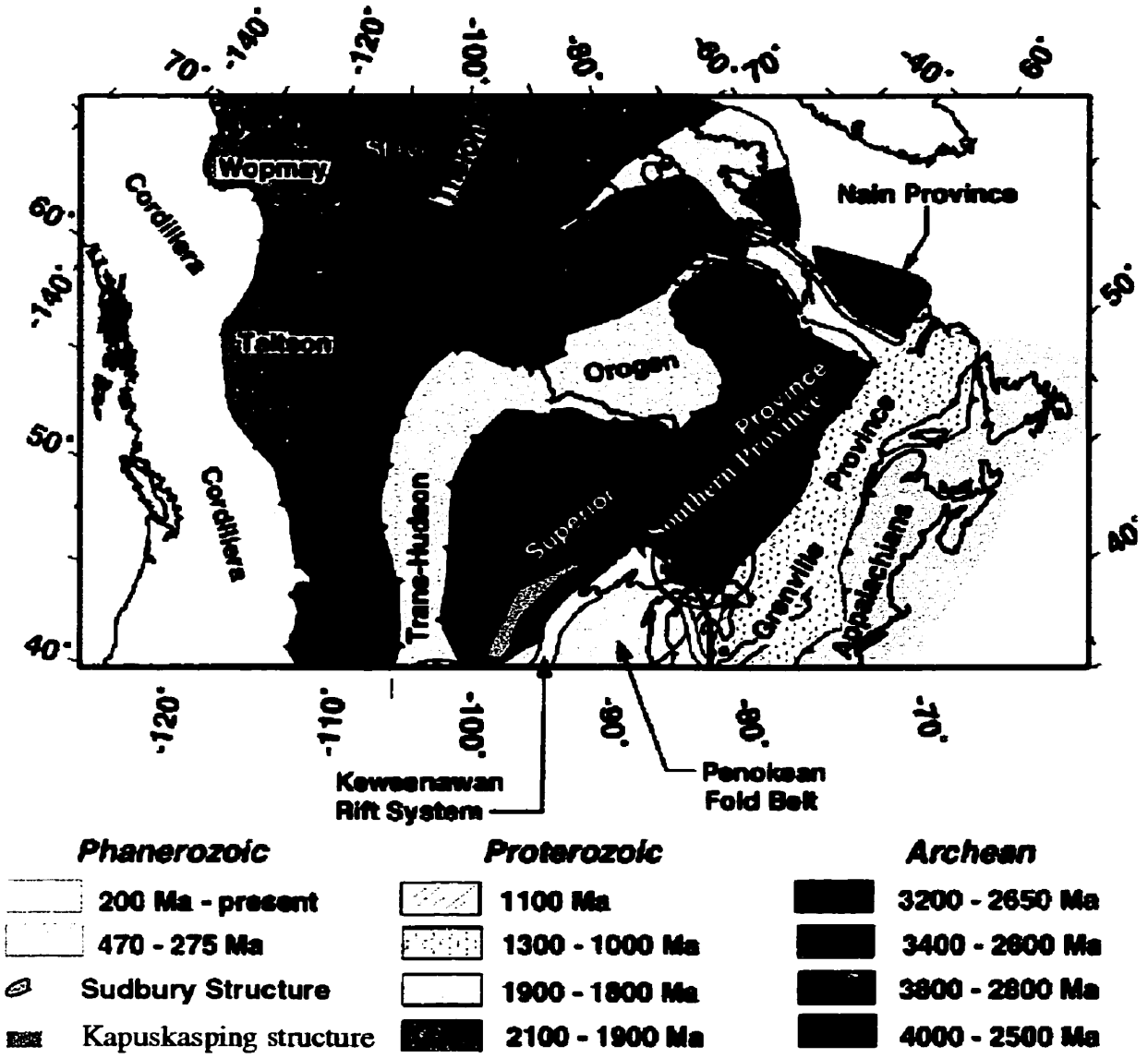

Figure 2.1 Location of the Sudbury Structure relative to the regional tectonic elements of North America (Modified from http://www.science.ubc.ca/~eoswr/slideshow/accounts/lithoprobe/slides/earth1.html) [accessed on June 10, 2000]. The Sudbury Structure is in the circled area.

2.1.1 Regional Geological Setting

1. Superior Province

The southern Abitibi subprovince of the Archean Superior Province, bordering the northern side of the Sudbury Structure (Figure 2.2), includes greenstone belts, metasedimentary belts, granitoid plutons and high-grade gneissic belts. The characteristic feature of the Abitibi subprovince is the alternation of belts of greenstone with granitoid intrusions and metasedimentary rocks (Card, 1990). Massive felsic plutons intruded tonalite, and amphibolite-granodiorite gneiss as well as metavolcanics north of Sudbury in the late Archean between 2.7-2.62 Ga (Card et al., 1984; Card, 1990; Meldrum et al., 1997). Immediately north of the Sudbury Igneous Complex, the Levack Gneiss Complex (2.71-2.65 Ga) is exposed on the surface in a 3-5 km wide belt and underlies the Sudbury Igneous Complex to constitute the basement of the northern half of the Sudbury Igneous Complex (Card et al., 1984; Krogh et al., 1984; Meldrum et al., 1997; Figure 2.2). The Cartier batholith (~2.64 Ga), one of the Algoman batholith bodies, which intruded north of the Levack Gneiss Complex, forms the northern footwall of the Sudbury Igneous Complex. The batholith is a result of crustal recycling, which commonly occurred in the early Archean. The northern margin of the Cartier batholith intruded the Benny Greenstone Belt. The western margin might "grade into other Algoman plutons" (although no critical evidence has been found) (Meldrum et al., 1997), whereas to the east, it underlies a Paleoproterozoic metasedimentary unit, the Cobalt Group of the Southern Province. Geochemical studies indicate that the Cartier batholith could have developed from a magma resulting from approximately 33% partial melting of the Levack Gneiss Complex (Meldrum et al., 1997).

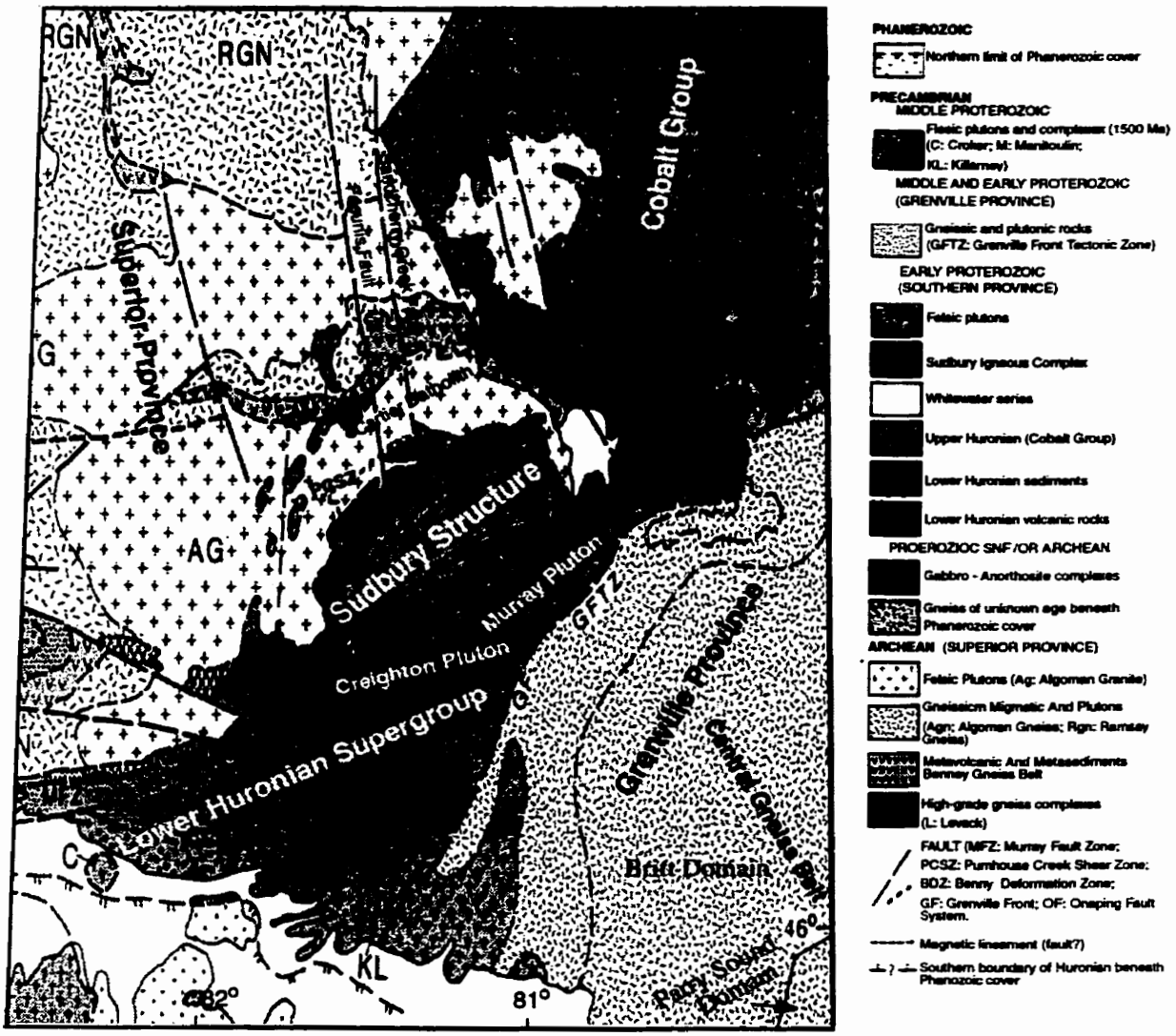

Figure 2.2 General geology map of the Subdury area (Modified from Card et al., 1984; Green et al., 1988; Ketchum et al., 1998; Meldrum et al., 1997).

Rocks of the Levack Gneiss Complex were metamorphosed from upper amphibolite to lower granulite facies during the Archean (Card et al., 1984). The Levack Gneiss Complex contains supercrustal and intrusive rocks such as migmatitic, tonalitic gneiss and paragneiss. The Cartier batholith contains high-grade gneiss and migmatitic units. Its rock-types are biotite monzogranite to granodiorite.

During the Paleoproterozoic (<2.5 Ga), Blezardian tectonism (2.47-2.422 Ga) activated the southern margin of the Abitibi subprovince which was a cratonic margin (Cowan et al., 1999); the sedimentary basin of the Southern Province developed on this margin (Cowan et al., 1999; Riller et al., 1999).

2. Southern Province

The Southern Province in Ontario is mainly a clastic wedge (the Huronian Supergroup), deposited on the flank of the southern margin of the Abitibi subprovince of the Superior craton. The Huronian Supergroup in the eastern part of the Southern Province south and east of the Sudbury Structure (Figure 2.1) was deposited between ~2.5 and 2.22 Ga in the tectonic fold belt produced by the eastern Penokean orogeny (1.89-1.83 Ga) (Bennett et al., 1991; Roscoe and Card, 1992; Riller et al., 1999); it dips and thickens toward the south. It uncomformably overlies the granitoid-greenstone basement of the Archean Superior Province. The Southern Province is characterized by two types of rock sequences, metasedimentary and metavolcanic rocks. The Huronian Supergroup includes the Elliot Lake, Hough Lake, Quirke Lake and Cobalt Groups in ascending chronological order. The Elliot Lake Group contains volcanic rocks (tholeiitic basalt-rhyolite) up to 5 km thick (Roscoe and Card, 1992). The Hough Lake and Quirke

Lake Groups overlying the Elliot Lake subsequent sediment, are characterized by megacyclic deposition sequences, comprised of a lower polymictic paraconglomerate unit, middle pelite-wacke units, and thick upper quartz-arenite units. The Cobalt Group, the uppermost group, is the thickest succession and the most extensive east of the Sudbury Igneous Complex (Figure 2.2), and consists of glaciogenic siltstone, and quartz, and hematite-rich sandstone (Roscoe and Card, 1992).

The elongated Creighton (~2.33 Ga) (U-Pb zircon; Frarey et al., 1982) and Murray (~2.39 Ga) (U-Pb zircon; Krogh et al., 1984) granitoid plutons are exposed along the northern margin of the Huronian Supergroup and contact the Sudbury Igneous Complex to the north (Figure 2.2). Remelted Creighton granite intruding into the South Range of the Sudbury Igneous Complex has been observed (Dressler, 1984). Therefore, the supergroup and Creighton and Murray granitoid plutons underlying the Sudbury Igneous Complex constitute the basement to the southern half of the Sudbury Igneous Complex. Nipissing diabases were intruded uniformly throughout the Sudbury area including the Archean basement and the Huronian Supergroup at about 2.22 Ga (Roscoe and Card, 1992). However, there is no evidence of any correlation between major tectonic events and Nipissing intrusions. The Creighton and Murray plutons contain plagioclase, perthitic microcline and minor biotite (Dressler, 1984). Nipissing intrusions comprise gabbro sills, dikes, and cone-sheets (Card and Pattison, 1973; Bennett et al.,1991).

3. Grenville Province

The Grenville orogeny (~1 Ga) (Krogh, 1994) truncated the Southern Province to the north and the boundary between the Grenville orogen and the Southern Province is the

Grenville Front. The Grenville orogenic belt, or Grenville Front Tectonic Zone, tends northeast-southwest and is approximately 30 km wide (Card et al., 1984). In Ontario, the Grenville Province is divided into the northwestern part of the Central Gneiss Belt and southeastern Central Metasedimentary Belt. The northwestern part of the Central Gneiss Belt mainly consists of the Britt and Parry Sound Domains (Figure 2.2). The parautochthonous Britt Domain underlies the Parry Sound Domain to the north. The Central Metasedimentary Belt will not be discussed in this study because it is outside of the study area. New Nd isotope data indicate that late Archean and Paleoproterozoic rocks occur up to 60 km south of the current Grenville Front (Bennett et al., 1991). Therefore, Bennett et al. (1991) suggested that the position of the Grenville Front could be relocated 60 km south.

The Grenville Province is characterized by plutonism, metamorphism and deformation (1.4-1.0 Ga) (Dressler, 1984). In the Parry Sound domain, laminated gneiss overlies metasediments (van Breeman et al., 1986). The lower unit of the Parry Sound domain contains a basal assemblage and mafic gneiss (Culshaw et al., 1994), whereas the upper unit contains amphibolite facies. The Britt Domain is dominated by the parautochthonous rocks containing mafic dikes and pre-Grenville metamorphism and intrusions (~1.6 Ga) (Ketchum et al., 1998). The Grenville Front Tectonic Zone is characterized by a mylonitized fault zone and amphibolite to granulite facies gneisses that show southeastward progressively stacked deformations from brittle to ductile (Green et al., 1988; Epili and Mereu, 1991; Bethune, 1997).

2.2 Sudbury Structure

The Sudbury Structure includes the Sudbury Igneous Complex, the Sudbury Basin (Figure 2.3), the Sublayer and Sudbury breccia country rocks surrounding the Sudbury Igneous Complex. The shape of the Sudbury Structure reflects the elliptical outline of the Sudbury Igneous Complex in plan view (Giblin, 1984). The Sudbury Igneous Complex is the main mass of the Sudbury Structure, overlying the Archean Superior and Proterozoic Southern provinces and forming the basement of the sedimentary Whitewater Group of

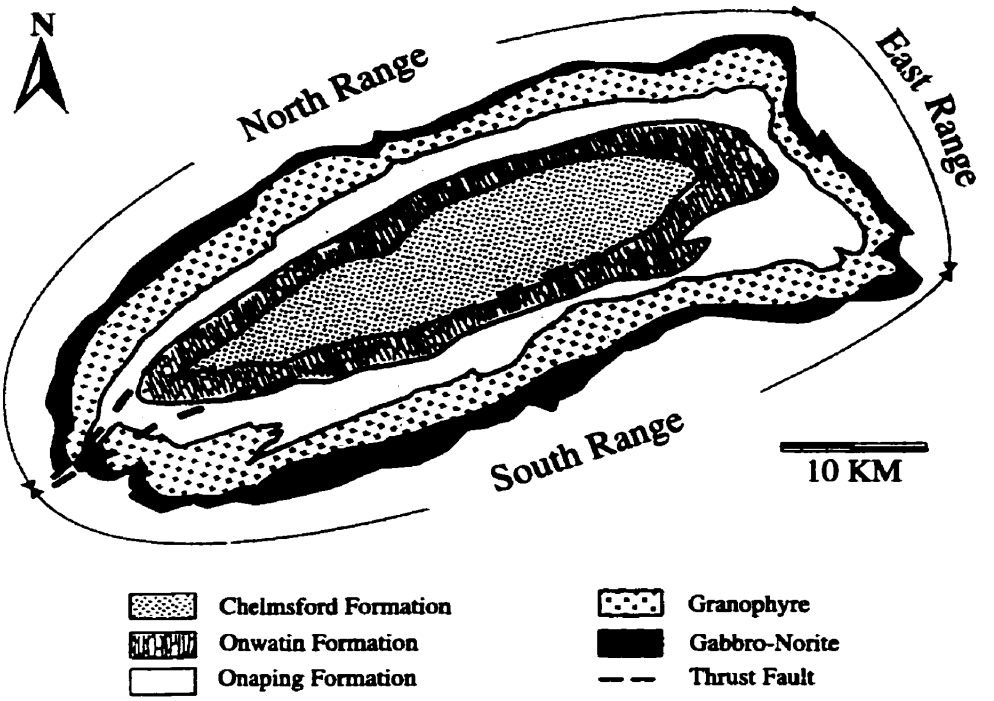

Figure 2.3 Simplified geological map of the Sudbury basin structure (After Miao, 1995).

the Sudbury Basin. The lithostratigraphic succession of the Whitewater Group comprises heterolithic breccias, mudstones, and wackes, corresponding to the Onaping, Onwatin and Chelmsford formations, respectively (Dressler, 1984).

2.2.1 Sudbury Igneous Complex

U-Pb dating of zircon and baddeleyite of North Range norite and South Range norite and granophyre suggests a 1.85 Ga age of the Sudbury Igneous Complex (Krogh et al., 1984). The Sudbury Igneous Complex has an elliptical shape with its long axis (~60 km) northwest-trending and its short axis (~27 km) northeast-trending (Figure 2.3). The Sudbury Igneous Complex mainly comprises norite, quartz gabbro and granophyre. The thickness of the norite is 2-5 km, the gabbro is 0.6-1.8 km thick and the granophyre is 0.6-3.5 km thick (Dressler et al., 1991; Naldrett and Hewins, 1984). Little is known about the deep structure of the Sudbury Igneous Complex from geological studies. However, high-resolution seismic reflection data have recently revealed the shallow subsurface structure. The seismic data indicate that the Sudbury Igneous Complex extends to ~12 km depth under the South Range. Seismic reflection data also reveal shallow south-dipping features beneath the North Range (corresponding to the lithologic units of the Sudbury Igneous Complex), whereas the lithologic units beneath the South Range are characterized by numerous, steep south-dipping reflections. The dipping reflections under the South Range were interpreted as a series of thrust faults (Milkereit et al., 1992; Wu et al., 1994), which indicates that the Sudbury Structure could have been shortened in the northwestern direction since its formation (Milkereit et al., 1992; Wu et al., 1994, 1995). Further reviews of this seismic study will be given in Chapter 3.

Lithologically, the Sudbury Igneous Complex is composed of three phases referred so as the lower, middle and upper layers (Figure 2.4). In the North Range, the lower layer contains felsic norite and mafic norite, containing medium to coarse grained plagioclase and hypersthene as cumulus phases (Dressler, 1984). The middle layer is a highly oxidized plagioclase augite-ulvospinel orthocumulate in the North Range. The upper layer contains coarse grained plagioclase. In the East Range, the rocks of the Sudbury Igneous Complex resemble those in the North Range. Rocks of the South Range are complex due to metamorphic overprint (Dressler et al., 1991). In the South Range, the lower layer contains norite and quartz-rich norite, mainly composed of coarse grained cumulus plagioclase and hypersthene, intercumulus titaniferous magnetite, and fine grained plagioclase (Dressler et al., 1991). The middle layer contains oxide-rich gabbro similar to that in the North Range. The gabbro grades into granophyre at the top of the layer (Naldrett, 1984). The granophyre of the upper layer was sheared in the South Range; otherwise, the petrography is similar to that in the North Range.

2.2.2 Whitewater Group of the Sudbury Basin

1. Onaping Formation

The Onaping Formation, the lowermost sedimentary unit of the Whitewater Group, has a thickness of ~1.6 km, forming the most voluminous sedimentary unit (Dressler et al., 1984). The Onaping Formation is divided into three major stratigraphic units (Figure 2.4): the Basal Member, Gray Member and Black Member. The discontinuous Basal Member may be up to hundreds of meters and is characterized by breccias, which were

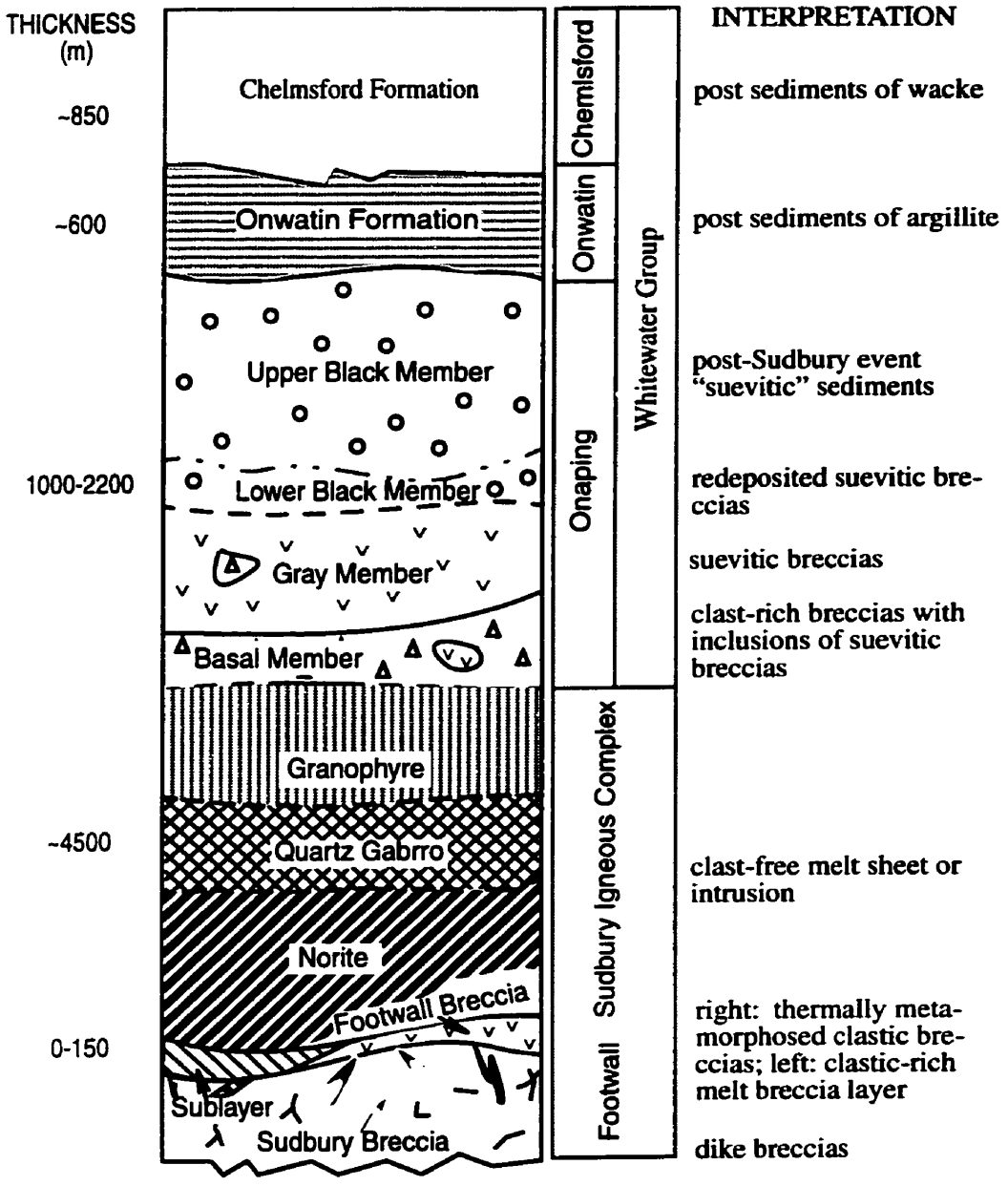

Figure 2.4 Schematic lithologic column of the Sudbury Structure (Modified from Deutsch, 1994; Naldrett and Hewins, 1984).

intruded by granophyre of the Sudbury Igneous Complex. These breccias contain the fragments of Archean country rocks, fragments of the Huronian country rocks, and recrystallized country rocks. The Basal Member gradationally or sharply contacts the underlying granophyre of the Sudbury Igneous Complex and sharply contacts the overlying Gray Member. The Gray Member overlies the Basal Member and is 0.2-0.7 km thick. The breccias generally contain country rock fragments, crystal fragments, recrystallized glass, and fluidal-textured materials (Dressler et al., 1991). The country rock fragments are characterized by rock types derived from granite, gneisses, and metavolcanic and metasedimentary rocks of the Archean Superior and Southern provinces. Some shock metamorphic features in quartz and plagioclase, as well as shock metamorphic glasses, were found in lithic and crystal fragments (Dressler et al., 1991). The Gray member gradually contacts the overlying Black Member. The Black Member, with a thickness from 0.8 to 1.2 km, is the major breccia unit in the Sudbury Basin. The composition of the breccias is similar to that of the Gray Member, including the shock metamorphic features. The Black Member has locally gradational contacts with the overlying Onwatin Formation.

2. Onwatin and Chelmsford Formations

The Onwatin Formation which is ~0.6 km thick has conforming-gradual contacts with the overlying Chelmsford Formation (Rousell, 1984) (Figure 2.4). Rocks of the Onwatin Formation mainly contain massive laminated siltstone to minor wacke (Dressler et al., 1991). Carbonaceous pyritic argillite and siltstone locally characterize the Onwatin Formation. The abundance of pelagic sediments demonstrates that it formed in oxygenic

bottom waters in a restricted basin. The lithological difference between the Onwatin and Onaping formations suggests that the source of the Onwatin sediments was outside of the basin and that it was not derived from the Onaping (Rousell, 1984).

The top unit of the Sudbury Basin is the Chelmsford Formation which is about 0.85 km thick (Rousell, 1984), but was originally thicker and more extensive. The formation comprises mostly wacke and siltstone. It was deposited rapidly from turbidity paleocurrents in a northwesterly trending, elongated trough with a source to the northwest of the Sudbury Basin (Rousell, 1984). No shock metamorphic features in quartz and feldspar have been observed in this formation. The southern contact of the Chelmsford with the Onwatin was unaffected by thrusting. This indicates that the Chelmsford sediment was deposited after the shortening deformation (Wu et al., 1995).

2.2.3 Breccias

The Footwall rocks of the Sudbury Igneous Complex contain Sudbury Breccia, Footwall Breccia and Sublayer which are directly related to the Sudbury Event, a large and violent release of energy. Sudbury Breccia can be described as pseudotachylytes (Dressler et al., 1991) or irregular bodies (Naldrett, 1984). Sudbury Breccia has been found ~50-80 km to the northeast of the Sudbury Igneous Complex, ~50 km to the southwest, and as far as the Grenville Front in the Huronian Supergroup (Müller-Mohr, 1992). There is a variation in the size of brecciation zones (Peredery et al., 1984), ranging from a few millimeters thick to a 0.5 by 11 km breccia zone exposed in the Huronian Supergroup (Dressler et a., 1991). The breccia bodies usually sharply contact the host rocks.

Footwall Breccia or granite breccia is most commonly in sharp contact with the lower part of the Sudbury Igneous Complex in the East and North Ranges as discontinuous lens and sheets (Dressler, 1984). Dressler (1984) also proposed that the Footwall Breccia originally contained a parautochthonous mass of shock-metamorphosed rocks. The Footwall Breccia grades into the Sudbury Breccia at depth.

Rocks of the Footwall Breccia are heterolithic and are mostly derived locally (granoblastic and granophyric textures). The Footwall Breccia is more commonly found in the upper than the lower crust as it is more abundant in the North Range than the South Range (Dressler et al., 1991).

The Sublayer is a thin, clastic-rich melt breccia layer (Figure 2.4), containing Ni-Cu deposits. It either directly contacts at the base of the Sudbury Igneous Complex or appears as offset dikes. The Sublayer is characterized by sulphide mineralization and a variety of inclusions derived from footwall rocks, and enigmatic mafic to ultramafic inclusions.

2.3 Tectonic History

The Sudbury Event happened ~1.85 Ga during the Penokean orogeny (1.89-1.83 Ga) (Table 2.1) on the border of the southern margin of the Abitibi subprovince of the Archean Superior craton and the Huronian Supergroup of the Southern Province. The Huronian Supergroup of the Southern Province was highly deformed during the eastern Penokean orogeny except for the Cobalt Group exposed northeast of the Sudbury Igneous Complex (Riller et al., 1999) (Figure 2.2). The eastern Penokean orogeny resulted in

Table 2.1 Major tectonic events and rock units in the Sudbury area

Tectonic Events	Rock Units	Ages (Ga)
Mesoproterozoic Grenville orogeny	Proterozoic gneissic rocks	1
Pre-Grenville metamorphism	Mafic dikes	1.6
Paleoproterozoic Deformation and metamorphism (late Penokean)		1.83
Sudbury event	Sudbury Igneous Complex Whitewater Group	1.85
Deformation and metamorphism (early Penokean)		1.89
Mafic magmatism	Nipissing diabase	2.22
Sedimentation, volcanism, magmatism	Huronian Supergroup dikes, granite gabbro-anorthosite intrusions, mafic-felsic volcanics	2.45 2.45-2.50
Archean Late deformation and plutonism	Metamorphism, Algoman granites	2.62
Early deformation and plutonism	Granodiorite-tonalite plutons	2.67-2.68
Volcanism and sedimentation	Abitibi belt greenstones	2.7-2.75

(After Card et al., 1984; Card, 1990; Krogh et al., 1984; Meldrum et al., 1997; Riller et al., 1999; Roscoe and Card, 1992).

steeply south-dipping reverse faults that thereafter dominated structural units in the southwestern Huronian Supergroup (Zolnai et al., 1984; Riller et al., 1999). The Murray fault in the Southern Province is a major crustal transverse fault zone in the eastern

Penokean orogen; it is characterized by dextral transpression and strike-shear which was overprinted on crustal architecture formed during a possible earlier (Blezardian) orogeny (~2.47-2.22 Ga) (Cowan et al., 1999; Riller et al., 1999).

During the Sudbury Event, the Sudbury Igneous Complex developed first but was overlain immediately by the Onaping Formation (Krogh et al., 1984). The Sudbury Igneous Complex intruded the Creighton (~2.3 Ga) and Murray (2.47 Ga) granitoid plutons in the South Range. The Onwatin sediment subsequently covered the Onaping Formation during the late regional deformation. Finally the Chelmsford group was deposited at the top of the basin in a northeast-southwest trend and was unaffected by the tectonism which caused the northwesterly shortening and produced the elliptical shape of the Sudbury Structure. The Southern Range Shear Zone (Figure 2.2) might have acted as a thrusting-glide interface and played a key role in the considerable deformation in Sudbury during the late Penokean orogeny (Shanks and Schwerdtner, 1991a; Riller and Schwerdtner, 1997).

There was no significant tectonism in the study area between the Penokean (1.89-1.83 Ga) and Grenville (~1 Ga) orogenies except for magmatism near the Grenville Front at ~1.75 Ga and 1.45 Ga (Riller et al., 1999). The age of the high-grade metamorphism (~1.04 Ga) in the Britt Domain marks the beginning of the Grenville orogenic tectonism (Riller et al., 1999). From 1.02 to 1.01 Ga, the Grenville Province underwent thermally-active extension. During the period of 1.01-0.98 Ga, thrust tectonism was reactivated and migrated northwesterly to the Grenville Front Tectonic Zone. The Grenville Front separating the Southern Province and the Grenville Front Tectonic Zone has been considered as the suture of the Grenville orogeny for years. However, it was suggested

that the tectonic suture between the Southern Province and the Grenville Province be moved to the south, ~60 km south of the Grenville Front (Dickin and McNutt, 1989) because rocks within the ~60 km wide zone adjacent to the Grenville Front in the southwestern Grenville Province are of Archean and Paleoproterozoic age. In the Southern Province and the Sudbury Structure, the Grenville orogeny only produced brittle deformation and thermal events superimposed on the earlier Penokean deformation belt (Stephan and Dalziel, 1974; Riller et al., 1999).

2.4 Hypotheses on the Origin of the Sudbury Structure

The origin of the Sudbury Structure had been modeled mainly as an endogenic volcanic process until the early 1960's. The discovery of shatter cones in Sudbury by Dietz (1964) introduced the possibility of an external cause of formation in the form of a meteorite impact. Since then, concepts of external and internal processes have been vigorously argued. Since 1964, more and more meteorite impact-related evidence in the Sudbury area has been reported, such as shock metamorphism, pseudotachylytes, impact diamonds and geochemical and geophysical evidence (French, 1972; Dressler, 1984; Faggart and Basu, 1985; Milkereit et al., 1992; Chubb et al., 1994; Thompson and Spray, 1994; Masaitis et al., 1999). Therefore, the impact origin of the Sudbury Structure has now been accepted by most geoscientists. Nevertheless, there are still important questions to be answered. Was the structure related to an impact-produced volcanic center, was the Sudbury Igneous Complex formed as a melt sheet or as a result of an igneous intrusion related to impact-induced volcanic activity, and was the Onaping Formation deposited as

a great fall-back breccia associated with the external impact process or by internal volcanic ash flow?

2.4.1 Hypothesis on Internal Volcanic Origin

Many geological features in Sudbury can be explained easily as products of endogenic activities (Muir, 1984). Some components of the Sudbury Structure are similar to features of endogenic structures such as the explosion breccia products (the Basal Member of the Onaping Formation), and the brecciated country rocks (the Footwall breccias).

1. Evidence and Arguments Against an Impact Formation

Essential arguments against an impact hypothesis focus on the spatial relationship between the Sudbury geological and regional setting, and differences between its geology and that of a typical impact crater. Card and Hutchinson (1972) proposed that the Sudbury Structure uniquely developed at the junction of three structural provinces of the Canadian Shield and argued that the structure could not therefore have been created by a random impact event. The Sudbury geology and mineral deposits in many aspects can be interpreted as a volcanic formation. For example, Ni-Cu sulfides formed from sulfide-facies iron formation from the Huronian rocks; Pb, Zn-Cu deposits can be interpreted as typical volcanic products (Card and Hutchinson, 1972). Stevenson and Stevenson (1980) cited the possible development of shock metamorphism and shatter cones in endogenic volcanic processes. Stevenson (1990) explained the Basal and Black Members of the

Onaping Formation as volcanic ash flow formations. A volatile-rich internal explosive basal eruption could produce shocked quartz (Loper and McGartney, 1988). However, the deformation in quartz produced by endogenic activities is not equivalent to that created by impact events (French, 1990).

2. Volcanic Model

Muir (1984) summarized eight endogenic models for the Sudbury Structure which were previously proposed by other authors, and from this he developed two basic endogenic models. One model was based on a deep crustal release of gas that rose to the surface to explode, and was followed by volcanism and post-volcanic plutonism (Figure 2.5). The model suggests that the structural area might have been located over a mantle hot spot. In the earlier stages (A_1 in Figure 2.5), diatreme-like processes occurred along several fractures; explosions happened near the surface and formed the elongated crater and cavity; shock metamorphic features and Sudbury and Footwall Breccias formed due to crashing. In the later stages (A_2 and A_3), the breccias of the Basal, Gray and Black Members of the Onaping Formation erupted which possibly triggered the intrusion of the Sudbury Igneous Complex. In the post-Sudbury event (A_4), volcanism waned and infilling of the basin was dominated by sedimentation; the Onwatin Formation was deposited as fine volcanic detritus and mud filled up the internal lake; the basin was subsiding and the Chelmsford Formation (turbidites) formed from material slumping off basin sides. The Sudbury Igneous Complex finally formed during multi-phase intrusions with deformation, however, the timing is unknown. The second basic model proposed by Muir (1984) involved initial volcanic intrusions, regarded as "a precursor to the pre-

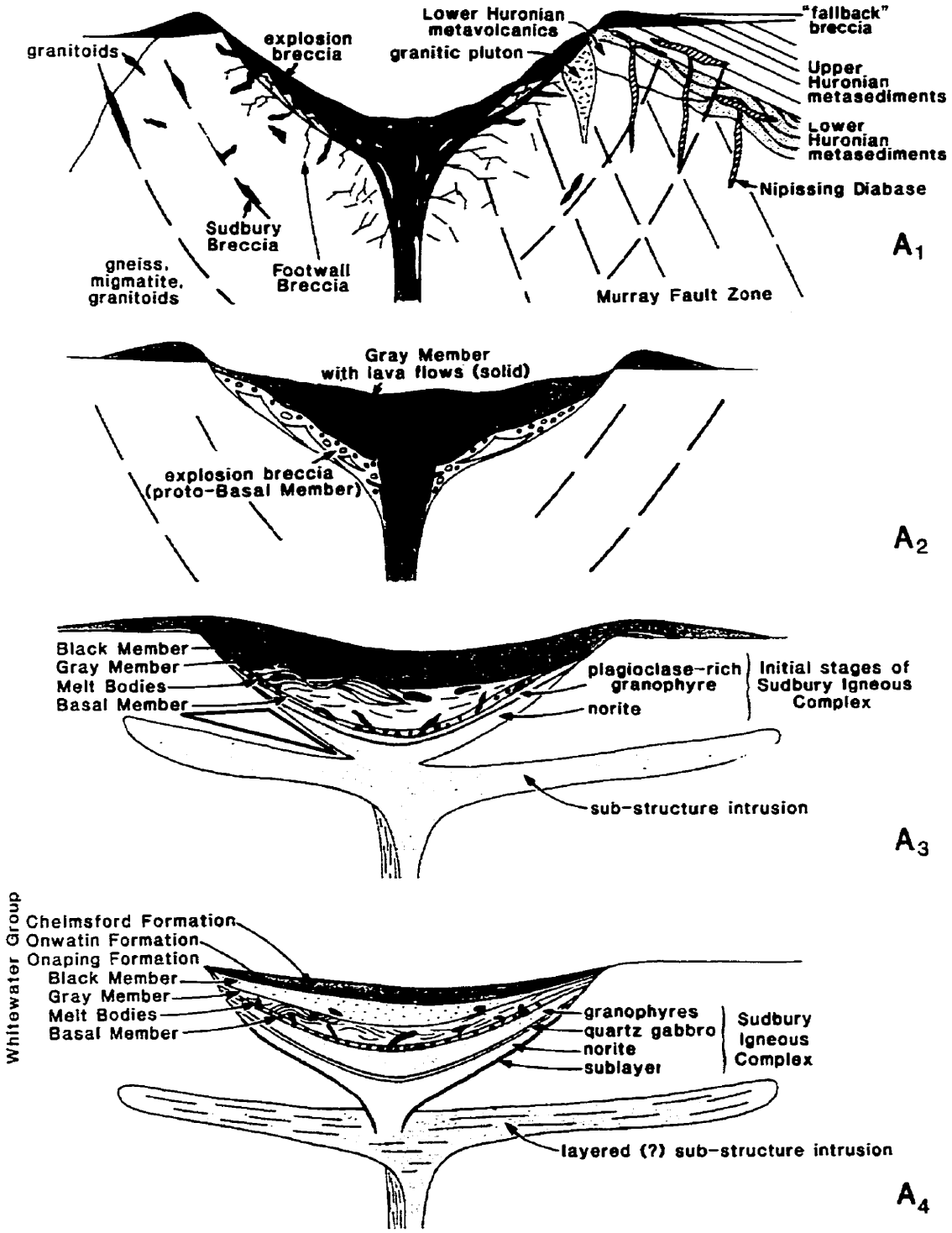

Figure 2.5 Development sequence of an endogenic model proposed by Muir (1984). A_1: earlier stage; A_2 and A_3: later stages; A_4: post-Sudbury event stage (see the text for details).

Onaping formation", followed by a large extent of explosive brecciation. Large volcanic eruptions and plutonism then occurred in the final stage.

2.4.2 Hypothesis on Meteorite Impact Origin

The large number of planetary and terrestrial impact craters indicates that impact events are a common phenomenon on many planets (Grieve, 1992). During the Proterozoic era, there was a special circumstance that resulted in an increased cratering rate on Earth because "a massive star or a molecular cloud stripped the outer part of the Oort comet cloud" (Shoemaker, 1998). Therefore, a meteorite impact event during the Proterozoic could be regarded as a possible episode in the geological history in Sudbury.

1. Evidence and Arguments for an Impact Structure

There are many indicators as well as evidence that can be used to identify terrestrial impact craters and structures such as shatter cones. Shatter cones are small cones ranging in size from a few cm to 2 m long, formed on tensional release surfaces in rocks. They are products of high-velocity shock metamorphism (Robertson and Grieve, 1975). In general, shatter cones are abundant around an impact structure. Shocked planar deformation features in quartz are also an important indicator for meteorite impact events. Although deformation features in quartz, such as quartz lamellae, have also been documented in volcano-induced structures (Stevenson and Stevenson, 1980), the specific orientation feature of quartz lamellae parallel to a certain crystallographic plane has only been observed at exogenic sites and not at volcanoes (French, 1990). Therefore, abundant

shatter cones and planar deformation features in quartz are two critically important products of meteorite impact events.

Generally, pseudotachylyte produced in endogenic tectonic or volcanic structures is less than 2 m wide because less energy is produced during an explosion than a hyper-velocity shock wave (Spray and Thompson, 1995). In contrast, a shock wave induced by a large meteorite impactor could produce a pseudotachylyte deformation zone up to 100 m wide. Therefore, wide pseudotachylyte zones (>2 m) which were observed in Sudbury could be considered as a supplementary indicator for distinguishing impact structures from endogenic volcanic sites.

Since the abundant shatter cones and shocked planar deformation features were discovered in Sudbury in the 1960's and 1970's, other geological, geochemical and geophysical indicators that favor an impact origin have been steadily documented (Morrison, 1984; Faggart and Basu, 1985; Grieve et al., 1991; Walker et al., 1991; Milkereit et al., 1992; Thompson and Spray, 1994; Becker et al., 1996; Dickin et al., 1999; Masaitis et al; 1999). The components of the rocks of the Sudbury Igneous Complex were derived from ancient crust and partial melt according to Sm-Nd isotope dating of whole rocks and minerals of the Sudbury Igneous Complex (Faggart and Basu, 1985). Other isotopic data such as Rb-Sr and Re-Os also support the derivation of the Sudbury Igneous Complex from impact melt (Walker et al., 1991; Deutsch, 1994; Dickin et al., 1999). Consideration of the crater melt volume and ore genesis (Grieve et al., 1991; Golightly, 1992) further support an exogenic origin of the Sudbury Structure. Recently, observation of helium trapped in fullerences in Sudbury indirectly supports the extraterrestrial formation of the Sudbury Structure (Becker et al., 1996). Six diamonds

discovered from two samples of the Black Member of the Onaping Formation show similar microstructural characteristics to other impact diamonds (Masaitis et al., 1999). Multi-ring pseudotachylyte zones were observed north, east and west of the Sudbury Igneous Complex by Chubb et al. (1994), Thompson and Spray (1994, 1996) and Spray and Thompson (1995). Some zones are over 100 m wide, and could be produced only by exogenic-induced processes and not an endogenic mechanism (Spray and Thompson, 1995). Furthermore, the approximately multi-ring distribution of pseudotachylyte suggests that the Sudbury Structure might be the remnant of a large multi-ring impact crater (Spray and Thompson, 1995).

The original shape of an impact crater is normally circular or nearly circular. The current elliptical shape of the Sudbury Structure has been questioned by opponents of impact origin since it was first proposed in 1964. Lowman (1991) suggested that the shape of the Sudbury Structure could have been originally elliptical, and formed by a very low-angle impact; he based his proposal on the lower degree of deformation in the North Range.

Recently, high-resolution seismic reflection data have revealed a northwesterly subsurface thrust zone with multiple thrust faults under the Sudbury Basin (Milkereit et al., 1992; Wu et al., 1994) which terminate at the base of the Onwatin Formation (Wu et al., 1995). The seismic data provide strong evidence at depth that the Sudbury Structure experienced intensive thrust deformation directed in the northwest after the fall-back breccia formation (Onaping Formation), but before deposition of the Onwatin and Chelmsford Formations. Therefore, deformation produced by northwesterly thrust shortening is one possible solution for the non-circular shape of the Sudbury Structure.

An original circular or nearly circular shape of the Sudbury Structure was also studied by an analysis of a correlation of strain to magnetic susceptibility, a finite-element analysis of the geological structure, and decomposition analysis of geophysical potential field data (Hirt et al., 1993; Shanks and Schwerdtner, 1991b; Roest and Pilkington, 1994). The results from all these studies support the initially circular shape origin.

As a great deal of geological, geochemical and geophysical evidence and indicators support an exogenic formation of the Sudbury Structure, its meteorite impact origin is favored by most scientists. Nevertheless, important questions such as whether the Sudbury Igneous Complex was formed by an impact melt sheet or igneous intrusion, and whether the Onaping Formation was formed as a huge blanket of fall-back breccia generated by a giant meteorite impact event or was a magmatic-related product, and how the original size of the Sudbury Structure is, still remain to be answered (Faggart and Basu, 1985; Grieve et al., 1991; Walker et al., 1991; Avermann and Brockmayer, 1992; Avermann, 1994; Norman, 1994; Corfu and Lightfoot, 1996; Lightfoot et al., 1997; Riller and Schwerdtner, 1997, 1999; Ames et al., 1998; Dressler and Sharpton, 1999). If the Sudbury Igneous Complex and Onaping Formation rocks were produced by an internal magmatic event, then the magmas were probably derived from the lower crust or mantle; evidence of magma in the form of a mafic root zone or a "feeding root" should exist at depth in the crustal rocks beneath the Sudbury Igneous Complex. Progress in the debate on the origin of the Sudbury Igneous Complex and Onaping Formation can be made by using geophysical data to image and evaluate the subsurface geological structure under the Sudbury Basin.

2. Impact Model

Meteorite impact models have been discussed by several authors. Peredery and Morrison, (1984) proposed an impact model that included a magmatic origin of the Sudbury Igneous Complex, impact formation of the Onaping sediment, and central uplift in the deep crust beneath the Sudbury Structure. Grieve (1994) developed a Sudbury impact model with a ~200 km original crater diameter estimated by an analysis of the volume of the impact melt sheet (Figure 2.6). In Grieve's model, the original crater, Sudbury Igneous Complex and Onaping Formation were developed in minutes immediately after a meteorite struck Sudbury during the time of the Penokean orogeny (a, b, c and d in Figure 2.6). The Onaping Formation was formed as a Fall-back debris (e and f in Figure 2.6). The Onaping Formation was highly deformed by northwesterly shortening in the South Range soon after deposition, whereas most of the Sudbury Igneous Complex remained almost undeformed because of incomplete consolidation due to slow cooling. Profile g indicates the present deformed structure. Finally, the Sudbury Structure experienced erosion during the Penokean and Grenville orogenies.

Generally, estimation of the horizontal dimension of the Sudbury impact model is difficult, because of deformation and erosional modification of the structure. Nevertheless, estimates of model dimensions have been made by using current knowledge of various kinds of impact evidence obtained from geological, geochemical and geophysical studies (Grieve et al., 1991; Shanks and Schwerdtner, 1991b; Hirt et al., 1993; Deutsch, 1994; Rondot, 1994, Stöffler et al., 1994). Stöffler et al. (1994) estimated the original diameter of the impact crater at approximately 220 km which is similar to that given by Grieve (1992) (~200 km). The total volume of the impact-produced melt sheet

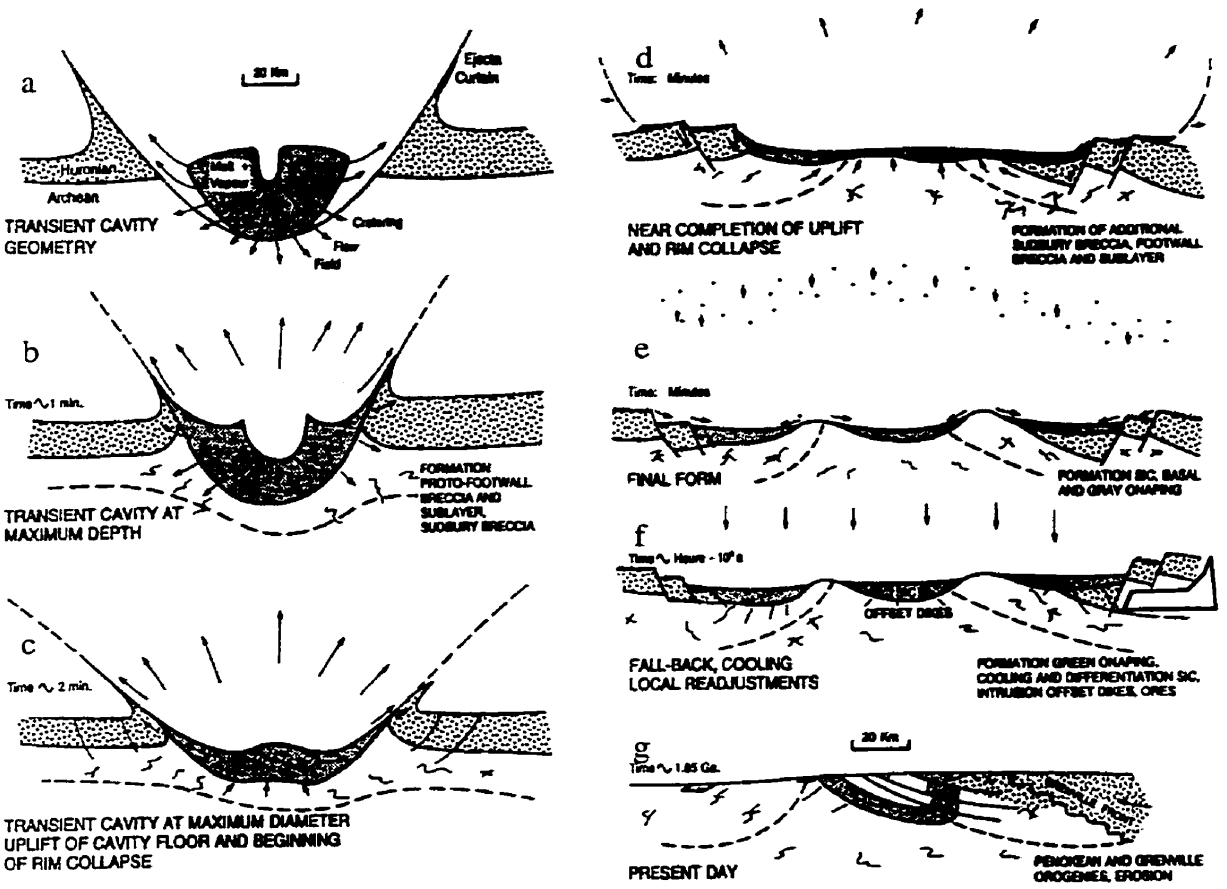

Figure 2.6 Development sequence of the exogenic meteorite impact model proposed by Grieve (1992). a, b, c and d represent the formation of the original crater and the Sudbury Igneous Complex in minutes after a meteorite stuck Sudbury. e and f indicate the Formation of the Onaping Formation as a fall-back debris. g represents the current deformed structure.

(Sudbury Igneous Complex) was given as 12,500 km^3. Furthermore, the depth of the transient cavity, the maximum depth of excavation, and the maximum depth of melting were estimated as 28-37 km, 15-21 km and 25-35 km, respectively by Stöffler et al. (1994). They suggested that the Sudbury Structure was generated by a large meteorite impact with a total energy of $8.6x10^{23}$ J and the diameter of the projectile was 14 km with a density of 3 g/cm^3. In 1999, Dressler and Sharpton summarized the size of the rim diameter in Sudbury estimated by previous researchers. The rim diameter is defined as the diameter of the furthest border from the center of a crater. The elevation of the rim is higher than the surrounding area. The size of the diameter of the Sudbury crater is in a range of 150-280 km. Assessment of the vertical dimension is usually more difficult than estimation of the horizontal dimension because of limited constraints at depth. Therefore, the estimation of depth of the crater is approximate. The vertical dimension of the Sudbury model was discussed by Shanks and Schwerdtner (1991b) and Rondot (1994). Shanks and Schwerdtner (1991b) used finite-element modeling of the structural geometry to reconstruct the original crater depth which was inferred to have been < 20 km by an analysis of the relationship between the crater depth and metamorphic grade. On the basis of a similarity to the Ries crater model, Rondat (1994) estimated the size of the Sudbury Structure as 154 km in diameter, and then deduced a crater depth of 15.4 km by using an empirical linear relation between depth and diameter (which is that the depth equals the product of 0.1 and the crater diameter). Dressler and Sharpton (1999) estimated that a ~15 km of erosion had taken place since the Sudbury impact (at ~1.85 Ga as obtained from paleomagnetic data).

Chapter 3

Review of Previous Geophysical Studies

There have been a large number of geophysical surveys carried out in the Sudbury and surrounding areas, including many small-scale geophysical surveys conducted by exploration industries. The thesis research focused on the regional geological structure and therefore only the large-scale previous geophysical studies in the Sudbury area are reviewed here. Specifically, it discusses the high-quality geophysical data and modeling results obtained in the early 1990's (such as the regional and high-resolution seismic experiments, including reflection and refraction surveys, potential field data, EM data and remote sensing satellite data).

3.1 Seismic Studies

Previous seismic studies in Sudbury involved seismic reflection and refraction approaches as basic methods in the investigation of crustal structure, as well as borehole logging and vertical seismic profiling (VSP) methods. The following three sections describe the results obtained from those methods.

3.1.1 Seismic Reflection

In 1985, a high-resolution seismic reflection experiment was conducted in the North Range in the Sudbury Basin to test the seismic imaging technique in mapping the deep nickel-mineralized zones (Moon et al., 1990). Since 1990, a large number of high-resolution seismic surveys have been carried out by Lithoprobe. A total of six seismic reflection profiles (lines 1, 40, 41, 42, 43 and 44) were surveyed in the Sudbury basin area by Lithoprobe, in co-operation with industry and the Ontario provincial government, to delineate the three-dimensional geometry (Figure 3.1). Five profiles crossed the Sudbury Basin and line 42 extended from the north-western boundary of the Sudbury Igneous Complex to the north to investigate the Levack Gneiss Complex and the northern half of the basement of the Sudbury Igneous Complex.

The subsurface geometry beneath the Sudbury Structure was first clearly revealed by high-resolution seismic reflection data along lines 40 and 41 (Milkereit et al., 1992) (Figure 3.2). A series of south-dipping reflections imaged under the Sudbury Basin were interpreted as northwest-southeast thrust faults (Milkereit et al., 1992, 1994; Wu et al., 1994), and implied that considerable shortening had occurred after formation of the Sudbury Structure. The current non-circular shape of the structure was interpreted as a result of such thrust deformation.

In 1994, Wu et al. reprocessed lines 40 and 41 using an advanced pseudo-3D processing strategy, including careful first break muting, refraction and surface consistent residual static corrections, and phase shift migration. The enhanced images obtained from the reprocessed seismic reflection data indicate that a previously unrecognized imbricated

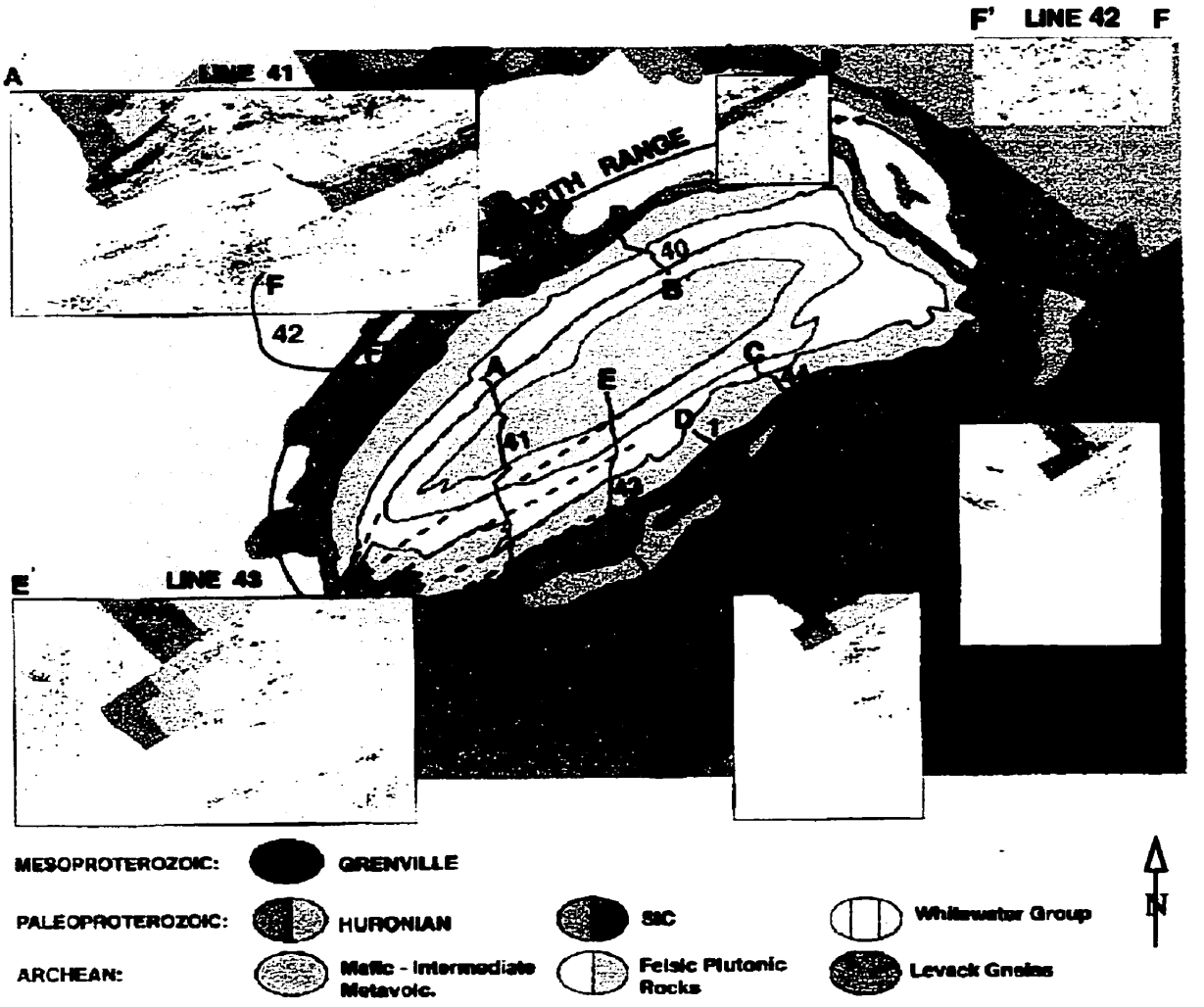

Figure 3.1 Locations of the seismic reflection profiles and sample images (Modified from Clowes, 1997).

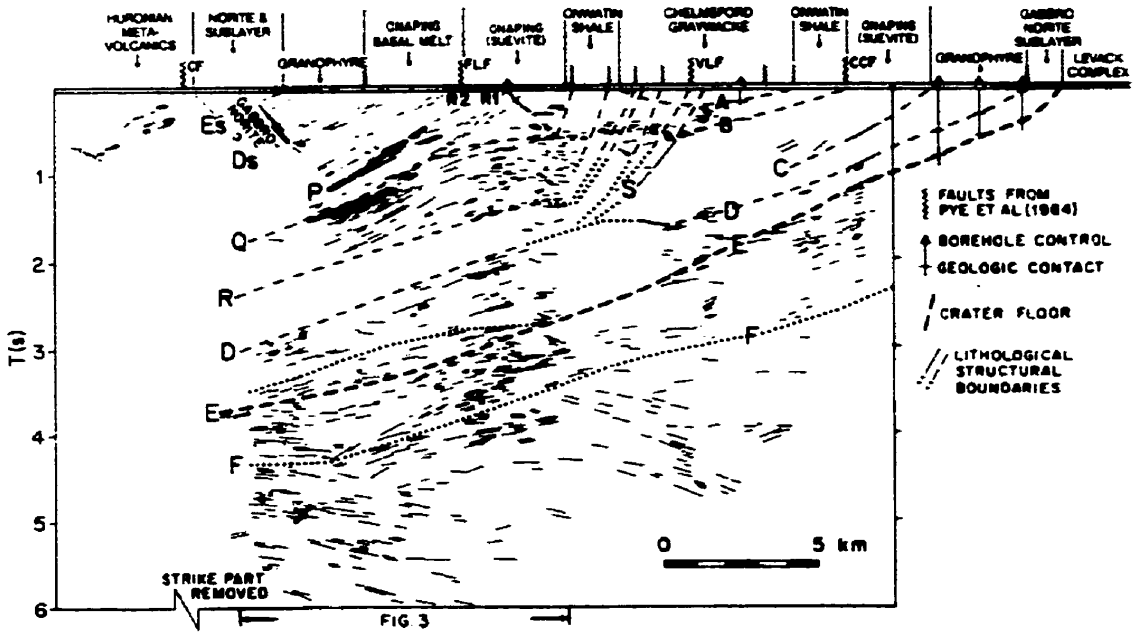

Figure 3.2 Migrated seismic image of line 41. A, B, C, D, E, F, Q, P, R, S, Es and Ds are seismc reflectors. CF: Creighton Fault; FLF: Fairbank Lake Fault; VLF: Vermilion Lake Fault; CCF: Cameron Creek Fault (After Milkereit et al., 1992).

northwest-dipping thrust fault zone penetrates into the base of the Onwatin argilite under the Sudbury Basin (Wu et al., 1995) (Figure 3.3). The imbricated northwestern thrust features provided an important timing constraint for the deformation event. The thrust features also implied that the overlying Chelmsford turbidites were deposited in a southwest paleoslope oriented parallel to the basin axis and have not undergone intensive deformation (Wu et al., 1995).

Line 42 was designed to examine the nature of the Levack Gneiss Complex and the contact relationship between the gneiss and granite intrusion (Moon and Miao, 1997). The reprocessed image for line 42 indicated that the interface between the Levack Gneiss

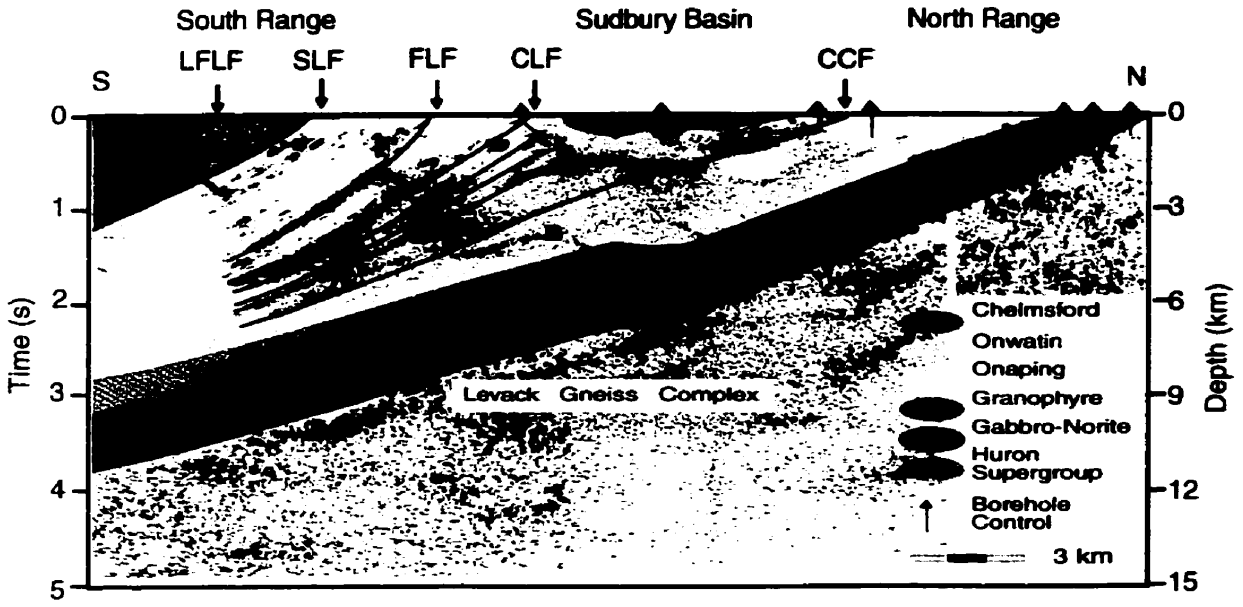

Figure 3.3 Seismic reflection image and geological interpretation of reprocessed seismic data. LFLF: Little Fairbank Lake Fault; SLF: Skill Lake Fault; FLF: Fairbank Lake Fault; CLF: Cameron Lake Fault; CCF: Cameron Creek Fault. (After Wu. et al., 1995)

Complex and the Cartier granite corresponds to an eastward-dipping event in the in-line direction (Miao, 1995; Moon and Miao, 1997). This feature is marked AA' on the reprocessed image (Figure 3.4). The Pumphouse creek fault was imaged and marked as event R_1 (Figure 3.4). Three previously unknown southeast-dipping reflection events, marked by R_2, 1 and 2 on Figure 3.4, were detected. The R_2 event was interpreted as a shear zone by Miao (1995) and Moon and Miao (1997). The surface position of the R_2 event corresponds to the outer limit of the first major pseudotachylyte-abundant zone ~11 km north of the Sudbury Igneous Complex, documented by Thompson and Spray (1994). However, the relationship between the R_2 event and the pseudotachylyte abundant zone, and the interpretation of the subsurface-dipping events 1 and 2, need to be investigated further by

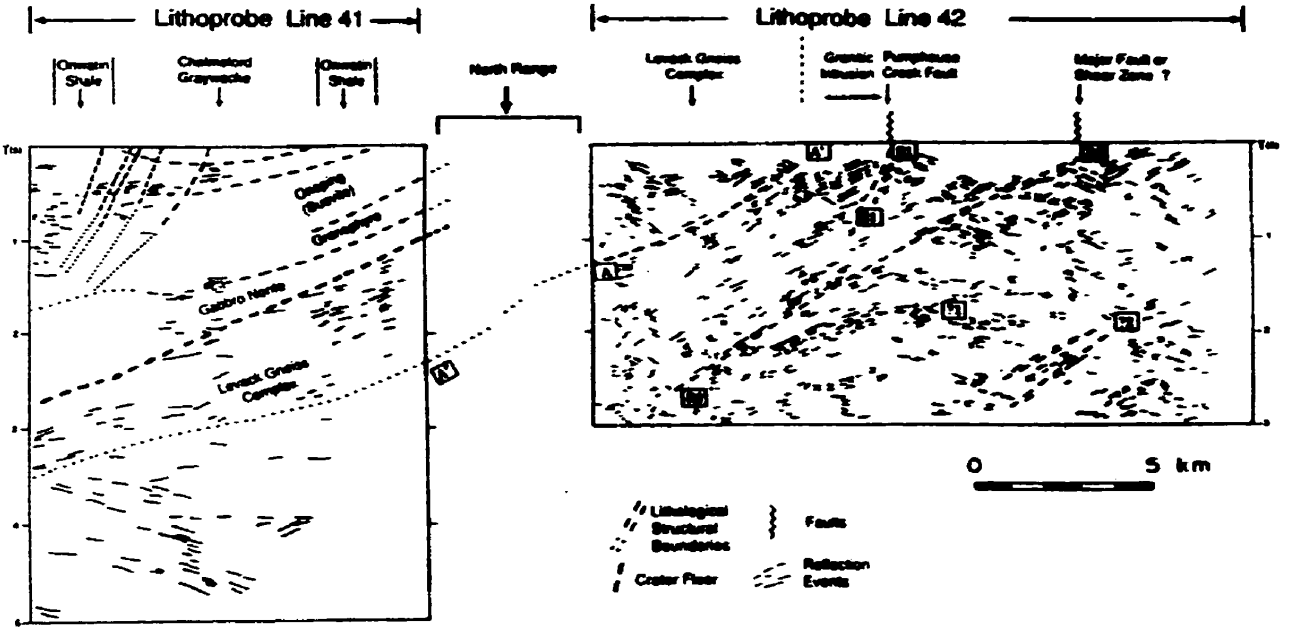

Figure 3.4 Seismic images of lines 42 and 41. AA', R_1R_1', R_2R_2', 1 and 2 are reflection interfaces revealed on line 42 (After Miao, 1995).

both geological and geophysical methods.

Seismic data along lines 1, 43 and 44 all indicated southeastward-dipping events which were interpreted as thrust faults (Milkereit et al., 1996; Clowes, 1997) and correlated with those revealed by seismic images along lines 40 and 41 (Figure 3.1). On the basis of the series of seismic images, an asymmetric 3-D geometry of the Sudbury Basin was inferred. The characteristics of the fault zone thrusting into the bottom of the Onwatin Formation suggested that the deformation in the Sudbury Structure occurred at the early stage of the Onwatin deposition (Wu et al., 1995). Consequently, seismic reflection data provided a critical interpretation of the current elliptical shape of the Sudbury Igneous Complex, i.e., that it resulted from northwest-southeast compression during the Penokean

orogeny.

3.1.2 Seismic Refraction

A high-resolution wide-angle reflection and refraction seismic survey in Sudbury was carried out during the 1992 Lithoprobe Abitibi-Grenville Transect seismic experiment. Two profiles, AB and XY, were surveyed. Miao (1995) first processed the data and developed preliminary models but did not investigate further. 2-D tomographic images along two profiles were provided by Winardhi and Mereu (1997) (Figure 3.5). However, geological structural interfaces could not be investigated by the 2-D tomographic technique. A detailed review of the previous seismic refraction studies is given in Chapter 5.

3.1.3 Borehole and VSP

Two borehole well logs were recorded in the upper layer of the Sudbury Igneous Complex containing granophyre in the North Range; these data were interpreted by Milkereit et al. (1994) and White et al. (1994b). The borehole penetrated from granophyre to the transition zone of quartz gabbro and ended in the Footwall breccia rocks. Not only were compression-wave (p) and shear-wave (s) velocities recorded but also density, Poisson's ratio and the gamma ray response (Figure 3.6a and 3.6b). Two significant reflective contacts were sharply indicated on the logging records. One reflection was of the contact between the granophyre (~5.9 to 6.0 km/s) and the transition zone of a high density layer of quartz Ti-Fe oxide-rich gabbro and norite (~6.3 km/s). The other reflector corresponds to the contact between the norite of the Sudbury Igneous Complex, and Footwall rocks

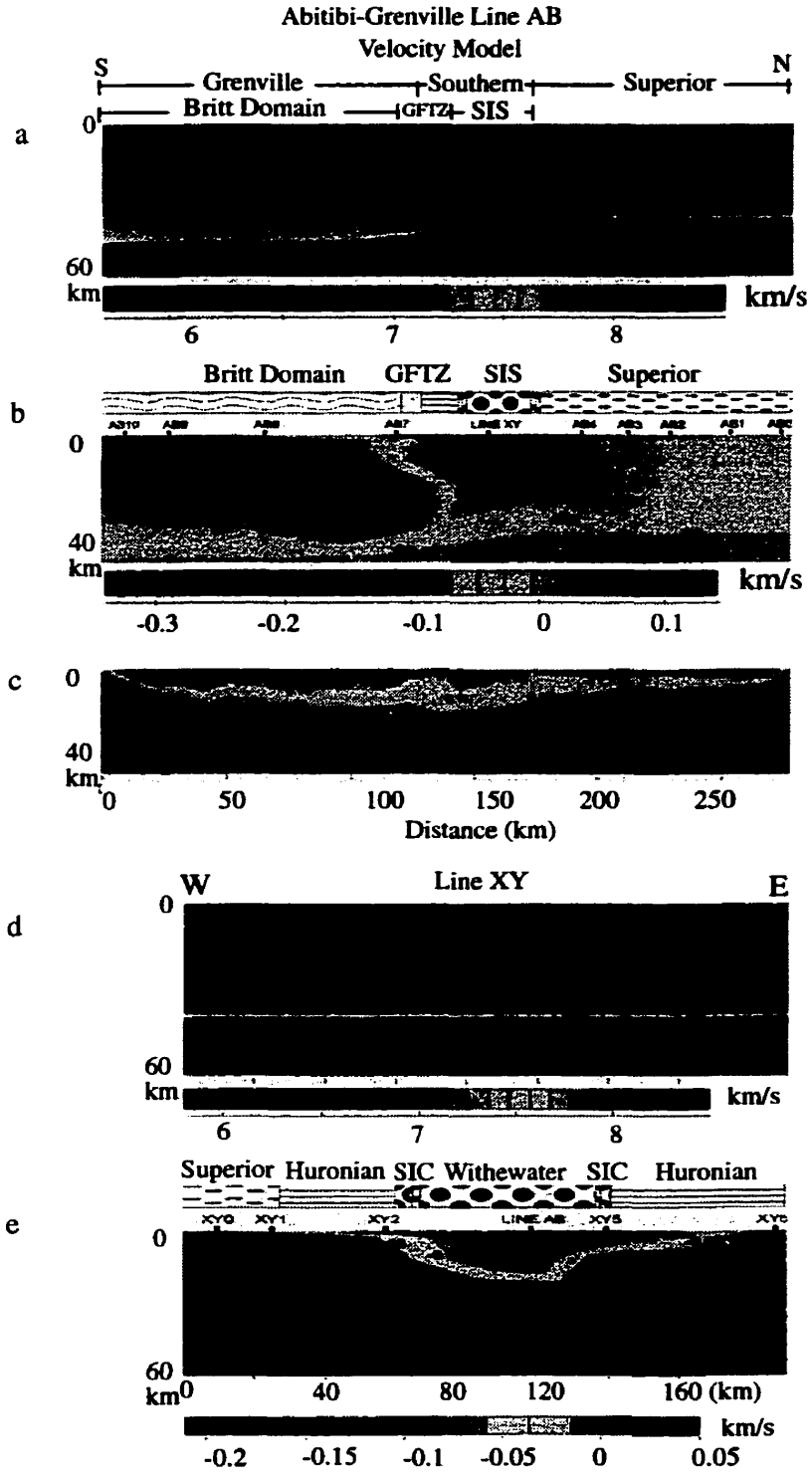

Figure 3.5 2-D tomographic velocity model. a: final velocity model of line AB; b: velocity anomaly of line AB; c: velocity uncertainty of line AB; d: final velocity model of line XY; e: velocity anoamly of line XY (After Winardhi and Mereu, 1997).

a

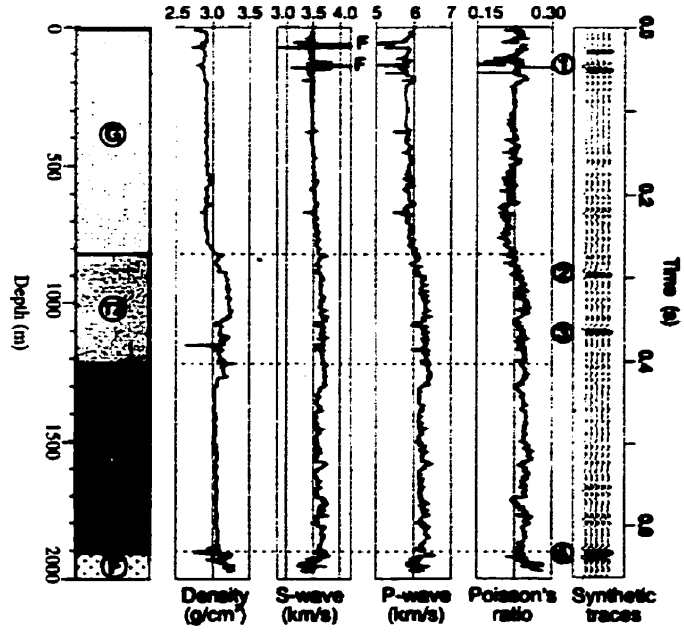

b

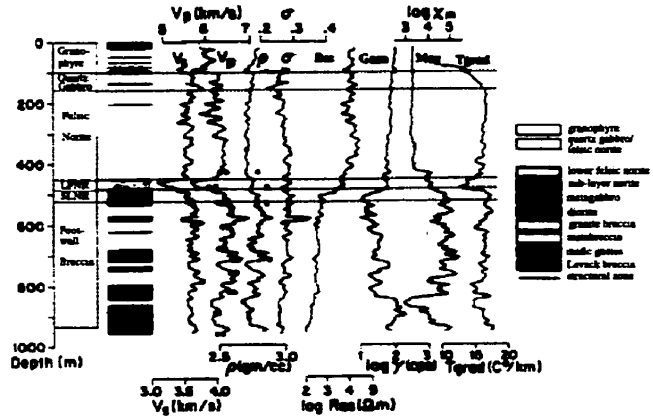

Figure 3.6 Borehole geophysical data in Sudbury. Density, P- and S- wave velocities, derived Poisson's ratio and synthetic seimogram for a 30-140 Hz source are indicated in **a**. G: Granophyre; TZ: Quartz Gabbro; N: Norite; F: Footwall Complex. **b** shows well data of density, P- and S- wave velocities, Poisson's ratio radioelements (**a** after Milkereit et al., 1994; **b** after White et al., 1994b).

(~6.5 km/s) which contain more mafic rocks. These in situ p-wave velocities are consistent with laboratory velocity measurements (Salisbury et al., 1994) (Table 3.1). The borehole velocities were used to calibrate surface seismic data and improve the interpretation of the lithologic contacts indicated by reflective events.

Table 3.1 Seismic (P-wave) velocities of rocks in the Sudbury area

Rock Type	Sample Number	Velocity from Sample Measurement (km/s)	Velocity from Borehole Surveys (km/s)
Chelmsford greywacke	13	5.91 ±0.18	n/a
Onwatin shale	11	5.16 ±0.30	n/a
Onaping tuff	28	6.09 ±0.25	n/a
Granophyre	23	6.20 ±0.13	~6.0
Norite	28	6.47 ± 0.24	~6.3
Levack gneiss	21	6.57 ± 0.20	~6.5

A three component VSP survey was conducted in the metasedimentary Whitewater series in Sudbury. The final VSP synthetic seismogram was generated by combining results from seismic data processing such as velocity analysis, wavefield separation, shear wave analysis, and waveform modeling, with an interpretation of borehole geophysical data (Miao et al., 1994; Miao, 1995). The synthetic VSP model correlated well with the

the surface seismic profile (Figure 3.7).

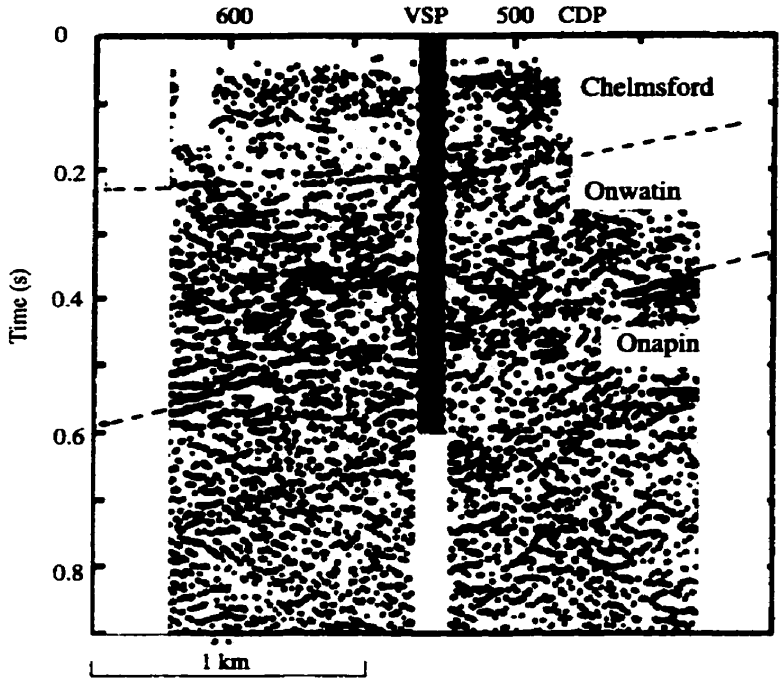

Figure 3.7 Corridor-stacked VSP section and seismic reflection image (After Miao, 1995).

3.2 Other Geophysical Studies

Geophysical potential field data, such as gravity and magnetic data, were processed and modeled across the Sudbury Basin along Lithoprobe seismic line 41. Electromagnetic sounding survey data were imaged along a short profile crossing the South Range of the Sudbury Igneous Complex (Boerner et al., 1994). In addition, magnetotelluric data were collected with a view towards deep mineral exploration. The tectonic and metamorphic history of the Sudbury Structure have been examined through an analysis of paleomagnetic data. Remote sensing data including ERS-1 SAR (synthetic aperture radar), airborne

SAR and airborne multi-sensor geophysical data were also acquired and investigated (Lowman, 1991, 1992, 1994; Singh et al., 1993). This section briefly describes interpretations of these geophysical data.

3.2.1 Potential Field Studies

Geological characteristics at the surface or in the subsurface can be inferred by analysis of gravity and magnetic anomalies. Interpretations of geophysical potential field data are inherently non-unique, which complicates their analysis.

1. Gravity Study

Generally, the gravity anomalies in the Sudbury Structure and adjacent area are divided into three prominent features (Figure 3.8): (1) the Sudbury positive gravity anomaly; (2) negative gravity anomalies over granite plutons (A, D), and sedimentary rocks (H, K); and (3) positive anomalies correlated to relatively high density rocks such as those of the greenstone belt (B), anorthosite gabbro and anorthosite complex (G), mafic rocks (M) and/or mixed zone of norite (X) as described by McGrath and Broome (1992, 1994).

The deep geometry of the Sudbury Structure was examined by Popelar (1972) and Gupta et al. (1984) by modeling the gravity anomalies for a 2-D profile across the Sudbury Basin, from northwest to southeast. In 1984, Gupta et al. improved Popelar's models by using additional gravity surveying data and numerous new density measurements in addition to newly surveyed geology. The average background density was taken as 2.73 g/cm^3 by Gupta et al. (1984). Two 2-D gravity models were proposed by Gupta et al. (1984), the

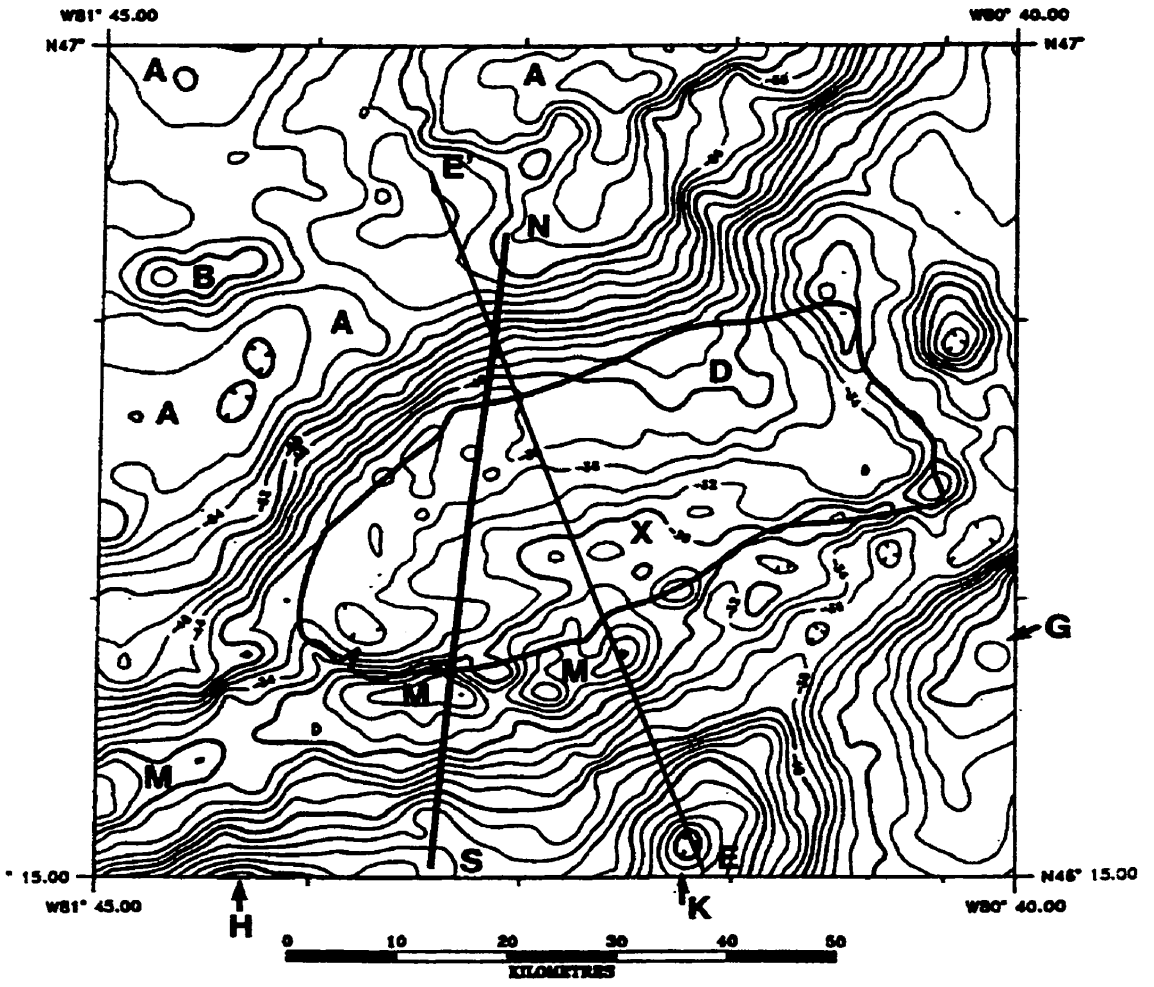

Figure 3.8 Bouguer gravity anomaly map in the Sudbury Area. EE' is the gravity profile of Gupta et al.'s model A whereas NS is the profile of the new 2.5 gravirty model. Interpretations corresponding to these two profiles are indicated in Figure 3.9a and 3.9b respectively. Anomalies A, B, D, H, K, M and X are referred to the text. (After McGrath and Broome, 1994).

first of which ("model A") is shown in Figure 3.9a. A large sub-horizontal sill-shaped, and high-density body under the Sudbury Basin was required to fit the large positive gravity anomaly; this body does not outcrop. The gravity anomaly is "too broad and too intense to be caused by any downward extension of the rocks in Sudbury" (Gupta et al., 1984). Gupta et al. interpreted this layered hidden body as a mafic or ultramafic intrusion containing rocks such as anorthosite gabbro, olivine gabbro, or dunite with densities of 3.0-3.3 g/cm^3.

As previously noted, the intrinsic ambiguity in gravity interpretation causes difficulty in data analysis. Furthermore, the fewer the constraints applied in modeling, the greater the subjectivity involved in interpretation. Therefore, without constraints provided by high-resolution seismic data, the gravity models obtained in the 1980's remained in doubt.

Recently, a new 2.5 dimensional gravity model (Figure 3.9b) was developed which was tightly constrained by a high-resolution seismic reflection model frame (McGrath and Broome, 1992, 1994). The new gravity model indicates that the broad and intense gravity anomaly is mainly attributable to an external source, the basement rock, not the Sudbury Structure itself. The positive gravity anomaly south of the Sudbury Igneous Complex, extending in the east-west direction, was suggested to be correlated to high density material effects of Huronian mafic or ultramafic rocks marked by M in Figure 3.8 (McGrath et al., 1994). The decreased gravity parallel to the northern margin of the Sudbury Igneous Complex is caused by the background density basement rocks (2.73 g/cm^3) north of the dense Levack gneiss and low-density rocks of the Cartier granite pluton (2.65 g/cm^3). The new gravity model shows the possible contact boundary between gneiss and granite as

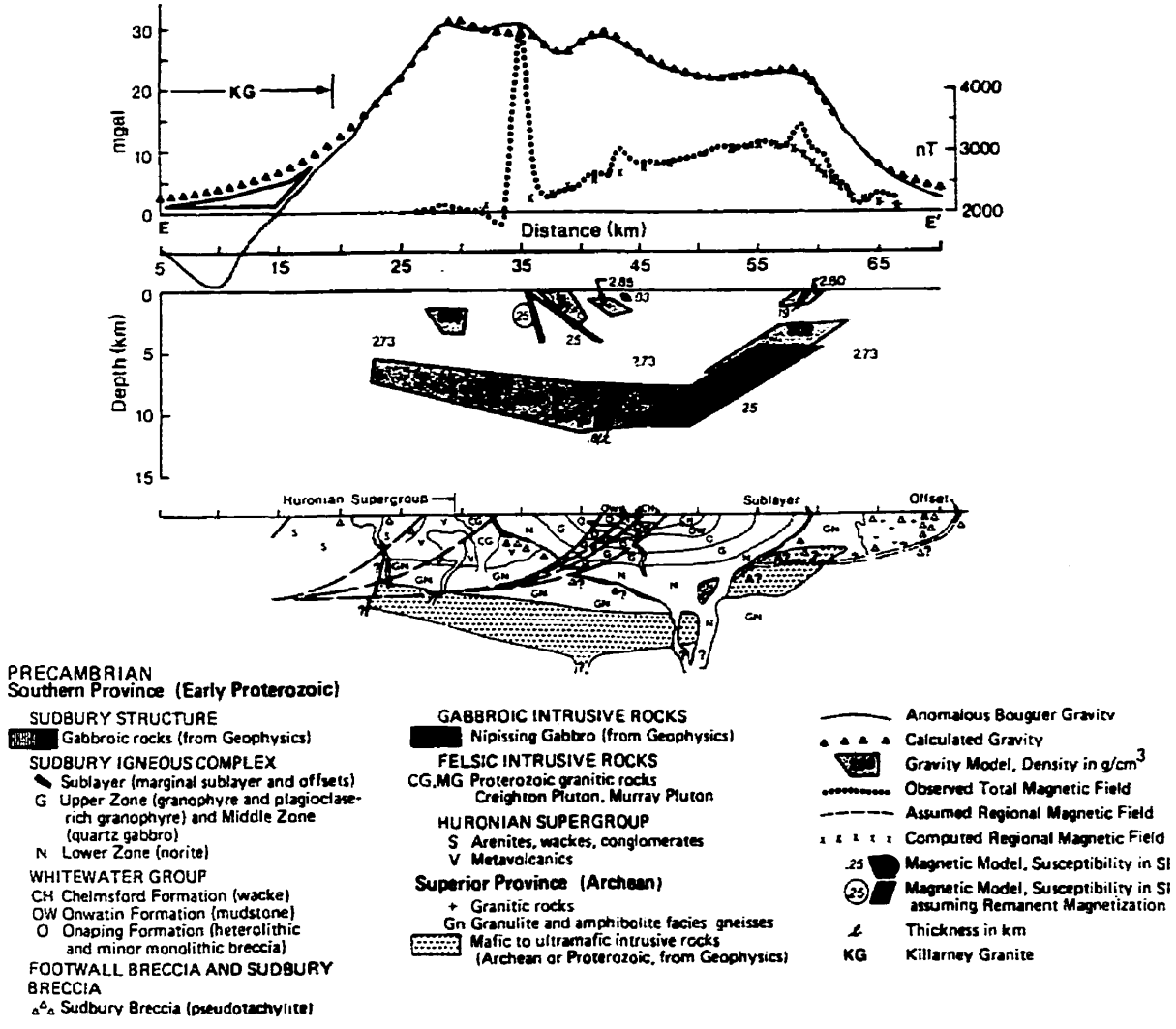

Figure 3.9a Geological interpretation of gravity model A (After Gupta et al., 1984).

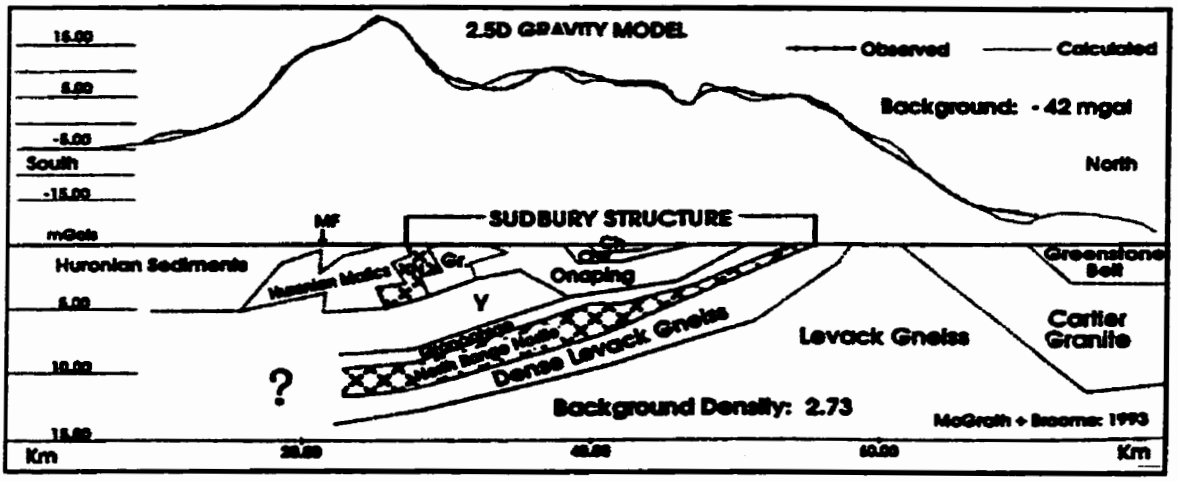

Figure 3.9b The 2.5 -D gravity model proposed by McGrath and Broome (1994). MF: Murray Fault; Gr: Granophyre; Ow: Onwatin; Ch: Chelmsford.

northward dipping. However, this could not be constrained by the newly processed seismic reflection data (line 42) (Figure 3.4) because of the limited profile length. The density model in the northern part of the profile thus needs a careful interpretation. In contrast, the density model under the Southern Range is well constrained by seismic reflection data and provides relatively reliable interpretation. It is significant that the new gravity model does not require a hidden high density layer or a mafic body hidden under the Sudbury Basin to fit the observed data.

2. Magnetic Study

There are various types and scales of magnetic data available in the Sudbury area, and geologists have routinely used both local and regional magnetic maps for their geological interpretation. The regional total-field aeromagnetic anomaly map in the Sudbury area was

compiled in 1984. The magnetic model responsible for the residual aeromagnetic data was developed by Gupta et al. (1984). Moon et al. (1988) converted the magnetic data by Hilbert transform and determined that the isolated positive anomaly in the south of the Sudbury Basin corresponded to the South Range norite.

Recently, a detailed 2-D magnetic model along seismic transect line 41 has been developed by Hearst et al. (1992, 1994) on the framework of the subsurface geometry provided by the seismic reflection data. The lithologic magnetic parameters, such as magnetic susceptibility and remnant magnetization, were measured in situ. The initial model, which was rigidly restricted to the seismic geometry, did not result in a satisfactory fit between the observed and calculated magnetic data. This misfit was analyzed and explained as the magnetic sensitivity to variations in geological structure (especially near-surface structure) and significant spatial variation in the magnetization of rock units caused by heterogeneity (Hearst et al., 1992). Hearst et al. modified their initial model by adding local magnetized bodies or dikes (between the surface and 5 km depth). The final magnetic model which gave the best match between the observed and calculated data indicated that the Levack Gneiss Complex (susceptibility in the range from 200 $x10^{-6}$ to 1700 $x10^{-6}$ SI) provides a broad regional magnetic anomaly (Figure 3.10a and b). The magnetic high between the Onwatin and Onaping formations was explained as the result of the contribution from a zone of hydrothermal mineralization. The high magnetic anomaly in the South Range of the Sudbury Igneous Complex was ascribed to the natural remnant magnetization.

The complex magnetic model therefore revealed local variations of geological features in the Sudbury Structure and implied that different tectonic processes occurred in the

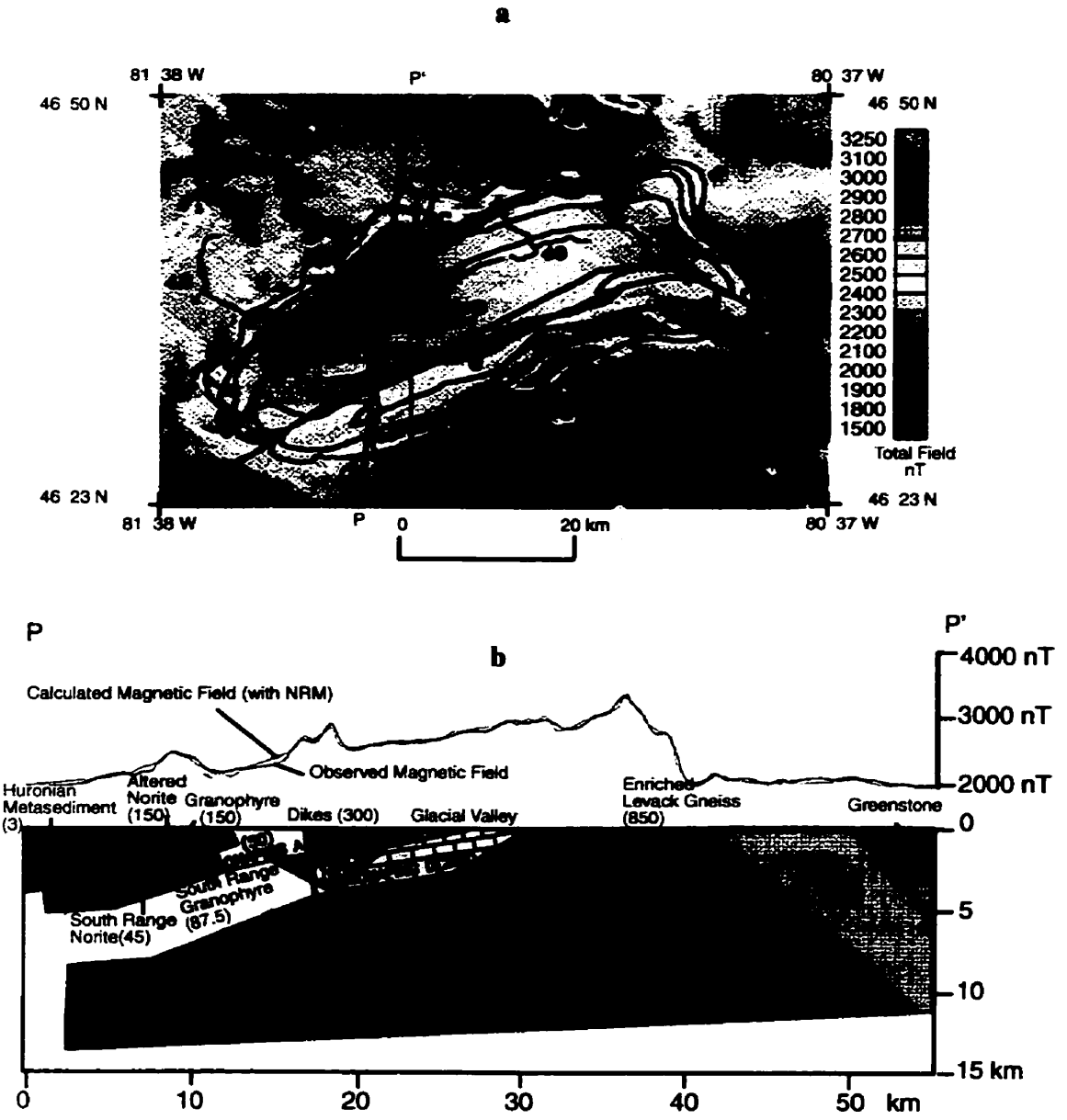

Figure 3.10 Total field magnetic anomalies (a) and magnetic model (b). C-O: Chelmsford and Onwatin; O: Onaping: G: Granophyre; N: Norite; LGC: Levack Gneiss Complex; CG: Cartier Granite. D: Electromagnetic survey profile (After Hearst et al., 1994).

South and North Ranges. Nevertheless, the magnetic model also raised some geological problems. The enhanced magnetization in the Levack Gneiss Complex zone along the North Range cannot be supported by the current rock samples collected on the surface crossing the North Range contact and thus this question remains for future discussion.

3.2.2 Electromagnetic and Other Surveys

Surface electromagnetic surveying (Figure 3.10a) using the UTEM system across the South Range of the Sudbury Igneous Complex was carried out in 1991 (Boerner et al., 1994). A southward-dipping conductive zone (7 siemens) of the Black Member of the Onaping Formation was discovered by the UTEM resistivity profile (Boerner et al., 1994). This zone marked by Q-R in Figure 3.11 could be interpreted as a result of graphitization effects in the carbonaceous Black Member (Boerner et al., 1994). The result is consistent with the low resistivity (7-20 Ω m) of the Black Member measured from drillcore samples (Katsube and Salisbury, 1994). From the Gray Member of the Onaping Formation down to the base of the Sudbury Igneous Complex, the rocks are uniformly characterized by high resistivity (10^4-$7\text{x}10^4$ Ω m) (Figure 3.11). The low-conductivity zone bounded by two reflectors Q and R (Figure 3.11) might be considered as a basic contact in the Sudbury Structure which represents the transition from the lower melt to the upper prominent fall-back lithology. Boerner et al. (1994) suggested that northwest-southeast thrusting might glide along such a zone within the Onaping Formation possibly graphitized during thermal process. However, the genesis of the low resistivity in the Black Member is still not fully explained.

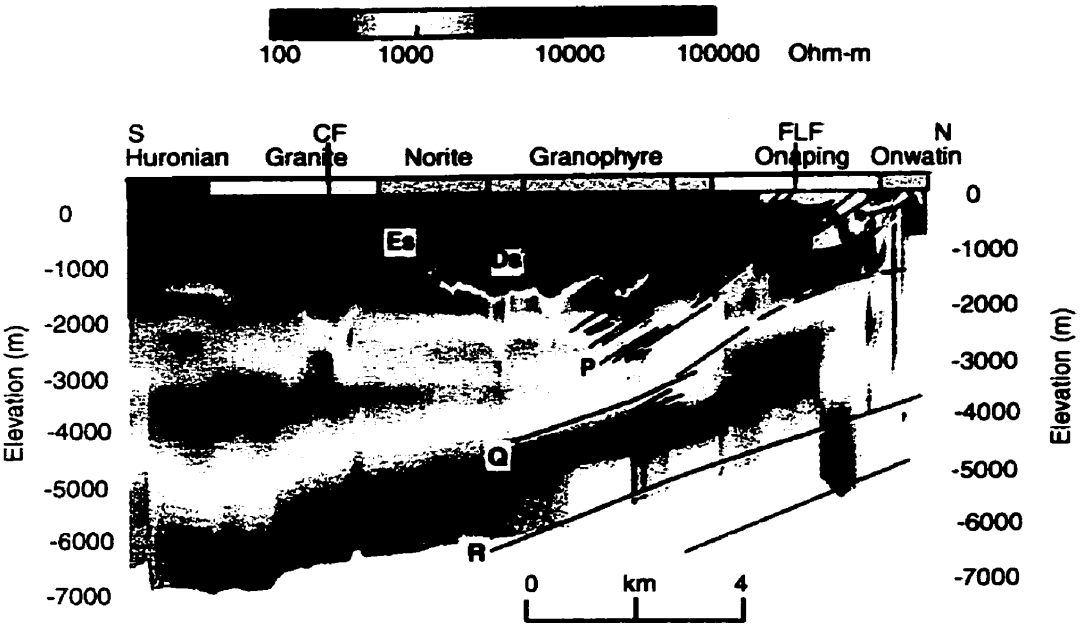

Figure 3.11 Resistivity versus depth profile interpreted from UTEM survey. The dipping lines are reflectors indicated on the seismic image shown in Figure 3.2. Es, Ds, P, Q, and R corresponds to reflectors pointed out in Figure 3.2. (CF: Creighton Fault; FLF; Fairbank Lake Fault.) (After Boerner et al., 1994).

A magnetotelluric study has been recently conducted on the western flank of the Sudbury Igneous Complex for deep mineral exploration. 2-D and 3-D models extending down to several km in depth were analyzed but no positive conclusion was obtained (Lively-brooks et al., 1996).

The paleomagnetic studies in Sudbury revealed a significant difference in the direction of remnant magnetization between two types of specimens sampled from the South and North Ranges (Hood, 1961; Morris, 1984). The remnant magnetization along the Sudbury Igneous Complex was interpreted from a demagnetization experiment as being of the ther-

moremnant type (Hood, 1961). The paleomagnetic data also proved that the Sudbury Structure and the Southern Province were less deformed than the Grenville Province (Morris, 1984) and only affected by thermal overprinting (Hood, 1961) during the Grenville orogeny. These paleomagnetic results did not give arguments for the Sudbury meteorite impact origin.

3.2.3 Remote Sensing

Since 1990, remote sensing data in Sudbury have been collected and processed for geological purposes. Won (1993) showed that the surface geology was better depicted by airborne SAR images than by ERS-1 SAR images. Butler (1994) did a lineament-extracting analysis on the Sudbury Landsat imagery. The strong arc patterns invisible to the naked eye in the northeast and northwest beyond the Sudbury Structure were extracted by analysis of a lineament length, direction, and intensity of topographic expression. A total of five ring arcs were identified. These ring features correspond to the boundaries of the major pseudotachylyte zones (>10 cm thick) defined by Thompson and Spray (1994) and Spray and Thompson (1995). Generally, a large impact site is characterized by multi-ring geological features around the crater such as pseudotachylyte zones. Sudbury multi-ring features suggest that this is a large complex impact feature.

Remote sensing imagery has proven to be a useful tool in geological mapping. The northwest-trending Fecunis and Sandcherry Creek faults of the Onaping fault systems (Figure 2.2), are well defined in SAR images (Lowman, 1991; Rivard et al., 1994; Rivard and Toutin, 1995). In 1991, Lowman reported several previously-unknown linear features

associated with faults and dikes northwest of the Sudbury Igneous Complex, recognized on processed airborne C- band SAR imagery. Two subparallel lineaments tending east-west in the Benny Deformation Zone cut the north-west-north faults of the Onaping fault system (Rivard and Toutin, 1995). Three dike sets with east-north-east, east-south-east and arcuate orientations in the Benny Deformation Zone are possibly related to Sudbury diabase swarms identified on the SAR image in combination with the airborne magnetic data.

Airborne multi-sensor geophysical data including magnetic and VLF (very low frequency) electromagnetic and gamma ray spectrometer data were collected in 1989 in Sudbury (Singh et al., 1993). A set of distinctive lineament features northwest of the Sudbury Structure was identified on the electromagnetic total field and quadrature images (Figure 3.12a). They are ascribed to north-west trending conductive bodies such as diabase dikes and fluid-filled fracture belts. The gamma ray spectrometer images delineated the boundary between the Onaping Formation and the Sudbury Igneous Complex (Figure 3.12b).

In general, Singhroy et al. (1993) and Lowman (1994) determined that a narrow-swath image or SAR (C-HH) image is useful for detailed mapping of geological structures (dikes, faults and geological units). On the other hand, wide-swath SAR images are applied as a standard tool for mapping regional geology. Integrated SAR images overlain by geophysical data could delineate significant lithologic units and contact boundaries (Fig 3.12c).

a

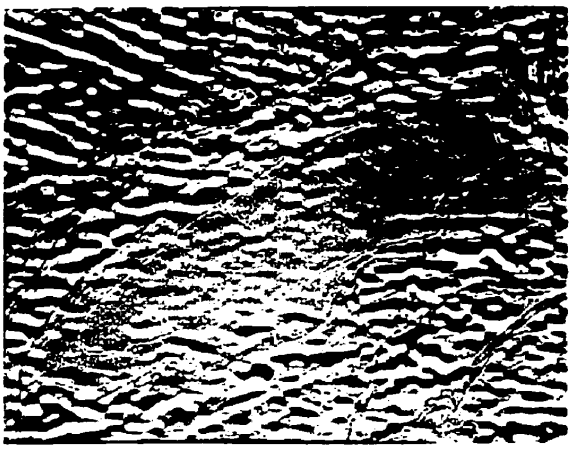

b

c

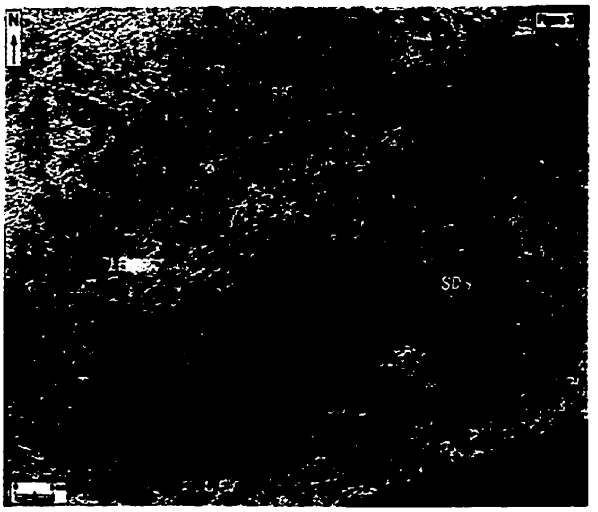

Figure 3.12 Remote sensing images overlain by geophysical and radioelement data. **a.** VLF (very low frequency) electromagnetic image. Lines are geological formation boundaries. **b.** composite radioelements image with geological formation boundaries. **c.** integration of airborne SAR (synthetic aperture radar) C-HH overlain by vertical magnetic gradient data (**a** and **b** after Singh et al., 1993; **c** after Singhroy et al., 1993).

Chapter 4

Seismic Refraction Survey

Although the post-deformed Sudbury structure has been intensively studied using geological and high-resolution seismic reflection techniques, the detailed processes involved in the formation of the Sudbury Structure are not well understood. The tectonic relationship between the Sudbury Structure and the adjacent area, and structure features in the lower crust and upper mantle, are not fully defined. In order to probe the Sudbury Structure in 3-D, a large-scale high-resolution refraction seismic experiment across the Sudbury area was conducted as a part of the Lithoprobe Abitibi-Grenville transect experiments. The objective was to answer fundamental questions including those related to the impact hypothesis.

Profiles AB and XY across the Sudbury Basin (Figure 4.1) were surveyed during the 1992 Lithoprobe seismic refraction experiment. Seismic data acquisition was carried out by an international multi-scientific research group including the Geological Survey of Canada (GSC), the United States Geological Survey (USGS), Lithoprobe, Geophysica GPR International Inc., University of Western Ontario, University of Manitoba, Ecole Polytechnique, University Lava and Dalhousie University. Seismic instruments, survey parameters and data processing are described in this chapter.

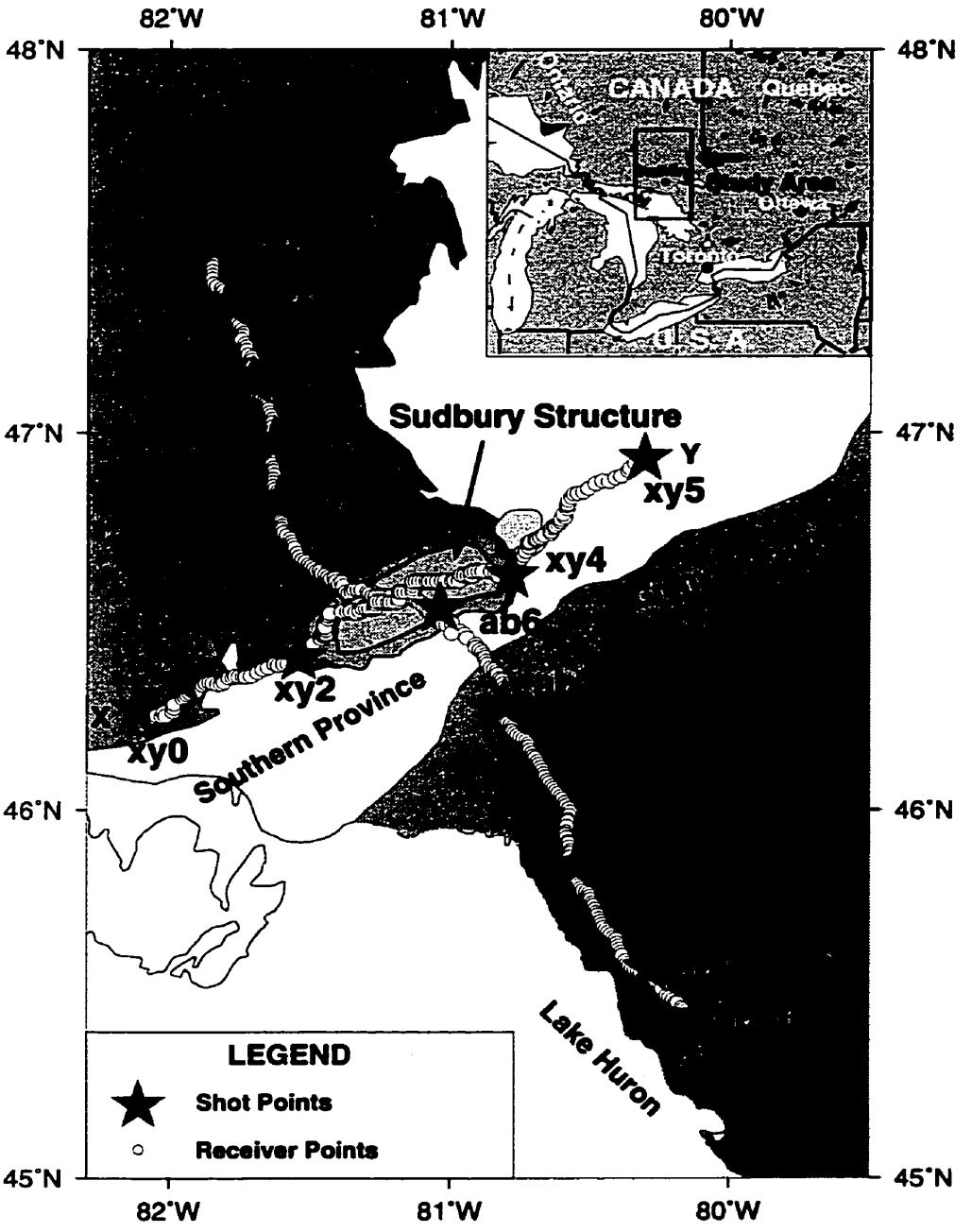

Figure 4.1 Source and receiver locations for the 1992 Lithoprobe high-resolution wide-angle reflection and refraction seismic survey (After Moon and Jiao, 1998).

4.1 Instruments

Two kinds of seismic recording instruments were deployed during the survey. A total of 185 vertical component PRS1 (Portable Refraction Seismograph 1) and 47 three-component PRS4 (Portable Refraction Seismograph 4) were provided by the GSC. Mark Product 2 Hz L4A detectors were used with the majority of the GSC's geophones. The shot time windows were downloaded into the instruments before deployment and the recorded data were uploaded after shooting using eight personal computers.

A total of 140 vertical component single geophone Seismic Group Recorders (SGR), and 50 vertical component geophones were provided by the USGS, with 2 Hz single and 8 Hz string detectors respectively. After shooting, the recorded data were uploaded from the cartridge tapes in the recorders into an Everex 1800 microcomputer system. The following section briefly describes the recording system principle of the GSC's PRS1 instrument as an example of the recording systems used.

4.1.1 The Geological Survey of Canada's PRS1

The PRS1 with a single channel was designed by the Instrumentation Laboratory of the Geophysics Division of the GSC in the early 1980s. The instrument had to meet requirements of the Lithoprobe project including being light, easy to use, cheap and requiring little battery power consumption. A precise clock (such as a GPS - geographical position system - satellite clock) and a computer (PC) installed with Litho SEIS software are needed to work with the PRS1.

Table 4.1 lists the instrument parameters. Figure 4.2 shows the main components of the

Table 4.1 Design parameters of the PRS1 recording system (After Asudeh et al., 1992)

Feature	Specifications	Status
Input	One analog source	*
	Balanced configuration	*
	Band-pass filters with 40 db rejection at half the sampling frequency	*
	High-pass corner at 0.568 Hz	*
	Provision for slaving several units together	o
Sensitivity	1 nanometer per second ground velocity per bit	*
Accuracy	Less than 1% systematic error	*
System noise	Less than 1 nm/s RMS	*
Full scale capacity	2 mm/s ground motion	*
A/D converter	12 bit resolution	*
Dynamic range	132 db peak to peak	*
Gain-ranging	Selects optimum gain for each measurement	*
Sampling rate	60 or 120 samples per second	o
Time accuracy	Correctable to 5 ms after a deployment of 48 hours	*
Typical sensor	Light weight 2 Hz geophone	*
Weight	Not to exceed 10 kg	*
Physical size	About 4 x 20 x 24 cms	*
Operating environs	From -30° to +40°	*
	Reasonably shock resistant	*
	Suitable for deployment in hot, cold, or wet weather	*
Mission duration	Minimum of 200 hours continuous operation, preferably 500 hours	*
Internal battery	6 to 14 V dc, 100 mA peak current	*
Connectors	Geophone	*
	Data I/O, terminal	*
	External battery	x
Data Storage	0.5 Mbytes solid-state	*
Controls	One push-button switch	*
Display	4 LEDs under processor control	*
Internal program	Bootstrap loader and communications only. Running program with all operating parameters are downloaded from external field computer	*
Field calibration	Manually initiated pulse calibration	*

*** = implemented, o= partially implemented, x= not implemented.**

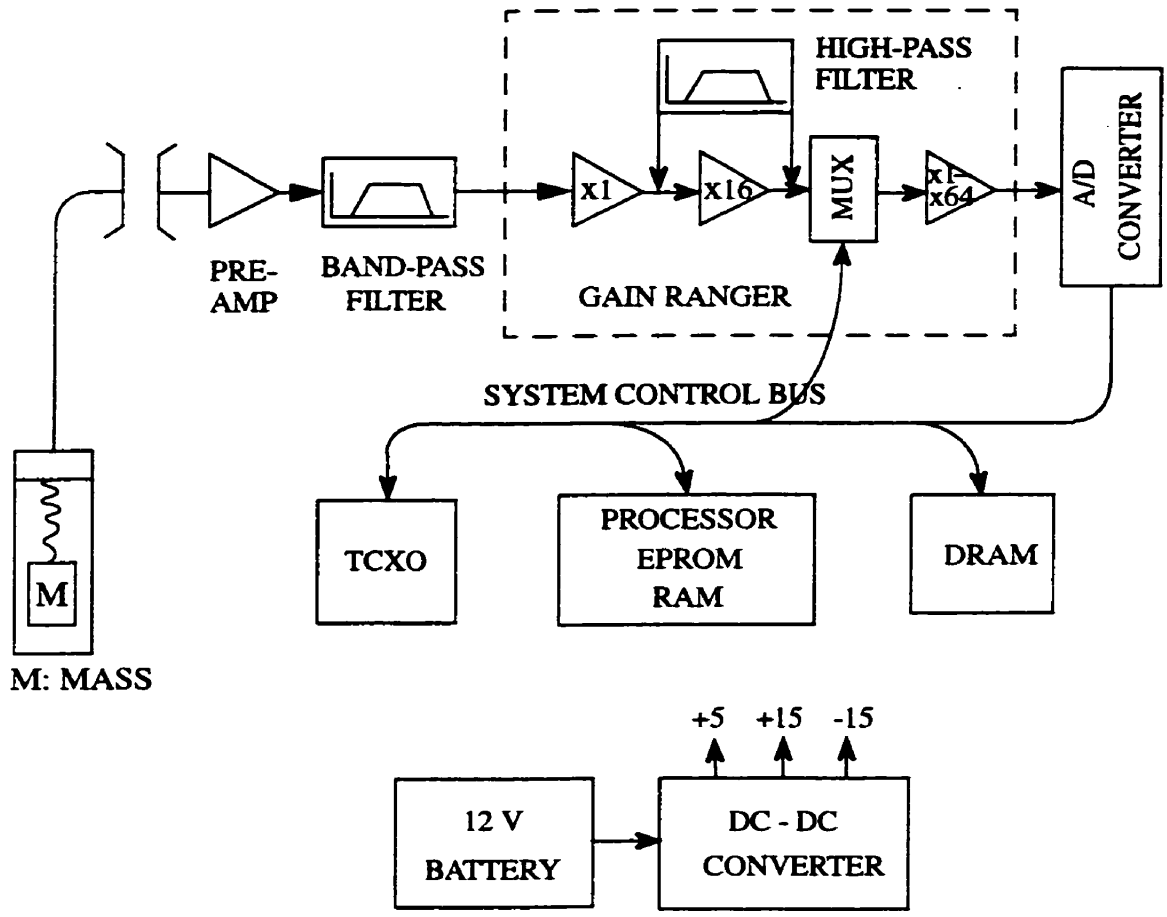

Figure 4.2 Main components of the PRS1 (After Asudeh et al., 1992). M: mass; MUX: multiplexer system control bus; TCXO: temperature compensated crystal oscillator.

PRS1. The ground motion detected by the Mark Product 2 Hz L4A seismometer is transferred into an electrical signal (Figure 4.2). The electrical signal output from a geophone is pre-amplified by a 17.24 gain factor to the minimum level which is required by the subsequent circuitry. The output signal from the pre-amplifier is then sent to a band pass filter (Figure 4.2), and a Bessel low-pass filter, which reduces the aliasing effects caused by the finite sampling rate.

The signal filtered by the band-pass filter is in turn input to a gain-ranging device, where the amplification of the system is modified according to incoming signal for obtaining the optimum gain. The dynamic range of the recording system is 132 dB (Table 4.1). A 12-bit A/D (analogy-to-digital) converter is used in the PRS1 instrument. However, 'a 12 bit converter supplies 72 dB, and the remaining 60 dB must be provided by the gain-ranging circuity' (Asudeh et al., 1992). The gain-ranger has two amplifiers, X1 and X16 (Figure 4.2). X1 has a gain of unity and X16 has a gain of 16. A high-pass filter is used to remove the drifts in the gain range. The last component of the circuitry has a selectable gain from 1 to 64 to amplify the output of one from X1 and X16. The MUX (a multiplexer system control bus) records X1 and X16 outputs in channels 1 and 2 respectively and monitors the battery voltage in channel 0.

Finally, the amplified signal is sent to the 12 bit (with 5 millivoltage per bit sensitivity) A/D converter, and saved in a dynamic memory RAM (DRAM) of a Hitachi HD 6303 XP processor which has 1 Megabyte storage capacity and a 8 bit CPU (Asudeh et al., 1992).

The precise time for the system is obtained using a temperature compensated crystal oscillator (TCXO). The power system includes a 12 V battery and a DC-DC converter.

4.2 Seismic Survey

In July 1992, the Lithoprobe Abitibi-Grenville subtransect high-resolution wide-angle reflection and refraction seismic experiment was carried out in the Sudbury area (Figure 4.1). Parameters for the survey geometry, shooting and recording, and data processing are described in detail in the following sections.

4.2.1 Survey Parameters

The exact location of all shot and receiver sites was determined by TRIMBLE Pathfinder GPS receivers with a base station at the INCO Copper Cliff Exploration office (Irving et al., 1993). Accuracy of the horizontal position at the differential positioning mode was estimated to be approximately 5 m after the necessary corrections (Miao, 1995). Eight Geocentric Earth Orbiting Satellite (GEOS) clocks provided an absolute time system for shot time correction and synchronization of shooting and recording time.

Survey geometric parameters include the length and direction of two high-resolution seismic profiles. Line AB extended ~265 km in length from northwest to southeast, crossing part of the Superior Province, Sudbury Basin, Southern Province, Grenville Front and ending at Parry Sound Domain in the Grenville province (Irving et al., 1993). Line XY was designed to form a cross-array with line AB, extending ~165 km in length from southwest to northeast, crossing the Southern Province, the Sudbury Basin, and ending in the eastern Southern Province (Figure 4.1).

4.2.2 Shooting and Recording

Originally, seventeen shots were planned along profiles AB and XY but two of them, ab5 and xy3, were abandoned because of environmental and safety concerns. Fifteen shot holes were then drilled with a diameter of 20.4 cm and depths of 35~43 m. Shot and receiver spacings were 30 km and 1-1.5 km respectively. Dynamic charge sizes were in a range of 200 to 1600 kg. The dynamite type was Hydromex T3 and the detonation velocity was approximately 5400 m/s.

A total of 278 receivers were deployed along line AB and 168 along XY. The sampling rate and recording length of the GSC instruments are 120 samples per second (sps) and 120 seconds (s) respectively. The sampling rate and recording time of the USGS's instrument are 125 sps and 60 s. The amplitude scaling factors for the USGS data are 2.5 x 10^6 and 5.4 x10^6 for signal and string geophones respectively. Shot time correction was applied before the SEGY (the data format defined by Society of Exploration Geophysicists) tapes were made. However, a receiver time correction was made by processors according to trace information in SEGY header bytes 217-218.

Table 4.2 summarizes the survey, shooting and recording parameters.

4.2.3 Data Processing

As the survey employed two different kinds of instruments with different recording systems, it was necessary to convert both types of seismic data into one standard data format, i.e. SEGY format. The USGS data were originally sampled at a rate of 125 sps. In order to merge them with the GSC data, the USGS data were re-sampled at a rate of 120 sps by using the Fast Fourier Transform method (Irving et al., 1993). After the USGS data were re-sampled, the GSC and USGS data were merged. All traces corresponding to each shot were then gathered. Finally, shot gather data in SEGY format were created and saved on Exabyte tapes for distribution and implementation of further processing and modeling. The record length was set to 60 s extending from -5 to 55 s.

Table 4.2 Refraction survey geometry, timing system and data recording instrument parameters (After Asudeh et al., 1992)

Contents	Parameters			
Shot information	No. of shot holes	15	Dynamite type	Hydromex T3
	Depth of holes	35 or 43 m	Detonation velocity	5400 m/s
	Diameter of holes	20.4 cm	Size of charges	200-1600 kg
	Ave. shot interval	30 km		
Receiver information	No. of receivers for line AB	278	No. of receivers of line XY	168
	Ave. receiver interval	1-1.5 km		
GSC instruments	PRS1 seismograph	1 vertical component Sampling rate 120 /s Recording length 120 s		
	PRS4 seismograph	3 components Sampling rate 120 /s Recording length 120 s		
	Geophone	2Hz L4A for vertical components L28 LBH 4.5 Hz for horizontal components		
USGS instruments	Seismograph	SGR (Seismic Group Recorder) 1 vertical component Sampling rate 125 /s Recording length 60 s		
	Geophone	2Hz L4C and 8 Hz string detectors Amplitude scaling L4C $2.5*10^6$ 8Hz $5.4*10^6$		
Timing system	GEOS (Geocentric Earth Orbiting Satellite) clock			
Navigation	TRIMBLE Pathfinder GPS using differential mode			

Chapter 5

Modeling of In-Line Data

(Profile AB)

Cerveny's dynamic ray tracing algorithm allows the forward modeling of in-line seismic refraction data in inhomogeneous media. The velocity structure is complex along profile AB and was modeled using this method. This chapter discusses Cerveny's ray tracing method, and its application to the modeling of the high-resolution seismic reflection and refraction data. The first section describes Cerveny's basic ray tracing theory. Then, the chapter discusses the processing and modeling of the seismic data along profile AB. The modeling provides subsurface velocity structures shown in a subsequent section.

5.1 Cerveny Ray Tracing Algorithm

Cerveny's ray tracing algorithm is based on a powerful dynamic ray tracing approach (Cerveny and Hron, 1980; Cerveny, 1985), which can trace the propagation of a seismic wave from source to receiver in complex geological media. The method provides the complete wave field generated by a line or point source including the elementary waves, such as reflection, refraction, converted, and multiple reflected waves. This section describes the basic ray theory, the determination of the source signal function, and the computation of the ray path traveltime and amplitude.

5.1.1 Basic Principles in Ray Theory

In an inhomogeneous elastic and isotropic medium, the linearized equation of motion can be written as (Cerveny and Ravindra, 1971)

$$\rho\frac{\partial^2 \boldsymbol{U}}{\partial t^2} = (\lambda+\mu)\nabla(\nabla\cdot\boldsymbol{U}) + \mu\nabla^2\boldsymbol{U} + \nabla\lambda(\nabla\cdot\boldsymbol{U}) + \tag{5.1}$$

$$\nabla\mu\times(\nabla\times\boldsymbol{U}) + 2(\nabla\mu\cdot\nabla)\boldsymbol{U},$$

where ρ is the density in the medium, λ and μ are Lamé parameters, $\boldsymbol{U}$ is the particle displacement vector, and t represents time. It is assumed that the wavefront is described by $t=\tau(x, y, z)$, where τ is a time function, and x, y, and z are spatial coordinates in the Cartesian system. The general form of the displacement vector in equation 5.1 is given by

$$\boldsymbol{U}(x, y, z, t) = \sum_{k=0}^{\infty} \boldsymbol{U}_k(x, y, z)F_k(t-\tau(x, y, z)), \tag{5.2}$$

where $\boldsymbol{U}_k(x, y, z)$ is the amplitude coefficient of the ray series and the source signal function F_k obeys the relation of

$$F'_k(\xi) = F_{k-1}(\xi). \tag{5.3}$$

The F'_k is the derivative of F_k. The F_k is commonly written as complex function

$$F_k(\xi) = f_k(\xi) + ig_k(\xi), \tag{5.4}$$

where $f_k(\xi)$ and $g_k(\xi)$ are real functions which are a pair of the following Hilbert transform

$$g_k(\xi) = \pi^{-1} \int_{-\infty}^{\infty} f_k(x)(x-\xi)^{-1} dx. \tag{5.5}$$

Furthermore, if the time function f_k is given, then F_k can be easily constructed by using equations 5.3, 5.4 and 5.5.

Substituting the displacement vector of equation 5.2 into equation 5.1, one obtains the important amplitude coefficient fundamental equation expressed in terms of $\boldsymbol{N}$, $\boldsymbol{M}$ and $\boldsymbol{L}$ (Cerveny et al., 1986):

$$\boldsymbol{N}(\boldsymbol{U}_k) - \boldsymbol{M}(\boldsymbol{U}_{k-1}) + \boldsymbol{L}(\boldsymbol{U}_{k-2}) = 0, \qquad k = 0, 1, 2, \ldots, \tag{5.6}$$

where we have $\boldsymbol{U}_{-1}=\boldsymbol{U}_{-2}=0$, and $\boldsymbol{N}$, $\boldsymbol{M}$ and $\boldsymbol{L}$ are respectively given by

$$\begin{aligned}
\boldsymbol{N}(\boldsymbol{U}_k) &= -\rho \boldsymbol{U}_k + (\lambda+\mu)\nabla\tau(\boldsymbol{U}_k \cdot \nabla\tau) + \mu(\nabla\tau)^2 \boldsymbol{U}_k, \\
\boldsymbol{M}(\boldsymbol{U}_k) &= (\lambda+\mu)[\nabla(\boldsymbol{U}_k \cdot \nabla\tau) + \nabla\tau(\nabla \cdot \boldsymbol{U}_k)] + \mu[2\nabla(\tau \cdot \nabla)\boldsymbol{U}_k + \\
&\qquad (\nabla^2\tau)\boldsymbol{U}_k] + \nabla\lambda(\boldsymbol{U}_k \cdot \nabla\tau) + \nabla\mu \times (\nabla\tau \times \boldsymbol{U}_k) + 2(\nabla\mu \cdot \nabla\tau)\boldsymbol{U}_k, \\
\boldsymbol{L}(\boldsymbol{U}_k) &= (\lambda+\mu)\nabla(\nabla \cdot \boldsymbol{U}_k) + \mu\nabla^2\boldsymbol{U}_k + \nabla\lambda(\nabla \cdot \boldsymbol{U}_k) + \\
&\qquad \nabla\mu \times (\nabla \times \boldsymbol{U}_k) + 2(\nabla\mu \cdot \nabla)\boldsymbol{U}_k \ .
\end{aligned} \tag{5.7}$$

The fundamental ray equation 5.7 is used frequently in derivations of the solutions of the amplitude and "ray tracing system" in the Cerveny's algorithm.

The compressional P wave and shear S wave propagate independently in the case of high frequency signal (Cerveny and Hron, 1980; Cerveny et al., 1986). Thus we can study P and S waves separately. We express the amplitude coefficient $\boldsymbol{U}_k$ of a ray as a combination of three orthogonal components along a unit tangent vector direction ($\mathbf{t}$), normal vec-

tor direction (**n**) and unit binormal vector direction (**b**). The amplitude coefficient is then written as

$$\boldsymbol{U}_k = U_k^{\mathrm{P}}\mathbf{t} + U_k^{\mathrm{S}^1}\mathbf{n} + U_k^{\mathrm{S}^2}\mathbf{b}, \tag{5.8}$$

where U_k^{P} is amplitude coefficient for P wave propagation in the direction parallel to the ray **t**, $U_k^{\mathrm{S}^1}$ and $U_k^{\mathrm{S}^2}$ are the coefficients for two S wave propagations in the directions perpendicular to the ray, **n** and **b**. To obtain a simple expression for the amplitude coefficient solution, the Cartesian coordinate system (x, y, z) is replaced by a ray coordinate system (τ, γ_1, γ_2), where τ defines the propagation time of a ray, and γ_1 and γ_2 represent curve ray coordinates which are also called ray parameters. We can define a function J as

$$J = \left| \frac{\partial \boldsymbol{X}}{\partial \gamma_1} \times \frac{\partial \boldsymbol{X}}{\partial \gamma_2} \right|, \tag{5.9}$$

where $\boldsymbol{X}=\boldsymbol{X}(\tau, \gamma_1, \gamma_2)$, and γ_1 and γ_2 define a particular ray at time τ (Figure 5.1). J is the Jacobian of the transformation from the Cartesian coordinate system into the ray coordinate system, and is the critical function in resolving the amplitude of a ray, as will be discussed later in this section.

5.1.2 Source Functions

The ray tracing algorithm provides for the evaluation of the source time function which is also known as a Gaussian envelope signal because of its presumed shape. The proper selection of source signal parameters enables the algorithm to simulate various seismic signals. This chapter discusses only a simple, rapid estimation of the source

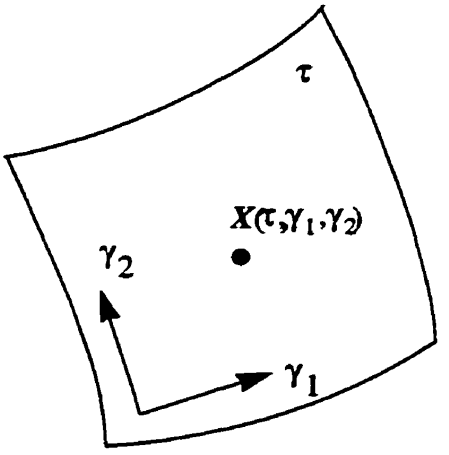

Figure 5.1 A ray coordinate system.
X: point coordinate at which a ray intersects an interface; τ time; γ_1 and γ_2: ray parameters.

signal. The first step to construct the source signal is to assume that the time function has the following zero order approximation (Cerveny et al., 1986)

$$f_0(t) = e^{-(2\pi f_M(t-t_0)/\gamma)^2} cos(2\pi f_M(t-t_0)+\nu), \tag{5.10}$$

where t is time, f_M denotes the primary frequency of a harmonious signal carrier, and γ, ν and t_0 are the parameters of the source time function. If ν is large, $g(t)$ can be estimated as $g_0(t) - -e^{-(2\pi f_M(t-t_0)/\gamma)^2} sin(2\pi f_M(t-t_0)+\nu)$. As discussed above, in equation 5.4 the source signal time function $F(t)$ is complex. However, only its real part physically contributes to the calculation of the source signal. The real part of $F(t)$ is derived in terms of $f(t)$ and $g(t)$ and is $F_0(t) = f_0(t)cos(\theta) - g_0(t)sin(\theta)$, where θ is a phase angle and the subscript 0 denotes zero order. Consequently, we can simplify the

above equation to

$$F_0(t) = e^{-(2\pi f_M(t-t_0)/\gamma)^2} cos(2\pi f_M(t-t_0) + \nu - \theta). \qquad (5.11)$$

Equation 5.11 is valid as the zero order approximation. To obtain a source signal time function for $k \geq 1$, we have to repeatedly integrate the low-order signal time function over the range of $-\infty$ to t. The result is an inversion of equation 5.3 and can be written as

$$F_k(t) = \int_{-\infty}^{t} F_{k-1}(\zeta)d\zeta. \qquad (5.12)$$

With equations 5.11 and 5.12, the source signal time function can be rapidly generated.

5.1.3 Determination of Ray Path, Traveltime and Amplitude

1. Ray Path and Traveltime

The basic function for determining a ray path and its traveltime is the well-known eikonal equation which was derived by Cerveny and Hron (1980) and Aki and Richards (1980). In this thesis, the derivation of the eikonal equation will not be repeated and only the final solution is described for tracing a ray and calculating the traveltime. The eikonal equations are partial differential equations, which can be written as

$$(\nabla\tau)^2 = \alpha^{-2} \qquad \text{for P wave}, \qquad (5.13)$$

$$(\nabla\tau)^2 = \beta^{-2} \qquad \text{for S wave}.$$

Slowness is the inverse of velocity. By defining the slowness vector as $\boldsymbol{p}=(p_1, p_2, p_3)$, we obtain $\nabla\tau = \boldsymbol{p}$, or $\frac{\partial\tau}{\partial x}\mathbf{i} + \frac{\partial\tau}{\partial y}\mathbf{j} + \frac{\partial\tau}{\partial z}\mathbf{k} = p_1\mathbf{i} + p_2\mathbf{j} + p_3\mathbf{k}$, where $\mathbf{i}$, $\mathbf{j}$ and $\mathbf{k}$ are three

orthogonal unit vectors in the Cartesian coordinate system. A substitution of p_i into equation 5.13 results in

$$p_i p_i = v^{-2}, \qquad i = 1, 2, 3, \; v = \alpha \text{ for a P wave}, \qquad (5.14)$$
$$v = \beta \text{ for an S wave.}$$

In general, ordinary differential equations defining characteristic curves are employed to solve a partial differential equation. In the case of seismic wave propagation, the characteristic curves associated with the corresponding ordinary differential equations represent rays. The eikonal equation (5.14) therefore produces the following ordinary differential equation

$$\frac{dx_i}{d\tau} = v^2 p_i, \qquad \frac{dp_i}{d\tau} = -\frac{\partial \ln v}{\partial x_i}, \qquad i = 1, 2, 3, \qquad (5.15)$$

where x_i represents the point coordinate (x_1, x_2, x_3) or (x, y, z). The above equation is also called a "ray tracing system" (Cerveny and Hron, 1980).

Equation 5.15 can also be rewritten in a spherical coordinate system. The relation between the two different coordinate systems is given by

$$p_1 = v^{-1} \cos\varphi \sin\delta, \qquad p_2 = v^{-1} \sin\varphi \cos\delta, \qquad p_3 = v^{-1} \cos\delta, \qquad (5.16)$$

where the angle φ is defined as the angle between the positive x-axis and the line projected by a ray on the horizontal x-y plane and is in the range of 0 to 2π. The angle δ represents the angle between the positive z-axis and a ray, and is in the range of 0 to π. By substitution of equation 5.16 into equation 5.15, the five ordinary differential equations representing a "ray tracing system" may be written as

$$\begin{aligned}
\frac{dx_1}{d\tau} &= v\cos\varphi\sin\delta, \\
\frac{dx_2}{d\tau} &= v\sin\varphi\sin\delta, \\
\frac{dx_3}{d\tau} &= v\cos\delta, \\
\frac{d\varphi}{d\tau} &= (v_1\sin\varphi - v_2\cos\varphi)\sin\delta, \\
\frac{d\delta}{d\tau} &= -(v_1\cos\varphi + v_2\sin\varphi) + v_3\cos\delta,
\end{aligned} \tag{5.17}$$

where $v_i = \frac{\partial v}{\partial x_i}$, i = 1, 2, 3.

In 2-D, the number of transformation equations (5.16) is reduced to two because $dy = 0$, $\varphi = 0$. Equation 5.16 thus becomes

$$p_x = v^{-1}\sin\delta, \qquad p_z = v^{-1}\cos\delta, \tag{5.18}$$

where p_x and p_z are slowness components in x and z directions respectively. The five ordinary differential equations of the "ray tracing system" in 3-D then reduce to three ordinary differential equations in 2-D:

$$\begin{aligned}
\frac{dx_1}{d\tau} &= v\sin\delta, \\
\frac{dx_3}{d\tau} &= v\cos\delta, \\
\frac{d\delta}{d\tau} &= -v_1\cos\delta + v_3\sin\delta.
\end{aligned} \tag{5.19}$$

If we replace x_1, x_3, v_1 and v_3 by x, z, v_x and v_z respectively, the above equations directly lead to

$$\frac{dx}{d\tau} = v\sin\delta,$$

$$\frac{dz}{d\tau} = v\cos\delta \tag{5.20}$$

$$\frac{d\delta}{d\tau} = -v_x\cos\delta + v_z\sin\delta\,,$$

where v_x and v_z are partial derivatives with respect to x and z respectively. Equation 5.20 is the final basic formula used in this approach to trace a ray path and calculate traveltime in 2-D.

In inhomogeneous media, the numerical solution of these first order ordinary differential equations can be obtained by an iteration approach. In Cerveny's ray tracing algorithm, the Runge-Kutta method was used to obtain a desired approximate solution (Cerveny et al., 1986). Numerical methods usually require input of initial values. The Runge-Kutta technique is no exception. The initial values for the parameters in equation 5.20 can be any reasonable values, $\tau = \tau_0$, $(x, z) = (x_0, z_0)$, $\varphi = \varphi_0$, $\delta = \delta_0$. If a ray intersects a velocity interface, equation 5.20 can be still used at the discontinuity by giving new initial values of τ, x, z, φ and δ derived according to Snell's law (Cerveny et al., 1986).

2. Amplitude

The amplitude of a displacement vector is determined by the amplitude coefficient $U_k(x, y, z)$ and source signal time function which were discussed in terms of equations 5.2 and 5.12. The source signal function can be approximately determined by using equations 5.11 and 5.12. On the basis of the fundamental equation 5.6, Cerveny et al. (1986) derived the amplitude-coefficient ordinary differential equations which are also called transport equations. The final, simplified transport equations for compressions P waves are given by

$$\frac{dU_k^P}{d\tau} + \frac{1}{2}U_k^P\left(\alpha^2\nabla^2\tau + \frac{d}{d\tau}ln(\rho\alpha^2)\right) = g_k^{(1)}(\tau), \tag{5.21}$$

where $g_k^{(1)} = \alpha(2\rho)^{-1}(\boldsymbol{L}(\boldsymbol{U}_{k-1}) - \boldsymbol{M}(\boldsymbol{U}_k^{\perp})) \cdot \nabla\tau$. This represents the principle component. The additional components of the amplitude coefficients are contributed by S waves and are given by

$$\boldsymbol{U}_k^{\perp} = -\alpha^2(\lambda+\mu)^{-1}(\boldsymbol{M}(\boldsymbol{U}_{k-1}) - \boldsymbol{L}(\boldsymbol{U}_{k-2})). \tag{5.22}$$

All parameters in equations 5.21 and 5.22 have the same meanings as described in the previous discussion of equations 5.1, 5.2, 5.6, 5.7, 5.8 and 5.13. For S waves, the amplitude coefficient transport equations have a more complex form than those for P waves expressed in equations 5.21 and 5.22. The equations representing the principle component of S waves include

$$\begin{aligned}
&\frac{dU_k^{S^{(1)}}}{d\tau} - \beta T U_k^{S^{(2)}} + \frac{1}{2}U_k^{S^{(1)}}\left(\beta^2\nabla^2\tau + \frac{d}{d\tau}ln(\rho\beta^2)\right) = g_k^{(2)}(\tau), \\
&\frac{dU_k^{S^{(2)}}}{d\tau} - \beta T U_k^{S^{(1)}} + \frac{1}{2}U_k^{S^{(2)}}\left(\beta^2\nabla^2\tau + \frac{d}{d\tau}ln(\rho\beta^2)\right) = g_k^{(3)}(\tau),
\end{aligned} \tag{5.23}$$

where $g_k^{(2)}(\tau) = (2\rho)^{-1}((\boldsymbol{L}(\boldsymbol{U}_{k-1}) - \boldsymbol{M}(U_k^P\mathbf{t})) \cdot \mathbf{n})$,
$g_k^{(3)}(\tau) = (2\rho)^{-1}((\boldsymbol{L}(\boldsymbol{U}_{k-1}) - \boldsymbol{M}(U_k^P\mathbf{t})) \cdot \mathbf{b})$,

and T is the torsion of a ray curve. The additional amplitude coefficient equation for S waves is

$$U_k^P = \beta^2(\lambda+\mu)^{-1}((\boldsymbol{M}(\boldsymbol{U}_{k-1}) - \boldsymbol{L}(\boldsymbol{U}_{k-2})) \cdot \mathbf{t}). \tag{5.24}$$

Equations 5.21 and 5.23 produce the essential components of the amplitude coefficients for P and S waves respectively corresponding to high frequency source signals.

If a source signal is characterized by a wide range of frequencies or dominated by low frequency, we have to derive a general solution of the transport equations. In a smoothly varying medium, the general solution of the transport equation at the zero order approximation has the simple form

$$U_0(\tau) = U_0(\tau_0)\left(\frac{J(\tau_0)\rho(\tau_0)v(\tau_0)}{J(\tau)\rho(\tau)v(\tau)}\right)^{\frac{1}{2}}, \tag{5.25}$$

where τ_0 is initial value of the τ, J was discussed in terms of equation 5.9, and $U_0(\tau)$ represents the amplitude coefficient for P or S waves. Generally, the zero order approximate formula of the amplitude coefficient can be generalized to include any reflected and transmitted waves or even multiples in heterogeneous layered media.

When a ray intersects a curved interface, the amplitude coefficients corresponding to reflected and transmitted waves have a complicated form. In this case, the displacement cannot be expressed by an analytic expression as discussed above. The following equation is then used to express the displacement in terms of amplitude A and source signal function F,

$$U_\xi(M) = AF(t-\tau, \varphi_\xi), \tag{5.26}$$

where ξ represents coordinates x, y, and z, $U_\xi(M)$ represents the amplitude component along x, y, and z axes respectively, M denotes the point (x, y, z, τ), $A = V\left|gQq_\xi L^{-1}\right|$ and $\varphi_\xi = arg(gQq_\xi L^{-1})$, g represents the source direction, q_ξ is an appropriate ray transform coefficient, L is the geometric expression which is related to J, V can be expressed in terms of velocity and density in inhomogeneous media, and Q is the product of the coeffi-

cients of reflection or transmission reflectivities. g, q_ξ, and Q and V have their own specific expressions corresponding to the properties of wave transmission or reflection, source parameters in media, and reflectivities. Determination of the function J in L plays the key role in resolving the amplitude coefficients, which is also the case indicated in equation 5.25.

In 2-D, J can be approximated by $\left|\frac{\Delta\chi}{\Delta\gamma_1}cos\delta\right|J_\perp$ where $\Delta\chi$ denotes the distance between the two points at which two rays intersect an interface at an incident angle δ. The ray coordinates of two points are (γ_1, γ_2) and $(\gamma_1 + \Delta\gamma_1, \gamma_2)$ respectively (where $\Delta\gamma_1$ is small). $J_\perp = 1$ for a line source and $J_\perp = |\chi|$ for a point source.

At this point, the amplitude coefficients can be considered solvable. The displacement of a ray is then obtained. Furthermore, a synthetic seismogram is generated. The physical principles and the important algorithmic procedures on which a ray synthetic seismogram is based were described in detail by Cerveny (1985).

The dynamic ray tracing method is important in exploration seismology because of the easy computation of the second derivatives of the traveltime with respect to spatial coordinates (Cerveny, 1987), and is extensively used in the study of complicated geological media.

5.2 Modeling of In-line Profile AB

Profile AB extends in a northwest-southeast direction, crossing the Sudbury Structure and the complicated Grenville front structure (Figure 4.1). Complicated structures such as

this cannot be accurately modeled by presently available inversion algorithms. Therefore, interpretation of the seismic data from profile AB was only performed by forward modeling (using the Cerveny's ray tracing algorithm). The initial model was estimated on the basis of the previous results of seismic studies and analysis of the apparent velocities.

5.2.1 Reflectors Suggested by Previous Seismic Studies

The 1990 Lithoprobe high-resolution seismic reflection experiment revealed a good reflector (Figures 3.2 and 3.3) corresponding to the Sudbury Igneous Complex (Milkereit et al., 1992; Wu et al., 1994, 1995). Velocity measurement of sample rocks suggested that the granophyre and norite in the Sudbury Igneous Complex have relatively high velocity (Table 3.1) (Salisbury et al., 1994). The presence of the norite in the Sudbury Igneous Complex was also revealed by the 2-D gravity model (in which the complex/norite has a density of 2.81 g/cm^3) (McGrath and Broome, 1994). Thus, the Sudbury Igneous Complex is expected to be a good reflector in the refraction data.

The Grenville Front is in contact with the Huronian Supergroup rocks approximately 30 km southeast of the Sudbury Structure. The Grenville Front Tectonic Zone separating the Southern Province from the Grenville Province is marked by a ductile mylonite zone (Epili and Mereu, 1991; Gibb et al., 1983) and characterized by a series of southeast-dipping stacked shear zones (or stacked microterranes). The GLIMPCE (Great Lake International Multidisciplinary Program on Crustal Evolution) deep seismic reflection and refraction experiment for the first time delineated the dipping structure under the Grenville Front Tectonic Zone along profile J (Figure 5.2). Figure 5.3 indicates strong reflections

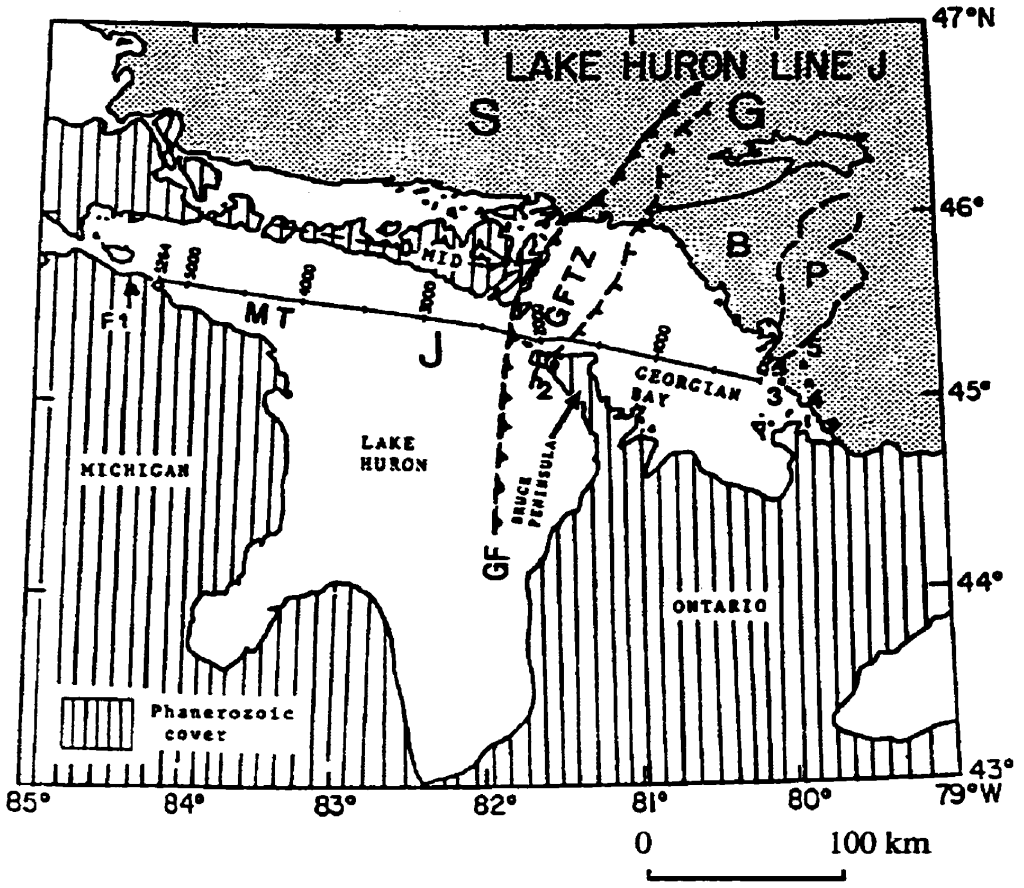

Figure 5.2 Location map of profile J of the GLIMPCE seismic experiment across Lake Huron (After Epili and Mereu, 1991).

dipping towards the east at angles of 20° to 35° (Green et al., 1989, 1990). The reflective feature can be traced down to the lower crust (Figure 5.3b). In the Britt Domain, the reflectivity is characterized by more moderately east-dipping feature.

The wide-angle reflection and refraction seismic data collected along profile J also revealed dipping structures suggested by "shingle-like" events (Figure 5.4a) (Epili and Mereu, 1991; Mereu et al., 1990). The shingle events required six dipping reflectors representing six layers under the Grenville Front and the Britt Domain. The depth to the Moho

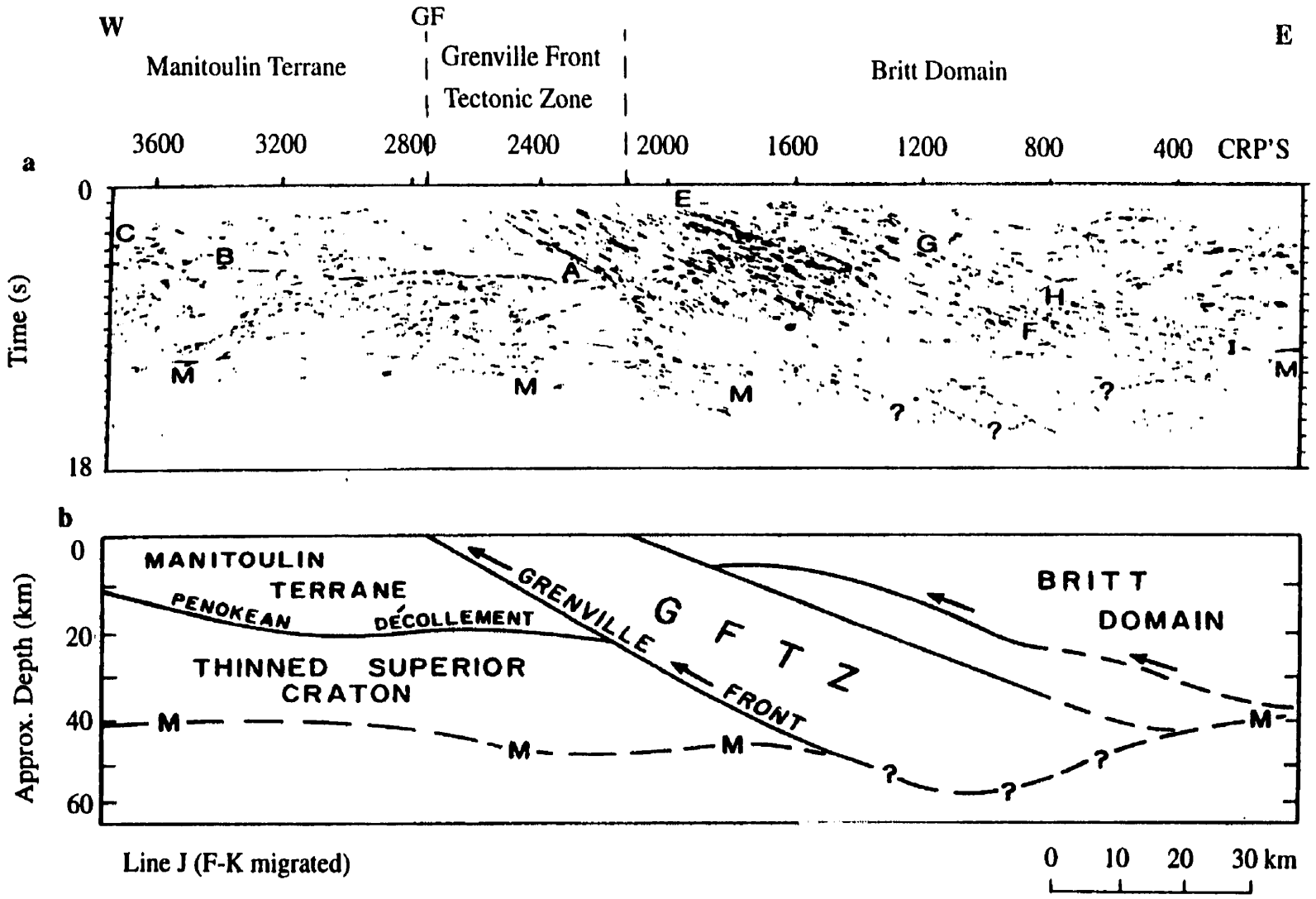

Figure 5.3 Reflection section (a) and its interpretation (b) along profile J in the eastern part of the GLIMPCE experiment crossing the Grenville Front in Lake Huron (After Clowes et al., 1992).

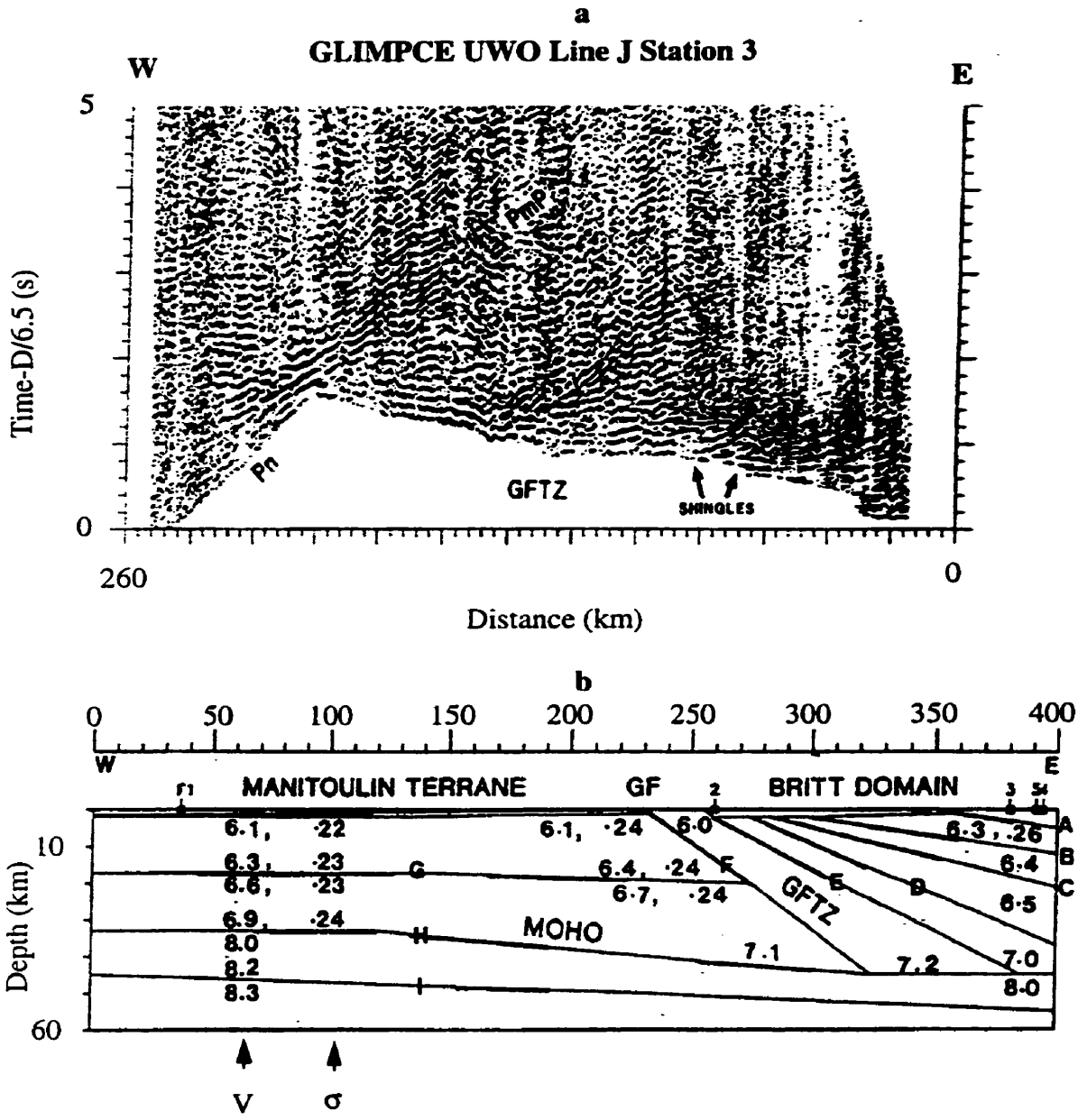

Figure 5.4 2-D seismic refraction section with shingle-like events (**a**) and interpreted velocity model (**b**) (After Epili and Mereu, 1991).

discontinuity increases from ~35 km deep in the west (in the Manitoulin terrane) to ~45 km deep in the east (in the Grenville Province) (Figure 5.4b).

The seismic data from reflection line 15 over the Grenville Front to the northeast of the Sudbury Structure (Figure 5.5) revealed a different dipping structure. Horizontal

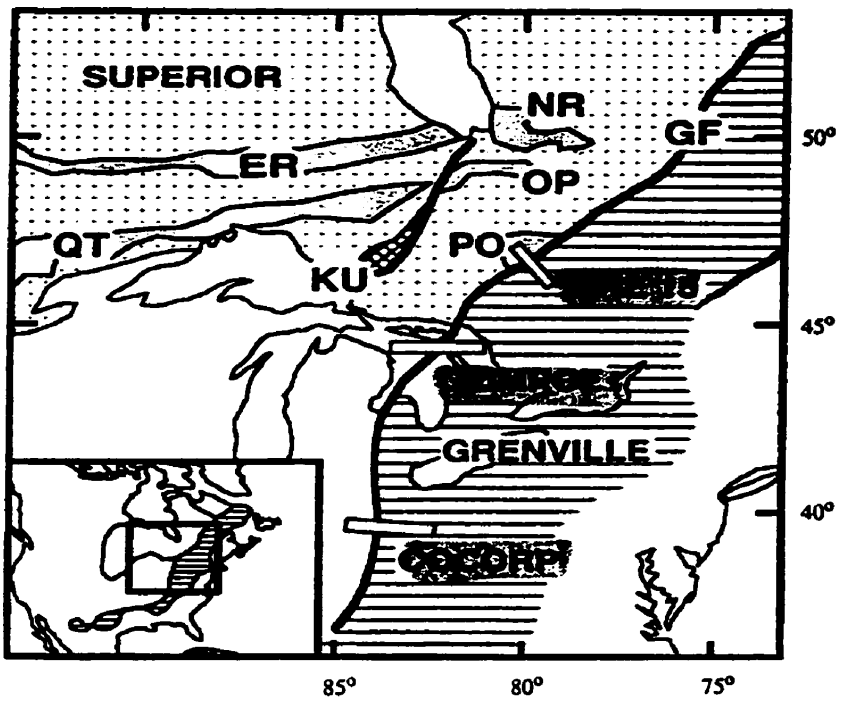

Figure 5.5 Location map of Abitibi-Grenville Lithoprobe line 15 (After Kellett et al., 1993).

reflectivity is more significant than dipping reflectors along profile 15 especially at depth (Figure 5.6) (Kellet et al., 1993). At shallow depth, the Grenville Front is characterized by steep reflectors. Gently dipping faults mark the mid-lower crustal features in the Grenville front zone.

The preliminary velocity model along profile AB was obtained by Miao (1995) using the same seismic refraction data. The Pg phases were, however, not considered in the

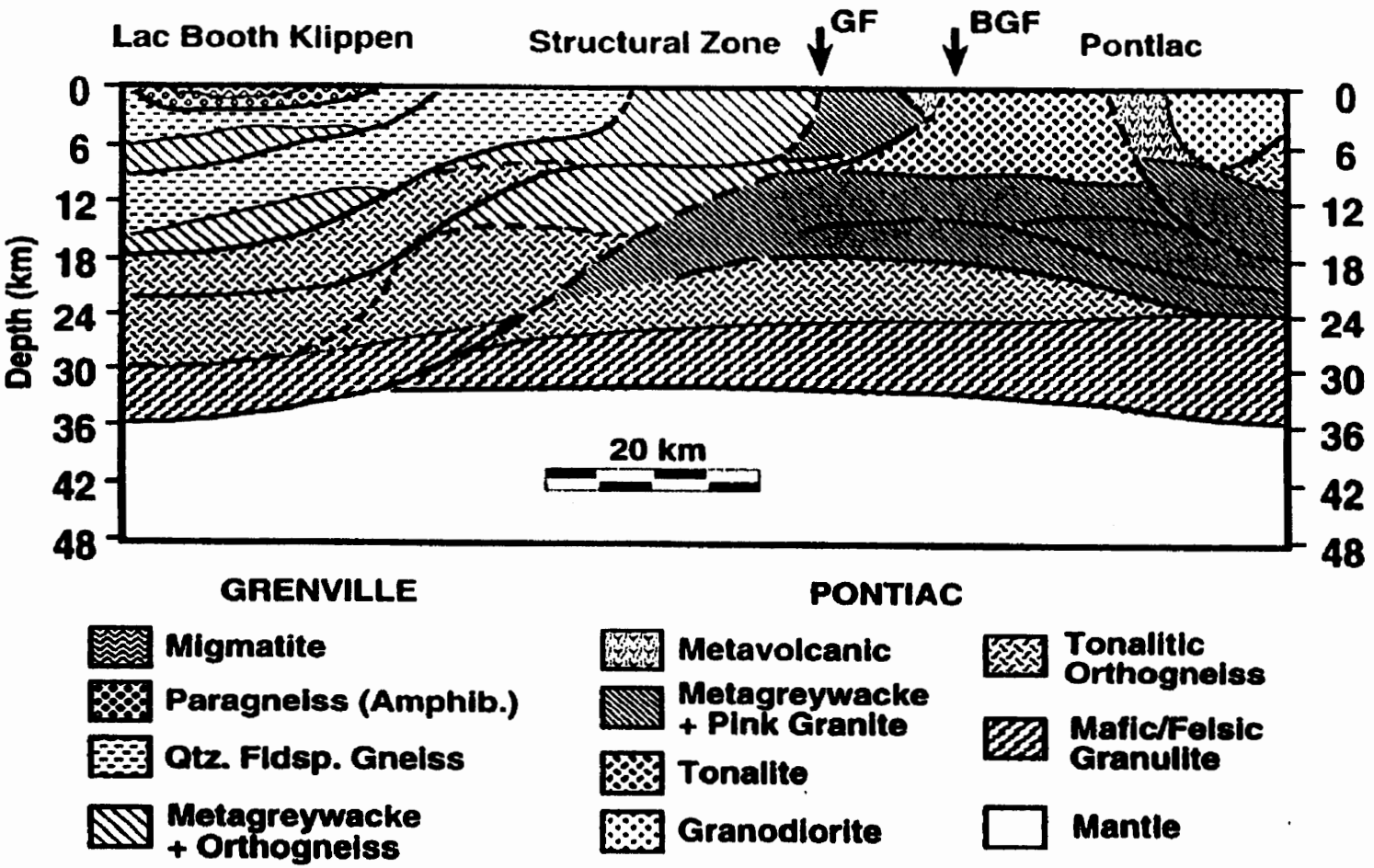

Figure 5.6 Geological section interpreted by a combination of seismic reflection data from line 15 and gelogical information (Kellett et al., 1993).

modeling. Horizontal interfaces in the middle and lower crust were determined in the Archean and Southern provinces (Figure 5.7). Four dipping layers truncating horizontal boundaries under the Grenville Front were responsible for the shingle events observed on profile AB (Figure 5.7). The anomalous velocity body near the surface under the Sudbury Basin was also modeled along both profiles and interpreted as the Sudbury Igneous Complex. This preliminary model is referred to as the initial model for detailed modeling and interpretation in this thesis.

5.2.2 Seismic Refraction Data Processing and Displaying

The seismic refraction data collected during the 1992 Lithoprobe seismic experiment were originally processed by Miao (1995). Miao first converted the data from SEGY format into IT&A INSIGHT format. Then, the seismograph clock errors, which were stored in a header file, were corrected on all traces. In addition, the S/N ratio was improved by applying 8-35 Hz bandpass filtering, median filtering, automatic gain-control (with a 0.8 s time window) and spectral balancing (with a 0.5 s sliding time window). High-frequency electric-storm noise and the air wave in the near-shot traces were thus suppressed and the subsequent reflection and refraction events were enhanced (Miao, 1995).

The seismic data in a time recording range of -5 to 55 s were firstly displayed as reduced time sections with a 8 km/s reducing velocity presented in the survey report (Irving et al., 1993). Miao plotted the processed seismic sections using a 6.8 km/s approximate reducing velocity corresponding to the average velocity in the lower crust rather than 8 km/s because a seismic section with a 6.8 km/s reducing velocity can reveal significant intermediate reflections as well as deep Moho events significantly. Therefore, the 6.8 km/s reducing velocity is applied to plot seismic sections of the Sudbury seismic refraction data

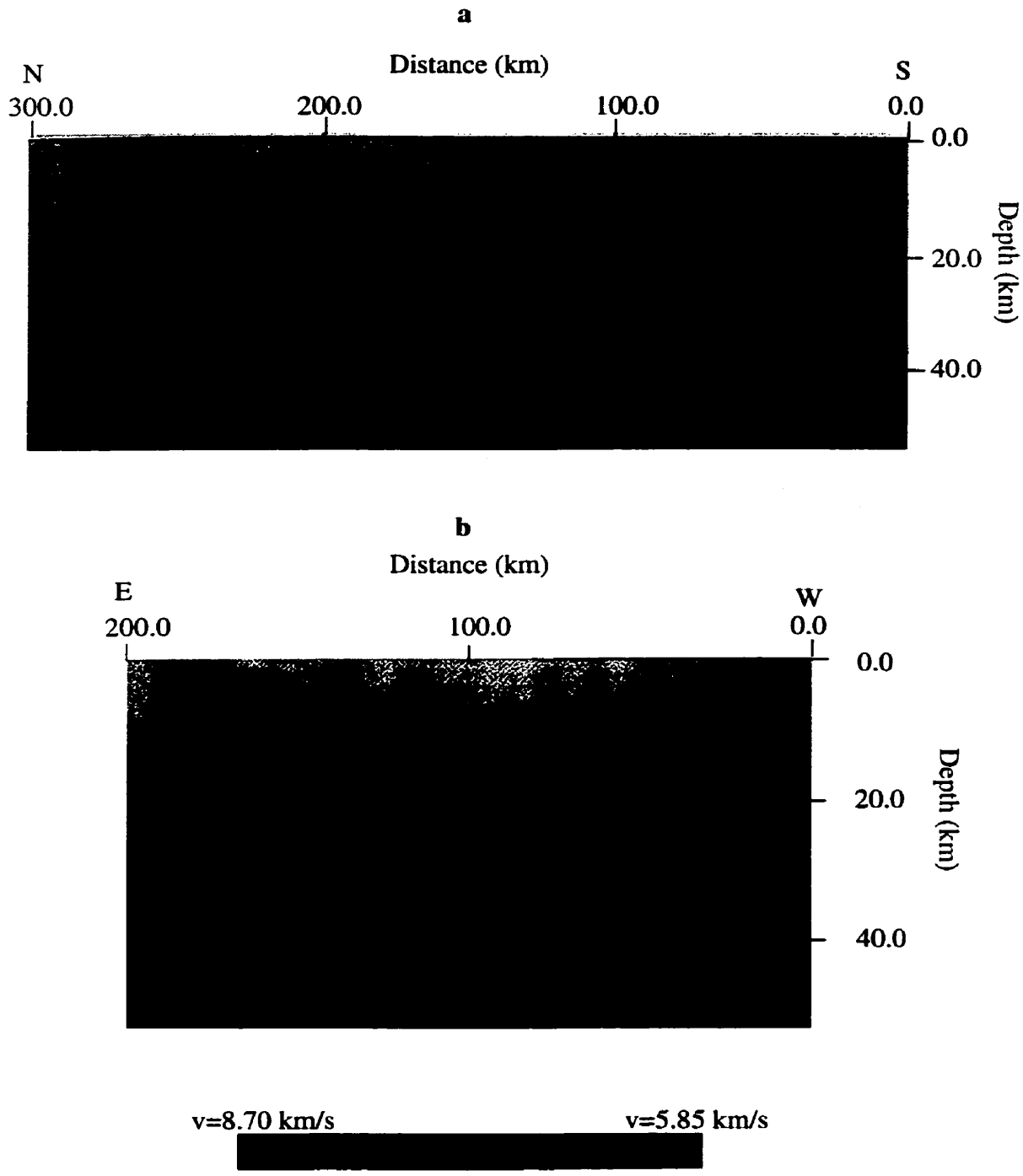

Figure 5.7 Velocity models along profiles AB (**a**) and XY (**b**) from the 1992 Lithoprobe seismic refraction survey across Sudbury (After Miao,1995).

in this thesis.

The amplitude of the seismic data was normalized according to all traces of a section rather than being equalized on each trace as done by Miao (1995). The amplitude on each trace in a section was normalized by the specific amplitude value obtained by averaging all amplitudes of whole section data, excluding the maximum and minimum values of the amplitude. The normalized seismic section can then be used to compare the observed energy on the synthetic seismogram.

The seismic sections were displayed in wiggle mode superimposed on a variable area mode commonly used in displaying seismic refraction sections. A postscript code was created by a computer program developed in the thesis work, to precisely display seismic data. Ten seismic sections from shots ab0 to ab10 are plotted in Figures 5.8-5.17. The vertical axis in a seismic section represents the reduced time in seconds and the horizontal axis refers to distance in kilometers corresponding to the distance between shot ab0 and the receiver.

5.2.3 Seismic Phase Analysis

Seismic wide-angle reflection and refraction data are commonly analyzed and modeled according to "identifiable and laterally coherent" (Zelt and Forsyth, 1994) phase events correlated over a number of traces in each section. In traditional refraction terminology, Pg represents P waves that reflect or refract/turn in the upper crust; Pc represents P waves which refract/turn at the mid-crustal interface; and Pn represents P waves that refract/turn at the Moho discontinuity which separates the crust and upper mantle. PcP and PmP represent reflections that reflect at the mid-crustal and Moho boundaries respectively. Pr, as used in this thesis, denotes a strong reflection coherent in a limited number of traces,

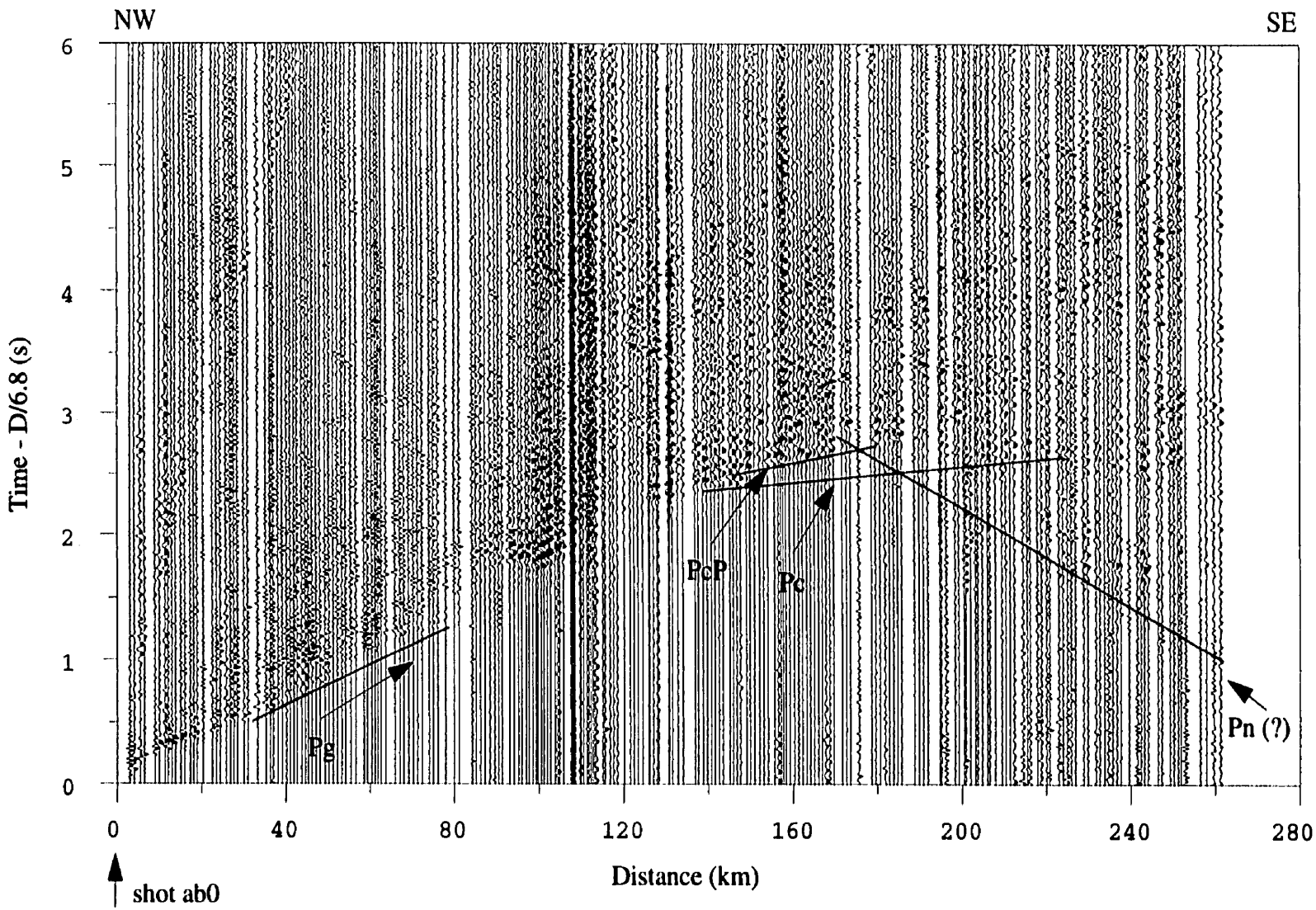

Figure 5.8 Wide-angle seismic reflection and refraction section for in-line ab0.

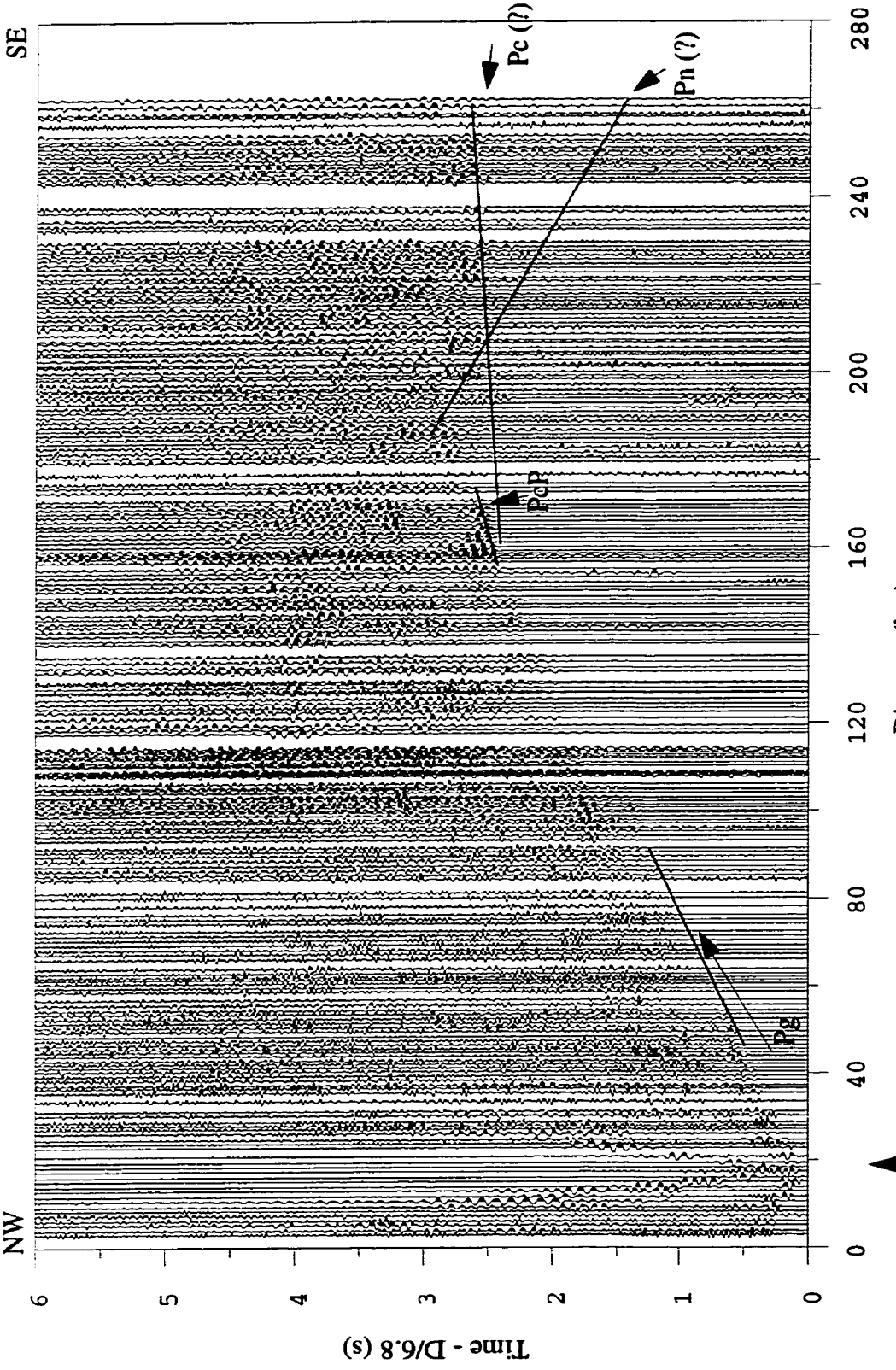

Figure 5.9 Wide-angle seismic reflection and refraction section for in-line ab1.

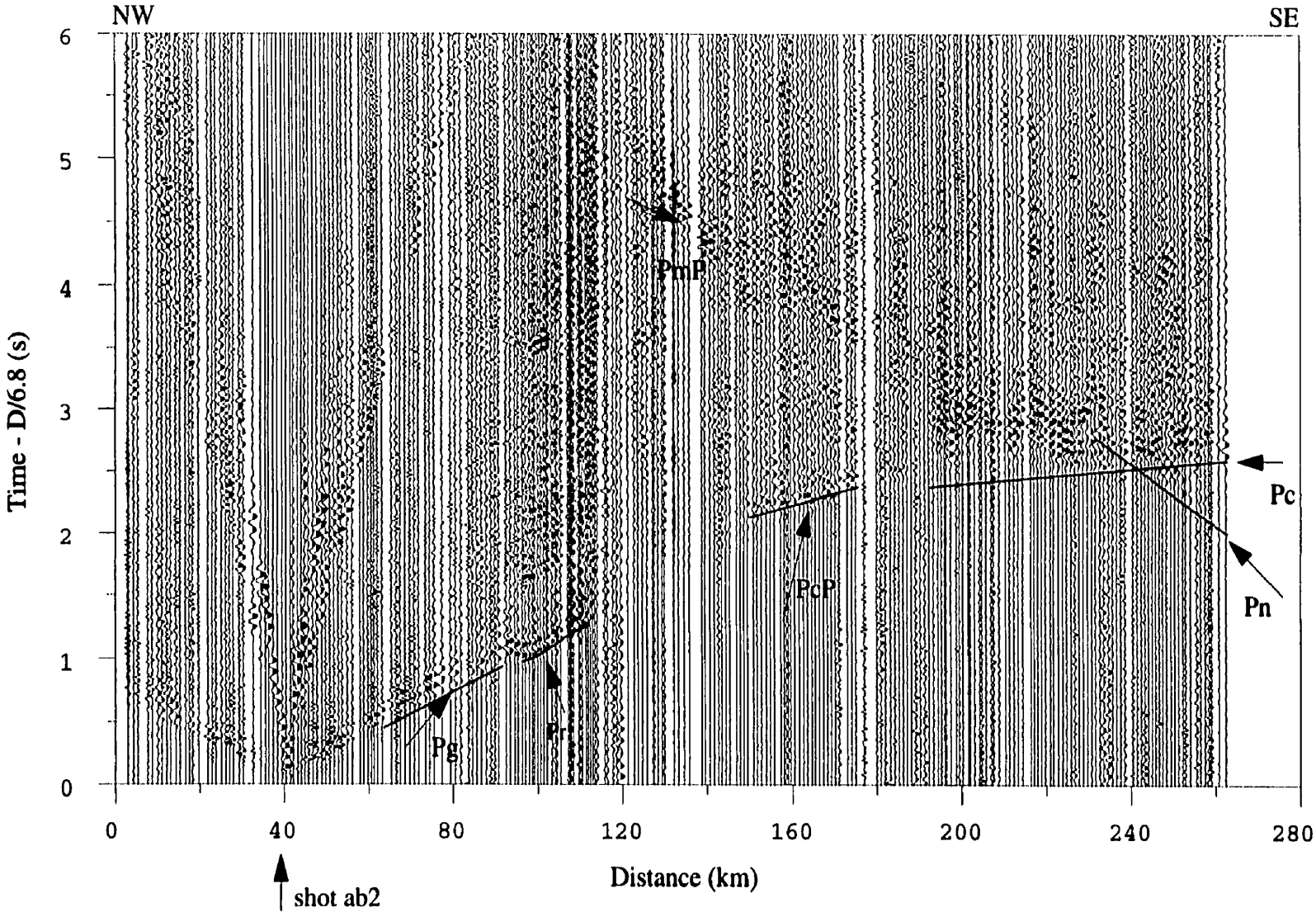

Figure 5.10 Wide-angle seismic reflection and refraction section for in-ine ab2.

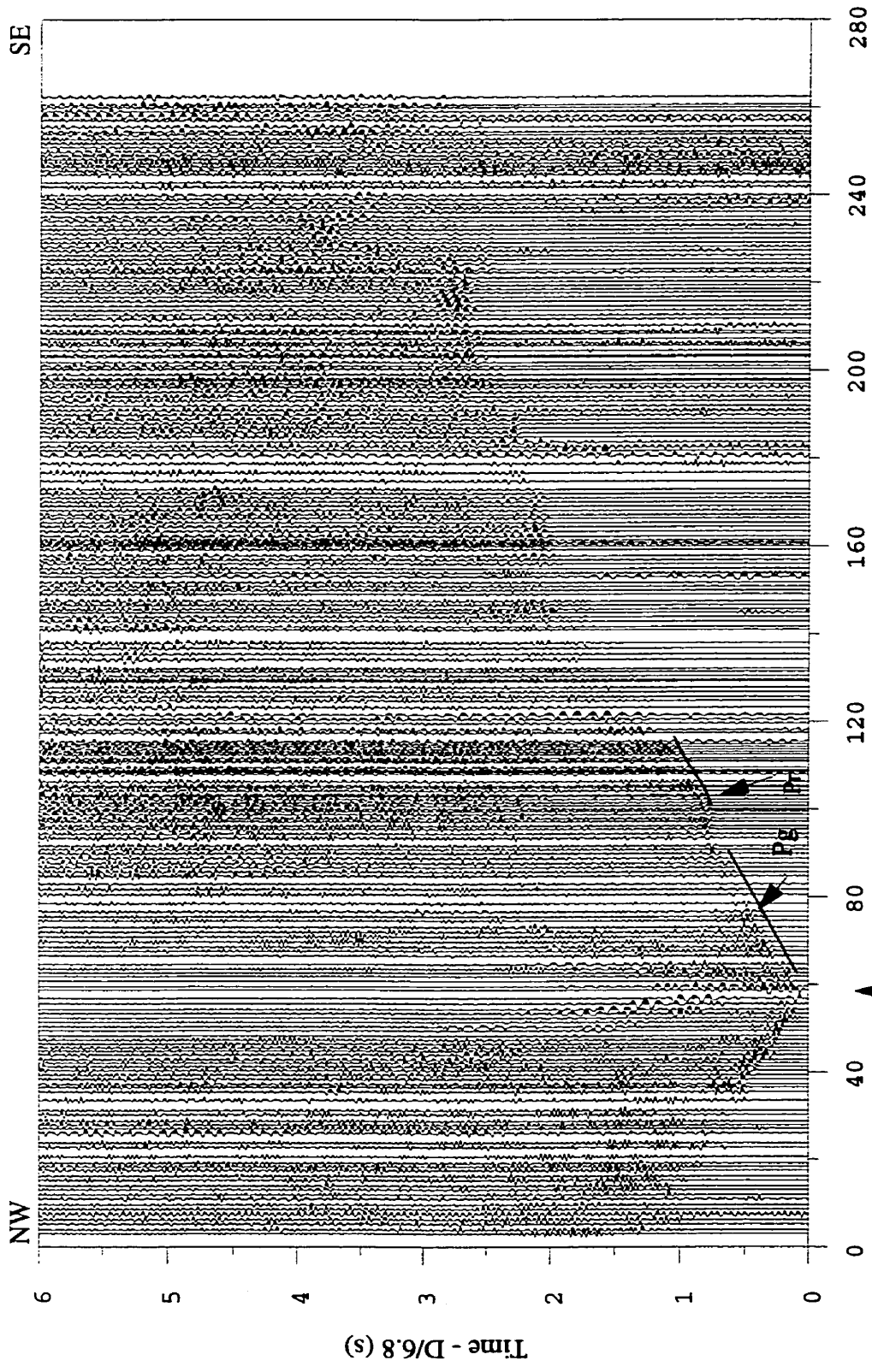

Figure 5.11 Wide-angle seismic reflection and refraction section for in-line ab3.

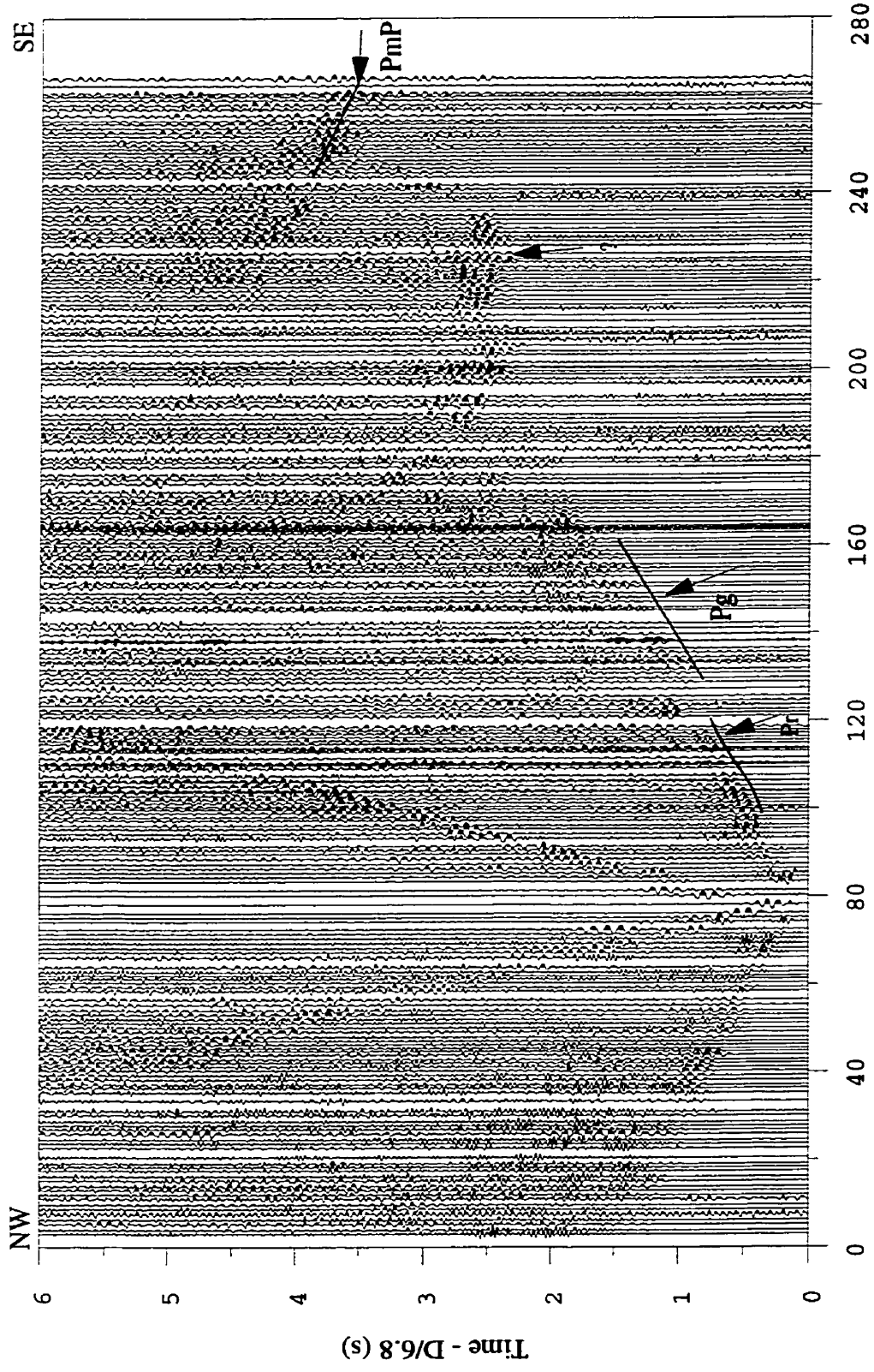

Figure 5.12 Wide-angle seismic reflection and refraction section for in-line ab4.

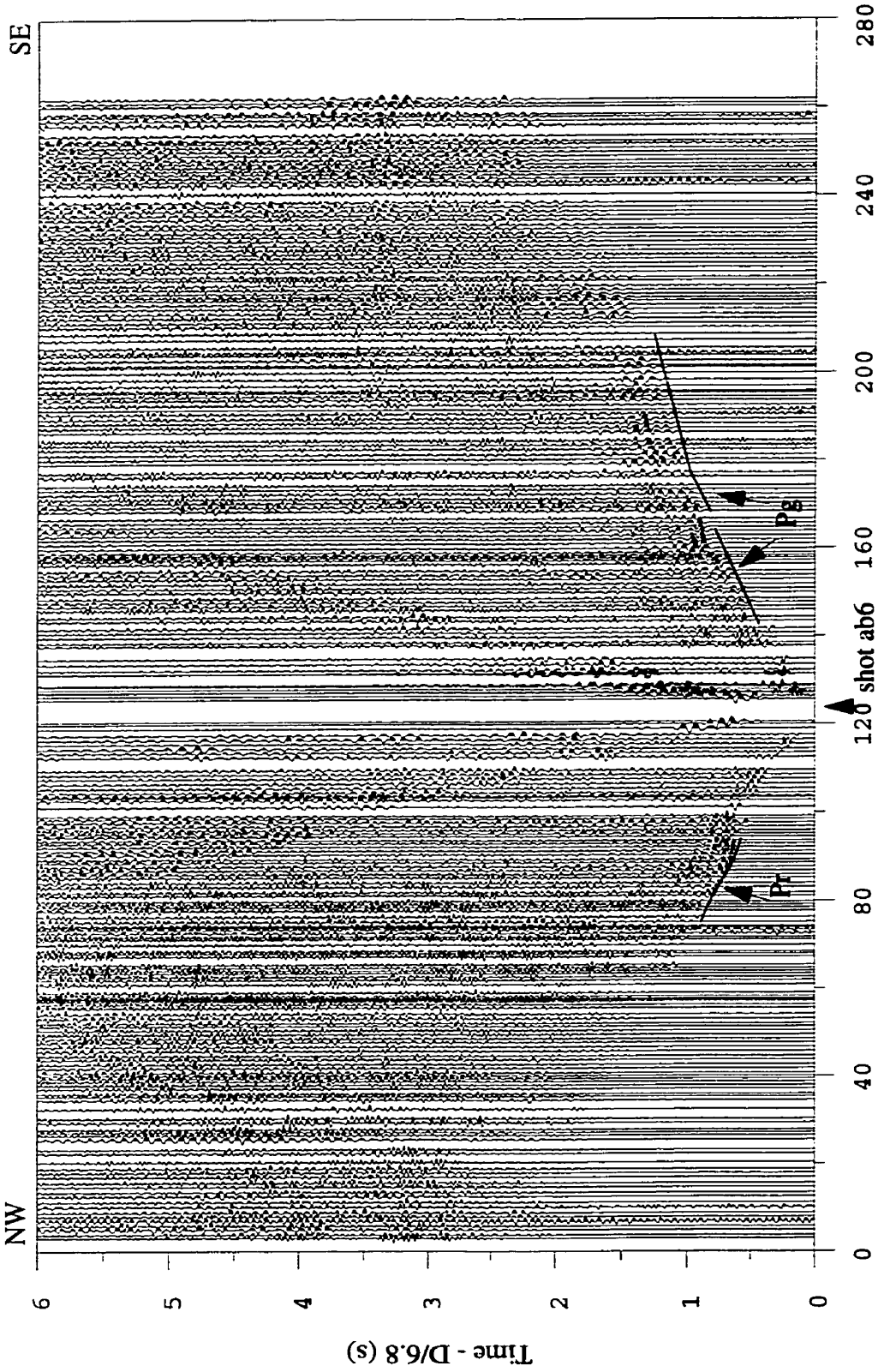

Figure 5.13 Wide-angle seismic reflection and refraction section for in-line ab6.

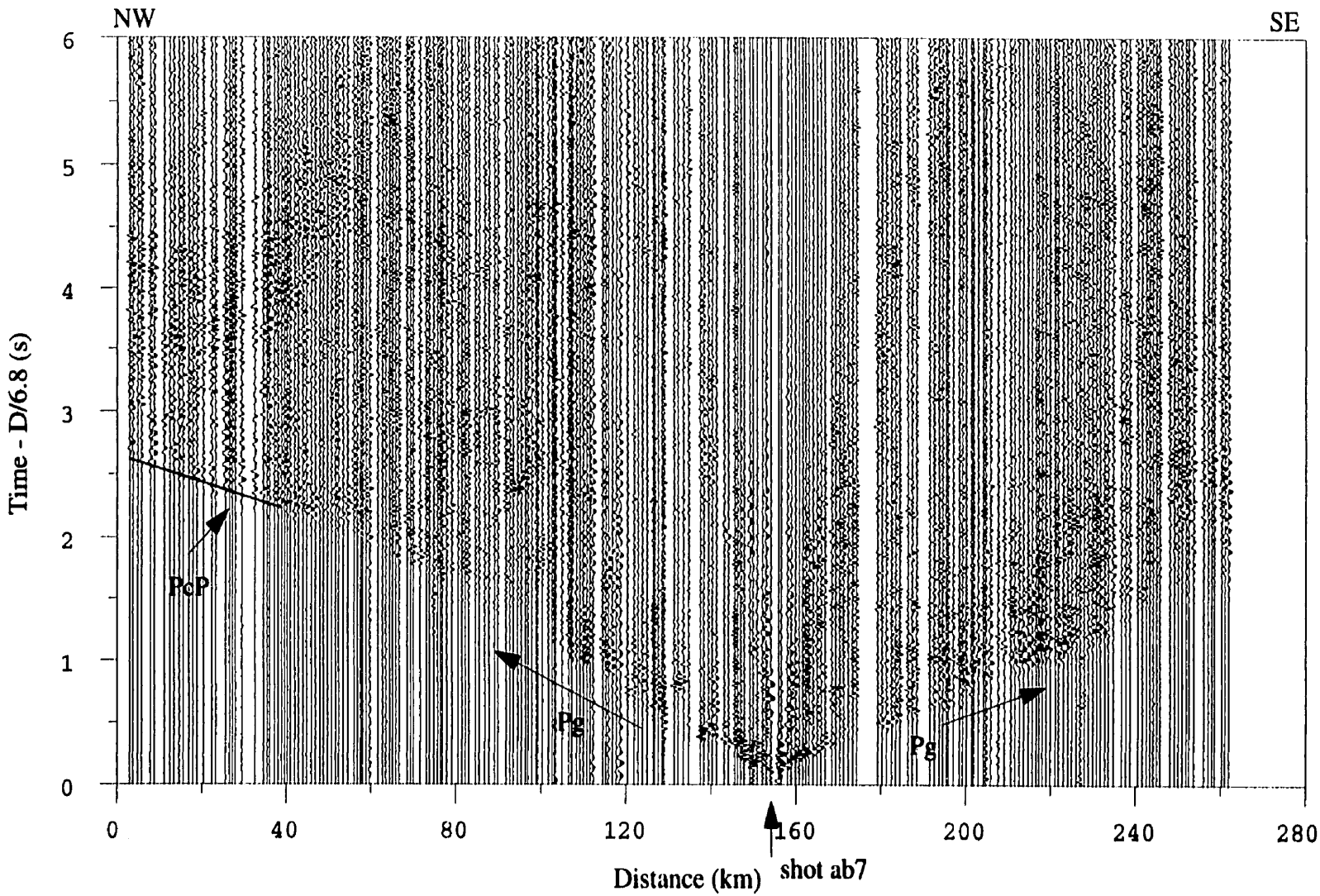

Figure 5.14 Wide-angle seismic reflection and refraction section for in-line ab7.

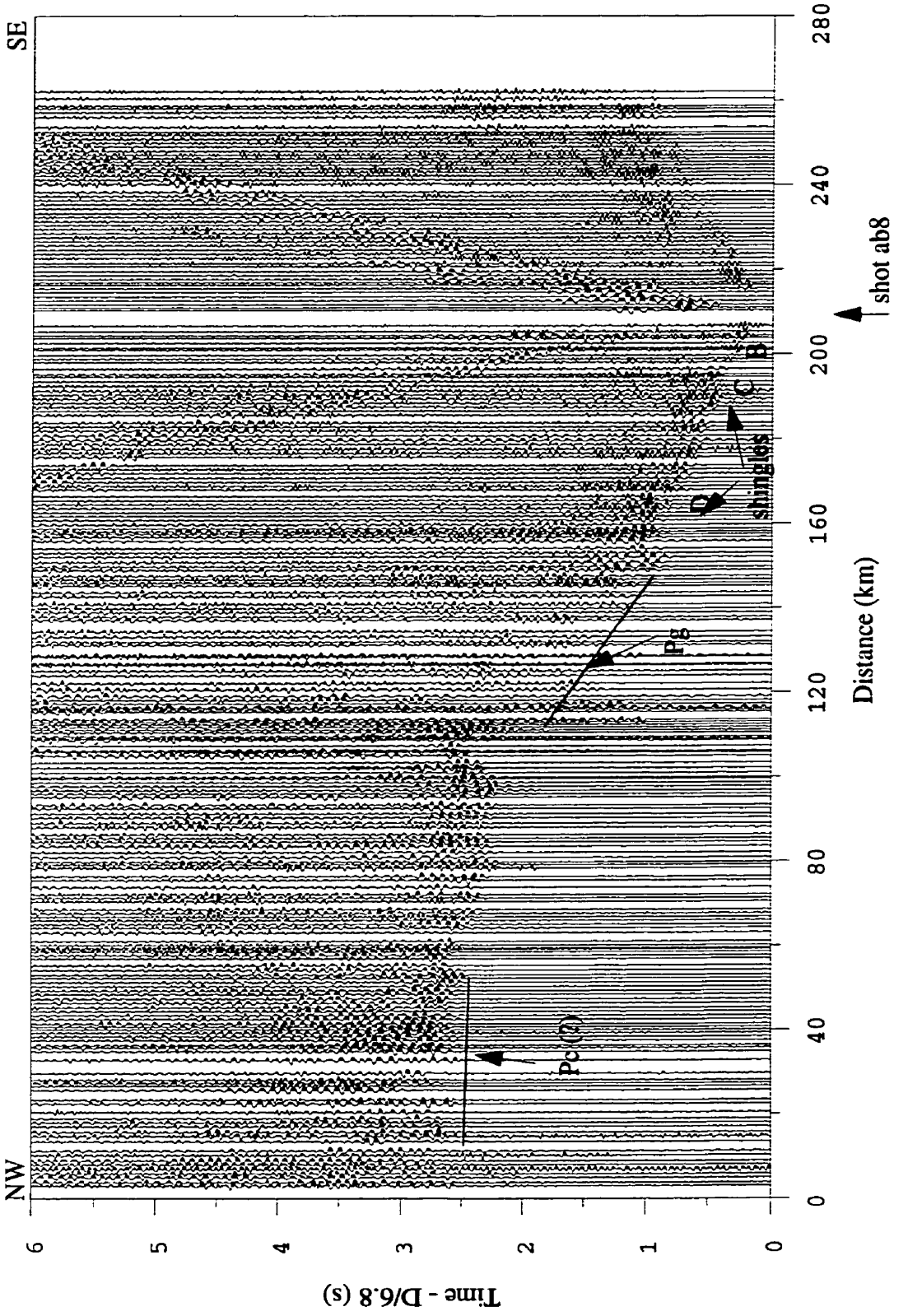

Figure 5.15 Wide-angle seismic reflection and refraction section for in-line ab8.

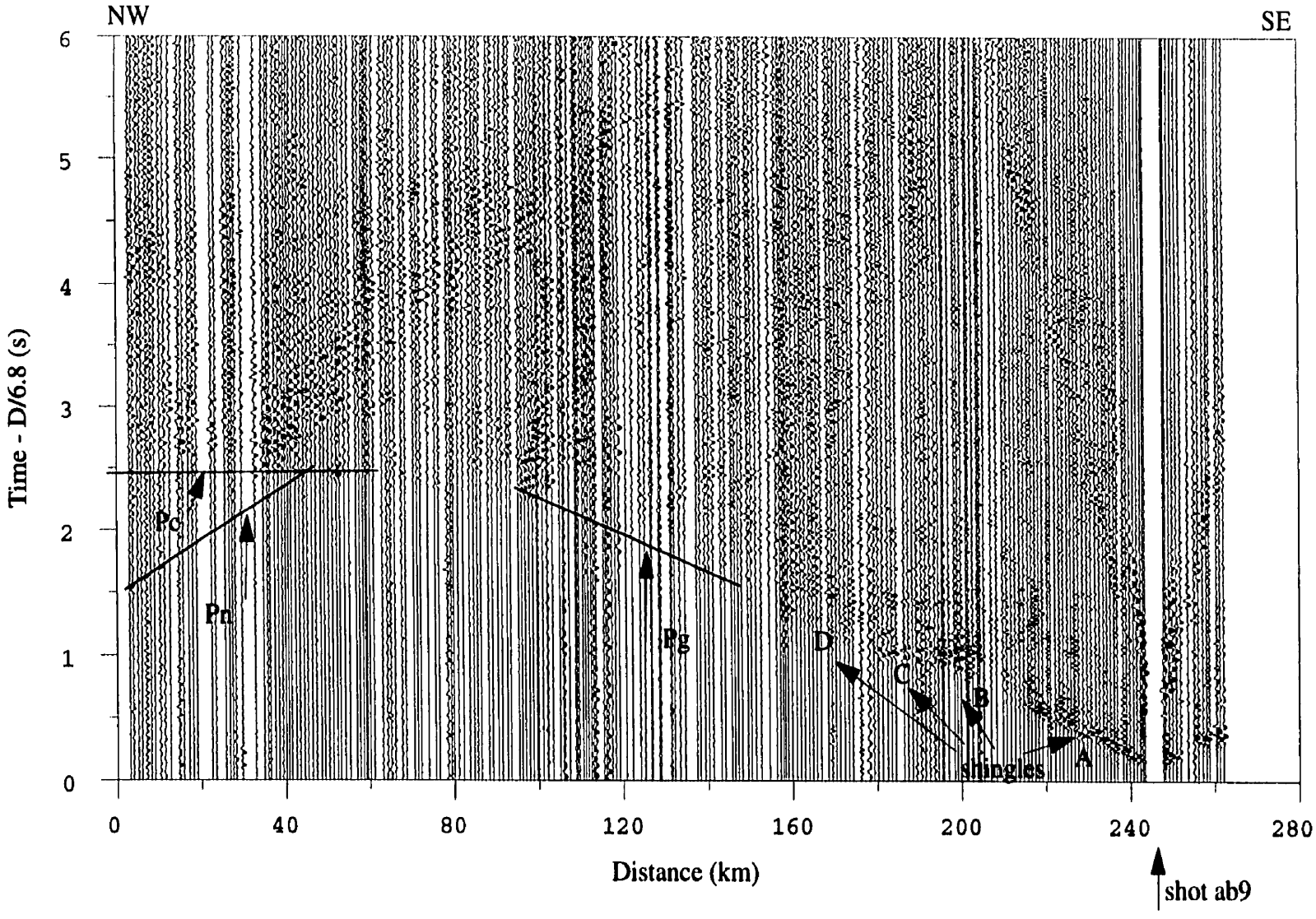

Figure 5.16 Wide-angle seismic reflection and refraction section for in-line ab9.

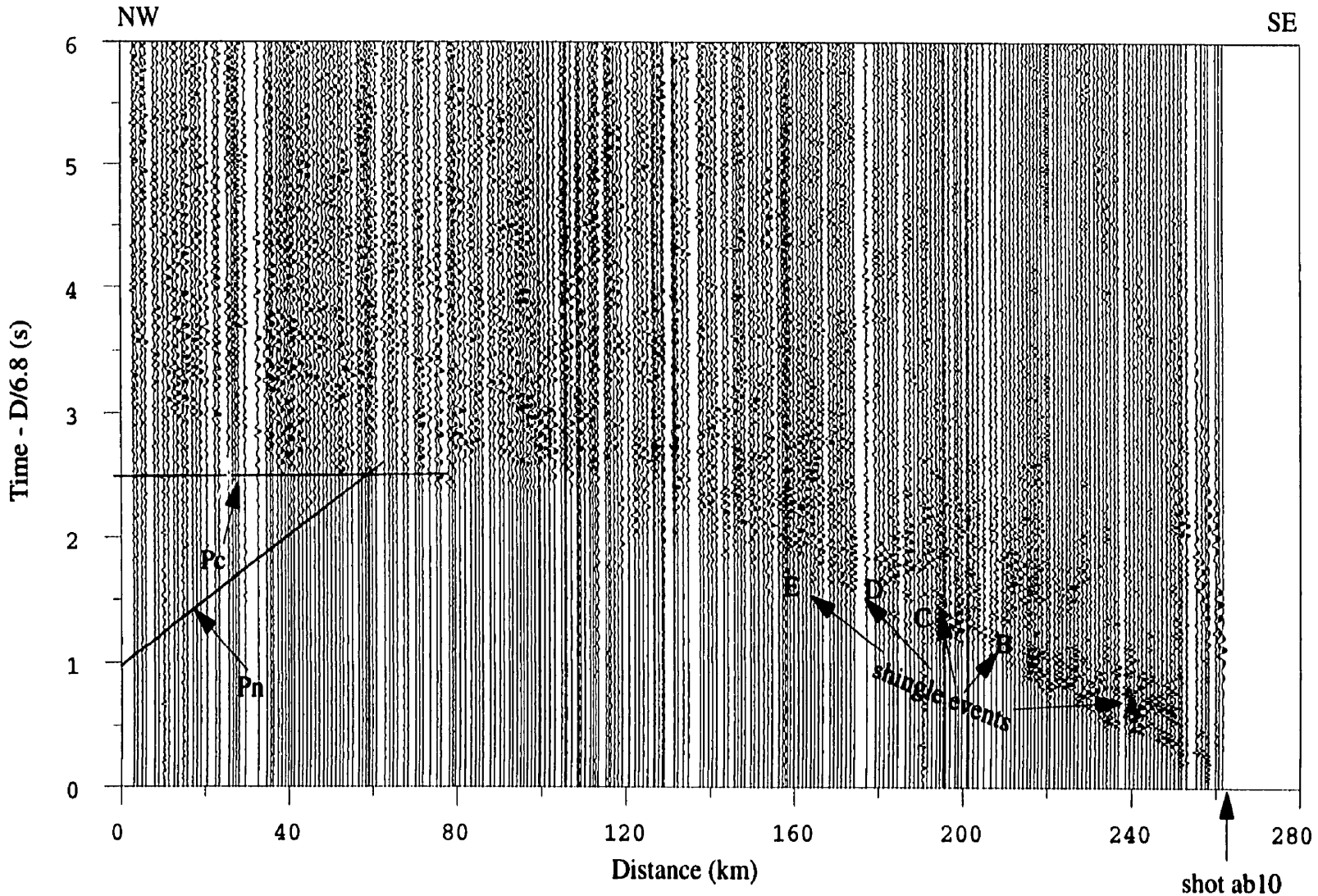

Figure 5.17 Wide-angle seismic reflection and refraction section for in-line ab10.

arising from reflections off small-scale structural interfaces such as structural boundaries and faults with high reflectivity. The reflected and refracted waves are generally correlated across shot sections. However, Pr events might not be identifiable from section to section because they represent small-scale phenomena.

1. Pg Phase

First arrivals at near offsets are Pg phases which travel along the near-surface low-velocity layer which is referred to an area extending from the surface to several kilometers deep. The maximum offset (distance between receiver and corresponding shot) at which Pg phases appear and the variation of the apparent velocity depend on the velocity structure and thickness of this layer.

The Pg phase has a relatively high S/N ratio at near offsets less than 80 km for shot ab0, whereas, the S/N ratio is low beyond the offsets of 80 km because of noise contamination (Figure 5.8). The energy of Pg phases is strong at offsets less than 40 km. This feature appears on most of the sections except shots ab9 and ab10. The amplitude of Pg wave suddenly drops at distances of 80-95 km. This decrease must relate to the local shallow low-velocity structure.

There are significant anomalous reflections coherent over a few traces identified on shots ab2, ab3, ab4 and ab6 (Figures 5.10-5.13). Strong Pg phases (or Pr discussed later in this section) could relate to a local reflective structure. For shot ab2, such event appears at offsets between 50 and 65 km on the right side of the shot point. It was detected at offsets of 35 to 50 km for shot ab3. For shot ab4, the reflection with strong energy was observed at receiving offsets of 15-40 km in the southwest. However, the reflection was found at a 90 km distance for shot ab6. On the basis of an analysis of the reflection, the location of

the structure corresponding to the strong anomalous reflection was inferred to be at a distance of ~100 km from shot ab0, corresponding to the location of the Sudbury Basin. Hence, the strong reflection could be associated with the Sudbury Structure, especially the Sudbury Igneous Complex.

Figures 5.15-5.17 (shots ab8, ab9 and ab10) reveal a number of interesting events which form a "shingle-like" pattern. The "shingle-like" pattern can be observed clearly at offsets of 0-100 km (Figure 5.17). Shingle events A, B and C are characterized by the block distribution of the amplitude energy. Each reflection event has a non-uniform energy, which implies that each velocity layer might be heterogeneous. Events A-D are also evident on sections of shots ab8 and ab9 at offsets less than 80 and 40 km respectively (Figures 5.15 and 5.16). Event E is not as clearly observed as the other events. This "shingle-like" pattern was observed on profile J of the GLIMPCE experiment (Epili and Mereu, 1991). Mereu et al. (1990) analyzed these events and suggested that the shingles resulted from a group of shear zone structures in the Grenville Province overlying the Southern Province. Epili and Mereu (1991) modeled a group of six dipping reflectors to correspond to the shingle patterns (Figure 5.4b).

The apparent velocity of the Pg phase is approximately 5.82-6.32 km/s. At near offsets (<10 km), the apparent velocity ranges from 5.82 to 6.27 km/s, whereas at far offsets (20-80 km), the apparent velocity is in the range of 5.83-6.32 km/s. This variation of apparent velocity indicates a thin low-velocity layer overlying a high-velocity basement. At near offsets (<5 km), northwest of shot ab6, the apparent velocity is approximately 5.82 km/s. At far offsets (15-75 km), the apparent velocity is 5.88-5.97 km/s. These apparent velocities are smaller than those estimated for the northern end of the profile, which indicates a relatively low-velocity structure near the surface at distances between 100 and 120 km. At

far offsets (35-80 km), southeast of shots ab6 and ab7, the apparent velocity ranges from 5.83 to 6.32 km/s. The variation of the apparent velocity between both sides of shot ab6 for a constant offset indicates that the velocity in the northwest is lower than in the southeast. The analysis of the apparent velocity yields an estimate of the velocity in the first layer of ~6.0 km/s.

2. PcP Phase

Although the PcP phase represents a weak lateral arrival, it can be observed clearly on shots ab0, ab1, ab2, ab4 and ab7 (Figures 5.8-5.10, 5.12 and 5.14). Shot ab0 reveals the PcP reflection at distances of 150-180 km. It appears at distances between 160 and 180 km on shot ab1. Strong reflections between 150-190 km indicate PcP events on shot ab2. A PcP reflection also appears at a distance of ~40 km for shot ab7 (Figure 5.14). The apparent velocity estimated from shots ab0, ab1, ab2 and ab7 ranges from 6.15 to 6.28 km/s at offsets of 122-172 km. The small variation in apparent velocity implies that there is little lateral variation in the upper crust. Using these values, the velocity in the upper crustal layer could be initialized to be 6.1 km/s at the top and 6.28 km/s at the bottom. The close apparent velocity estimates indicate that the upper crust varies less in velocity and geometry than the shallow layer previously discussed.

3. Pc Phase

The Pc phase is the weakest event observed. Two first arrival events related to Pc are identified for shots ab0 and ab8 (Figures 5.8 and 5.15). The apparent velocity is approximately 6.6 km/s for shot ab0, and 6.48 km/s for shot ab8 at the same offset. The apparent velocity of Pc phases at these offsets represents the velocity at the top of the lower crust in

the northern part of the profile. Therefore, the velocity at the top of the lower crustal layer was constrained to be between 6.48 and 6.6 km/s. Although only two sections recorded a weak Pc phase, the existence of this event is verified by the synthetic seismogram.

4. PmP Phase

The PmP phase is a strong, later arrival which is seen clearly on the section for shot ab2 (Figure 5.10). A coherent PmP phase with large amplitude is observed at offsets of 140-190 km for shot ab4. The apparent velocity was estimated from shot ab2 to be ~6.97 km/s. The velocity model along profile J gave a velocity of 6.9 km/s at the base of the crust. Hence, a velocity within the range of 6.9-6.97 km/s was considered as an initial value for the velocity at the bottom of the crust.

5. Pn Phase

The Pn phases are clearly observed as the first arrivals on sections of shots ab2 and ab10 at offsets greater than ~205 km (Figures 5.10 and 5.17), suggesting a crustal thickness of ~40 km. For shot ab2, the first arrival at the far offset of 205 km is identified as Pn phase. The event is coherent over 10 traces to the 215 km offset. The arrivals could not be traced at distances greater than 215 km because of noise contamination. For shot ab10, the Pn arrivals are recorded clearly at offsets between 209 km and 233 km. The apparent velocity estimated from shot ab2 (at 222 km distance) was ~8.1 km/s and from shot ab10 (at 212 km distance) it was ~8.0 km/s. The value of 8.04 km/s for the apparent velocity was then applied in estimation of the velocity of the upper mantle.

6. Pr Phase

There is a special reflection, Pr, recorded as the first arrivals at certain offsets for shots ab2, ab3 ab4, southeast of the shot points and for shot ab6, northwest of the shot point (Figures 5.10-5.13), which was described above in details in the analysis of the Pg phase. The apparent velocity for these small-scale structures could not be determined accurately from the phase analysis. The velocity of the anomalous body responsible for the Pr phase might be estimated by assuming that the strong Pr reflection is related to the Sudbury Igneous Complex. The well-log velocity data and measurement of sample rocks suggested that the velocity of the Sudbury Igneous Complex is in a range of 6.2 to 6.5 km/s (Table 3.1) (Salisbury et al., 1994). Therefore, the initial velocity of this anomalous body is taken to be ~6.4 km/s. There is also a strong reflection observed at distances of 180-230 km and marked by a question mark in Figure 5.12. As this reflection is observed on only one section, it could relate to a strong local reflective structure possibly located off the survey line. Therefore, there will be no further modeling of this event in this thesis.

5.2.4 Modeling Procedure

The model parameterization was done first by referring to apparent velocity analysis and the previous studies of Sudbury and surrounding areas (Epili and Mereu, 1991; Miao, 1995). The traveltimes were then computed according to the given model. The model parameters were adjusted until the desired agreement between the observed and calculated traveltime was obtained. Then, the amplitudes between the observed and calculated phases were compared and the model parameters adjusted to obtain a good fit. Thus, the velocity and geometry model along profile AB was determined. The forward modeling is straight

forward. The first step is to give an initial model according seismic phase analysis and previous study results. Then the forward modeling is performed. On the basis of the variation between the observed and calculated traveltimes, a modification of the model is the third step. The fourth step is to repeat the second and third steps until one obtains a desired misfit between the observed and calculated traveltimes. A slight modification is required to adjust the calculated amplitude to match the observed.

In this section, the modeling results will be discussed after a description of the model parameterization.

1. Model Parameterization

The velocity model was parameterized mainly on the basis of the apparent velocity analysis, the preliminary velocity model in Sudbury obtained by Miao (1995) and the velocity model along profile J (Epili and Mereu, 1991). The characteristics of Pg phases analyzed above indicate that the near-surface low-velocity layer is very shallow. The depth of the base of this layer is in the range of ~0.3 to ~1.0 km (and it has a velocity of 6.0 km/s). Its greatest thickness is at a distance of 100 km. There is a rhomboid-shaped high-velocity body suggested by unusually strong reflections corresponding to the Sudbury Igneous Complex (Miao, 1995) at a location of 100 km distance and 5 km depth (with a velocity of 6.4 km/s). PcP and Pc phases suggest an interface separating the upper and lower crust in the northern part of the profile. The depth of the interface at the northern part of the profile (~17 km) was based on the velocity model obtained by Epili and Mereu (1991). The velocity of the upper crustal layer was defined to be 6.1 km/s at the top and 6.3 km/s at the base. The Moho discontinuity dips towards the southeast as interpreted by Epili and Mereu (1991) and Miao (1995). The velocity of the lower crustal layer in the

northwestern part of the profile was defined to be 6.6 km/s at the top and 6.92 km/s at the base. The velocity of the upper mantle was taken as 8.06 to 8.10 km/s. In the southeastern part of the profile, five southeast-dipping layers constitute the complex stacked-sheet crustal structures beneath the Grenville Front Tectonic Zone and the Grenville Province. The existence of the five layers is based on the observation of the shingle events and is a little different from the four layers suggested by Miao in 1995 (Figure 5.7). The dipping layers truncate the subhorizontal middle crustal boundary in the north at the Grenville Front.

The following subsections discuss the modeling results according to near-surface, upper crustal, lower crust and dipping structures respectively. Figure 5.18 shows the initial model.

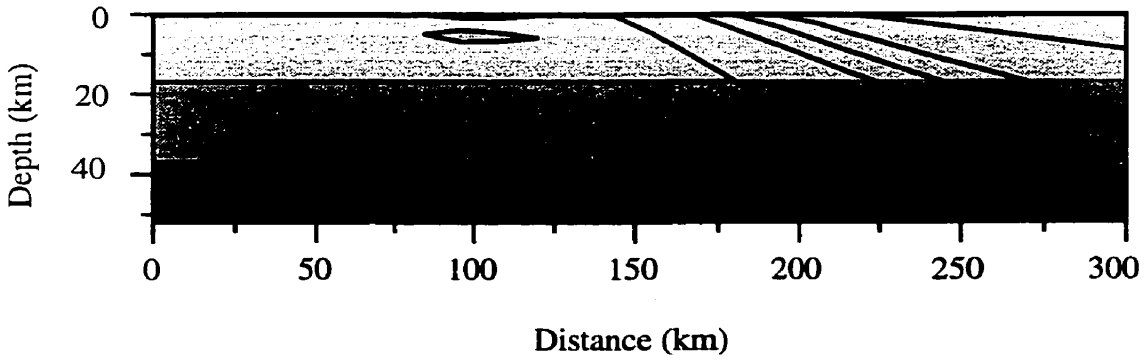

Figure 5.18 Initial velocity model along profile AB obtained by forward modelling. Solid lines represent the structural boundaries.

2. Near-surface Structure

The velocity within the near-surface layer and the interface geometry were constrained mainly using the Pg phases. During modeling, reflections, head waves and turning waves were used. For all shots, the observed and calculated traveltimes fitted very well (Figures 5.19a-5.28a). The line linked by circles in the figures represents the calculated traveltime corresponding to seismic reflections (Pg, PcP, Pc, PmP, Pn and Pr). The near-offset arrivals did not indicate large lateral variations of velocity near the surface. The depth to the interface increases gradually from ~0.2 km at two ends of the profile to ~1.0 km at the Sudbury Basin. At the northwestern and southeastern parts of the profile, the velocity in this layer is modeled as 6.09 km/s, whereas, at a distance of ~100 km the velocity decreases to 5.95 km/s. This velocity value is close to velocities of the sedimentary rocks of Chelmsford greywacke and Onwatin shale (5.16-5.91 km/s) of the Sudbury Basin. A comparison of Figure 5.18 and Figure 5.7 reveals the information added to the initial model on the basis of the present study.

3. Upper Crustal Structure

The velocity variations in the upper crust (between the near-surface low-velocity layer and the mid-crustal interface) were determined using mainly PcP phases and the turning rays of Pg phases recorded at far offsets. In the northwestern part of the profile, the velocity at the top of this layer was determined from the forward modeling to be 6.1 km/s (which was also found along profile J shown in Figure 5.4b). A velocity of 6.3 km/s was obtained at the bottom of this layer. The depth to the base or mid-crustal interface was determined to be ~17 km. The attitude of this interface is subhorizontal. The structural

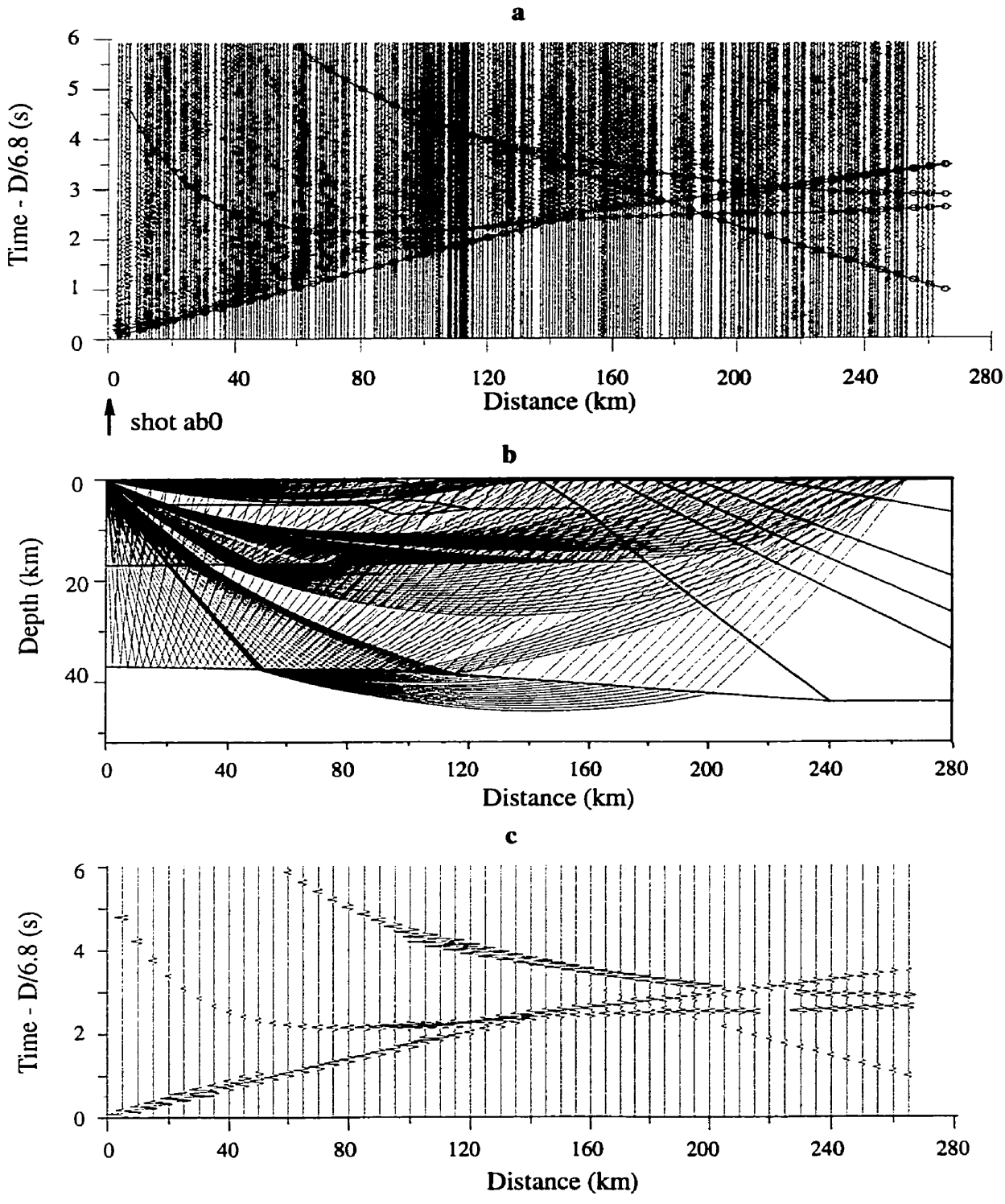

Figure 5.19 Wide-angle seismic reflection and refraction section for in-line ab0.
a: seismic section; **b**: ray path; **c**: synthetic seismogram.
⊖–⊖ : calculated traveltime.

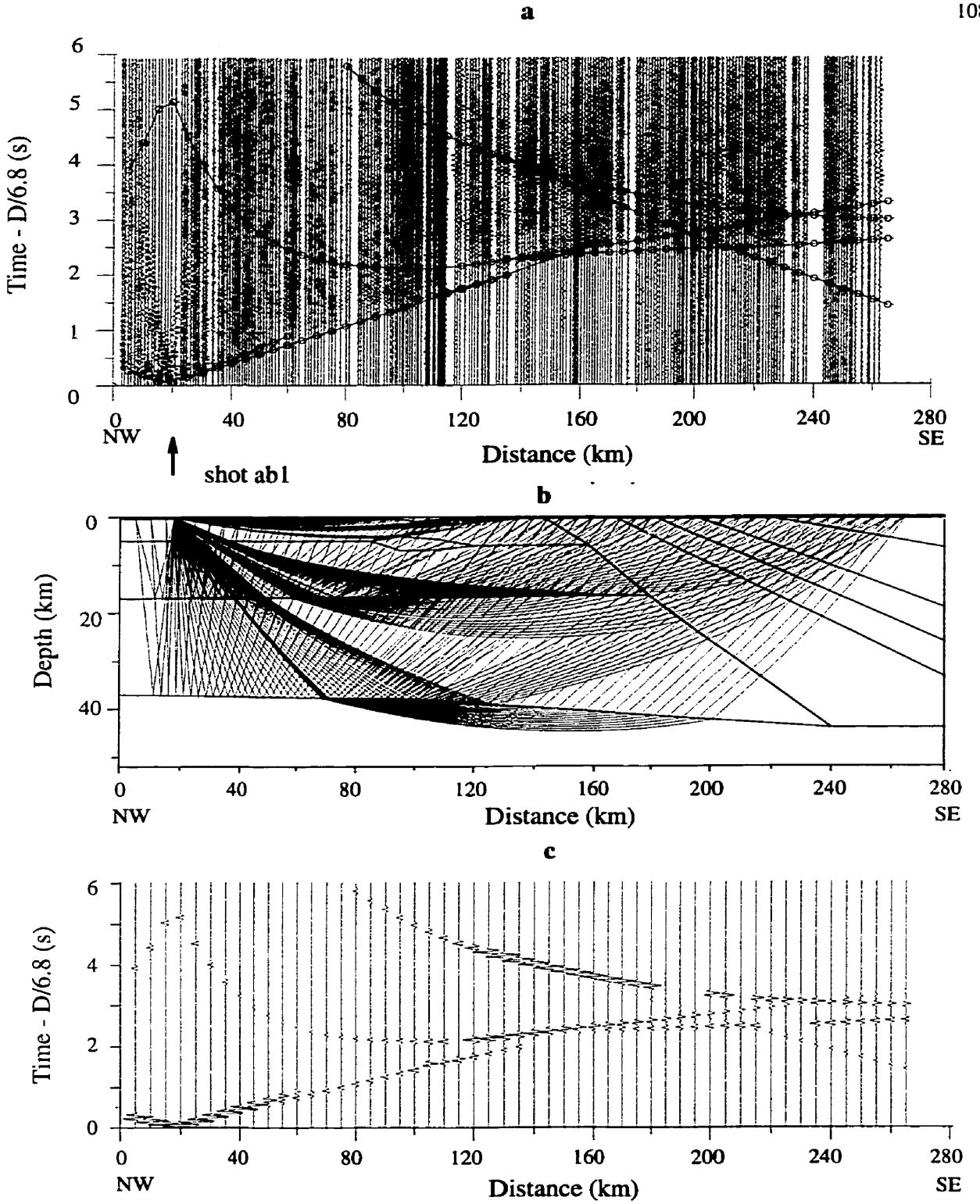

Figure 5.20 Wide-angle seismic reflection and refraction section for in-line ab1.
a: seismic section; **b**: ray path; **c**: synthetic seismogram.
⊖⊖ : calculated traveltime.

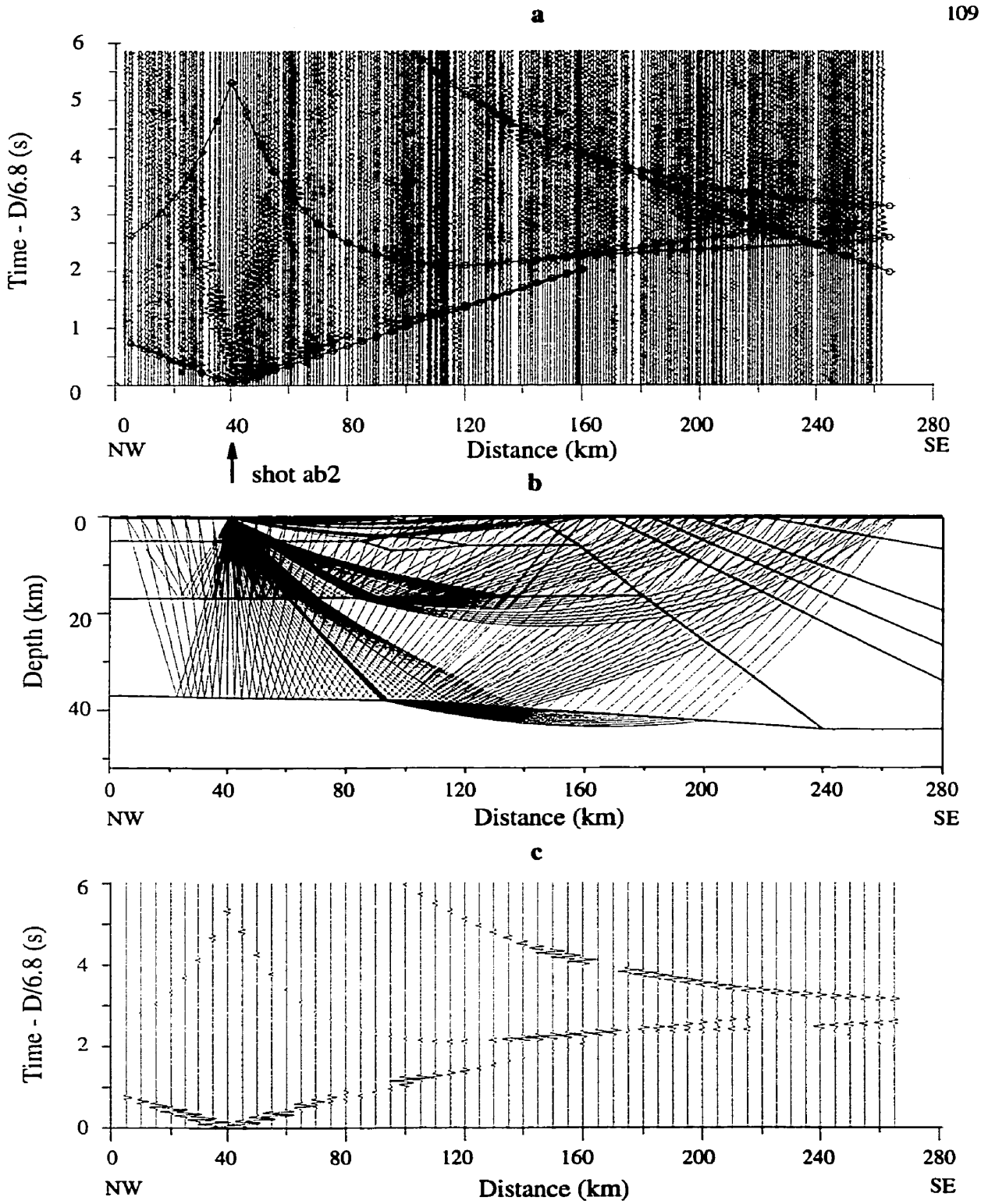

Figure 5.21 Wide-angle seismic reflection and refraction section for in-line ab2.
a: seismic section; **b**: ray path; **c**: synthetic seismogram.
⊖–⊖ : calculated traveltime.

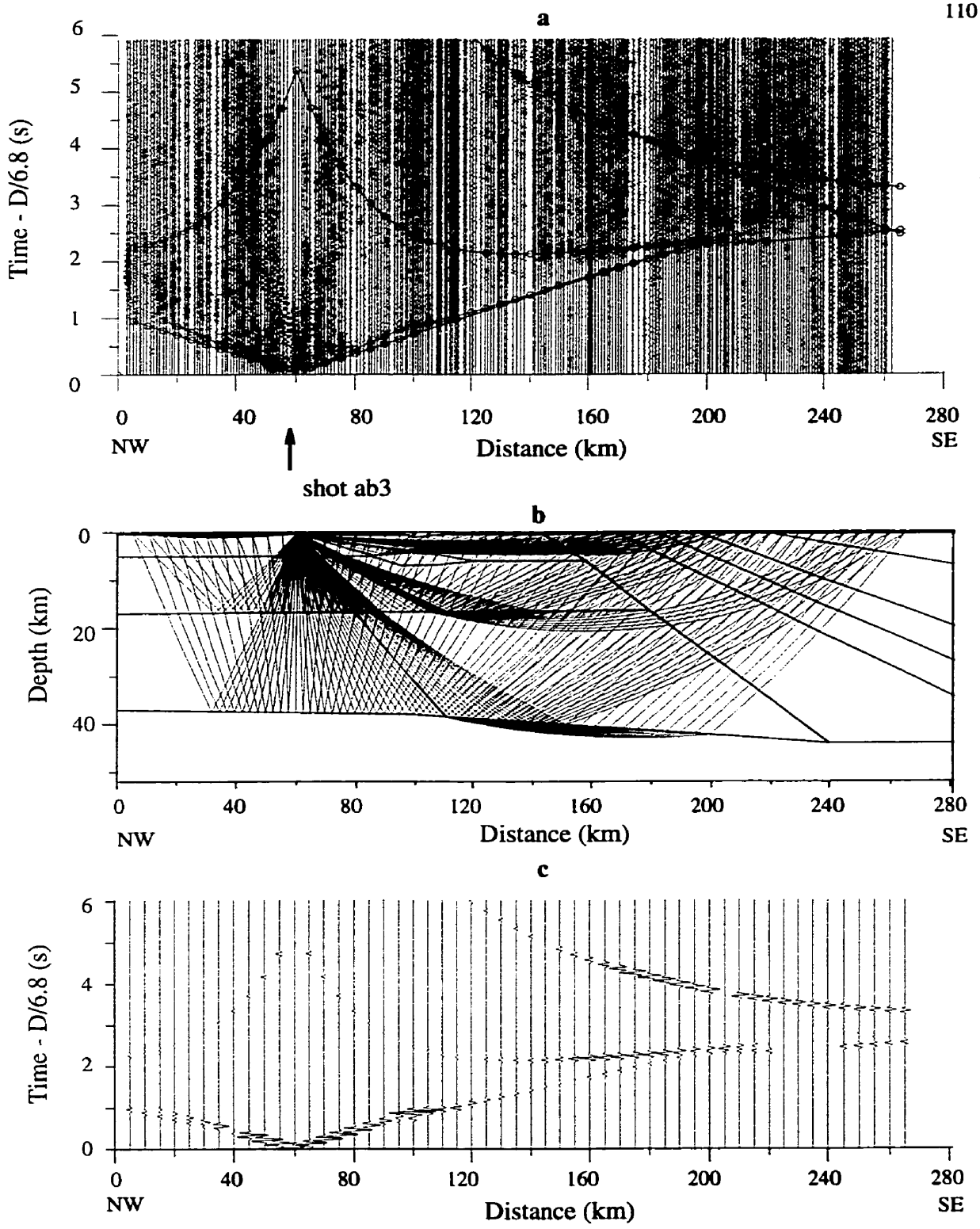

Figure 5.22 Wide-angle seismic reflection and refraction section for in-line ab3.
a: seismic section; **b**: ray path; **c**: synthetic seismogram.
o–o : calculated traveltime.

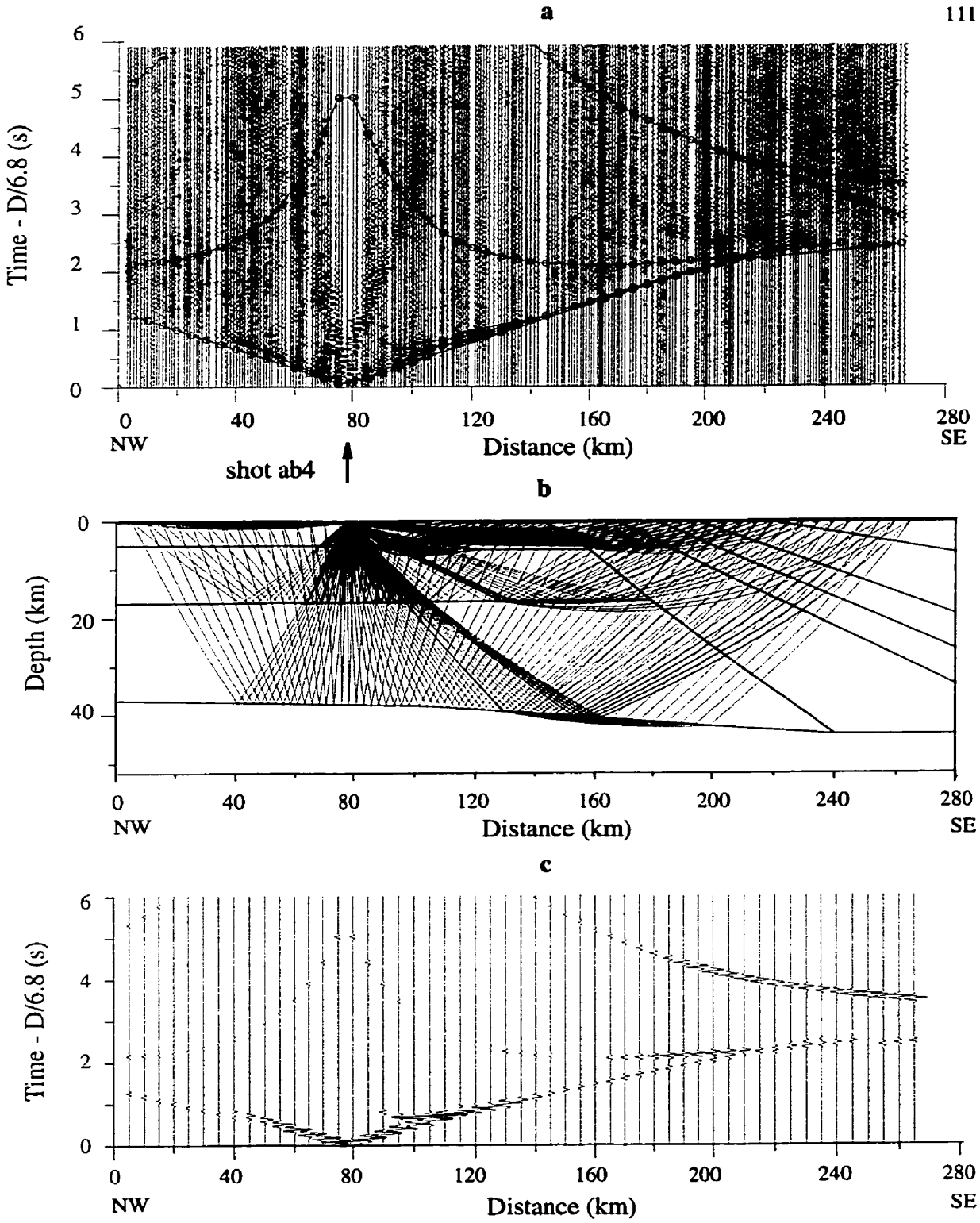

Figure 5.23 Wide-angle seismic reflection and refraction section for in-line ab4.
a: seismic section; **b**: ray path; **c**: synthetic seismogram.
⊖–⊖ : calculated traveltime.

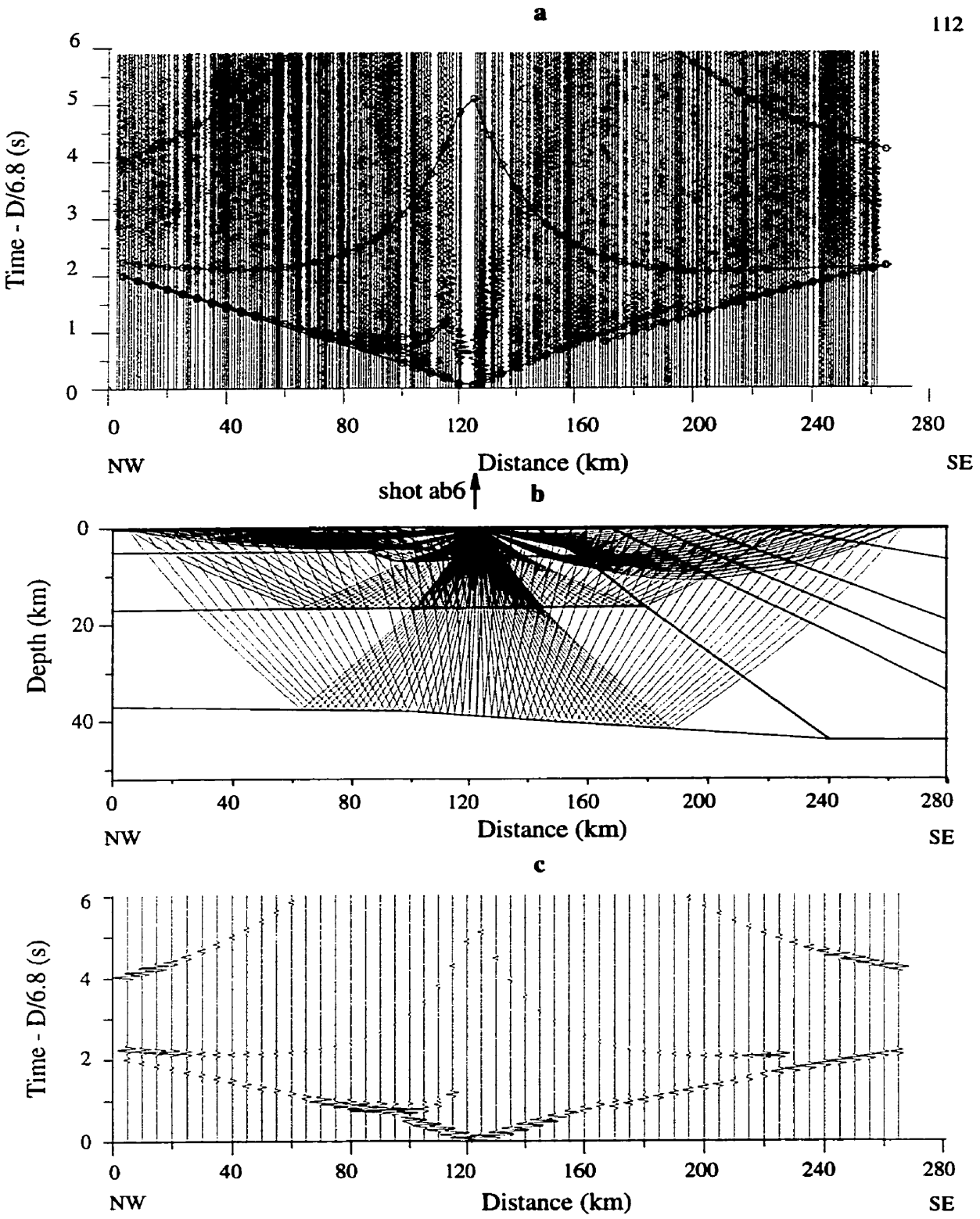

Figure 5.24 Wide-angle seismic reflection and refraction section for in-line ab6.
a: seismic section; **b**: ray path; **c**: synthetic seismogram.
⊖–⊖ : calculated traveltime.

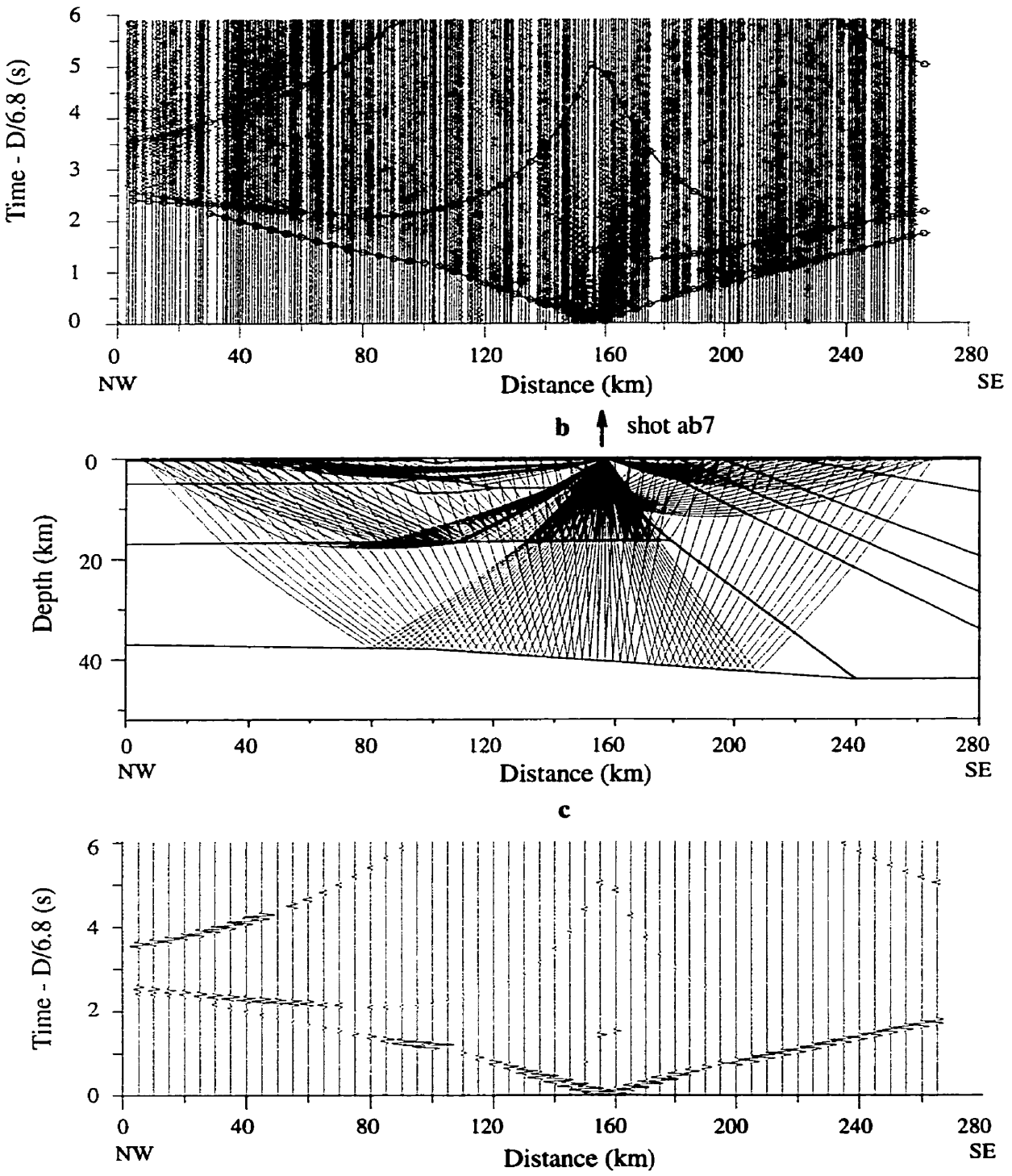

Figure 5.25 Wide-angle seismic reflection and refraction section for in-line ab7.
a: seismic section; **b**: ray path; **c**: synthetic seismogram.
⊖–⊖ : calculated traveltime.

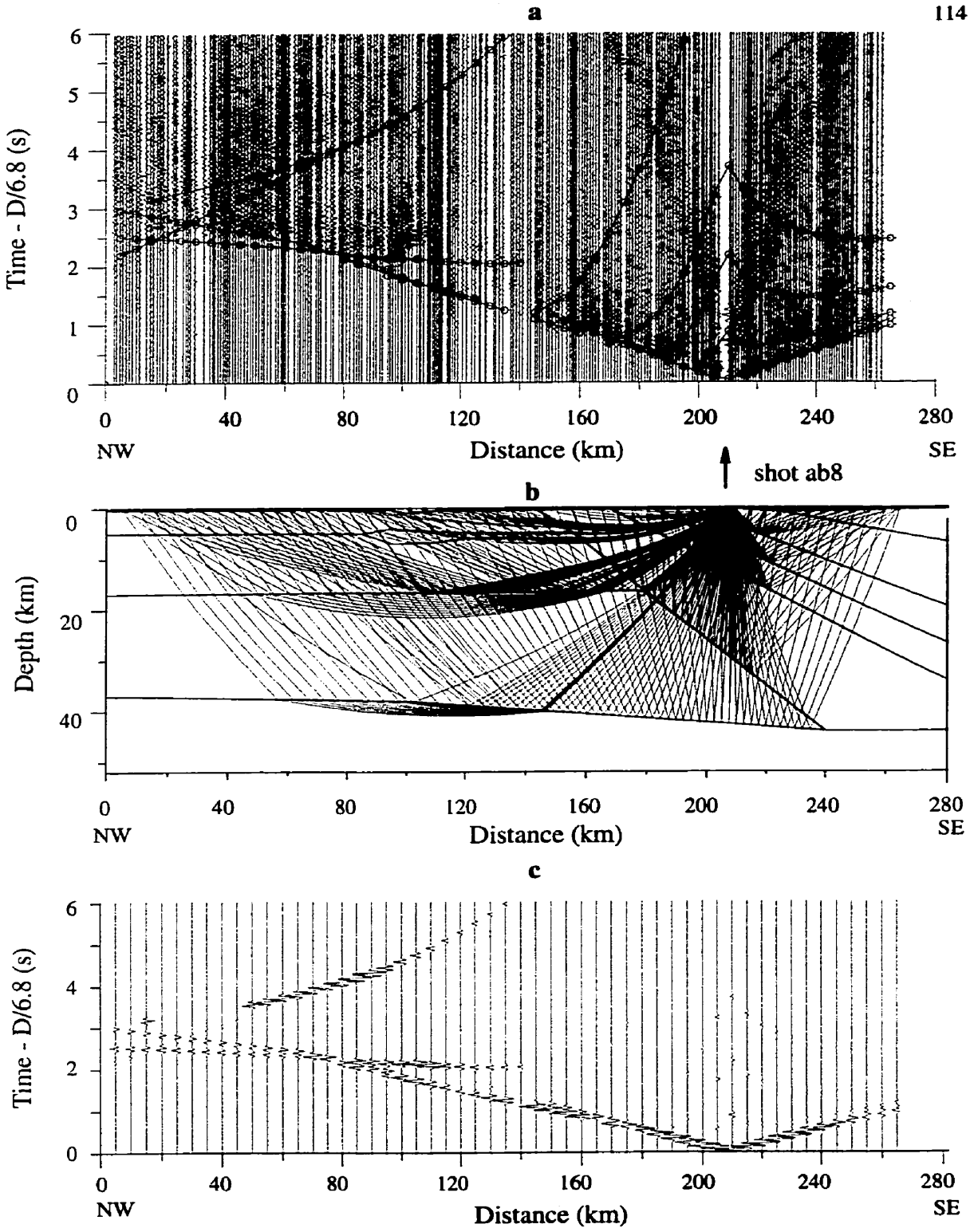

Figure 5.26 Wide-angle seismic reflection and refraction section for in-line ab8.
a: seismic section; **b**: ray path; **c**: synthetic seismogram.
⊖–⊖ : calculated traveltime.

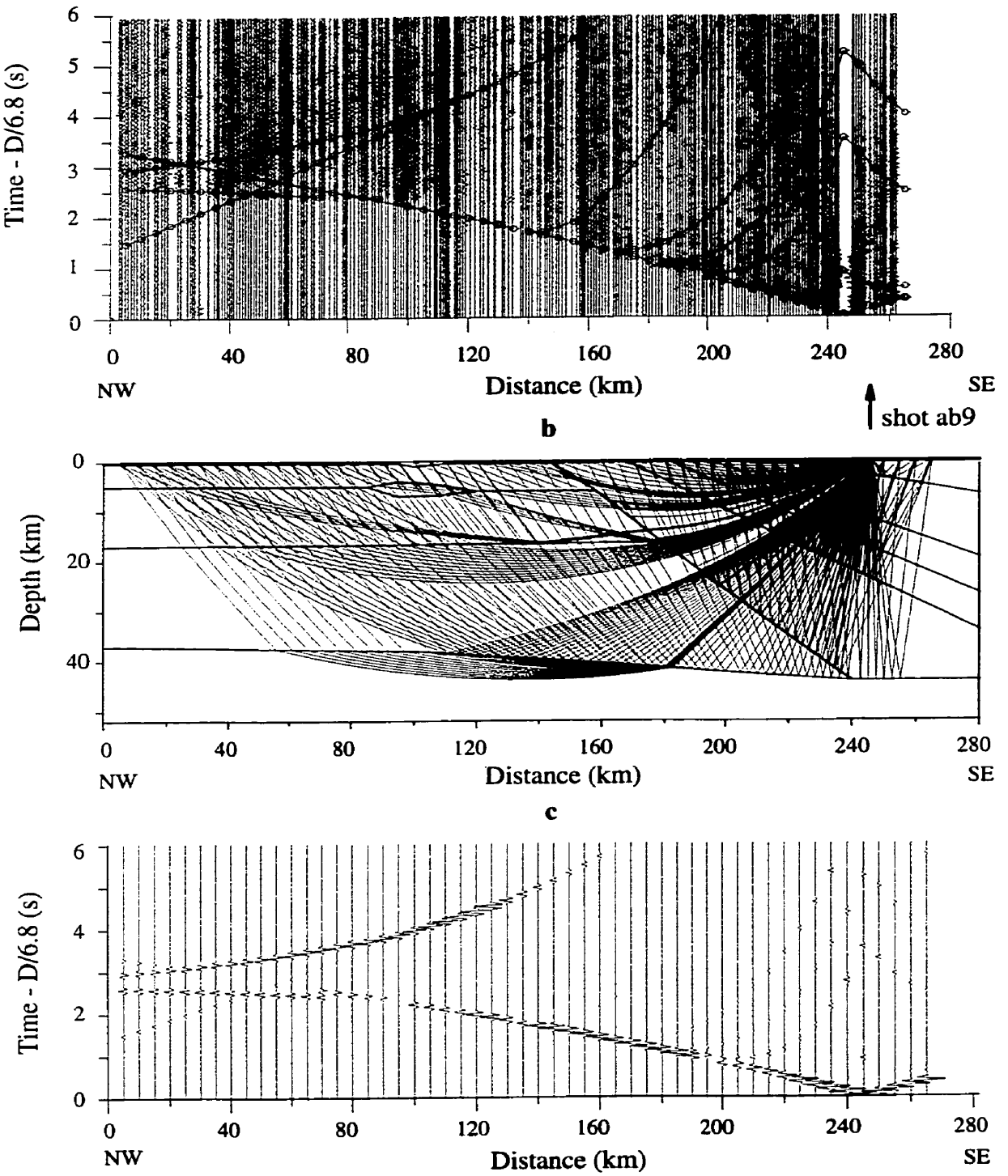

Figure 5.27 Wide-angle seismic reflection and refraction section for in-line ab9.
a: seismic section; **b**: ray path; **c**: synthetic seismogram.
⊖⊖ : calculated traveltime.

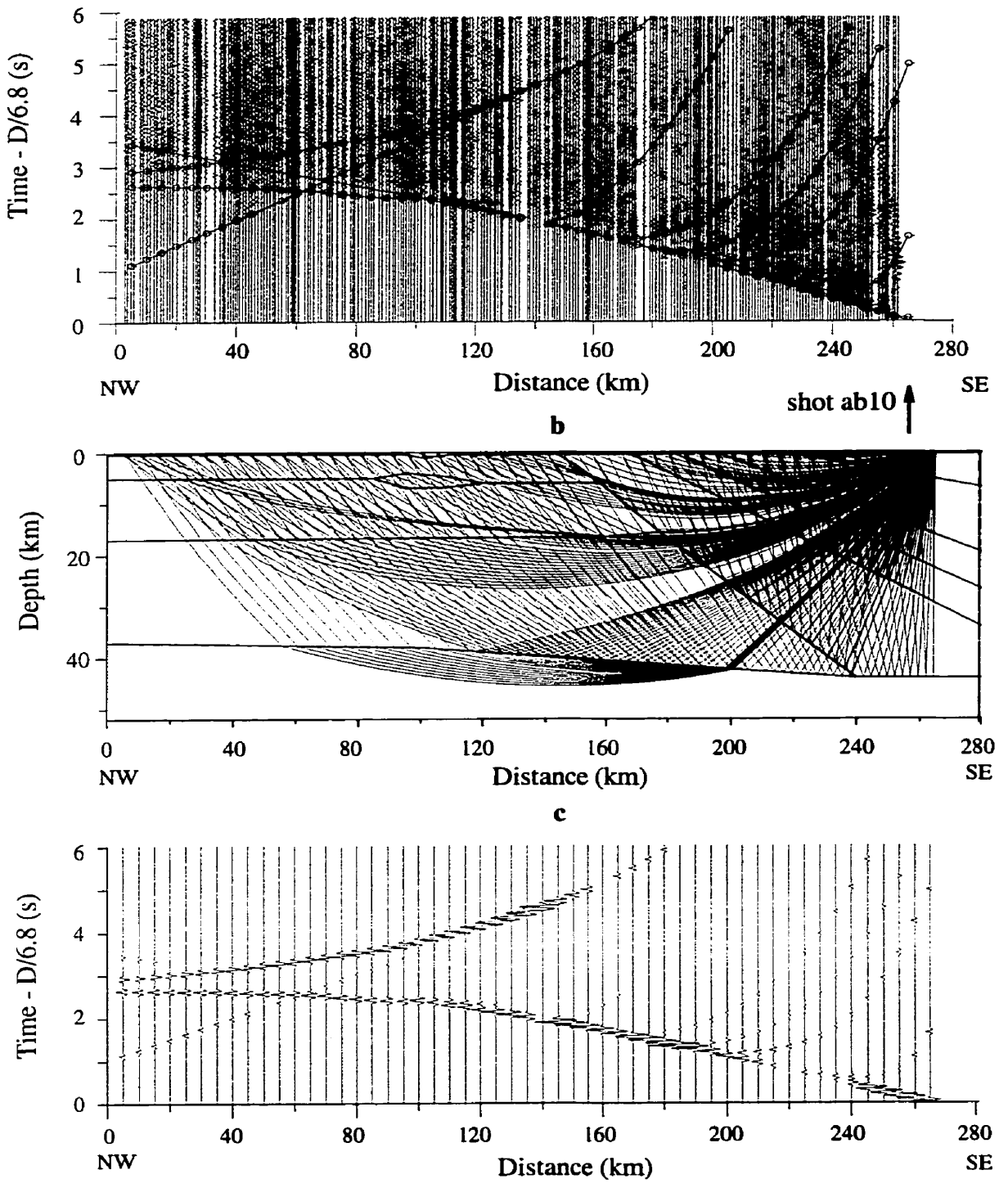

Figure 5.28 Wide-angle seismic reflection and refraction section for in-line ab10.
a: seismic section; **b**: ray path; **c**: synthetic seismogram.
⊖–⊖ : calculated traveltime.

feature in the southeast of the profile will be discussed in the later subsection of Dipping Stacked Structure.

4. Lower Crustal and Upper Mantle Structures

The reflection features at far offset suggest that a single layer in the lower crust in the northwestern part of the profile is sufficient to model the observed velocity gradient. Modeling of the Pc phase yielded a value of 6.6 km/s for the velocity at the top of the lower crust. A velocity gradient in the layer was constrained by PmP and Pn arrivals. A constant velocity of 6.92 km/s at the base of the crust provides a good fit to PmP and Pn traveltimes as shown on sections of shots ab2, ab4 and ab10 (Figures 5.21, 5.23 and 5.28). The subhorizontal Moho discontinuity was modeled as a depth of ~37 km at distances of 0-100 km. Beyond 100 km, the depth of the Moho discontinuity gradually decreases to a depth of ~44 km at a distance of 240 km. The model has a constant Moho depth of 44 km at the southeastern end of the profile.

The velocity in the upper mantle was constrained by Pn arrivals. The final velocity obtained from time modeling is ~8.06 km/s in the northwestern part of the profile and 8.10 km/s in the southeastern part with a constant 0.012 1/s vertical gradient, which produce an excellent fit to the observed Pn arrivals (Figures 5.21 and 5.28).

5. Dipping Stacked Structure

The "shingle-like" events were modeled as a series of five southeast-dipping reflectors. The reflectors truncate the subhorizontal structure to the south and are exposed on the surface at distances of 140-270 km. They dip southeast and extend down to the bottom of

the crust. The initial velocity of the five layers was determined from the previous studies by Epili and Mereu (1991) and Miao (1995). From forward modeling in this present study, the velocity at the top of the high-velocity body was found to be ~6.10 km/s, and 6.28 km/s at 9 km depth at its bottom. The apparent dip angle is moderate (7°). The reflection from this layer corresponds to the first arrival single event A on shot ab10. The velocity of the second top layer was determined to be 6.1 km/s at the top of the layer and 6.46 km/s at the bottom (24 km depth), and the layer dips towards the southeast at a 25° angle. This structure is responsible for the shingle event B. The third and fourth layers were modeled by relatively thin layers, which are sub-parallel to the second layer. They fitted the third and fourth shingle-like events (C and D) respectively. The velocity increases from 6.2 km/s at the top to 6.6 km/s at the base (32 km) for the third layer, and from 6.2 km/s at the top to 6.7 km/s at depth of 40 km for the fourth layer. The fifth layer dips southeast at an angle of 30° and has velocities of 6.1 km/s at the top and 7.1 km/s at the base (44 km). This layer was not as well constrained as the other four because of the weak reflections observed.

These shingle events are more complicated than those observed along profile J (Figure 5.4a). The block distribution of amplitude energy implies that the velocity is highly heterogeneous in both lateral and vertical directions. The shingle events indicate that subsurface dipping reflectors might not be a simple layered structure but a group of dipping and stacked microterranes as revealed by the seismic reflection image (Figures 5.3 and 5.6).

6. Near-surface Strong Reflection

The other unusual event observed in the Sudbury seismic refraction data is the strong

coherent near-surface reflection recorded as a Pg arrival but characterized subsequently as a Pr arrival (Figures 5.10-5.13). This reflection was interpreted as the reflected wave from the high-velocity body associated with the Sudbury Igneous Complex (at a distance of 100 km) (Miao, 1995). In this present study, the high-velocity body was modeled as dipping slightly to the southeast. The depth of the body was modeled as 4-7 km for the top and 5-7.5 km for the base. The velocity was modeled to be ~6.4 km/s. The bottom geometry of the anomalous body was not well constrained because of sparse ray coverage.

7. Amplitude Comparison

Amplitude modeling is very difficult in seismic modeling because the true amplitude of the signal is very hard to estimate in seismic recording. In addition, the superposition of seismic traces alters the true amplitude of seismic events, especially for late arrival signals. Therefore, only relative amplitudes are compared in this study for the purpose of providing additional constraints on velocity gradients and velocity contrasts across layer boundaries. The model velocities obtained by traveltime modeling can be modified according to the discrepancy between the observed and calculated amplitudes. However, the traveltime modeling should be given a higher priority than amplitude modeling (Zelt and Forsyth, 1994).

The velocity parameters along profile AB were adjusted based on a comparison of the observed and synthetic amplitudes. Cerveny's forward modeling software has the capability of generating a synthetic seismogram. The amplitudes of traces at offsets (less than 20 km) were normalized such that when the largest amplitude would not overlap a neighboring trace. This modification was done by this thesis work.

The synthetic seismogram for each section was plotted at the bottom of Figures 5.19-5.28 (using GMT-Geographical Mapping Tools). In the synthetic seismogram, for shots ab0, ab1 and ab2, the Pg arrivals at near offsets (<50 km) are characterized by strong reflection energy (Figures 5.19a-5.21a), which suggests a relatively large velocity gradient in the upper crust. In contrast, for shot ab3, the observed Pg arrivals at offsets between 110 km to 140 km indicate a very weak amplitude which corresponds to the small velocity gradient in the northwestern part of the profile. Therefore, the velocity assigned to the upper crust was modified according to the amplitude variation. As a result of the amplitude adjustment, at the northern end of the profile, the velocity was increased from 6.15 km/s to 6.19 km/s at a depth of ~7 km, whereas the velocity at a distance of ~150 km was decreased from 6.15 km/s to 6.12 km/s at a depth of 7 km. The velocities were modified from 6.10 km/s to 6.07 and 6.08 km/s at the tops of the fourth and fifth dipping layers respectively in order to increase the vertical velocity gradient, and thus match the relatively large amplitude observed.

For shot ab0, the amplitude variation with distance in the synthetic seismogram matches the energy distribution. In particular, at distances less than 50 km the large amplitude of the Pg arrival was fitted well. The amplitude decreases over the distance range of 50-100 km. The amplitude then increases slightly at distances between 100-115 km, as a result of small-scale phenomena associated with the Sudbury Structure. At a distance of 140 km, a region where Pg, PcP and Pc arrivals cross, the amplitude of the observed arrivals increases due to the superposition of three reflections. An increased amplitude of PcP as a second arrival at distances between 150 and 189 km was observed. All these amplitude variations in observed data were well matched by the synthetic seismogram. The

amplitude at distances greater than ~200 km could not be compared with synthetic data due to a low S/N ratio. For shot ab1, the observed amplitude variation is similar to that for shot ab0. The energy distributions for Pg, PcP and Pc were well fitted (Figures 5.20a and 5.20c).

For shots ab2, ab3, ab4 and ab6, the strong reflections of the Pr phase at a distance of ~100 km agree well with the observed data and synthetic seismograms (Figures 5.21-5.24). For shot ab2, observed PcP arrival amplitudes indicate high energy at an offset of ~120 km. In the southeastern end of the profile Pc amplitudes shown in the synthetic figures agree well with the observed amplitude (Figures 5.21a and 5.21c). For shot ab7, the amplitude of the Pg phase matched well except at distances between 85 and 100 km, where a strong reflection in the synthetic seismogram corresponds to the refracted wave from the high-velocity body. The Pn amplitude of the observed data was well matched by that of the synthetic data (Figure 5.28c), indicating that the crustal model provides a good fit to the observed data.

The "shingle-like" events (Figures 5.27 and 5.28) could not be analysed by comparing amplitude variations because shingle events were not identified as simple, coherent reflections but rather as block energy reflection features. This energy distribution was generated by rays propagating through a velocity body which is heterogeneous in both vertical and horizontal directions.

The final velocity model is shown in Figure 5.29. The comparison of the this model with Figure 5.18, the new results provided by the present inversion are indicated. In the northwest, the structure is characterized by subhorizontal features. The depth of the top layer drops at a distance of ~100 km. There is a hyperbolic high-velocity body modeled in

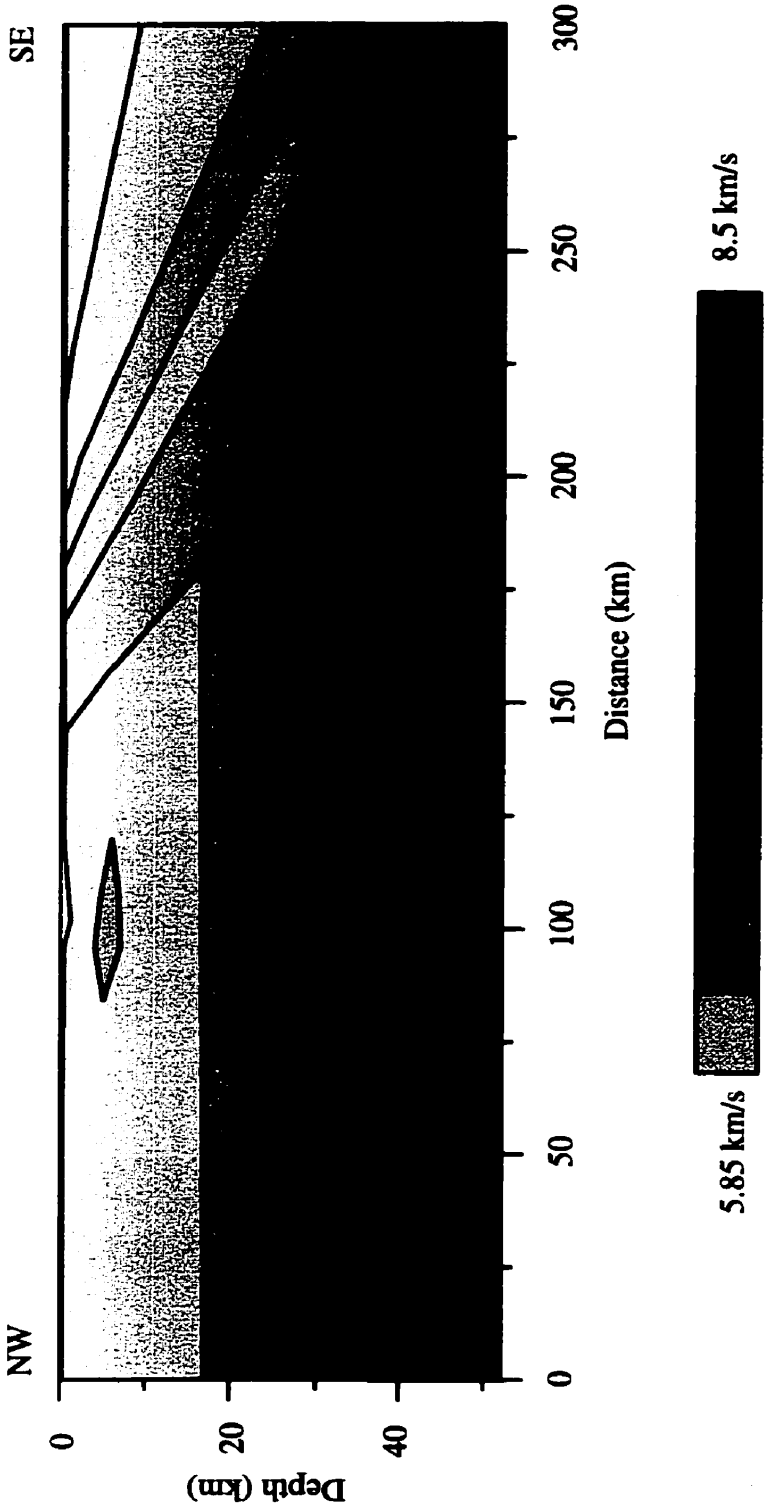

Figure 5.29 Velocity structure along profile AB obtained by forward modelling. Solid lines represent the structural boundaries.

the upper crust. It is located at distances of 80-120 km and at depths of 4-7 km. The thickness of the body is ~2-4 km. The subhorizontal structures in the northwest are truncated by five individual southeastern dipping layers at angles of 20°-45°. The thickness of these dipping layers varies. The Moho discontinuity decreases from ~37 km in the northwest to ~44 km in the southeast.

5.3 Summary

In Cerveny's dynamic ray tracing algorithm, the eikonal function is the fundamental equation for determining a ray path and calculating its traveltime. A first order ordinary differential equation ray tracing system was derived for obtaining the solution of the eikonal equation (equation 5.13). In the algorithm, the Runge-Kutta technique was applied to obtain approximate solutions for ray path and traveltime. In addition, synthetic seismograms can also be estimated by solving the transport equation (equations 5.21 and 5.23) and determining the source signal function. The algorithm was derived for an inhomogeneous elastic medium; therefore, it is a method suitable for the study of complicated geological structures such as beneath profile AB in Sudbury.

The initial velocity model along profile AB was determined mainly by the velocity model along profile J of the GLIMPCE project, the preliminary model obtained from this seismic data set (Miao, 1995), and seismic phase analysis conducted in this research. A significant feature of the first arrivals on sections of shots ab2, ab3 ab4 and ab6 is that there is a strong reflection with a short traveltime and a limited number of coherent traces observed at a distance of ~100 km. The reflection event was modeled as a reflection from

the boundary of the high-velocity body, which confirmed the previously preliminary result. In the present study, this high-velocity body was modeled as a rhomboid wedge buried at distances of ~80-120 km at depths of ~4-7 km. The velocity of the anomalous body was determined to be ~6.4 km/s.

In the northern part of the profile, the Moho discontinuity and mid-crustal interface were modeled as subhorizontal at depths of 37 and 17 km respectively (Figure 5.29), which are similar to the previous result obtained by Miao (1995). The velocity at the bottom of the crust was modeled to be 6.92 km/s. In the southern part of the profile, the initial model is characterized by a series of southeasterly dipping layers suggested by shingle events observed on sections of shots ab8, ab9 and ab10. These shingle events were also observed on profile J, and six dipping layers (Epili and Mereu, 1992) were suggested to be responsible for these events. In the present study, the structure was modeled using five dipping layers, corresponding to the complicated form of dipping microterranes in the Grenville Province. The Moho depth increases from ~37 km in the Superior Province to ~40 km under the Grenville Front Tectonic Zone and ~44 km in the Grenville Province. The velocity at the bottom of the crust in the Grenville Province increases to 7.1 km/s. Crustal thickness and velocity at the base of the crust follow the global pattern suggested by Durrheim and Mooney (1991).

Chapter 6

Modeling of In-line Data (Profile XY)

The Cerveny forward modeling method allows treatment of a complex geological model but does not provide estimates of model resolution and parameter uncertainty. In contrast, the RAYINVR inversion modeling algorithm estimates the model resolution and parameter uncertainty at the cost of model simplification. The RAYINVR algorithm was employed to investigate the (relatively simple) geological structure along profile XY using the in-line seismic data. This chapter describes the in-line RAYINVR ray tracing algorithm in the first section. It then discusses the application of the algorithm in the second section.

6.1 RAYINVR Ray Tracing Inversion Algorithm

The RAYINVR ray tracing inversion algorithm simultaneously determines velocity and interface parameters for seismic P wave events in 2-D and was developed by Zelt and Smith (1992). This algorithm modifies model parameters (velocity and depth of interface) by using computer-based iteration so as to obtain a good fit between the observed and calculated data after each forward modeling step. In addition, it also provides quantitative estimates of model parameter resolution and uncertainty.

6.1.1 Model Parameterization

The ray tracing algorithm requires the parameterization of the geological model in terms of velocity and interfaces in 2-D. The model consists of layered, variably sized trapezoids with isotropic velocity. Therefore, the structure being modeled is simplified to match this model. Each layer boundary is required to cross the model from left to right and to not cross other interfaces (Figure 6.1). This requirement is the same as that specified by Cerveny's method. The number and spacing of boundary blocks in each layer is arbitrary. A curved interface is represented by multiple segment lines.

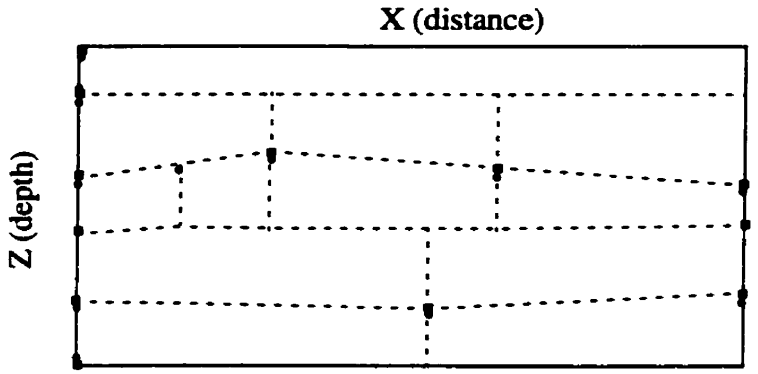

Figure 6.1 Example of model parameterization
- - - - - : layer interfaces and layer blocks; • : interface block boundary notes; . : velocity nodes.

Filled squares and filled circles marked in Figure 6.1 are interface boundary nodes and velocity nodes respectively. Interface nodes and velocity nodes represent locations of boundaries and specified velocities respectively which will be modified during inversion. A single velocity node in a layer indicates a laterally constant velocity, whereas multiple velocity nodes represent a laterally varying velocity field. The entire velocity field in a trapezoid is defined by linear interpolation between the velocity values at the upper and

lower interface points within the trapezoid block rather than cubic-B spline interpolation as applied in Cerveny's approach. The velocity within a trapezoid block is then determined by the simple expression (Zelt and Smith, 1992):

$$v(x, z) = \frac{(c_1 x + c_2 x^2 + c_3 z + c_4 xz + c_5)}{(c_6 x + c_7)}, \tag{6.1}$$

where

$$\begin{aligned}
c_1 &= s_2(x_2 v_1 - x_1 v_2) + b_2(v_2 - v_1) - s_1(x_2 v_3 - x_1 v_4) - b_1(v_4 - v_3), \\
c_2 &= s_2(v_2 - v_1) - s_1(v_4 - v_3), \\
c_3 &= x_1 v_2 - x_2 v_1 + x_2 v_3 - x_1 v_4, \\
c_4 &= v_1 + v_4 - v_3 - v_2, \\
c_5 &= b_2(x_2 v_1 - x_1 v_2) - b_1(x_2 v_3 - x_1 v_4), \\
c_6 &= (s_2 - s_1)(x_2 - x_1), \\
c_7 &= (b_2 - b_1)(x_2 - x_1).
\end{aligned}$$

v_i (i=1, 2, 3, 4) denotes the velocity at four corners of a trapezoid; and s_1, b_1, s_2, and b_2 are parameters of line functions for the upper and lower interfaces with index 1 and 2 respectively (Figure 6.2). This algorithm requires an adequate number of trapezoids to fully represent the lateral variation in a velocity field (Zelt and Smith, 1992).

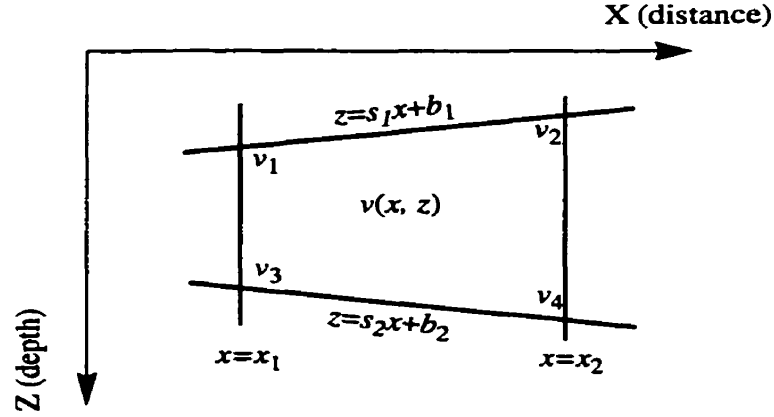

Figure 6.2 The velocity and interface parameterization in a trapezoid boundary block.

6.1.2 Ray Tracing (Forward Modeling)

The basic ray tracing equations in the algorithm are the same as equation 5.20 which was derived by Cerveny et al. (1986) and discussed in Section 5.1. Based on equation 5.20, the ray tracing system for simulating a near horizontal ray path in 2-D can be further rewritten as

$$\frac{dz}{dx} = \cot\delta, \qquad \frac{d\delta}{dx} = \frac{v_z - v_x \cot\delta}{v}, \tag{6.2}$$

where $v_x = \frac{\partial v}{\partial x}$ and $v_z = \frac{\partial v}{\partial z}$. The alternate forms of the system for tracing a ray with a near vertical path are similarly derived as

$$\frac{dx}{dz} = \tan\delta, \qquad \frac{d\delta}{dz} = \frac{v_z \tan\delta - v_x}{v}. \tag{6.3}$$

To solve these ordinary derivative equations (equations 6.2 and 6.3), the Runge-Kutta numerical method is employed in this algorithm as it is in the method of Cerveny et al. (1986).

The RAYINVR ray tracing uses an iterative search procedure (Zelt and Ellis, 1988) to determine the maximum and minimum take-off angles for each ray group such as reflection, refraction and head waves. Rays in the groups of reflection and turning waves are then traced with the take-off angle increasing from the minimum to the maximum value allowing some rays to reach the surface as needed (Figures 6.3a and 6.3b). Rays in the group of head waves, propagating along a sublayer boundary and refracting upward to the surface at the critical angle or take-off angle, are determined by the critical angle (Figure 6.3c).

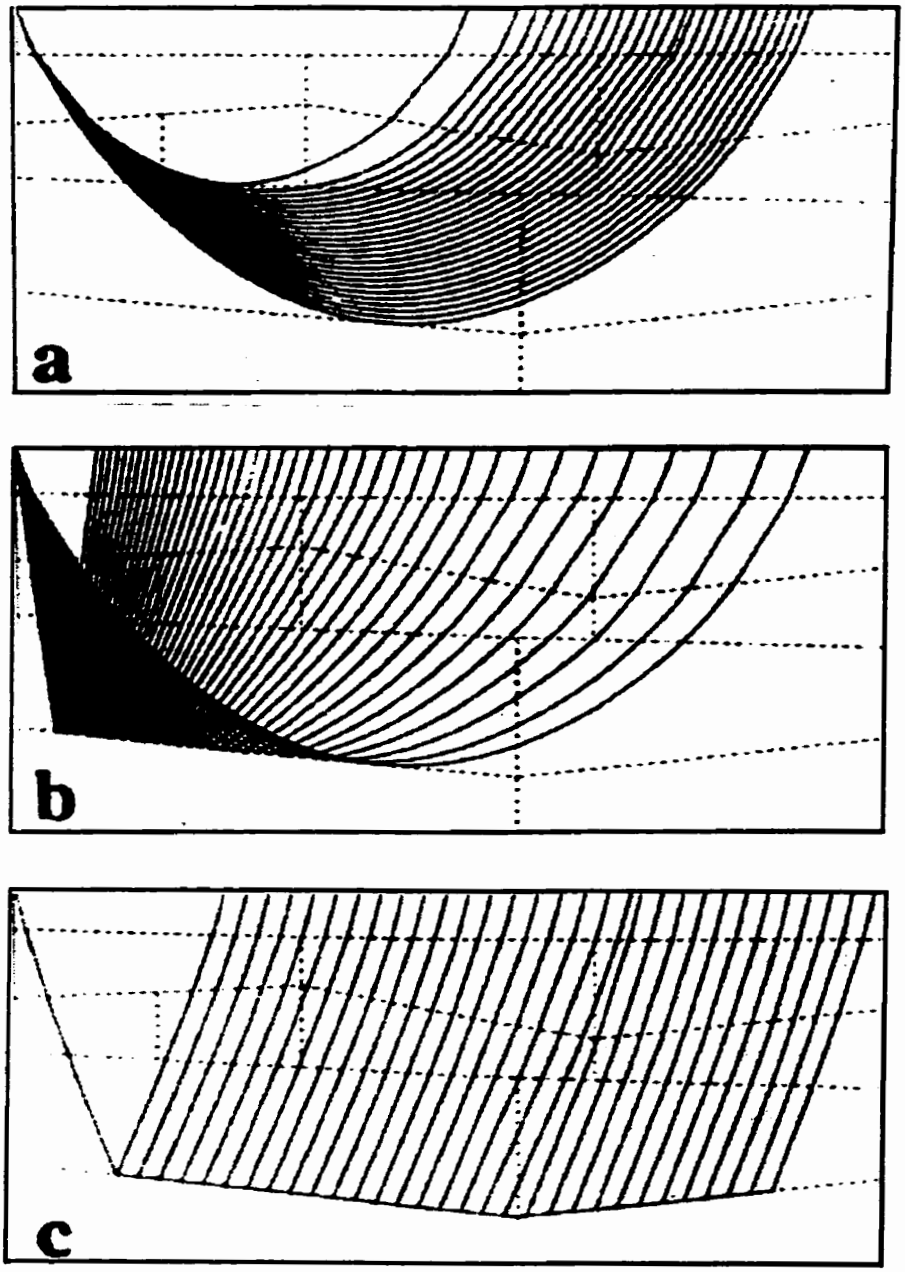

Figure 6.3 Take-off angles for turning (**a**), reflection (**b**), and refraction (**c**) waves (After Zelt and Smith, 1992).

Abrupt changes at layer boundaries produce the problem of "geometrical shadow zones at the surface" (Zelt and Smith, 1992), which is caused by the linear interpolation of velocity during parameterization. In order to perform the forward modeling effectively, a three point averaging technique was used to smooth the sharp boundaries. The "block-ness" effect was thus reduced and traveltimes could be obtained at most end-point boundaries on the surface.

An important difference between the algorithm provided by Zelt and Smith (1992) and Cerveny's method is that in Zelt and Smith's method a ray traveltime related to a shot and specific receiver is linearly interpolated from traveltimes calculated associated for the two closest rays, rather than being determined by tracing an exact ray path from a shot to the receiver (Cerveny, 1971). In addition, the model parameters are much simpler in Zelt and Smith's approach than in Cerveny's classical method. Therefore, the RAYINVR algorithm uses less computer time than Cerveny's method. This saving allows the implementation of a iterative inversion algorithm for modeling parameters.

6.1.3 Inversion

The RAYINVR ray tracing algorithm provides the automatic determination of velocity and depth of interface structures during the inversion procedure. The inversion is performed by a damped least-squares technique which iteratively updates the parameters of the velocity and boundary depth. Root mean square (RMS) traveltime residual, parameter resolution and normalized chi-squared χ^2 misfit, are the main factors used to define the termination criteria of the inversion iteration and the selection of the final

model.

The discrete form of the traveltime function, which is the basic equation in the traveltime inversion, is written as

$$t_k = \sum_{i=1}^{n} \frac{l_{i,k}}{v_i}, \tag{6.4}$$

where the t_k represents traveltime recorded at the kth receiver at the surface; $l_{i,k}$ are path lengths of a ray propagating through the ith velocity node upward to the kth receiver; v_i is the velocity corresponding to the ith velocity node and n denotes the number of the velocity nodes passed by the ray. The traveltime in equation 6.4 is a nonlinear function. It can be approximated by a linear equation related to the first-order expansion of the equation into a Taylor series. The matrix form of the linear traveltime equation is then given as

$$\boldsymbol{t} = \boldsymbol{t_0} + \boldsymbol{A}(\boldsymbol{M} - \boldsymbol{M_0}), \tag{6.5}$$

where $\boldsymbol{t}$ is the observed traveltime vector (with dimensions N x 1), $\boldsymbol{t_0}$ is the calculated traveltime vector, $\boldsymbol{M}$ is the true model parameter vector (with dimensions M x 1) and $\boldsymbol{M_0}$ is the calculated model parameter vector. $\boldsymbol{A}$ (with dimensions M x N) is the partial derivative matrix which contains elements consisting of the partial derivatives of traveltimes with respect to model parameters. M is the number of the observed traveltimes and N is the number of model parameters. Rewriting the above linear traveltime equation by moving $\boldsymbol{t_0}$ from the right-hand-side to the left-hand-side of the equation, we can obtain the well-known linear traveltime perturbation vector equation in terms of the product of the partial derivative matrix and model parameter perturbation

vector, which is

$$\Delta t = A\,\Delta M, \tag{6.6}$$

where Δt is the traveltime residual vector; and ΔM is the vector containing the model parameter adjustments.

The linear equation (6.5) is solved by using a damped least-squares inversion technique in the Zelt and Smith algorithm. Generally, the damped least-squares solution is given in the following form (Zelt and Smith, 1992)

$$\Delta M = (A^{T}C_t^{-1}A + DC_m^{-1})^{-1}A^{T}C_t^{-1}\Delta t, \tag{6.7}$$

where D is a damping parameter, C_t is the diagonal variance matrix of the observed data which in the case of uncorrelated data errors is equal to diag$\{\sigma_i^2\}$, and C_m is the diagonal covariance matrix of the estimated model which in the case of uncorrelated data errors is equal to diag$\{\sigma_j^2\}$. σ_i and σ_j are the estimated uncertainties of the ith traveltime measurement and the priori estimation of the uncertainty of the jth model parameter respectively. The model resolution matrix R in the solution is written as (Zelt and Smith, 1992)

$$R = (A^{T}C_t^{-1}A + DC_m^{-1})^{-1}A^{T}C_t^{-1}A. \tag{6.8}$$

A lower bound for the true parameter errors can be estimated by taking the square root of the diagonal elements of $C = (I - R)C_m$ (where I denotes the identity matrix), and represents the standard error of parameters (Zelt and Smith, 1992).

The least-squares inversion for a nonlinear problem is an iteration procedure which minimizes the difference between the calculated and observed traveltimes by modifying

the model parameters. In the RAYINVR algorithm, an empirical method is used to determine the termination criteria for the iteration. Generally, if the number of model parameters increases the traveltime residual will reduce rapidly; however, the overall model parameter resolution will also decrease. Therefore, the final model is determined by the "desired trade-off between RMS traveltime residual and parameter resolution" (Zelt and Smith, 1992).

The final model is also assessed by its ability to trace all received rays and by the normalized misfit parameter χ^2 (Zelt and Forsyth, 1994). The normalized misfit χ^2 is expressed by $\left[\left(\sum_{i=1}^{n}((t_{o_i}-t_{c_i})/u_{o_i})\right)/n\right]^{1/2}$, where t_{o_i} is the observed traveltime, t_{c_i} is the calculated traveltime, u_{o_i} is the uncertainty of the observed traveltimes, and n is the number of the observed traveltimes. When the normalized $\chi^2 = 1$ (a desired value), the misfit between the calculated and observed traveltime is close to the uncertainty of the data. In this case, the calculated data fit the observed data well within the given uncertainties. If $\chi^2 \ll 1$, the observed data are overfits and the model contains details which may not represent the required data. If $\chi^2 \gg 1$, the calculated traveltimes do not fit the observed data well. In the inversion, if χ^2 for some phases has the desired value 1, the $\chi^2 < 1$ can be expected and accepted for all phases (Zelt and Forsyth, 1994). Therefore, in seismic modeling, a value of χ^2 of approximately 1 is accepted. The value of χ^2, parameter resolution and RMS traveltime residual constitute three important criteria to determine the final model when using the RAYINVR ray tracing inversion algorithm.

6.2 Modeling of In-line Profile XY

Line XY extends from southwest to northeast across line AB in the Sudbury Basin. Line XY does not cross the dipping-thrust crustal tectonic zone; therefore, the regional geometry beneath this line is expected to be relatively simpler than the geometry along profile AB. Furthermore, the analyses of seismic data along the profile are carried out using both forward and inverse modeling with the RAYINVR software package. The expected reflectors and the seismic data processing and display methods have been discussed in detail in Subsections 5.2.1 and 5.2.2. Therefore, in this section, only the seismic phase analysis and the modeling procedure are described.

6.2.1 Seismic Phase Analysis

Seismic phase analysis provides an estimate of apparent velocities and derives an initial model for the inversions. A total of five shots were recorded along line XY which extends ~165 km (Figures 6.4-6.8). For shots xy0, xy1 and xy5 there were parts of traces with low S/N ratio due to noise (Figures 6.4, 6.5 and 6.8). The data quality for shots xy2 and xy4 is high (Figures 6.6 and 6.7). Solid lines on Figures 6.4-6.8 mark clearly picked phases identified on sections. As line XY is a short profile, PmP and Pn, PcP and Pc phases were not clearly recorded. In particular, Pn and Pc were not observed as first arrivals along this line.

1. Pg Phase

Pg arrivals have a high S/N ratio on all five sections. For shot xy0, a strong Pg phase

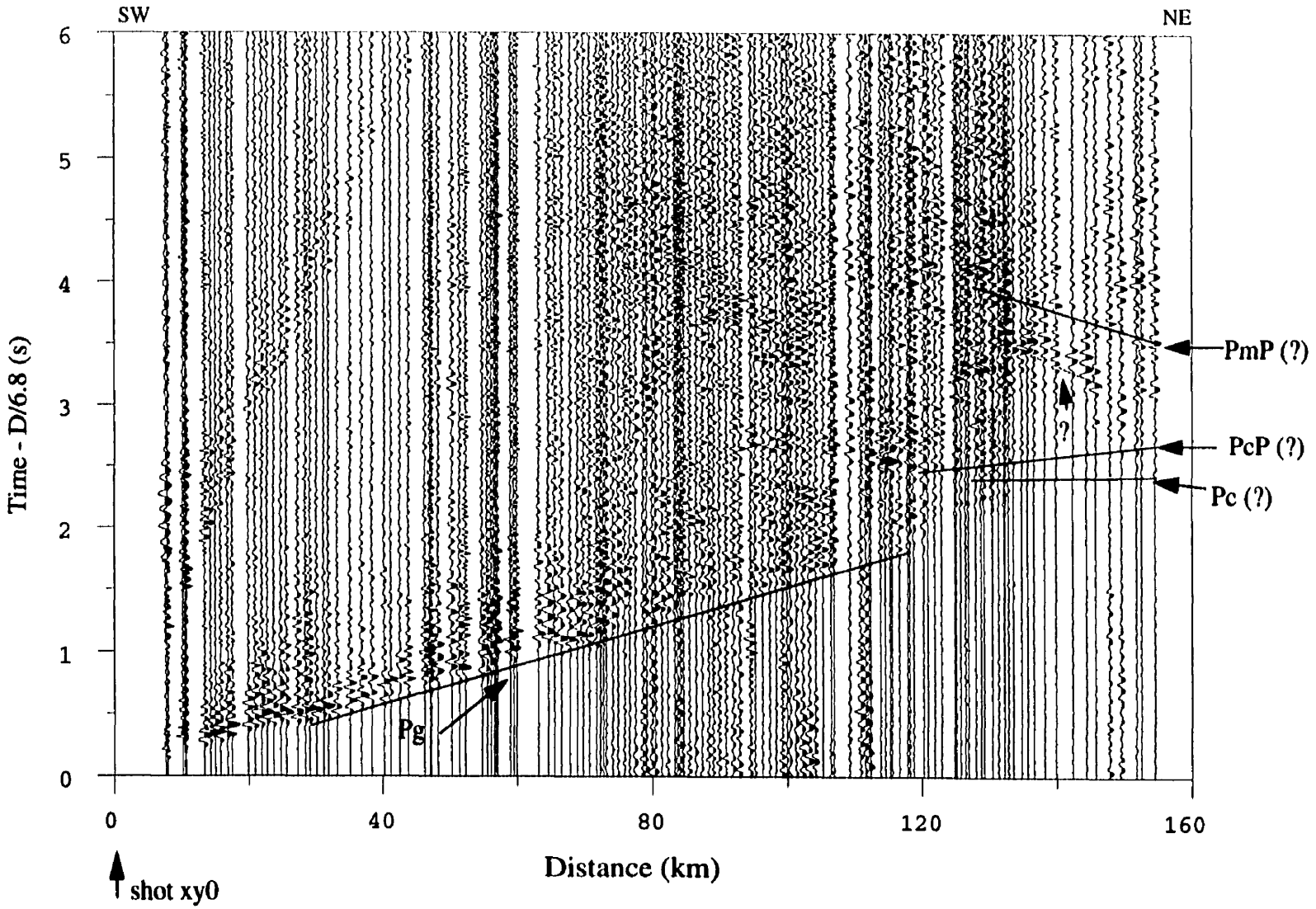

Figure 6.4 Wide-angle seismic reflection and refraction section of shot xy0 on in-line XY.

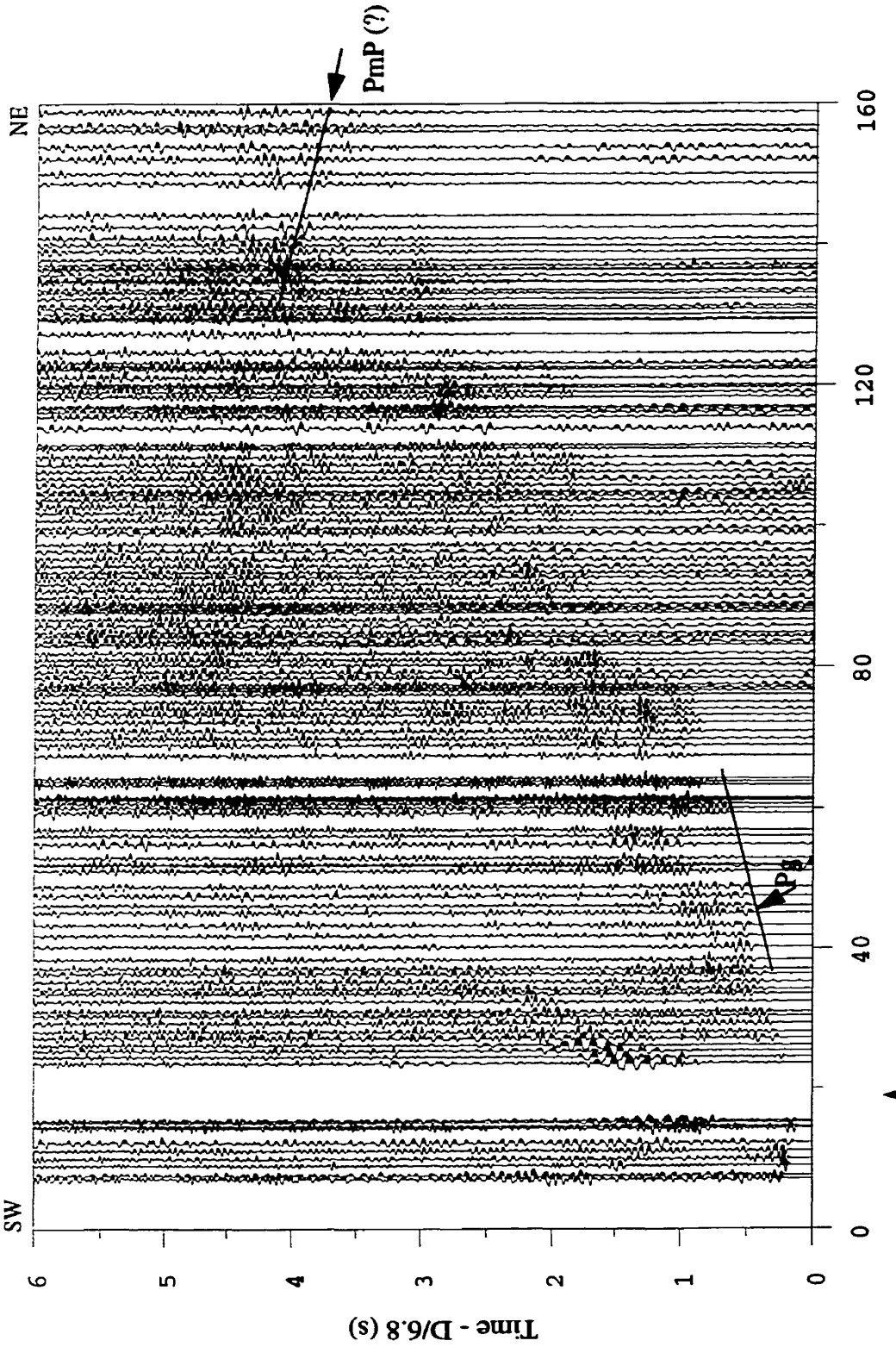

Figure 6.5 Wide-angle seismic reflection and refraction section ofshot xy1 on in-line XY.

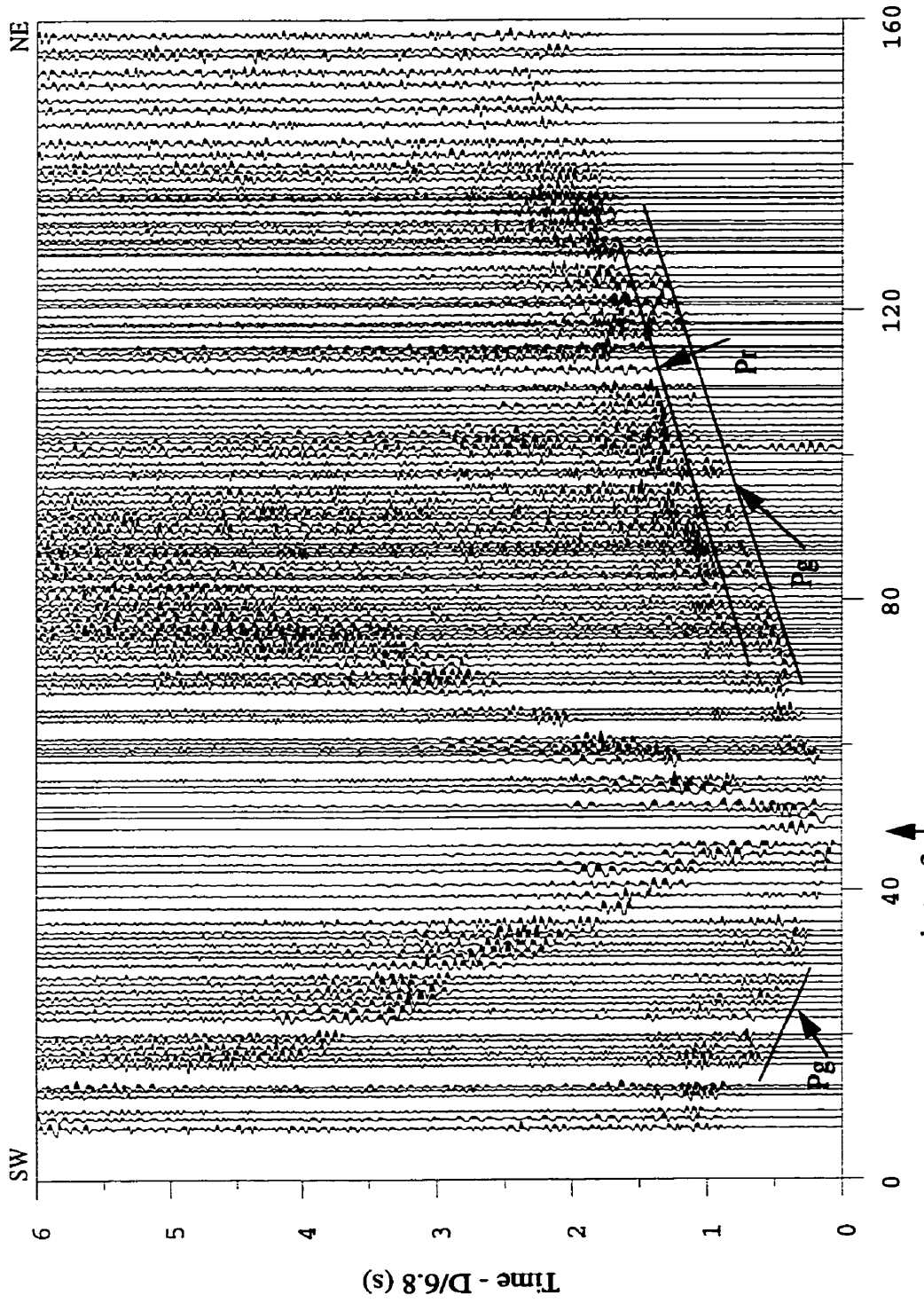

Figure 6.6 Wide-angle seismic reflection and refraction section of shot xy2 on in-line XY.

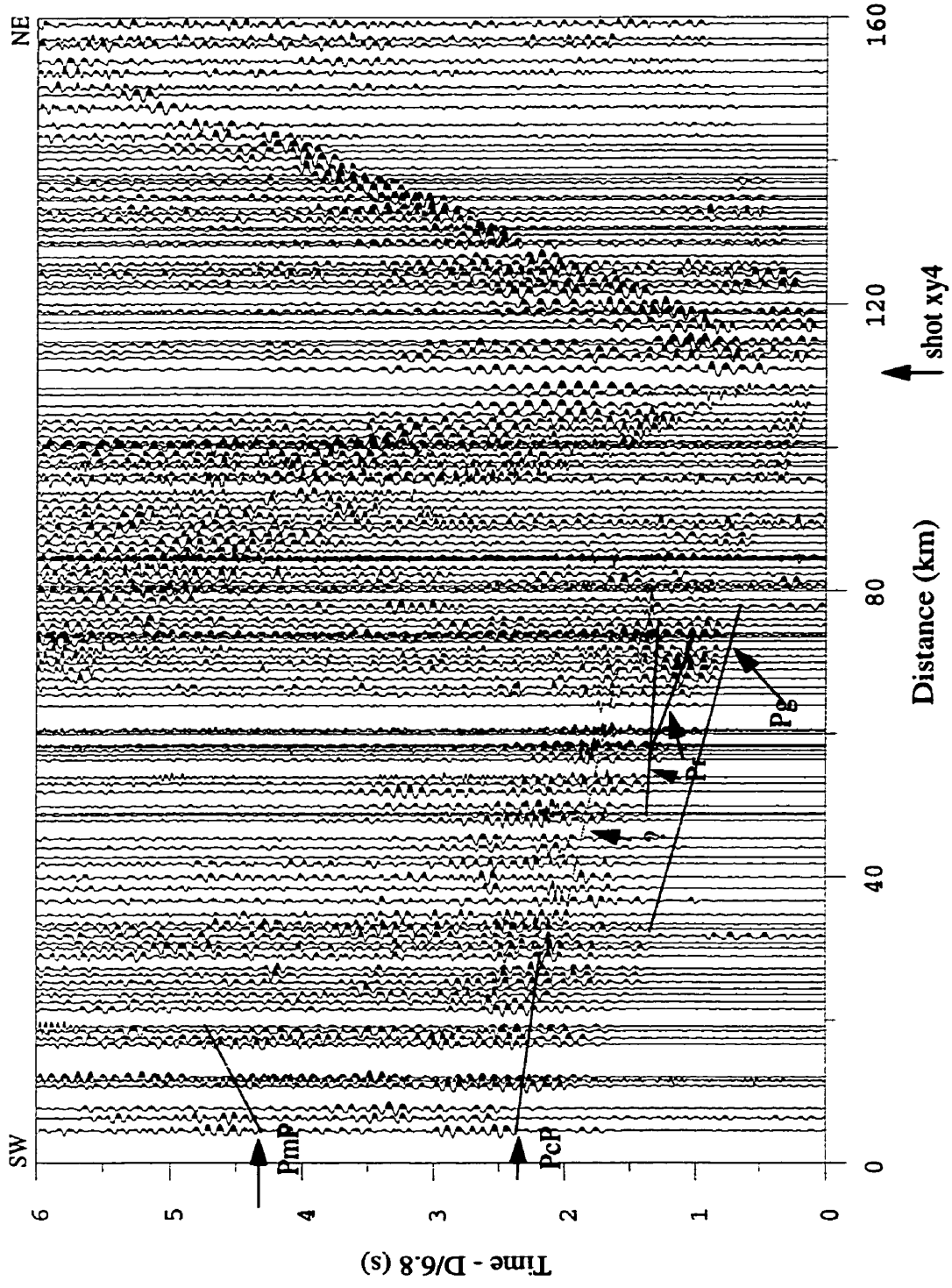

Figure 6.7 Wide-angle seismic reflection and refraction section of shot xy4 on in-line XY.

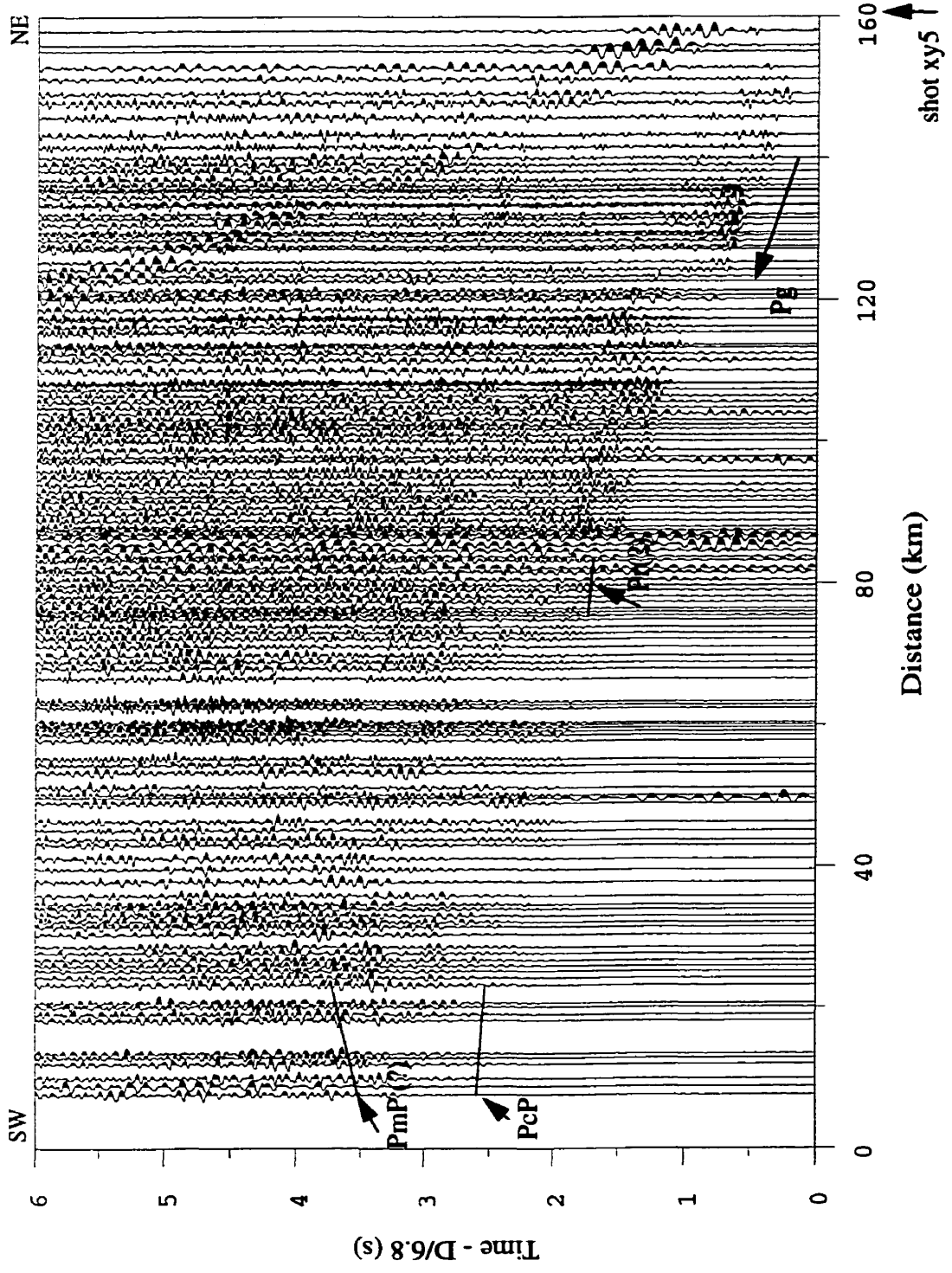

Figure 6.8 Wide -ngle seismic reflection and refraction section of lshot xy5 on in-line XY.

can be identified at offsets less than 70 km. At distances between 70 and 112 km, noise contaminates the seismic traces. However, since the first arrivals have strong amplitudes, the Pg phases within these offsets can still be observed clearly. The amplitude of Pg arrivals decreases at offsets greater than 112 km. For shot xy1, the first arrivals at offsets greater than 60 km have a very low S/N ratio and could not be picked for modeling. The amplitude of the Pg phases at offsets less than 10 km is weak compared with that for shot xy0. Shot xy2 provides high quality data. For shot xy2, the amplitude of the Pg phases at receivers in the southwest is less than that on traces at the corresponding offset in the northeast. This difference implies the existence of near-surface lateral velocity heterogeneity. The energy of first arrivals gradually decreases with increasing offset.

For shot xy4, which is located in the northeast of the Sudbury Basin, only a small number of traces were affected by noise. Therefore, the majority of Pg phases could be picked accurately. All Pg phases indicate weak energy. This phenomenon is probably caused by a strong attenuation effect near the shot point. Shot xy4 is located at the eastern edge of the Sudbury Basin. Hence, the locally complicated geological structure of the basin might produce strong scatter and thus reduce the amplitude of the recorded signals. Pg phases for shot xy5 are also observed to have weak amplitude, except at offsets between 25 and 35 km. As this anomaly is not identified on other sections, it is possibly associated with a very small-scale structure, and will not be interpreted further in this thesis.

Near offset (<5 km) Pg arrivals have apparent velocities of between 5.9 and 6.08 km/s. At offsets between 10 and 40 km, the apparent velocities range from 6.0 to 6.25 km/s. This rapid change of velocity indicates that the near-surface low-velocity layer is very thin and

overlies a high-velocity basement, which is similar to the velocity model along profile AB. At greater offsets (60-80 km), the apparent velocities are in the range of 5.83 to 6.18 km/s. At the farthest offsets (>115km), two measurements of the apparent velocity indicate values of 6.08 and 6.16 km/s.

The variation in the apparent velocity for Pg arrivals observed at near offset increases with increasing offset. The maximum apparent velocity (6.25 km/s) was determined for a distance of 30 km. At greater offset the apparent velocity decreases with increasing distance. At a distance of 110 km, it reaches its minimum value of 5.83 km/s. With increasing distance to the end of the profile, the apparent velocities increases again to 6.08 km/s. The broad range of apparent velocities at a consistent offset for Pg arrivals suggests that there is lateral velocity variation in the near-surface of the upper crust.

2. PcP Phase

PcP phases form weakly-coherent later arrivals. They are identified and picked on all shot sections, often with relatively large picking uncertainty, by referring to sections along profile AB. The apparent velocity for the PcP phase is estimated using only sections of shots xy0 and xy4 (Figures 6.4 and 6.7), which provide clearer phases than other sections. The apparent velocity of PcP arrivals at a 135 km offset is estimated to be 6.48 km/s for shot xy0, and the apparent velocity at an offset of 115 km is estimated to be 6.38 km/s for shot xy4. The similar traveltime of the phases at similar offset on different shots indicates that the middle crustal interface has little relief.

3. Pc Phase

The weak Pc phase arrivals were identified on shot xy0 at offsets greater than 120 km (Figure 6.4). For shots xy1 and xy5, they were picked by referring to sections of profile AB and to synthetic seismogram results. The apparent velocity for Pc phases was analysed only on the basis of shot xy0 at an offset of 152 km. The apparent velocity is 6.67 km/s. This value, combined with the velocity model along profile AB, provides an estimation of the velocity in the upper lower crust, which is taken to be 6.65 km/s.

4. PmP and Pn Phases

PmP phases were picked with large uncertainties on four sections from shots xy0, xy1, xy4 and xy5 (Figures 6.4, 6.5, 6.7 and 6.8). Shot xy4 provides high quality recordings of PmP phases. Therefore, the apparent velocity of PmP arrivals was estimated from the data of shot xy4, and at an offset of 155 km was found to be 6.90 km/s. Similarly, considering the velocity value of 6.92 km/s modeled at the base of the crust along profile AB, the velocity in the base of the crust could be initialized at 6.90-6.92 km/s. The similar travel-times of PmP phases at similar offsets for each of four shots suggests that the Moho interface has little geometric relief.

As line XY has a length of only ~165 km, a Pn phase could not be observed as a first arrivals along the profile. The Pn phase is a weak reflection compared with PcP and PmP phases. Therefore, the arrivals of Pn phases are hard to recognize in the sections. The apparent velocity could not be estimated from the sections for shots xy0 and xy1 because of low reliability. As discussed above, the initial velocity below the Moho boundary was assigned to be 8.06 km/s and the vertical velocity gradient in the mantle was initialized to

0.012 1/s on the basis of the velocity model obtained along line AB.

4. Pr Phase

The unusually coherent Pr phase with strong reflected energy (which appears as a second arrivals) was observed on section xy2 at offsets between 20 and 85 km (Figure 6.6). These strong coherent reflections can be related to a near-surface geological interface as discussed in Section 5.2.4. The reflection location corresponding to this event indicates that the phase is possibly associated with the Sudbury Structure. In addition, there are short coherent Pr phases identified on shots xy4 and xy5 (Figures 6.7 and 6.8). The preliminary interpretation for these relates to the same structure responsible for the strong reflection recorded on the section of shot xy2 (Miao, 1995). Therefore, they were picked and modeled.

There is a relatively strong reflection apparent at the reduced time of 3.4 s at offsets between 135 and 145 km for shot xy0. In addition, there is a weakly coherent reflection apparent at the reduced time of 1.75 s over distances of 30 to 60 km on the section for shot xy4. These two events are marked on the figures only by question marks. The former event correlates over a limited number of traces and is recorded on only one section. Therefore, it will not be further modeled in this thesis. The latter event appears weakly coherent over a number of traces, and is possibly associated with small geological structures beneath the Sudbury Igneous Complex or is outside survey line XY. As only one section revealed this event, modeling of the weak coherent reflection might be unreliable and will not be included in this study.

6.2.2 Modeling Procedure

Ray-based traveltime inverse modeling (RAYINVR, Zelt and Smith, 1992) was performed to interpret the seismic data along profile XY. The initial model was determined from estimates of the apparent velocities and modeling results from profile AB. An improved velocity model was then obtained by fitting the observed traveltimes. The final model was determined by modification of velocities according to a comparison of the amplitudes of the observed and calculated data and maximum ray coverage in the modeling.

1. Phase Picking

Phase picking is the first step in the ray-based traveltime inverse modeling of the wide-angle seismic reflection and refraction data. A total of 1497 traveltimes were picked for Pg, PcP, PmP, Pn and Pr phases. Table 6.1 lists the number of the picked phases and the

Table 6.1 Number of arrival time picks and uncertainties for line XY

Phase / Shot	Pg	PcP	Pc	PmP	Pn	Pr	Total
xy0	144(57)	89(61)	31(54)	57(63)	28(63)		349(50)
xy1	50(54)	104(59)	7(60)	73(70)	9(70)		243(63)
xy2	158(56)	91(58)				72(54)	321(56)
xy4	143(56)	80(57)		31(64)		48(51)	302(56)
xy5	142(52)	75(52)	26(50)	31(60)		8(50)	282(53)
Total	637(52)	439(58)	64(53)	192(65)	37(65)	128(53)	1497(57)

Note: (): picking uncertainty in milliseconds.

picking uncertainties for each shot. The total number of Pg arrivals picked from the five shots is 637 and the average picking uncertainty is 52 milliseconds (ms). The PcP phase provides the second largest group of events picked. The total number of picks is 439 with an average uncertainty of 58 ms. A total of 192 traveltimes were picked for the PmP phase, with a relatively large picking error of 65 ms. The anomalous reflection, Pr phase, was identified from 128 arrivals. Its picking error is 53 ms. A total of 64 Pc and 37 Pn arrivals were picked with 53 ms and 65 ms picking errors respectively.

2. Model Parameterization

The initial velocity model was based on an analysis of the apparent velocities. Three layers and a lenticular high velocity body beneath the Sudbury Basin constitute the main structure (Figure 6.9). The first layer is defined by a sub-horizontal basal interface with a

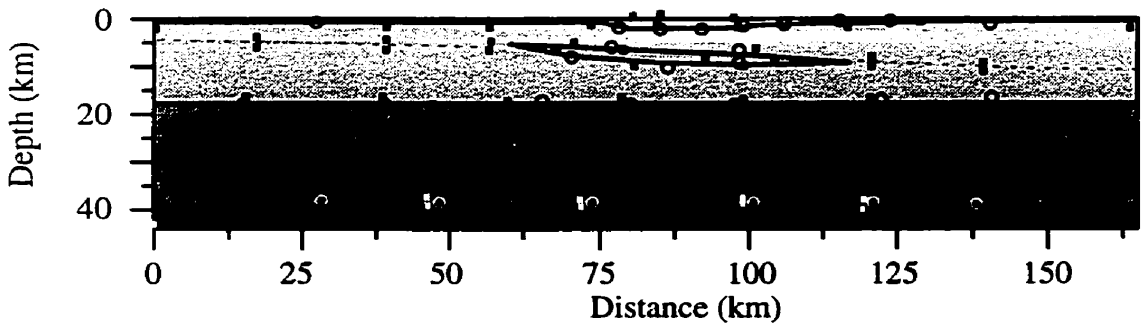

Figure 6.9 Model parameterization of profile XY. Solid lines denote the interface boundaries. Dash lines represent the velocity boundaries. Open circles represent the interface boundaries node and filled squares represent velocity nodes.

shallow depth (~0.5 km) at the two ends of the profile. The depth to the layer increases to ~2.2 km at the center of the profile in the Sudbury Basin, representing a thickening the

low-velocity sediment of the Whitewater series. The thickness of the Whitewater series was based on the seismic reflection image which suggested a thickness of 2 km (Milkereit et al., 1990; Wu, et al., 1994). The initial velocity for the layer was 6.0 km/s. The base of the second layer separated the upper and lower crust at a constant depth of 17.8 km. The third interface represents the Moho discontinuity and is a subhorizontal interface at a depth of 39.4 km. The model includes a lenticular body with a thickness of ~2.5 km in the center (and tapers off at the two ends), at distances of 65 km in the west and 120 km in the northeast of the profile respectively. The body is dipping towards the east from 5 km depth at its southwestern and down to 9 km depth at the eastern end. The initial velocity for the body is 6.3-6.4 km/s.

3. Traveltime Inversion and Amplitude Comparison

Traveltime inversion adjusts the velocity values on the velocity nodes and the depth of the interface boundary nodes to obtain the optimum fit between the observed and calculated data by an iterative procedure. In this thesis, all parameters were modeled simultaneously. Amplitude modeling and comparison between the observed and calculated amplitudes provided supplementary constraints for adjusting the specific parameters.

4. Near-surface Structure

The initial velocity value within the near-surface velocity layer was set to a constant 6.0 km/s. The initial interface boundary geometry is shown in Figure 6.9. After one inversion iteration, the velocity at the top of the layer decreased slightly from 6.0 km/s to 5.95 km/s in the western end of the profile, and from 6.0 km/s to 5.86-5.92 km/s at distances

between 80 km and 103 km, corresponding to the location of the Sudbury Basin. However, the velocity increases to 6.08 km/s towards the eastern end of the profile. The velocity gradient at the bottom of the near-surface layer at the center of the profile, at a distance of 80 km, was then modeled as 0.18 s^{-1}. In the center of the profile at distances of 88-115 km, the vertical velocity gradient is small: ~0.02 s^{-1}. The absolute velocity value is low (5.88 to 5.96 km/s) and corresponds to the velocity values of the Whitewater series sediments (Table 3.1). The velocity at the edges of the profile is close to the modeled velocity (5.95-6.09 km/s) along profile AB. The Pg traveltimes were fitted well with a normalized χ^2 value of 1.48 for this phase (Figures 6.10a, b-6.14a, b).

The amplitudes of the observed data and the synthetic seismogram were compared. The velocity values were modified slightly to minimize discrepancies in the amplitudes of the observed and calculated data as well as to obtain the maximum ray coverage. Velocities of three nodes at the bottom of the eastern end of the profile were reduced from 6.07, 6.08 and 6.08 km/s to 6.0, 5.98 and 5.98 km/s, respectively, in order to match the observed amplitude of a ray propagating from the west. The velocities at the bottom of the low-velocity layer corresponding to the velocity nodes at distances of 103 km and 100 km were also adjusted by increasing the velocity for nodes at distances of 103 km an 100 km from their values 5.78 and 5.88 km/s to 5.95 and 6.02 km/s, respectively. Following these changes, the amplitude modeling indicates a good match between the calculated and observed velocities for the majority of Pg phases (Figures 6.10a, c-6.14a, c). Figure 6.15 shows ray paths according to three kinds of rays: 1) turning rays (Pg1) (Figure 6.15a); 2) refractions (Pg2) travelling along the bottom of the layer (Figure 6.15b); and 3) turning

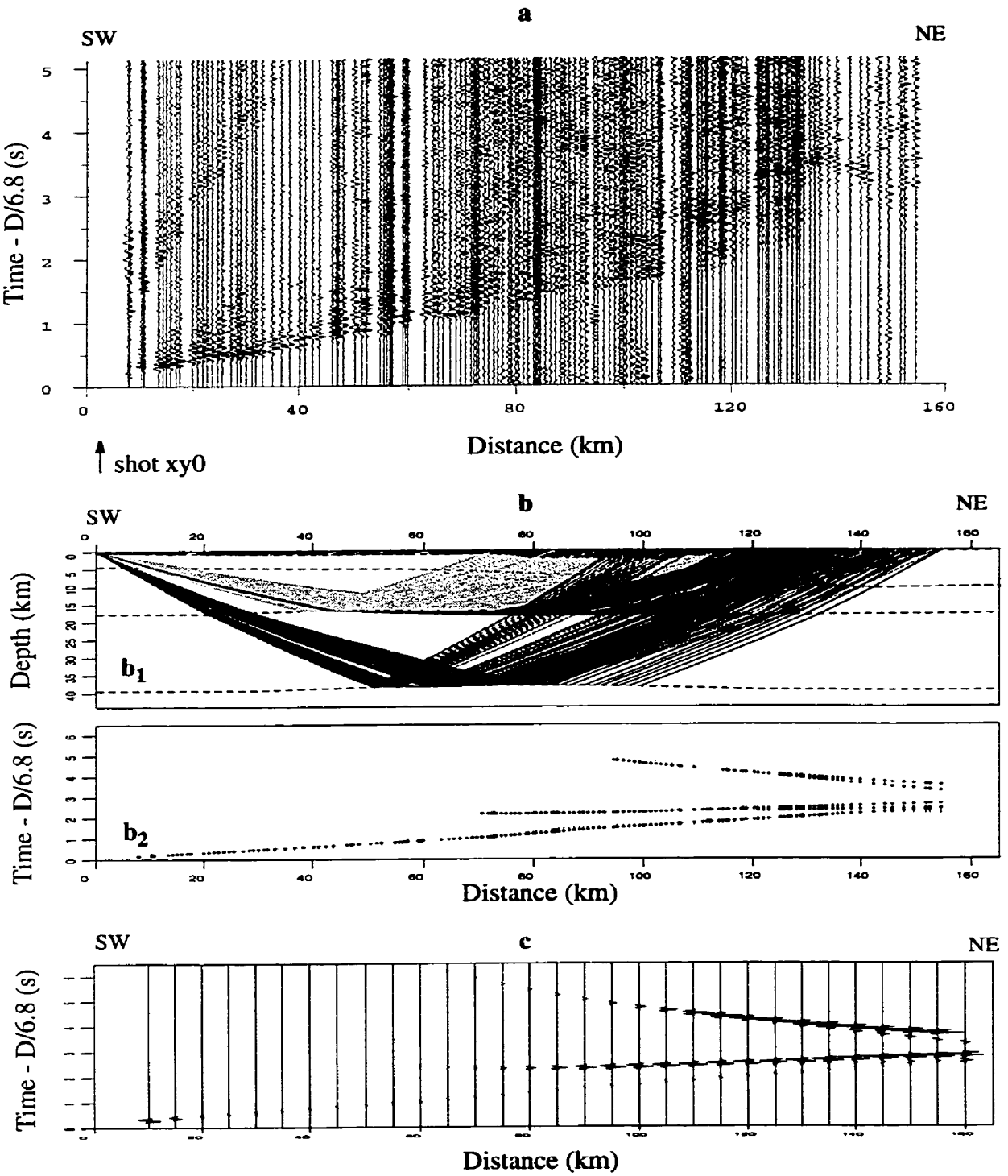

Figure 6.10 In-line seismic section for shot xy0. **a**: seismic section with picked traveltimes; **b**: ray path ($\mathbf{b_1}$) and observed and calculated traveltimes ($\mathbf{b_2}$); **c**: synthetic seismogram. The solid line in **a** represents the picked traveltimes.

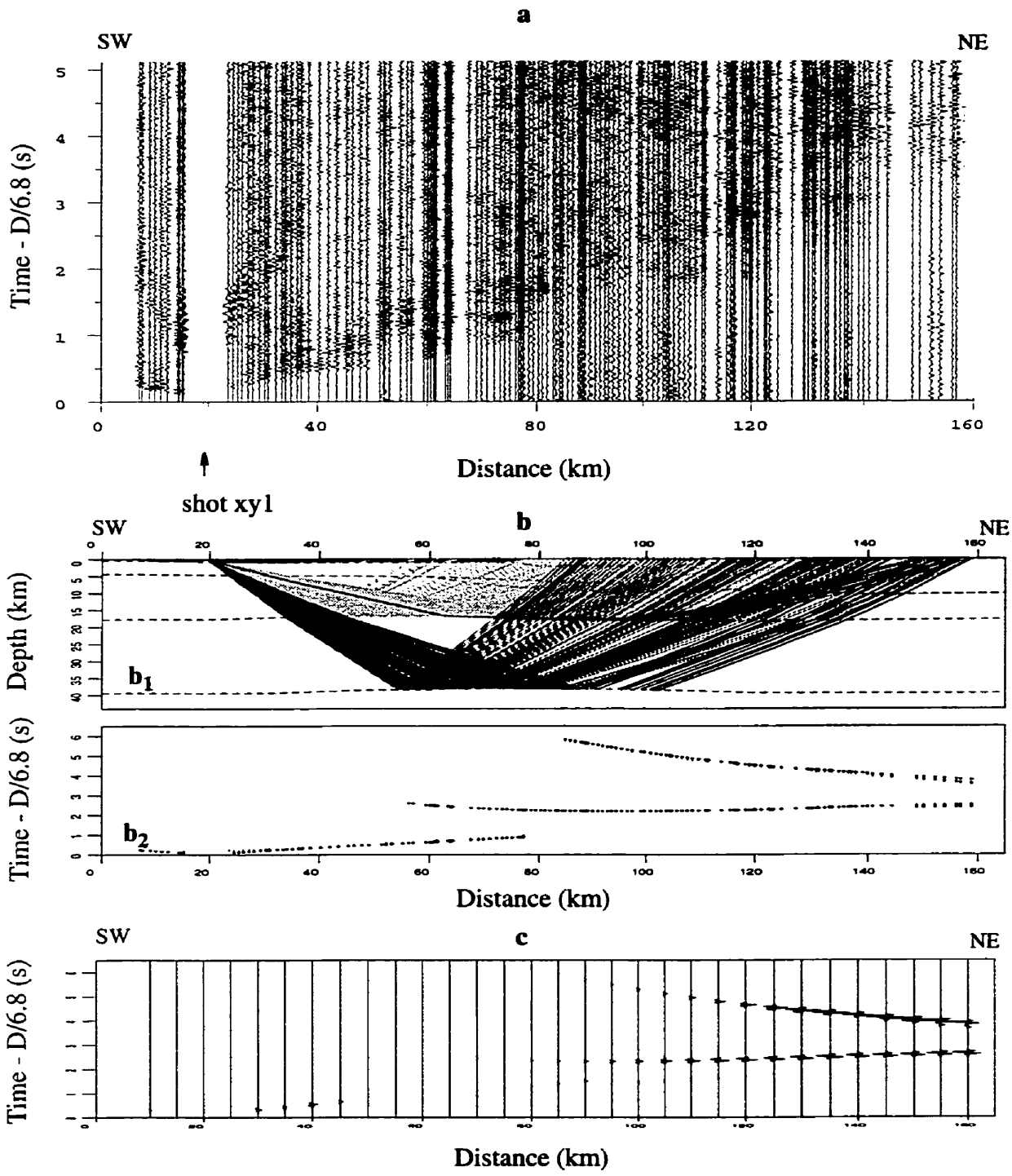

Figure 6.11 In-line seismic section for shot xy1. **a**: seismic section with picked traveltimes; **b**: ray path ($\mathbf{b_1}$) and observed and calculated traveltimes ($\mathbf{b_2}$); **c**: synthetic seismogram. The solid line in **a** represents the picked traveltimes.

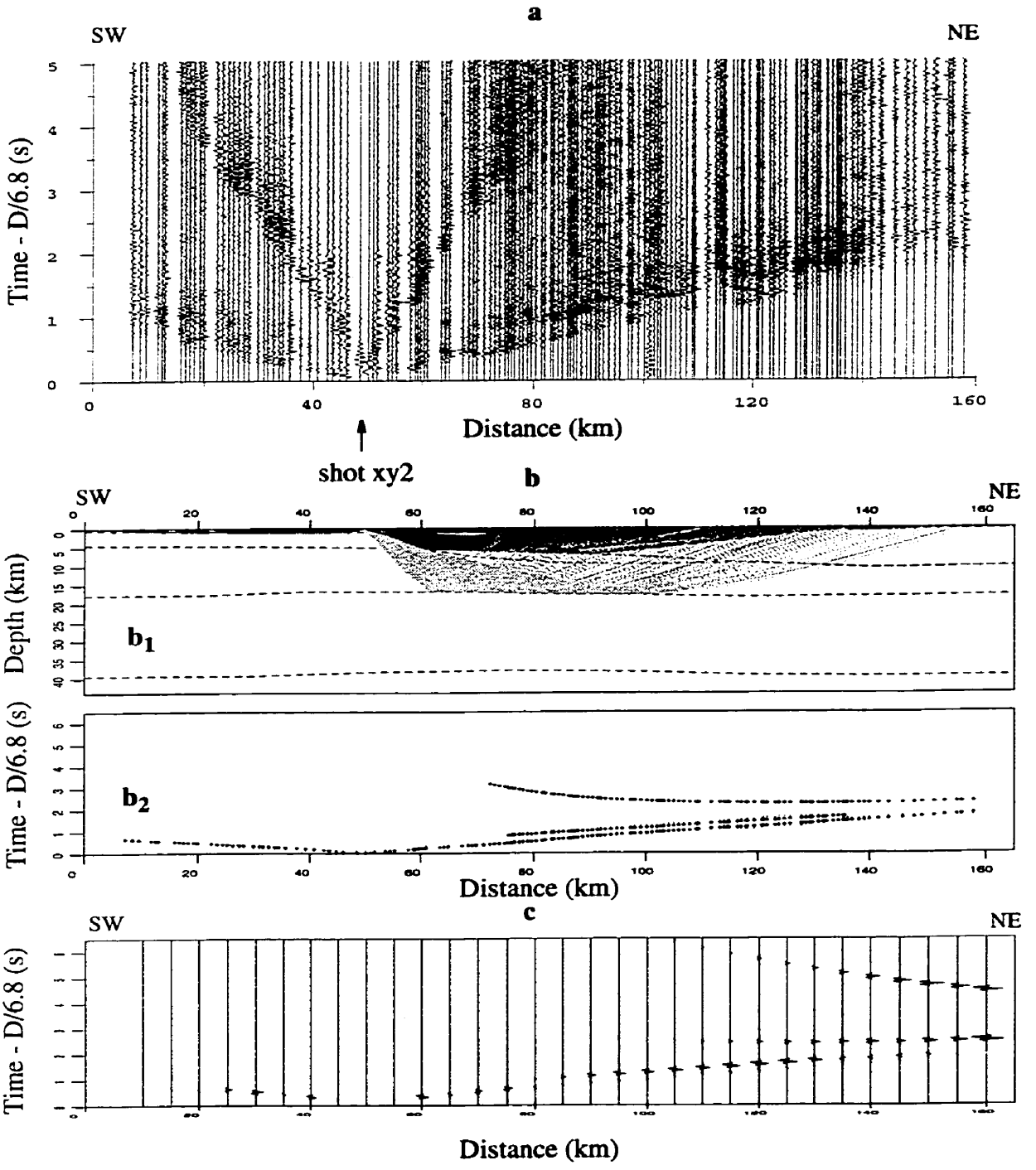

Figure 6.12 In-line seismic section for shot xy2. **a**: seismic section with picked traveltimes; **b**: ray path ($\mathbf{b_1}$) and observed and calculated traveltimes ($\mathbf{b_2}$); **c**: synthetic seismogram. The solid line in **a** represents the picked traveltimes.

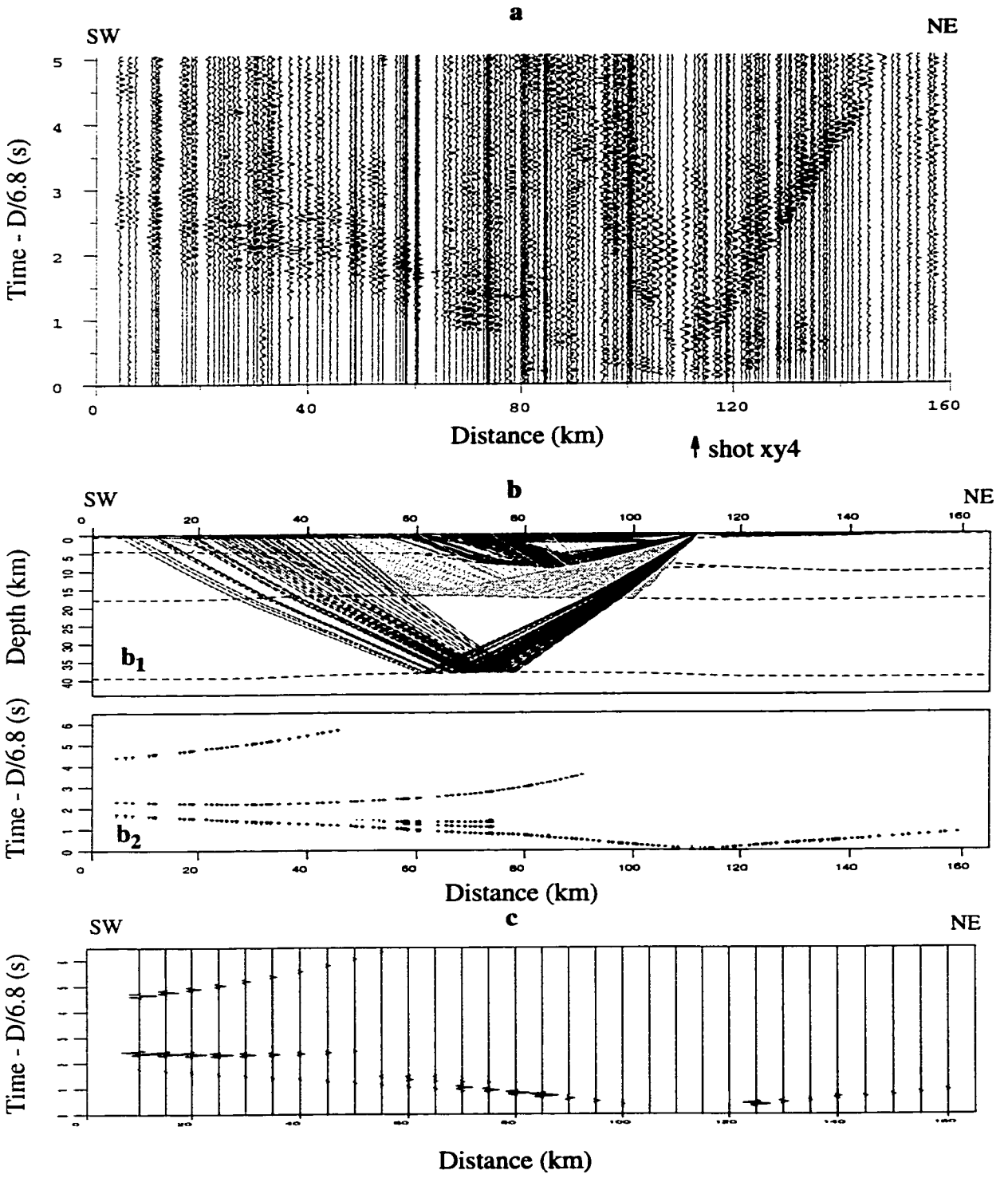

Figure 6.13 In-line seismic section for shot xy4. **a**: seismic section with picked traveltimes; **b**: ray path ($\mathbf{b_1}$) and observed and calculated traveltimes ($\mathbf{b_2}$); **c**: synthetic seismogram. The solid line in **a** represents the picked traveltimes.

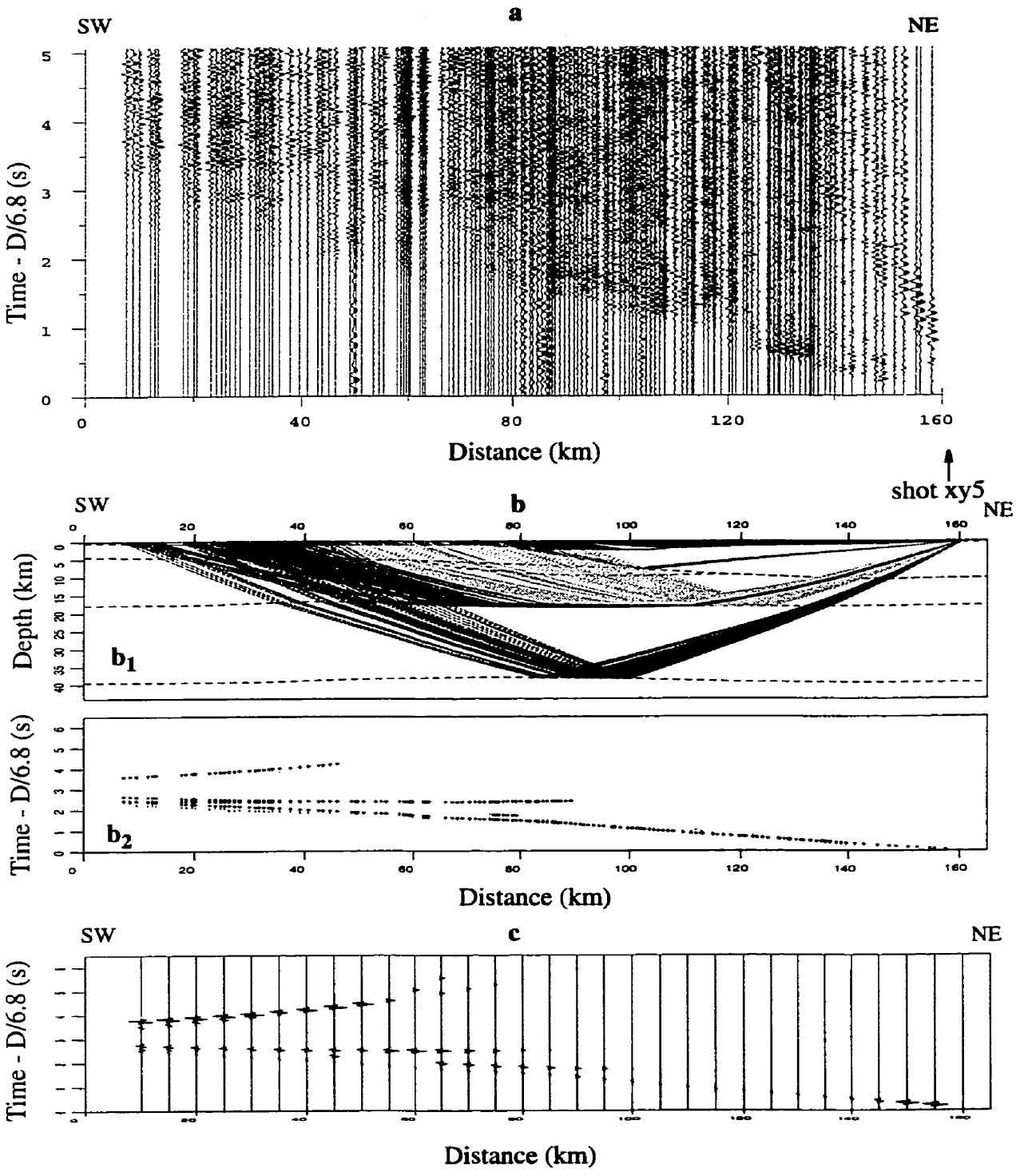

Figure 6.14 In-line seismic section for shot xy5. **a**: seismic section with picked traveltimes; **b**: ray path ($\mathbf{b_1}$) and observed and calculated traveltimes ($\mathbf{b_2}$); **c**: synthetic seismogram. The solid line in **a** represents the picked traveltimes.

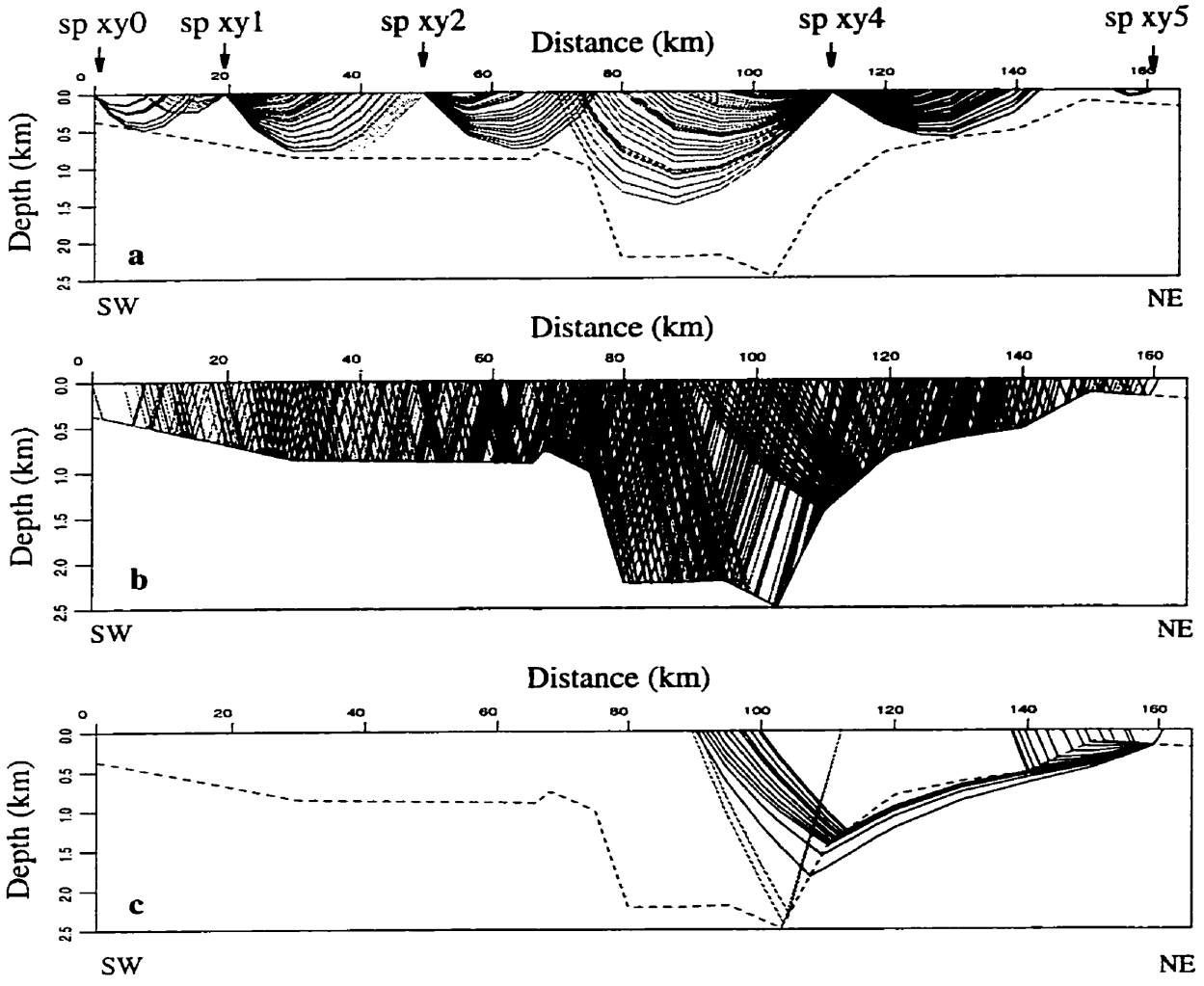

Figure 6.15 Ray paths for turning Pg waves (**a**), head wave refractions (**b**) and turning wave propagating through the first layer and the upper second layer (**c**). sp indicates shot points.

waves through the top of the second layer (Pg3) (Figure 6.15c). The modeling results for these three waves is also listed in Table 6.2.

Table 6.2 RMS traveltime residual and χ^2 in the inversion of the seismic refraction data of profile XY

Seismic Phase	No. of Picks	RMS t. r. (s)	χ^2
Pg1	593	0.07	1.54
Pg2	159	0.06	1.25
Pg3	92	0.04	0.74
Pg	632	0.07	1.48
PcP, Pc	504	0.02	0.17
PmP, Pn	228	0.03	0.29
Pr	122	0.04	0.48
Total	1483	0.05	0.77

Note: Pg1: turning wave in the first layer
Pg2: refraction along the bottom of the first layer
Pg3: turning wave propagating in the top of the second layer
χ^2 : normalized chi-square
RMS t. r.: root mean square traveltime residual (s)

5. Upper Crustal Structure

The upper crust is defined in the seismic structure as the zone between the near-surface velocity layer and the boundary interface between the upper and lower crust. The velocities at the top of the upper crustal layer were determined partly by refraction head waves travelling along the low-velocity interface. There is a high-velocity discontinuity defined within this zone. The purpose of including this velocity discontinuity is to investi-

gate the lateral velocity heterogeneity in the area surrounding the Sudbury Basin. The depth of this discontinuity is approximately 4 km at the western end of the profile. The depth of the boundary of the discontinuity increases linearly to 6 km at 60 km distance. To northeast, it extends along the interface of the top boundary of the high-velocity anomalous body. At a distance of 117 km, the depth increases to 9 km. The depth of the discontinuity continually increases to 10 km at the eastern end of the profile. There are seven velocity nodes in the mid-crustal interface (Figure 6.9).

The velocity of the node at the top of the high-velocity interface at a distance of 88 km was modified by decreasing its velocity by 0.05km/s from 6.18 to 6.13 km/s for improvement of ray coverage. The other three velocity values along the velocity discontinuity were also adjusted for ray coverage improvement and in order to match the observed amplitude of the Pr phase. At a distance of 40 km, the velocity increased from 6.04 to 6.08 km/s. At a distance of 68 km, it was adjusted by +0.06 km/s. The final velocity at this node was given as 5.89 km/s. The velocity at the third node was modified the most. It increased from 5.92 km/s to 6.01 km/s. However, all four modifications were within the estimated velocity uncertainty (0.1 km/s).

The velocity modeled at the top of the upper crustal layer is characterized by one relatively high-velocity zone and one low-velocity zone. In the inversion model, the relatively high-velocity zone was modeled at distances between 20 and 40 km with an average velocity of 6.23 km/s. The velocity at distances of 68-88 km was approximately 6.13 km/s. Then, the velocity at the top of the layer was dropped to 6.03 km/s at a distance of 110 km, which was near the northeastern end of the Sudbury Basin. The velocity finally increased to 6.13 km/s at distances of 120 to 140 km. The low velocity might correspond

to the sedimentary formations in the Sudbury Basin, whereas the high-velocity feature outside of the Sudbury Basin might be associated with the local high-velocity anomalous body in the southwestern part of the profile.

In the inversion model, there are two pairs of velocity nodes which indicate that there are significant changes between the velocities above and below the velocity discontinuity corresponding to the same location. One was modeled at a distance of 40 km; the other at a distance of 120 km. At 120 km distance, the difference between velocities above and below the discontinuity was ~0.23 km/s. The velocity jumped from 6.01 km/s to 6.24 km/s crossing the velocity discontinuity. The distance of 120 km indicates that this node lies inside the eastern edge of the Sudbury structure. Therefore, the abrupt change in velocity at a depth of 9 km is related to the Sudbury Structure or Sudbury Igneous Complex. In contrast, the positive velocity contrast of 0.16 km/s cross the interface at 40 km distance seems to correspond to the anomalous source of a positive gravity anomaly in the southwest of the Sudbury Basin as observed in Figure 3.5.

In the inversion model, the velocity at the bottom of the upper crustal layer is in the range of 6.26-6.45 km/s. Beneath the Sudbury Basin, the velocity is approximately 6.35 km/s. The total number of picked traveltimes for PcP and Pc phases involved in modeling is 504 and the value of the normalized χ^2 is 0.17 with an RMS traveltime residual of 0.023 s. The χ^2 value indicates an overfit in the modeling for the phases of PcP and Pc. One possible reason for this overfit is the large number of velocity and interface nodes selected. Since the velocity in the upper crust is varying laterally (which will also be indicated in 3-D tomographic images discussed in Chapter 8), a large number of velocity and

interface nodes had to be included to represent the actual velocity structure. In this case, the velocity model for profile AB is used to compare the velocity in the mid-crust at the cross point.

The cross point between profile XY and AB is located at a 77 km distance on profile XY and at 98 km distance on profile AB. On the profile XY the average velocity in the near-surface layer at a distance of 76 km is 5.94 km/s and the layer thickness is slightly greater than 1.0 km. On profile AB, at a distance of 98 km the velocity in the near-surface layer is modeled as 5.95 km/s with a layer thickness of 1.0 km. On profile AB, at the top of the upper crust, the velocity is 6.10 km/s and at the bottom of the upper crustal layer it is 6.34 km/s with a 17.3 km upper crustal thickness. These numbers compare well to 6.13 and 6.32 km/s for the velocities and 17.4 km for depth at the cross point on profile XY. Therefore, the models of the upper crust along two profiles were well tied at the cross point.

For shot xy0, the theoretical amplitude could not be matched very well with the observed data because there are high amplitude phases apparent at 0.5 s and 0.4 s at distances of 122 km to 158 km which affect the trace amplitude energy. Therefore, we cannot compare measured and modeled amplitudes for that region (Figures 6.10a and 6.10c). Shot xy1 represents a similar case (Figures 6.11a and 6.11c). For shot xy4 strong amplitudes for the PcP wave were modeled at offsets between 80 and 100 km. This pattern is compatible with the observed phases (Figures 6.13a and 6.13c). There is also a very good fit between calculated and observed amplitudes for shot xy5 (Figures 6.14a and 6.14c). The theoretical amplitude of PcP phases is larger than those of the Pg and Pc phase but

smaller than that of the PmP phase. Figure 6.16a shows the ray paths of the PcP and Pc reflections for all shots involved in modeling.

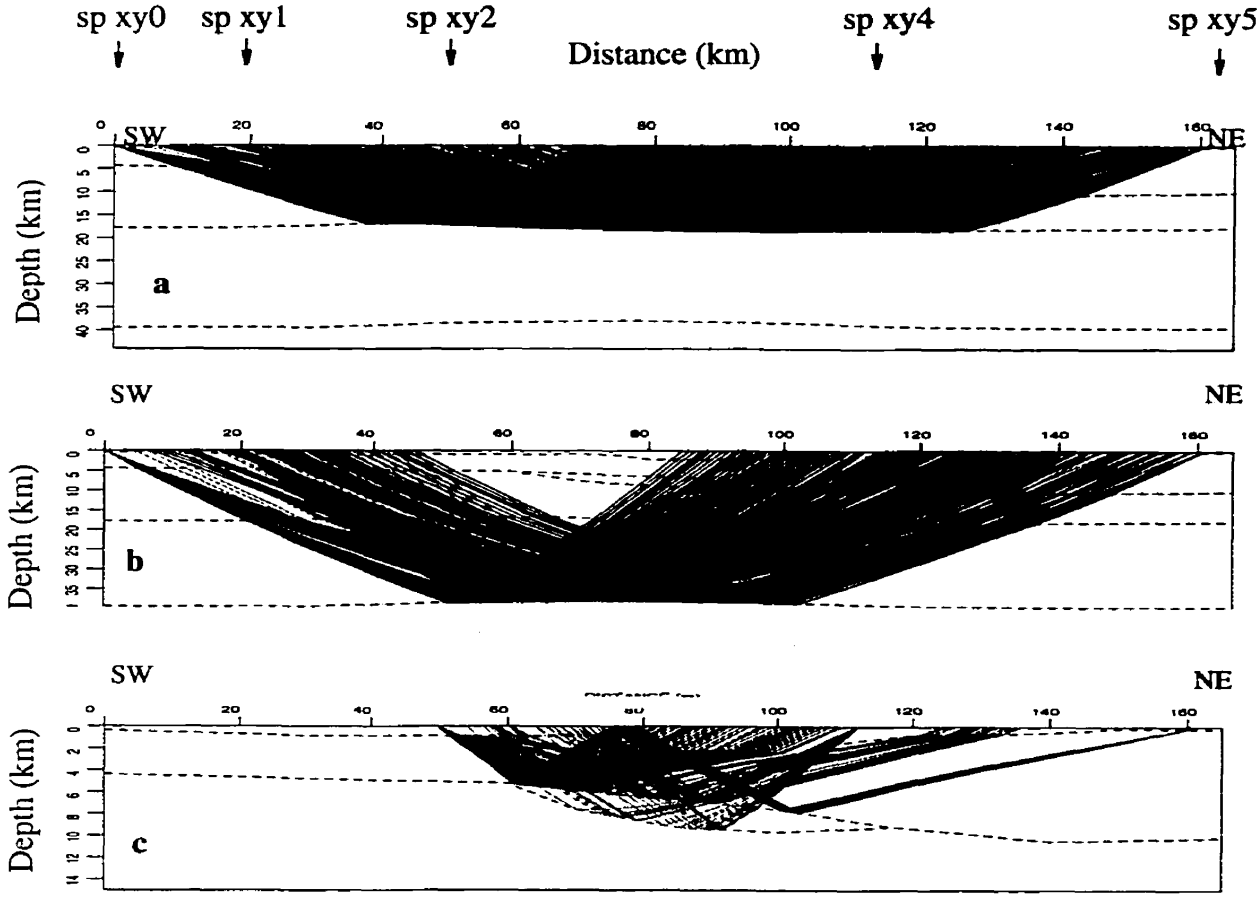

Figure 6.16 A selective plot of ray paths of Pr (**a**), PcP and Pc (**b**), and PmP and Pn (**c**) phases.

7. Lower Crustal and Upper Mantle Structures

The lower crustal and upper mantle structure were not constrained well by seismic data along profile XY because no Pn phases were observed due to the limited length of the profile. The velocity, especially in the upper mantle, is constrained partially by the velocity model of profile AB.

A total of 228 arrivals of PmP and Pn phases were picked for inversion modeling with 6 velocity nodes at the bottom of the lower crust and 6 interface nodes for reconstruction of the Moho discontinuity. The velocity at the top of the lower crust layer is constrained mainly by Pc phases. In the inversion model, the modeled velocity lies in the range of 6.56 km/s at a 30 km distance to 6.71 km/s at a 75 km distance. At a distance of 100 km, the velocity is approximately 6.6 km/s. At the cross point, it is 6.70 km/s. Forward modeling along profile AB gave 6.6 km/s for the velocity at the cross point. Although there is a 0.1 km/s difference between these values, the velocity uncertainty of the inverse modeling is also 0.1 km/s. Figure 6.16b shows ray coverage for the PmP and Pn phase for all receivers used in the modeling.

The RMS traveltime residual was 0.034 s for the PmP and Pn phases with the value of normalized χ^2 equal to 0.29 which indicates overfitting. At the cross point, the velocities above and below the Moho discontinuity are 7.0 and 8.08 km/s respectively. The velocities modeled along profile AB show comparable values at the cross point, 6.92 and 8.08 km/s respectively. The depth of the Moho boundary at the point is also well tied by values of 37.9 km on profile XY and 37.7 km for profile AB.

The amplitudes of the synthetic seismograms for PmP and Pn phases provide a good fit to the observed amplitudes, particularly for shot xy4 and xy5 (Figures 6.13a, c and 6.14

a, c). Figure 6.16b shows the PmP and Pn ray paths.

8. Structure Associated with Strong Near-surface Reflection

Anomalous reflections, Pr phases, were observed as second and third arrivals on shots xy2, xy4 and xy5 (Figures 6.6a-6.8a). Two Pr phase events were identified at offsets of 35 km to 60 km for shot xy4. The separate Pr arrivals join together at an offset of 50 km which implies the Pr phases could be caused by a velocity structure or body at an offset of 30 km. This offset corresponds to a distance of 80 km along the profile and thus to the location of the Sudbury Basin. The top of the Sudbury Igneous Complex beneath the Sudbury Basin was identified as a strong reflection interface in a high-resolution seismic reflection image (Milkereit et al., 1992; Wu et al., 1994). Therefore, the initial model for the interpretation of Pr phases was assigned a high anomalous velocity body dipping towards the east with a central thickness of 2.5 km.

Four velocity nodes were selected; two controlled the top of the anomalous body and the other two defined the velocity at the bottom. The total number of upper and lower boundary nodes was 5 (Figure 6.9). A total of 122 traveltimes were picked for the Pr phases. The initial velocity of the anomalous body was assigned values of 6.35 to 6.4 km/s. The velocity values in the inversion model at the top of the upper layer of the high-velocity body is 6.35-6.37 km/s. However, there was no ray traveling through the area of velocity node of 6.35 km/s. Therefore, the velocity of 6.35 km/s was modified by reducing it by 0.04 km/s to increase the ray coverage. The final velocity was found to be in the range of 6.31 to 6.37 km/s which is reasonably close to the 6.4 km/s obtained in forward modeling along profile AB. These discrepancies are within the velocity uncertainty of 0.1

km/s. The RMS traveltime residual is 0.04 s with the value of normalized χ^2 equal to 0.48. The ray paths corresponding to these reflections are shown in Figure 6.16c.

The amplitude modeling indicates a good match between the synthetic seismogram and observed reflection data. The final velocity values corresponding to the velocity nodes are shown in Figure 6.17.

The final velocity model with a high-velocity body at distances of ~75-120 km beneath the Sudbury Basin. The depth of the base of the near-surface layer decreases to ~2 km in the center of the profile at the Sudbury Basin. The mid-crustal interface and Moho discontinuity were modeled as subhorizontal layers. There is no significant center uplift in the lower crust and upper mantle. There is no high-velocity zone in the lower crust and upper mantle.

9. Discussion of Resolution and Uncertainty

Table 6.3 lists the least-squares modeling resolution for important parameters involved in the inversion. For the first layer, more than half of the parameter nodes have high modeling resolution (>0.5). In the middle crust layer, a majority of parameters were modeled with good resolution. In the lower crust and upper mantle, there were fifteen parameters with high-resolution, and five parameters with low modeling resolution of 0.2-0.41 and there are thirteen parameters with very low resolution. These thirteen parameters correspond to locations at the edge of the profile. Therefore, this low resolution could be caused by insufficient ray coverage. For the high-velocity body, five parameters were obtained with a resolution higher than 0.42. The other four have resolutions from 0.07 to 0.32. The

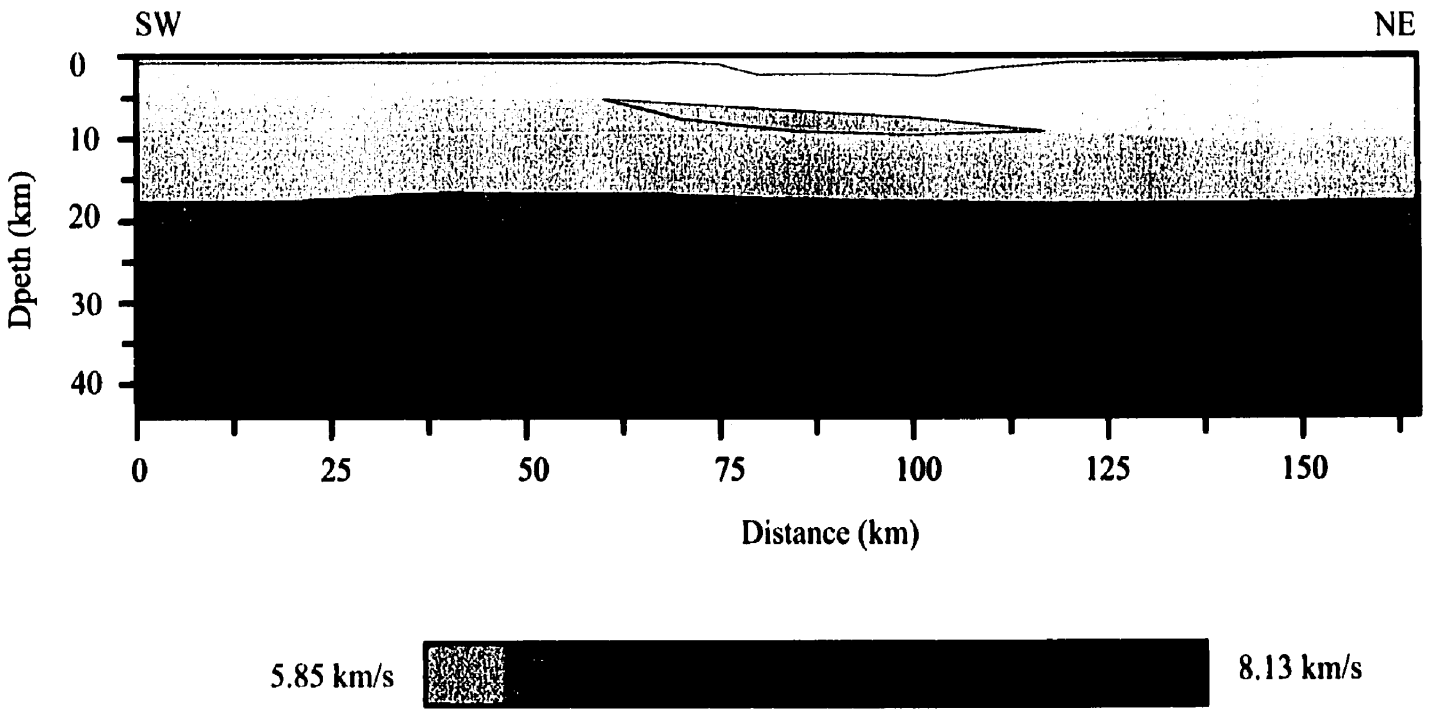

Figure 6.17 The seismic velocity structure modeled by using RAYINVR ray tracing forward and inverse modeling along proble XY. The solid line represents the interface boundaries.

relatively low model resolution for the anomalous velocity body is explained by the large number of velocity and interface boundary nodes parameterized. In other words, the data require a much more simplified model than this. Conversely, denser sampling in space is required to model adequately small-scale features of a complex geological structure like the Sudbury Structure.

One advantage of inversion modeling is to provide the possibility of estimating reliability in terms of model resolution and uncertainty. It is very difficult to quantify the resolution and uncertainty with respect to the "true" model because of the non-uniqueness inherent in geophysical inversions in general. However, the resolution and uncertainty for the inverse model can be estimated.

Zelt and Smith (1992) suggested a model perturbation approach to investigate model reliability. The method can be defined in terms of three steps: (1) positively and negatively perturb the velocity or interface depth for each nodes; (2) calculate the traveltime corresponding to the modified model parameters; and (3) compare the discrepancy of the calculated and observed data in terms of the value of χ^2, and the ability to obtain reasonable ray coverage. This estimation thus depends partly on empirical experience.

Louder and Fan (1998) discussed the error analysis of the final model using a different perspective from Zelt and Smith's approach. Louder and Fan (1998) applied the vertical resolution estimation used for exploration seismic reflection data to obtain the vertical interface uncertainty for seismic wide-angle reflection data. They derived the velocity uncertainty formula as $dv = \frac{dl}{t} - \frac{l dt}{t^2} \le \frac{|dl|}{t} + \frac{l|dt|}{t^2}$, where v denotes velocity, t repre-

sents time and l is the length of the ray path. The above formula was obtained by differentiating the velocity equation, $v = l/t$. However, when they estimated the uncertainty of velocity, $|dl|$ was assumed to be the vertical interface uncertainty. Since a ray in seismic refraction modeling does not have a near-vertical orientation as is the case of stacked data in exploration seismology, the ray path uncertainty could not be precisely represented by the vertical ray path uncertainty. In this thesis, the model parameter uncertainty is therefore analysed following a modified version of the approach of Zelt and Smith.

Parameter uncertainties of the final model of profile XY were estimated according to Zelt and Smith's perturbation assessment method. However, a single parameter perturbation was replaced by the simultaneous perturbation of parameters at the same depth level. Therefore, parameters at the same depth level can positively and negatively be perturbed at the same time to obtain parameter uncertainties. Since several velocity parameters have been modified to fit the amplitude and to improve ray coverage, these parameters will not be used in estimation of uncertainty.

On the basis of the resolution analysis, the near-surface layer velocity and boundary depth parameters have uncertainties of ±0.1 km/s and ±0.3 km, respectively. The perturbed velocity values of this magnitude cause an 11-26% increase in the normalized χ^2 in the Pg phase modeling, for example. A positive 0.3 km perturbation in boundary nodes give rise to a 22% increase in χ^2, whereas a negative perturbation reduces the ray coverage by ~19%. Therefore, ±0.1 km/s and ±0.3 km were considered as the maximum modeling uncertainties in the velocity and depth respectively. However, for five modified velocities indicated in Table 6.3., the uncertainty is as high as 0.15 km/s. Similarly, uncer-

Table 6.3 Model resolution of main parameters

type	orig. par.	uncert.	adjust.	new par.	resol.	std. error
2	6.0000	0.1000	-0.0429	5.9571	0.8085	0.0438
2	6.0000	0.1000	-0.0477	5.9523	0.8210	0.0423
2	6.0000	0.1000	-0.1615	5.8385	0.6260	0.0612
2	6.0000	0.1000	-0.1209	5.8791	0.7441	0.0506
2	6.0000	0.1000	-0.0805	5.9195	0.8638	0.0369
2	6.0000	0.1000	0.0651	6.0651	0.7831	0.0466
2	6.0000	0.1000	0.0755	6.0755	0.2655	0.0857
2	6.0000	0.1000	0.0763	6.0763	0.3836	0.0785
2	6.0000	0.1000	-0.0439	5.9561	0.4413	0.0747
2	6.0000	0.1000	-0.2177	5.7823	0.3459	0.0809
2	6.0000	0.1000	-0.1239	5.8761	0.1918	0.0899
1	0.6500	0.5000	-0.4574	0.1926	0.4846	0.3590
1	0.6800	0.5000	0.0720	0.7520	0.8760	0.1761
1	2.0500	0.5000	0.2225	2.2725	0.3399	0.4062
1	2.0000	0.5000	0.1949	2.1949	0.2930	0.4204
1	2.0000	0.5000	0.1639	2.1639	0.3192	0.4125
1	1.2000	0.5000	1.2180	2.4180	0.4310	0.3772
1	1.0000	0.5000	0.5518	1.5518	0.6237	0.3067
1	0.8900	0.5000	-0.0964	0.7936	0.5967	0.3175
1	0.6000	0.5000	0.0662	0.6662	0.6558	0.2933
1	0.6000	0.5000	-0.0854	0.5146	0.5590	0.3321
1	0.6200	0.5000	-0.4044	0.2156	0.3245	0.4109
1	0.6000	0.5000	-0.3415	0.2585	0.1324	0.4657
2	6.1000	0.1000	0.0978	6.1978	0.9825	0.0132
2	6.1000	0.1000	0.1574	6.2574	0.9915	0.0092
2	6.1000	0.1000	0.0397	6.1397	0.9727	0.0165
2	6.1000	0.1000	0.0816	6.1816	0.9722	0.0167
2	6.1000	0.1000	-0.0657	6.0343	0.9441	0.0236
2	6.1000	0.1000	0.0215	6.1215	0.9398	0.0245
2	6.1000	0.1000	0.0450	6.1450	0.9377	0.0250
2	6.1000	0.1000	-0.0701	6.0299	0.6391	0.0601
2	6.1000	0.1000	0.0242	6.1242	0.2266	0.0879
2	6.1000	0.1000	-0.0607	6.0393	0.3324	0.0817
2	6.1000	0.1000	-0.2693	5.8307	0.9137	0.0294
2	6.1000	0.1000	-0.1805	5.9195	0.9180	0.0286
2	6.1000	0.1000	-0.0358	6.0642	0.7373	0.0513
2	6.1000	0.1000	-0.0884	6.0116	0.7328	0.0517
2	6.1000	0.1000	0.1014	6.2014	0.5481	0.0672
1	8.0000	0.5000	-0.4518	7.5482	0.5218	0.3458

1	9.2000	0.5000	-0.0238	9.1762	0.0728	0.4815
2	6.3500	0.1000	-0.0394	6.3106	0.2400	0.0872
2	6.3500	0.1000	-0.0104	6.3396	0.0227	0.0989
2	6.4000	0.1000	0.0145	6.4145	0.5639	0.0660
2	6.3500	0.1000	0.0081	6.3419	0.3195	0.0825
1	7.9000	0.5000	-0.1613	7.7387	0.5571	0.3328
1	9.3800	0.5000	-0.1753	9.2047	0.7795	0.2348
1	9.5000	0.5000	0.1130	9.6130	0.4375	0.3750
2	6.2000	0.1000	0.0017	6.2017	0.5829	0.0646
2	6.2500	0.1000	-0.0083	6.2417	0.6608	0.0582
2	6.2500	0.1000	0.0388	6.2888	0.8416	0.0398
2	6.2500	0.1000	-0.1246	6.1254	0.6795	0.0566
2	6.2500	0.1000	-0.0143	6.2357	0.4457	0.0744
2	6.2500	0.1000	0.0391	6.2891	0.1919	0.0899
2	6.3500	0.1000	-0.0618	6.2882	0.4754	0.0724
2	6.3500	0.1000	-0.0867	6.2633	0.6474	0.0594
2	6.3500	0.1000	0.0218	6.3718	0.6668	0.0577
2	6.3500	0.1000	-0.0422	6.3078	0.6602	0.0583
2	6.3500	0.1000	0.1455	6.4955	0.6520	0.0590
2	6.3500	0.1000	-0.0560	6.2940	0.4817	0.0720
2	6.3500	0.1000	0.0261	6.3761	0.1464	0.0924
1	17.8000	0.5000	-0.0775	17.7225	0.2105	0.4443
1	17.8000	0.5000	-1.1043	16.6957	0.9212	0.1403
1	17.8000	0.5000	-0.8511	16.9489	0.9597	0.1004
1	17.8000	0.5000	-0.4133	17.3867	0.9259	0.1361
1	17.8000	0.5000	0.0260	17.8260	0.9643	0.0944
1	17.8000	0.5000	0.2053	18.0053	0.6566	0.2930
1	17.8000	0.5000	0.1709	17.9709	0.1419	0.4632
2	6.7000	0.1000	-0.1397	6.5603	0.3720	0.0792
2	6.7000	0.1000	-0.0258	6.6742	0.7192	0.0530
2	6.6500	0.1000	0.0449	6.6949	0.8355	0.0406
2	6.6500	0.1000	-0.0503	6.5997	0.8022	0.0445
2	6.6500	0.1000	0.0441	6.6941	0.4050	0.0771
2	6.6500	0.1000	0.0549	6.7049	0.1038	0.0947
2	6.9000	0.1000	0.0822	6.9822	0.4090	0.0769
2	6.9000	0.1000	0.1089	7.0089	0.5816	0.0647
2	6.9000	0.1000	0.0320	6.9320	0.4742	0.0725
2	6.9000	0.1000	0.0784	6.9784	0.1299	0.0933
1	39.4000	0.5000	-1.1273	38.2727	0.8142	0.2155
1	39.4000	0.5000	-1.6031	37.7969	0.8616	0.1860
1	39.4000	0.5000	-1.1392	38.2608	0.6010	0.3158
1	39.4000	0.5000	-0.1211	39.2789	0.0456	0.4885
2	8.0600	0.1000	-0.0545	8.0055	0.1343	0.0930
2	8.0600	0.1000	0.0206	8.0806	0.7196	0.0529

2	8.0600	0.1000	0.0042	8.0642	0.5516	0.0670
2	8.0600	0.1000	-0.0008	8.0592	0.0916	0.0953
2	8.1300	0.1000	0.0000	8.1300	0.0000	0.1000

Damping factor: 1.0

Note: **type**: 1:depths of interfaces; **type** 2: velocities;
orig. par.: original parameters. 1 is for depth in km and 2 is for velocity in km/s; **uncert.**: uncertainty of parameter; **adjust.**: adjustment of parameter; **new par.**: new parameters; **resol.**: model resolution; **std. error**: standard error (see the text).
The data underlined were modified within the prior uncertainties for amplitude fitting and ray coverage.

tainties of ±0.12 km/s in velocity and ±1.0 km in depth could be obtained for the upper crust model where such perturbation caused the χ^2 to increase to 1.93. For the high-velocity body in the upper crust, the parameter uncertainties are mainly constrained by Pr phases, which have relatively high values of ±0.2 km/s and ±1.5 km due to insufficient ray coverage. In the lower crust, the velocity uncertainty is in the range of ±0.18 km/s and a boundary depth uncertainty of ±1.0 km. In the upper mantle, the velocity uncertainty is high at ±0.2 km/s. The general variation in parameter uncertainties indicates that the uncertainty increases at greater depths because of decreasing ray coverage.

6.3 Summary

The RAYINVR ray tracing forward and inversion algorithm applied the basic ray tracing system discussed in equation 5.20. The solution of the ray tracing system was obtained by numerical iteration as described in Chapter 5. However, in the forward mode-

ling of the RAYINVR method, a ray traveltime from shot to receiver was linearly interpolated using two computed traveltimes associated with the two closest rays but not determined by tracing an exact ray path which was applied in the method. The model parameters are simpler in this approach than in the Cerveny's ray tracing algorithm. In inversion, a damped least-squares technique was employed. The RAYINVR algorithm provides estimates of the model resolution and parameter uncertainty which cannot be given by forward modeling.

Analyses of seismic phases and gravity models indicate that the structure near the surface and in the upper crust along profile XY is laterally heterogeneous. Therefore, there are large numbers of velocity nodes and interface boundaries in the velocity model to allow for a good estimate of the real structure. In addition, in the middle and lower crust, a relatively large number of parameters are required to allow for the possibility of a mafic block and central uplift feature as expected by some hypotheses of the Sudbury formation. However, the RAYINVR algorithm requires a limited number of parameters in a model in order to obtain a high model resolution. The final model along profile XY includes a large lateral variation in velocity required by the real situation, at the cost of a lower model resolution than expected.

In this study, the preliminary model (Miao, 1995) was confirmed, modified and refined by the inversion modeling. The unusual structure, responsible for the strong reflection (Pr) mainly observed on the section of shot xy2, was modeled as a lenticular high-velocity body. The location of the body was refined at distances between ~65 and ~120 km and buried at depths of ~4 to 9 km, with apparent dip towards the east. The velocity of the anomalous body is approximately 6.34 km/s which is close to the 6.4 km/s obtained in the

forward modeling along profile AB. The velocity model has a RMS traveltime residual of 0.04 s and a normalized χ^2 of 0.48. The velocity and boundary uncertainties are ±0.2 km/s and ±1.5 km, respectively.

The velocity in the upper crust is highly variable in both lateral and vertical directions. The thesis study results indicate that there is a high-velocity body (6.26 km/s) modeled near the surface at a distance of ~30 km, which is probably associated with mafic rocks responsible for the western part of the linear gravity high anomaly. For the upper crustal model parameters, the normalized χ^2 is 1.48 and uncertainties are ±0.12 km/s in velocity and ±1.0 km in depth. In the middle and lower crust, velocity does not significantly vary laterally, and the mid-crustal interface and the Moho discontinuity are subhorizontal. The velocity structure was tied at the cross point of profiles XY and AB. The uncertainties of velocity and depth are ±0.18 km/s and ±1.0 km respectively. Generally, there is a good match between the observed and calculated amplitudes.

Chapter 7

Fan-shot Data Modeling

During the 1992 Lithoprobe Abitibi-Grenville transect high-resolution seismic reflection and refraction experiment, not only were in-line seismic data recorded but also several sets of broadside fan-shot data. The broadside fan-shot data can be used to extract 3-D crustal structure and velocity information (Kanasewich and Chiu, 1985). This chapter describes a 3-D ray tracing forward and inverse modeling algorithm developed during the early part of this Ph. D. thesis research. It then describes an investigation of the 3-D velocity structure of the Sudbury Structure using this algorithm. The field layout, including shot and receiver locations, was discussed in Chapter 4, and will not be repeated here. Figure 7.1 shows the fan-shot survey pattern. The minimum and maximum offsets are typically ~11 km and ~175 km respectively.

7.1 3-D Modeling Method

7.1.1 Fletcher Reeves Ray Tracing

The calculation of traveltime for a simplified 3-D model was implemented by solving a set of nonlinear equations (Kanasewich and Chiu, 1985). The estimation of the solution is usually obtained by a numerical iterative method such as the steepest descent or gradient method. However, this approach may not provide the desired solution if the

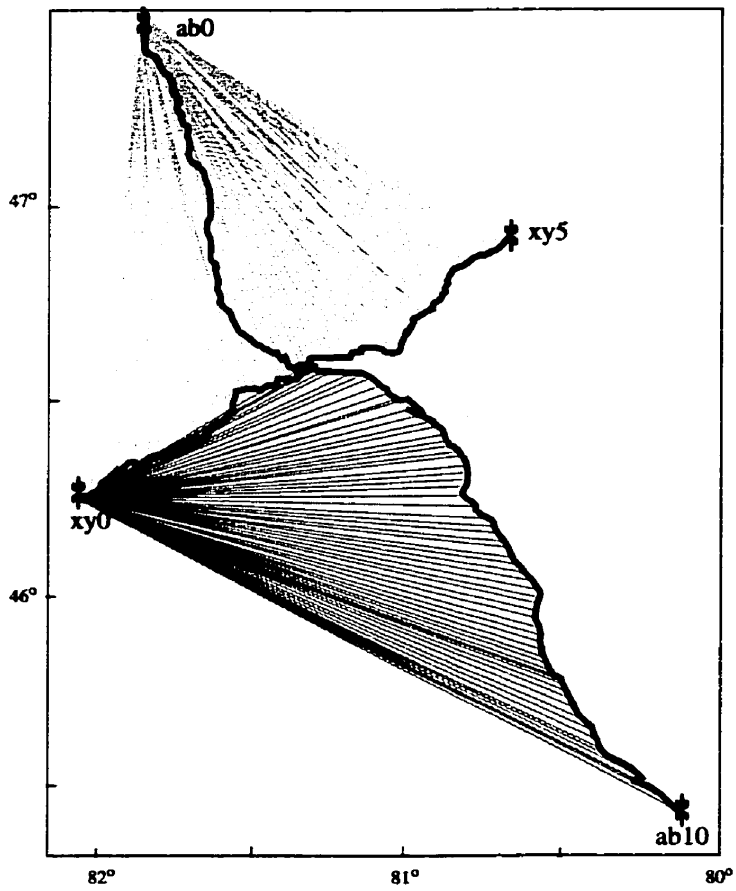

Figure 7.1 A sketch of the fan shot survey pattern in a plane view. ⌐: receiving line; • shot point; ab0: shot number; : line linking shot of ab0 and receiver along profile XY; — : line linking shot xy0 and receiver along the southern part of the cross point of profile AB; : line linking shot xy5 and a receiver along the southern part of the cross point of profile AB.

initial values are not good estimates of the solution. In 3-D forward modeling, it is not easy to provide a good initial estimate. Hence, the Fletcher Reeves conjugate gradient technique was considered to avoid this difficulty. In this method, the ray path with the minimum traveltime from the chosen source to receiver points is traced according to Fermat's principle by determining the coordinates at which the ray intersects interfaces. Afterwards the traveltime is computed using the corresponding velocities.

1. Model Parameterization

Plane interfaces and constant velocities between interfaces are assumed in the algorithm. The number of interfaces is determined by the number of observed coherent reflection and refraction seismic events. The equations of m planes in Cartesian coordinates are given by

$$a'_i x_{i,j} + b'_i y_{i,j} + c'_i z_{i,j} + d'_i = 0 \ , \tag{7.1}$$

where a'_i, b'_i, c'_i, and d'_i are the coefficients of the equation of the ith plane; i is in the range of 1 to m; $(x_{i,j}, y_{i,j}, z_{i,j})$ represent the coordinates of the intersection point on the ith interface; j equals 1 for a down-going ray and 2 for an up-going ray. Generally, the planes being modeled do not intersect at the origin of Cartesian coordinates. Normalizing equation 7.1 by d'_i, one has

$$a_i x_{i,j} + b_i y_{i,j} + c_i z_{i,j} + 1 = 0 \tag{7.2}$$

where a_i, b_i and c_i are normalized coefficients of plane equations. Equation 7.2 is the basic plane equation used in the 3-D modeling discussed here.

2. Traveltime Function

As discussed in the previous chapter, the traveltime equation is nonlinear. The traveltime of a ray propagating in the simplified model in Cartesian coordinates is simply given by

$$t = \sum_{i=1}^{m} \sum_{j=1}^{2} \frac{r_{i,j}}{v_i} + \frac{R}{v_{m+1}}, \tag{7.3}$$

where $r_{i,j} = ((x_{i,j} - x_{i-1,j})^2 + (y_{i,j} - y_{i-1,j})^2 + (z_{i,j} + z_{i-1,j})^2)^{1/2}$,

$R = ((x_{m,2} - x_{m,1})^2 + (y_{m,2} - y_{m,1})^2 + (z_{m,2} + z_{m,1})^2)^{1/2}$, for refracted waves,

$R = 0$, for reflected waves,

$i = 1, 2, 3, 4, ..., m; j = 1, 2.$

m represents the number of interfaces; v_i denotes the velocity in the layer between the ith and $(i\text{-}1)$th interfaces; v_{m+1} represents the velocity of the bottom layer; $r_{i,j}$ denotes the distance between two points at which a ray intersects two immediately adjacent interfaces, labeled i and $(i\text{-}1)$. Figure 7.2 shows a schematic example of a model parameterization and ray paths.

According to Fermat's principle, the ray path from shot to receiver yields a minimum traveltime. In our model, this reduces to the simple requirement that the partial derivatives of t in equation 7.3 with respect to the coordinates ($x_{i,j}$ and $y_{i,j}$) are equal to zero. The solution of a set of these partial derivative equations provides the point coordinates at which the required ray intersects the layers (Kanasewich and Chiu, 1985). The traveltime of the ray can then be obtained for a given velocity model. For a reflected

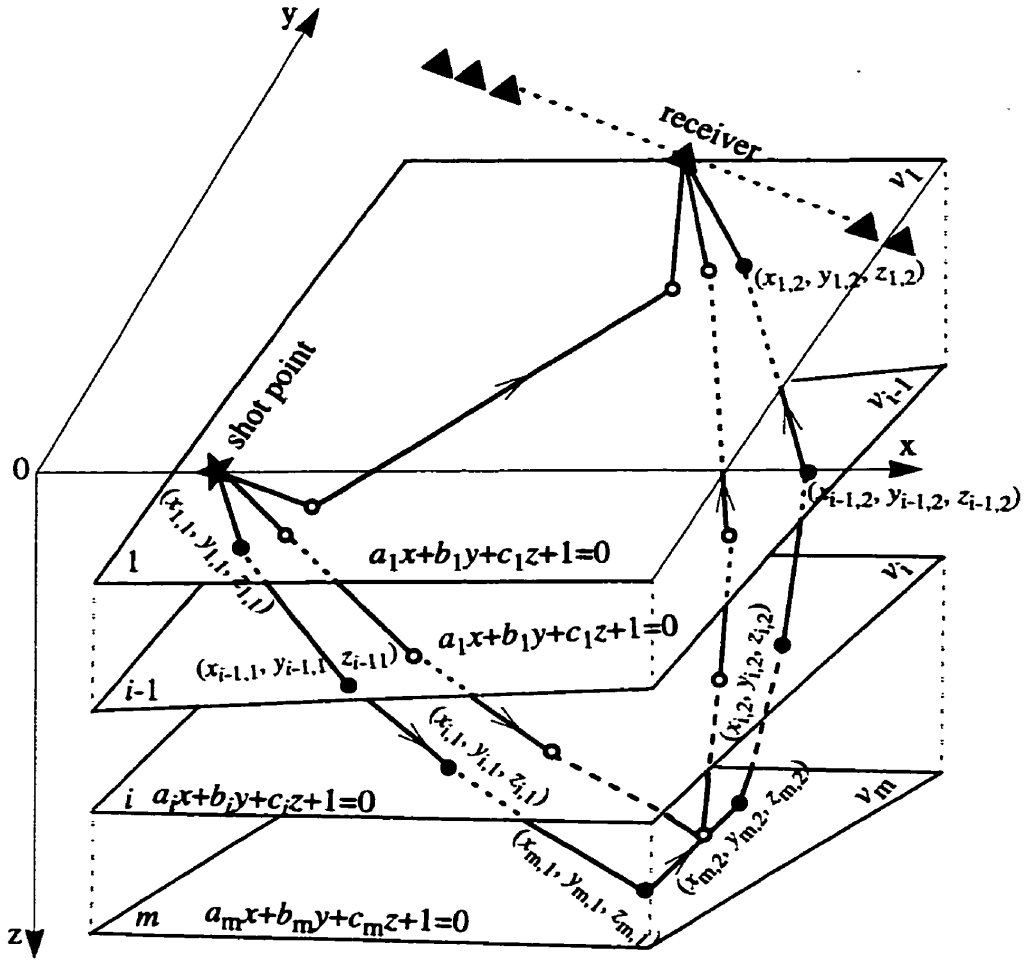

Figure 7.2 Schematic drawing of the model parameterization. Planes are defined by equation 7.2. v_i denote the constant velocities between two adjacent layers; *i* represents the layer index; ★: shot point; ▲: receiver point; o : unlabelled coordinate point; ● : labelled coordinate point. Three ray paths are drawn in the diagram which correspond to the refraction at the first interface, the reflection at the *m*th interface, and the refraction at the *m*th interface. In the diagram, only the coordinates associated with the ray refracted at the *m*th layer are labeled.

ray, there are (4*m*-2) partial derivative equations which are written as follows

$$
\begin{cases}
\dfrac{\partial t}{\partial x_{i,j}} = \left(x_{i,j} - x_{i-1,j} - \dfrac{a_i}{c_i}(z_{i,j} - z_{i-1,j})\right)/(v_i \cdot r_{i,j}) + \\
\qquad \left(x_{i,j} - x_{i+1,j} - \dfrac{a_i}{c_i}(z_{i,j} - z_{i+1,j})\right)/(v_{i+1} \cdot r_{i+1,j}) = 0, \\
\dfrac{\partial t}{\partial y_{i,j}} = \left(y_{i,j} - y_{i-1,j} - \dfrac{b_i}{c_i}(z_{i,j} - z_{i-1,j})\right)/(v_i \cdot r_{i,j}) + \\
\qquad \left(y_{i,j} - y_{i+1,j} - \dfrac{b_i}{c_i}(z_{i,j} - z_{i+1,j})\right)/(v_{i+1} \cdot r_{i+1,j}) = 0, \\
\quad \vdots \qquad \text{for } i=1, 2, 3, \ldots, m\text{-}1;\ j=1, 2, \\
\dfrac{\partial t}{\partial x_m} = \left(x_m - x_{m-1,1} - \dfrac{a_m}{c_m}(z_m - z_{m-1,1})\right)/(v_m \cdot r_{m,1}) + \\
\qquad \left(x_m - x_{m,2} - \dfrac{a_m}{c_m}(z_m - z_{m,2})\right)/(v_m \cdot r_{m,2}) = 0, \\
\dfrac{\partial t}{\partial y_m} = \left(y_m - y_{m-1,1} - \dfrac{b_m}{c_m}(z_m - z_{m-1,1})\right)/(v_m \cdot r_{m,1}) + \\
\qquad \left(y_m - y_{m,2} - \dfrac{b_m}{c_m}(z_m - z_{m,2})\right)/(v_m \cdot r_{m,2}) = 0,
\end{cases}
\tag{7.4}
$$

For a refracted ray, there are 4*m* partial derivative equations required to be solved for the coordinates. The set of nonlinear equation systems for the refraction waves are written as

$$\frac{\partial t}{\partial x_{i,j}} = \left(x_{i,j} - x_{i-1,j} - \frac{a_i}{c_i}(z_{i,j} - z_{i-1,j})\right)/(v_i \cdot r_{i,j}) +$$

$$\left(x_{i,j} - x_{i+1,j} - \frac{a_i}{c_i}(z_{i,j} - z_{i+1,j})\right)/(v_{i+1} \cdot r_{i+1,j}) = 0,$$

$$\frac{\partial t}{\partial y_{i,j}} = \left(y_{i,j} - y_{i-1,j} - \frac{b_i}{c_i}(z_{i,j} - z_{i-1,j})\right)/(v_i \cdot r_{i,j}) +$$

$$\left(y_{i,j} - y_{i+1,j} - \frac{b_i}{c_i}(z_{i,j} - z_{i+1,j})\right)/(v_{i+1} \cdot r_{i+1,j}) = 0,$$

$$\vdots \qquad \text{for } i=1, 2, 3, \ldots, m\text{-}1; j=1, 2,$$

$$\frac{\partial t}{\partial \varsigma_{m,1}} = \left(\varsigma_{m,1} - \xi\varsigma_{m-1,1} - \frac{a_m}{c_m}(z_{m,1} - z_{m-1,1})\right)/(v_m \cdot r_{m,1}) + \qquad (7.5)$$

$$\left(\varsigma_{m,1} - \varsigma_{m,2} - \frac{a_m}{c_m}(z_{m,1} - z_{m,2})\right)/(v_{m+1} \cdot R) = 0,$$

$$\frac{\partial t}{\partial \varsigma_{m,2}} = \left(\varsigma_{m,2} - \varsigma_{m-1,2} - \frac{a_m}{c_m}(z_{m,2} - z_{m-1,2})\right)/(v_m \cdot r_{m,2}) +$$

$$\left(\varsigma_{m,2} - \varsigma_{m,1} - \frac{a_m}{c_m}(z_{m,2} - z_{m,1})\right)/(v_{m+1} \cdot R) = 0,$$

where ς represents x and y, and R denotes the distance between two refracted points at the bottom layer m. To solve this set of nonlinear equations, the best tool one can use is the numerical iteration approach. There are various numerical techniques for solving systems of nonlinear equations. In this research, the conjugate gradient technique was applied to obtain an accurate approximate solution to the system of partial derivative equations. The technique is faster and more effective than the gradient method (Press et

al., 1989). The conjugate gradient method modifies each downgoing direction of a time gradient with its conjugate information. The next subsection presents a detailed discussion on the application of the conjugate gradient method in 3-D seismic traveltime modeling.

3. Fletcher Reeves Conjugate Gradient Numerical Approach

The traveltime t in the nonlinear equation 7.3 can be rewritten as a quadratic form or a second-order Taylor expansion series (Cai, 1982; Press et al., 1989), assuming that the solution for t closely approaches the idea solution. The approximate second-order Taylor series solution may be written as

$$t(\boldsymbol{X}) \approx c - \boldsymbol{b} \cdot \boldsymbol{X} + \frac{1}{2}\boldsymbol{X}^T \cdot \boldsymbol{A} \cdot \boldsymbol{X}, \tag{7.6}$$

where the vector $\boldsymbol{X}$ contains points of intersection of a ray with the layers; $t(\boldsymbol{X})$ is the traveltime; c is the computed traveltime $t(\boldsymbol{X}^*)$ corresponding to the $\boldsymbol{X}^*$ vector which is the specific point regarded as the origin of the coordinate system; $\boldsymbol{b}$ is the downhill gradient of the traveltime which is given by $-\nabla t(\boldsymbol{X})\big|_{\boldsymbol{X}^*}$, and $\boldsymbol{A}$ is the Hessian matrix (Press et al., 1989) which contains the second partial derivative elements of the time function at $\boldsymbol{X}^*$, $\frac{\partial^2}{\partial X_i \partial X_j} t(\boldsymbol{X})\big|_{\boldsymbol{X}^*}$; i and j have been described in equation 7.1. Matrix $\boldsymbol{A}$ is used to derive the modified gradient direction but is not applied in the calculation procedure. This search procedure possesses the advantage of speeding up the calculation. Accordingly, the Fletcher Reeves conjugate gradient method needs only two search steps to find the

solution of the quadratic equation 7.6. The solution for a position vector minimizing the traveltime is obtained through an iterative procedure.

The first step in obtaining the traveltime is to give initial coordinate values. The initial coordinate vector, $\boldsymbol{X}^0$, is arbitrary. The first search direction $\boldsymbol{P}^0$ is defined as the local downhill gradient, $-\nabla t(\boldsymbol{X}^0)$. The next step is to construct the $\boldsymbol{P}^1$ which is the conjugate of $\boldsymbol{P}^0$ with respect to $\boldsymbol{A}$, that is,

$$(\boldsymbol{P}^0)^T \cdot \boldsymbol{A} \cdot \boldsymbol{P}^1 = 0. \tag{7.7}$$

Taking gradients in equation 7.6 with respect to $\boldsymbol{X}^0$ and $\boldsymbol{X}^1 = \boldsymbol{X}^0 + \lambda^0 \boldsymbol{P}^0$ respectively, and subtracting one from the other, we obtain

$$\lambda^0 \boldsymbol{P}^0 = \boldsymbol{A}^{-1}(\nabla t(\boldsymbol{X}^1) - \nabla t(\boldsymbol{X}^0)), \tag{7.8}$$

where λ^0 is a scalar which minimizes the traveltime. Assuming that

$$\boldsymbol{P}^1 = -\nabla t(\boldsymbol{X}^1) + \beta^0 \boldsymbol{P}^0, \tag{7.9}$$

we substitute equations 7.8 and 7.9 into equation 7.7, and hence can derive the conjugate coefficient β^0 as

$$\beta^0 = \frac{\|\nabla t(\boldsymbol{X}^1)\|^2}{\|\nabla t(\boldsymbol{X}^0)\|^2}, \tag{7.10}$$

where

$$\|\nabla t(\boldsymbol{X}^k)\|^2 = \nabla^T t(\boldsymbol{X}^k) \nabla t(\boldsymbol{X}^k) \qquad k = 0, 1. \tag{7.11}$$

Thus the second steepest descent direction is modified and solved (equation 7.9). It is possible to write β^0 in approximate quadratic form by (Cai, 1983)

$$\beta^0 = \frac{\|\nabla t(X^1)\|^2 - \nabla^T t(X^1)\nabla t(X^0)}{\|\nabla t(X^0)\|^2}. \tag{7.12}$$

At the $(k+1)$th iteration step, P^{k+1} and β^k are given as

$$P^{k+1} = -\nabla t(X^{k+1}) + \beta^k P^k, \tag{7.13}$$

and

$$\beta^k = \frac{\|\nabla t(X^{k+1})\|^2 - \nabla^T t(X^{k+1})\nabla t(X^k)}{\|\nabla t(X^k)\|^2}, \tag{7.14}$$

respectively. The coordinate vector at the $(k+1)$th step is then determined by

$$X^{k+1} = X^k + \lambda^k P^k, \tag{7.15}$$

where λ^k is obtained by solving the equation $\frac{\partial t}{\partial \lambda^k} = 0$.

The termination criterion of the iteration is determined by $\|\nabla t(X^k)\|^2 < \varepsilon$, where ε is the desired minimum tolerance value. The traveltime is then computed using the point coordinates at which the ray crosses interfaces. Figure 7.3 shows a computing flow chart for the application of this approach.

7.1.2 Inversion

In the inversion procedure, the nonlinear traveltime function is expanded as a first-order Taylor series to produce a set of linear equations for the observed data, which is

$$T_l = t_l(g^*) + \sum_{j=1}^{N} \left.\frac{\partial t_l}{\partial g_j}\right|_{g=g^*} (g_j - g_j^*) \tag{7.16}$$

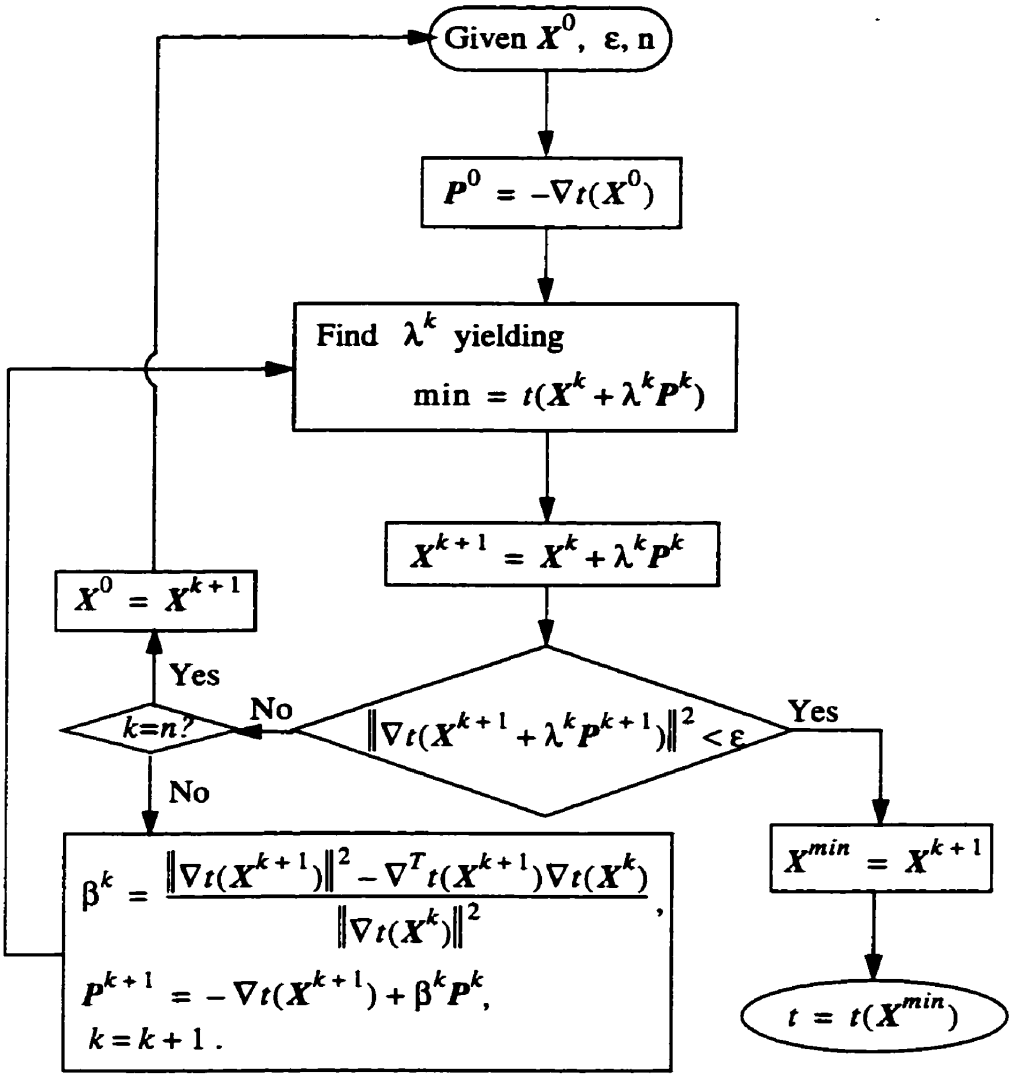

Figure 7.3 Flow chart for the Fletcher Reeves conjugate gradient method. n represents a maximum iteration number allowed. After iterations n, if the termination criterion is not satisfied, the calculation procedure is restarted by using a new initial value X^0 which equals X^{k+1} obtained from the previous iteration. If an iteration number is less than the maximum and the termination criterion is not satisfied, the conjugate coefficient will be modified and the a new iteration is required.

where T_l represents observed traveltime at the lth receiver; g^* is estimate of model parameters g; t_l denotes computed traveltime on the basis of the estimated model; l is an index corresponding to the receiver and equals 1, 2, ..., M; j is an index corresponding to the model parameter and equals 1, 2, ..., N.

Equation 7.16 can be rewritten in matrix form

$$\Delta \boldsymbol{T} = \boldsymbol{A}' \cdot \Delta \boldsymbol{G}, \tag{7.17}$$

where $\Delta \boldsymbol{T} = \langle T_l - t_l \rangle$: the traveltime residual vector with dimension M x 1,

$\boldsymbol{A}' = \langle \frac{\partial t_l}{\partial g_j} \rangle$: the matrix containing the partial derivative of the traveltimes with respect to the model parameters (with dimension M x N),

$\Delta \boldsymbol{G} = \langle g_j - g_j^* \rangle$: the model parameter adjustment vector with dimension N x 1.

Equation 7.17 has the same form as equation 6.5. Thus, the damped least-squares inversion technique can be employed to obtain plane interface and velocity parameters. This inversion procedure was discussed in Section 6.1.

The inversion damping factor is empirically selected (Zelt and Smith, 1992) to stabilize the inversion (Cimini, 1999). The damping factor for 2-D seismic refraction modeling is usually given as 1 (Zelt and Smith, 1992). However, if the number of model parameters is much smaller than the number of observed data, and the initial model is close to the 'desired one', the damping factor could be assigned a larger value. In fan-shot modeling, the damping factor was chosen in the range of 10-250 to stabilize the

inversion, depending on how close the initial model was to the real model.

7.2 Modeling of the Sudbury Data

The fan-shot (or broadside) seismic reflection and refraction data were modeled to obtain a cross-sectional view of the three-dimensional structure and velocity information for the Sudbury area. Fifteen shots were recorded by seismometers in broadside shooting during the 1992 Lithoprobe seismic experiments in Sudbury. In this section, the travel-times of identified phases are inverted without amplitude modeling and comparison in four quadrants (Figure 7.4). In other words, this section discusses 3-D kinetic modeling.

7.2.1 Fan-shot Data Processing and Displaying

The processing procedure applied to the in-line and the fan-shot data was similar. Therefore, there is no need to include detailed explanations on processing in this subsection. The fifteen fan-shot seismic sections were displayed in much the same way as the in-line sections. One difference is that for the fan shots the horizontal axis represents the azimuth rather than offset distances. The digital seismic data for each trace were normalized to the average amplitude excluding the minimum and maximum amplitude values. The fan-shot seismic sections are shown in Figures 7.5-7.19.

7.2.2 Seismic Phase Analysis and Picking

Pg, PcP and PmP phases were picked and the reliably picked PcP and PmP phases are marked by lines on corresponding sections. Generally, the fan-shot seismic data records

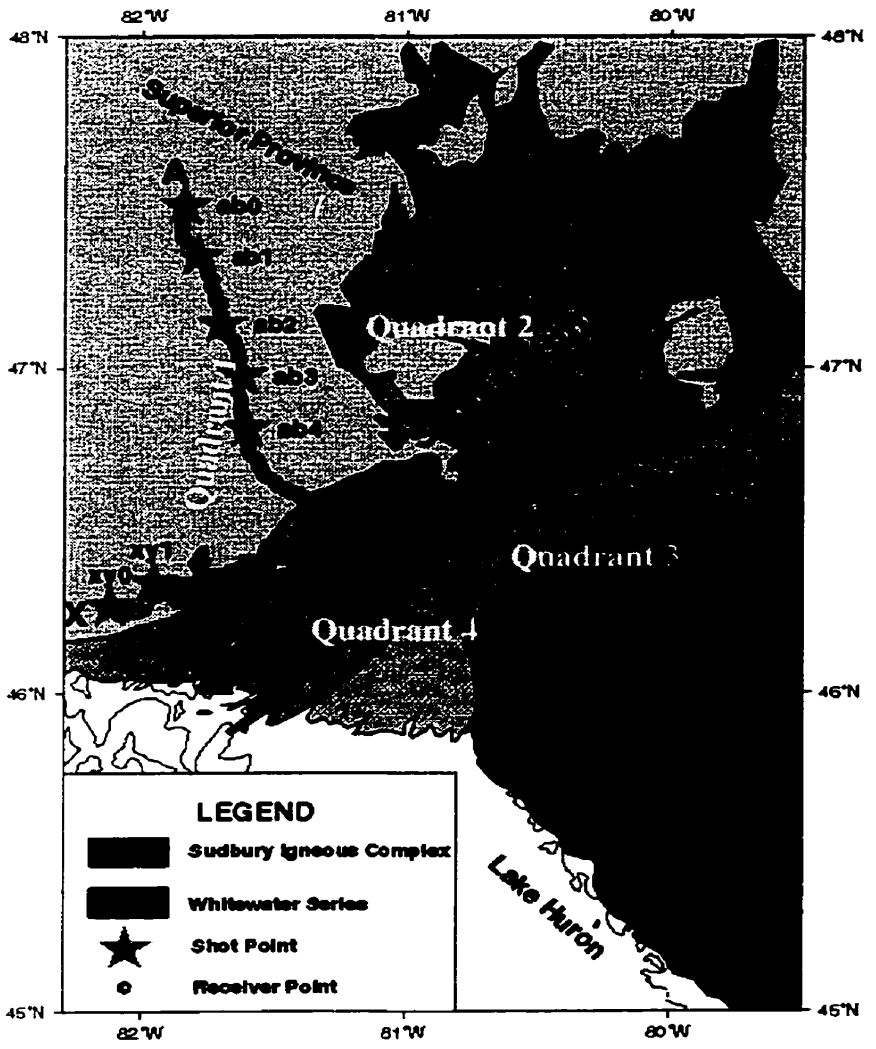

Figure 7.4 Locations of four quadrants separated by two seismic survey lines AB and XY.

are of good quality except one section from shot xy1 (Figure 7.16). Fan-shot xy1 represents the section recorded by receivers deployed along profile AB for the shot location xy1. On that section, the majority of traces were seriously affected by noise. In contrast, the data record from shot xy5 is of high quality (Figure 7.19).

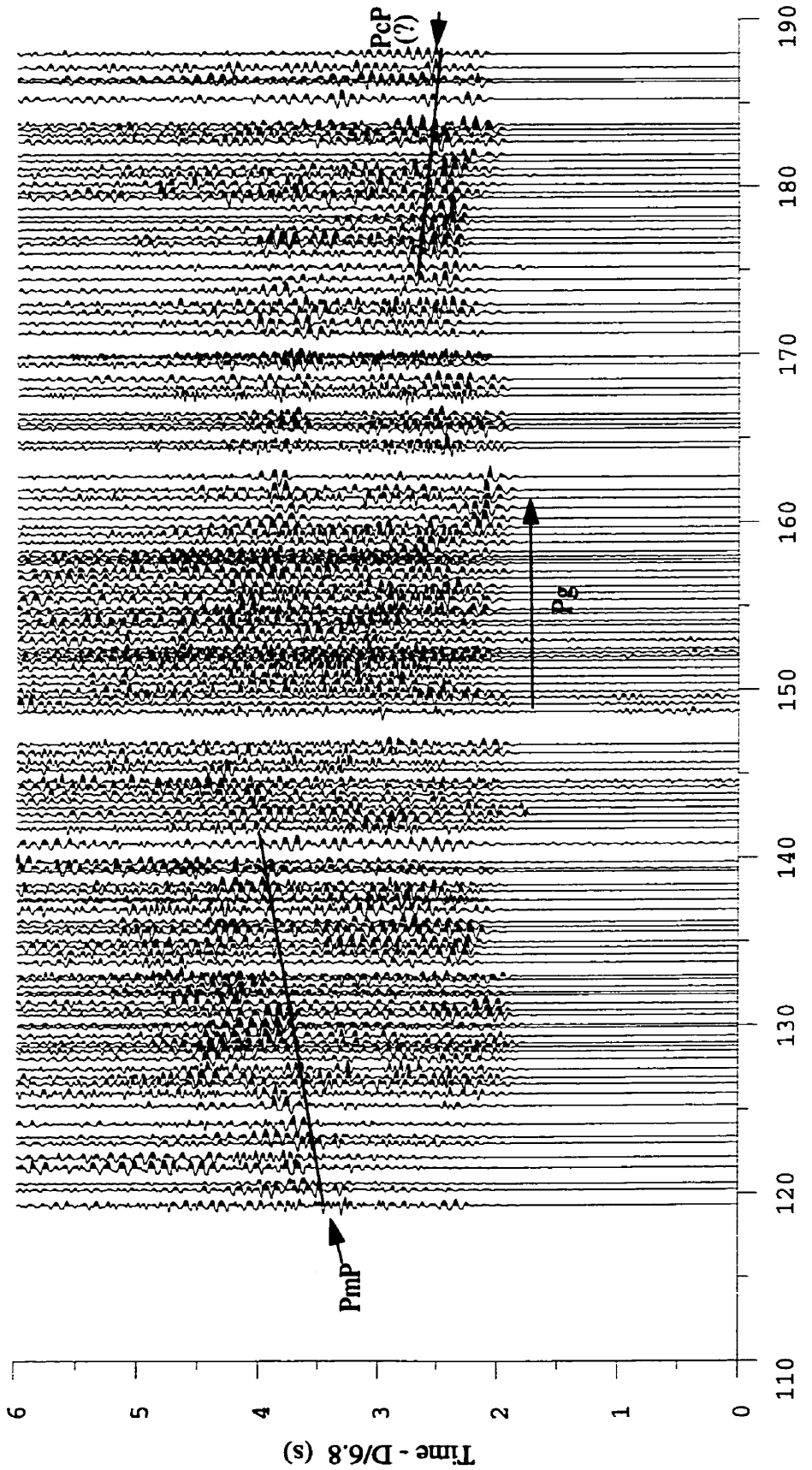

Figure 7.5 Fan-shot seismic section ab0.

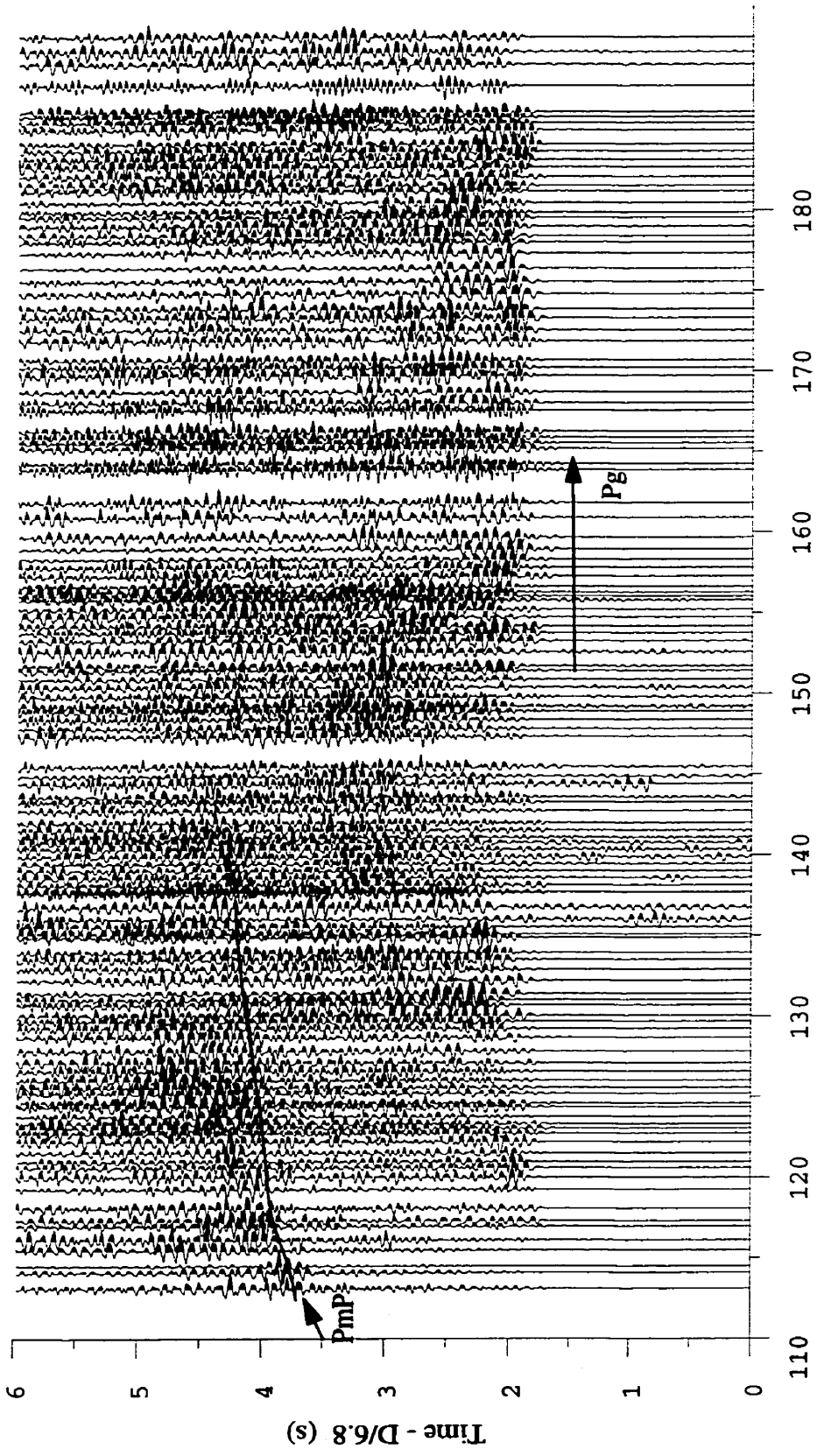

Figure 7.6 Fan-shot seismic section ab1.

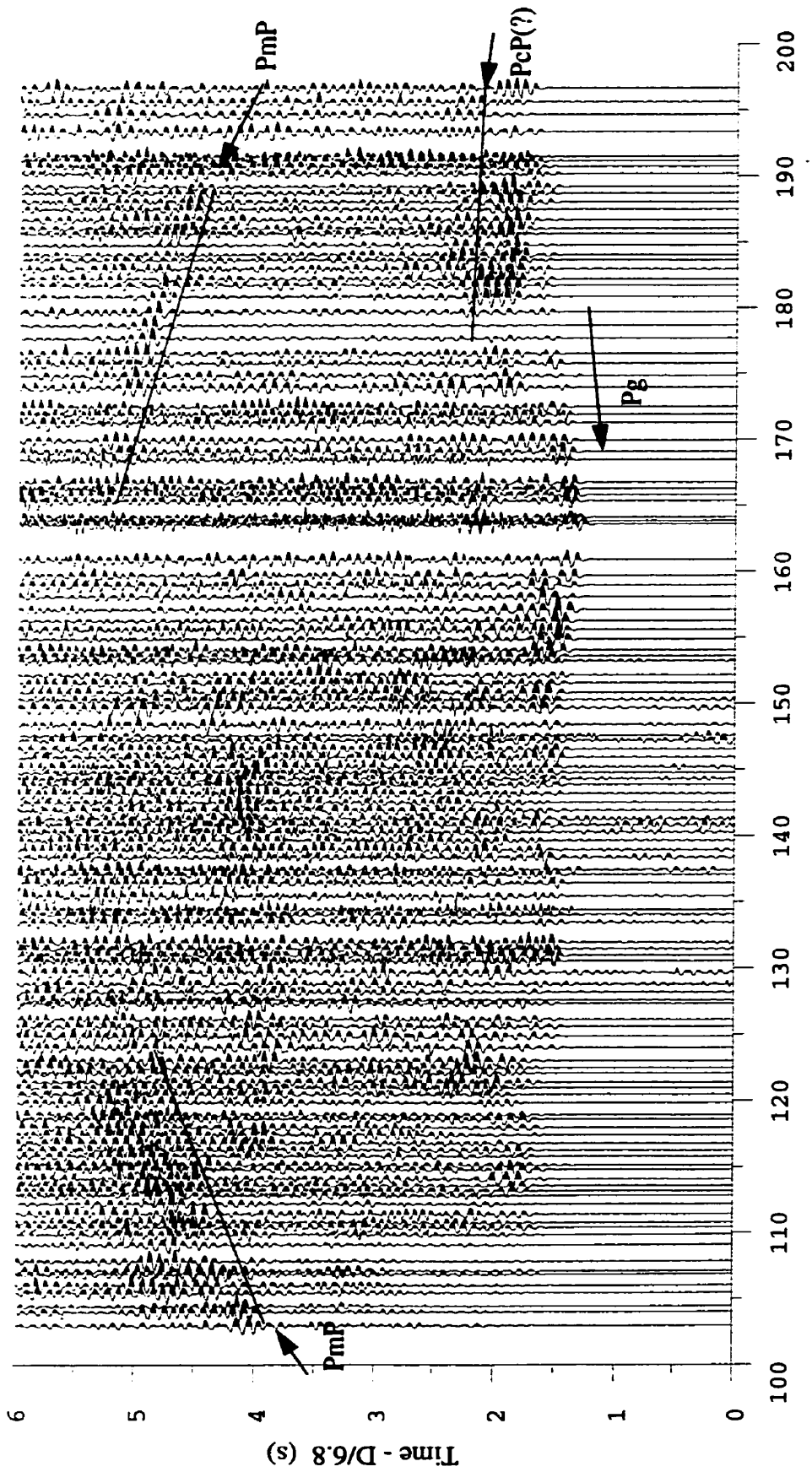

Figure7.7 Fan-shot seismic section ab2.

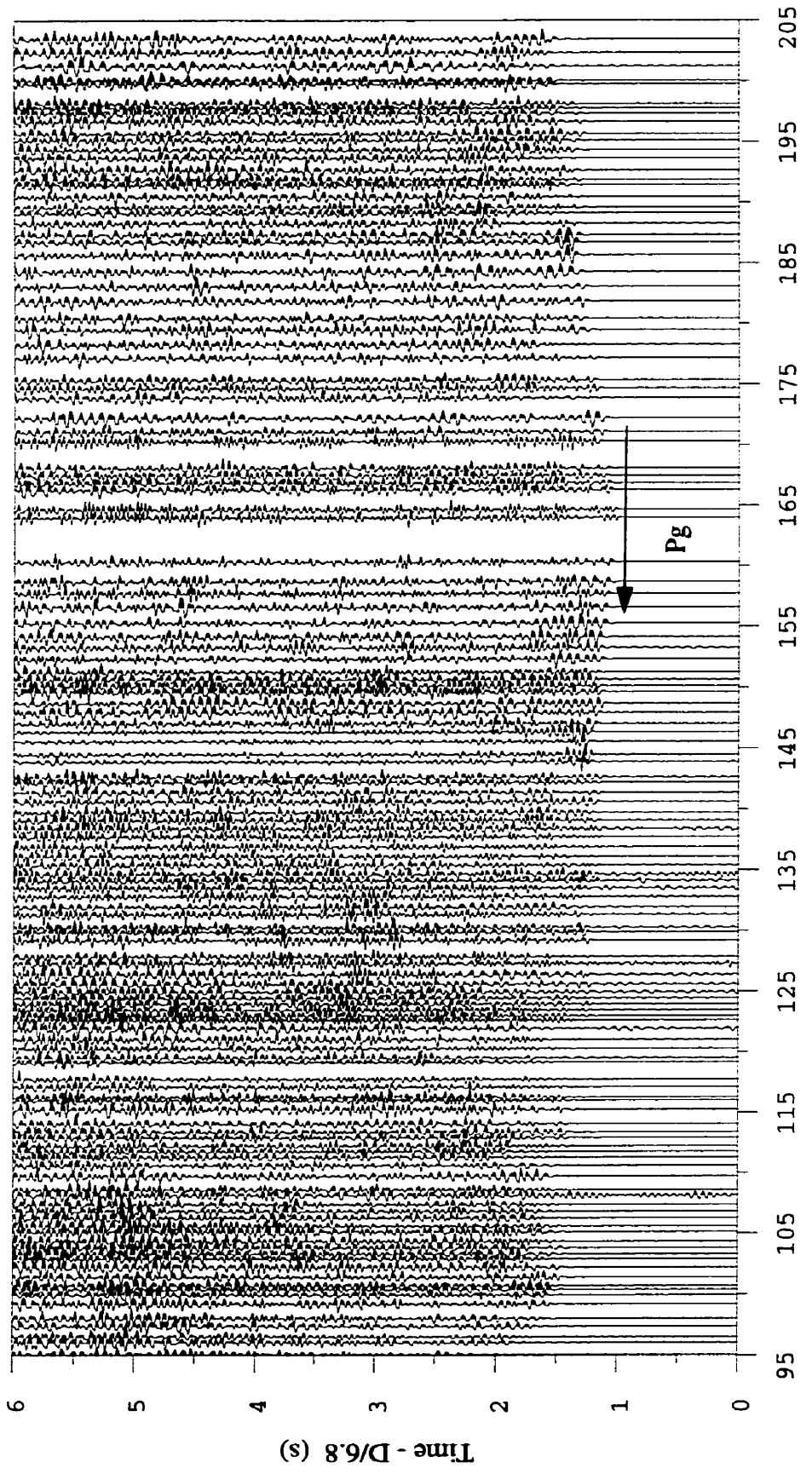

Figure 7.8 Fan-shot seismic section ab3.

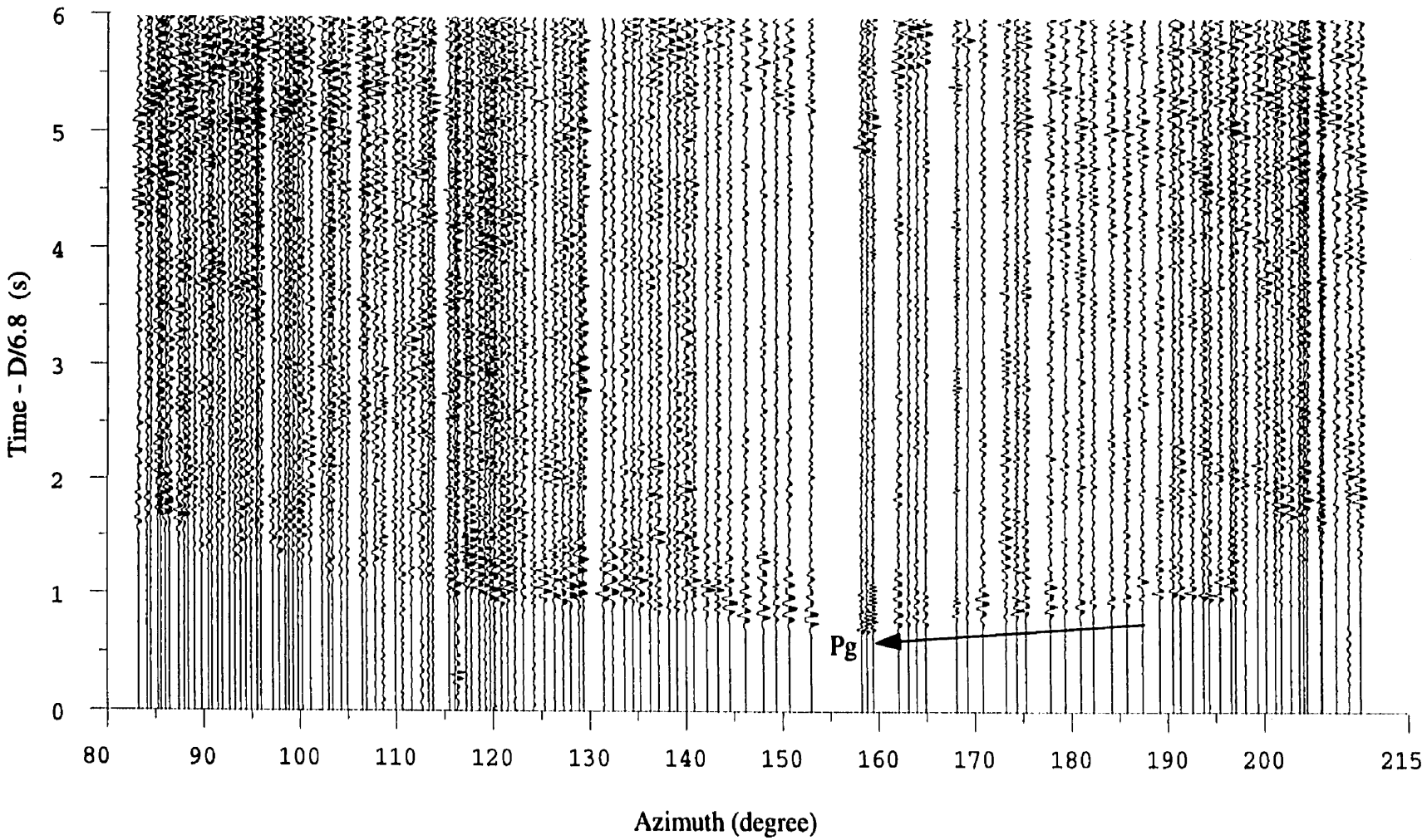

Figure 7.9 Fan-shot seismic section ab4.

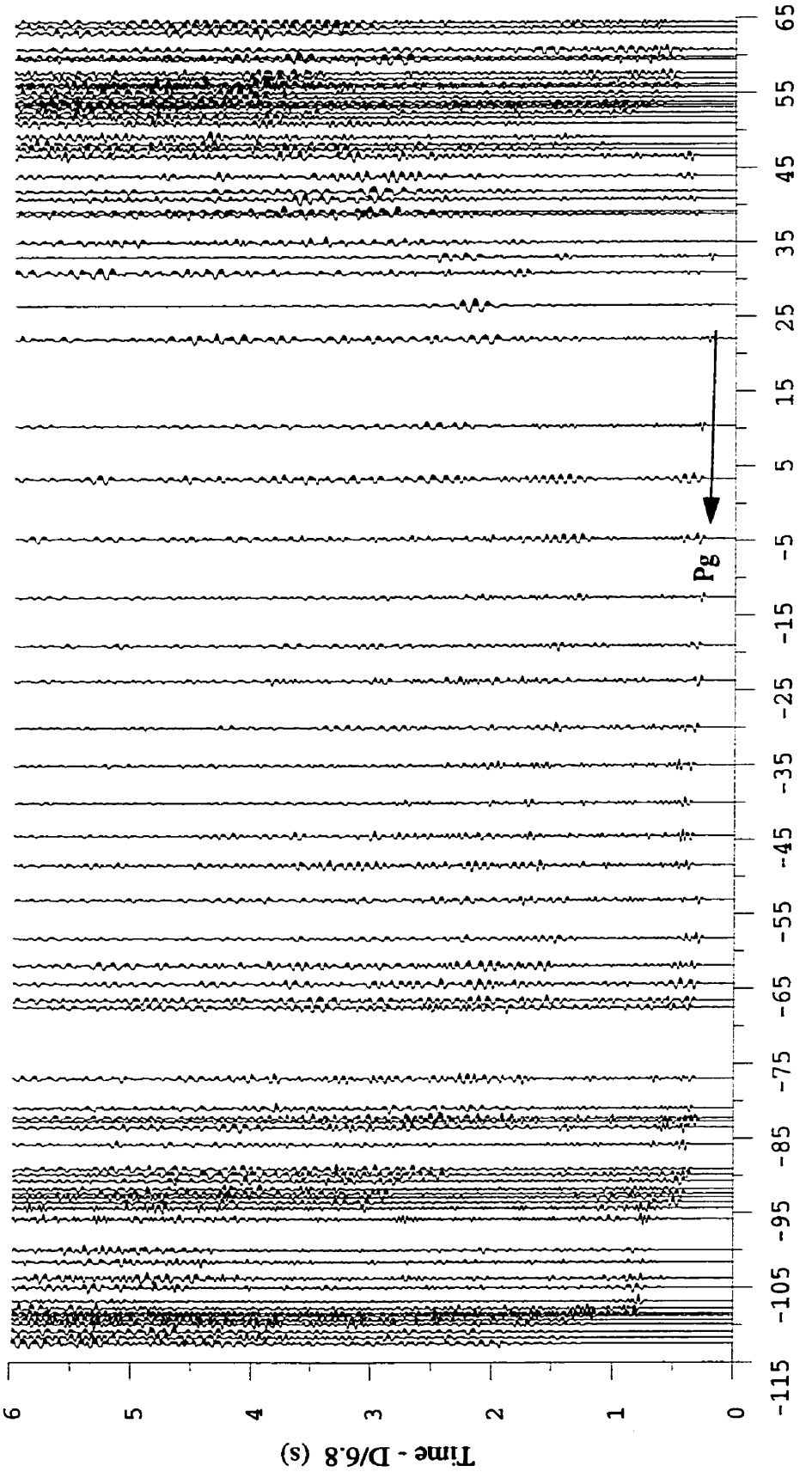

Figure 7.10 Fan-shot seismic section ab6.

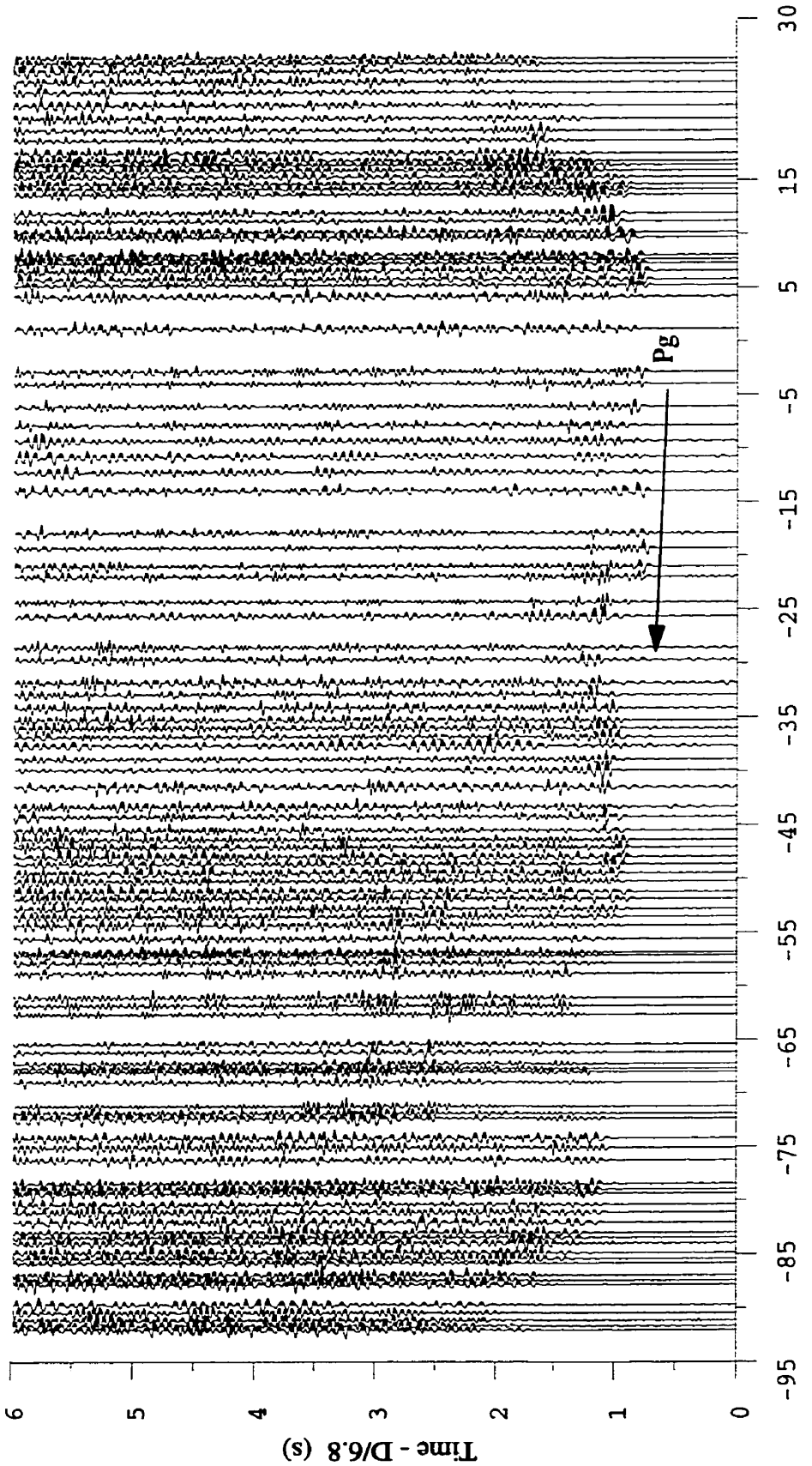

Figure 7.11 Fan-shot seismic section ab7.

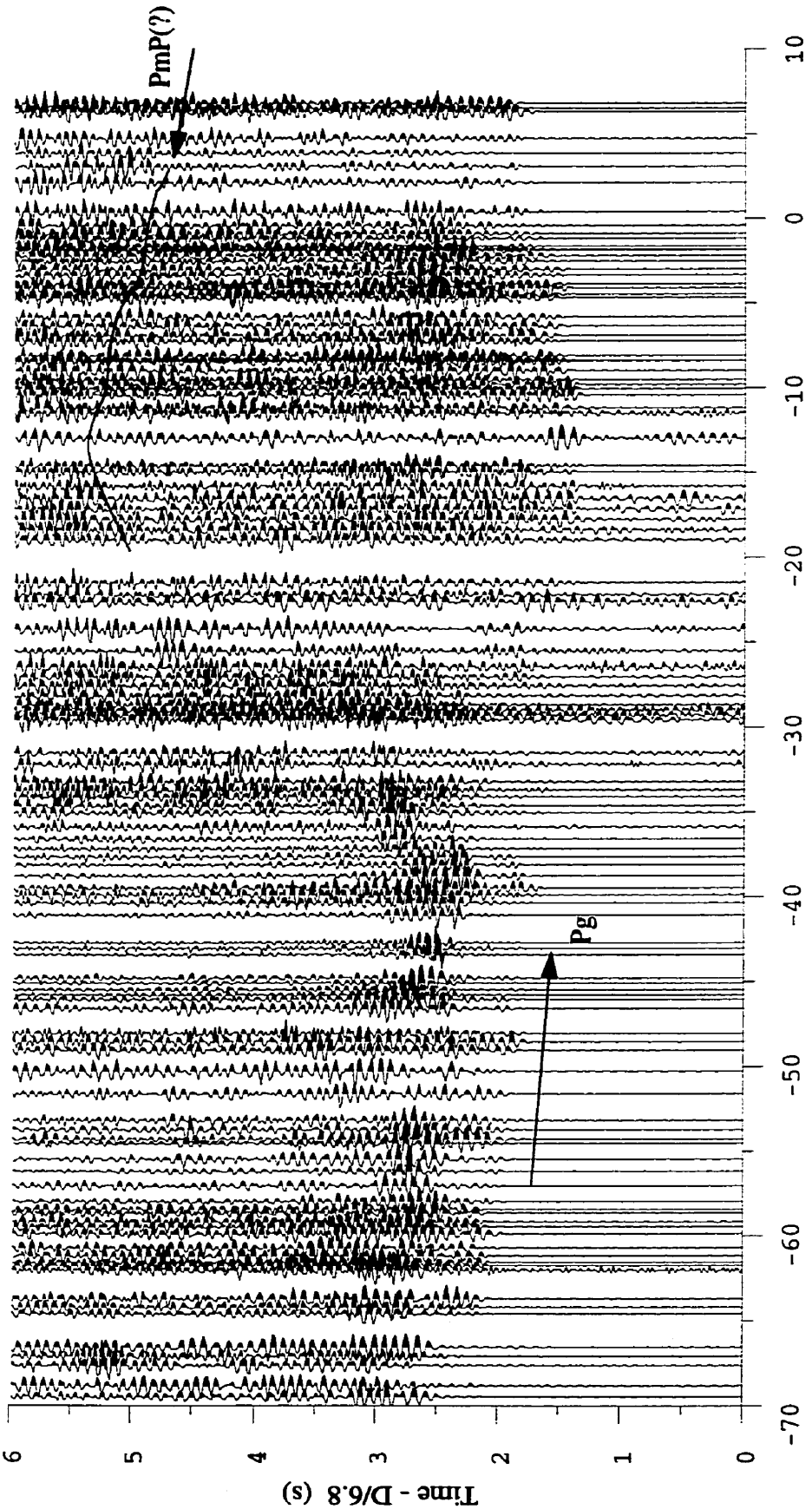

Figure 7.12 Fan-shot seismic section ab8.

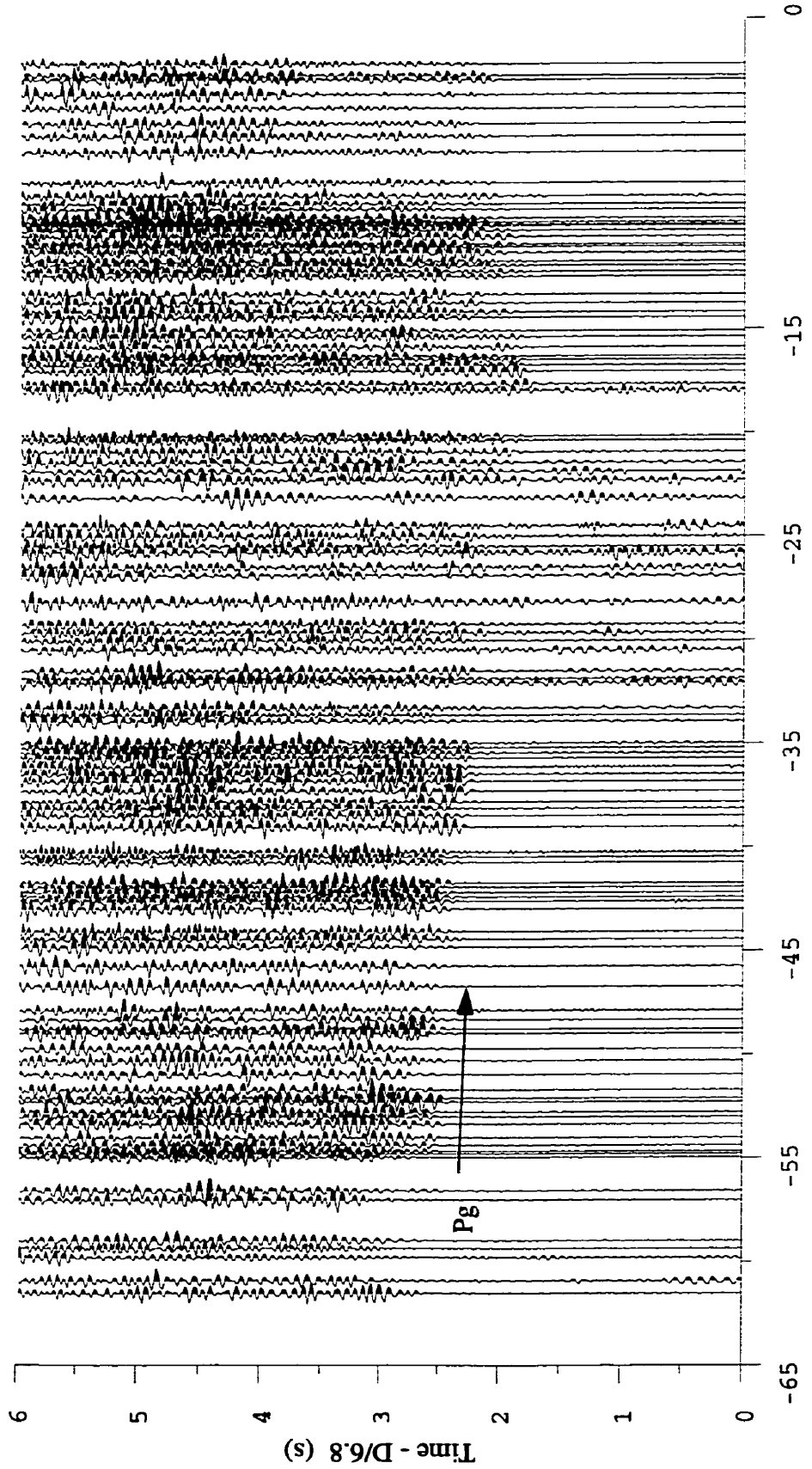

Figure 7.13 Fan-shot seismic section ab9.

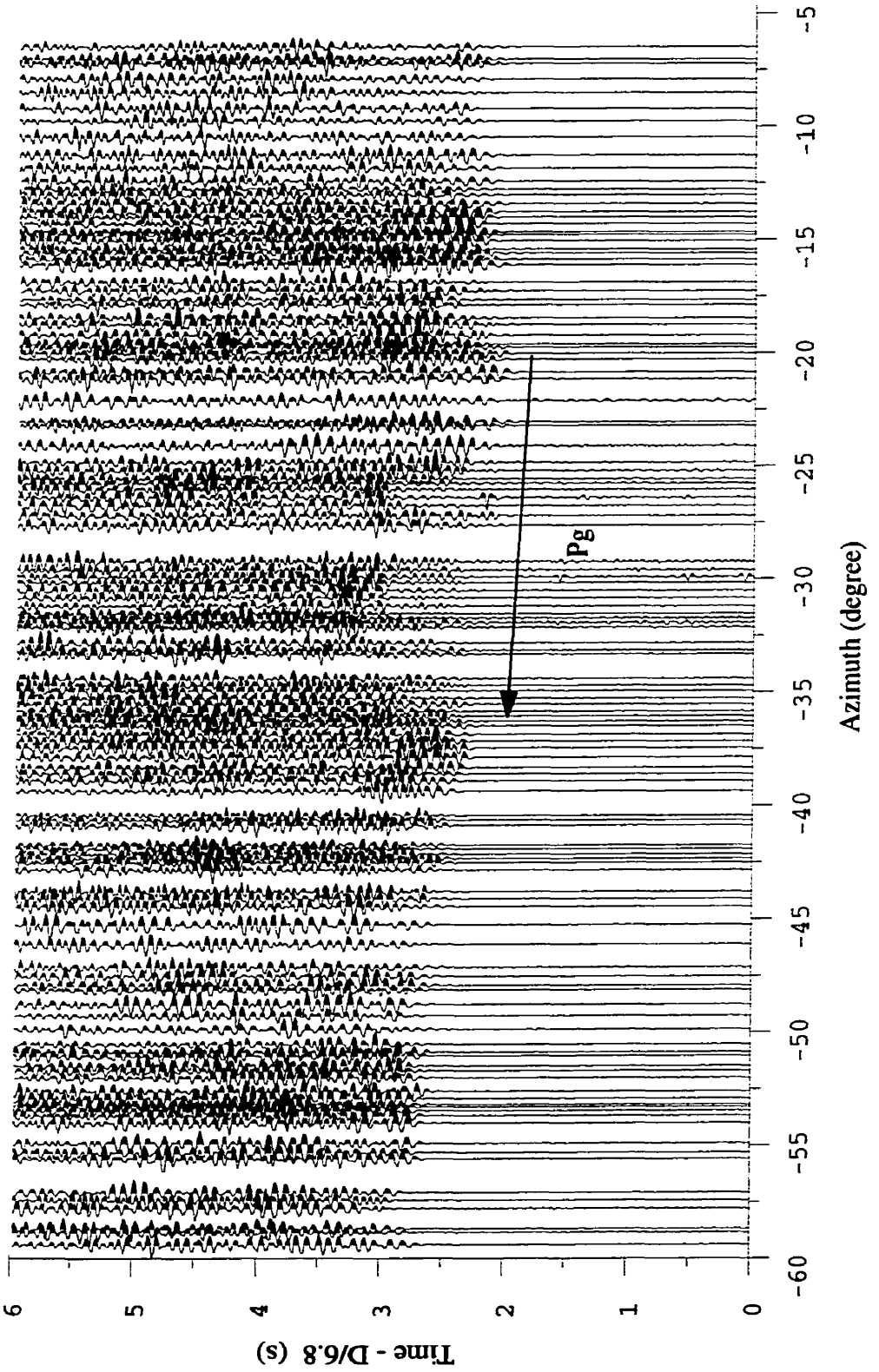

Figure 7.14 Fan-shot seismic section ab10.

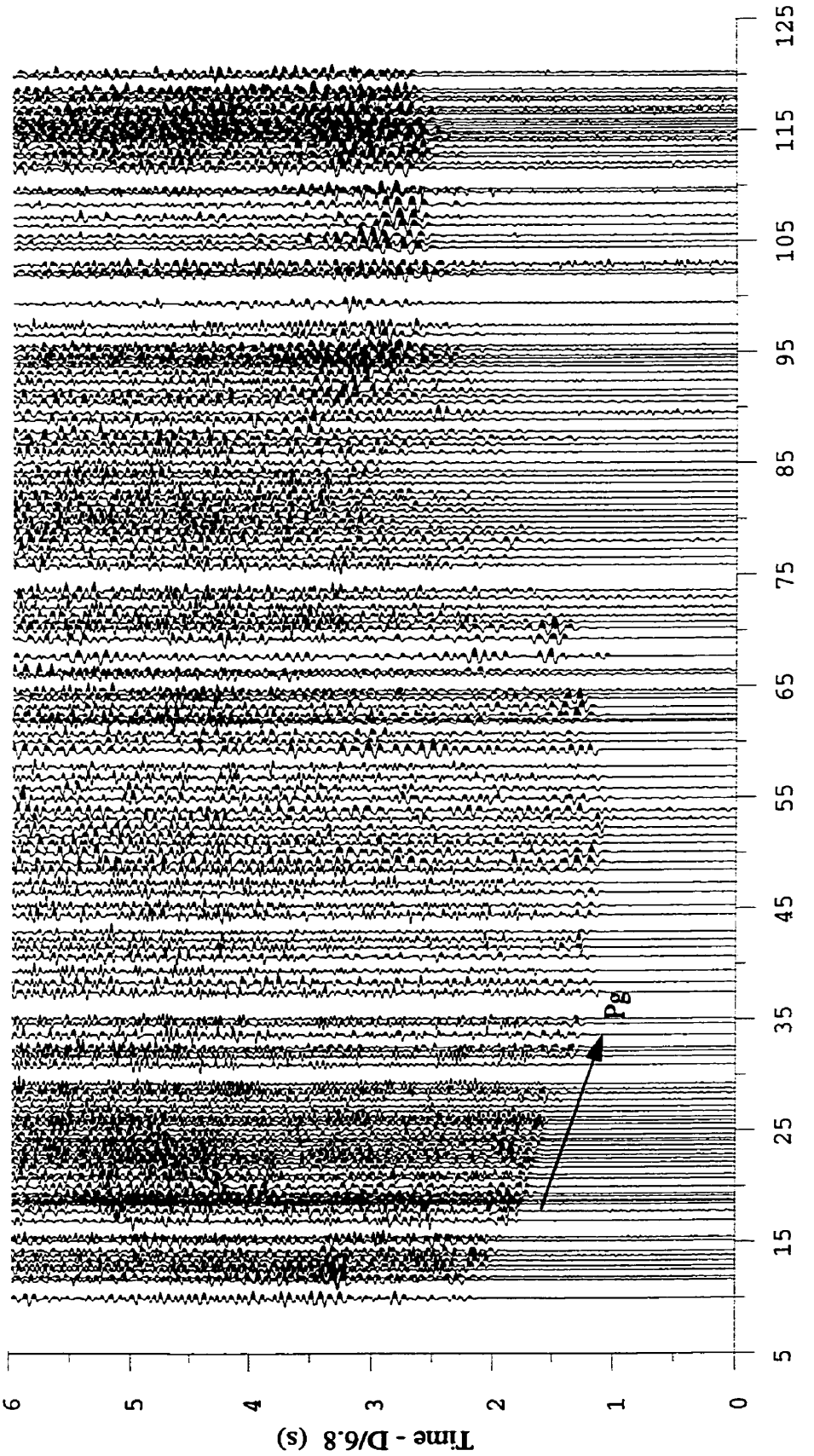

Figure 7.15 Fan-shot seismic section xy0.

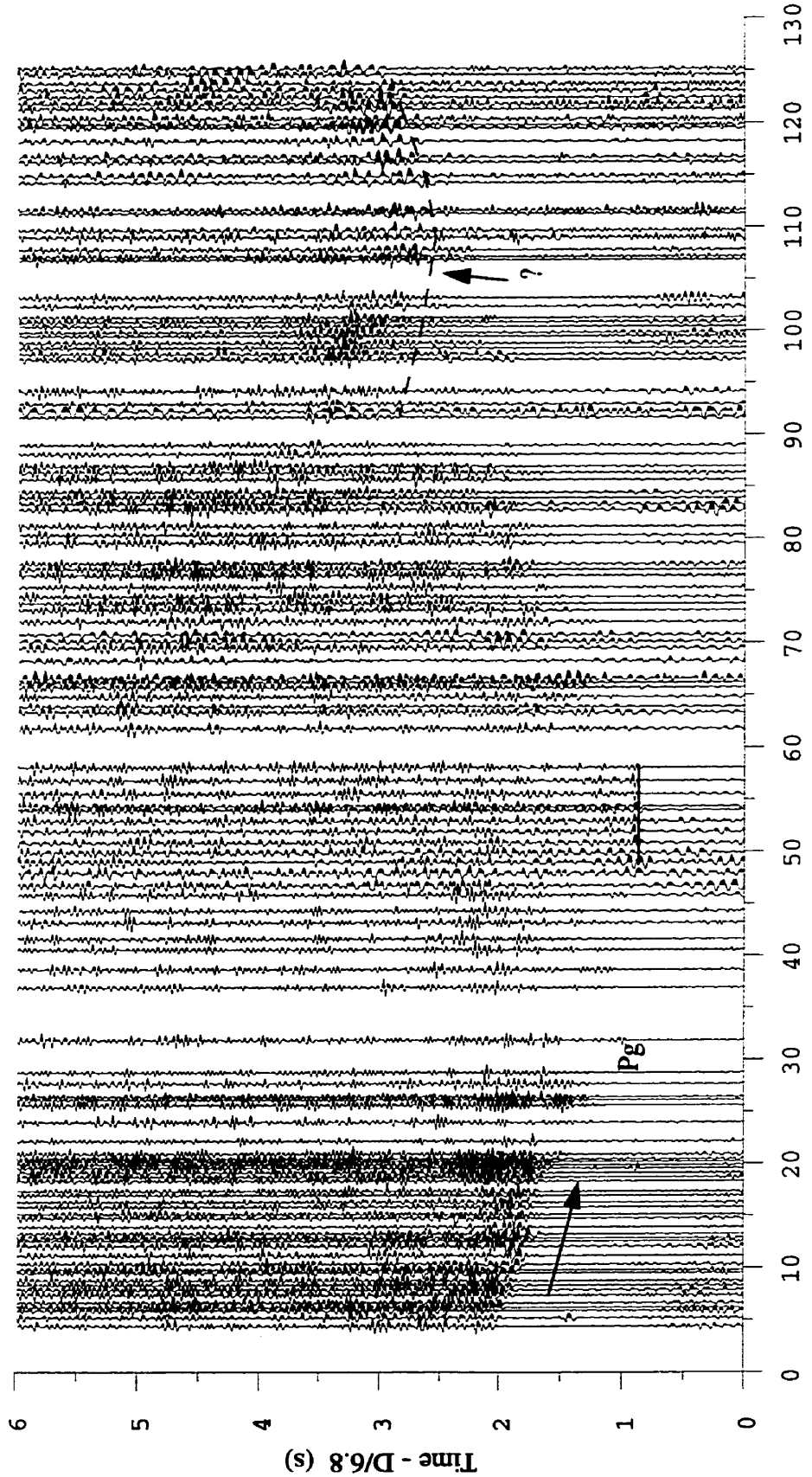

Figure 7.16 Fan-shot seismic section xy1.

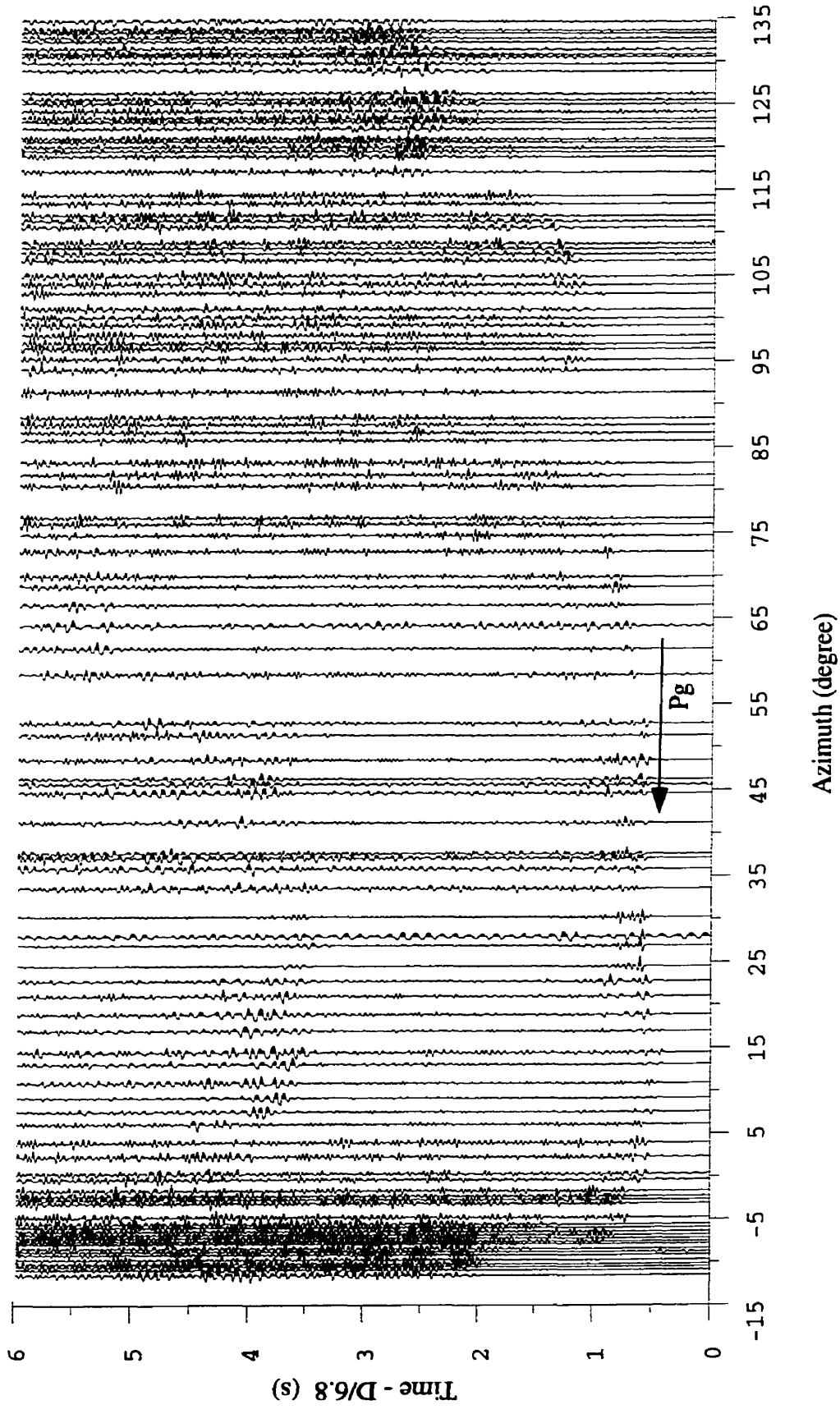

Figure 7.17 Fan-shot seismic section xy2.

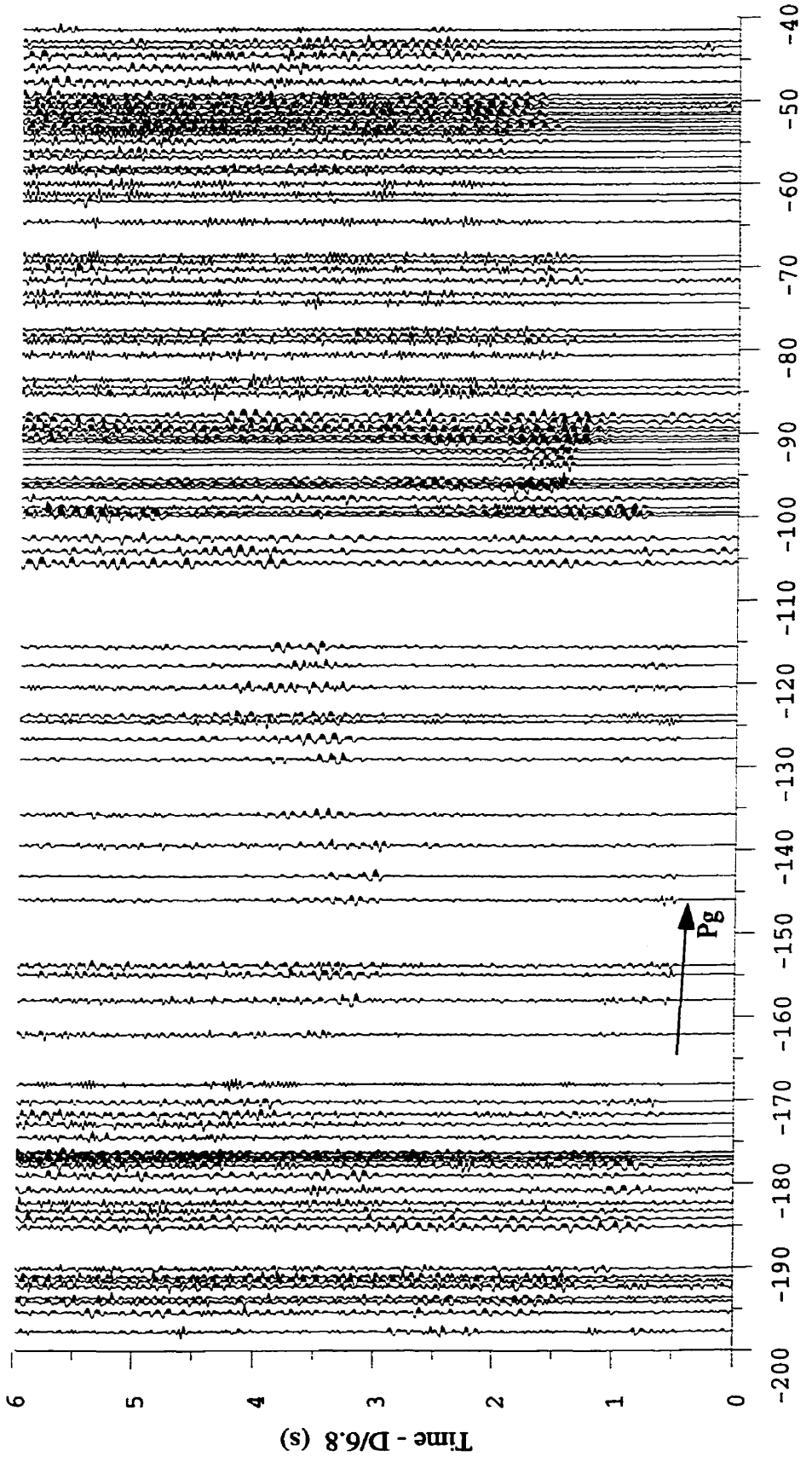

Figure 7.18 Fan-shot seismic section xy4.

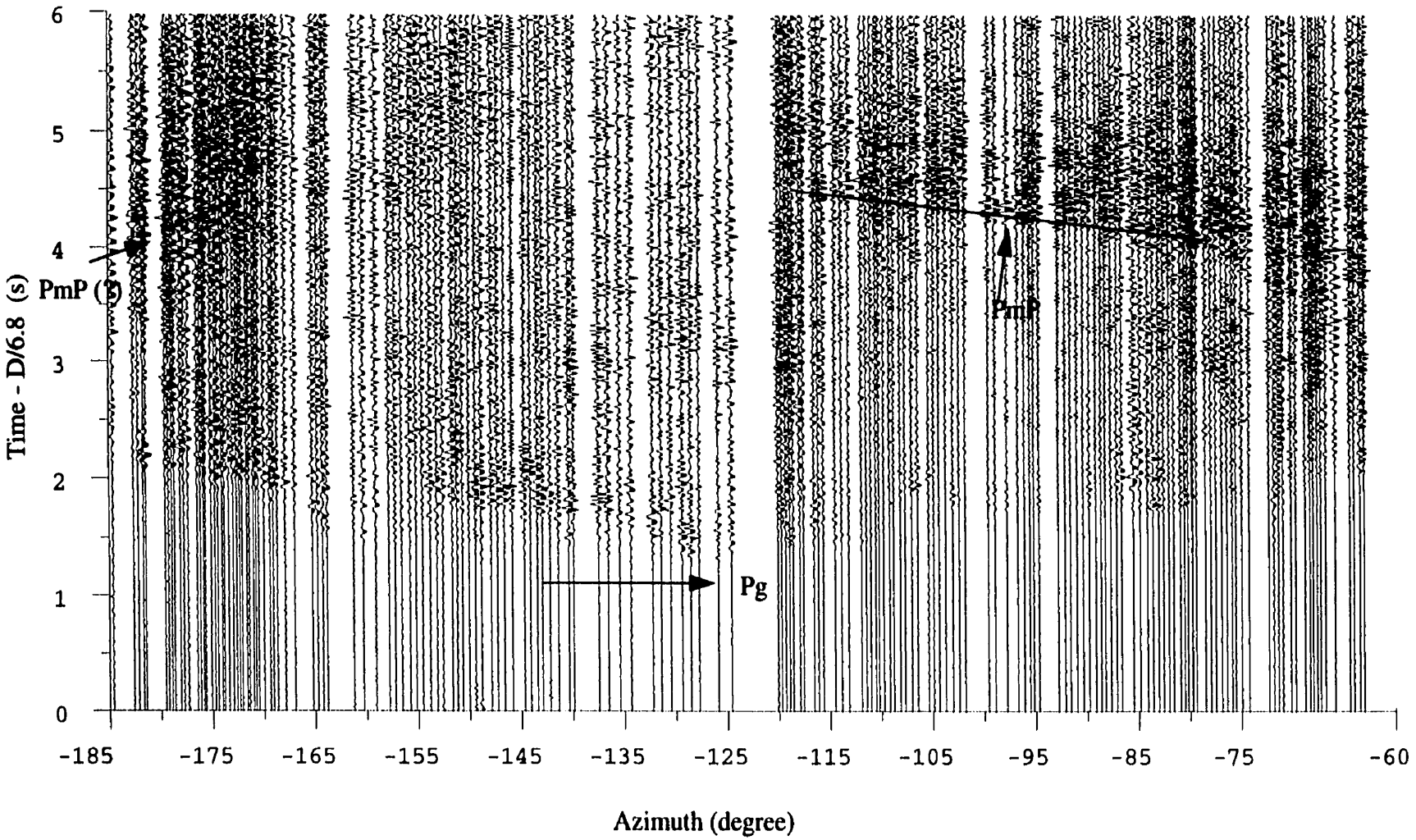

Figure 7.19 Fan-shot seismic section xy5.

1. Pg Phase

Pg phases are recorded as the first arrivals on each section and are believed to represent the head wave, or refraction, propagating along the bottom of the near-surface layer. The information on the picked Pg phases is listed in Table 7.1. A total of nine sections have a high S/N ratio and 90% of Pg arrivals were picked. For fan shots ab8, ab9, xy0 and xy2, one half to two thirds of Pg phases were picked (Figures 7.12-7.14 and 7.17). The data from shots xy1 and xy4 have the lowest S/N ratio among all fifteen data sets and in those two cases, only one quarter of Pg phases were picked for inversion modeling (Figures 7.16 and 7.18).

2. PcP Phase

PcP phases were not reliably identified in all fifteen fan-shot sections. Only shots ab0 and ab2 showed weak coherent PcP reflections over a limited section of traces (Figures 7.5 and 7.7). For fan shot ab0, at azimuths between188° to 183° at the right end of the profile, there is a coherent reflection extending over nine traces at ~2.5 s reduced time. This event could be traced towards an azimuth of ~174°. PcP phases were also picked at azimuths between 174° and 197° for fan shot ab2 (Figure 7.7).

3. PmP Phases

There are five sections which show PmP reflections from the Moho, including fan shots ab0, ab1, ab2, ab8 and xy5 (Figures 7.5-7.7, 12 and 19). For fan shot ab0, PmP phases were picked at azimuths of 123°-145° (Figure 7.5). In shot ab1 data, the Moho

reflection is very strong at azimuths between 113° and 120° (Figure 7.6). Although signals are generally weak, PmP phases can be traced towards an azimuth of 140° by using a combination of traces with strong amplitude and traces with phase change. The Moho reflection is recognized clearly in fan shot ab2 section with high S/N ratio. PmP phases were identified at azimuths of 113°-125° at 4.0-4.6 s reduced time (Figure 7.7). In addition, PmP phases are clearly observed at 4.4-5.0 s at azimuths of 175°-190° where they are characterized by a strong amplitude (Figure 7.7). Therefore, these PmP arrivals could be picked precisely. For fan shot ab8 (Figure 7.12), PmP phases can not be picked with a high S/N ratio but the Moho reflection is recognized at azimuths of -20° to 7° from coherent features in several traces. Because fan shot xy5 has a high S/N ratio, the Moho reflection was clearly observed, particularly at azimuths of -115° to -80° (Figure 7.19). A total of 77 arrivals were then picked from this section including 25 arrivals around -175° azimuth (Table 7.1).

7.2.3 Modeling Procedure

The starting model was a simple model containing three plane interfaces and constant velocities within layers. The inversion modeling was carried out for four quadrants separated by the refraction lines AB and XY (Figure 7.1). The initial velocity model in each quadrant was based on the forward and inversion modeling results along the in-line profiles AB and XY.

Table 7.1 Number of phases picked for inversion

Shot No.	No. of Pg (0.05)	No. of PcP (0.07)	No. of PmP (0.07)	Total
ab0	116	24	48	188 (0.06)
ab1	109		54	163 (0.06)
ab2	124	20	68	212 (0.06)
ab3	127			127 (0.05)
ab4	123			123 (0.05)
ab6	31			31 (0.05)
ab7	100			100 (0.05)
ab8	71		38	109 (0.05)
ab9	72			72 (0.05)
ab10	95			95 (0.05)
xy0	54			54 (0.05)
xy1	23			23 (0.05)
xy2	65			65 (0.05)
xy4	20			20 (0.05)
xy5	160		77	237 (0.06)
Total	1290	44	285	1619 (0.05)

Note: (): average picking uncertainty in seconds.

1. Model Parameterization

In 3-D fan-shot data modeling, the model parameters at interfaces do not represent depth but rather the coefficients of plane interfaces described in equation 7.2. There are only three independent coefficients per layer in equation 7.2. These three independent coefficients were used in 3-D modeling. The velocity parameter represents the average

velocity value within a layer.

In the northwest (quadrant 1), Pg, PcP and PmP phases were picked. Therefore, the data required a three-layer model which includes a near-surface interface, a mid-crustal interface and the Moho interface. A total of nine independent plane coefficients define these three layers. Thus, there are a total of 12 parameters in the model, including three velocity parameters. Table 7.2 lists the initial modeling parameters. Parameters in the

Table 7.2 Initial model parameters

Quadrant 1 (Superior Province)			**Quadrant 2 (Superior and Southern provinces)**			**Quadrant 3 (Southern Province and Grenville Front)**			**Quadrant 4 (Grenville Front and Grenville Province)**		
	Type	M.P.		Type	M.P.		Type	M.P.		Type	M.P.
I	1	0.022	I	1	-0.015	I	1	-0.027	I	1	0.005
	1	-0.013		1	-0.028		1	-0.003		1	0.028
	1	2.210		1	2.400		1	2.198		1	1.830
	2	5.950		2	5.950		2	5.950		2	5.950
				2	6.200		2	6.150		2	6.180
II	1	0.015	II	1	-0.011	II	1	0.038	II		
	1	0.015		1	-0.208		1	-0.034			
	1	18.000		1	37.800		1	37.636			
	2	6.200		2	6.550		2	6.550			
III	1	0.049									
	1	0.004									
	1	38.523									
	2	6.7860									

Note: I: low-velocity layer; II: middle crustal interface; III: Moho interface.
Type 1: independent coefficients of plane interfaces (see the text).
Type 2: velocities (km/s).
M.P. : model parameters.

northwest were initialized according to the velocity and interface depth modeled in the northwestern half of profile AB and in the western half of profile XY (Figure 7.4). The damping factor was initially taken as 10 for all 3-D modeling. If an inversion was unstable (e.g., unreasonable coefficients for the planes or low modeling resolution), the damping factors were increased until stable results were obtained.

No PcP phases could be identified and picked in the northeast and southeast (quadrants 2 and 3 respectively). Therefore, there were only two interfaces modeled, the base of the near-surface layer and the Moho boundary. The velocity within the middle layer is approximately equal to the average velocity in the crust which was determined to be 6.55 km/s from the in-line modeling described in Chapters 5 and 6. The initial velocity in the second layer was set to 6.55 km/s. This parameterization could raise a problem if the Pg and PmP phases are modeled simultaneously. According to the model, beyond a certain distance, Pg phases will propagate as a head wave at the bottom of the near-surface layer at the initial velocity of 6.55 km/s. In reality, the velocity below the near-surface low-velocity layer is approximately 6.1-6.2 km/s, as estimated from the in-line data discussed in previous chapters, rather than 6.55 km/s. The high value (6.55 km/s) could cause large misfits or unreasonable coefficients of the interface corresponding to the near-surface layer during the modeling. Therefore, the "layer stripping" (Zelt and Forsyth, 1994) modeling technique was applied in the northeast and southeast (quadrants 2 and 3). The near-surface low-velocity layer was modeled first with the velocity at the top of the second layer constrained to fit the Pg arrivals. Afterwards, the PmP phase was modeled with the coefficients of the interface representing the base of the near-surface velocity layer fixed to

the previously determined value. There are total nine parameters being modeled in the northeast and southeast.

There are no picked PmP and PcP arrivals picked in the southwest (quadrant 4). Therefore, only one interface, the base of the near-surface low-velocity layer, was thus modeled to match the Pg phases. The five initial parameters, including the velocity beneath the interface, were specified by consideration of modeling results from the in-line data in the southwestern half of profile XY and the southern half of profile AB (Table 7.2).

2. Crustal Structure in the Northwest (quadrant 1)

The Pg, PcP and PmP arrivals recorded in the northwest were modeled simultaneously. The total number of arrivals picked from eight shots is 504. Two iterations were required to obtain the final model with RMS traveltime residuals of 0.08, 0.072 and 0.036 s for Pg, PcP and PmP phases, with normalized χ^2 equal to 1.6, 1.03 and 0.52 respectively (Table 7.3). The RMS traveltime residual for all picked traveltimes was approximately 0.077 s with a normalized χ^2 of 1.5. The fit between the observed and calculated traveltimes is shown in Figures 7.20b-7.34b for all shots used in the modeling. The damping factor is 15 for this modeling. Final modeling parameters are listed in Table 7.4.

The velocity determined for the near-surface low-velocity layer is ~5.93 km/s (Table 7.4) corresponding to the velocity value (5.88-6.09 km/s) in this layer obtained using in-line data. The interface dips from ~0.6 km in the west and 1.5 km in the north to ~2.4 km towards the cross point of the two survey lines in the Sudbury Basin. The interface at the bottom of the upper crust was modeled to be in the range of 15.2-15.9 km which is com-

Table 7.3 RMS traveltime residuals and χ^2 for fan-shot data inversion modeling

Contents	No. of Picks (Seismic phases)	RMS t. r. (s)		χ^2	
Quadrant 1 (Superior Province)	428 (Pg) 44(PcP) 32(PmP)	0.080 0.072 0.036	0.077	1.60 1.03 0.52	1.51
Quadrant 2 (Superior and Southern provinces)	377(Pg) 190(PmP)	0.078 0.051		1.56 0.71	
Quadrant 3 (Southern Province and Grenville Front)	236(Pg) 63(PmP)	0.123 0.061		2.47 0.87	
Quadrant 4 (Grenville Front and Grenville Province)	249(Pg)	0.096		1.92	

Note: (): seismic phases; RMS t. r.: root mean square traveltime residual (seconds).

patible with the depth of 17.4-16.8 km for the middle crustal interface obtained from the in-line modeling. A velocity of 6.19 km/s was obtained for the upper crust, which corresponds well to the average velocity in the second layer (6.22 km/s) obtained from the in-line data. The velocity of the lower crustal layer was found to be 6.79 km/s (Table 7.4). The Moho depth (35.6-36.7 km) in the northwest of the study area is in agreement with the value of ~37 km of depth modeled from the in-line profiles.

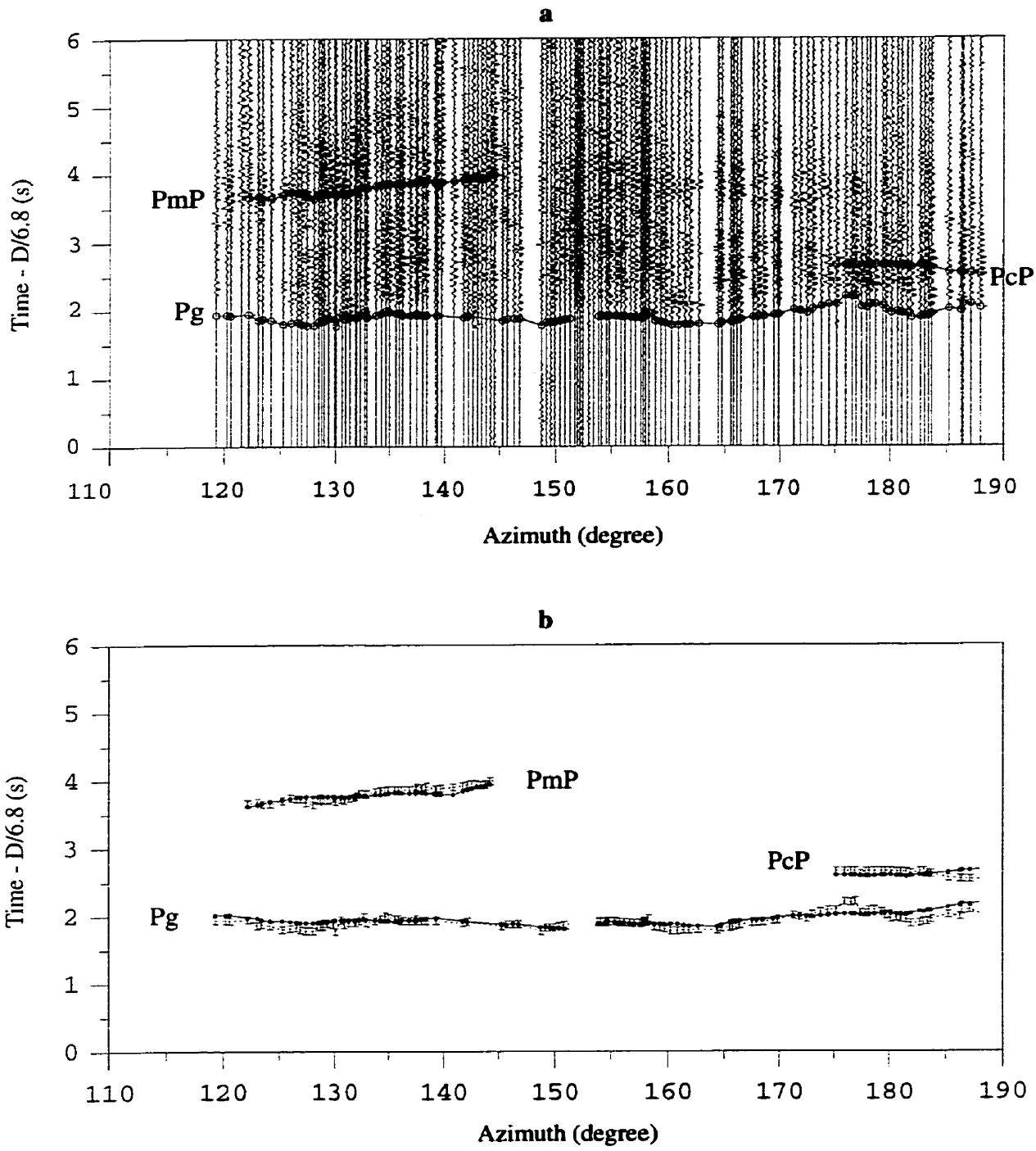

Figure7.20 Fan-shot seismic section ab0. **a**: traveltime section used for inversion modeling; **b**: the observed and calculated traveltime curves. ∞ : picked traveltime; ⋈ : picked traveltime with picking uncertainty; ⋯ : calculated traveltime.

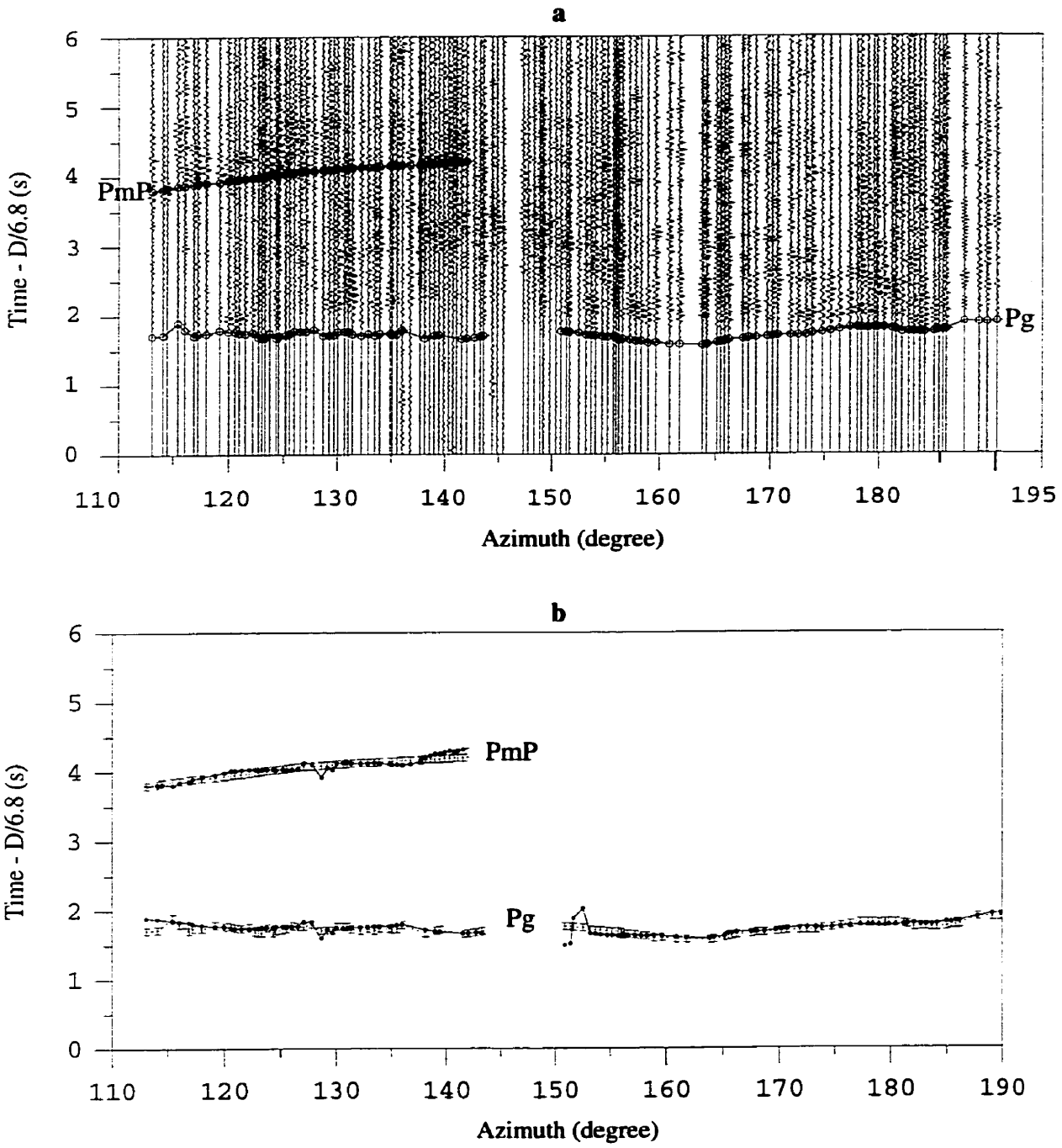

Figure7.21 Fan-shot seismic section ab1. **a**: traveltime section used for inversion modeling; **b**: the observed and calculated traveltime curves. ∞ : picked travel-time; ⋈ : picked traveltime with picking uncertainty; ●–● : calculated traveltime.

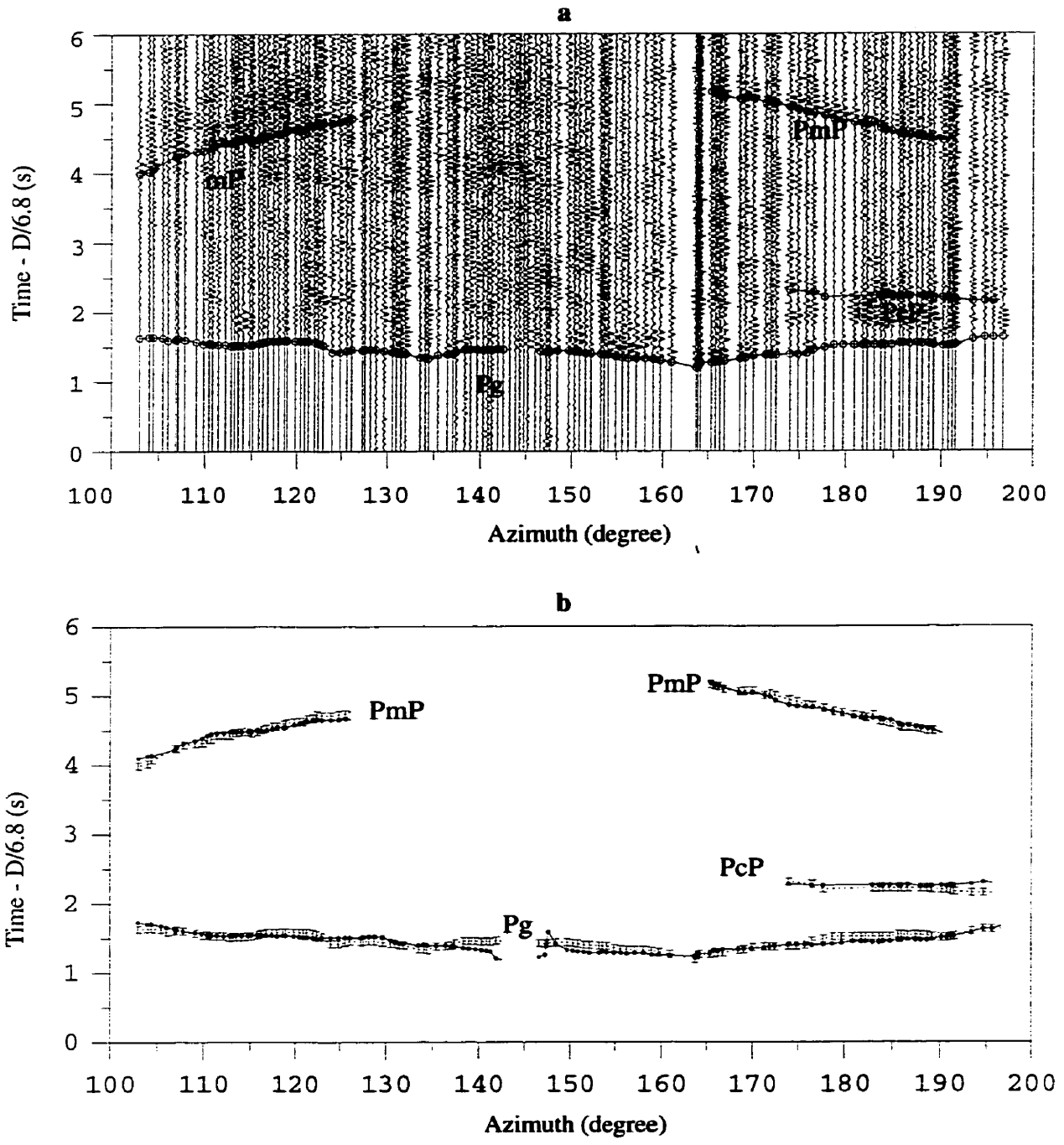

Figure7.22 Fan-shot seismic section ab2. **a**: traveltime section used for inversion modeling; **b**: the observed and calculated traveltime curves. ∞ : picked travel-time; ⋕ : picked traveltime with picking uncertainty; •-• : calculated traveltime.

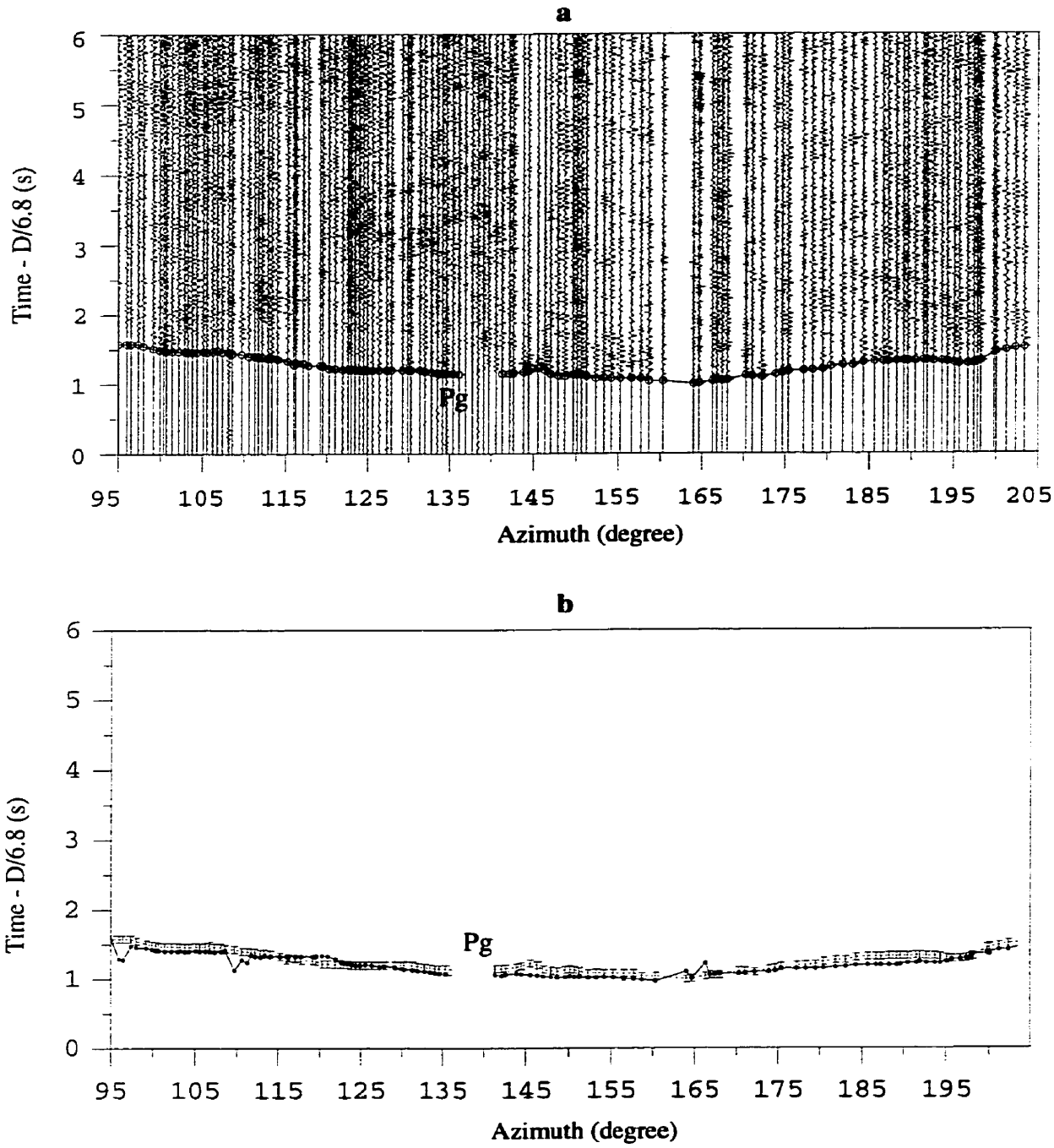

Figure7.23 Fan-shot seismic section ab3. **a**: traveltime section used for inversion modeling; **b**: the observed and calculated traveltime curves. ⚯ : picked traveltime; ⧗ : picked traveltime with picking uncertainty; ⚬—⚬ : calculated traveltime.

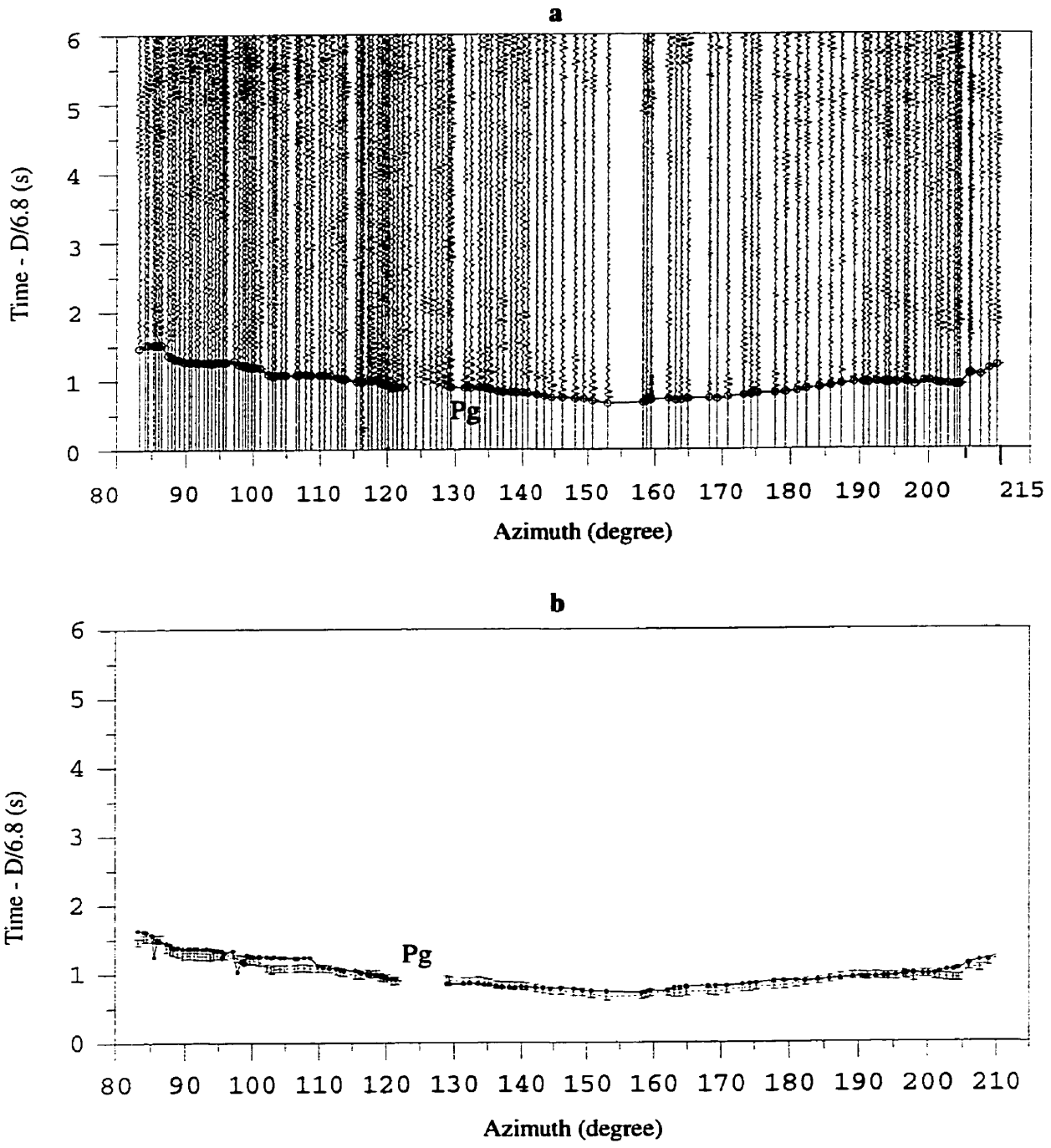

Figure7.24 Fan-shot seismic section ab4. **a**: traveltime section used for inversion modeling; **b**: the observed and calculated traveltime curves. ∞ : picked traveltime; ⋈ : picked traveltime with picking uncertainty; •—• : calculated traveltime.

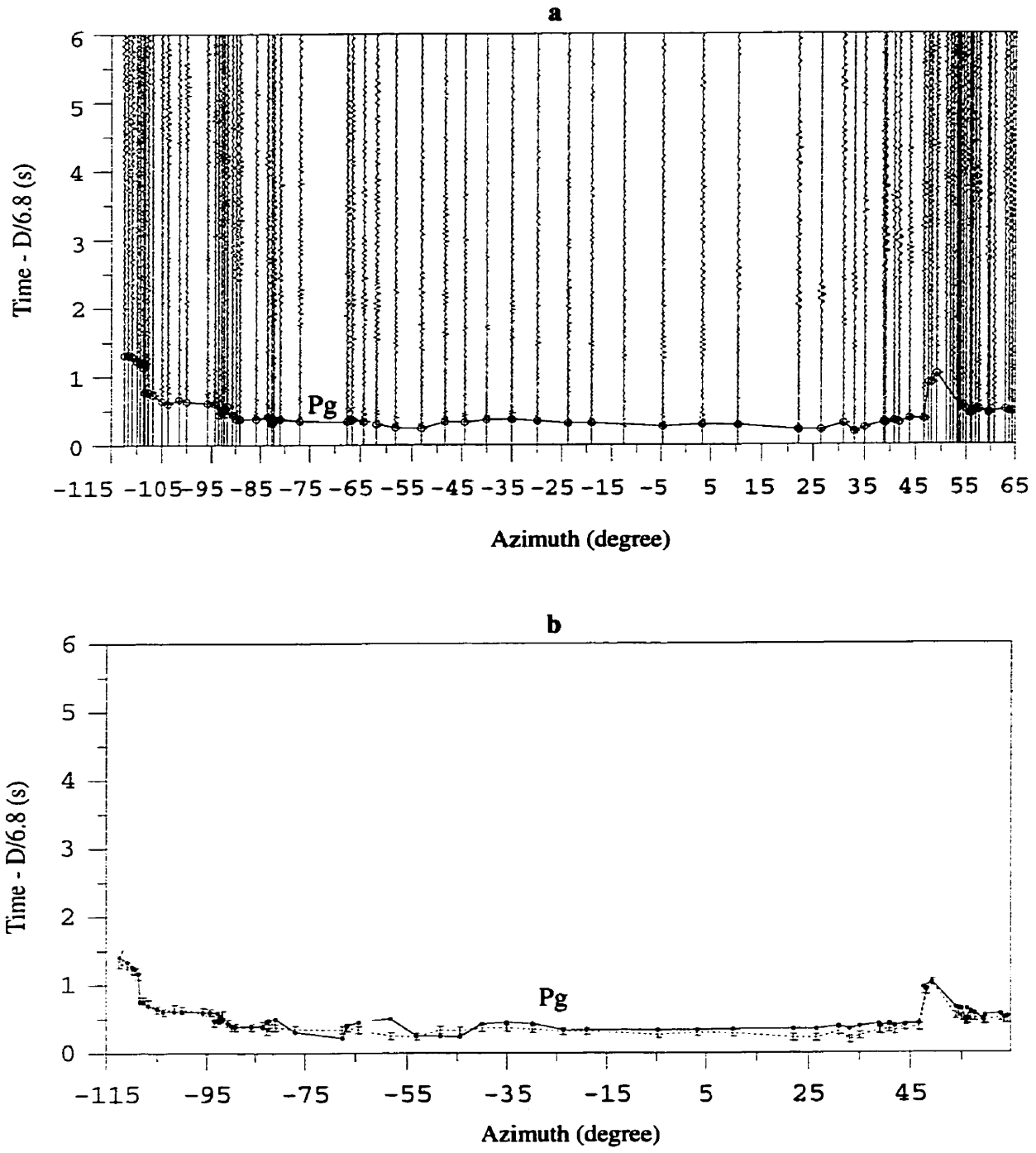

Figure7.25 Fan-shot seismic section ab6. **a**: traveltime section used for inversion modeling; **b**: the observed and calculated traveltime curves. ⊶ : picked traveltime; ⊣⊢ : picked traveltime with picking uncertainty; •—• : calculated traveltime.

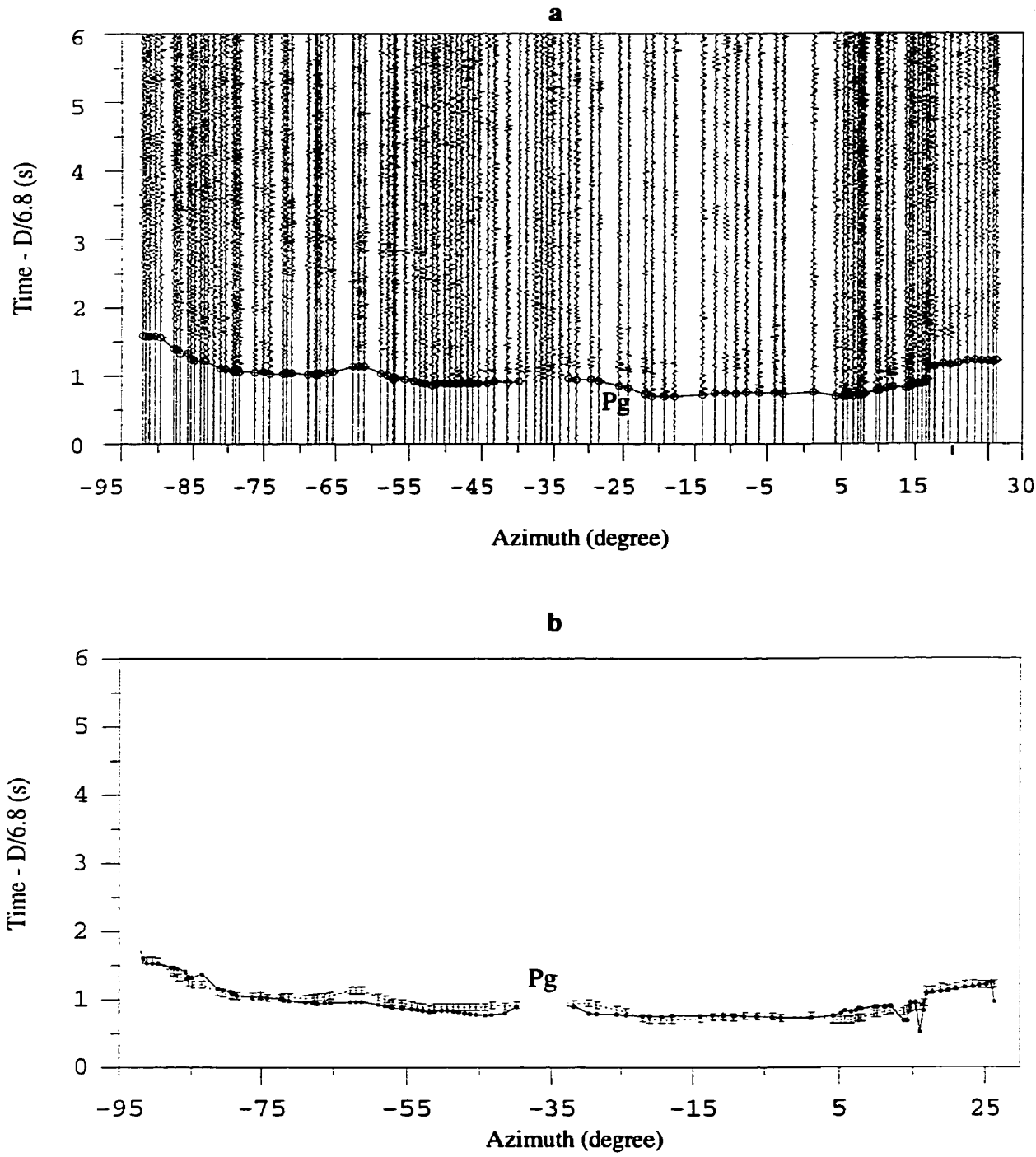

Figure7.26 Fan-shot seismic section ab7. **a**: traveltime section used for inversion modeling; **b**: the observed and calculated traveltime curves. ⚯ : picked traveltime; ⧗ : picked traveltime with picking uncertainty; ⚯ : calculated traveltime.

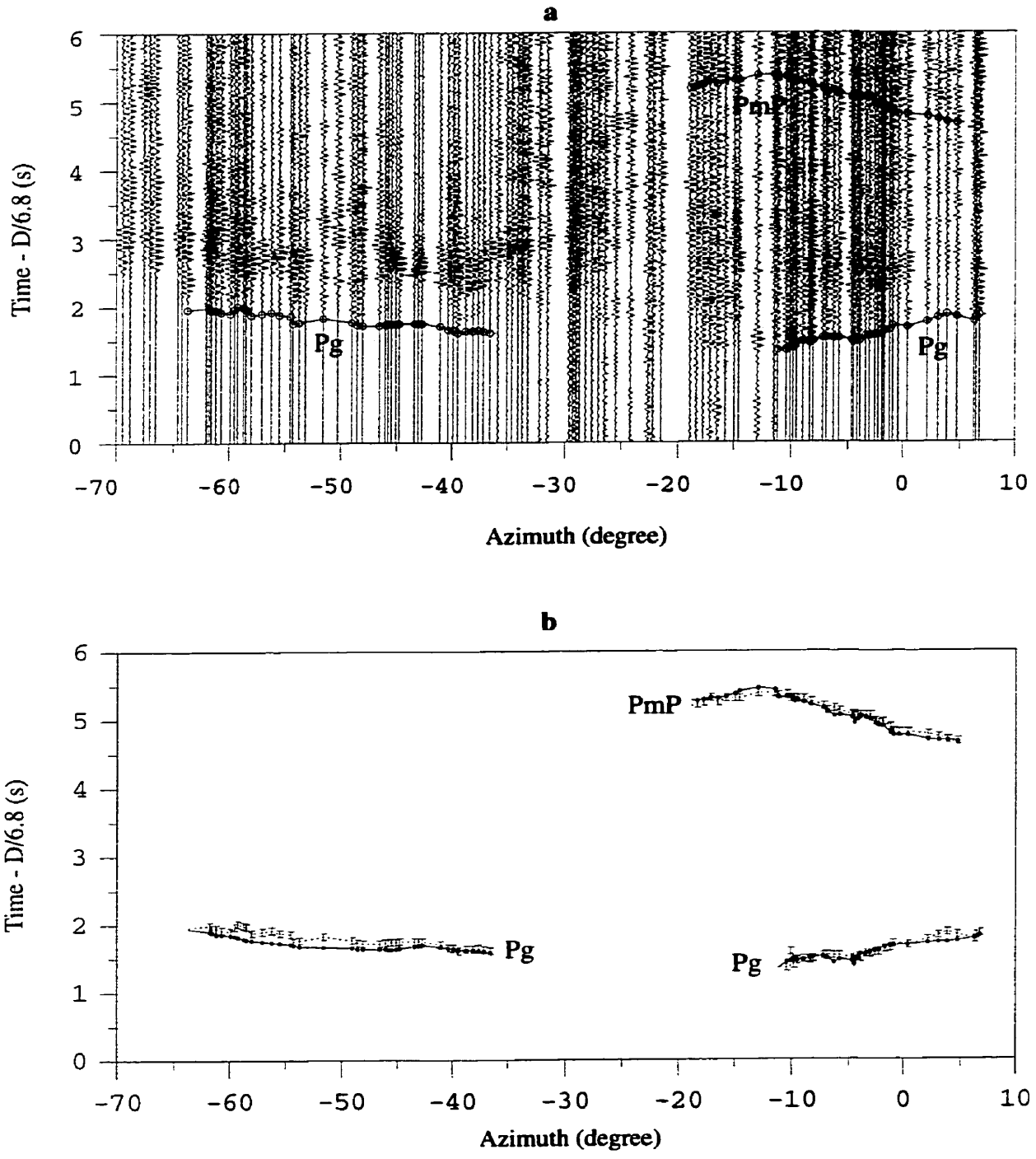

Figure7.27 Fan-shot seismic section ab8. **a**: traveltime section used for inversion modeling; **b**: the observed and calculated traveltime curves. ⚬⚬ : picked traveltime; ⧓ : picked traveltime with picking uncertainty; ⚬—⚬ : calculated traveltime.

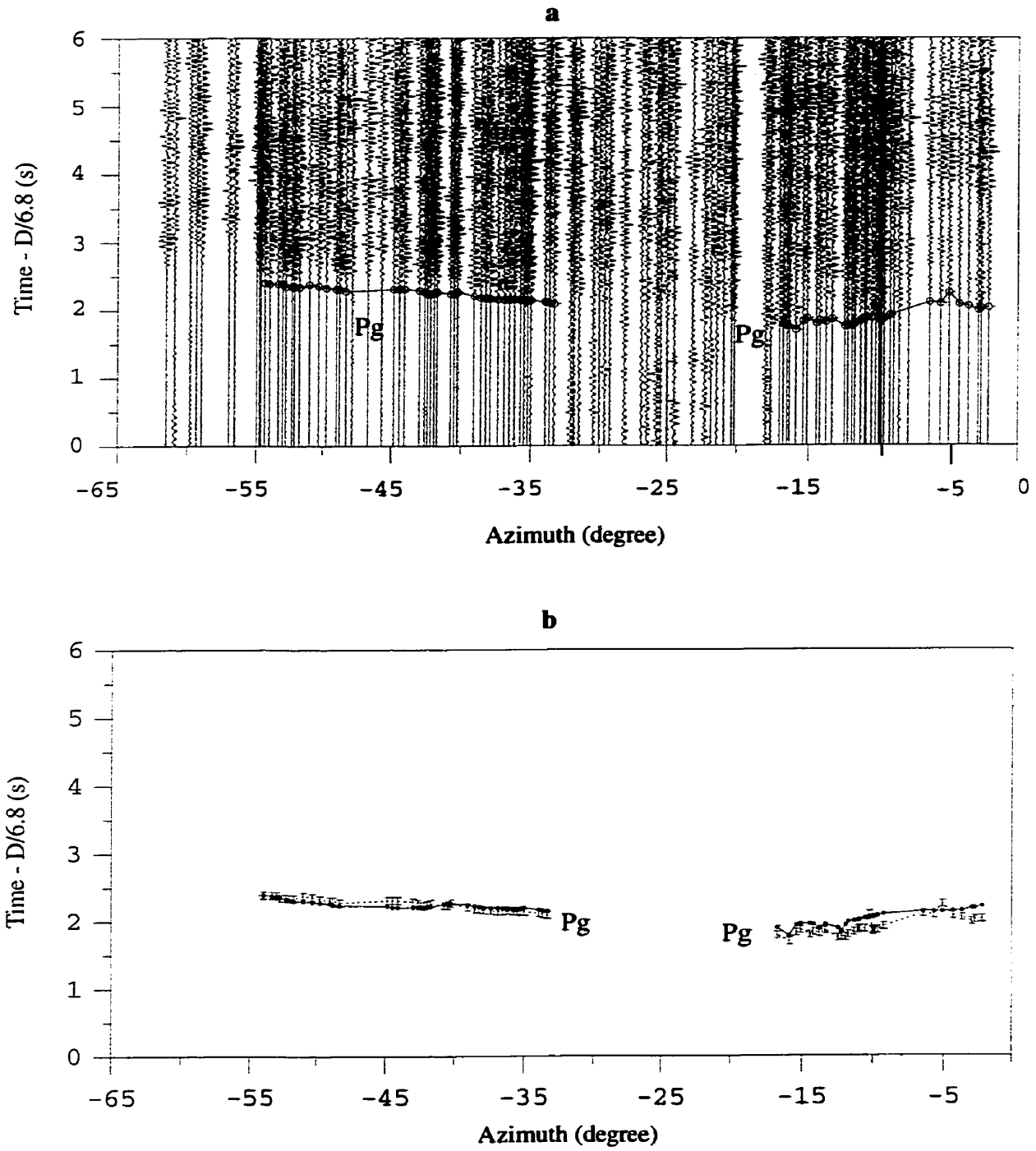

Figure7.28 Fan-shot seismic section ab9. **a**: traveltime section used for inversion modeling; **b**: the observed and calculated traveltime curves. ∞ : picked traveltime; ⋕ : picked traveltime with picking uncertainty; •-• : calculated traveltime.

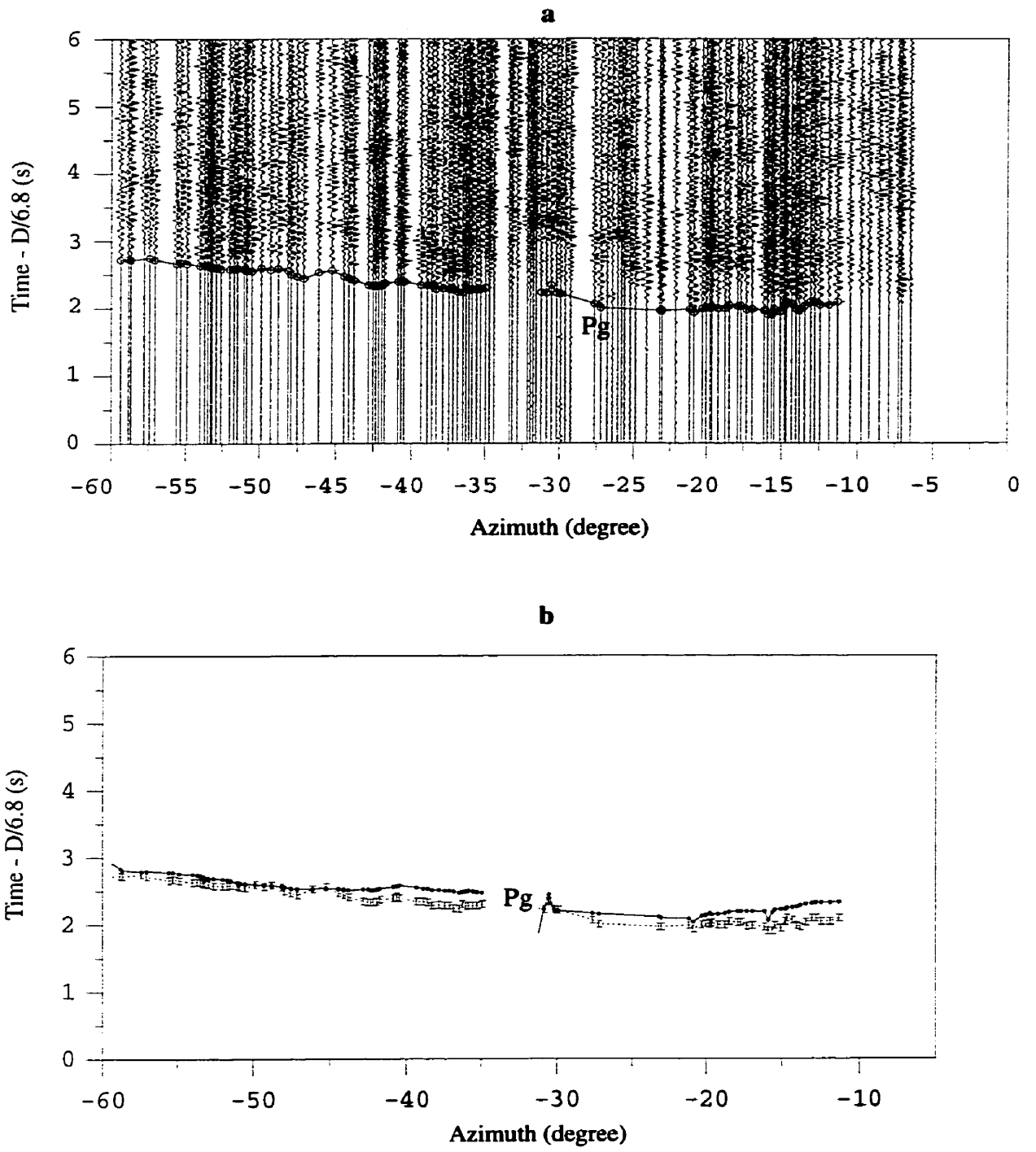

Figure7.29 Fan-shot seismic section ab10. **a**: traveltime section used for inversion modeling; **b**: the observed and calculated traveltime curves. ∞ : picked travel-time; ⋕ : picked traveltime with picking uncertainty; •—• : calculated traveltime.

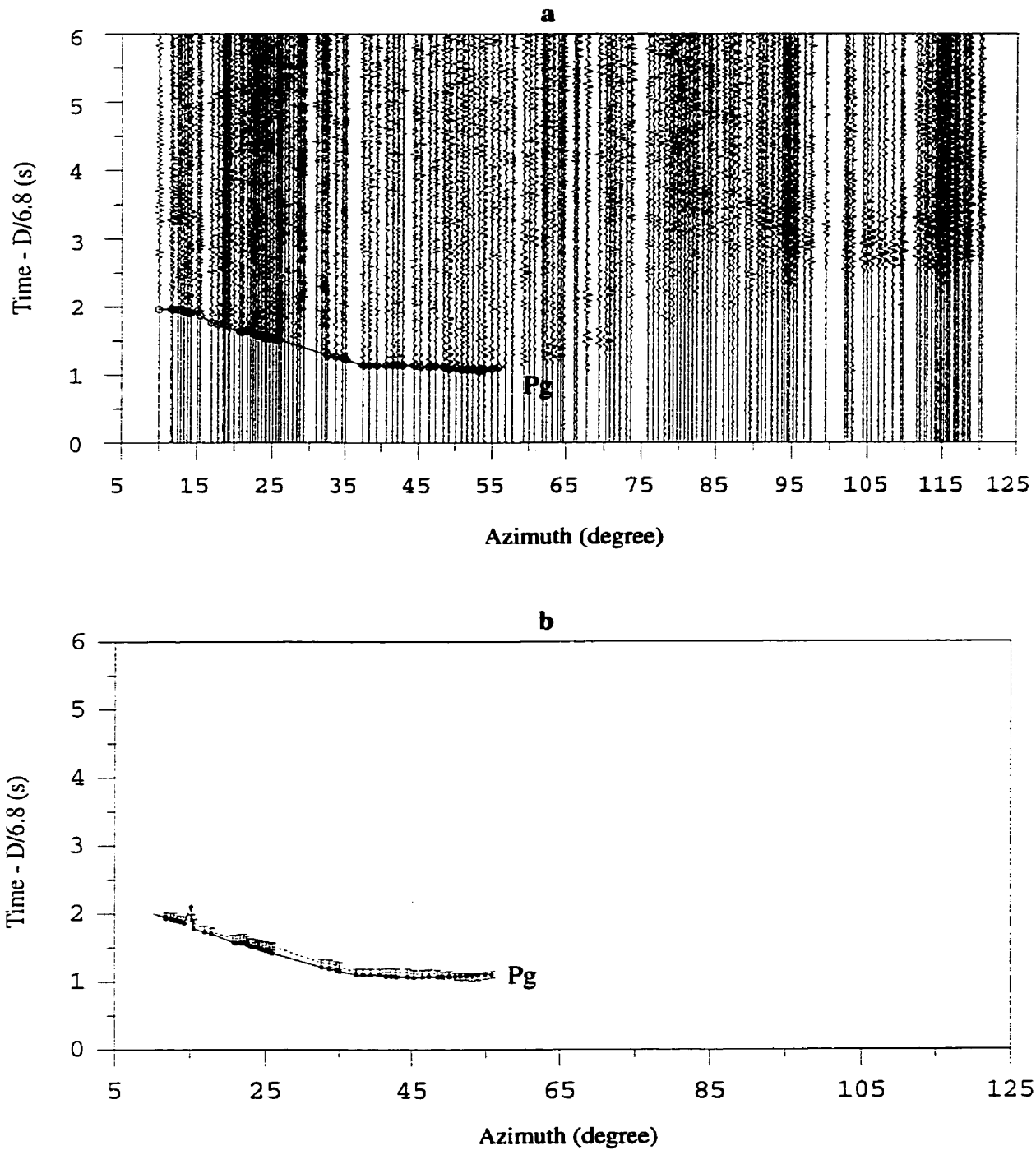

Figure7.30 Fan-shot seismic section xy0. **a**: traveltime section used for inversion modeling; **b**: the observed and calculated traveltime curves. ⊶ : picked traveltime; ⊣⊢ : picked traveltime with picking uncertainty; •—• : calculated traveltime.

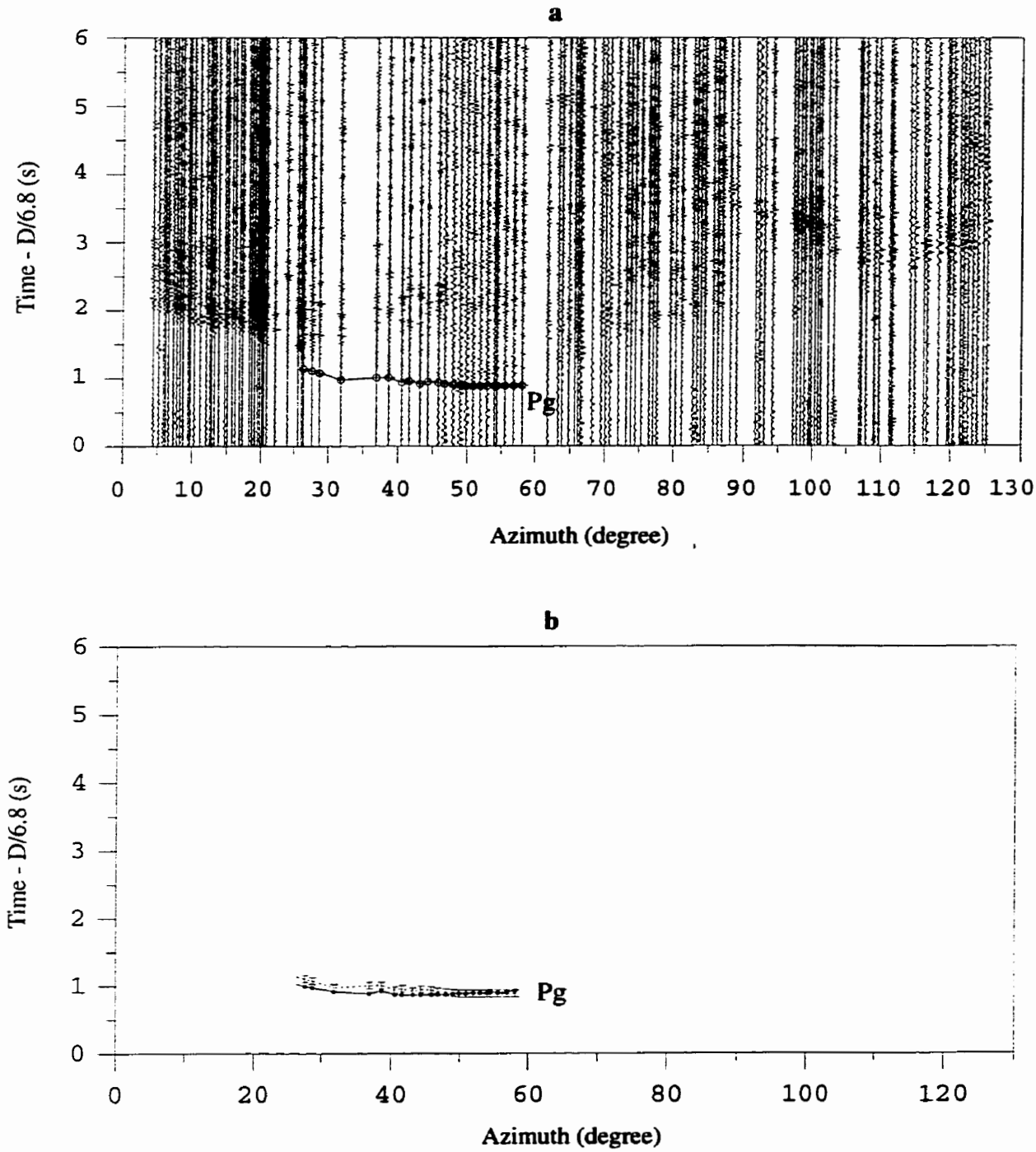

Figure7.31 Fan-shot seismic section xy1. **a**: traveltime section used for inversion modeling; **b**: the observed and calculated traveltime curves. ⊶ : picked traveltime; ⊶ : picked traveltime with picking uncertainty; ⊶ : calculated traveltime.

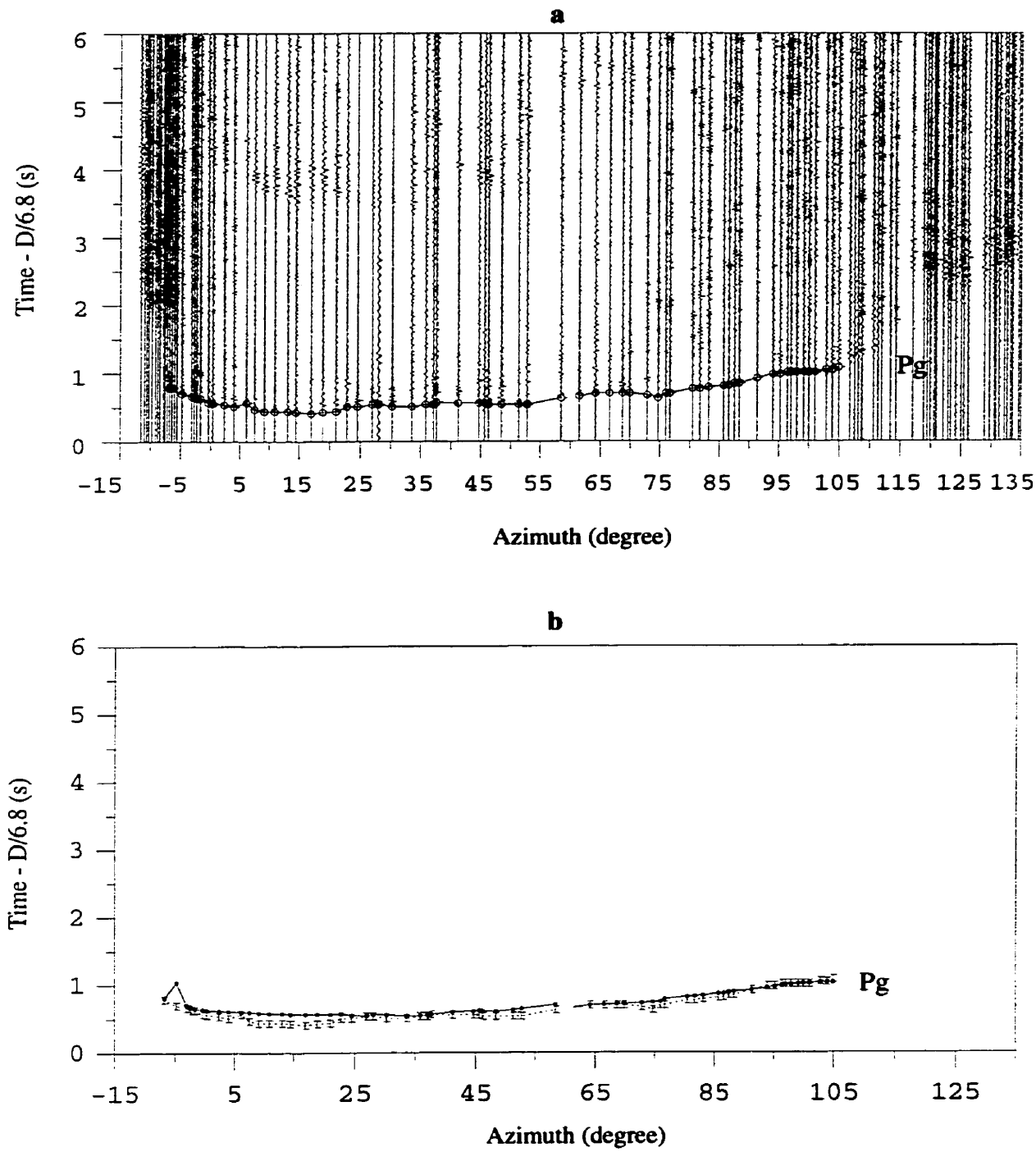

Figure7.32 Fan-shot seismic section xy2. **a**: traveltime section used for inversion modeling; **b**: the observed and calculated traveltime curves. ⚬⚬ : picked travel-time; ⧺⧻ : picked traveltime with picking uncertainty; ⚬—⚬ : calculated traveltime.

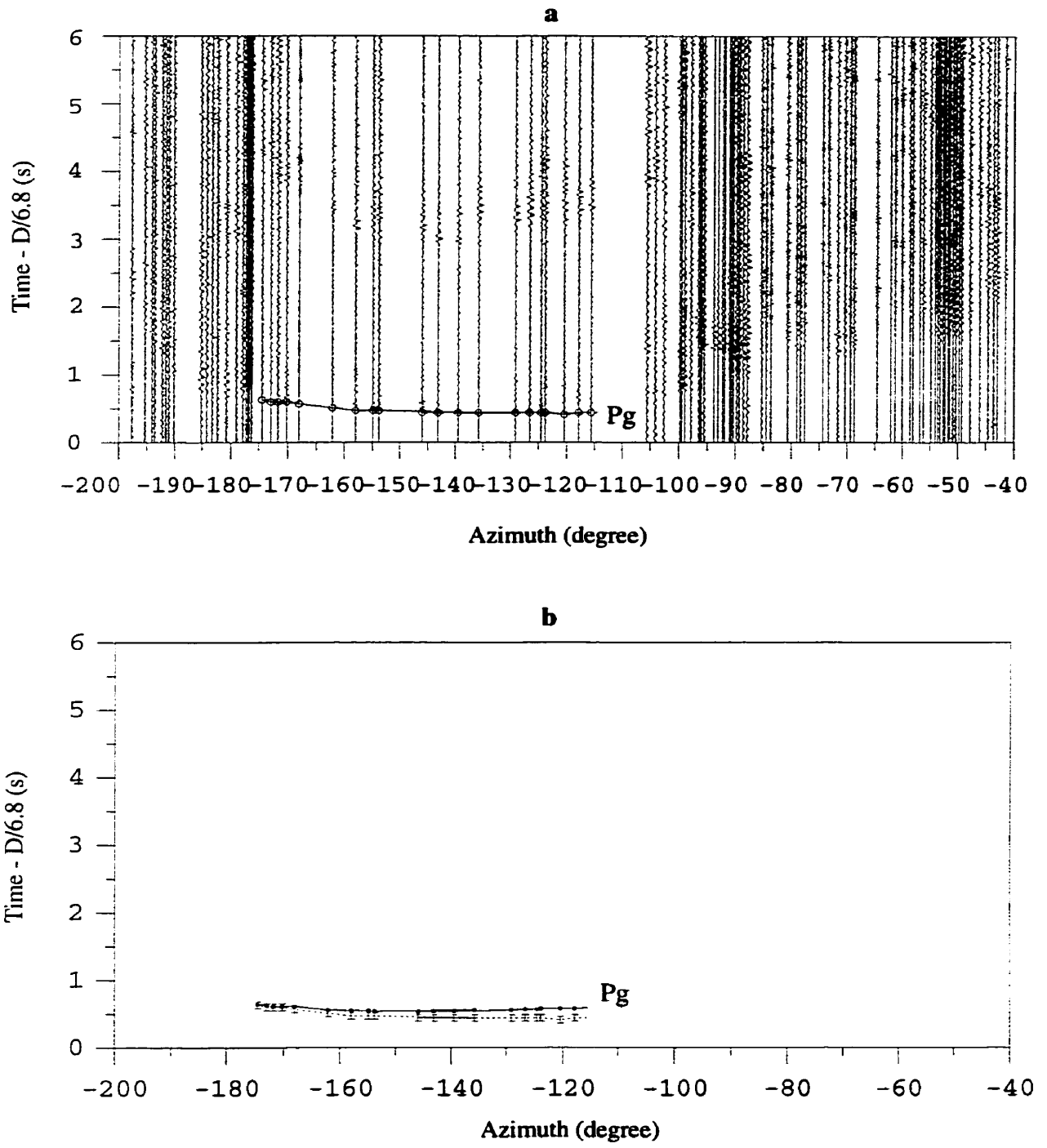

Figure7.33 Fan-shot seismic section xy4. **a**: traveltime section used for inversion modeling; **b**: the observed and calculated traveltime curves. ⚯ : picked traveltime; ⧖ : picked traveltime with picking uncertainty; ⚯ : calculated traveltime.

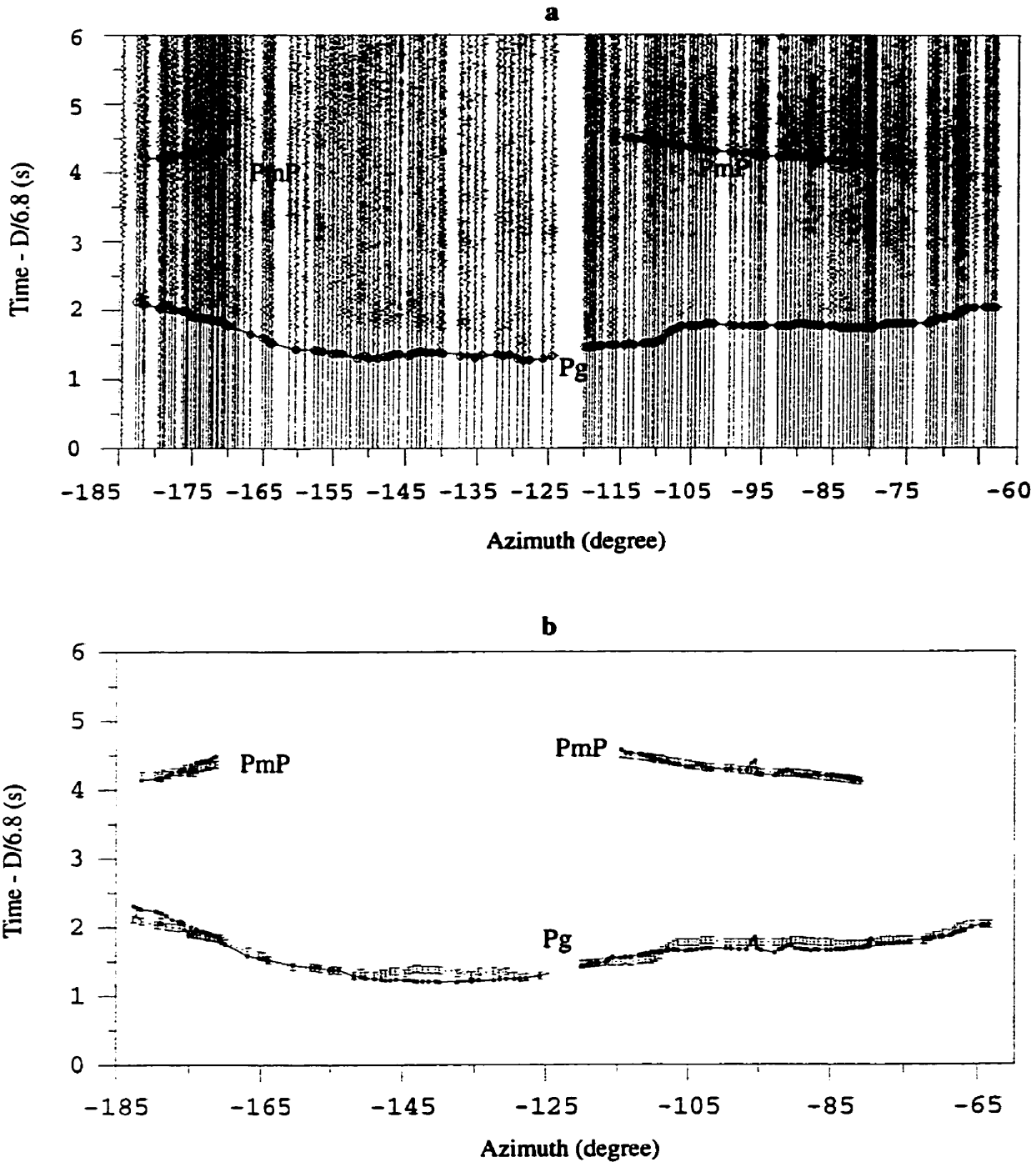

Figure7.34 Fan-shot seismic section xy5. **a**: traveltime section used for inversion modeling; **b**: the observed and calculated traveltime curves. ∞ : picked travel-time; ⋈ : picked traveltime with picking uncertainty; •—• : calculated traveltime.

Table 7.4 Results of inversion in the Northwest (quadrant 1)

	type	orig. par.	uncert.	adjust.	new par.	resol.	std. error
Iteration 1	1	0.022	0.0150	-0.0017	0.0239	0.4613	0.0110
	1	-0.013	0.0150	-0.0157	0.0030	0.6801	0.0085
	1	2.210	1.0000	-0.3464	2.5564	0.7543	0.4957
	2	5.950	0.1000	0.0114	5.9386	0.2011	0.0894
	1	0.015	0.0150	-0.0175	0.0325	0.3271	0.0123
	1	0.015	0.0150	-0.0059	0.0209	0.1636	0.0137
	1	18.000	1.0000	1.1831	16.8169	0.5582	0.6647
	2	6.200	0.1000	0.0169	6.1831	0.9486	0.0227
	1	0.049	0.0250	-0.0059	0.0550	0.5935	0.0159
	1	0.004	0.0250	-0.0024	0.0063	0.2307	0.0219
	1	38.526	1.0000	-0.0339	38.5597	0.4456	0.7446
	2	6.786	0.1000	-0.0022	6.7881	0.0540	0.0973
	Damping factor: 15.						
	type	**orig. par.**	**uncert.**	**adjust.**	**new par.**	**resol.**	**std. error**
Iteration 2	1	0.024	0.0250	0.0036	0.0203	0.6309	0.0152
	1	0.003	0.0250	-0.0061	0.0091	0.7686	0.0120
	1	2.556	1.0000	0.0616	2.4948	0.6756	0.5696
	2	5.939	0.1000	0.0086	5.9301	0.2552	0.0863
	1	0.032	0.0250	-0.0089	0.0414	0.5399	0.0170
	1	0.021	0.0250	-0.0195	0.0404	0.2877	0.0211
	1	16.817	1.0000	-0.0003	16.8172	0.3738	0.7913
	2	6.183	0.1000	-0.0086	6.1916	0.9127	0.0296
	1	0.055	0.0250	-0.0010	0.0560	0.5878	0.0161
	1	0.006	0.0250	-0.0010	0.0073	0.2296	0.0219
	1	38.560	1.0000	-0.0796	38.6393	0.4405	0.7480
	2	6.788	0.1000	0.0022	6.7859	0.0638	0.0968
	Damping factor: 15.						

Note: **type** 1: 1: independent coefficients of plane interfaces (a_i, b_i, c_i)(i=1, 2, 3) representing the first layer, second layer and third layer respectively. From the top, the first three coefficients denote the coefficients of the first plane, the second three represent the coefficients of the second plane and the third three represent the coefficients of the third layers); **type** 2; velocities; **orig. par.**: original parameters; **uncert.**: uncertainties of parameters; **adjust.**: adjustment of parameters; **new par.**: new parameters; **resol.**: model resolution; **std. error**: standard error (see Section 6.2 in Chapter 6).

3. Crustal Structure in the Northeast (quadrant 2)

In the northeast portion of the study area, the near-surface low-velocity layer and Moho interface were determined separately using 377 Pg and 190 PmP arrivals picked from fan shots ab0, ab1, ab2, ab3, ab4 and xy5 (Figures 7.5-7.9 and 7.19). The RMS traveltime residual for the Pg phase is ~0.078 s and the value of normalized χ^2 is equal to 1.56 (Table 7.3). The damping factor for Pg phase modeling is 10. An RMS traveltime residual of 0.051 s and normalized χ^2 value of 0.71 were obtained in the PmP phase modeling. The damping factor for PmP phase modeling was increased to 50 to stabilize the modeling. A good modeling resolution (>0.5) of seven parameters out of nine were obtained (Table 7.5).

The velocity in the northeast in the near-surface low-velocity layer is approximately 5.93 km/s which is equal to that obtained from the in-line seismic data. The depth to the base of this layer dips towards the cross point (from ~0.3 km in the north and ~1.4 km in the east to ~2.4 km at the cross point). The average crustal velocity is ~6.55 km/s and the Moho depth is in the range of 35.4 km to 36.6 km in this area (Figure 7.35).

4. Crustal Structure in the Southeast (quadrant 3)

In the southeast quadrant between the two profiles AB and XY, the traveltime modeling was similar to that in quadrant 2. A total of 236 Pg arrivals were picked from fan shots ab7, ab8, ab9, ab10, xy4 and xy5 (Figures 7.11-7.14, 7.18 and 7.19) and a total of 63 arrivals of PmP reflections were picked from the data of shots ab8 and xy5 (Figures 7.12 and 7.19). Pg arrivals from shot ab6 were not modeled because the shot and receivers were

Table 7.5 Results of inversion in the Northeast (quadrant 2)

	type	orig. par.	uncert.	adjust.	new par.	resol.	std. error
Layer 1	1	-0.0153	0.0100	-0.0120	-0.0032	0.6646	0.0058
	1	-0.0277	0.0100	-0.0019	-0.0259	0.2167	0.0089
	1	2.4000	0.5000	-0.2713	2.6713	0.3310	0.4090
	2	5.9500	0.1000	0.0226	5.9274	0.5588	0.0664
	2	6.2000	0.1000	0.0106	6.1894	0.9542	0.0214
	Damping factor: 10.						
	type	**orig. par.**	**uncert.**	**adjust.**	**new par.**	**resol.**	**std. error**
Layer 2	1	-0.0111	0.0250	0.0140	-0.0251	0.7267	0.0131
	1	-0.0208	0.0250	0.0101	-0.0308	0.5946	0.0159
	1	37.8000	1.0000	0.2983	37.5017	0.5399	0.6783
	2	6.5500	0.1000	-0.0053	6.5553	0.6842	0.0562
	Damping factor: 50.						

Note: **type** 1: 1:independent coefficients of plane interfaces (a_l, b_l, c_l); **type** 2: velocities; **orig. par.**: original parameters; **uncert.**: uncertainties of parameters; **adjust.**: adjustment of parameters; **new par.**: new parameters; **resol.**: model resolution; **std. error**: standard error (see Section 6.2 in Chapter 6).

almost in line and modeling of these traveltimes would contribute little to the 3-D structure.

A RMS traveltime residual of 0.123 s was obtained for Pg reflections after 2 iterations with a normalized χ^2 of 2.47. The value of χ^2 indicates that the parameters are underfit in this case. This result could be caused by the over-simplified model. In other words, the geological structure or velocity structure in the southeast is more complicated than in the

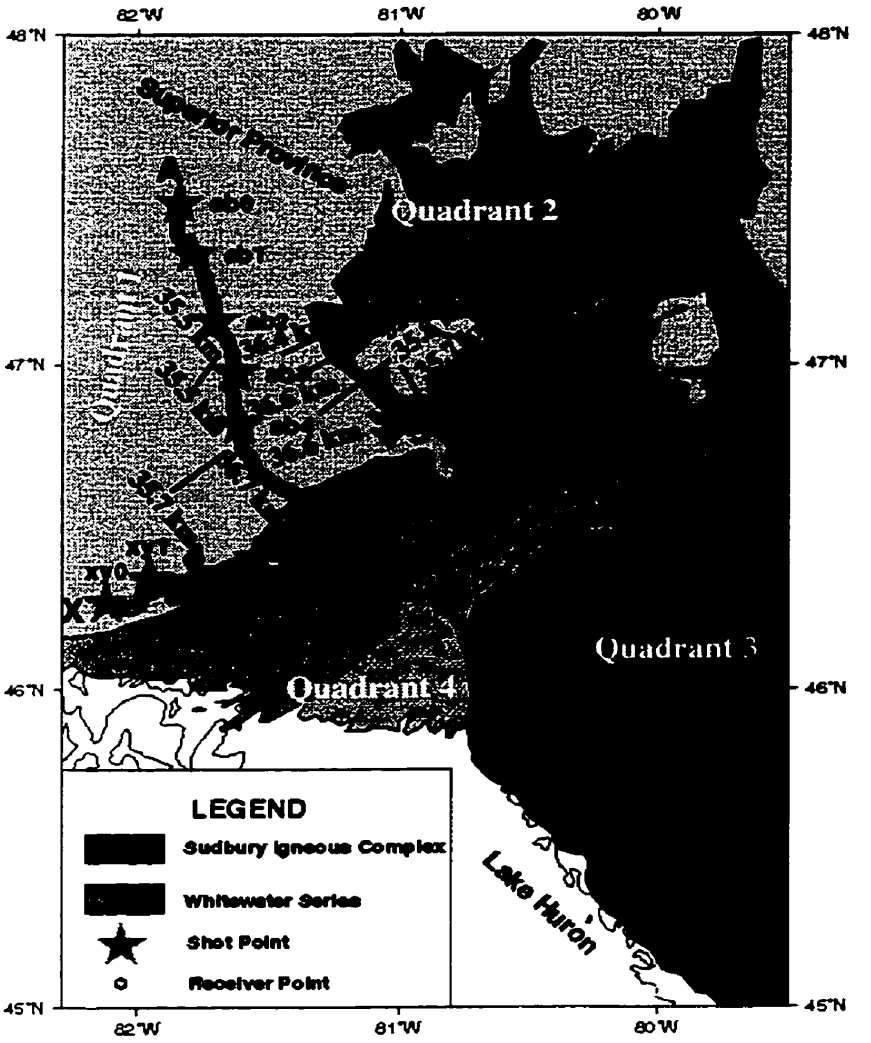

Figure 7.35 Crustal thickness map obtained by using the 3-D ray tracing inversion. ____: thickness location; numbers in km: crsutal thickness.

north so that it cannot be interpreted well using simple plane layers with constant velocities. The damping factor for Pg phase modeling had to be increased to 250 to stabilize the solution in the southeast. The large damping factor might also be necessary because of complicated near-surface structure which could not be fitted well by a plane structure model. Because of limited data availability, this model was accepted as a final result for the southeast quadrant. The PmP arrivals have a RMS traveltime residual of 0.061 s with a normalized χ^2 of 0.87 indicating a better fit to the phases with deeper travel paths. The damping factor for PmP phase modeling is 10. The observed and calculated traveltimes of PmP reflections are well matched (Figures 7.26b-7.29b and 7.34b). Table 7.6 lists the resolution and standard error of the model parameters (the standard error was explained in Section 6.2). All six parameters obtained have a high resolution (>0.5).

The velocity of the near-surface low-velocity layer in the southeast is ~5.94 km/s which is approximately equal to that in the northwest quadrant. The interface at the base of the layer dips towards the south from ~0.9 km in the north to ~2.0 km. The thickness of the first layer increases slightly from the AB-XY cross point to the east where it reaches 1.9 km under shot xy5. This quadrant includes the Grenville Front Tectonic Zone (Figures 7.4 and 7.35). The crustal velocity is ~6.57 km/s and the Moho depth is in the range of 40.4-41.6 km (Figure 7.35).

5. Crustal Structure in the Southwest (quadrant 4)

PmP and PcP phases could not be identified in the southwest because of the low S/N ratio. Therefore, only 249 Pg phases were picked from fan shots ab6, ab7, ab8, ab9, ab10 and xy2 for modeling the near-surface low-velocity layer (Figures 7.10-7.14 and 7.17).

Table 7.6 Results of inversion in the Southeast (quadrant 3)

	type	orig. par.	uncert.	adjust.	new par.	resol.	std. error
Layer 1 Iteration 1	1	-0.0271	0.0250	-0.0020	-0.0252	0.2042	0.0223
	1	-0.0029	0.0250	-0.0184	0.0155	0.3399	0.0203
	1	2.1979	0.5000	-0.0813	2.2792	0.1100	0.4717
	2	5.9500	0.1000	0.0175	5.9325	0.1128	0.0942
	2	6.1500	0.1000	-0.0602	6.2102	0.8116	0.0434
	Damping factor: 250.						
	type	**orig. par.**	**uncert.**	**adjust.**	**new par.**	**resol.**	**std. error**
Layer 1 Iteration 2	1	-0.0252	0.0250	-0.0149	-0.0103	0.4607	0.0184
	1	0.0155	0.0250	0.0096	0.0059	0.5693	0.0164
	1	2.2792	0.5000	-0.0572	2.3364	0.1358	0.4648
	2	5.9325	0.1000	-0.0058	5.9383	0.0759	0.0961
	2	6.2102	0.1000	-0.0148	6.2250	0.9082	0.0303
	Damping factor: 250.						
	type	**orig. par.**	**uncert.**	**adjust.**	**new par.**	**resol.**	**std. error**
Layer 2	1	0.0376	0.0250	-0.0002	0.0378	0.3807	0.0197
	1	-0.0340	0.0250	0.0101	-0.0441	0.6437	0.0149
	1	37.6455	1.0000	-0.0675	37.7130	0.5396	0.6785
	2	6.5500	0.1000	-0.0221	6.5721	0.7645	0.0485
	Damping factor: 10.						

Note: **type** 1: 1: independent coefficients of plane interfaces (a_l, b_l, c_l); **type** 2: velocities; **orig. par.**: original parameters; **uncert.**: uncertainties of parameters; **adjust.**: adjustment of parameters; **new par.**: new parameters; **resol.**: model resolution; **std. error**: standard error (see Section 6.2 in Chapter 6).

The traveltimes of the Pg phases were fitted well with a RMS traveltime residual of 0.096 s (Figures 7.25-7.29 and 7.32). The normalized χ^2 is approximately 1.92 which indicates an underfit in the modeling. This result suggests that the presence of considerably more structural complexity than expected for this quadrant. Another possible reason could be mis-picking of Pg phases at far offsets. The picked Pg phases contain ten traces on the section of fan shot ab10 for which the distance between the shot and receiver (160-175 km) is just slightly over 160 km. Analysis of the in-line seismic data for shots ab9 and ab10 indicated that the Pc phases could be observed as first arrivals at an offset of ~160 km. Therefore, the first arrivals on the fan shot for ab10 are possibly Pc phases rather than Pg phases. These phase picking errors could affect the final model. However, the errors are estimated to be only 5%. Therefore, the primary reason for the underfit of the model must be model parameterization.

The velocity in the near-surface layer is approximately 6.03 km/s and the velocity beneath the near-surface low-velocity layer is approximately 6.13 km/s. The depth to the base of the layer increases towards the cross point from 0.7 km to 1.7 km in the southwest. Three parameters out of five that were modeled have good resolution (>0.88) (Table 7.7).

7.3 Summary

This research developed a Fletcher Reeves conjugate gradient ray tracing algorithm for modeling fan-shot seismic data in 3-D to investigate the velocity structure in the area adjacent to the Sudbury Structure. In the forward modeling, the traveltime and ray path are obtained by solving the nonlinear traveltime function numerically with the conjugate gra-

Table 7.7 Results of inversion in the Southwest (quadrant 4)

type	orig. par.	uncert.	adjust.	new par.	resol.	std. error
1	0.0050	0.0500	0.0023	0.0027	0.8757	0.0176
1	0.0280	0.0500	0.0146	0.0134	0.9535	0.0108
1	1.8300	0.5000	0.2237	1.6063	0.3549	0.4016
2	5.9500	0.1000	-0.0765	6.0265	0.3005	0.0836
2	6.1800	0.1000	0.0481	6.1319	0.9476	0.0229

Damping factor: 20.

Note: **type** 1: 1: independent coefficients of a plane interface (a_l, b_l, c_l); **type** 2: velocities; **orig. par.**: original parameters: uncertainties of parameters; **adjust.**: adjustment of parameters; **new par.**: new parameters; **resol.**: model resolution; **std. error**: standard error (see Section 6.2 in Chapter 6).

dient technique. A simplification of the velocity model is needed for this algorithm. Plane interfaces and constant velocity within each layer are assumed. In the inversion modeling, a damped least-squares method is applied.

The velocity structure was modeled in four areas separated by the two profiles AB and XY. In the northwest of the study area (quadrant 1), the crustal thickness is ~36.0 km and the depth of the mid-crustal layer is ~15.6 km. The average velocity of the lower crust is 6.79 km/s. There is a good fit between the observed and calculated traveltimes (RMS error of 0.077 s) with a normalized χ^2 of 1.5. In the northeast (quadrant 2), the crustal thickness ranges from 35.4 to 36.6 km (Figure 7.35) with an average velocity of ~6.55 km/s. A RMS traveltime residual of 0.051 s and a normalized χ^2 of 0.71 were obtained. In the southeast (quadrant 3), the near-surface layer modeled using Pg phases was underfitted because of

the complicated structure of the Grenville Front Tectonic Zone. The Grenville Front Tectonic Zone was modeled as several dipping layers or microterrane stacked sheets shown in Figures 5.4 and 5.29 by seismic refraction data. Therefore, this structure could not be fitted well by a simplified plane model. The Moho depth under the Grenville Front Tectonic Zone was found to be approximately 40.4-41.6 km (with a RMS traveltime residual of 0.061 s and a normalized χ^2 of 0.87) which corresponds to the depth obtained from the in-line modeling of profile AB. In the southwest, only the near-surface layer was modeled, using Pg phases. This model was also underfitted because of the complex structure of the subsurface in the Southern Province.

Chapter 8

3-D Seismic Tomography

Advanced 3-D seismic tomography was done during this thesis research using the high-resolution seismic reflection and refraction data collected in the Sudbury area. The first section of this chapter describes the 3-D weighted backprojection seismic tomographic algorithm which was developed by Hole (1992). The fast finite-difference technique proposed by Vidale (1990) was applied in the forward modeling. The weighted backprojection method is an inversion procedure and is described in the following subsection. The second section describes the results of applying the tomographic technique to the Sudbury seismic data. The chapter ends with a summary of 3-D seismic tomography in the Sudbury area.

8.1 Algorithm

A nonlinear 3-D seismic traveltime tomographic algorithm was developed by Hole (1992). It reconstructs high-resolution velocity images with large velocity contrasts from seismic data. Generally, 3-D seismic tomographic applications and interpretations are limited by two factors: nonlinearity causing the computation to be very expensive, and limited spatial resolution. In the forward modeling in Hole's algorithm, a fast finite-difference algorithm (Vidale, 1990) was applied, rather than the time consuming 3-D

two-point ray tracing approach. The nonlinear tomographic inversion method employed in Hole's algorithm reduces computer time by replacing the nonlinear traveltime problem with a linear traveltime perturbation problem. The resulting high-resolution 3-D seismic tomographic algorithm used in this thesis (Hole, 1992) is a fast procedure which can be applied to large volumes of available seismic data.

8.1.1 Finite-difference Forward Modeling

Backprojection tomography constructs velocity variations in grids or cells. In forward modeling, the first arrivals are computed rapidly and iteratively using a finite-difference extrapolation method (Vidale, 1990). The model is parameterized in terms of small cubes. In the present research, the initial 3-D velocity field is determined by linear interpolation of the 1-D velocities increasing with depth. This linear increasing velocity was determined on the basis of the 2-D and 3-D ray tracing modeling results.

The basic partial derivative equation for determining traveltime is the eikonal function which was discussed in Chapter 5 (equation 5.13). In the Cartesian coordinate system, one can replace the traveltime τ and velocity α or β in equation 5.13 with $t(x, y, z)$ and slowness $s(x, y, z)$, where x, y and z are the coordinates, and obtain the following alternative form of the eikonal equation

$$\left(\frac{\partial t}{\partial x}\right)^2 + \left(\frac{\partial t}{\partial y}\right)^2 + \left(\frac{\partial t}{\partial z}\right)^2 = s^2(x, y, z)\,. \tag{8.1}$$

The iterative process of calculating the traveltimes in 3-D is similar to the solution for the 2-D eikonal function using the finite-difference technique provided by Vidale (1988).

The finite-difference algorithm provides three schemes to calculate traveltimes in an

equally spaced grid. Scheme A uses known traveltime values at seven corners of a cubic cell to estimate the arrival time at the 8th corner (Figure 8.1). The traveltime equation at the 8th corner point is given as (Vidale, 1990)

$$t_7 = t_0 + \frac{1}{2}\sqrt{6h^2s^2 - (t_1 - t_2)^2 - (t_2 - t_4)^2 - (t_4 - t_1)^2 - (t_3 - t_5)^2 - (t_5 - t_6)^2 - (t_6 - t_3)^2} \quad (8.2)$$

where t_i is the traveltime at the ith point (i=0, 1, 2, ..., 7), h is the grid spacing in each cube, and s is the average slowness of the eight corner points in a cube.

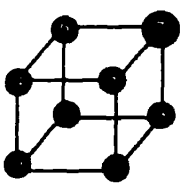

Figure 8.1 A cubic cell for scheme A. ●: known traveltime points; ●: calculated traveltime point.

Scheme B calculates a traveltime at one grid point in terms of five known traveltimes at corners of two adjacent cubes, as illustrated in Figure 8.2. The traveltime at the 6th (Figure 8.2) grid point t_5 is determined according to the following function (Vidale, 1990)

$$t_5 = t_2 + \sqrt{2h^2s^2 - \frac{1}{2}(t_0 - t_3)^3 - (t_2 - t_4)^2}. \quad (8.3)$$

The last scheme, C, computes a traveltime for a 6th corner extrapolated from five known arrivals at corners of four adjacent cubic cells (Figure 8.3). The formula for the traveltime is given by Vidale (1990)

$$t_5 = t_2 + \sqrt{h^2 s^2 - \frac{1}{4}[(t_1 - t_3)^2 + (t_0 - t_4)^2]}. \qquad (8.4)$$

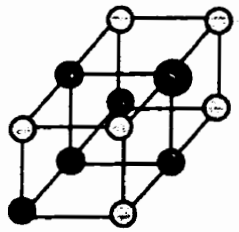

Figure 8.2 Two cubic cells for scheme B. ●: known traveltime points; ⊙ : unknown traveltime points; ● : calculated traveltime point.

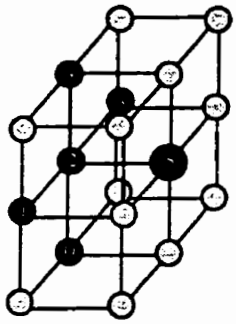

Figure 8.3 Two cubic cells for scheme C. ●: known traveltime points; ⊙ : unknown traveltime points; ● : calculated traveltime point.

Therefore, traveltimes at any points in a cubic cell can be computed iteratively on the basis of equations 8.2, 8.3 and 8.4. The approximation error for these iterative extrapolations was examined by Vidale (1990). Scheme A has the lowest error when the algorithm is applied in a uniform medium, whereas schemes B and C have relatively larger errors (Figure 8.4) (Vidale, 1990). As Vidale (1990) discussed, scheme A is

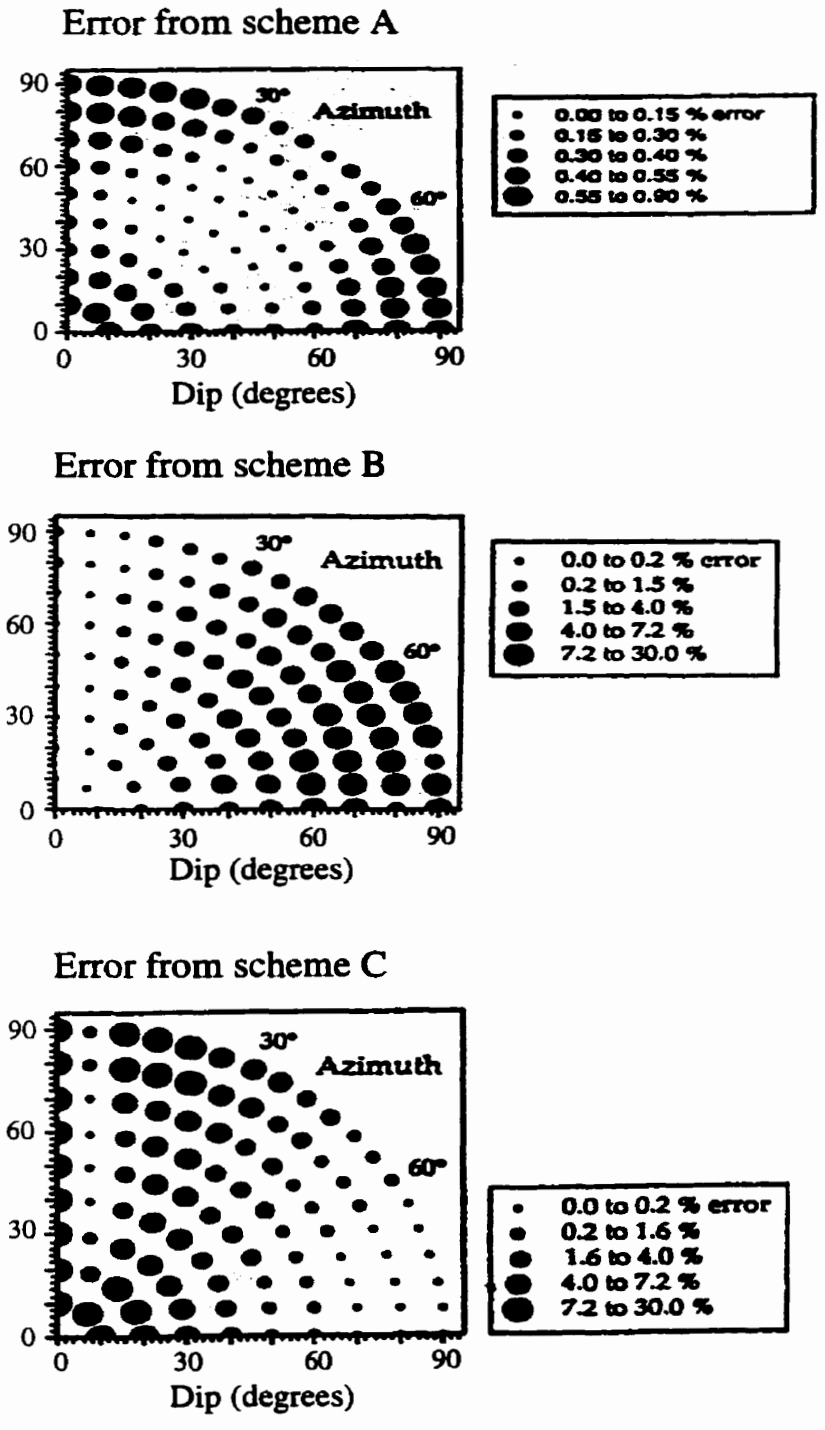

Figure 8.4 Errors expected for the three schemes for a uniform medium at the range of 10 grid points (After Vidale, 1990).

applied in more than 90% of calculations of traveltimes. Scheme B is used in approximately 9%, and scheme C in less than 1% of calculations. The traveltime can be computed to good accuracy if cubic cells are small. The average discrepancy between the traveltimes computed in a nonuniform media using the finite-difference and ray tracing algorithms for a data set of dimensions of the order of 100 by 100 by 100 grid points is approximately 0.11% or less (Vidale, 1990). Therefore, the finite-difference forward traveltime modeling algorithm is fast and accurately computes first arrivals. It can thus be applied effectively in seismic imaging when the seismic data are densely sampled.

8.1.2 Backprojection Tomographic Inversion

The fast computation of traveltimes using the finite-difference algorithm allows us to model densely-sampled data through a nonlinear tomographic inversion. The integral form of the nonlinear traveltime equation is given by

$$t = \int_{l[u(r)]} u(r)dl, \tag{8.5}$$

where $u(r)$ denotes the slowness, r is a position vector, $l[u(r)]$ presents the integral ray path. Considering the slowness to be composed of two parts, a reference part and a perturbation part, equation 8.5 can be rewritten as

$$t = \int_{l[u_0(r)+\delta u(r)]} u_0(r)dl + \int_{l[u_0(r)+\delta u(r)]} \delta u(r)dl, \tag{8.6}$$

where $\delta u(r)$ is the slowness perturbation and $u_0(r)$ refers to a reference slowness. According to Fermat's principle which states that "a ray path is stationary with respect to the slowness" (Waters, 1987), the integral ray path $l[u_0(r)+\delta u(r)]$ can be replaced by

$l[u_0(r)]$ (Hole, 1992). Therefore, the traveltime perturbation function, which is the second part on the right-hand side of equation 8.6, is expressed as (Hole, 1992)

$$\delta t = \int_{l[u_0(r)]} \delta u(r) dl . \tag{8.7}$$

Equation 8.7 indicates that the relationship between traveltime residual δt and slowness perturbation δu is linear. Therefore, the nonlinear traveltime problem has been simplified into a linear problem (Hole, 1992). Equation 8.8 is utilized as the basic formula in the 3-D tomographic algorithm.

Generally, a linear problem can be expressed in an integral form as

$$d_i = \iiint m(r) g_i(r) dr \qquad i = 1, 2, 3, \ldots, M , \tag{8.8}$$

where the $g_i(r)$ are called the kernels and $m(r)$ is the model parameter function which is a superposition of a basic function of $h_j(r)$ and parameters α_j in the jth cell

$$m(r) = \sum_{j=1}^{N} \alpha_j h_j(r) . \tag{8.9}$$

The discrete integration of a linear transformation equation is defined as

$$d_i = \sum_{j=1}^{N} \alpha_j \Gamma_{ij} , \tag{8.10}$$

where $\Gamma_{ij} = \iiint h_j(r) g_i(r) dr$. In seismic problems, the physical meaning of Γ_{ij} is the length of the ith ray in the jth cell. Hole (1992) defined a ray in 3-D as a beam centered at the ray path with a cross-sectional area of A. Then the parameters α_j are derived as

$$\alpha_j = \frac{A\delta t_j}{l_j}, \tag{8.11}$$

where δt_j denotes the traveltime residuals for the jth ray and l_j represents the total length of the jth ray path. The following discrete integration equation gives the slowness perturbation solution which is

$$\delta u(r) = \sum_{j=1}^{M} \frac{\delta t_j}{l_j} Ag_j(r), \tag{8.12}$$

where $Ag_j(r) = 1$ along the jth ray,

$Ag_j(r) = 0$ elsewhere.

More simply, we can rewrite the slowness perturbation at each grid point as a weighted average form

$$\delta u(r)(\text{grid}) = \frac{1}{K} \sum_{k=1}^{K} \frac{\delta t_k}{l_k}, \tag{8.13}$$

where K is the number of rays penetrating the neighboring cells around a grid point.

The model was assumed to be divided into small cubic cells. The velocity in each cell is determined by solving the linear equation 8.7. The solution of equation (8.13) was derived by using the technique of the beams centered at a ray path (Hole, 1992). The backprojection tomographic function is then obtained on the basis of the general solution

$$\langle \delta u(r) \rangle = \frac{1}{\sum_k w_k(r)} \sum_k w_k(r) \frac{\delta t_k}{l_k}, \tag{8.14}$$

where $w_k(r)$ is the length of the portion of the kth ray, and t_k and l_k are the time and the ray path length corresponding to the kth ray in the beam box. Equation 8.14 is called the

backprojection solution with a different weight for each ray. The high-resolution velocity structure can be reconstructed using dense seismic data.

The resolution kernel of this linearization problem depends only on the basic function or ray coverage $g_i(\boldsymbol{r})$ and not on the data values (Hole, 1992). The resolution kernel is defined as

$$R(\boldsymbol{r}, \boldsymbol{r}_0) = \frac{1}{\sum_i w_i(\boldsymbol{r}_0)} \sum_i \frac{w_i(\boldsymbol{r}_0)}{l_i} g_i(\boldsymbol{r}), \tag{8.15}$$

where $w_i(\boldsymbol{r}_0)$ is the ith ray segment length inside a small box of volume V centered at $\boldsymbol{r}_0$. In terms of a grid point, the resolution corresponding to the single ray is given by

$$R_i = \frac{w_i}{l_i}. \tag{8.16}$$

The resolution at the grid point for rays penetrating through the volume V, which is defined by a superposition of the eight neighboring grid cell volumes, is obtained by weighted integration of equation 8.16. As discussed above, the resolution of this linear modeling equation can be alternatively considered as a kind of ray coverage.

8.2 3-D Seismic Tomographic Imaging of the Sudbury Structure

The 3-D weighted backprojection tomographic technique was used to image the velocity structure in Sudbury. Although the seismic data in Sudbury is not densely sampled, a seismic imaging in 3-D was still carried out in the thesis research in order to

highlight velocity heterogeneity near the surface in Sudbury, and to show the importance of the application of 3-D seismic imaging in the investigation of complicated geological structure. The first subsection of this section describes the model parameterization. The study area was divided into the number of cubic cells with a constant velocity assigned to each cell. The second subsection includes the tomographic modeling procedure and velocity imaging. The first arrival time from source to receiver was computed. The discrepancy between the observed and calculated arrivals was then assigned to the initially assumed ray path and converted into a velocity discrepancy in each cell. On the basis of velocity discrepancy, the velocities in associated cells were modified. This procedure was repeated until the stopping criterion was met.

8.2.1 Model Parameterization

The coordinate system used in the modeling is the UTM (zone 17) projection. The coordinates of the origin of the volume being modeled are (5031, 412, -2.0) in km which is at the southwest corner of the study area (Figure 8.5). The negative value for z represents the height above sea level. In the x direction, there are 158 cells with a cell length of 1 km. Therefore, there are a total of 159 cell nodes associated with 158 cells. In the y direction, there are 230 cells, and there are 27 cells in the z direction. The dimension of the parameterized model is thus 159 x 231 x 28.

The initial velocity model consists of a 1-D distribution with the vertical gradient defined using the in-line and fan-shot modeling results. The 1-D initial velocity was

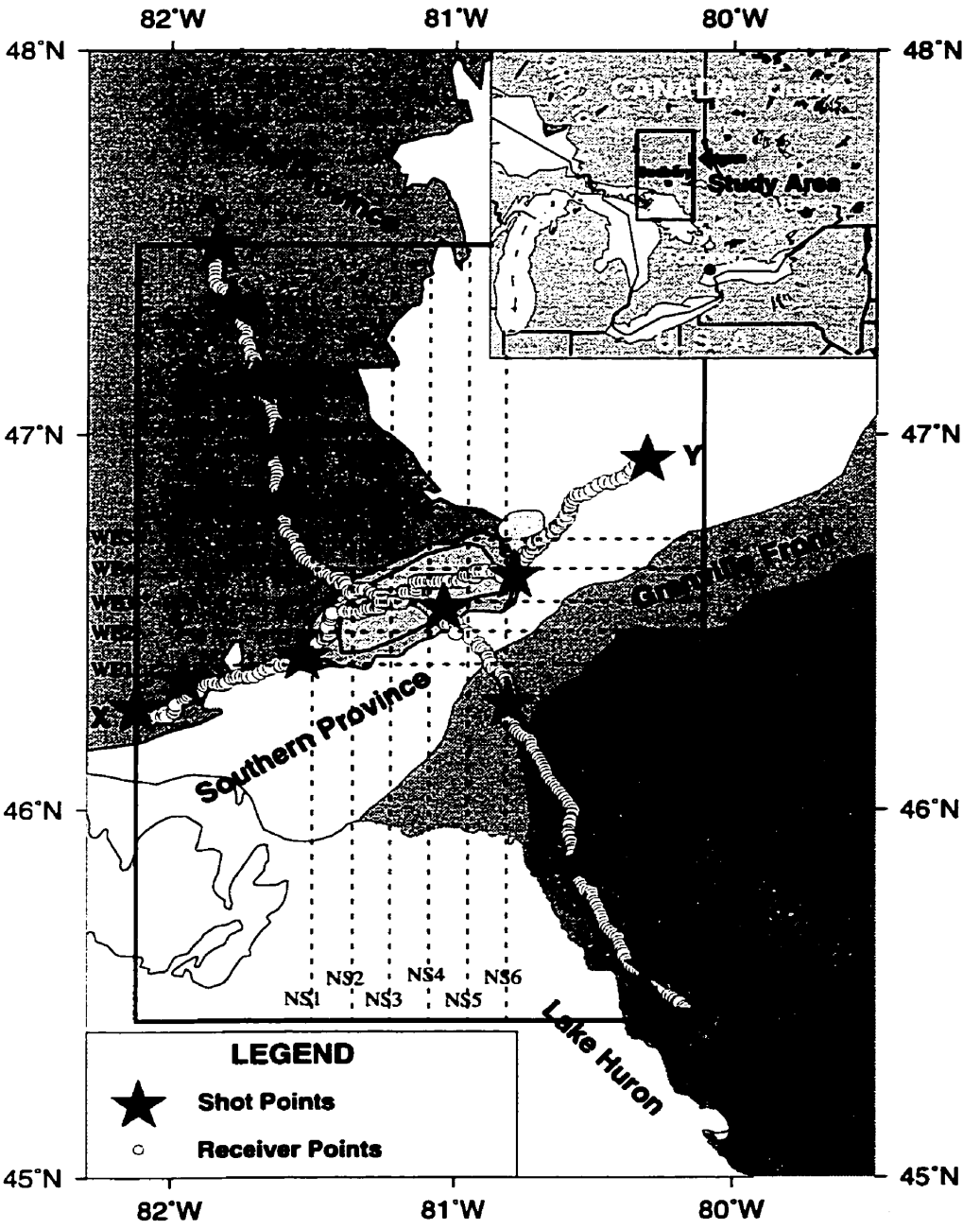

Figure 8.5 Tomographic imaging area indicated by the thick framed line. Dashed lines represent the velocity imaging profiles; characters and numbers beside dashed lines denote velocity imaging profiles.

given as 6.0 km/s at the surface, 6.1 km/s at 3 km depth, 6.3 km/s at 10 km depth, 6.7 km/s at 20 km depth and 6.8 km/s at 30 km depth. The computer code (Hole, 1992), called vel1d, extends the 1-D velocity to 3-D and the velocity in each cubic cell was then finally initialized.

8.2.2 3-D Tomographic Modeling

1. Modeling

A total of 4223 first arrivals were picked from 30 sections including in-line and fan-shot data (Table 8.1). There were 1045 more arrivals picked from the 15 in-line sections than from the 15 fan-shot sections because coherent phases were more easily traced in the in-line data than in the fan-shot data. An arbitrary weighting (1-10) is assigned to the picked arrivals depending on the data quality. If the data have very high S/N ratio, they are given a high weighting, otherwise a low weighting is assigned. For the Sudbury seismic data, a weighting 5 was assigned to the majority of in-line data except those of shot xy5 to which the weighting of 3 was assigned. It was necessary to give low weighting to the fan-shot data because the first break picks are less accurate than in the case of the in-line data. The reason is that a majority of these fan-shot sections was contaminated by noise and the first arrivals could not be accurately picked. The first break in in-line data is more easily traced than in fan-shot data. Therefore, a weighting 3 was assigned to fourteen fan-shot data sets. However, the fan-shot data from shot xy5, with a high S/N ratio, was given a weighting of 5.

After five iterations of the inversion procedure described above, an acceptable RMS

Table 8.1 First arrival picking information for each shot

No.	Shots	Weighting for fan shots	No. of picked first arrivals for fan shots	Weighting for in-line shots	No. of picked first arrivals for in-line shots	Total
1	xy0	3	80	5	144	224
2	xy1	3	60	5	60	120
3	xy2	3	71	5	145	216
4	xy4	3	20	5	141	161
5	xy5	5	176	3	143	319
6	ab0	3	132	5	168	300
7	ab1	3	128	5	164	292
8	ab2	3	130	5	198	328
9	ab3	3	133	5	194	327
10	ab4	3	129	5	168	297
11	ab6	3	77	5	251	328
12	ab7	3	109	5	237	346
13	ab8	3	115	5	177	292
14	ab9	3	113	5	200	313
15	ab10	3	116	5	244	360
Total			1589		2634	4223

traveltime residual (0.168 s) was obtained (Table 8.2). Table 8.2 indicates that for the data from 25 shots, a good fit between the observed and calculated traveltimes was obtained with the RMS traveltime residual for each shot being less than 0.2 s. Only five

Table 8.2 RMS traveltime residuals of the modeling

No. of shots	Shot names	No. of picked first arrivals for fan shots	RMS traveltime residuals for fan shots (s)	No. of picked first arrivals for in-line shots	RMS traveltime residuals for in-line shots (s)
1	xy0	80	0.121	144	0.052
2	xy1	60	0.271	60	0.043
3	xy2	71	0.071	145	0.035
4	xy4	20	0.029	141	0.029
5	xy5	176	0.055	143	0.045
6	ab0	132	0.052	168	0.068
7	ab1	128	0.077	164	0.068
8	ab2	130	0.065	198	0.075
9	ab3	133	0.083	194	0.109
10	ab4	129	0.077	168	0.069
11	ab6	77	0.151	251	0.129
12	ab7	109	0.132	237	0.167
13	ab8	115	0.189	177	0.312
14	ab9	113	0.276	200	0.360
15	ab10	116	0.168	244	0.340
Total		1589	0.136	2634	0.184

RMS traveltime residual for the whole data set: 0.168 s
Note: RMS: root mean square.

shots had relatively high RMS traveltime residuals (0.27-0.36 s). Four of these are located at the southern end of profile AB (fan shot ab9, in-line shots ab8, ab9 and ab10). The RMS traveltime residuals of fan shots ab8, ab10 and in-line ab7 were also relatively high (0.16-0.19 s). This result implies that the subsurface structure or velocity variation in the south (e.g., associated with dipping stacked sheets under the Grenville Front Tectonic Zone) could be complicated. The model parameterization is too coarse to fit the data well. In considering the low ray coverage formed by the survey pattern of profiles AB and XY, the velocity model from the 5th iteration was accepted as the final 3-D tomographic image (with a total RMS traveltime residual of 0.168 s).

2. Velocity Images on WE Profiles

Velocity images of five profiles traversing the Sudbury Structure in an east-west direction will now be discussed (Figure 8.5). The velocity image and ray coverage for each profile are displayed in both grey and color scales. The ray coverage image in a grey scale is designed to show the intensity of ray coverage whereas one in a HSV color scale generated in Khoros (Release 2.02) is designed to show locations of at least minimal ray coverage. It is not necessary to show a color scale for ray coverage because the color plot is introduced only to outline locations of ray coverage.

Figure 8.6 indicates the velocity image of profile WE1 extending from west to east and crossing the southern edge of the Sudbury Basin. There is a lenticular low-velocity zone (~6.07-6.2 km/s) revealed approximately at the center of the profile, extending from the surface down to a depth of ~16 km (Figures 8.6a and 8.6b). Three high-velocity zones were imaged at offsets of 40 km (~6.25 km/s), 70 km (~6.36 km/s) and 110 km (~6.25

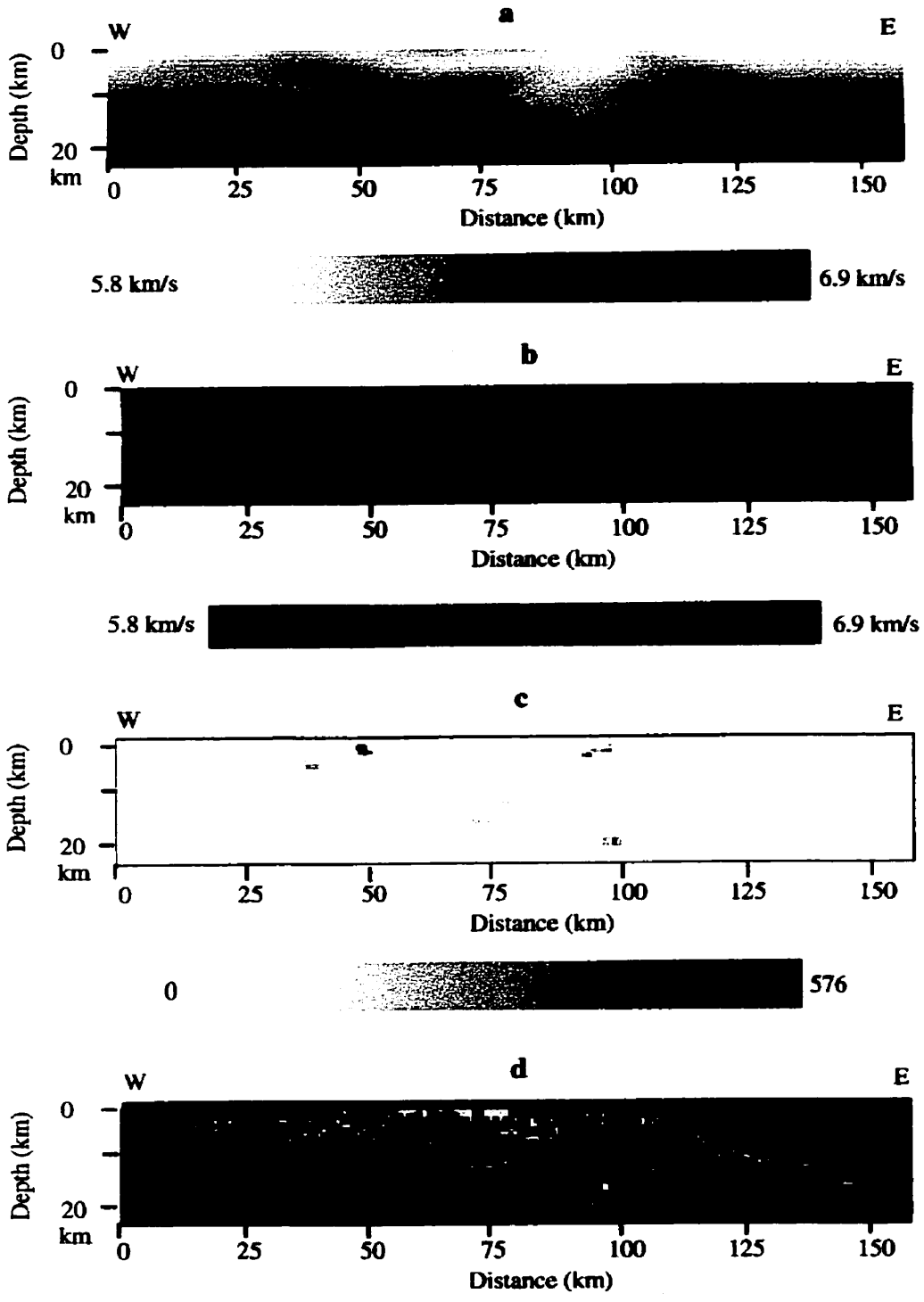

Figure 8.6 Seismic tomographic velocity image of profile WE1 (**a** in a grey scale and **b** in a color scale) and corresponding ray coverage (**c** in a grey scale and **d** in a HSV color scale generated in Khoros (Release 2.02).

km/s) at depths of ~4 km, 7 km and 6 km respectively. The offsets used in this chapter refer to the distance between the current location and the western end (for WE profiles) or the southern end (for NS profiles) of a profile. The high-velocity anomaly at an offset of 40 km could relate to the relatively high-velocity zone (~6.26 km/s) near the surface at 1 km depth at offsets of 20-40 km modeled along profile XY. Figures 8.6c and 8.6d illustrate ray coverage resolution with the maximum value of 576 near the surface at an offset of 50 km. At shallow depth, especially between 1 and 5 km, there is greater ray coverage at offsets from 10 to 100 km than in the other areas. The deepest ray propagation is to a depth of 22 km at an offset of 97 km.

Figures 8.7a and 8.7b show the velocity image along the west-east profile WE2 which is 1 km north of profile WE1. A velocity structure similar to the previous one is observed except for the low-velocity zone which is further west than on WE1 (Figures 8.7a and 8.7b). The ray coverage for WE2 has a similar form to that for WE1 (Figures 8.7c and 8.7d).

Figures 8.8a and 8.8b are the velocity images along profile WE3, which crosses the center of the Sudbury Basin. A lenticular high-velocity zone is visible near the surface at offsets between ~40 and ~115 km and is supported by relatively high ray coverage (Figures 8.8c and 8.8d). The depth of base at the center of this zone was determined to be ~7 km with a velocity of ~6.48 km/s. Beneath this zone, there is a low-velocity anomaly imaged, extending down to ~20 km deep. The structure is defined by partial ray coverage (Figures 8.8c and 8.8d). Three local high-velocity anomalies are observed in this image. The high-velocity zone at offsets between 15 and 30 km at depths of ~2 to 7 km has a velocity of ~6.1-6.3 km/s. The second high velocity anomaly (~6.3-6.6 km/s) was imaged

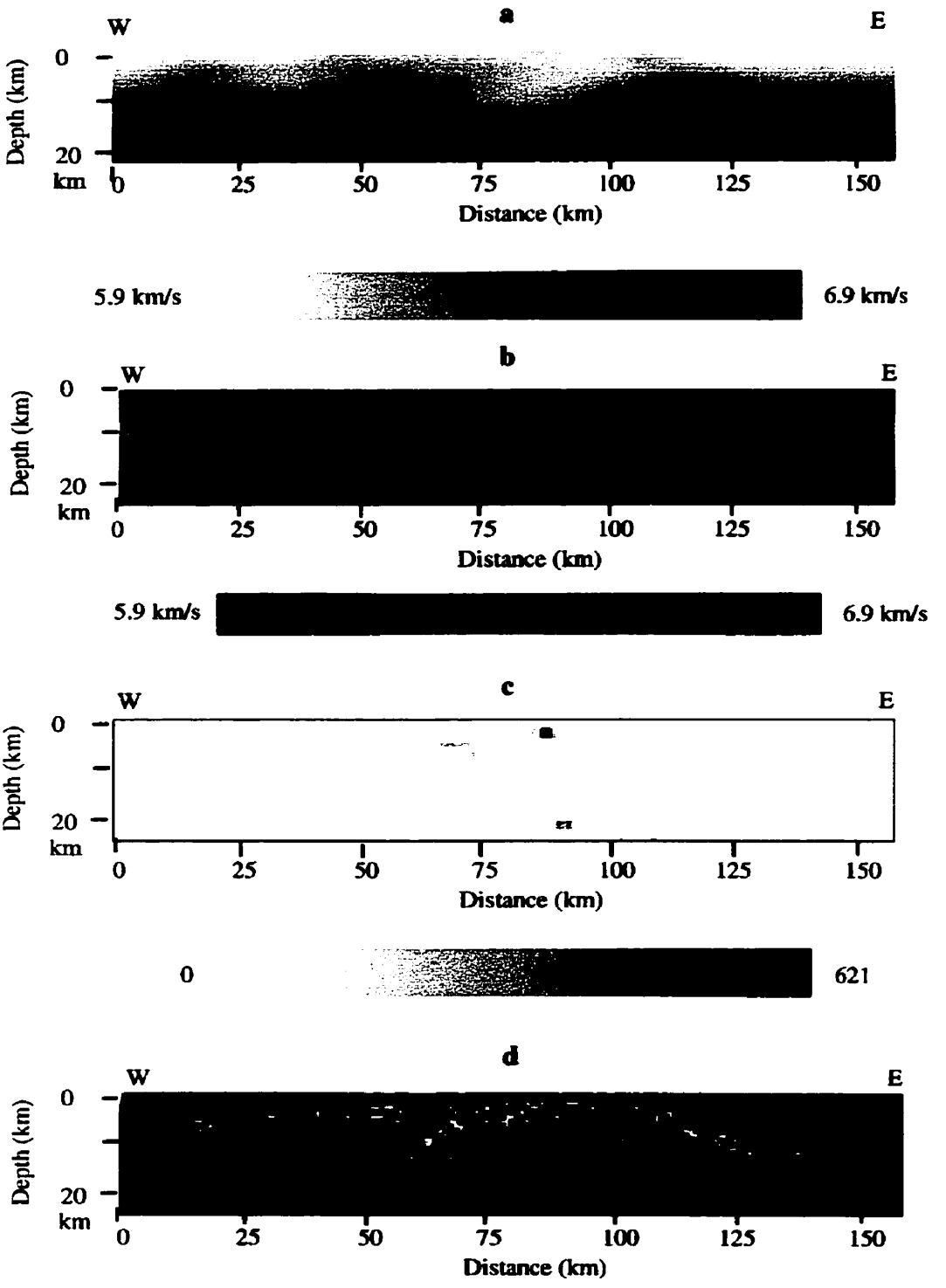

Figure 8.7 Seismic tomographic velocity image of profile WE2 (**a** in a grey scale and **b** in a color scale) and corresponding ray coverage (**c** in a grey scale and **d** in a HSV color scale generated in Khoros (Release 2.02).

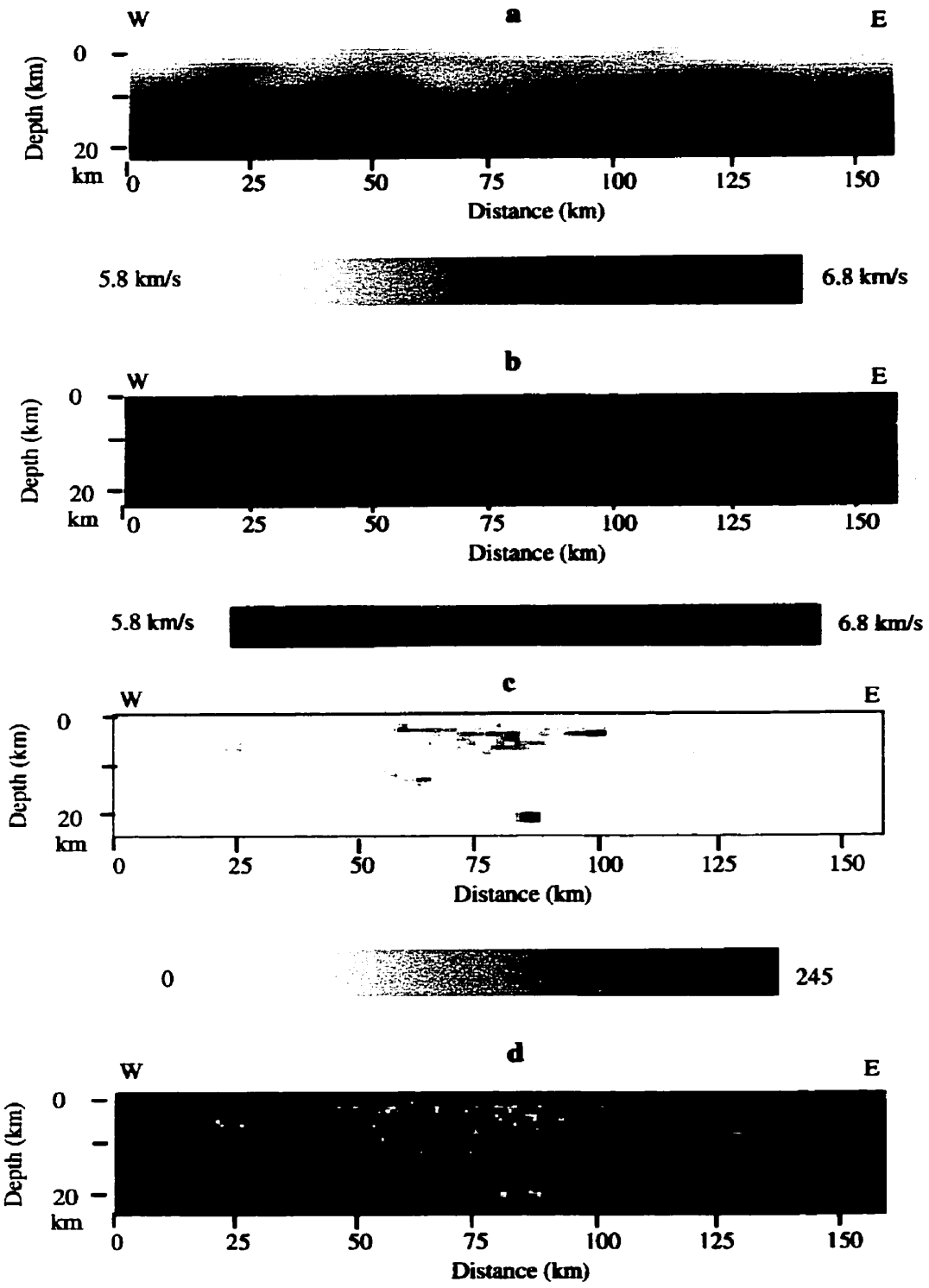

Figure 8.8 Seismic tomographic velocity image of profile WE3 (**a** in a grey scale and **b** in a color scale) and corresponding ray coverage (**c** in a grey scale and **d** in a HSV color scale generated in Khoros (Release 2.02).

at offsets of ~40 to 60 km, extending down to depths of ~7 to 13 km. However, the base of the anomaly is not well defined because of poor ray coverage (Figures 8.8c and 8.8d). The third high-velocity anomaly (~6.35 km/s) is visible at ~8 km depth, at an offset of ~120 km. This anomaly corresponds to the large positive velocity gradient anomaly (+0.23 s^{-1}) across the velocity interface at depth of ~9 km (Subsection 6.2.2) modeled by using the in-line XY data (Figure 6.17). The velocity anomalies shown on profiles WE4 and WE5 are similar.

The lenticular-shaped high-velocity anomaly near the surface was also imaged on both profiles WE4 and WE5 shown in Figures 8.9a, 8.9b, 8.10a and 8.10b. There are two high-velocity anomalies revealed to the west of the low-velocity anomaly on both profiles. The high-velocity anomaly (~6.3 km/s) at an offset of ~30 km and a depth of ~4 km was well controlled by ray coverage (Figures 8.10c and 8.10d). In contrast, the high-velocity anomaly at an offset of ~50 km and a depth of ~7.5 km was poorly controlled by ray coverage.

2. Velocity Images on NS Profiles

A total of six profiles crossing the Sudbury Structure (Figure 8.5) in the north-south direction are displayed in Figures 8.11-8.16 and velocity features observed along these profiles are now explained. There is a high-velocity anomaly zone (~6.3 km/s) at an offset of 105 km and at depth of ~5 km in the center of profile NS1 as shown in Figures 8.11a and 8.11b. North of this structure, there is a high-velocity anomaly revealed to be slightly south-dipping. The lower part of the anomaly is less well resolved because of the

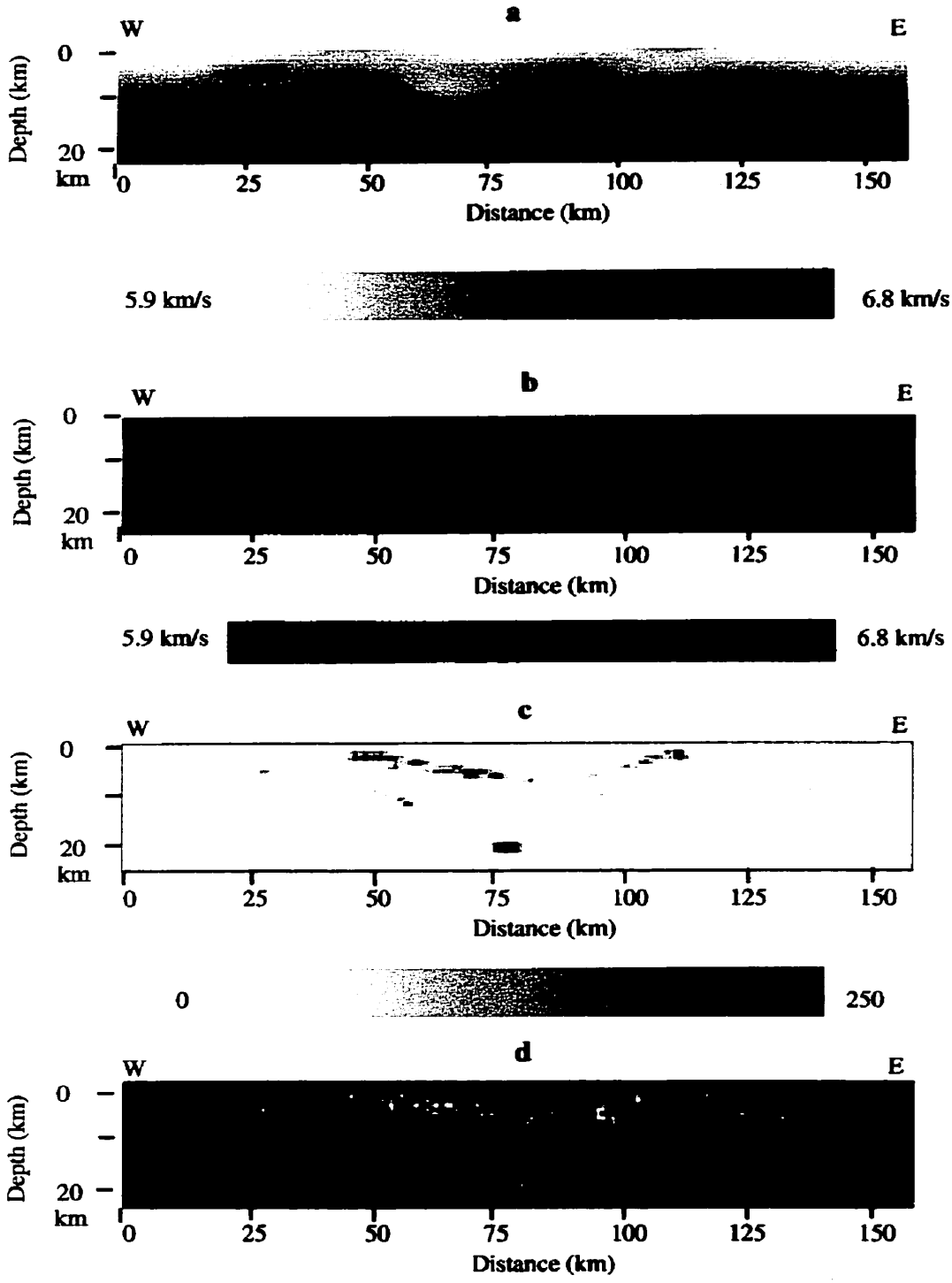

Figure 8.9 Seismic tomographic velocity image of profile WE4 (**a** in a grey scale and **b** in a color scale) and corresponding ray coverage (**c** in a grey scale and **d** in a HSV color scale generated in Khoros (Release 2.02).

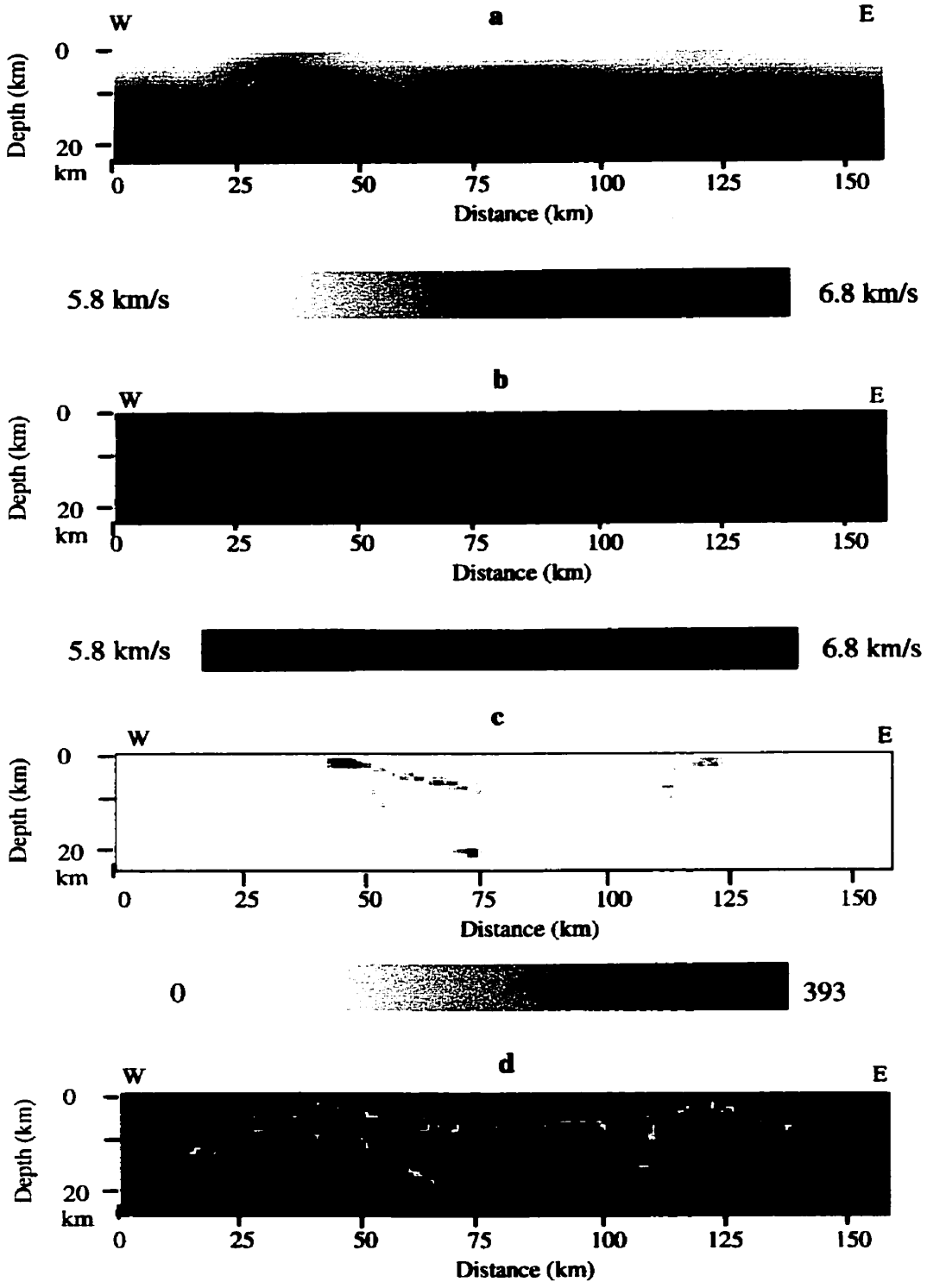

Figure 8.10 Seismic tomographic velocity image of profile WE5 (**a** in a grey scale and **b** in a color scale) and corresponding ray coverage (**c** in a grey scale and **d** in a HSV color scale generated in Khoros (Release 2.02).

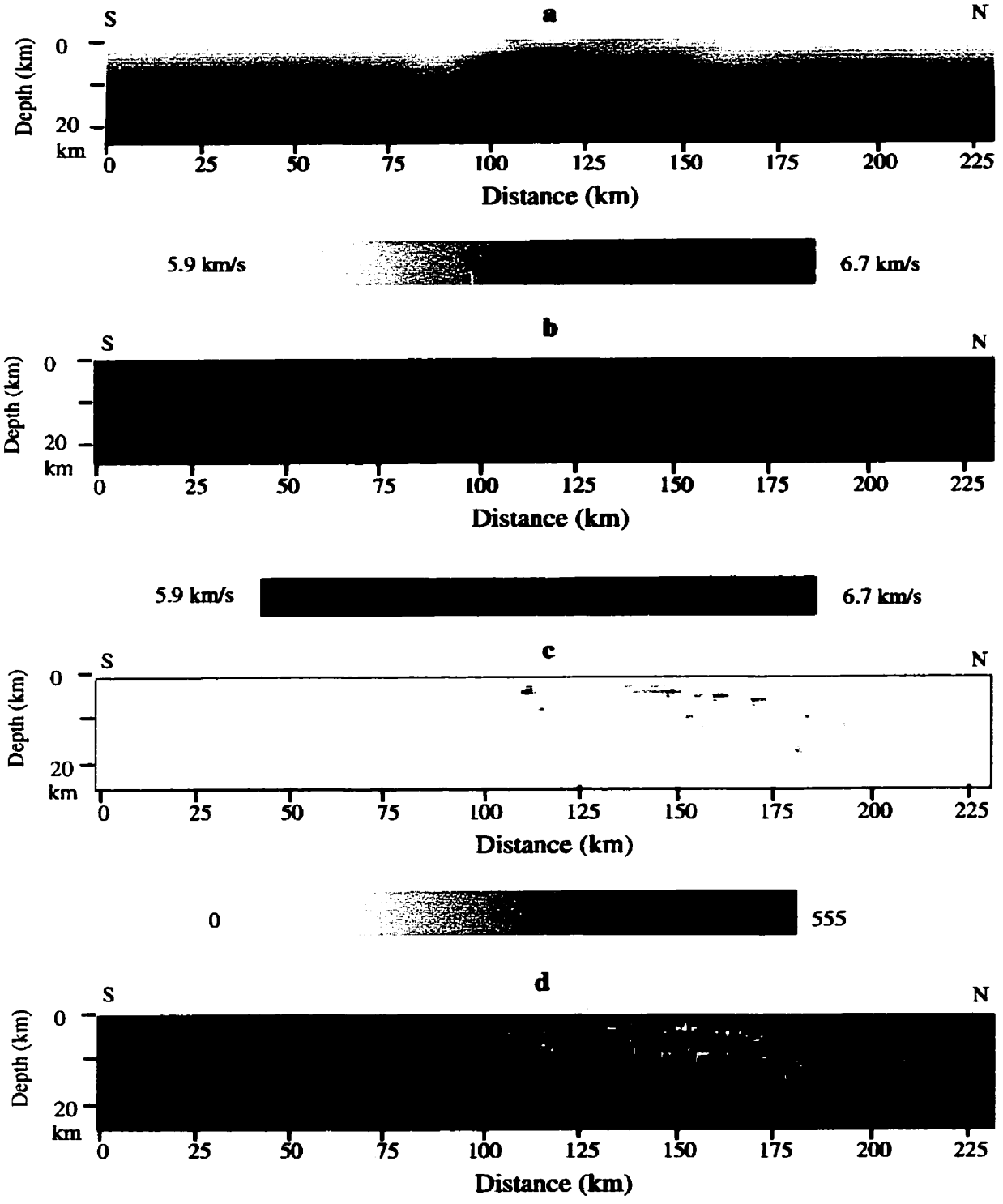

Figure 8.11 Seismic tomographic velocity image of profile NS1 (a in a grey scale b in a color scale) and corresponding ray coverage (c in a grey scale and d in a HSV color scale generated in Khoros (Release 2.02).

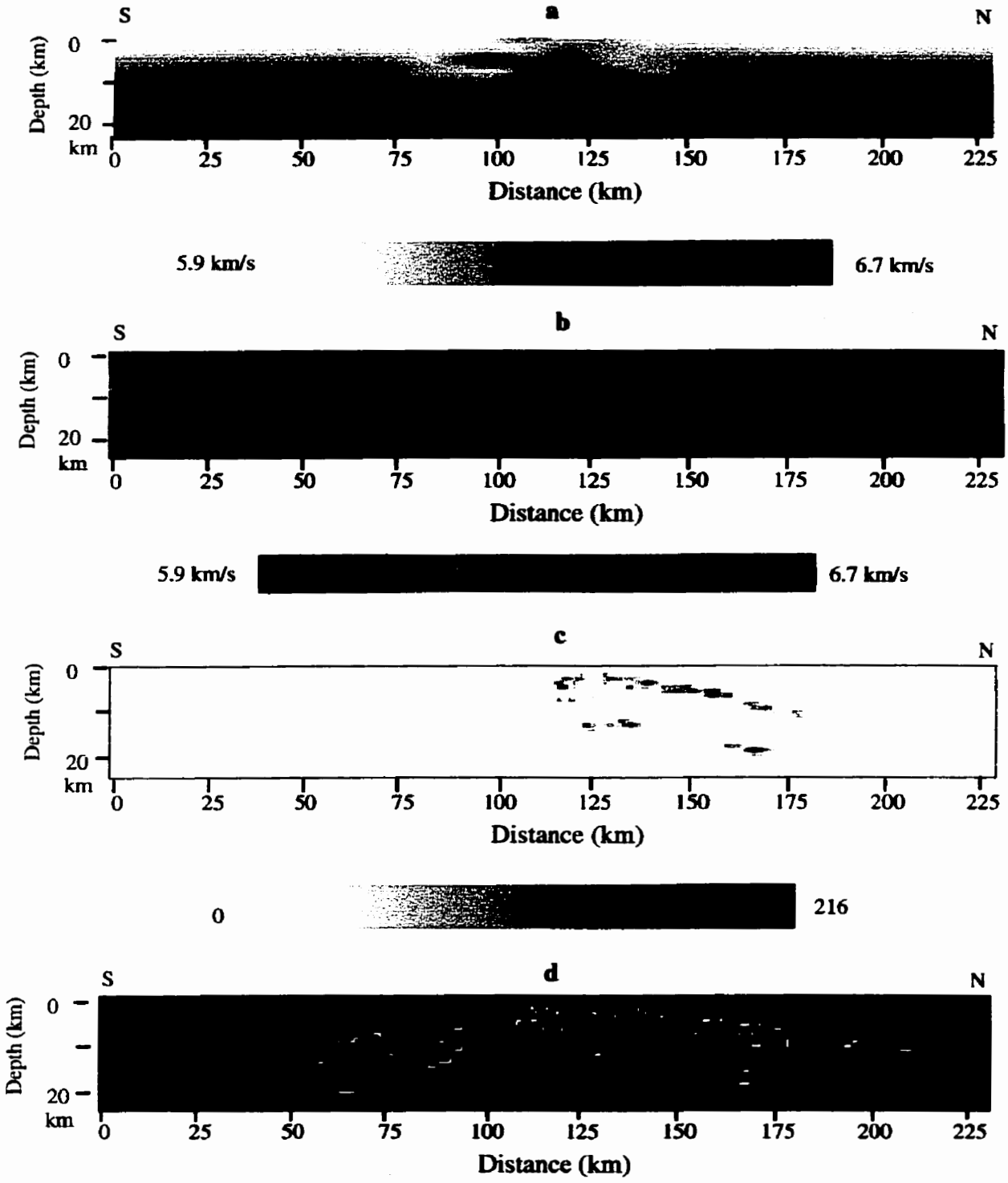

Figure 8.12 Seismic tomographic velocity image of profile NS2 (a in a grey scale b in a color scale) and corresponding ray coverage (c in a grey scale and d in a HSV color scale generated in Khoros (Release 2.02).

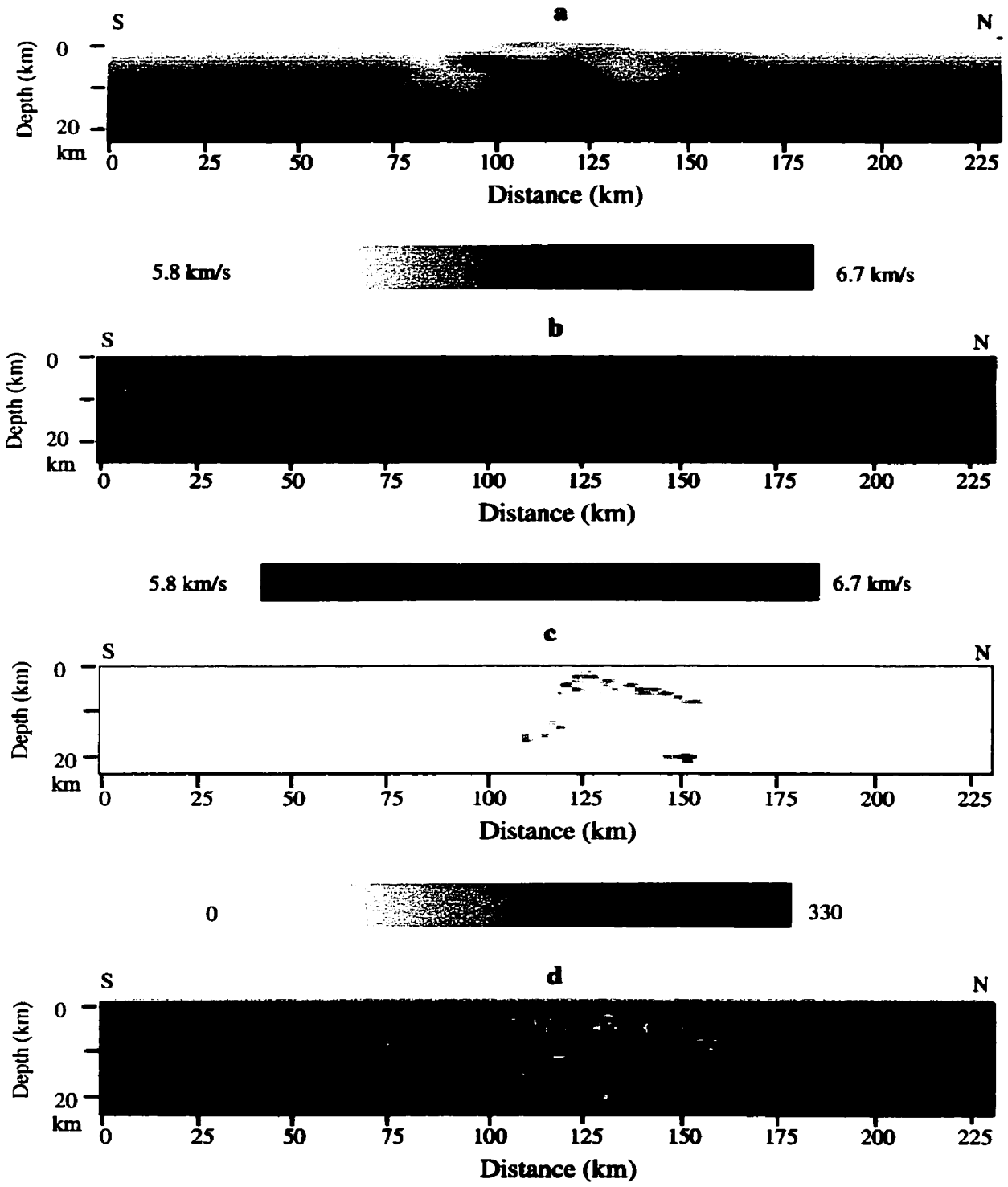

Figure 8.13 Seismic tomographic velocity image of profile NS3 (a in a grey scale b in a color scale) and corresponding ray coverage (c in a grey scale and d in a HSV color scale generated in Khoros (Release 2.02).

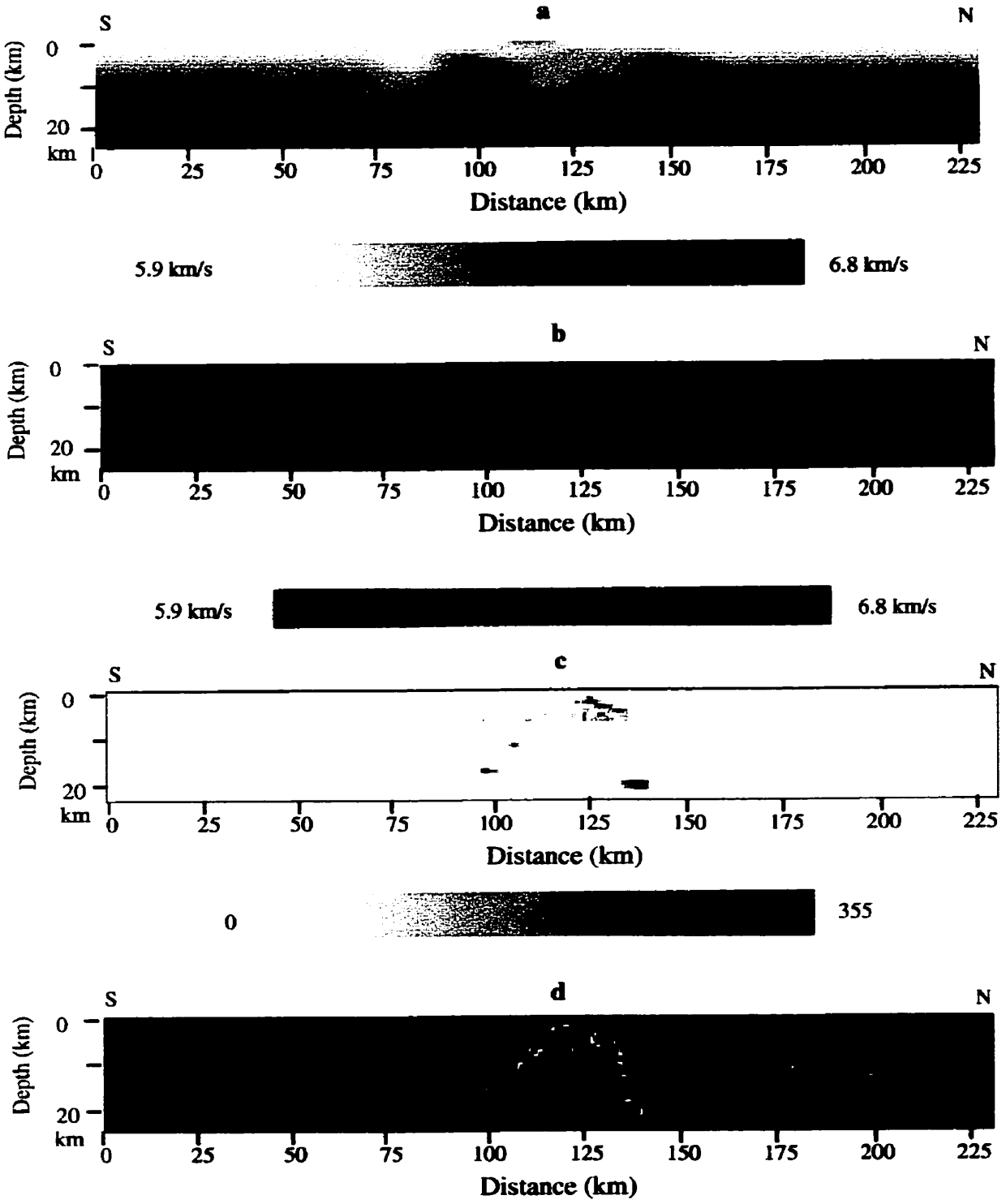

Figure 8.14 Seismic tomographic velocity image of profile NS4 (a in a grey scale b in a color scale) and corresponding ray coverage (c in a grey scale and d in a HSV color scale generated in Khoros (Release 2.02).

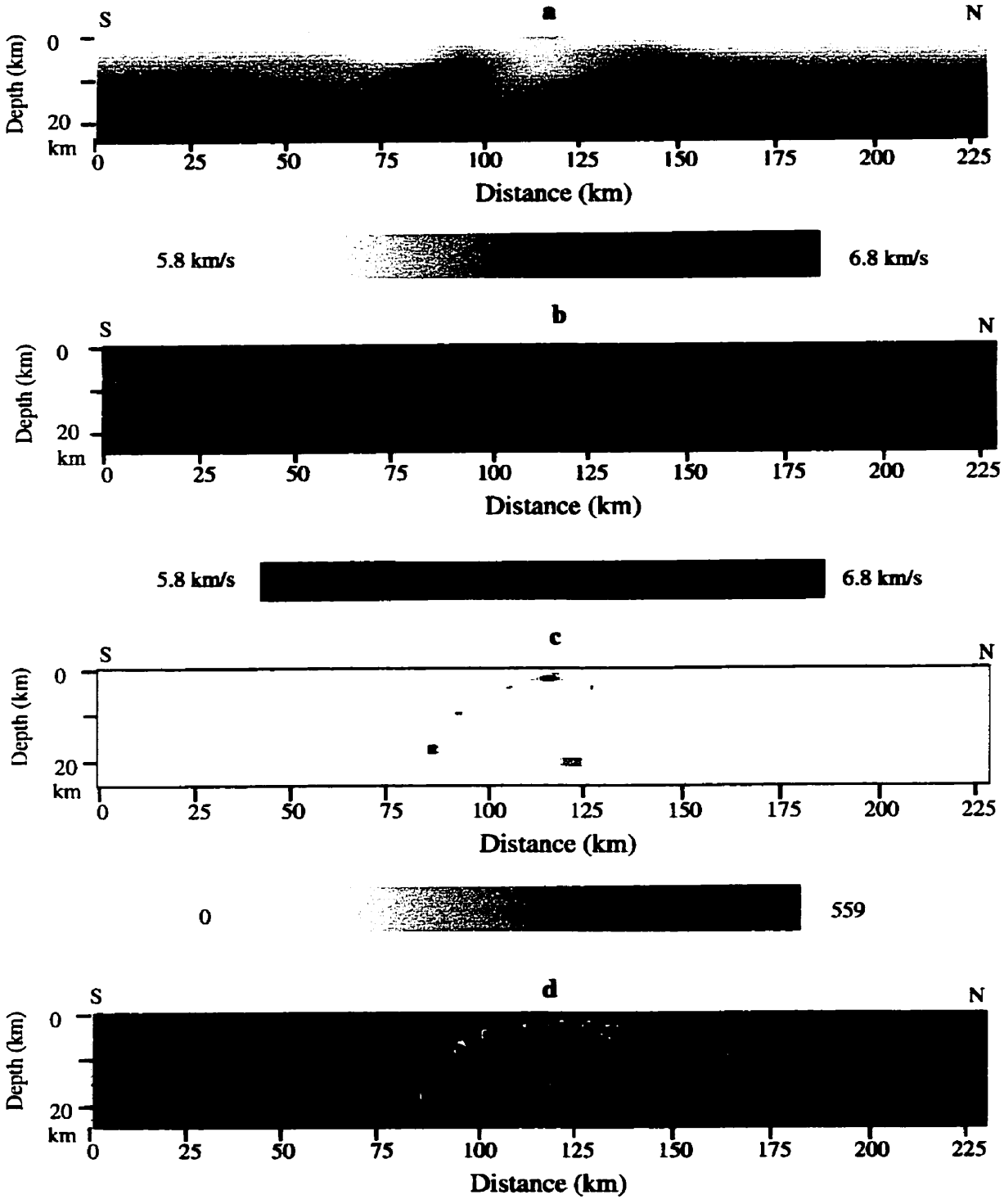

Figure 8.15 Seismic tomographic velocity image of profile NS5 (a in a grey scale b in a color scale) and corresponding ray coverage (c in a grey scale and d in a HSV color scale generated in Khoros (Release 2.02).

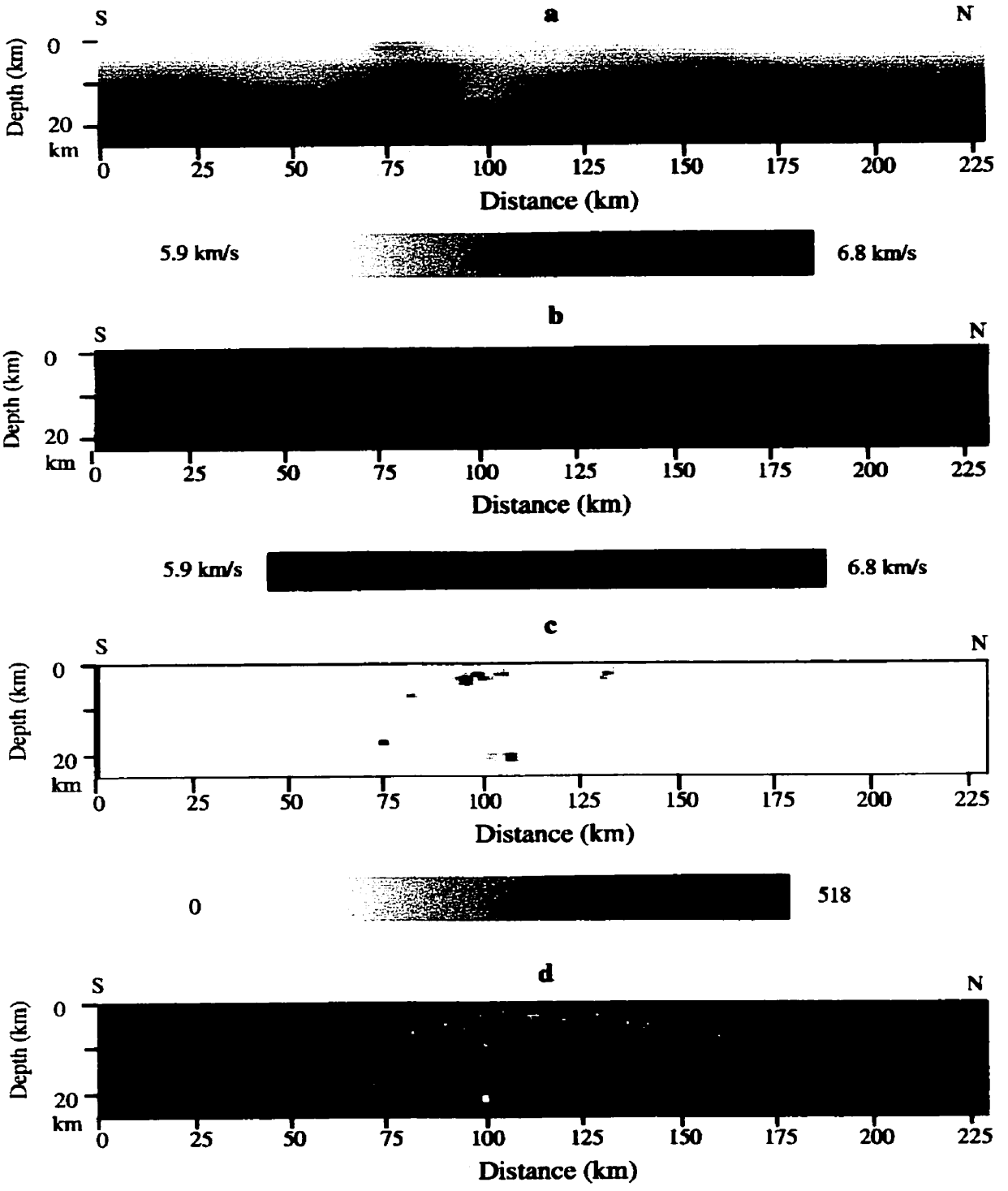

Figure 8.16 Seismic tomographic velocity image of profile NS6 (a in a grey scale b in a color scale) and corresponding ray coverage (c in a grey scale and d in a HSV color scale generated in Khoros (Release 2.02).

low ray coverage (Figures 8.11c and 8.11d).

Velocity images on profiles of NS2 and NS3 illustrate similar characteristics to those formed on NS1. There is a low-velocity zone in the center at offsets between ~65 and 160 km, extending to a depth of ~15 km (Figures 8.12a, 8.12b, 8.13a and 8.13b). This velocity feature is located beneath the Sudbury Basin. The low-velocity zone is thus associated with the Sudbury Structure. There are three zones of anomalous velocity observed in the images within the low-velocity zone. A high-velocity anomaly zone (~6.2 km/s) dips southward from the surface at an offset of 125 km down to a ~5 km depth. At greater depth, there is a high-velocity anomalous wedge (~6.4-6.65 km/s) at offsets of ~90 and 130 km, which dips southward at depths from ~10 to ~20 km. There is good ray coverage only at the top of this zone (Figures 8.12c, 8.12d, 8.13c and 8.13d). The third high-velocity anomaly body is located within the low-velocity zone at a depth of ~5 km at offsets of 90-105 km and is defined by poor ray coverage.

The velocity images shown in Figures 8.14a, 8.14b, 8.15a and 8.15b indicate similar features. Good ray coverage is indicated in Figures 8.14c, 8.14d, 8.15c and 8.15d at offsets of ~100 to 145 km at depths above ~8 km. A significant positive variation in velocity (~6.3 km/s) is observed at a depth of ~5 km between offsets of ~95 to 110 km in the south-north direction (Figures 8.14a and 8.14b). This anomaly could relate to an anomaly body in the south of the Sudbury Basin, responsible for the gravity high discussed in Appendix C. Figure 8.16 indicates a velocity image along profile NS6 (Figure 8.5). The ray coverage shown in Figures 8.16c and 8.16d is poor. Therefore, the variation in velocity will not be described in detail.

2. 2-D Velocity Images on Depth Slices

Three velocity images for depth slices at 2 km, 5 km and 10 km are now examined. Figures 8.17a and 8.17b show the velocity anomaly at a depth of 2 km in grey and color scales respectively. Variations in velocity in the areas surrounding two refraction profiles AB and XY are observed. A high-velocity anomaly is imaged at the southern end of profile AB. However, as discussed in Subsection 8.2.2, the values of the RMS traveltime residuals of shots located in the south of profile AB are very high (0.27-0.36 s). Therefore, this anomaly is underfitted and is not appropriate to be interpreted although there is reasonable ray coverage (Figures 8.17c and 8.17d). At the western part of profile XY, a relatively high-velocity anomaly with a velocity of ~6.25 km/s (with good ray coverage) is revealed. This feature correlates with the high-velocity body (with velocity of ~6.26 km/s) obtained from the in-line XY data. The location of the anomaly corresponds to the linear high-gravity anomaly parallel to the South Range of the Sudbury Igneous Complex.

Figures 8.18a and 8.18b show the velocity structure of a depth slice at 5 km. The ray coverage is low at both ends of the survey lines (Figures 8.18c and 8.18d). A high-velocity anomaly (~6.38 km/s) is delineated clearly at an offset of ~96 km of south-north profiles and at the center of west-east profiles with a good coverage. The ray coverage of the velocity image sliced at a depth of ~10 km is even more sparse (Figures 8.19c and 8.19d). The velocity variation shown in Figures 8.19a and 8.19b will not be interpreted in detail. Therefore, there is no further discussion of this velocity image from a plane of view in this thesis.

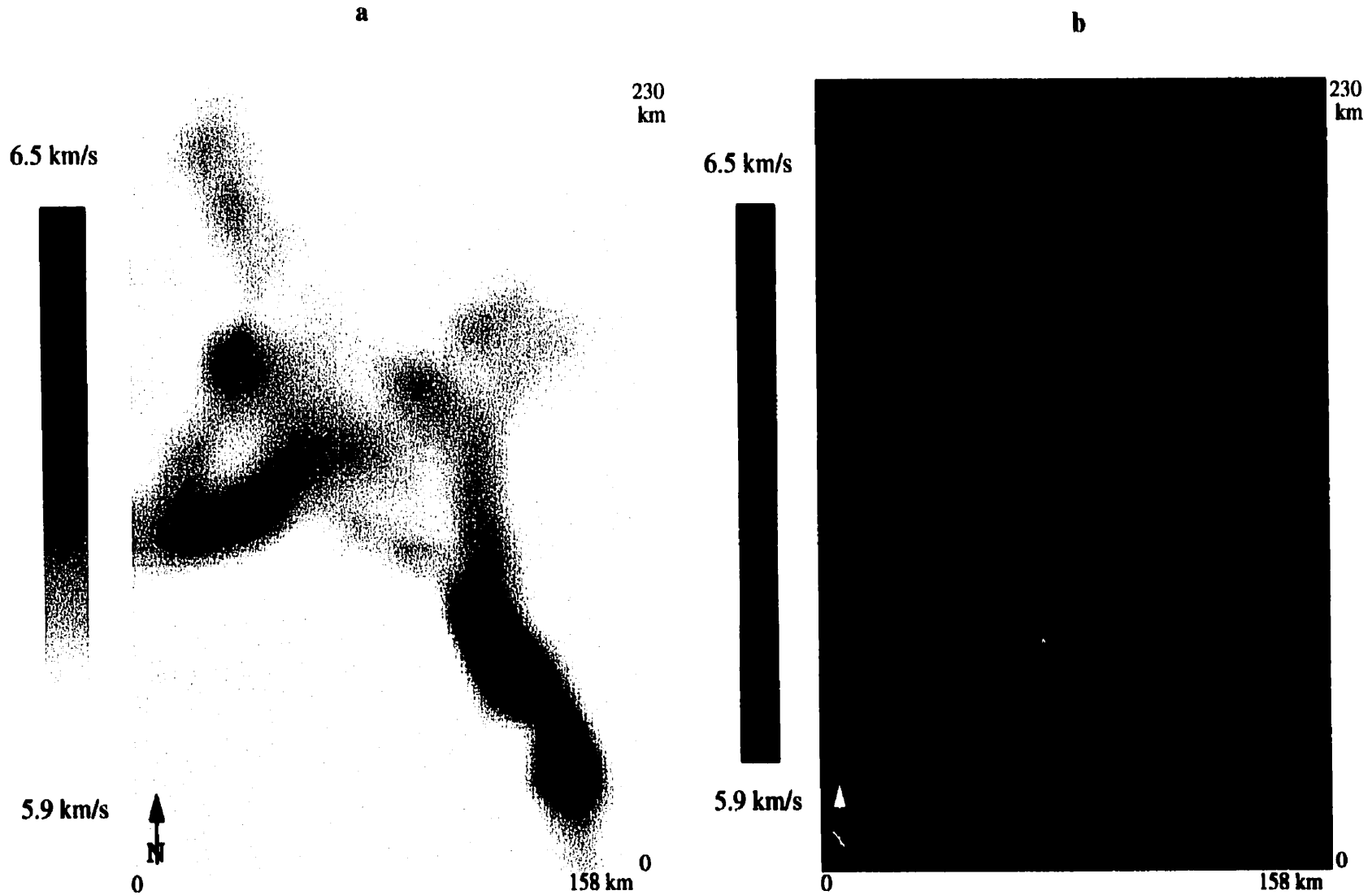

Figure 8.17 Seismic velocity images of the depth slice at 2 km deep (**a**, **b**) and corresponding ray coverage (**c**, **d**). **a** shows velocity in grey scale; **b** shows velocity in color scale; **c** diplays ray coverage in grey scale and **d** shows ray coverage in a HSV color scale generated in Khoros (Release 2.02).

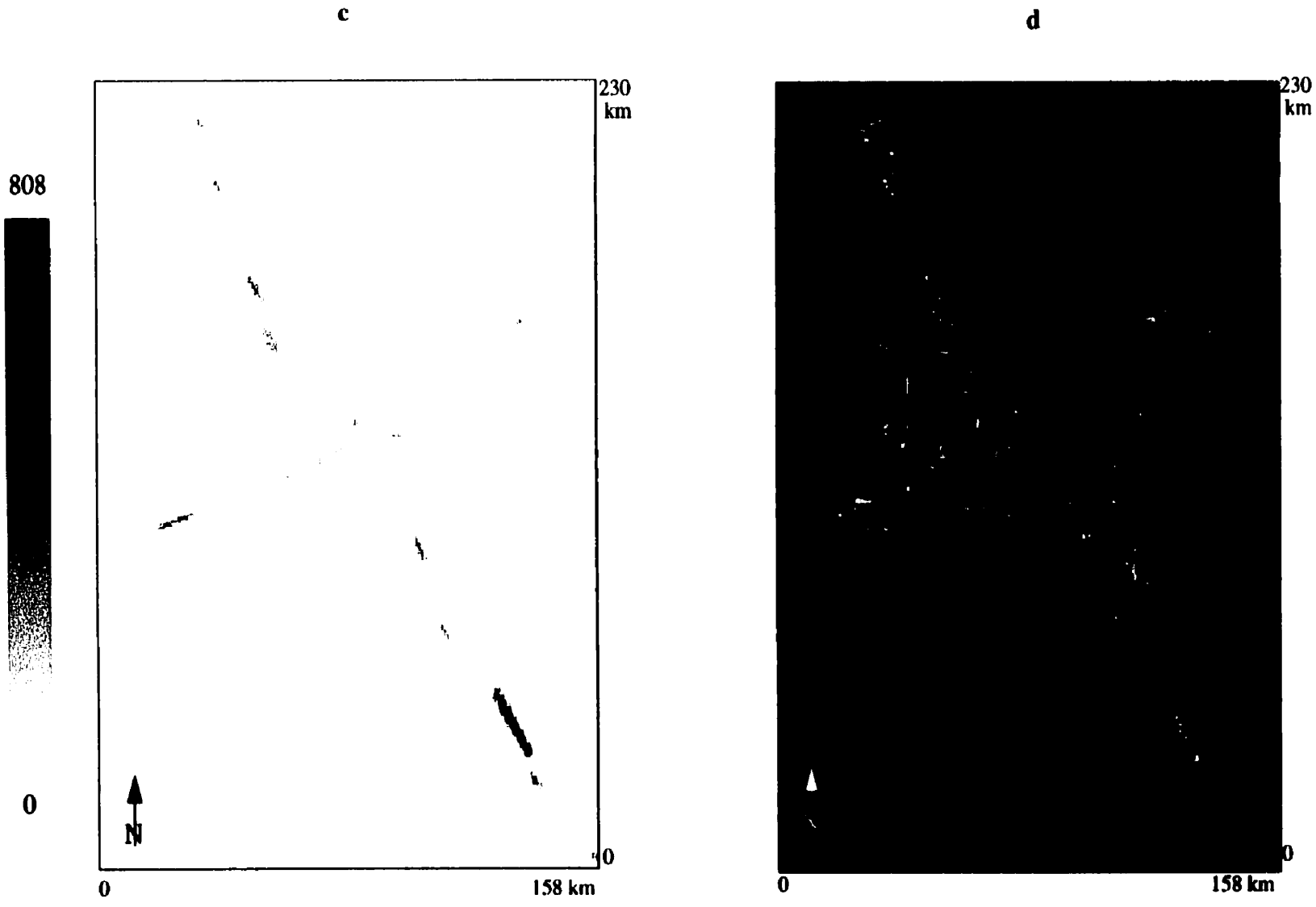

Figure 8.17

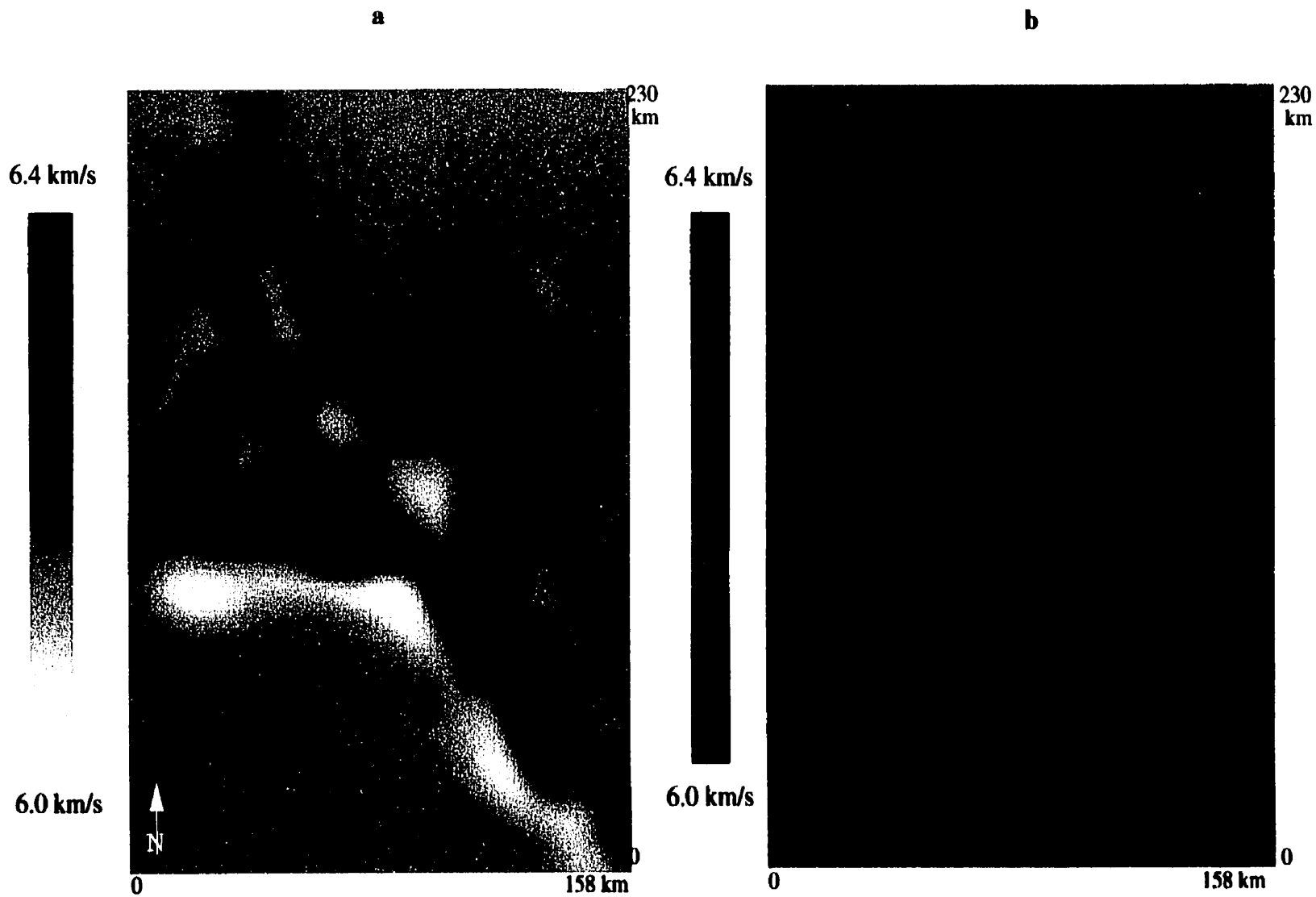

Figure 8.18 Seismic velocity images of the depth slice at5 km deep (**a**, **b**) and corresponding ray coverage (**c**, **d**). **a** shows velocity in grey scale; **b** shows velocity in color scale; **c** diplays ray coverage in grey scale and **d** shows ray coverage in a HSV color scale generated in Khoros (Release 2.02).

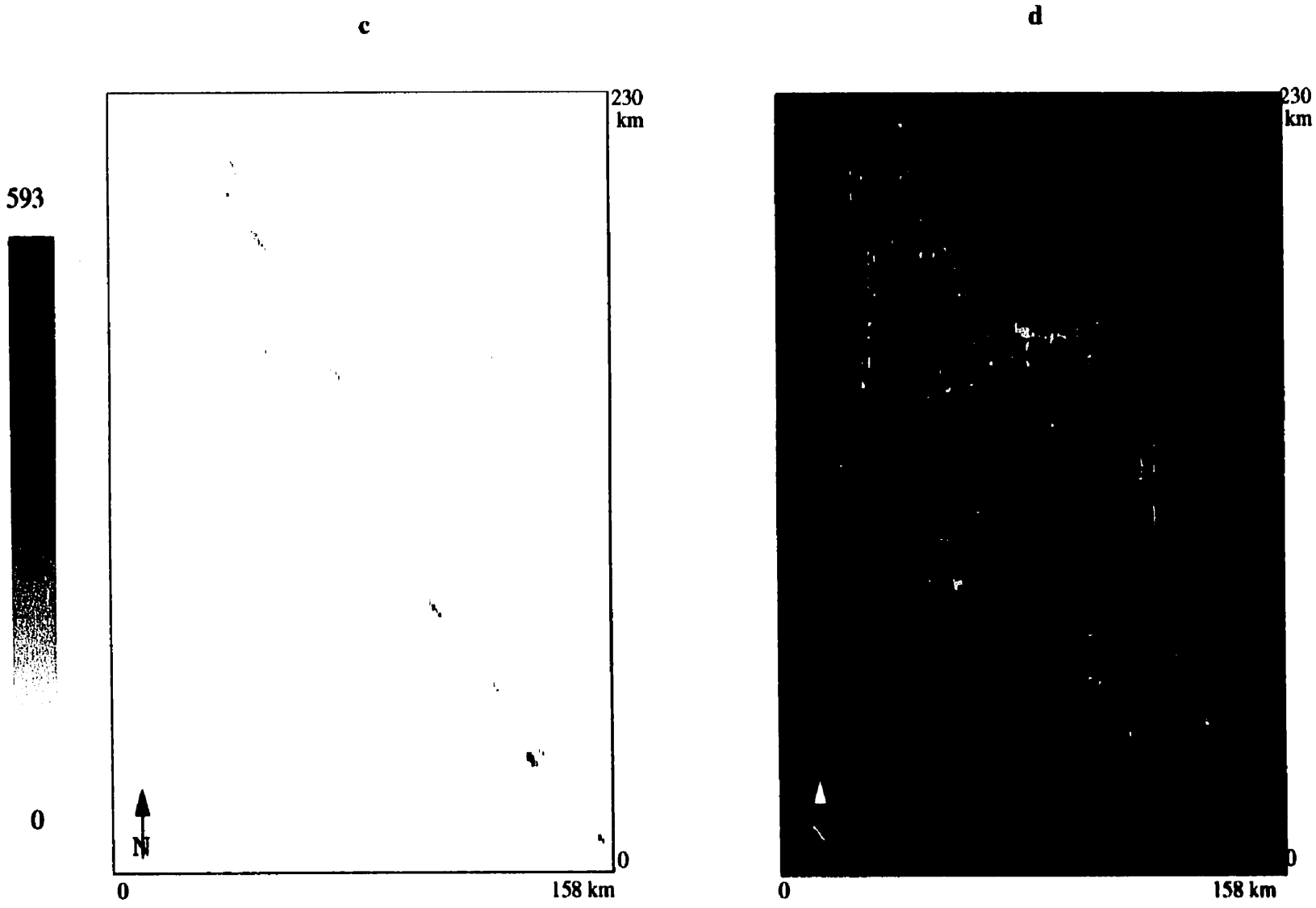

Figure 8.18

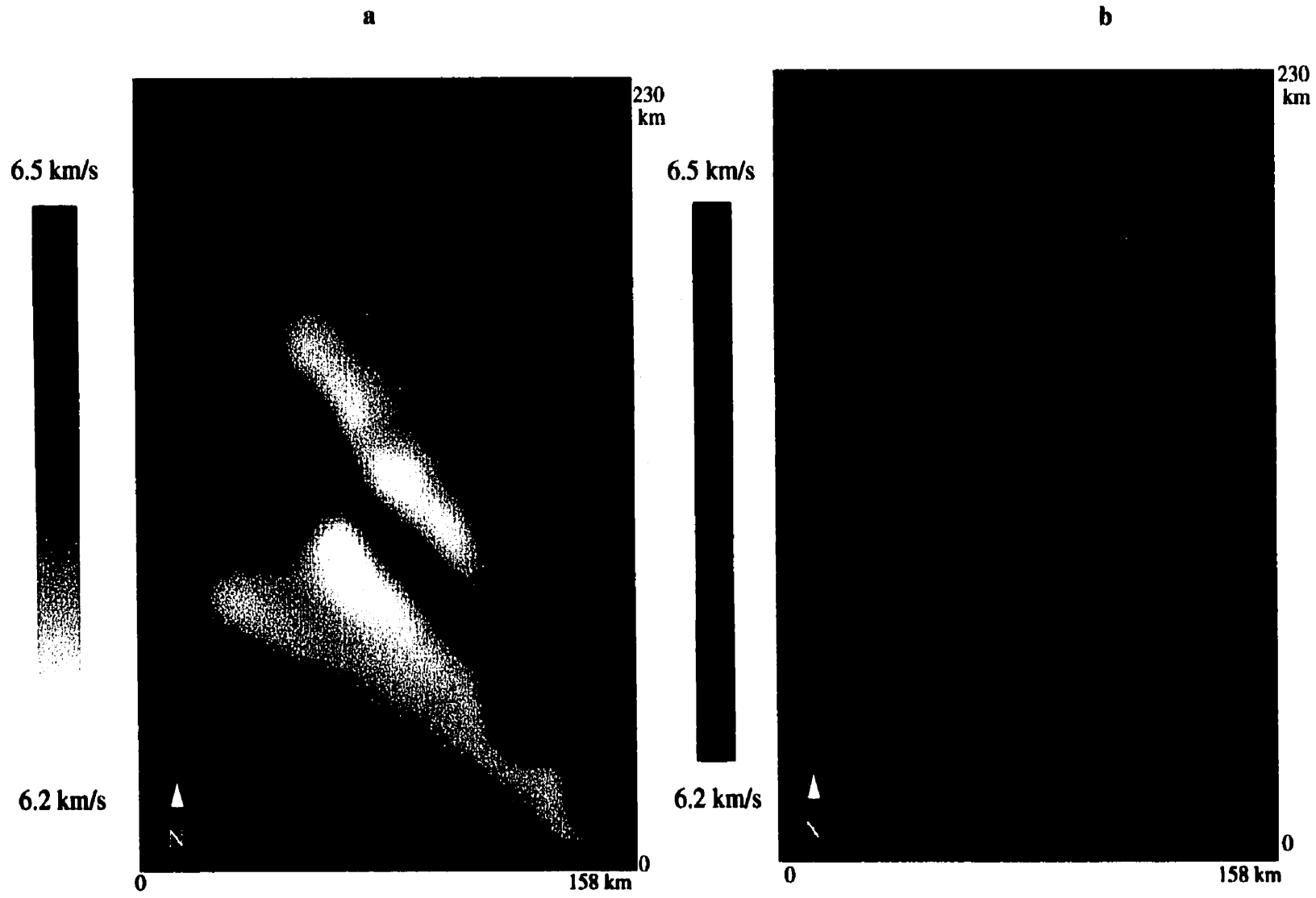

Figure 8.19 Seismic velocity images of the depth slice at 10 km deep (**a**, **b**) and corresponding ray coverage (**c**, **d**). **a** shows velocity in grey scale; **b** shows velocity in color scale; **c** diplays ray coverage in grey scale and **d** shows ray coverage in a HSV color scale generated in Khoros (Release 2.02).

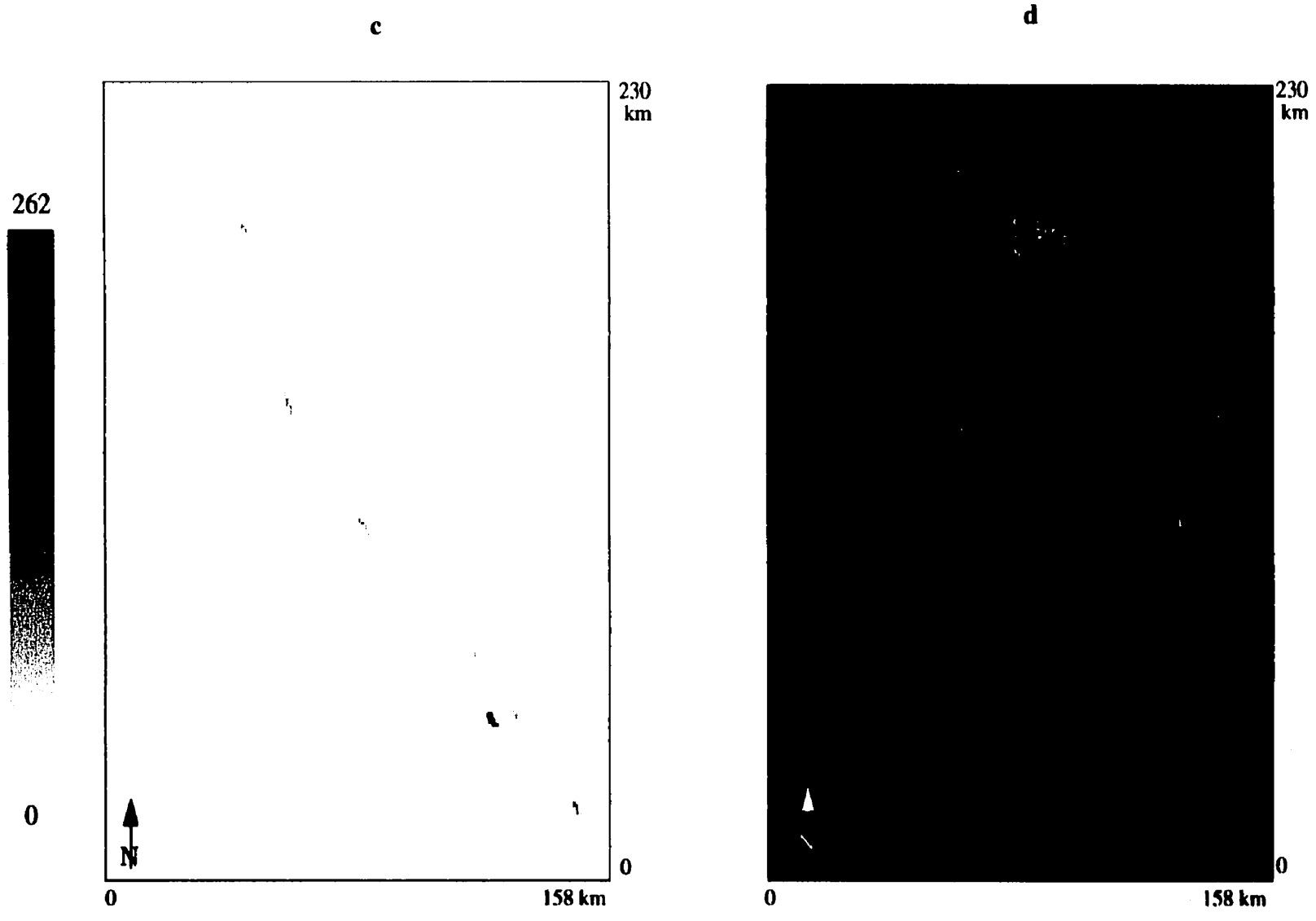

Figure 8.19

8.3 Summary

The 3-D weighted backprojection tomographic algorithm applies a fast finite-difference method in the forward modeling and a nonlinear tomographic inversion method to reduce the computing time and to reconstruct the velocity field while using a large amount of seismic data. The finite-difference algorithm for computing first arrivals was derived on the basis of the eikonal function (Vidale, 1990), and the tomographic inversion was derived from the nonlinear traveltime equation. In the 3-D tomographic algorithm, the nonlinear traveltime equation is replaced by the linear traveltime perturbation equation (Hole, 1992). Therefore, the nonlinear problem is simplified to a linear problem. The solution of the linear traveltime perturbation equation was obtained by using the weighted backprojection tomographic technique.

If a different initial velocity model was given (for example, if the initial velocity was changed slightly in the vertical gradient (+0.01 1/s)), the velocity images would indicate similar shapes.

In this study, the results of the final velocity images show that there is a lenticular high-velocity zone at distances of ~40 to 115 km under the Sudbury Basin imaged on WE profiles, particularly on profile WE3. The depth (~7 km) of this zone is relatively small in comparison with the depth (~9 km maximum) of the lenticular high-velocity body modeled by the in-line seismic data. Beneath this zone, a low-velocity anomaly was imaged which extends down to a depth of ~20 km. There is a small high-velocity block at a distance of 40 km at 4 km depth imaged along profile WE1.

A small high-velocity zone was imaged at a depth of ~5 km at the southern margin of

profiles NS2, NS3 and NS4. A high-velocity anomaly along the western part of profile XY is supported by the velocity slice at a depth of 2 km.

Adequate ray coverage in 3-D seismic tomographic modeling is important for providing a reasonable velocity field and allowing a confident interpretation of the velocity model. In this seismic study in Sudbury, the ray coverage is not sufficiently dense to reconstruct a complete and reliable velocity field over the whole area. Hence, the velocity features interpreted in detail are based on regions with a good ray coverage.

Chapter 9

Discussion and Model of the Sudbury Structure

This chapter includes the interpretation and modeling results obtained from the wide-angle seismic reflection and refraction data. A total of four algorithms were applied in the seismic data modeling (2-D Cerveny ray tracing forward modeling, 2-D RAYINVR ray tracing inverse modeling, 3-D ray tracing forward and inverse modeling and 3-D tomographic imaging). The interpretation and discussion presented in this chapter will be based on these four modeling results. The meteorite impact model of the Sudbury Structure is then examined. This chapter ends with a discussion of the geological models.

9.1 Interpretation and Discussion of the Results

9.1.1 2-D Modeling

An important step in the interpretation of refraction seismic data is the 2-D forward and traveltime inversion modeling. A 2-D parameterized model not only reveals the velocity variations in lateral and vertical directions but also provides us with information on the geological boundaries. Such a model can provide a realistic geological image of the Sudbury Basin. Cerveny's two-point dynamic ray tracing algorithm allows a model to

be parameterized so that it can represent complex geological structure containing steep dipping boundaries, isolated velocity blocks, and lateral and vertical velocity heterogeneities. Therefore, this algorithm was used to model the complex velocity structure along profile AB.

Model resolution cannot be estimated in the ray tracing forward algorithm. However, RAYINVR's forward and inverse method has the advantage of being able to estimate model resolution at the cost of simplification in the geological model. The west-east profile, line XY, was analyzed with such inversion modeling. The near-surface velocity along profile XY is heterogeneous, as is clearly indicated by variations of gravity data (Figure 3.8). In the inversion modeling, the velocity structure along profile XY has to be compared using the modeling results of profile AB at the cross point of the two profiles. This procedure is followed in order to compensate for non-optimal model resolution of profile XY caused by the large number of velocity nodes applied for the velocity heterogeneity. In addition to the traveltime modeling, comparison of amplitudes between the observed and theoretical data can further constrain specific model features.

In the north of the study area, an average thickness of ~37 km of the Archean crust was obtained from the in-line modeling in this study. This average crustal thickness is in the range of the global Archean crustal thickness of ~37 to 42 km (Durrheim and Mooney, 1991). However, in comparison with the crustal thickness of 38-53 km in the central Superior province (which is 130 km northwest of the Sudbury Basin) (Boland and Ellis, 1989), the crust in the southern margin of the Archean craton is relatively thin. This thin crust may be formed by extension or thinning of the Archean crust mainly related to the evolution of a south-facing continental margin during 2.4-2.5 Ga (Green et al., 1988)

and subsequent regional uplift and erosion sequence associated with the Penokean (1.83-1.89 Ga) and Grenville orogenies (~1 Ga). A mid-crustal discontinuity in the Superior and Southern provinces was identified by weak seismic reflectors and modeled in this study at approximately 17 km depth. This mid-crustal interface correlates to the Penokean decollement at the 18-22 km depth (1.83-1.89 Ga) suggested by reflection seismic data from profile J recorded during the GLIMPCE experiment (Green et al., 1988).

The lower crust appears to be composed of "deformed Archean granulite facies rocks or interleaved mafic-intermediate gneiss" (Grandjean et al., 1994) with a relatively high velocity (6.6-6.9 km/s). The upper crust in Sudbury consists of the deformed Huronian strata and Archean basement including metaplutonic and metasedimentary rocks (Grandjean et al., 1994). The significant variation in velocity in shallow subsurface (at ~3 km depth) obtained from the in-line inversion modeling along profile XY indicates that the upper crust is laterally heterogeneous. The anomalous high-velocity block (6.26 km/s) located 40 km southwest of the Sudbury Igneous Complex and at depths of ~1 to 4 km along profile XY is probably associated with high-density rocks (mafic?) implied from a linear gravity high anomaly (McGrath and Broome, 1994). The near-surface low-velocity layer could be associated with the shallow supercrustal assemblages or allochthonous veneer (Grandjean et al., 1995).

In the southern and southeastern parts of the study area, the subhorizontal crustal structure in the Archean craton is truncated sharply by the Grenville Front Tectonic Zone (Figure 5.29), an intense deformation zone and high-grade metamorphic terrane (Green et al., 1988). The Moho depth increases from ~37 km in the north to 44 km under the Grenville Province. In the Grenville Front Tectonic Zone and Grenville Province, the

velocity model requires five southeast-dipping layers (with dips of 7°-30°) corresponding to "shingle-like" events recorded along profile AB. In general, block distribution of amplitude energy is attributed to horizontal and vertical heterogeneities in the subsurface velocity structure. This interpretation is based on comparison of the synthetic seismograms for a theoretical velocity model and one in which the velocity structure contains fractal noise (Crossley and Jensen, 1989). Therefore, the nonuniform energy distribution in shingle events implies lateral and vertical heterogeneity of velocity within each layer. This heterogeneity could be interpreted as being associated with the southeast-dipping stacked microterranes. These zones are characterized by a highly-reflective shear and mylonite zone which was also imaged on seismic reflection profile J (Figure 5.4) (Mereu et al., 1990; Epili and Mereu, 1991), and Lithoprobe Abitibi-Grenville reflection line 15 (Figure 5.6). The dipping layers modeled in the present study extend to the base of the lower crust, which is interpreted as thrust faults extending to the lower crust. The present analysis revealed thick crust under the Grenville Front Tectonic Zone and Grenville Province (40-44 km) which might be considered to be a result of the stacking of microterranes or ductile thrusting during the Grenville orogeny (~1.0 Ga) (Figure 5.29). The thick crust also correlates with the global average thickness for the Proterozoic crust (~45 km in thickness) (Durrheim and Mooney, 1991).

In the Sudbury Basin, the low-velocity (5.83-5.95 km/s) shallow crustal structure modeled under the Sudbury Basin is interpreted to correspond to sedimentary rocks, specifically the Chelmsford greywackes (5.91±0.18 km/s) and Onwatin shale (5.16±0.30 km/s) (Table 3.1). Below this near-surface low-velocity layer (~2.2 km in thickness), the

velocity, modeled in the range of 6.03~6.14 km/s, is compatible with the velocities determined for the Onaping tuff (6.09±0.25 km/s) and granophyre (6.20±0.13 km/s). A rhomboid-shaped high-velocity body under the Sudbury Basin was modeled using both 2-D modeling techniques, and found to lie at a depth of 4-9 km. Along profile XY, the body dips northeastward whereas it dips slightly toward southeast along profile AB. The velocity of the body is 6.31 to 6.4 km/s, which is higher than the velocity in the surrounding area (Figures 5.29 and 6.17). Salisbury et al. (1994) summarized velocities of the Sudbury Igneous Complex, measured from sample rocks, and listed velocities of 6.20±0.13 km/s for granophyre (with a density of ~2.70 g/cm^3), 6.47±0.24 km/s for norite (with a density of ~2.81 g/cm^3), and 6.57±0.20 km/s for the Levack gneiss (with density of 2.73-2.86 g/cm^3) underlying the Sudbury Igneous Complex. These measured velocity results indicate that the granophyre/norite contact is a good reflector. On the basis of comparison of the modeled velocities and the velocities measured from rock samples, the high-velocity body could primarily be associated with the norite of the Sudbury Igneous Complex. The 2-D crustal model obtained in this study also shows a good agreement between the depth range of the high-velocity body (4-9 km) (Figure 5.29) and the interpreted depth of the granophyre and norite revealed on the image of high-resolution seismic reflection line 41 (6-12 km) (Figure 3.4). The difference in the exact depth of the seismic reflection and refraction results may be due to the velocity used in the seismic reflection interpretation. Therefore, the bottom of the lenticular-shaped high-velocity body corresponds approximately to the base of the norite of the Sudbury Igneous complex.

9.1.2 3-D Modeling

Although the modeling technique employed, and the very sparse data coverage, limit the precise interpretation of the geological structure, a cross-array pattern over Sudbury did provide an opportunity to investigate the 3-D form of the crustal velocity structure. Fan-shot modeling gives information on both velocities and velocity boundaries using a simplified model of the geological structure. The Fletcher Reeves conjugate gradient traveltime algorithm, developed during the early stages of this thesis research, can rapidly trace a two-point ray path and thus avoid time-consuming traveltime calculations in 3-D. The rapid algorithm requires a simple mode parametrization consisting of plane interfaces and constant layer velocities. A 3-D velocity structure was imaged in the whole study region using a tomographic technique.

The low-velocity near-surface structure determined from the fan-shot data correlates well with the modeling results of the in-line data. The depths to the mid-crustal interface and Moho discontinuity in both the northwestern and northeastern cross-sectional regions are 15.2-15.9 km and 35.4-36.7 km, respectively. These values are reasonably compatible with ~17 km (mid-crustal interface) and ~37 km (Moho discontinuity) depths modeled along two in-line profiles. 3-D ray tracing modeling results also reveal that there is no significant variation of the crustal thickness in the southern Superior and eastern Southern provinces. This uniformity could imply that these two regions underwent a similar tectonic environment during the geological history. The 3-D ray tracing modeling indicates that under the Grenville Front Tectonic Zone the Moho depth increases to ~41.6 km, which agrees well with the depth obtained from the in-line refraction seismic data in

this area.

The 3-D tomographic velocity images should be interpreted carefully because of the very sparse ray coverage and nonuniform ray distribution. This coverage can sometimes yield images containing features that are not correlated to geological structures (Chang, 1996). Therefore, the geological interpretation of results from a survey with sparse ray coverage must consider the distribution of rays.

The lenticular high-velocity body under the Sudbury Basin was also revealed on tomographic images, especially on the west-east profiles. Figure 8.8a indicates that the top of the lenticular high-velocity body is shallow (~2 km deep). The base of the body is at approximately 7 km depth. The thickness of the sedimentary rocks of the Onwatin shale and Chelmsford greywacke, which overlie the Onaping tuff, is approximately 1.5 km (Figures 2.4 and 3.3). The underlying Onaping tuff has a velocity of ~6.09 km/s, whereas the Onwatin and Chelmsford have velocities of ~5.16 and 5.91 km/s respectively (Table 3.1). Therefore, the lenticular high-velocity body may correlate to Onaping tuff, granophyre (6.20 km/s) and norite (6.47 km/s) of the Sudbury Igneous Complex (Figure 8.8a). The base of the lenticular high-velocity body corresponds to the base of the Sudbury Igneous Complex.

There is a lower velocity zone directly below the Sudbury Basin in the lower upper crust (at ~12 km depth) revealed by velocity images, particularly at a 130 km offset on profile WE3 (Figure 8.8a). Generally, the ray coverage is poor at depth. However, the velocity image in the lower crust in the center of profile WE3 was defined by a reasonable ray coverage (Figure 8.8b). Therefore, this deep velocity structure is sufficiently reliable to be interpreted. This study suggests that the low-velocity zone

could relate to the Footwall and Sudbury Breccias with the relatively low velocity caused by shock-induced loss of structure strength. However, this interpretation needs further investigation.

A small, shallow, high-velocity body (~6.3 km/s) at an offset of 95 km and at a depth of 5 km was imaged along profile NS2 (Figure 8.12a). Good ray coverage was obtained on profile WE1. The location of this body corresponds to the position of Huronian mafic volcanic rocks (with a density of 2.88 g/cm^3) (McGrath and Broome, 1994), which are responsible for the gravity high at the South Range of the Sudbury Igneous Complex (Figure 3.3). Therefore, the seismic anomaly might relate to the high-density volcanic rocks.

Figure 8.17 shows that there is an anomalous high-velocity body in the western part of profile XY, imaged at a depth of 2 km with a reasonable ray coverage. This high-velocity anomaly (~6.25 km/s) corresponds to the near-surface high-velocity structure (6.26 km/s) at offsets of 20-40 km revealed by the in-line inversion modeling along profile XY (Chapter 6.2). There is a gravity high at the corresponding location (Figures C.2a and C.2b). McGrath and Broome (1994) interpreted this linear gravity anomaly as being due to mafic Huronian volcanic rocks (2.88 g/cm^3) buried near the surface.

A complex 3-D velocity structure in Sudbury was revealed using the seismic tomographic technique. A good ray coverage was obtained close to the arms of the cross of the two survey profiles, although there is an insufficient coverage of rays in the rest area for definitive interpretation of the anomalies. The tomographic study indicated that 3-D velocity imaging is a powerful tool for investigating the complicated geological

structure. However, in order to obtain reliable and detailed images of the Sudbury Structure using 3-D seismic tomography, and to reveal the complete velocity structure, more densely sampled seismic data are required.

The velocity structure modeled in this research indicates that there is no high-velocity and dense mafic rock body or igneous "feeding root" in the lower crust and upper mantle directly beneath the Sudbury Basin. A significant component of the endogenic hypothesis is that there is a mafic source or "feeding root" in depth (implied by Muir, 1984). Hence, there is no evidence in seismic refraction results to support the endogenic hypothesis for the formations of the Sudbury Structure and Sudbury Igneous Complex. The lenticular high-velocity body related to the major component of the norite of the Sudbury Igneous Complex under the Sudbury Basin might result from an impact-generated melt sheet, which supports the hypothesis that the Sudbury Structure is the relic of a large terrestrial impact crater.

Seismic results (no "feeding root" in lower crust and upper mantle) do not support the hypothesis of a volcanic origin of the Onaping Formation. The Onaping Formation is implied to be formed by an impact event (or derived from fallback debris created by the meteorite impact) (Grieve et al., 1991).

The subhorizontal crustal structure in Sudbury modeled using the seismic refraction data suggests that there is no significant central-uplift. Generally, a typical large meteorite impact crater has a central uplift feature (Grieve et al., 1991). The Sudbury Structure is not a typical large impact crater because of no central-uplift feature. The thrusting deformation in the Sudbury area, which is related to the Penokean (1.83-1.89 Ga) and Grenville (~1.0 Ga) orogenies, is one explanation for the lack of local central-

uplift in the large impact structure. Therefore, this thesis research provides the geophysical solutions to persistent questions on origin of the Sudbury Structure, and on the formation and nature of the Sudbury Igneous Complex and Onaping Formation from the point of the crustal seismology.

To investigate the Sudbury Igneous Complex and small high-velocity bodies at its base in detail in the future, a survey with a square pattern (150 by 150 km) centered in the Sudbury Basin would be designed. Receivers should be placed around and inside the interior of the square with ~1 km spacing in in-line and fan-shot configurations. Sources should be placed along the margin of the square with perhaps ~20 km spacing. A detailed seismic velocity structure under the Sudbury Structure would be expected to be revealed using the 3-D seismic data collected by the designed survey.

9.1.3 Discussions of Other Studies Conducted during this Thesis Work

1. Seismic Phase Picking

There are three seismic inversion modeling approaches that were used in this study. The first step before all these methods were performed was to pick the seismic events from the seismic sections. Computer-based fractal techniques for picking seismic phases were developed during the thesis research for obtaining the consistent and accurate picks.

The variance fractal dimension technique was used to detect the first breaks as well as late arrival signals. If there is auto-correlated noise in seismic trace signals, a random noise with amplitude equivalent to the average of the correlated noise is required to add to seismic trace signals to obtain accurate picking time by breaking up the correlation of the

noise. A detailed description of the method developed is given in Appendix A. The length fractal dimension technique was used to distinguish first breaks from the background noise. This method requires a normalization of trace signals according to the maximum amplitude on a trace. Appendix B discusses this method in detail.

2. Potential Field Data Processing and Radar Imaging

Geophysical potential field data in Sudbury were processed by applying commonly used techniques for investigation of the spatial distribution features of geological structures. The techniques used include low-pass filtering, upward- and downward-continuation filters, and the pseudo-sun angle (shading-relief) technique to enhance linear features of various orientations. A full description of this work may be found in Appendix C.

The processed geophysical potential field data delineate the spatial distribution of the geological structure in Sudbury (Figures C.2-C.3). An interesting ring-shaped feature located ~30 km north and northwest of the North Range of the Sudbury Igneous Complex was revealed on the upward-continuation shaded-relief total aeromagnetic images (Figure C.4). Its location correlates to the second pseudotachylyte ring zone which was observed at distances of 25-35 km from the North Range of the Sudbury Igneous Complex (Spray and Thompson, 1995). Multi-ring features in large meterorite impact craters have been observed (for example, lunar Copernicus crater in Figure C.5). However, the questions on the relationship between the magnetic anomaly and the impact-induced structure, the magnetization process and magnetic carriers remain to be answered.

A radar image generated by Radarsat-1 provides a basic geological mapping database. The geological boundaries in the Sudbury area were digitized and overlain on

the radar image, in order to yield a basic map for visualization of geophysical data for enhancing geological features in specific directions.

9.2 Model of the Sudbury Structure

9.2.1 Impact Model

There are two parameters to quantitatively describe an impact model: horizontal diameter and vertical depth. Dressler and Sharpton (1999) summarized research to conclude that the diameter of the Sudbury crater is in the range of 150-280 km. The depth of a crater is difficult to estimate because only limited constraining information is available. However, there is a scaling relationship between crater depth and diameter, which was obtained by statistical analysis of the dimensions of 211 lunar craters (Figure 9.1) (Melosh, 1989). The relationship provides an opportunity for determination of the depth of the Sudbury crater. A scaling relationship between the depth and diameter of large terrestrial craters (>17km in diameter) was estimated and plotted in Figure 9.2. Based on this scaling relationship, the best estimate of the original depth of the Sudbury impact crater is between 11.2 and 21.2 km, corresponding to diameters of 150 and 280 km respectively (Figure 9.2).

The maximum depth to the base of the high-velocity body (the norite of the Sudbury Igneous Complex) is estimated to be approximately 9 km based on the current refraction seismic study. Grieve et al. (1991) suggested that during the Sudbury impact event, shock melting might have extended to the bottom of the original transient cavity for a large

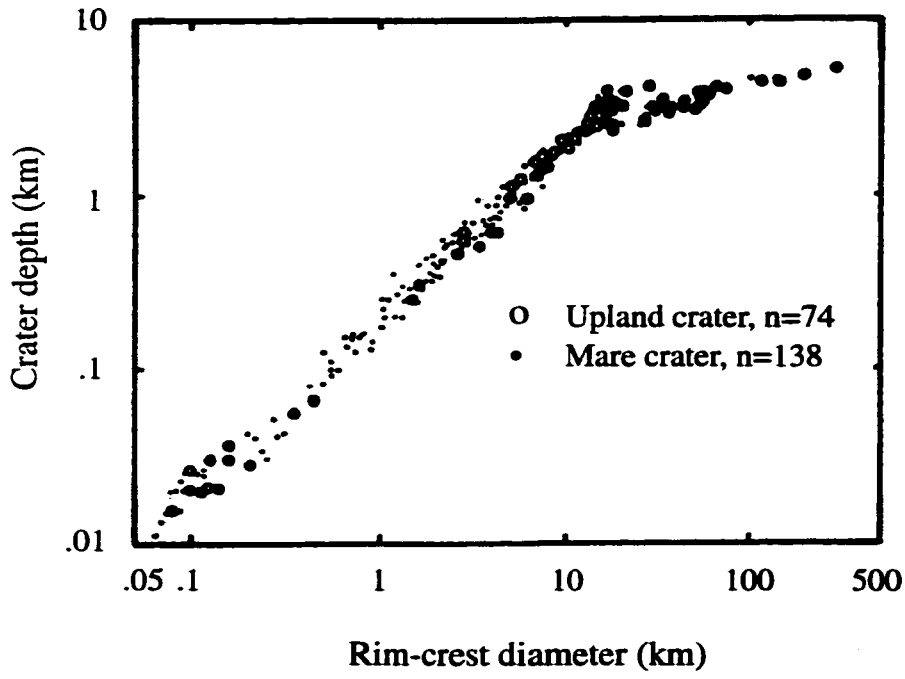

Figure 9.1 Relationship between the depth and diameter of fresh, unflooded lunar craters (After Melosh, 1989).

impact crater. Therefore, the assumption was made that the maximum depth of the Sudbury Igneous Complex is approximately equal to the depth of the transient crater which is assumed to be comparable to the depth of the final crater. The difference between the current depth and original depth implies the amount of the regional erosion. Therefore, there must have been approximately 2.2 to 12.2 km of regional erosion throughout the geological evolution of the Sudbury area following the impact.

9.2.2 Development of Geological Sequences

In this study, the seismic modeling results support the hypothesis of the meteorite impact origin of the Sudbury Structure. Figure 9.3 shows the speculative development

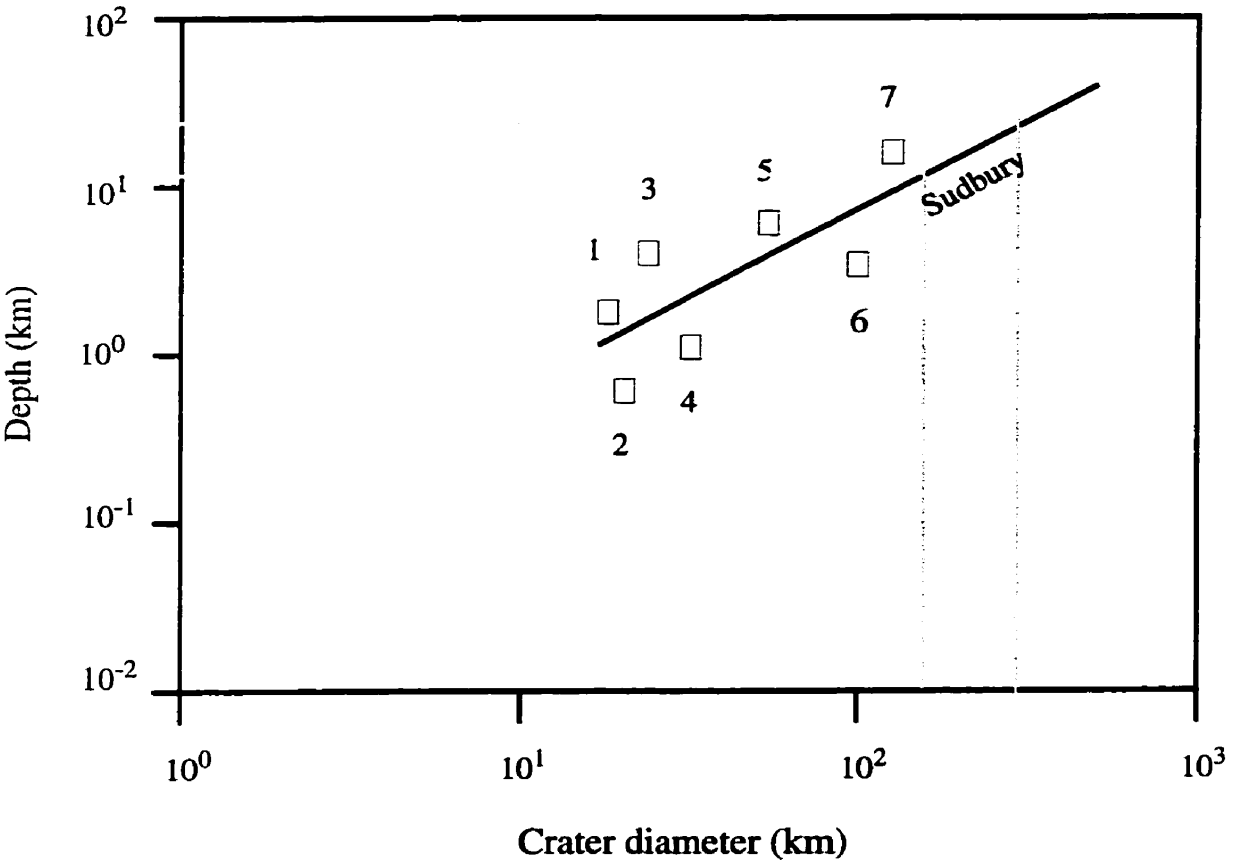

Figure 9.2 Relationship between the depth and diameter of large complex terrestrial craters: 1. El'gygytgyn, Russia; 2. Haughton, Canada; 3. Ries, Germany; 4. West Clearwater Lake, Canada; 5. Siljian, Sweden; 6. Manicouagan, Canada; 7. Vredefort, South Africa (Based on Pilkington and Grieve, 1992 Rondot, 1994).

stages of the Sudbury impact structure. Impact cratering, melting and vaporizing (~1.85 Ga) in Huronian and Archean rocks constitute the first stage of the exogenic formation (Figures 9.3a and 9.3b) (Grieve, 1992). The Sudbury Breccia, Footwall Breccia and impact melting sheet (Sudbury Igneous Complex) were then formed and the Onaping breccia was subsequently deposited over the impact crater (Figure 9.3c) (Grieve, 1992). Thrust deformation occurred in the northwest-southeast direction in Sudbury during the

Penokean orogeny (Wu et al., 1995), whereas the impact structure was only slightly deformed in the northeast-southwest direction. The crater was deformed and the Onwatin Formation overlaid the Onaping Formation on the deformed crater (Figure 9.3d) (Wu et al., 1995). The Chelmsford Formation was deposited on the Onwatin Formation by turbidity currents in a northwesterly trend (Figure 9.3e). The Sudbury Structure is believed to have been further eroded, deformed and modified during the subsequent Grenville orogeny (~1.0 Ga). Figure 9.4 shows the enlarged current structure profiling in the west-east direction. In this study, the seismic modeling results indicate that the Moho discontinuity and mid-crustal interface in the northern part of the Sudbury Structure are subhorizontal (Figures 5.29 and 6.17). These features imply that there is no significant uplift in the Moho discontinuity and the mid-crustal interface beneath the structure. The present Sudbury structure was therefore formed by a large meteorite impact without development of a significant central-uplift.

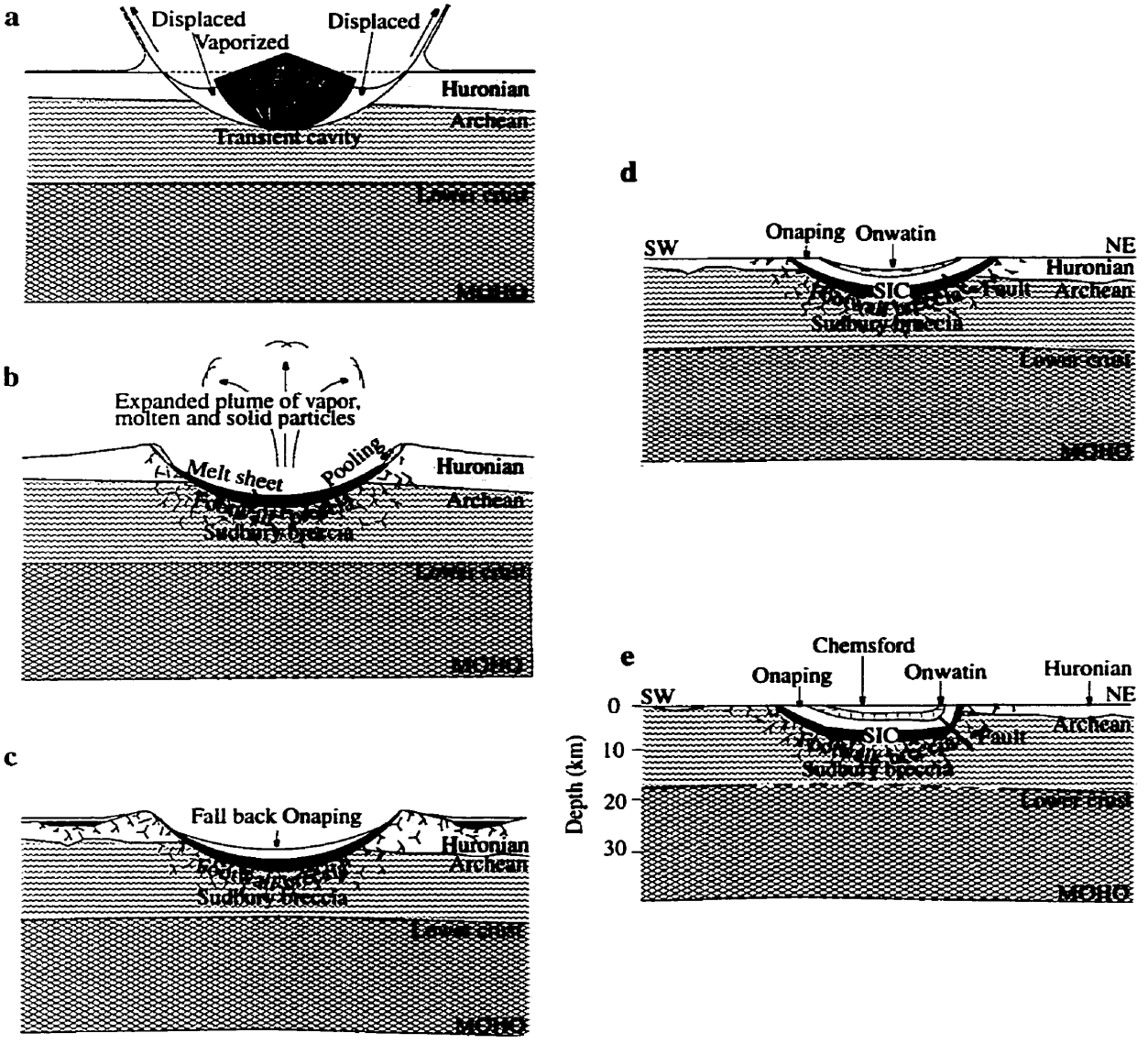

Figure 9.3 Schematic cartoon of the development sequences of the Sudbury impact structure: (a) Impact cratering, vaporizing and melting (based on Grieve et al., 1991); (b) Formation of melting sheet and the Sudbury Breccia and Footwall Breccia (after Avermann et al., 1994 and Miao, et al., 1995); (c) Final stage of the impact cratering and emplacement of the melting sheet; (d) Formation of the sediments, thrusting and erosion; (e) The present Sudbury structure after strong northwest-southeast compressive deformation and subsequent erosion during the Penokean and Grenville orogenies.

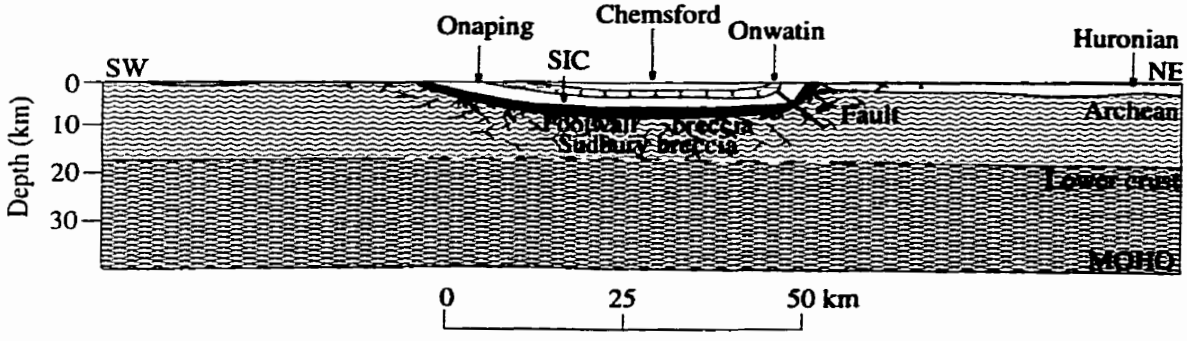

Figure 9.4 Enlarged picture of the present Sudbury structure after severe northwest-southeast deformation and erosion during the Penokean and Grenville orogenies. The mid-crustal velocity boundary beneath the Sudbury structure was drawn by a dashed line to reflect the model resolution.

Chapter 10

Conclusions

The main objectives of the Lithoprobe Abitibi-Grenville transects and this research include imaging of the 3-D subsurface geological structure of the Sudbury area, investigation of the relationships between the geological structures in the Sudbury Basin and the adjacent areas, and testing of the key geophysical constraints on the formations of the Sudbury Structure, Sudbury Igneous Complex and Onaping Formation. Preliminary results of modeling (2-D) and interpretation of the seismic reflection and refraction data were previously carried out by Miao (1995) and Winardhi and Mereu (1997). This thesis research further refined the detailed structures in both 2-D and 3-D for better understanding of the deeper structural setting, and was designed to provide constraints on the origin of the Sudbury Structure and the formation of the Sudbury Igneous Complex and Onaping Formation. In this thesis, the 1992 Lithoprobe Abitibi-Grenville high-resolution wide-angle seismic reflection and refraction in-line and fan-shot data sets were processed. Various modeling techniques (forward, inverse and 3-D modeling) were utilized to investigate the complex subsurface structure in Sudbury and its surrounding areas, because a single modeling technique cannot provide comprehensive results.

The Moho discontinuity under the Superior and Southern provinces, imaged using the in-line and fan-shot data, is approximately horizontal. The average Moho depth is

approximately 37 km and the average crustal velocity is 6.55 km/s. The depth of the Moho discontinuity gradually increases to ~40 km under the Grenville Front Tectonic Zone. The crustal structure under the Grenville Front Tectonic Zone is characterized by the southeast dipping crustal sheets which truncate a sub-horizontal structure to the north. The middle crustal interface is also a sub-horizontal feature in the northern part of the study area. This sub-horizontal discontinuity in the Superior and Southern provinces implies that there is no apparent uplift at the lower crust, indicating that there is no local central uplift feature under the Sudbury Structure throughout the geological setting. The current interpretation of the seismic refraction data proposes that there is no significant high-velocity anomalous body or igneous "feeding root" in the lower crust or upper mantle around the structure.

A lenticular high seismic velocity body under the Sudbury Basin is well defined in the in-line seismic velocity model and also in the 3-D tomographic inversion model. It does not seem appropriate to interpret this velocity body as a hidden ultramafic body because there is no "feeding root" modeled in the lower crust and upper mantle.

On the basis of an analysis of the velocity image of Lithoprobe Abitibi-Grenville Transect line 41 data and the measured velocities from rock samples, the base of the lenticular high-velocity body appears to be associated with the base of Sudbury Igneous Complex. This result implies that the Sudbury Igneous Complex could have been formed from the meteorite impact-induced melting sheet. As there is no evidence at depth for volcanic activities induced by the impact event, it is reasonable to interpret the origin of the Onaping Formation as a result of fallback debris produced by a giant meterorite impact.

The interpretation of the high-velocity anomalous body in Sudbury as revealed by the high-resolution seismic data (Milkereit et al, 1992; Wu et al., 1995), refraction data (this study), gravity (McGrath et al., 1994) and magnetic data along seismic reflection profile 41 (Hearst et al., 1994) generally agrees with the impact origin of the Sudbury Igneous Complex. Seismic interpretation from this study provides us with a strong geophysical constraint for the meterorite impact origin of the Sudbury Structure. The Sudbury Structure is not a typical large impact structure because of the lack of the central uplift. The Sudbury Event happened at ~1.85 Ga in the eastern part of the Penokean orogen (1.83~1.89 Ga). The absence of the significant central uplift could be related primarily to the thrusting compression during the Penokean orogeny. Nevertheless, geological interpretation of the anomalous velocity body under the Sudbury Structure and the mechanism of the absence of a central uplift structure in the Sudbury Structure as a complex large impact crater require further proof.

Geophysical potential field data reveal interesting spatial distributions in the Sudbury Structure, particularly the ring pattern unexpectedly observed on upward-continuation shaded-relief magnetic images. However, the magnetic source and formation mechanism of the magnetic carrier could not be completely interpreted here because of a lack of sufficient geophysical and experimental data. Remote sensing and GIS database established on the Sudbury Structure provides a useful tool to simultaneously visualize the topography, geological structure boundaries and characteristic geophysical properties for a comprehensive geophysical interpretation.

In addition to the investigation on the origin of the Sudbury geological structure, seismic phase picking techniques were also researched in this thesis. Two fractal analysis

methods were developed for the detection of seismic signal arrivals in the presence of background noise. The variance fractal dimension technique can be used to distinguish not only weak seismic first arrivals but also late arriving signals (ground roll and PmP phases) with a large window size. The sharp transition feature on the dimension trajectories generated by the variance fractal dimension and length fractal dimension techniques indicates the possibility of the application of the fractal dimension techniques to automatically pick first arrival times in seismic reflection and refraction data.

On the basis of this thesis research, it is suggested that in order to precisely image the 3-D subsurface geological structure and to completely understand a giant meteorite impact process and its impact-evolved structure, it is recommended that a future study should acquire a well planned dense seismic survey in and around Sudbury. In addition, a further research should be carried out on the large scale weak magnetic anomalies associated with various meteorite impact events. The weakly magnetized large ring-shaped magnetic anomalies outside the Sudbury Igneous Complex may hold a key information on the origin of the Sudbury Structure.

References

Aki, K., and Richards, P., 1980, Quantitative Seismology: Theory and Methods, Vol. II, W. H. Freeman and Co..

Ames, D. E., Watkinson, D. H., and Parrish, R. R., 1998, Dating of a regional hydrothermal system induced by the 1850 Ma Sudbury impact event, Geology, 26, 447-450.

Asudeh, I., Anderson, F., Parmelee, J., Vishnubhatla, S., Munro, P., and Thomas, J., 1992, A portable refraction seismograph PRS1, Geological Survey of Canada, Open File 2478.

Avermann, M., 1994, Origin of the polymict, allochthonous breccias of the Onaping Formation, Sudbury Structure, Ontario, Canada, *in* Large Meteorite Impacts and Planetary Evolution, edited by B. O. Dressler, R. A. F. Grieve, and V. L. Sharpton, the Geological Society of America, Special Paper 293, 265-274.

Avermann, M., 1999, the Green Member of the Onaping Formation, the collapsed fireball layer of the Sudbury impact structure, Ontario, Canada, *in* Large Meteorite Impacts and Planetary Evolution II, edited by B. O. Dressler and V. L. Sharpton,the Geological Society of America, Special Paper 339, 323-330.

Avermann, V., and Brockmayer, P., 1992, The Onaping Formation of the Sudbury Structure (Canada): An example of allochthonous impact breccias, Tectonophysics, 216, 227-234.

Becker, L., Poraka, R. J., and Beda, J. L., 1996, Extra-terrestrial helium trapped in fullerenes in the Sudbury impact structure, Science, 272, 249-251.

Bennett, G., Dressler, B. O., and Robertson, J. A., 1991, The Huronian Supergroup and associated intrusive rocks, *in* Geology of Ontario, edited by P. C. Thurston, H. R. Williams, R. H. Sutcliffe, and G. M. Stott, Ontario Geology Survey, Special Volume 4, Part I, 549-591.

Bethune, K. M., 1997, The Sudbury dyke swarm and its bearing on the tectonic development of the Grenville Front, Ontario, Canada, Precambrian Res., 85, 117-146.

Boerner, D. E., Milkereit, B., and Naldrett, A. J., 1994, Introduction to the Special Section on the LITHOPROBE Sudbury Project, Geophys. Res. Lett., 21, 919-922.

Boland, A. V., and Ellis, R. M., 1989, Velocity structure of the Kapuskasing uplift, northern Ontario, from seismic refraction studies, J. Geophys. Res., 94, 7189-7204.

Boschetti, F., Dentith, M. D., and List, R. D., 1996, A fractal-based algorithm for detecting first arrivals on seismic traces, Geophysics, 61, 1095-1102.

Butler, H. R., 1994, Lineament analysis of the Sudbury multiring impact structure, *in* Large Meteorite Impacts and Planetary Evolution, edited by B. O. Dressler, R. A. F. Grieve, and V. L. Sharpton, the Geological Society of America, Special Paper 293, 319-329.

Cai, X., 1982, Optimization and Optimum Control (in Chinese), Qinghua University Publication Press.

Card, K. D., 1990, A review of the Superior Province of the Canadian Shield, a product of Archean accretion, Precambrian Res., 48, 99-156.

Card, K. D., Gupta, V. K., McGrath, P. H., and Grant, F. S., 1984, The Sudbury Structure: Its regional geological and geophysical setting, *in* The Geology and Ore Deposits of

the Sudbury Structure, edited by E. G. Pye, A. J. Naldrett, and P. E. Giblin, Ontario Geological Survey, Special Volume 1, 25-56.

Card, K. D., and Hutchinson, R. W., 1972, The Sudbury Structure: its regional setting, *in* New Developments in Sudbury Geology, edited J. V. Guy-Bray, Geological Association of Canada, Special Paper 10, 67-78.

Card, K. D., and Pattison, E. F., 1973, Nipissing diabase of the Southern Province, Ontario, *in* Huronian Stratigraphy and Sedimentation, edited by G. M. Young, Geological Association of Canada, Special Paper 12, 7-30.

Cerveny, V., 1985, Ray synthetic seismograms for complex two-dimensional and three-dimensional structures, J. Geophysics, 85, 2-26.

Cerveny, V., 1987, Ray tracing algorithms in the three-dimensional laterally varying layered structures, *in* Seismic Tomography with Applications in Global Seismology and Exploration Geophysics, edited by G. Nolet, and D. Reidel, Publishing Company, 99-133.

Cerveny, V., and Hron, F., 1980, The ray series method and dynamic ray tracing system for three-dimensional inhomogeneous media, Bull. Seism. Soc. Am., 70, 47-77.

Cerveny, V., Molotkov, A., and Psencik, I., 1986, Ray methods in seismology (in Chi nese), translated by F. Liu, G. Hu, H. Wu, and Y. Quan, Chinese Geological Publication Press.

Cerveny, V., and Ravindra, R., 1971, Theory of seismic head waves, University of Toronto Press.

Chang, X., 1996, Relationship between ray distribution and reconstructed velocity image in reflection tomography, J. App. Geophys., 35, 145-150.

Chang, X., 1997, First arrival picking in seismic data using the Hausdroff fractal dimension technique (Abstract), the 2nd symposium of the Chinese geoscientists, Beijing, China, 18-20.

Chubb, P. T., Vogel, D. C., Peck, D. C., James, R. S., and Keays, R. R., 1994, Occurrences of pseudotachylyte at the east Bull Lake and Shakespeare-Dunlop intrusion, Ontario, Canada, Can. J. Earth Sci., 31, 1744-1748.

Cimini, G. B., 1999, P-wave deep velocity structure of the Sothern Tyrrhenian Subduction Zone from nonlinear teleseismic traveltime tomography, Geophys. Res. Lett., 26, 24, 37-9-3712.

Clowes, R. M., 1989, LITHOPROBE Phase III proposal, submitted to NSERC and the Geological Survey of Canada.

Clowes, R., 1993, Studies of the evaluation of a continent, Lithoprobe Phase IV Proposal of Studies of the Evolution of a Continent.

Clowes, R., 1997, Evolution of a continent revealed, Lithoprobe Phase V Proposal of Evolution of a Continent Revealed.

Clowes, R., Cook, F. A., Green, A. G., Keen, C. E., Ludden, J. N., Percival, J. A., Quinlan, G. M., and West, G. F., 1992, Lithoprobe: new perspectives on crustal evolution, Can. J. Earth Sci., 29, 1813-1864.

Coles, R. L., and Clark, J. F., 1982, Lake St. Martin Impact Structure, Manitoba, Canada: Magnetic anomalies and magnetizations, J. Geophys. Res., 87, 7087-7095.

Corfu, F., and Lightfoot, P. C., 1996, U-Pb Geochronology of the Sudbury environment, Sudbury Igneous Complex, Ontario, Economic Geology, 91, 1263-1269.

Corner, B., Durrheim, R. J., and Nicolaysen, L. O., 1990, Relationships between the Vredefort Structure and the Witwatersrand Basin within the tectonic framework of the Kaapvaal Craton as interpreted from regional gravity aeromagnetic Data, Tectonophysics, 171, 49-61.

Cowan, E. J., Riller, U., and Schwerdtner, W. M., 1999, Emplacement geometry of the Sudbury Igneous Complex: Structural examination of a proposed impact melt-sheet, *in* Large Meteorite Impacts and Planetary Evolution II, edited by B. O. Dressler and V. L. Sharpton,the Geological Society of America, Special Paper 339, 399-418.

Crossley, D. J., and Jensen O. G., 1989, Fractal velocity models in refraction seismology, Pure Applied Geophysics, 131, 62-76.

Culshaw, N. G., Ketchum, J. W. F., Wodicka, N., and Wallace, P., 1994, Deep crustal ductile extension following intrusion in the southwestern Grenville Province, Ontario, Can. J. Earth Sci., 31, 160-175.

Dietz, R. S., 1964, Sudbury Structure as an astrobleme, J. Geology, 72, 412-434.

Deutsch, A., 1994, Isotope systematics support the impact origin of the Sudbury Structure (Ontario, Canada), *in* Large Meteorite Impacts and Planetary Evolution, edited by B. O. Dressler, R. A. F. Grieve, and V. L. Sharpton, the Geological Society of America, Special Paper 293, 279-302.

Dickin, A. P., and McNutt, R. H., 1989, Nd model age mapping of the southeast margin of the Archean foreland in the Grenville Province of Ontario, Geology, 17, 299-302.

Dickin, A. P., Nguyen, T., and Crocket, J. H., 1999, Isotopic evidence for a single impact melting origin of the Sudbury Igneous Complex, *in* Large Meteorite Impacts and

Planetary Evolution II, edited by B. O. Dressler and V. L. Sharpton,the Geological Society of America, Special Paper 339, 361-371.

Dressler, B. O., 1984, General geology of the Sudbury Area, *in* The Geology and Ore Deposits of the Sudbury Structure, edited by E. G. Pye, A. J. Naldrett, and P. E. Giblin, Ontario Ministry of Natural Resources, 57-82.

Dressler, B. O., Gupta, V. K., and Muir, T. L., 1991, The Sudbury Structure, *in* Geology of Ontario, edited by P. C. Thurston, H. R. Williams, R. H. Sutcliffe, and G. M. Stott, Ontario Geological Survey, Special Volume 4, Part I, 593-625.

Dressler, B. O., and Sharpton, V. L., 1999, Sudbury Structure 1997: A persistent enigma, *in* Large Meteorite Impacts and Planetary Evolution II, edited by B. O. Dressler and V. L. Sharpton,the Geological Society of America, Special Paper 339, 299-304.

Durrheim, R. J., and Mooney, W. D., 1991, Archean and Proterozoic crustal evolution: Evidence from crustal seismology, Geology, 19, 606-609.

Earle, P. S., and Shearer, P. M., 1994, Characterization of global seismograms using an automatic-picking algorithm, Bull. Seism. Soc. Am., 84, 366-376.

Elming, S., and Bylund, G., 1991, Paleomagnetic and the Siljan Impact Structure, central Sweden, Geophys. J. Int., 105, 757-770.

Epili, D., and Mereu, R. F., 1991, The Grenville Front Tectonic Zone: Results from the 1986 Great Lakes onshore seismic wide-angle reflection and refraction experiment, J. Geophys. Res., 96, 16335-16348.

Faggart, B. E., and Basu, A. R., Jr., 1985, Origin of the Sudbury Complex by meteorite impact: neodymium isotopic evidence, Science, 230, 436-439.

Frarey, M. J., Loverbridge, W. D., and Sullivan, R. W., 1982, A U-Pb zircon age for the

Creighton granite, Ontario, *in* Rb-Sr and U-Pb Isotopic Age Studies, Report 5, Current Research, Part C, Geological Survey of Canada, Paper 82-1C, 129-132.

French, B. M., 1967, Sudbury Structure, Ontario: Some petrographic evidence for origin by meteorite impact, Science, 156, 1094-1097.

French, B. M., 1972, Shock-metamorphic features in the Sudbury Structure, Canada: A review, *in* New Developments in Sudbury Geology, edited by J. V. Guy-Bray, the Geological Association of Canada, Special Paper 10, 19-28.

French, B. M., 1990, 25 Years of the impact-volcanic controversy: Is there anything new under the Sun or inside the Earth?, EOS Trans. AGU, 71, 411-414.

Gelchinsky, B., and Shtivelman, V., 1983, Automatic picking of first arrivals and parameterization of traveltime curves, Geophys. Pros., 31, 915-928.

Gibb, R. A., Thomas, M. D., Lapointe, P. L., and Mukhopadhyay, M., 1983, Geophysics of Proposed Proterozoic Sutures in Canada, Precambrian Res., 19, 349-384.

Giblin, P. E., 1984, History of exploration and development of geological studies and development of geological concepts, *in* the Geology and Ore Deposits of the Sudbury Structure, edited by E. G. Pye, A. J. Naldrett, and P. E. Giblin, Ontario Geological Survey, Special Volume 1, 3-23.

Godano, C., Alonzo, M. L., and Bottari, A., 1996, Multifractal analysis of the spatial distribution of earthquakes in southern Italy, Geophys. J. Int., 125, 901-911.

Golightly, J. P., 1994, The Sudbury Igneous Complex as an impact melt: evolution and ore genesis, *in* Proceedings of the Sudbury - Noril'sk Symposium, Ontario Geological Survey, Special Volume 5, 105-117.

Grandjean, G., Wu, H., White, D., Mareschal, M., and Hubert, C., 1995, Crustal velocity models for the Archean Abitibi greenstone belt from seismic refraction data, Can. J. Earth Sci., 32, 149-166.

Grant, F. S., 1985, Aeromagnetic geology and ore environments, I. magnetite in igneous, sedimentary and metamorphic rocks: An Overview, Geoexploration, 23, 303-333.

Green, A. G., Cannon, W. F., Milkereit, B., Hutchinson, D. R., Davison, A., Behreultt, J. C, Spence, C., Lee, M. W., morela-L'Huissier, P., and Agena, W. F., 1989, A "GLIMPCE" of the Great Lakes, *in* Properties and Processes of Earth's Lower Crust, Edited by R. F. Mereu, St. Mudler, and D. M. Fountain, American Geophysical union, Geophysical Monographon, 51, 65-80.

Green, A. G., Milkereit, B., Percival, J., Davidson, A., Parrish, R., Cook, F., Geis, W., Cannon, W., Hutchinson, D., West, G., and Clowes, R., 1990, Origin of deep crustal reflections: seismic profiling across high grade metamorphic terranes in Canada, Tectonophysics, 173, 627-638.

Green, A. G., Milkereit, B., Spencer, C., Hutchinson, D. R., Cannon, W. F., Lee, M. W., Agera, W. F., Behrendt, J. C., and Hinze, W. J., 1988, Central structure of the Grenville Front and adjacent terranes, Geology, 16, 788-792.

Gregotski, M. E., Jensen, O., and Arkani-Hamed, J., 1991, Fractal stochastic modeling of aeromagnetic data, Geophysics, 56, 1706-1715.

Grieder, W. S., 1996, Variance fractal dimension for signal feature enhancement and segmentation from noise, M. Sc. Thesis, The University of Manitoba, Winnipeg, Canada.

Grieder, W., and Kinsner, W., 1994, Speech segmentation by variance fractal dimension, Proceedings of 1994 Canadian Conference on Electrical and Computer Engineering, II,

481-485.

Grieve, A. F., 1990, Shocked minerals and K/T controversy, EOS Trans. AGU, 71, 1792.

Grieve, R. A. F., 1992, An impact model of the Sudbury Structure, *in* Large Meteorite Impacts and Planetary Evolution, edited by B. O. Dressler, R. A. F. Grieve, and V. L. Sharpton, the Geological Society of America, Special Paper 293, 119-132.

Grieve, R. A. F., 1994, An impact model of the Sudbury Structure, *in* Proceedings of the Sudbury - Noril'sk Symposium, Ontario Geological Survey, Special Volume 5, 119-132.

Grieve, R. A. F., Stöffler, D., and Deutsch, A., 1991, The Sudbury Structure: Controversial or misunderstood?, J. Geophys. Res., 96, 22753-22764.

Gupta, V., Grant, F. S., and Card, K. D., 1984, Gravity and magnetic characteristics of the Sudbury Structure, *in* the Geology and Ore Deposits of the Sudbury Structure, edited by E. G. Pye, A. J. Naldrett, and P. E. Giblin, Ontario Geological Survey, Special Volume 1, 381-410.

Hearst, R. B., Morris, W. A., and Thomas, M. D., 1992, Magnetic interpretation along the Sudbury Structure Lithoprobe transect, *in* Large Meteorite Impacts and Planetary Evolution, edited by B. O. Dressler, R. A. F. Grieve and V. L. Sharpton, the Geological Society of America, Special Paper 293, 33-43.

Hearst, R. B., Morris, W. A., and Thomas, M. D., 1994, Magnetic interpretation along the Sudbury Structure Lithoprobe transect, Geophys. Res. Lett., 21, 951-954.

Hirt, A. M., Lowie, W., Clendenen, W. S., and Kligfield, R., 1993, Correlation of strain and the anisotropy of magnetic susceptibility in the Onaping Formation: Evidence for a near circular origin of the Sudbury Basin, Tectonophysics, 225, 231-254.

Hole, J. A., 1992, Nonlinear high resolution three dimensional seismic traveltime tomography, J. Geophys. Res., 97, 6553-6562.

Hood, P., 1961, Paleomagnetic study of the Sudbury Basin, J. Geophys. Res., 66, 1235-1241.

Irving, R., Asudeh, I., Forsyth, D., Mortimer, D., Argyle, M., Zelt, C., Mereu, R., Hamilton, D., Kohler, W., Carrol, P., Vasudevan, K., Barnes, A., Kellet, R., Moon, W. M., Seguin, M., and Jessop, J., 1993, 1992 LITHOPROBE Abitibi-Grenville seismic refraction survey: Acquisition and processing report, LITHOPROBE Report #30.

Jiao, L., and Moon, W. M., 1998, Application of Length Fractal Dimension Technique for Automatic Picking of First Arrival Times: Lithoprobe Seismic Processing Facility, Newsletter, 11, 69-72.

Jiao, L., and Moon, W. M., 2000, Detection of Seismic Refraction Signal using Variance Fractal Dimension Technique, Geophysics, 64, 286-292.

Jiao, L., Moon, W. M., and Kinsner, W., 1997, Variance fractal dimension analysis of seismic refraction signals, *in* Proceedings of IEEE WESCANEX 97 Conference on Communications, Power and Computing, 116-120.

Kanasewich, E. R., and Chiu, S. K. L., 1985, Least squares inversion of spatial seismic refraction data, Bull. Seism. Soc. Am., 75, 865-880.

Katsube, T. J., and Salisbury, M., 1994, Implications of laboratory electrical measurements on interpretation of EM-surveys and origin of the Sudbury Structure, Geophys. Res. Lett., 21, 947-950.

Kellett, R. L., Barnes, A. E., and Rive, M., 1993, The deep structure of the Grenville

Front: A new perspective from western Quebec, Can. J. Earth Sci., 31, 282-292.

Ketchum, J. W. F., Heaman, L. M., Krogh, T. E., Culshaw, N. G., and Jamieson, R. A., 1998, Timing and thermal influence of late orogenic extension in the lower crust: A U-Pb geochronological study from the southwest Grenville orogen, Canada, Precambrian Res., 89, 25-45.

Kinsner, W., 1996, Fractal and chaos engineering (Lecture Notes), The University of Manitoba, Winnipeg, Canada.

Krogh, T. E., 1994, Precise U-Pb ages for Grenvillian and pre-Grenvillian thrusting of Proterozoic and Archean metamorphic assemblages in the Grenville Front Tectonic Zone, Canada, Tectonics, 13, 963-982.

Krogh, T. E., Davis, D. W., and Corfu, F., 1984, Precise U-Pb zircon and baddeleyite ages for the Sudbury area, *in* The Geology and Ore Deposits of the Sudbury Structure, edited by E. G. Pye, A. J. Naldrett, and P. E. Giblin, Ontario Geological Survey, Special Volume 1, 431-446.

Lee, M. W., 1990, Traveltime inversion using transmitted waves of offset VSP data, Geophysics, 55, 1089-1099.

Lightfoot, P. C., Keays, R. R., Morrison, G. G., and Bite, A., 1997, Geochemical relationships in the Sudbury Igneous Complex: Origin of the main mass and offset dikes, Economic Geology, 92, 289-307.

Livelybrooks, D., Mareschal, M., Elais, E., and Smith, J. T., 1996, Magnetotelluric delineation of the Trillabelle massive sulphide body in Sudbury, Ontario, Geophysics, 61, 972-986.

Loper, D. E., and McGartney, K., 1988, Catastrophic volcanism as a cause of iridium and shocked quartz found at the K/T boundary, EOS Trans. AGU, 69, 302.

Louder, K. Z., and Fan, J., 1998, Crustal structures of Grenville, Makkovik, and southern Nain provinces along the Lithoprobe ECSOOT transect: regional seismic refraction and gravity models and this tectonic implications[1], Can. J. Earth Sci., 35, 583-601.

Lowman, P. D., Jr., 1991, Original shape of the Sudbury Structure, Canada: A study with airborne imaging radar, Can. J. Remote Sensing, 17, 152-161.

Lowman, P. D., Jr., 1992, The Sudbury Structure as a terrestrial mare basin, Rev. Geophys., 30, 227-243.

Lowman, P. D., Jr., 1994, Radar geology of the Canadian Shield: A 20-year review, Can. J. Remote Sensing, 20, 198-209.

Masaitis, V. L., Shafranovsky, G. I., Grieve, R. A. F., Langenhorst, F., Peredery, W. V., Therriault, A. M., Balmasov, E. L., and Fedorova, I. G., 1999, Impact diamonds in the Suevitic Breccias of the Black Member of the Onaping Formation, Sudbury Structure, Ontaio, Canada, *in* Large Meteorite Impacts and Planetary Evolution II, edited by B. O. Dressler and V. L. Sharpton, the Geological Society of America, Special Paper 339, 317-321.

Maus, S., and Dimri, V. P., 1994, Scaling properties of potential fields due to scaling sources, Geophys. Res. Lett., 21, 891-894.

McGrath, P. H., and Broome, H. J., 1992, A gravity model for the Sudbury Structure, *in* Proceedings of the Sudbury - Noril'sk Symposium, Ontario Geological Survey, 21-31.

McGrath, P. H., and Broome, H. J., 1994, A gravity model for the Sudbury Structure

along the LITHOPROBE seismic lines, Geophys. Res. Lett., 21, 955-958.

Meldrum, A., Abdel-Rahman, A. F. M., Martin, R. F., and Wodicka, N., 1997, The nature, age and petrogenesis of the Cartier Batholith, north flank of the Sudbury Structure, Ontario, Canada, Precambrian Res., 82, 265-285.

Melosh, H. J., 1989, Impact Cratering: A Geologic Process, Oxford University Press, New York.

Mereu, R. E., Epili, D., and Green, A. G., 1990, Pg shingles: Preliminary results from the onshore GLIMPCE refraction experiment, Tectonophysics, 173, 617-626.

Miao, X. G., 1995, Integrated seismic study for the Sudbury Structure and surrounding area, Ph. D. Thesis, The University of Manitoba, Winnipeg, Canada.

Miao, X., Moon, W. M., Milkereit, B., and Mwenifumbo, C. J., 1994, Three component vertical seismic profiling (VSP) experiment in the Sudbury Basin, Geophys. Res. Lett., 21, 939-942.

Milkereit, B., Eaton, D., Wu, J., Perron, G., and Salisbury, M. H., 1996, Seismic imaging of massive sulfide deposits: Part II, reflection seismic profiling, Economic Geology, 91, 829-823.

Milkereit, B., Green, A., and Sudbury Working Group, 1992, Deep geometry of the Sudbury Structure from seismic reflection profiling, Geology, 20, 807-811.

Milkereit, B., Green, A., Wu, J., White, D., and Adam, E., 1994, Integrated seismic and borehole geophysical study of the Sudbury Igneous Complex, Geophys. Res. Lett., 21, 931-934.

Moon, W., and Jiao, L., 1998, Sudbury impact structure modeling with high resolution seismic refraction survey results, J. Royal Astr. Soc. Canada, 92, 250-257.

Moon, W., and Miao, X., 1997, Crustal structure northwest of the Sudbury meteorite-impact structure (LITHOPROBE reflection-seismic AGT line 42), Geos. J., 1, 189-201.

Moon, W., Serzu, M., and Kublick, E., 1990, Application of high resolution seismic technique in Precambrian terrain (Sudbury, Ontario), Technical Report #158, The University of Manitoba, Winnipeg, Canada.

Moon, W., Ushah, A, Singh, V., and Bruce, B., 1988, Application of 2-D Hilbert transform in geophysical imaging with potential field data, IEEE transactions on Geoscience and Remote Sensing, 26, 502-510.

Moriya, H., and Niitsuma, H., 1996, Precise detection of a P-wave in low S/N signal by using time-frequency representations of a triaxial hodogram, Geophysics, 61, 1453-1466.

Morris, W. A., 1984, Paleomagnetic constraints on the magmatic, tectonic, and metamorphism evolution of the Sudbury Basin region, *in* the Geology and Ore Deposits of the Sudbury Structure, edited by E. G. Pye, A. J. Naldrett, and P. E. Giblin, Ontario Geological Survey, Special Volume 1, 411-427.

Morrison, G. G., 1984, Morphological features of the Sudbury Structure in relation to an impact origin, *in* the Geology and Ore Deposits of the Sudbury Structure, edited by E. G. Pye, A. J. Naldrett, and P. E. Giblin, Ontario Geological Survey, Special Volume 1, 513-520.

Muir, T. L., 1984, The Sudbury Structure, considerations and models of an endogenic origin, *in* the Geology and Ore Deposits of the Sudbury Structure, edited by E. G. Pye, A. J. Naldrett, and P. E. Giblin, Ontario Geological Survey, Special Volume 1, 449-489.

Muir, T. L., and Peredery, W. V., 1984, The Onaping Formation, *in* the Geology and Ore Deposits of the Sudbury Structure, edited by E. G. Pye, A. J. Naldrett, and P. E. Giblin, Ontario Geological Survey, Special Volume 1, 139-210.

Müller-Mohr, V., 1992, Breccias in the basement of a deeply eroded impact structure, Sudbury, Canada, Tectonophysics, 216, 219-226.

Murat, M. E., and Rudman, A. J., 1992, Automated first arrival picking: A neural network approach, Geophys. Pros., 40, 587-604.

Naldrett, A. J., 1984, Summary, discussion and synthesis, *in* the Geology and Ore Deposits of the Sudbury Structure, edited by E. G. Pye, A. J. Naldrett, and P. E. Giblin, Ontario Geological Survey, Special Volume 1, 533-569.

Naldrett, A. J., 1999, Summary: Development of ideas on Sudbury geology, 1992-1998, *in* Large Meteorite Impacts and Planetary Evolution II, edited by B. O. Dressler and V. L. Sharpton,the Geological Society of America, Special Paper 339, 431-442.

Naldrett, A. J., and Hewins, R. H., 1984, The main mass of the Sudbury Igneous Complex, *in* the Geology and Ore Deposits of the Sudbury Structure, edited by E. G. Pye, A. J. Naldrett, and P. E. Giblin, Ontario Geological Survey, Special Volume 1, 235-274.

Norman, M. D., 1994, Sudbury Igneous Complex: Impact melt or endogenous magma? Implications for lunar crustal evolution, *in* Large Meteorite Impacts and Planetary Evolution, edited by B. O. Dressler, R. A. F. Grieve and V. L. Sharpton, the Geological Society of America, Special Paper 293, 331-341.

Peitgen, H.-O., Jurgens, H., and Saupe, D., 1992, Chaos and Fractals: New Frontiers of Sciences, Springer-Verlag.

Peredery, W. N., and Morrison, G. G., 1984, Discussion of the origin of the Sudbury

Structure, *in* the Geology and Ore Deposits of the Sudbury Structure, edited by E. G. Pye, A. J. Naldrett, and P. E. Giblin, Ontario Geological Survey, Special Volume 1, 491-511.

Pilkington, M., and Grieve, R. A. F., 1992, The geophysical signature of terrestrial impact craters, Rev. Geophys., 30, 161-181.

Pilkington, M., and Todoeschuck, J. P., 1993, Fractal magnetization of continental crust, Geophys. Res. Lett., 20, 627-630.

Pisarenko, V. F., Kushnir, A. F., and Savin, I. V., 1987, Statistical adaptive algorithm for estimation of onset moments of seismic phases, Phys. Earth Planet Inter., 47, 4-10.

Popelar, J., 1972, Gravity interpretation of the Sudbury area, *in* New Developments in Sudbury Geology, edited by J. V. Guy-Bray, the Geological Association of Canada, Special Paper 11, 103-115.

Press, W. H., Flannery, B. P., Teukolsky, S. A., and Vetterling, W. T., 1989, NUMERICAL RECIPES, Cambridge University Press.

Riller, U., and Schwerdtner, W. M., 1997, Mid-crustal deformation at the southern flank of the Sudbury Basin, central Ontario, Canada, Geol. Soc. Am. Bull., 109, 841-854.

Riller, U., Schwerdtner, W. M., Halls, H. C., and Card, K. D., 1999, Transpressive tectonism in the eastern Penokean orogen, Canada: Consequences for Proterozoic crustal kinematics and continental fragmentation, Precambrian Res. 93, 51-70.

Ristau, J., 1999, Application of synthetic aperture radar interferometry in the study of the Nahanni earthquake region, M. Sc. Thesis, The University of Manitoba, Winnipeg, Canada.

Rivard, B., Kellett, R. L., Sairt-Jean, R., and Singhroy, V., 1994, Characterization of

faulting and dyke intrusion in the Benny deformation zone, north range of Sudbury, from airborne magnetics and SAR, Can. J. Remote Sensing, 20, 324-328.

Rivard, B., and Toutin, T., 1995, A mosaic of airborne SAR imagery for geological mapping in rolling topography, Can. J. Remote Sensing, 21, 75-78.

Robertson, M. C., and Sammis, C. G., 1995, Fractal analysis of three-dimensional spatial distributions of earthquakes with a percolation interpretation, J. Geophys. Res., 100, 609-620.

Robertson, P. B., and Grieve, R. A. F., 1975, Impact structures in Canada: Their recognition and characteristics, J. Royal Astro. Soc. Canada, 69, 1, 1-21.

Robertson, P. B., and Roy, J. L., 1979, Shocked-diminished paleomagnetic remanent at the Charlevoir Impact Structure, Quebec, Can. J. Earth Sci., 16, 1842-1856.

Rondot, J., 1994, Recognition of eroded astroblemes, Earth Sci. Rev., 35, 311-365.

Roest, W. R., and Pilkington, M., 1994, Restoring post-impact deformation at Sudbury; A circular argument, Geophys. Res. Lett., 959-966.

Roscoe, S. M., and Card, K. D., 1992, Early Proterozoic tectonics and metallogeny of the Lake Huron region of the Canadian Shield, Precambrian Res., 58, 99-119.

Rousell, D. H., 1984, Onwatin and Chelmsford Formations, *in* the Geology and Ore Deposits of the Sudbury Structure, edited by E. G. Pye, A. J. Naldrett, and P. E. Giblin, Ontario Geological Survey, Special Volume 1, 211-218.

Salisbury, M. H., Iuliucci, R., and Long, C., 1994, Velocity and reflection structure of the Sudbury Structure from laboratory measurements, Geophys. Res. Lett., 21, 923-926.

Shanks, W. S., and Schwerdtner, W. M., 1991a, Structural analysis of the central and southwestern Sudbury Structure, Southern Province, Canadian Shield, Can. J. Earth Sci., 28, 411-430.

Shanks, W. S., and Schwerdtner, W. M., 1991b, Crude quantitative estimates of the original northwest-southeast dimension of the Sudbury Structure, south-central Canadian Shield, Can. J. Earth Sci., 28, 1677-1686.

Shoemaker, E. M., 1998, Impact cratering through geological time, J. Royal Astro. Soc. Canada, 92, 297-309.

Singh, V., Moon, W. M., Singhroy, V., and Slaney, V. R., 1993, Preliminary study of airborne multi-sensor geophysical data from Sudbury, Ontario, Can. J. Remote Sensing, 19, 160-169.

Singhroy, V., Slaney, R., Lowman, P., Harris, J., and Moon, W., 1993, Radarsat and radar geology in Canada, Can. J. Remote Sensing, 19, 338-351.

Spray, J. G., and Thompson, L. M., 1995, Friction melt distribution in a multi-ring impact basin, Nature, 373, 130-132.

Stephan, J. B., and Dalziel, I. W. D., 1974, The Sudbury Basin, the Southern Province, the Grenville Front, and the Penokean orogeny, Geol. Soc. Am. Bull., 85, 1571-1580.

Stevenson, J. S., 1990, The volcanic origin of the Onaping Formation, Sudbury, Canada, Tectonophysics, 171, 249-257.

Stevenson, J. S., and Stevenson, L. S., 1980, Sudbury, Ontario, and the meteorite theory, Geos. Canada, 7, 103-108.

Stöffler, D., Deutsch, A., Avermann, M., Bischoff, L., Brockmeyer, P., Buhl, D., Lakomy, R., and Muller-Mohr, V., 1994, The Formation of the Sudbury Structure, Canada:

Towards a unified impact model, *in* Large Meteorite Impacts and Planetary Evolution, edited by B. O. Dressler, R. A. F. Grieve, and V. L. Sharpton, the Geological Society of America, Special Paper 293, 303-318.

Thompson, L. M., and Spray, J. G., 1994, Pseudotachylytic rock distribution and genesis within the Sudbury impact structure, *in* Large Meteorite Impacts and Planetary Evolution, edited by B. O. Dressler, R. A. F. Grieve, and V. L. Sharpton, the Geological Society of America, Special Paper 293, 275-287.

Thompson, L. M., and Spray, J. G., 1996, Pseudotachylyte petrogenous constraints from the Sudbury impact structure, Contrib. Mineral Petrol., 125, 359-374.

Todoeschuck, J. P., and Jensen, O. G., 1988, Joseph geology and seismic deconvolution, Geophysics, 53, 1410-1414.

Turcotte, D. L., 1986, Fractals and fragmentation, J. Geophys. Res., 91, 1921-1926.

Turcotte, D. L., 1992, Fractals and Chaos in geological and geophysics, Cambridge University Press.

van Breemen, O., Davidson, A., Loveridge, W. D., and Sullivan, R. D., 1986, U-Pb zircon geochronology of Grenville tectonics, granulites and igneous precursors Parry Sound, Ontario, *in* The Grenville Province, edited by J. M. Moore, A. Davidson, and A. J. Baer, Geological Association of Canada, Special Paper 31, 191-207.

Vasudevan, K., Li, Q., Robley, K., and Cook, F. A., 1995, Fractal behavior of the crust in deep seismic reflection profiles, Lithoprobe seismic processing Facility, Newsletter, 8, 93-98.

Vidale, J. E., 1988, Finite-difference calculation of travel times, Bull. Seism. Soc. Am., 78, 2062-2076.

Vidale, J. E., 1990, Finite-difference calculation of traveltimes in three dimensions, Geophysics, 55, 521-526.

Walker, R. J., Morgan, J. W., Naldrett, A. J., Li, C., and Fassett, J. D., 1991, Re-Os isotope systematics of Ni-Cu sulfide ores, Sudbury Igneous Complex, Ontario: Evidence for a major crustal component, Earth and Planet. Sci. Lett., 105, 416-429.

Waters, K., H., 1992, Reflection Seismology: A tool for energy resource exploration, Krieger Publication Company.

White, D. J., Easton, R. M., Culshaw, N. G., Milkereit, B., Forsyth, D. A., Carr, S., Green, A. G., and Davison, A., 1994a, Seismic images of the Grenville orogen in Ontario, Can. J. Earth Sci., 31, 293-307.

White, D. J., Milkereit, B., Wu, J. J., Salisbury, M. H., and Mwenifumbo, J., 1994b, Seismic reflectivity of the Sudbury Structure North Range from borehole logs, Geophys. Res. Lett., 21, 935-938.

Winardhi, S., and Mereu, R. F., 1997, Crustal velocity structure of the Superior and Grenville provinces of the southeastern Canadian Shield, Can. J. Earth Sci., 34, 1167-1184.

Won, J. S., 1993, Inversion of synthetic aperture radar (SAR) data using Born approximation and SAR image enhancement for geological application, Ph. D. Thesis, The University of Manitoba, Winnipeg, Canada.

Wu, J., Milkereit, B., and Boerner, D., 1994, Timing constraints on deformation history of the Sudbury impact structure, Can. J. Earth Sci., 31, 1654-1660.

Wu, J., Milkereit, B., and Boerner, D. E., 1995, Seismic imaging of the enigmatic Sudbury Structure, J. Geophys. Res., 100, 4117-4130.

Young, G. A., 1972, Gosses Bluff airborne magnetic survey, Geophys. Pros., 30, 83-91.

Zelt, C. A., and Ellis, R. M., 1988, Practical and efficient ray tracing in two-dimensional media for rapid traveltime and amplitude forward modelling, Can. J. Expl. Geophys., 24, 16-31.

Zelt, C. A., and Forsyth, D. A., 1994, Modeling wide-angle seismic data for crustal structure: Southeastern Grenville Province, J. Geophys. Res., 99, 11687-11704.

Zelt, C. A., and Smith, R. B., 1992, Seismic traveltime inversion for 2-D crustal velocity structure, Geophys. J. Int., 108, 16-34.

Zolnai, A. I., Price, R. A., and Helmstaedt, H., 1984, Regional cross section of the Southern Province adjacent to Lake Huron, Ontario: implications of the tectonic significant of Murray Fault Zone, Can. J. Earth Sci., 21, 447-456.

Appendix A

Variance Fractal Dimension

Technique of Detecting Seismic Phases

Accurate determination of the traveltimes of various seismic phases is an important first step in many seismic forward and inverse modeling procedures, including wave propagation, seismic tomography. In this thesis, three algorithms out of four used in seismic modeling required picking seismic events before inverse modeling. The author picked first breaks, later arrivals such as PcP, Pc, PmP, Pn and Pr phases manually in the early research stage. The author quickly learned that the hand-picking of seismic events is ineffective and can contain easily subjective bias. As a part of this thesis research, computer-based picking techniques of seismic phases were investigated. Two fractal determination techniques were developed: a variance fractal dimension trajectory technique discussed in this Appendix A and a length fractal dimension technique discussed in Appendix B. Since the first technique was published in Geophysics, 2000, Appendix A only includes a copy of the paper titled by "Detection of seismic refraction signals using variance fractal dimension technique" (Jiao and Moon, 2000).

GEOPHYSICS, VOL. 65, NO. 1 (JANUARY-FEBRUARY 2000); P. 286–292, 12 FIGS.

Detection of seismic refraction signals using a variance fractal dimension technique

Lingxiu Jiao* and Wooil M. Moon*

ABSTRACT

Seismic signals in deep crustal surveys are often contaminated with various types of noise, mainly caused by the low signal-to-noise (S/N) earth environment. A variance fractal dimension (VFD) technique is investigated and tested with real data sets for detection of seismic refraction signals from background noise. The data tested in this study were collected during the 1992 Lithoprobe Abitibi-Grenville Transect high-resolution refraction and wide-angle reflection seismic experiments. The sharpness of transition features on the VFD trajectory is used as a criterion for distinguishing specific seismic phases. The window size and window interval applied in the application of VFD technique were determined using synthetic seismic data for generation of the optimum VFD trajectory. The window size of 48 samples and the window interval of 8 sample intervals were chosen to calculate the fractal dimension values and create the trajectories for detecting phases *Pg*, *Pn*, *PmP*, and ground roll. The VFD technique was also tested and applied for automatic detection of the first breaks in the high-resolution seismic reflection data collected during the 1990 Lithoprobe regional and high-resolution seismic surveys. The sharp transition features corresponding to the first arrivals in the seismic reflection data are distinct and provide us with a robust and powerful tool for separating the seismic signals from noise.

INTRODUCTION

Accurate determination of the traveltimes of various seismic phases is an important first step in many seismological forward and inverse modeling procedures, including wave propagation problems, seismic tomography, and seismic reflection data processing, and also in earthquake seismology. Generally, the recognizable onset of the signal amplitude and waveform features is used as a criterion for detecting the arrivals of various seismic signal phases. However, manual picking of seismic events can not provide consistent results (because of subjective bias) nor is it effective. Therefore, computer-based methods of detecting seismic signal arrivals are desirable if they can be more consistent and provide us with accurate unbiased traveltime estimation of seismic events.

There are various techniques provided for the automatic picking of seismic signals in the literature. Gelchinsky and Shtivelman (1983) proposed a method based on the specific correlation properties of seismic signals for determining the first arrivals. However, if noise is spatially correlated over a short distance, this correlation method is less effective. Pisarenko et al. (1987) developed a statistical adaptive algorithm to pick *P*-wave signals. Murat and Rudman (1992) developed a back-propagation neural network technique for detecting the first breaks in low signal-to-noise (S/N) data. Earle and Shearer (1994) developed an algorithm to detect earthquake events on the basis of the short-term average to long-term average ratio calculated from an envelope function of the seismographs. Moriya and Niitsuma (1996) detected *P*-wave signals in low S/N data in the time-frequency domain by a statistical test using a crosscorrelation coefficient. In general, automatic picking of the first arrivals depends on the characteristic features of the specific seismic phase and also on the S/N ratio. If the S/N ratio is low, accuracy becomes a very serious problem. Hence, it is usually very difficult to pick the late arriving seismic signals because of contamination of unwanted signals arriving prior to the ones being detected.

The concept of fractals has been applied to various earth processes and geophysical methods, such as geological fragmentation phenomena, earthquake-related tectonic features, analysis of geophysical potential field, and fractal and multifractal analysis of the spatial distribution of earthquakes (Turcotte, 1986, 1992; Todoeschuck and Jensen, 1988; Gregotski et al., 1991; Pilkington and Todoeschuck, 1993; Maus and Dimri, 1994; Robertson and Sammis, 1995; Godano et al., 1996). Since the 1980s, various fractal analysis techniques have been used in seismic data processing and interpretations, such as fractal characteristic analysis of seismic reflection patterns, fractal

Manuscript received by the Editor January 29, 1998; revised manuscript received March 03, 1999.
*Department of Geological Sciences, University of Manitoba, 240 Wallace Building, Winnepeg, Manitoba R3T 2N2, Canada. E-mail: lingxiu@cc.umanitoba.ca; wmoon@cc.umanitoba.ca.

scaling properties of seismic reflection data, and detection of first breaks (Crossley and Jensen, 1989; Vasudevan et al., 1995; Boschetti et al., 1996). Crossley and Jensen (1989) attributed block distribution of the amplitude energy of seismic events along a profile to horizontal and vertical heterogeneities of the subsurface velocity structure by comparison between the synthetic seismographs of the velocity structure introduced by fractal noise and the theoretical velocity model. Vasudevan et al. (1995) discussed the capability for designing filter parameters on a seismic reflection profile and the relationship between seismic attribute characteristics and regional geological features using a box dimension fractal technique. Boschetti et al. (1996) discussed first-break detection using the fractal-based "divider method" and "Hurst method," which show a gently slopping transition at the boundary between signal and noise on a fractal dimension curve.

In this paper, transition features on the variance fractal dimension (VFD) trajectory are applied to identification of the seismic refraction signals from relatively low S/N data and the first arrivals of the seismic reflection data. The VFD decreases rapidly for a correlated signal. On the other hand, the fractal dimension of uncorrelated noise is high. Therefore, there is a transition feature at the boundary of the signal wavelet and background noise on the VFD trajectory. The seismic signal is coherent within a wavelet time duration. Thus, the VFD technique can be used to detect the arrival of seismic signals including both first breaks and late arriving signals (Jiao et al., 1997). In order to create effective VFD trajectories of the observed seismic data, synthetic seismic data were first tested to determine the window size and window interval, which are two important parameters for generating the optimum trajectories.

VARIANCE FRACTAL DIMENSION

Fractal dimension analysis depends on the property of self-similarity or self-affinity in multiple scaling objects. The basic idea of VFD was discussed on the basis of Brownian motion (Grieder, 1996). For analysis of time series data, the VFD technique does not create window artifacts, which normally occur in fractal spectral analysis, because the requirement of a window in the Fourier sense is not needed (Kinsner, 1996). Therefore, VFD analysis is suitable for studying the internal processes of a time series signal.

Variance measurement for a given scale

For a 1-D discrete time series signal B with N samples and equal time sampling unit δt (Figure 1), the increment of the signal amplitude over the unit time increment is simply

$$b_{j1} = B_{j+1} - B_j, \tag{1}$$

where B_j is the signal amplitude at the jth sample, j is a sampling signal index, and b_{j1} is the increment of the signal amplitude over one time increment unit.

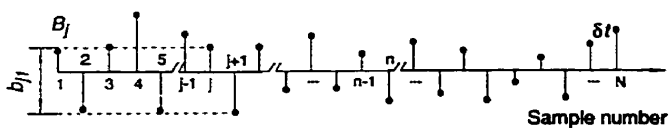

FIG. 1. One-dimensional digital time series signal B_j.

Considering a finite number n or a set of samples (Figure 1), the sample variance σ_{fs}^2 for a given set of samples n can be expressed as

$$\sigma_{fs}^2 = (1/n_1)\sum_{j=1}^{n_1}(b_{j1} - \overline{b_1})^2 \tag{2}$$

or

$$\sigma_{fs}^2 = \left[\sum_{j=1}^{n_1}(b_{j1})^2 - \left(\sum_{j=1}^{n_1} b_{j1}\right)^2 \Big/ n_1\right] \Big/ n_1, \tag{2a}$$

where n_1 is the number of the variable taken into account for the calculation of variance on one unit scale in the given set (n samples), and $\overline{b_1}$ is the arithmetic mean of the given set of samples. Rewriting equation (2) in terms of the mean $\bar{b}$ of the whole population of the samples (N), we have

$$\sigma_{fs}^2 = (1/n_1)\sum_{j=1}^{n_1}[(b_{j1} - \bar{b}) - (\overline{b_1} - \bar{b})]^2. \tag{3}$$

The expectation of the square of the difference between the amplitude increment b_{j1} and a mean $\bar{b}$ of a whole population of the signal is given as a variance σ^2, which has the form

$$E\left((b_{j1} - \bar{b})^2\right) = \sigma^2. \tag{4}$$

The expectation of $(\overline{b_1} - \bar{b})^2$ can then be derived as

$$\begin{aligned} E\left((\overline{b_1} - \bar{b})^2\right) &= E\left(\left((1/n_1)\sum_{j=1}^{n_1} b_{j1} - \bar{b}\right)^2\right) \\ &= E\left(\left[\left(\sum_{j=1}^{n_1}(b_{j1} - \bar{b})\right)\Big/ n_1\right]^2\right) \\ &\le E\left(\sum_{j=1}^{n_1}(b_{j1} - \bar{b})^2 \Big/ n_1\right)\Big/ n_1 = \sigma^2/n_1. \end{aligned} \tag{5}$$

Then, following relationship is obtained:

$$0 \le E\left((\overline{b_1} - \bar{b})^2\right) \le \sigma^2/n_1. \tag{6}$$

Taking the expectation of the sample variance of equation (3), we have

$$\begin{aligned} E(\sigma_{fs}^2) &= E\left(\left(\sum_{j=1}^{n_1}(b_{j1} - \bar{b})^2 - n_1(\overline{b_1} - \bar{b})^2\right)\Big/ n_1\right) \\ &= \left[\sum_{j=1}^{n_1} E\left((b_{j1} - \bar{b})^2\right) - n_1 E\left((\overline{b_1} - \bar{b})^2\right)\right]\Big/ n_1. \end{aligned} \tag{7}$$

If one puts the maximum value of $E((\overline{b_1} - \bar{b})^2)$ [i.e., $E((\overline{b_1} - \bar{b})^2) = \sigma^2/n_1$] into equation (7), one can obtain a factor for modifying the variance estimation from equation (2a) that is called biased estimation (Grieder and Kinsner, 1994; Kinsner, 1996):

$$E(\sigma_{fs}^2) = \left(\sum_{j=1}^{n_1}\sigma^2 - n_1\frac{\sigma^2}{n_1}\right)\Big/ n_1$$

or

$$E(\sigma_{fs}^2) = (n_1 - 1)/n_1 \cdot \sigma^2. \quad (8)$$

The biased variance estimation from equation (2a) is modified by the factor $n_1/(n_1 - 1)$. Then, the unbiased estimation ($\sigma_{fs'}^2$) for the variance of a given set in the whole population is given (Grieder, 1996; Kinsner, 1996):

$$\sigma_{fs'}^2 = (n_1/(n_1 - 1)) \cdot (1/n_1) \cdot \left[\sum_{j=1}^{n_1}(b_{j1})^2 - \left(\sum_{j=1}^{n_1} b_{j1}\right)^2 \Big/ n_1\right], \quad (9)$$

or, in a simple form,

$$\sigma_{fs'}^2 = \left[\sum_{j=1}^{n_1}(b_{j1})^2 - \left(\sum_{j=1}^{n_1} b_{j1}\right)^2 \Big/ n_1\right] \Big/ (n_1 - 1). \quad (10)$$

Equation (10) is used for the variance calculation for one unit time scale in analysis of the fractal dimension.

Dimension calculation for multiple scales

In the previous section, the variance calculation was formulated for signal amplitude increments over one unit time scale. If we consider multiple time scales, the increments of the signal amplitude over s unit time scales can be written as $b_{js} = B_{j+s} - B_j$, where s denotes the time increment sampling interval and is given by $1, 2, \ldots, K$. However, the variance measurements for multiple time scales can be carried out following the same procedure as described in the previous section. The relationship between the variance over s-unit time scales [Var(b_s)] and the time scales ($s\delta t$) can be established as the following power law (Kinsner, 1996):

$$\mathrm{Var}(b_s) \propto |s\delta t|^{2H}, \quad (11)$$

where H is the Hurst exponent and δt is one unit time sampling interval (a constant in this case). Furthermore, the exponent H can be expressed in logarithmic form as

$$\log \mathrm{Var}(b_s) = 2H \log |s\delta t| + C,$$

or simply,

$$\log \mathrm{Var}(b_s) = 2H \log |s| + C', \quad (12)$$

where C and C' are constants. The variance measurement over one single time scale provides one corresponding single point on the logarithmic plot of the variance of the signal amplitude increment versus the time increment.

In this paper, the scale index s is chosen to be 1, 2, 3, and 4 (Figure 2), as used in a noise separation technique (Grieder, 1996; Kinsner, 1996). The logarithmic values of time increments and the corresponding variances are calculated according to the following form:

$$X_s = \log(s), \quad (13)$$

$$Y_s = \log \mathrm{Var}(b_s). \quad (14)$$

The slope, S, of the log-log plot of X_s versus Y_s is determined by least squares. The Hurst exponent is then

$$H = S/2. \quad (15)$$

The VFD (D_σ) then becomes

$$D_\sigma = E + 1 - H, \quad (16)$$

where E is the embedding Euclidean dimension (Peitgen et al., 1992; Kinsner, 1996). For a 1-D time series signal, E is equal to 1. The location of the VFD value on 1-D time series signal corresponds to a point at the end of the current window (Figure 2).

Trajectory generation

The VFD calculated using the procedure described in the previous section gives a single point corresponding to the end point of the current window. By moving the current window to a new window location with a chosen window interval and following the dimension calculation procedure, one can obtain the new VFD value corresponding to the end point of the new window. By repeating this procedure over the entire signal length, one can generate the VFD curve or trajectory over the entire data set (Figure 2).

There are two important parameters here which critically affect the trajectory behavior: the window size and window interval. When the window size is small, the arrivals of adjacent signals can be identified by the transition features on the dimension trajectory. When the window size is large, the dimension

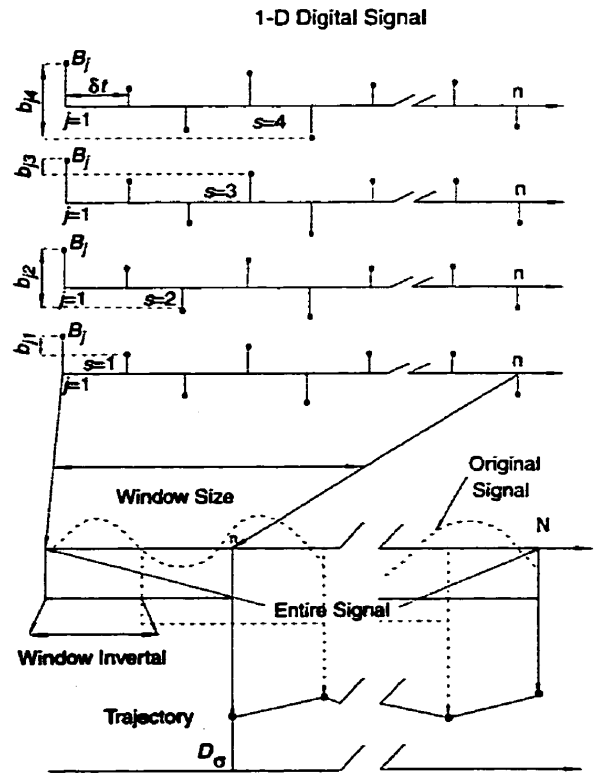

FIG. 2. A noise separation increment diagram and its trajectory generation.

variation effect of unwanted early arrivals on the trajectory can be reduced, and then the late arriving signals can be detected. A small spacing interval can cause a redundant calculation. In contrast, a large spacing interval will contribute to loss of the detail information on the trajectory. Thus, optimum suitable window size and window interval are important for generating effective trajectories.

SEISMIC DATA

Synthetic seismic refraction data were first computed using a simple velocity model to test the above algorithm. The test data were used not only to estimate the window size and window interval for generating effective VFD trajectories for the observed seismic data, but also to examine and evaluate the VFD technique for detecting seismic signals. Both seismic-refraction and high-resolution seismic-reflection data collected during the 1990 (Miao, 1995) and 1992 (Iring et al. (1993) Lithoprobe AGT seismic experiments in the Sudbury area were then tested for detecting real seismic signals from background noise.

Synthetic seismic data

The test synthetic seismogram was sampled at a rate of 0.01 s, which is similar to the field observed seismic refraction data in frequency. To calculate a realistic VFD, random noise with less than 1% of the maximum value of the signal amplitude was first added to the synthetic data for the variance measurement. During the measurement, overlapping or moving the time increment over one unit step was used. Figure 3 shows the power law relationship between the variance of signal amplitude increments and the time increments with four scalings ($1\delta t$, $2\delta t$, $3\delta t$, $4\delta t$) in the logarithmic plot. The slope of the least-squares regression lines shows a clear difference between the true seismic signal and background noise.

In this paper, four window sizes, each with 36, 48, 64 and 128 samples, were tested (Figure 4). When the size of the window becomes too large, the dimension of the later signal occurred within the time defined by the sum of the length of the window size and the period of the previous signal is affected and contaminated by the previous signal; a small window size is better to distinguish the late arrival signal on the dimension trajectory. Window sizes with 36 and 48 samples give good transition

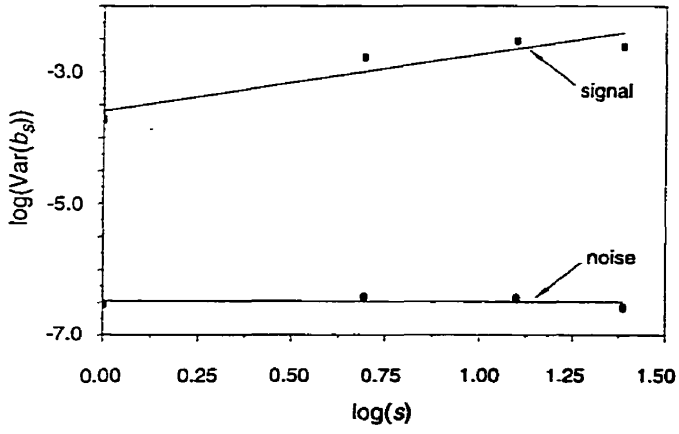

FIG. 3. Logarithmic plot of the variance of the amplitude increment (b_s) versus time increment (s) for signal and noise.

features on the dimension trajectories. However, considering various types of noise in seismic refraction data, including short period seismic diffraction pattern and scattered signals, the 48-sample window size was selected because it is less affected by short period noise (which can become serious if the window size becomes too small). Nevertheless, for the *PmP* phase reflected from the Moho, the window size was increased to 128 samples, and the transition feature improved because the influence of the dimension variation of early arriving seismic signals prior to the *PmP* phase was reduced.

Figure 5 shows trajectory features of the 48-sample window size with different window intervals (1, 4, 8, and 12 sampling intervals). The small window intervals of 1 and 4 sampling intervals show redundant calculations. If we use a large window interval (12 sampling intervals), the transition feature on the trajectory is smoothed too much. The 8-sampling window interval creates a good trajectory that represents the curvature

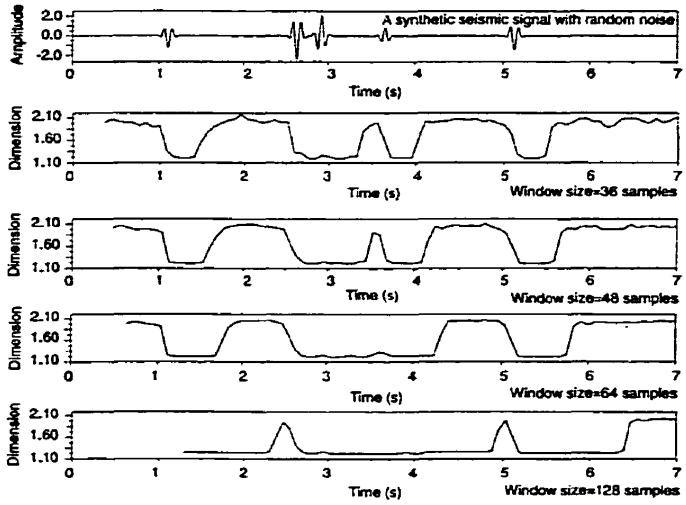

FIG. 4. Variance fractal dimension trajectories for a synthetic seismic signal with window sizes of 36, 48, 64, and 128 samples.

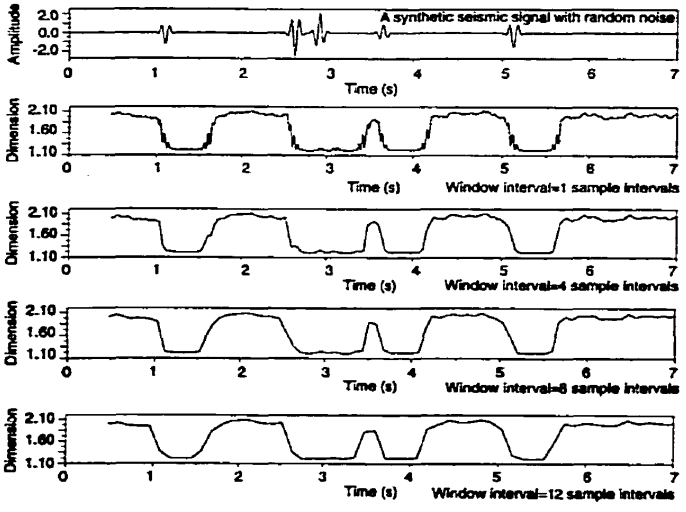

FIG. 5. Variance fractal dimension trajectories with window size of and window intervals of 48 samples and 1, 4, 8 and 12 sampling intervals.

of the transition features with sufficient details while saving computer time. Thus, the 8-sampling window interval was used in the subsequent processing of real field data.

High-resolution seismic-refraction data

The seismic refraction data traces used in this paper were selected from two in-line data sets ab2 and ab10 and one fan-shot data set ab2 recorded during the 1992 Lithoprobe AGT seismic experiments. The test seismic traces were resampled at about 120 samples per second and gain was reset. The data were processed with a 8 to 35 Hz band-pass filter, gain control, trace balancing, and bad trace editing. The fractal dimension analysis was then implemented on these preprocessed data.

In the case of the *Pg* phase (from the fan-shot ab2 data), there is a clear transition feature where the signal arrives (Figure 6). In other words, the trajectory curve changes sharply at the boundary between the signal and background noise. The dimension value of the signal is approximately 1.25, and the dimension value of the background noise is approximately 1.75. As offset distance increases, the *Pn* wave arrives first. Since the energy of the *Pn* phase is relatively weak, the *Pn* signal can easily be contaminated with background noise, and the *Pn* arrivals are then usually difficult to pick. However, the fractal dimension trajectory shows a sharp transition feature at the onset of the *Pn* signal (data from the in-line ab10 data) (Figure 7). This type of sudden changes in the trajectory can be used for identifying *Pn* arrivals. Figure 7 indicates that the dimension values of the *Pn* arrivals are approximately 1.35, whereas the fractal dimensions of the background noise are relatively high

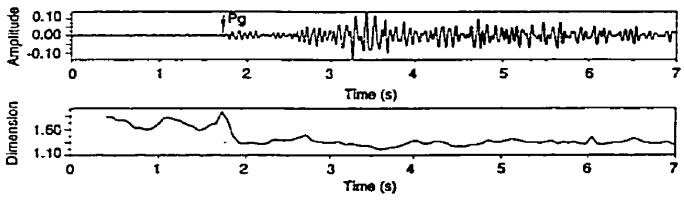

FIG. 6. Variance fractal dimension trajectory for the *Pg* seismic signal from the fan-shot ab2 data.

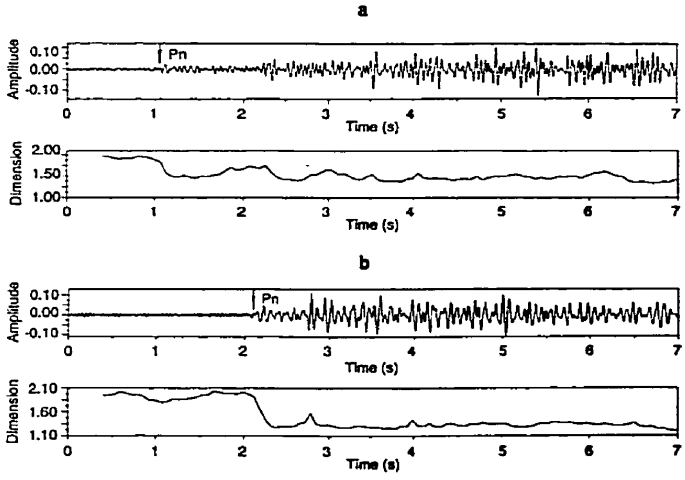

FIG. 7. Variance fractal dimension trajectory for the *Pn* seismic signal from the in-line ab10 data. (a) Trace 4, (b) trace 35.

1.85. The ground roll signal clearly visible in the in-line ab2 data has low-frequency and high-amplitude characteristics, and the estimated fractal dimension value is in the range of 1.1 to 1.2 (Figure 8). The fractal dimension value of the background noise increases to 2.10 in this data set.

For identification of the late arriving signals such as *PmP*, a large window size with 128 samples was selected to reduce the noise correlation arriving prior to the *PmP* signal. Figure 9 shows the processing sequence for the *PmP* phases with the large window size. There are only two clear transition features on the trajectories with a 128-sampling window size in both Figures 9a and 9b: the first transition corresponding to the first-break arrival and the second transition corresponding to the *PmP* phase arrival. Therefore, the dimension trajectory with a large window size more clearly reveals the arrival time of the *PmP* signal from background noise than a smaller window size because it can reduce small variations in the fractal dimension between adjacent signals. The fractal dimension values

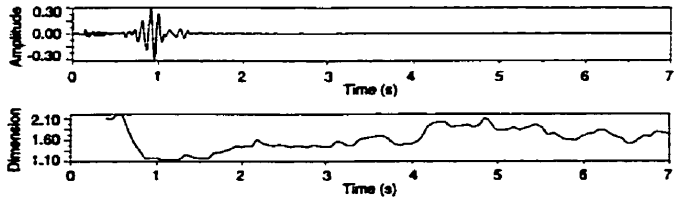

FIG. 8. Variance fractal dimension trajectory for the ground roll seismic signal from the in-line ab2 data.

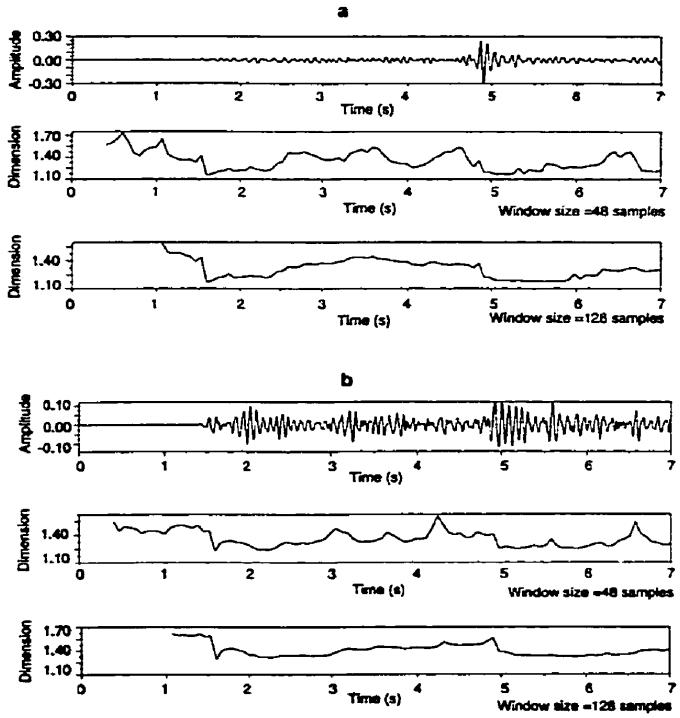

FIG. 9. Variance fractal dimension trajectory for the *PmP* seismic signal from the fan-shot ab2 data. (a) Trace 26, (b) trace 28. The upper and lower trajectories in (a) were computed using sample window sizes of 48 and 128, respectively. The upper and lower trajectories in (b) were computed using sample window sizes of 48 and 128, respectively.

corresponding to noise in both two traces are less than 1.70, whereas the fractal dimensions of the signal are in a range of 1.25 to 1.40. Although the fractal dimensions of the signals slightly increase with the large window size, the transitions on the trajectories can be effectively used for picking the arrivals of the *PmP* signals.

If the signal is badly contaminated with strongly correlated noise, the transition features cannot effectively detect the first arrival signals (Figure 10). However, after adding a random noise with amplitude values equivalent to those of the background noise into the signal, the transition feature at the boundary between the first arrival and the background noise is greatly improved (Figure 10). The VFD of a correlated noise signal is low, which shows a similar curvature to the correlated seismic signal (Figure 10). Hence, this causes a difficulty in detecting seismic signals from a correlated background noise. However, for a white noise signal, variances corresponding to four scaling time increments have similar values. This implies that its slope in a log-log plot of the logarithmic variance and time scale is small. Consequently, the VFD of a white noise is high. Thus, the VFD curvature of the background noise is dramatically changed from low value to high value after introducing a random noise whereas, because the amplitude of a random noise added in a seismic trace is small, the VFD curvature of the seismic signal keeps the similar feature created by the signal without an introduced random noise. Therefore, a random noise added into a signal can break up the correlated noise and improve the probability of distinguishing the seismic signals from the background noise.

High-resolution seismic-reflection data

The seismic reflection data tested were chosen from shot gather 516 of line 40-1 collected during 1990 Lithoprobe AGT regional and high-resolution seismic experiments. Four synchronized vibrators were employed as source with a sweep frequency from 30 to 140 Hz (Miao, 1995). The sampling interval was 2 ms. The fractal technique was applied on the correlated reflection data set. The values of the data were normalized, and a random noise with values less than 8% of the maximum value of the amplitude was added to all traces because of the correlated background noise. The 48-sample window size and 8-sampling window interval were applied in detecting the first breaks of the reflection data because the sampling number within a wavelet is comparable to that of the seismic refraction data.

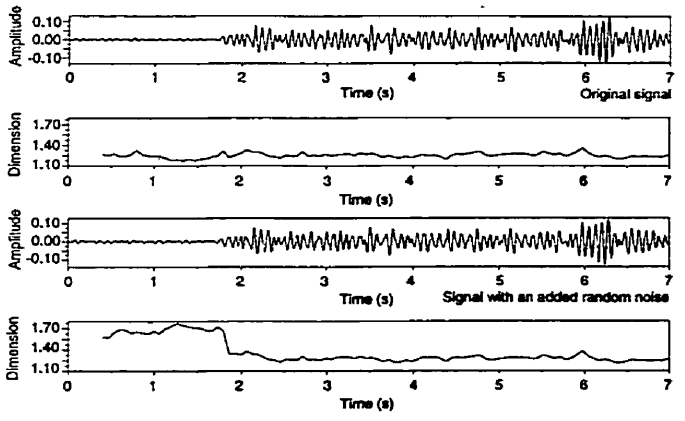

FIG. 10. The improved variance fractal dimension trajectory for the seismic refraction signal from the fan-shot ab2 data. The upper trajectory was computed from the original data, the lower trajectory was computed with added random noise.

Figure 11 shows the comparison between the VFD trajectory corresponding to the original signal (shot gather 516 of line 40-1) and the improved VFD trajectory corresponding to the signal with added random noise. Figure 12 indicates the sharp transition features on the trajectories associated with 10 traces (151–160). The dimension value of the reflection signals is approximately 1.35, and the dimension value of the noise is approximately 1.9. The clear sharp transition feature between the first arrival signal of the seismic reflection data and background noise presents a feasibility of the application of the VFD technique in detecting the first breaks of seismic reflection data.

CONCLUSIONS

The VFD technique provides us with a new approach which can detect coherent seismic signals from background noise by sharp transition features on the dimension trajectory. A window size of 48 samples and a window interval of 8 sampling intervals are optimum for generating clear transition features on the dimension trajectory for detecting seismic first arrivals and ground roll phases as well as arrival of the weaker *Pn* phase refracted from the Moho. In addition, the large window size with 128 samples can be used to reduce the effect of short period waves arriving prior to the *PmP* phase and distinguish the late arriving *PmP*.

The fractal dimension values of the observed seismic refraction and reflection signals are usually low at approximately 1.25 and 1.35, respectively, and those of noise are usually high at an average of 1.7 and 1.9, respectively.

For the data sets tested in this paper, a white noise with the maximum amplitude value equivalent to the maximum amplitude value of background noise can be added to the tested data to effectively break up strongly correlated noise and to

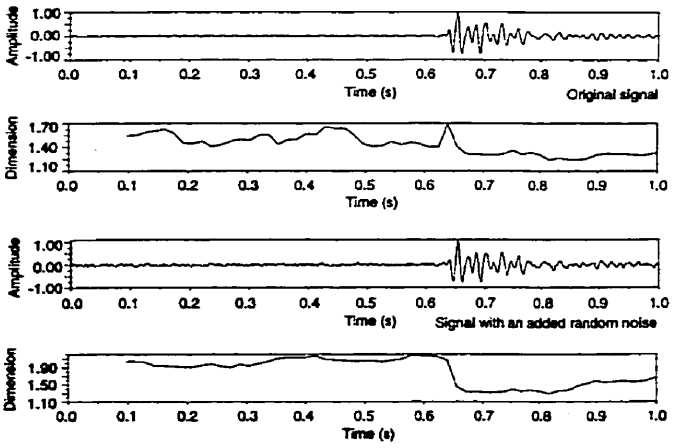

FIG. 11. The variance fractal dimension trajectories for the seismic reflection signal (trace 40 of the shot gather 516 of line 40-1). The upper trajectory was computed from the original data, the lower trajectory was computed with added random noise.

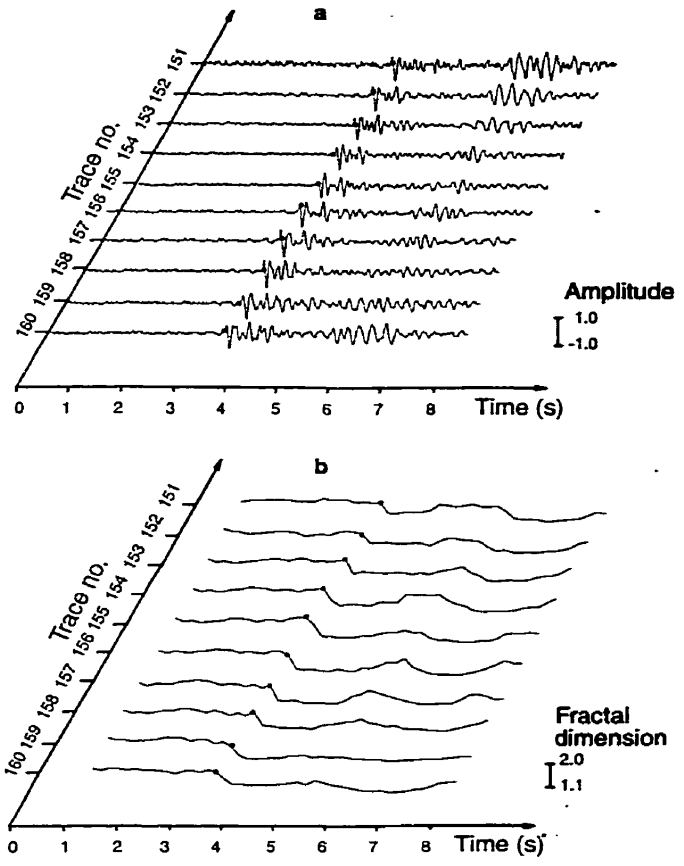

FIG. 12. Variance fractal dimension trajectories for the seismic reflection signals from traces 151–160 of the shot gather 516 of line 40-1. (a) Traces 151 to 160, (b) variance fractal dimension trajectories for traces 151–160. Dots represent the first arrivals picked by the technique.

generate the optimum VFD trajectory for identifying the *Pn* or *Pg* phases of seismic refraction signals from the noise. The pattern of the first arrival of seismic reflection signals is more recognizable than that of the weaker *Pn* phases of seismic refraction signals. The VFD technique proposed can be therefore effectively applied in detection of the first arrivals of seismic reflection signals and provides a powerful tool for the automatic picking of the first breaks in seismic reflection data.

AKNOWLEGMENTS

This research was funded by NSERC operating grant (A #7400) to W. M. Moon. The authors thank Prof. W. Kinsner for various innovative ideas, discussions, and supports during this research. Fanle Meng also provided continuing support during the study.

REFERENCES

Boschetti, F., Dentith, M. D., and List, R. D., 1996, A fractal-based algorithm for detecting first arrivals on seismic traces: Geophysics, **61**, 1095–1102.

Crossley, D. J., and Jensen, O. G., 1989, Fractal velocity models in refraction seismology: Pure Appl. Geophys., **131**, 62–76.

Earle, P. S., and Shearer, P. M., 1994, Characterization of global seismograms using an automatic-picking algorithm: Bull. Seis. Soc. Am., **84**, 366–376.

Gelchinsky, B., and Shtivelman, V., 1983, Automatic picking of first arrivals and parameterization of traveltime curves: Geophys. Prosp., **31**, 915–928.

Godano, C., Alonzo, M. L., and Bottari, A., 1996, Multifractal analysis of the spatial distribution of earthquakes in southern Italy: Geophys. J. Internat., **125**, 901–911.

Gregotski, M. E., Jensen, O., and Arkani-Hamed, J., 1991, Fractal stochastic modeling of aeromagnetic data: Geophysics, **56**, 1706–1715.

Grieder, W. S., 1996, Variance fractal dimension for signal feature enhancement and segmentation from noise: M.S. thesis, Univ. of Manitoba.

Grieder, W., and Kinsner, W., 1994, Speech segmentation by variance fractal dimension: Proc. 1994 Canadian Conf. on Electrical and Computer Engineering, **II**, 481–485.

Iring, R., Asudeh, I., Forsyth, D., Mereu, R., Kohler, W., and Working Group, 1993, 1992 Lithoprobe Abitibi-Grenville seismic refraction survey: Acquisition and processing report: Lithoprobe report 30.

Jiao, L., Moon, W., and Kinsner, W., 1997, Variance fractal dimension analysis of seismic refraction signals: Proc. IEEE WESCANEX 97 Conf. on Comm., Power and Computing, 116–120.

Kinsner, W., 1996, Fractal and chaos engineering (lecture notes): Univ. of Manitoba.

Maus, S., and Dimri, V. P., 1994, Scaling properties of potential fields due to scaling sources: Geophys. Res. Lett., **21**, 891–894.

Miao, X., 1995, Integrated seismic study for the Sudbury Structure, Canada, and surrounding area: Ph.D. thesis, Univ. of Manitoba.

Moriya, H., and Niitsuma, H., 1996, Precise detection of a *P*-wave in low S/N signal by using time-frequency representations of a triaxial hodogram: Geophysics, **61**, 1453–1466.

Murat, M. E., and Rudman, A. J., 1992, Automated first arrival picking: A neural network approach: Geophys. Prosp., **40**, 587–604.

Pisarenko, V. F., Kushnir, A. F., and Savin, I. V., 1987, Statistical adaptive algorithm for estimation of onset moments of seismic phases: Phys. Earth Plan. Int., **47**, 4–10.

Peitgen, H.-O., Jürgens, H., and Saupe, D., 1992, Chaos and fractals: New frontiers of sciences: Springer-Verlag.

Pilkington, M., and Todoeschuck, J. P., 1993, Fractal magnetization of continental crust: Geophys. Res. Lett., **20**, 627–630.

Robertson, M. C., and Sammis, C. G., 1995, Fractal analysis of three-dimensional spatial distributions of earthquakes with a percolation interpretation: J. Geophys. Res., **100**, 609–620.

Todoeschuck, J. P., and Jensen, O. G., 1988, Joseph geology and seismic deconvolution: Geophysics, **53**, 1410–1414.

Turcotte, D. L., 1986, Fractals and fragmentation: J. Geophys. Res., **91**, 1921–1926.

——— 1992, Fractals and chaos in geological and geophysics: Cambridge Univ. Press.

Vasudevan, K., Li, Q., Robley, K., and Cook, F. A., 1995, Fractal behavior of the crustal in deep seismic reflection profiles: Lithoprobe Seismic Processing Facility Newsletter, **8**, 93–98.

Appendix B

Length Fractal Dimension

Technique of Detecting Seismic Phases

In addition to investigating the feasibility of applying the variance fractal dimension technique in the detection of seismic phases, another type of fractal method, length fractal dimension technique, was also investigated and tested for distinguishing first breaks from high resolution seismic reflection data. Appendix A contains a paper providing a detailed description of the fractal concept, the method and procedure of a fractal technical performance. The fractal concepts and methodologies will not be repeated here. The method of computing the length fractal dimension is straightforward. Therefore, this Appendix B will not include a detail explanation of the concepts and procedure of the dimension calculation but only a description of its application. This information was originally published in the Newsletter of the Lithoprobe Seismic Processing Facility (Jiao and Moon, 1998).

B.1 Length Fractal Dimension

Fractal techniques have been recently applied in detection of seismic signals (Boschetti et al., 1996; Chang, 1997; Jiao et al., 1997, 2000). Boschetti et al. (1996) discussed the first-break detection using fractal-based 'Hurst method' with a gentle-sloping fractal

dimension curve. Chang (1997) applied Hausdroff dimension technique in detecting first arrivals in seismic reflection data and earthquake recording signals. In this appendix, a length fractal dimension technique is applied to demo and real data (processed with agc) for detection of first arrivals in seismic reflection signals. A sudden increase feature on the length fractal dimension curve (or trajectory) is used as a criterion for detecting first arrivals.

The length fractal dimension is determined through the measurement of geometric patterns and forms of a curve (Peitgen et al., 1992; Kinsner, 1996). The seismic signals in a trace can be simply regarded as geometric curve patterns. Hence, the fractal technique can be applied to the detection of seismic signals by analyzing of the complexity of the signal curve. Firstly, we select the measuring sticks or compasses at different scales. Then, we walk the stick or compass along a segment curve in a given time window counting the number of sticks and compasses. The length of the segment curve corresponding to the stick or compass can be easily obtained. The scaling relationship or the power law relation between the length and inverse of the scaling setting is exhibited by a straight line in log-log plot. The slope of the regression line in log-log plot is given as d. The length fractal dimension value is then calculated as the formula

$$D = 1 + d \tag{B.1}$$

where D is the length fractal dimension. This procedure of calculation of the length fractal dimension is repeated throughout one seismic trace by moving the given time window by a selected window spacing. Then, we obtain the length fractal dimension curve or trajectory (Kinsner, 1996). On the length fractal dimension curve or trajectory,

there is a sudden increase in the length dimension at the arrival time of the first break. This method is thus applied in picking first arrivals in seismic reflection data.

B.2 Application to Seismic Reflection Data

The demonstration data (sampled with 2 ms interval) from ITA INSIGHT seismic reflection data processing software package were first used to test the capability of the application of the length fractal dimension technique in detection of first arrivals. The basic stick or compass setting was given as one data point. Five scalings of stick or compass were then chosen with one data point increment respectively. The length of a segment curve within the given time window (10 data points segment) corresponding to the stick or compass was measured. Therefore, the length fractal dimension value was computed on the basis of the dimension formula described above. Generally, the picking time error is approximately 2 to 4 data points. Figures B.1 and B.2 show sudden increase features at the boundary between the first arrival and the background noise on the length fractal dimension curve or trajectory.

The seismic reflection data used in this study was chosen from profile 40 obtained during the 1990 Lithoprobe high resolution seismic reflection experiment in the Sudbury area. The seismic reflection data were sampled at 2 ms. To compare the dimension results with traces, the maximum amplitudes of the recording signals on traces were normalized to approximately 0.01. Figure B.3 shows the length fractal dimension curves or trajectories for traces 100 and 150 of profile 40. There is a sudden increase at the boundary between the first arrival and noise on the length fractal dimension curve or

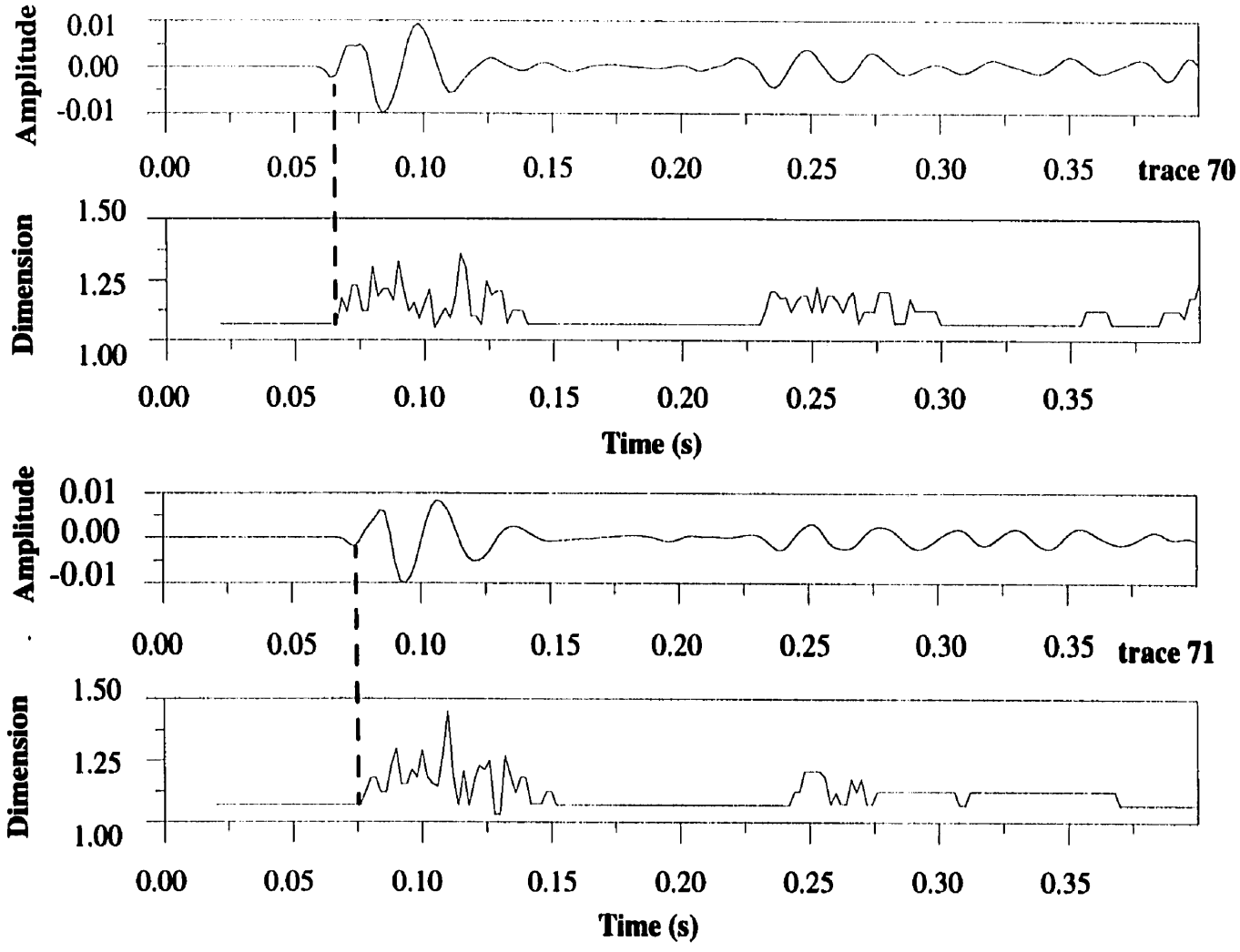

Figure B.1 Length fractal dimenison curves or trajectories for demo data (from ITA INSIGHT software package).

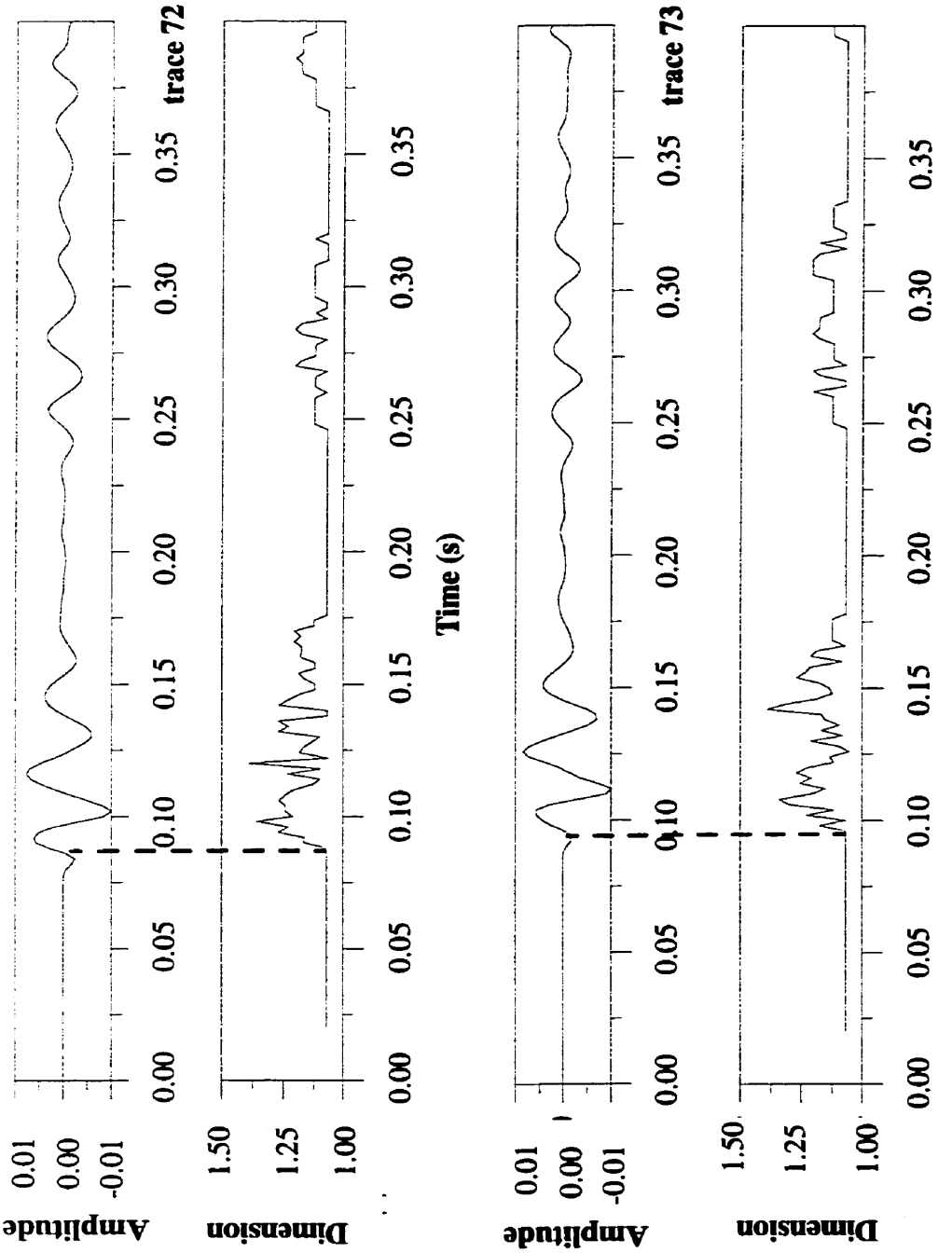

Figure B.2 Length fractal dimenison curves or trajectories for demo data (from ITA INSIGHT software package).

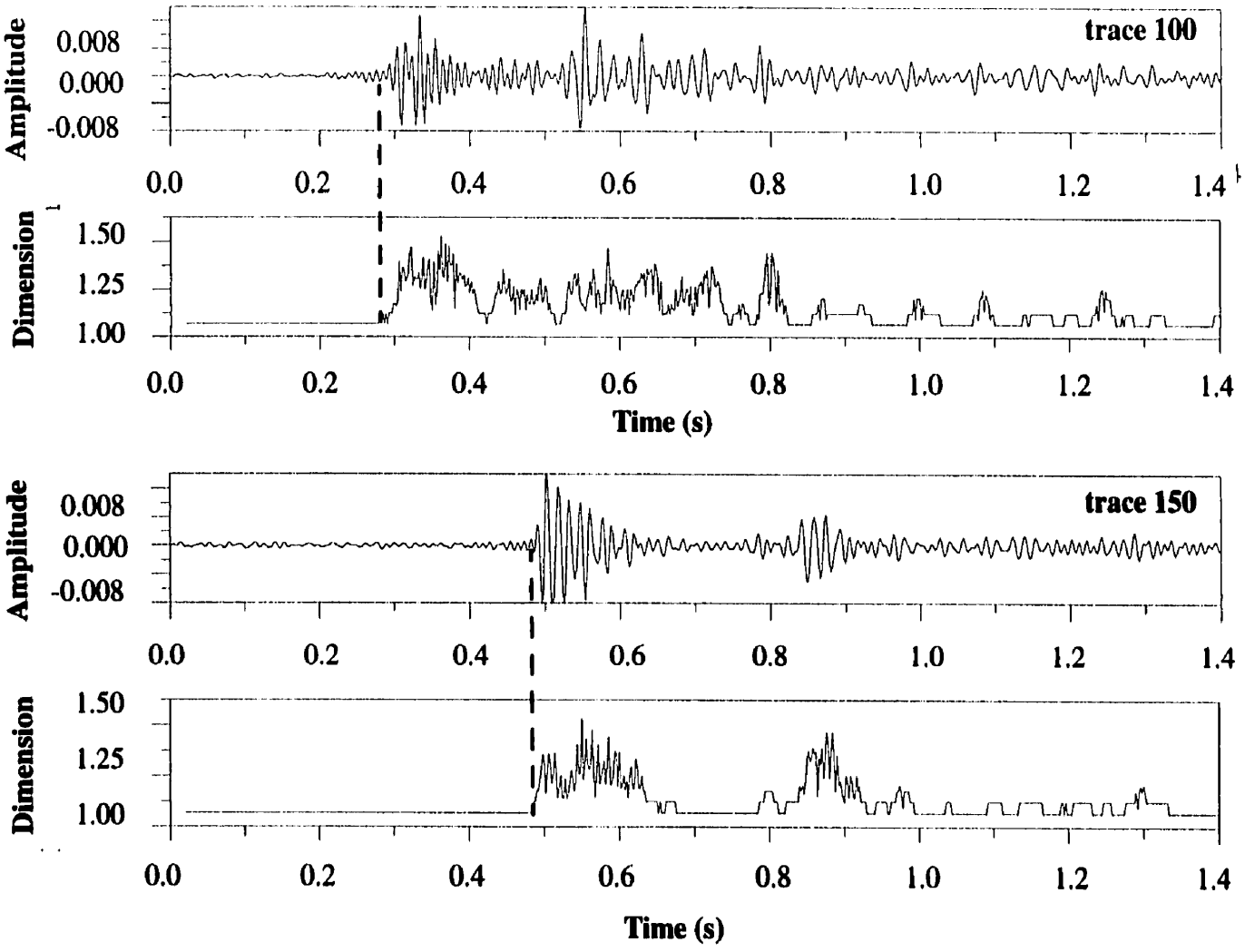

Figure B.3 Length fractal dimension curves for high resolution seismic reflection data (line in the Sudbury area).

trajectory, which identifies the first arrival. Figure B.4 indicates the picked first travel times for 21 traces from 170 to 190 of profile 40. The length dimension value of noise indicates a constant (about 1.06), whereas the dimension value of seismic signals increases (to about 1.1~1.5). Therefore, the sudden change on the length fractal dimension curve at the boundary between the signal and background noise shows us the capability of the length fractal dimension technique in automatic picking of the first arrival time of seismic reflection data.

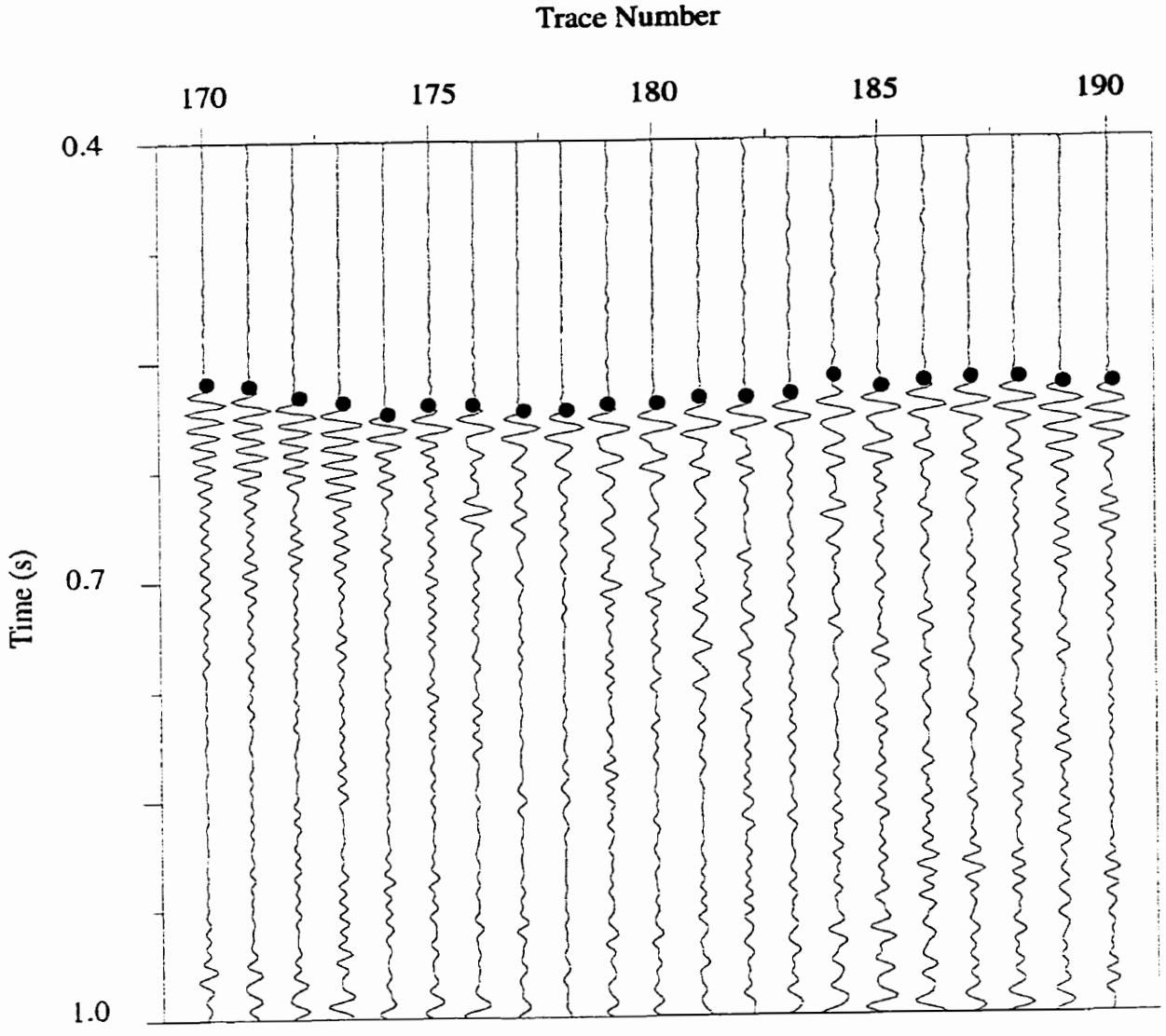

Figure B.4 Travel time pick for seismic reflection data (line 40) from Lithoprobe Sudbury survey. Dots: picked traveltimes.

Appendix C

Potential Field Data Processing and Anomalies

In addition to the investigation of the Sudbury geological structure using seismic methods, the available potential field data (gravity and magnetic), were also processed and imaged utilizing ER Mapper (Release 5.0/5.5) to obtain supplementary information. This appendix describes the basic processing steps and gives a preliminary interpretation of the structure delineated by the potential field data.

C.1 Processing Steps

As the main objectives of this study concerned the spatial distribution of the large-scaled structure, the gravity and magnetic data from the 1:1,000,000 Bouguer gravity and aeromagnetic anomaly maps compiled by the GSC in 1984 were used. The magnetic data were obtained from a geophysical database of the Sudbury study area established by Miao. The data coverage is illustrated in Figure C.1. The geological boundaries, such as the edge of the Sudbury Igneous Complex and major tectonic boundaries and faults, were also digitized and applied as the second layer to overlie geophysical images for more precise analysis and interpretation of the relationship between geophysical anomalies and tectonic structures.

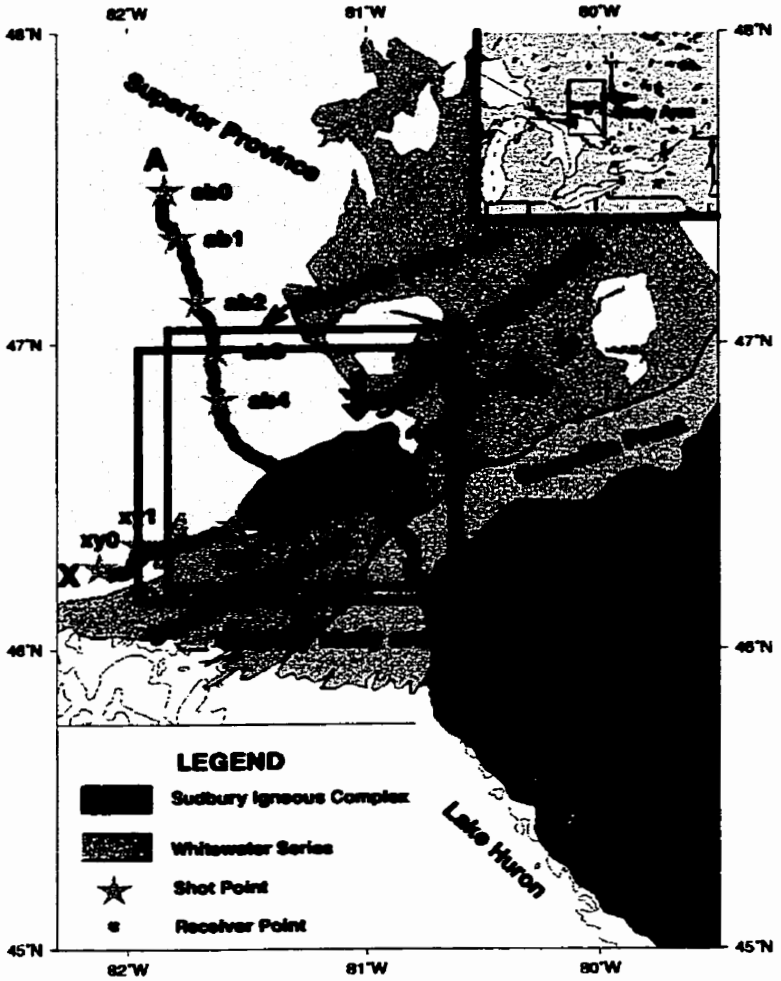

Figure C.1 Geological setting in the Sudbury study area and the potential field data coverage.

1. Gravity Data

The Bouguer gravity map was first digitized by using a Summagraphics digitizer and AutoCad (Release 13) installed on a PC running Windows 95. The digitized gravity data were interpolated to a regular grid form by using Grass (Release 4.1) installed on an IBM RS6000 workstation. The interpolated raster gravity data were then processed and visualized using ER Mapper.

Figure C.2a shows the Bouguer gravity anomaly image overlain by the geological boundaries of the Sudbury Structure and tectonic boundary of the Grenville Front Tectonic Zone. To illustrate the particular structural trend, a pseudo-sun angle (shading) technique provided in ER Mapper was applied to illuminate the gravity anomaly as if it represented a topographic surface. The elevation and azimuth of the sun angle represent the position of the artificial sun. The sun angle shading technique enhances structure trends perpendicular to or parallel to the azimuth. Figure C.2b represents a gravity image displayed at a sun angle shading of elevation 45^{o} and azimuth 45^{o} which emphasizes a southeastern linear high gravity anomaly located at the southern boundary of the Sudbury Structure. The anomaly extends to the southwest down to the southern edge at the study area.

The low-pass residual processing technique reduces short wavelength (local) anomalies responsible for gravity effects from shallow anomalous density bodies, and enhances long wavelength (regional) anomalies responsible for the effects from deeper buried anomalous bodies. Figure C.2c shows a low-pass residual gravity image shaded at a sun angle of elevation 4^{o} and azimuth 310^{o} which clearly illustrates the shapes of the Sudbury Basin and Sudbury Igneous Complex. A 5 km upward-continuation filter also enhances the long wavelength gravity anomalies in the Sudbury area (Figure C.2d).

2. Magnetic Data

A processing procedure similar to that employed in gravity data processing was also applied to total field aeromagnetic data. The aeromagnetic anomaly is illustrated as an image overlain by major geological boundaries (Figure C.3a). The shading technique is

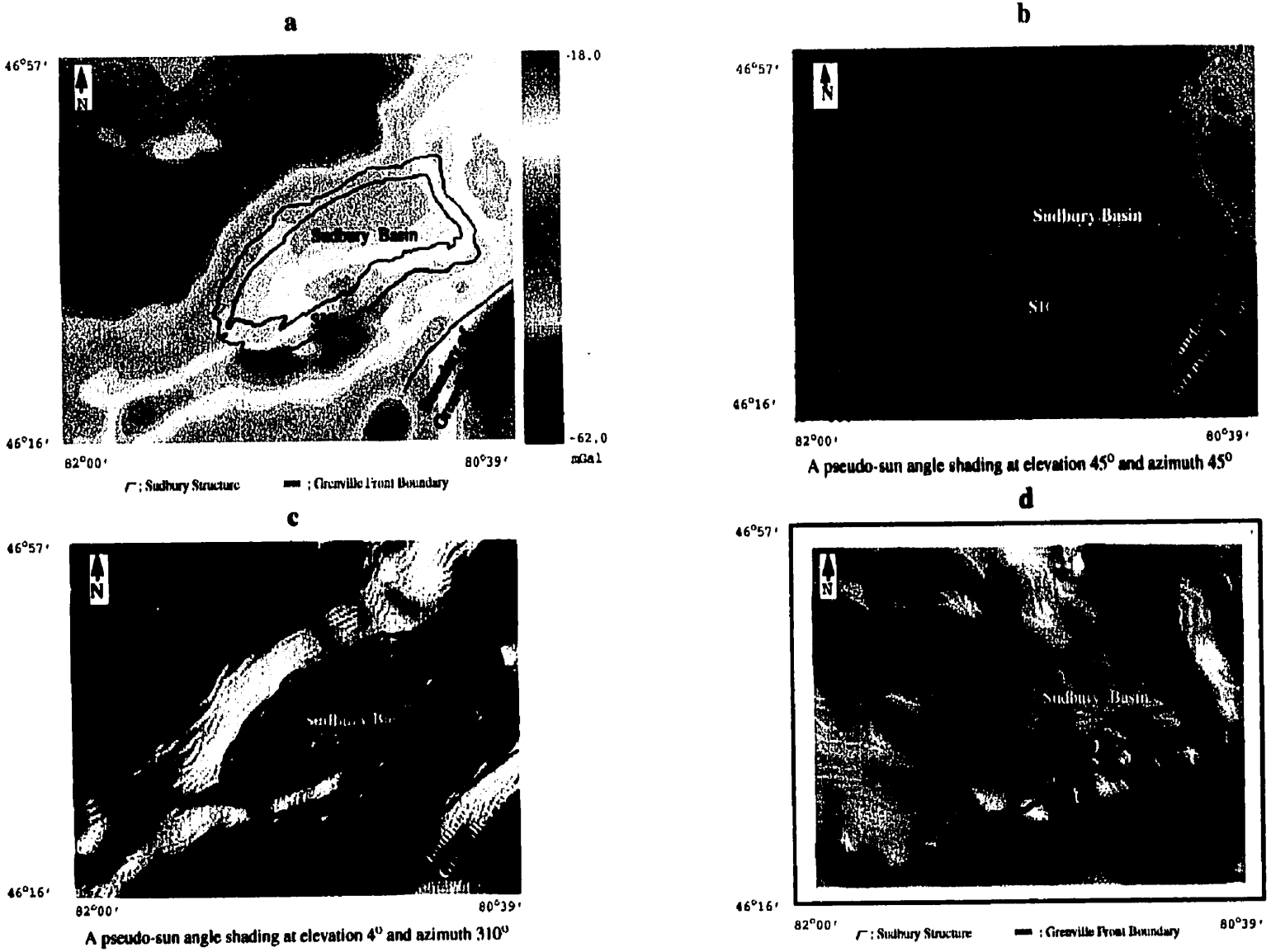

Figure C.2 **a**: Bouguar gravity anomaly in Sudbury; **b**: shaded relief Bouguer gravity anomaly image in the Sudbury area; **c**: low-pass residual shaded relief gravity anomaly image in the Sudbury area; **d**:5 km up-continuation Bouguer gravity anomaly in the Sudbury area.

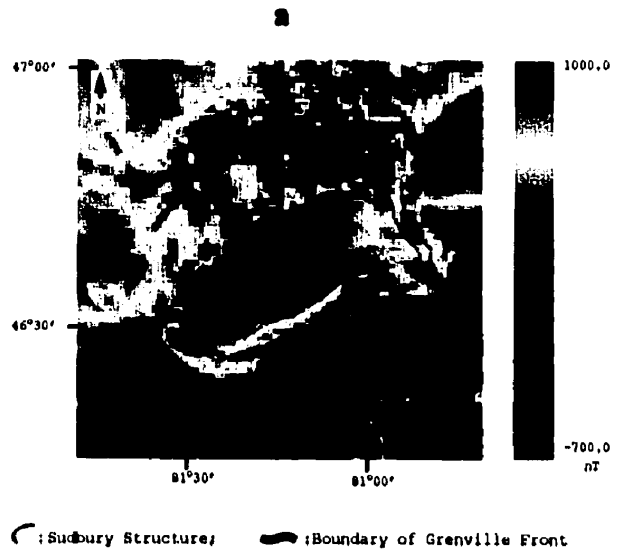

Figure C.3 **a**: Total field aeromagnetic anomaly map in the Sudbury area; **b**: shaded relief aeromagnetic anomaly image at a sun angle of elevation 45° and azimuth 45°; **c**: shaded relief aeromagnetic anomaly image at a sun angle of elevation 45° and azimuth 45°; **d**: second derivative aeromagnetic anomaly image.

important in visualization of magnetic images to emphasize linear structural features such as faults and dikes. Figure C.3b enhances a linear structure extending northwest to north-east direction visualized at the sun angle of azimuth 45° and elevation 45°. In contrast, an illumination at a sun angle of azimuth 267° and elevation 45° (Figure C.3c) was used to emphasize north-south or east-west trend structure features. Figure C.3d shows the second derivative gradient magnetic image which includes a number of very small anomalies outlining the boundary of the Sudbury Igneous Complex. Figures C.4a~C.4d indicate four 5 km upward continuation aeromagnetic anomaly images shaded at sun angles of elevation 45°, and azimuths of 45°, 134°, 219° and 267° respectively. An interesting ring-shaped magnetic anomaly surrounding the Sudbury Structure is revealed in all four images. The ring-shaped magnetic anomaly boundary is marked by a thick dashed line (Figures C.4a~C.4d).

C.2 Preliminary Interpretation

The Bouguer gravity anomaly features indicate that the Sudbury Structure occurs at a gravity gradient anomaly belt which trends in the northeast direction and possibly correlates to the Southern province rocks. There is a positive linear anomaly (Figures C.2a~C.2d) along the southern boundary of the Sudbury Igneous Complex that corresponds to high density mafic rocks (~2.88 g/cm^3) formed during the Proterozoic (McGrath and Broome, 1994). In the Bouguer gravity anomaly image (Figure C.2a), the Sudbury Igneous Complex was not sharply delineated due to its weak positive density contrast. However, it was clearly revealed by gravity images visualized by sun angle shad-

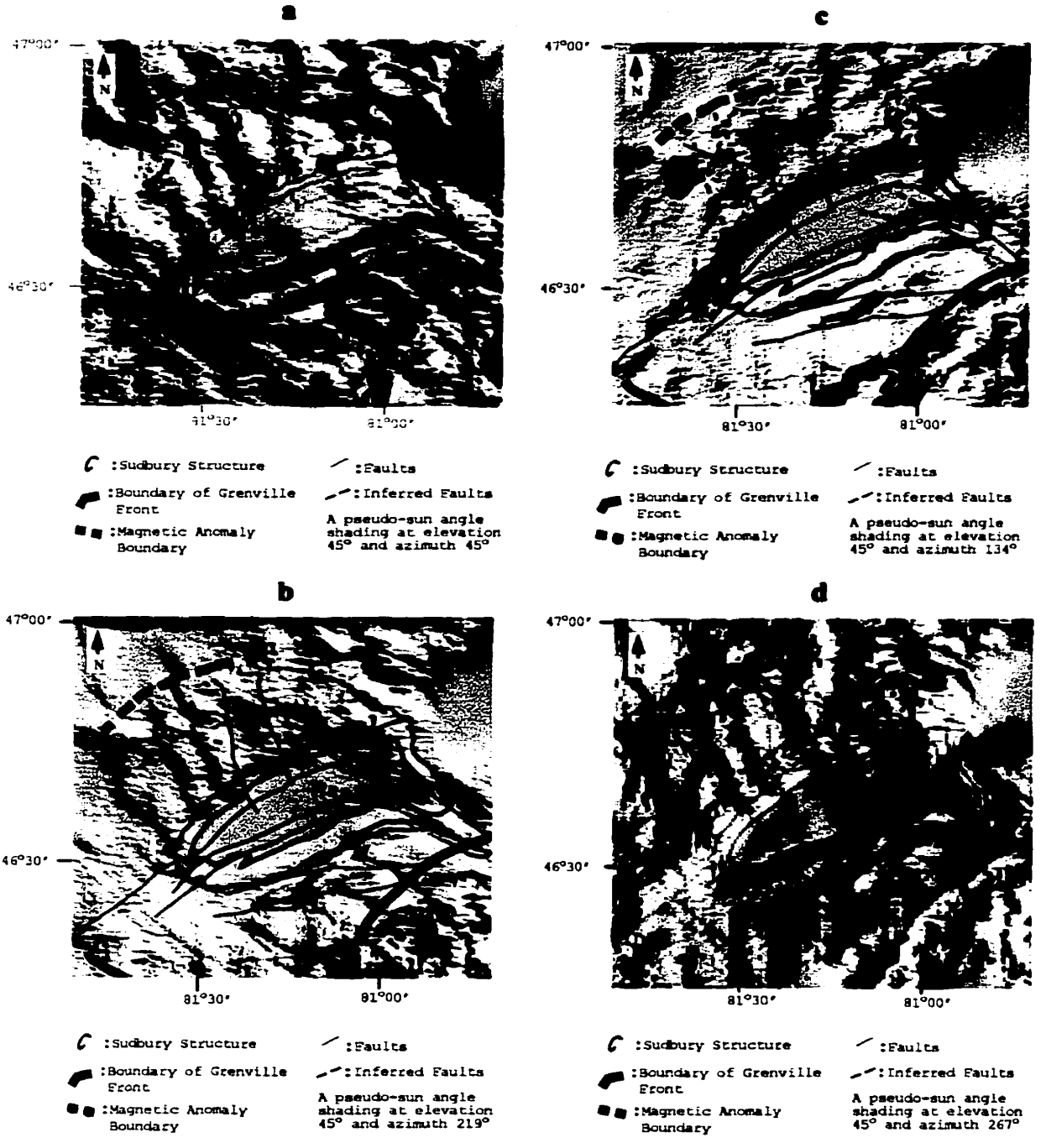

Figure C.4 **a**: shaded relief 5 km upward continuation areomagnetic anomaly image in the Sudbury area at a sun angle of elevation 45° and azimuth 45°; **b**: shaded relief 5 km upward continuation areomagnetic anomaly image at a sun angle of elevation 45° and azimuth 134° ; **c**: shaded relief 5 km upward continuation areomagnetic anomaly image at a sun angle of elevation 45° and azimuth 219°; **d**: shaded relief 5 km upward continuation areomagnetic anomaly image at a sun angle of elevation 45° and azimuth 267°.

ing technique and low-pass residual process (Figures C.2b and C.2c) where local gravity anomalies, such as the positive linear anomaly mentioned above, were reduced and a weak linear anomaly associated with the Sudbury Igneous Complex rocks especially in the northeast was enhanced.

The outline of the Sudbury Structure was more clearly delineated in the aeromagnetic anomaly image (Figure C.3a). The shaded relief magnetic images illuminated at a sun angle of elevation 45° and azimuth 45° delineates linear magnetic features with northwest and northeast trends corresponding to a series of faults and dikes (Figure C.3b). North-northwest faults, such as Sandcherry Creek Fault and Fecunis Fault in the north of the Sudbury Structure (Figure 2.2), were revealed clearly by linear magnetic features (Figure C.3b). The Sudbury structural boundary and the Grenville Front were clearly illuminated on the magnetic image shaded at a sun angle of elevation 45° and azimuth 267° (Figure C.3c). The second derivative gradient aeromagnetic anomaly in Figure C.3d shows that small-scaled magnetic anomalies surround the Sudbury Basin, whereas the anomaly in the center is relatively weak. These features suggest that the near-surface magnetic sources limit to the preferential edge of the Sudbury Basin. These magnetic anomalies could correspond to the highly magnetized rocks, such as norite (350×10^{-4} S. I.) of the Sudbury Igneous Complex in the North Range, South Range and East Range (Hearst et al., 1994). The 5 km upward-contained shaded-relief total-field aeromagnetic images (Figures C.4a~C.4d) show an interesting arcuate magnetic anomaly boundary ~25 km northwest and southwest of the Sudbury Igneous Complex. This anomaly boundary cannot be detected northeast of the Sudbury Igneous Complex due to the strong Temagami magnetic

anomaly. To south of the Sudbury Igneous Complex, this boundary might be affected by the Grenville Front Tectonic Zone. This arcuate magnetic anomaly boundary is interpreted to correlate to the second ring zone containing pseudotachylyte, 25-35 km from the North Range of the Sudbury Igneous Complex. The other unexpected magnetic anomaly shown on a shaded-relief magnetic images is a ray-shaped magnetic feature observed between the boundaries of the arcuate magnetic anomaly and the Sudbury Igneous Complex (Figures C.4a~C.4d). A typical ray-shaped structure induced by an impact event was observed by remote sensing images of lunar Copernicus crater (Figure C.5). However, the magnetic feature of this ray-shaped impact structure on the Moon could not be observed because of the current limited survey technique.

Interpretation of magnetic data is more difficult than that of gravity data because of complex magnetic properties of rocks. In addition, magnetic properties of rocks can be changed by exogenous activities, such as propagation of shock waves, mechanical deformation, high-temperature hydrous alternation, chemical effects and sulfide mineralization (Grant, 1985). There are a few documents discussing magnetization of magnetic reset of rocks inside craters caused by propagation of shock waves, temperature change and chemical effects induced by impact events and nuclear explorations (Young, 1970; Robertson and Roy, 1979; Coles and Clark, 1982; Corner et al., 1990; Elming et al., 1991; Pilkington and Grieve, 1992; Hirt et al., 1993). Moreover, there are few studies in magnetic properties of "undisturbed rocks" outside craters. Therefore, the ring- and ray-shaped magnetization process, magnetic carriers and the relationship between the magnetic anomaly and impact-induced structure in Sudbury are unclear and need to be studied further.

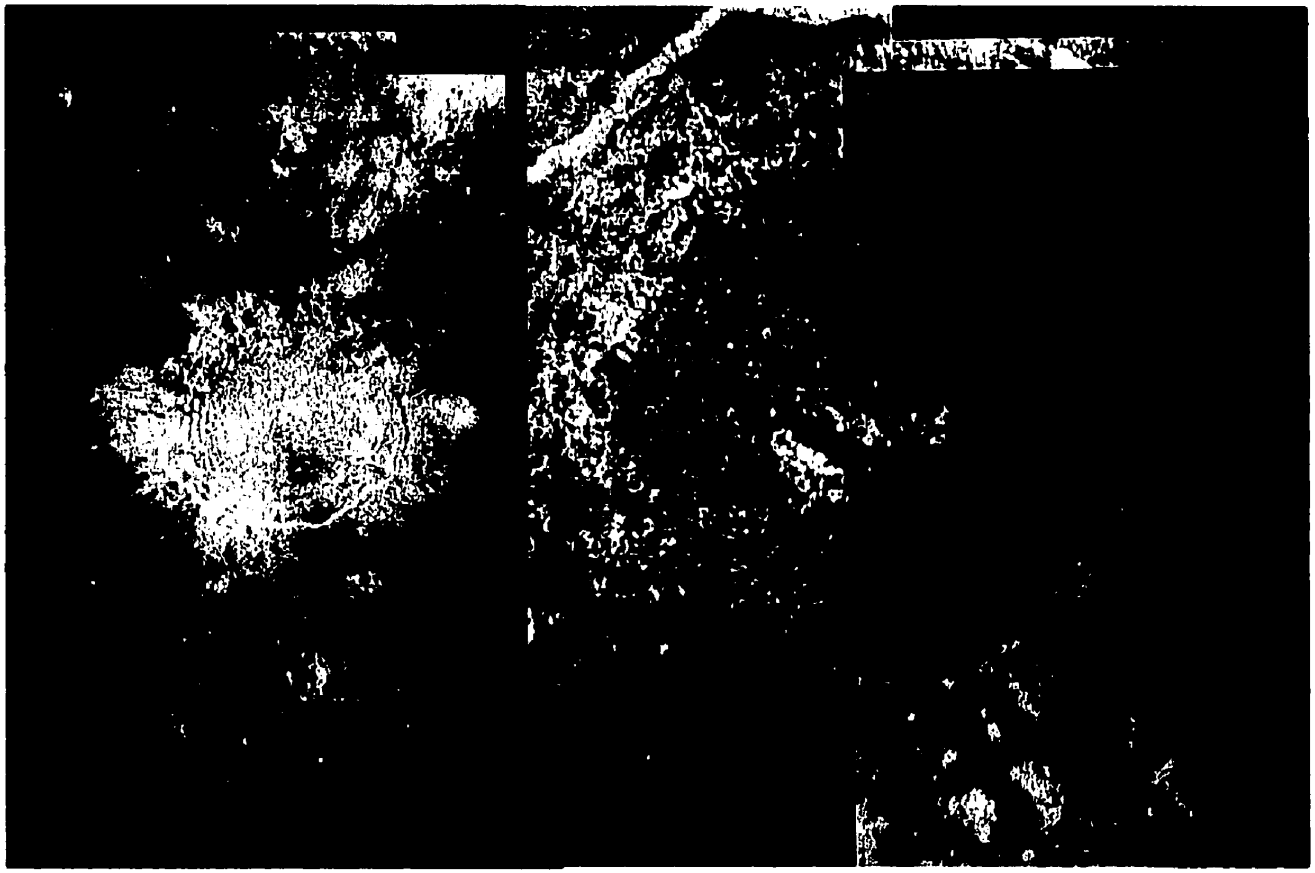

Location: 9°N, 20°W; Diameter: 95 km
(from Clementine UV-VIS, NASA images)

Figure C.5 Lunar Copernicus crater.

Appendix D

Remote Sensing Data and GIS Applications

This appendix contains a discussion of the preliminary processing of a radar image in Sudbury and the basic application of a GIS in displaying the radar image and geological information. The radar image of Radarsat-1 in Sudbury was received in June, 1996. The image covers a ~70x70 km area and was georeferenced using PCI (Release 6.6) software. A Forest filter in PCI was applied to reduce the speckle noise of the image. The radar image was then overlain by the digitized geological map and seismic survey location using ER Mapper (Release 5.5).

D.1 Preliminary Processing of Radar Image

There are three primary steps in the Sudbury radar image processing: (1) selecting control points for georeferencing; (2) georeferencing of the image data to assign geographical coordinates to each pixel; and (3) filtering of the data to reduce speckle noise.

The original radar image of the Sudbury area has not been georeferenced. Therefore, georeferencing was required to "allocate" coordinates for the Sudbury radar image. In

georeferencing, the important step is to select control points from high-resolution topographic maps. Control points are specific positions which can be precisely identified in a radar image. These locations include cross points of rivers and centers of small islands. Control points should be uniformly distributed throughout the imaging region in order to georeference the image properly. In Sudbury, a total of 21 control points covering the image area were chosen from 1:50,000 UTM topographic maps. The coordinates of the selected control points in Sudbury are listed in Table D.1. Figure D.1 shows the original radar image overlain by these control points marked by red crosses.

The coordinates were assigned to the pixels of the Sudbury image by using the GCP Works module of the PCI package installed on a Sun SPARC 20. The basic steps for georeferencing in PCI are described in the PCI GCP Works reference manual. As this processing is common and straight forward, the detailed processing procedure will not be described here. The final Sudbury georeferenced radar image contains the RMS errors of 2.97 pixel and 2.75 pixel.

D.2 Speckle Noise Reduction

The original image was contaminated by many small white spots (speckle noise). To remove the noise, filtering techniques were applied. A total of five filters were tested in a selected small-sized image (Figure D.2). The methods used include the enhanced Forest filter (7x7 pixel filter window or 7x7), Forest filters (7x7 and 5x5), average filters (5x5 and 3x3), Kuan filters (5x5 and 7x7) and Lee filter (7x7). Among the filtered images, the Forest filter with a 7x7 filter, window, provides the optimum result. Figure D.3 shows the

Table D.1 UTM coordinates of the control points (C.P.) and the corresponding pixel positions in the RADARSAT image

C. P. No.	Coordinates NS (m)	Coordinates EW (m)	Pixel Offset in Image	Line Offset in Image
1	5181431	522521	12702.4	4372.1
2	5139201	498411	10920.6	10186.9
3	5193801	459181	4652.2	4584.4
4	5159451	463581	6124.7	8662.7
5	5204681	520901	11875.7	1588.6
6	5179941	514851	11804.4	4772.6
7	5196561	535546	13878.3	2185.0
8	5202001	529801	13035.1	1672.1
9	5146001	434001	2878.9	11105.0
10	5139571	432825	2916.3	11920.0
11	5137946	455001	5660.9	11517.9
12	5131431	457226	6108.8	12255.2
13	5148746	472976	7560.9	9712.6
14	5142726	494141	10303.0	9873.5
15	5130291	483451	9337.9	11681.1
16	5128176	471386	7924.3	12267.8
17	5201951	461421	4703.0	3531.0
18	5206381	452926	3548.0	3223.9
19	5218551	448446	2669.0	1855.4
20	5229270	450100	2578.0	504.0
21	5189776	504436	10279.3	3854.3
Total: 21 control points				

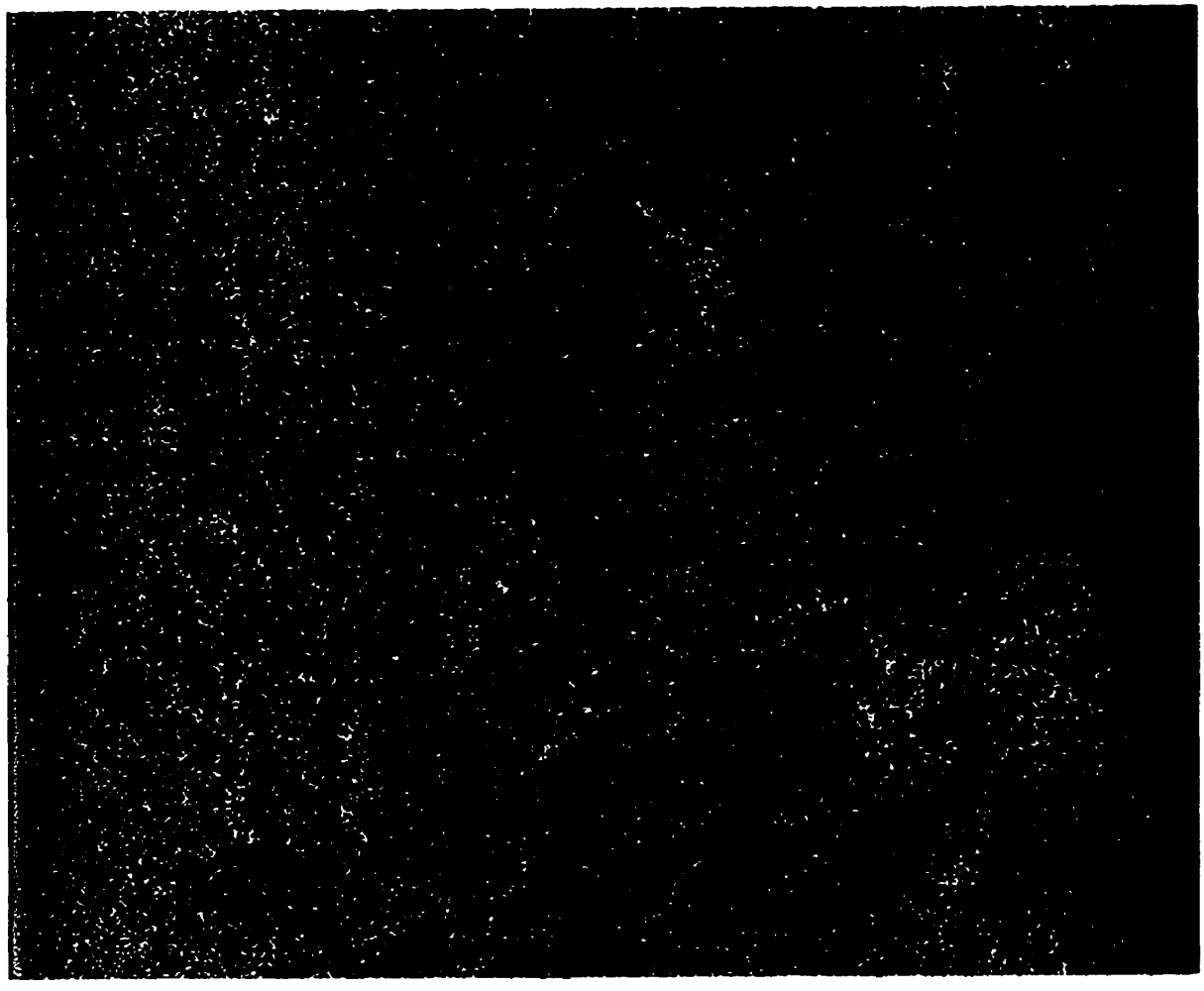

Figure D.1 Original radar image in Sudbury (1996) with 21 control points for geo-reference. Red crosses and numbers represent the control point.Yellow framed area is enlarged in Figure D.2.

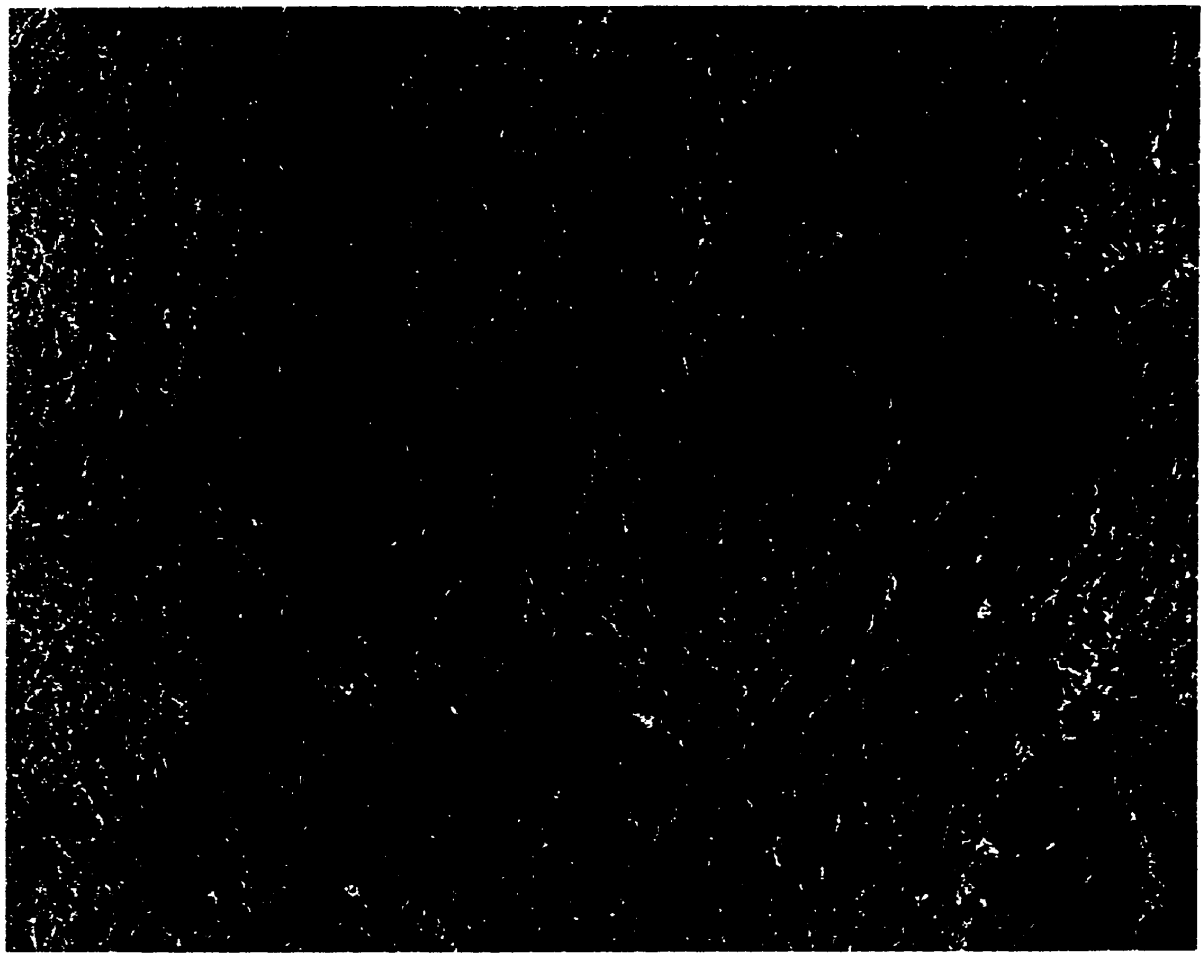

Figure D.2 Original radar image without filtering. The area is indicated by yellow frame in Figure D.1.

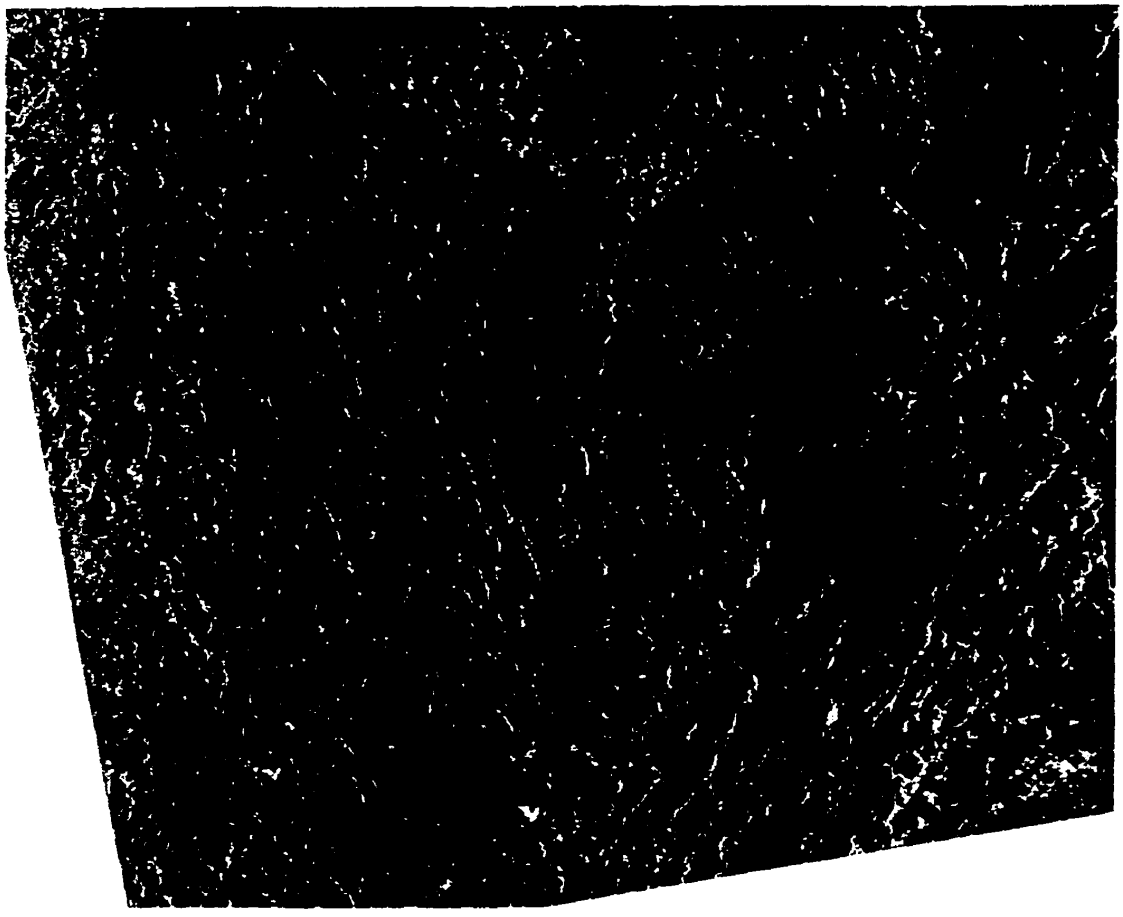

Figure D.3 The radar image filted by 7 x 7 Forest filter. The area corresponds to the region in Figure D.2.

small-sized image filtered by a 7x7 Forest filter. Finally, the 7x7 Forest filter was applied to the whole image. A detailed discussion of the filters used for image processing is given by Ristau (1999). Figure D.4 shows the georeferenced and filtered image which was displayed in UTM projection.

D.3 GIS Displaying

The Sudbury geological map, which contains mainly geological boundaries, was digitized using AutoCad (Release 13) and was edited using AutoCad (Release 14) and CorelDRAW (Version 8). Unfortunately, ER Mapper (Release 5.5) did not accept the filled area format of the digitized data which was used in the geological map digitizing. Therefore, the digitized geological map was saved in a standard image format (bmp) and imported into ER Mapper. Subsequently, the geological map was georeferenced in ER Mapper. Then, the georeferenced geological map was placed transparently on top of the processed radar image as a second layer. The vector data file containing the UTM coordinates of the seismic survey locations was generated in ER Mapper. Then, this vector data was overlain on the geological map and radar image as a third layer. This final image, along with seismic survey positions, is shown in Figure D.5. This figure displays the relationship between the geological structure and topography in the Sudbury area.

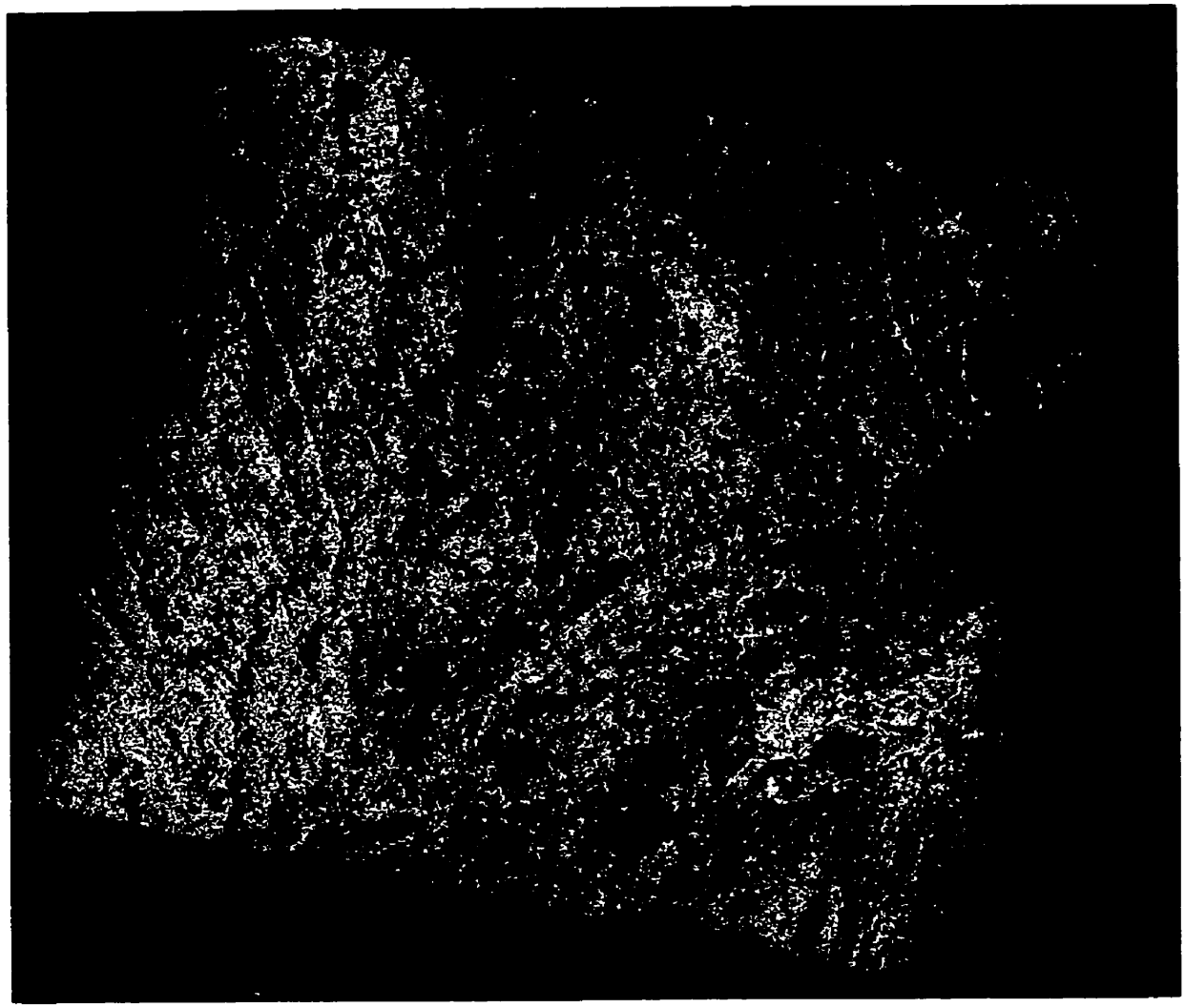

Figure D.4 The geoferenced and Forest (7 x 7) filtered radar image in Sudbury.

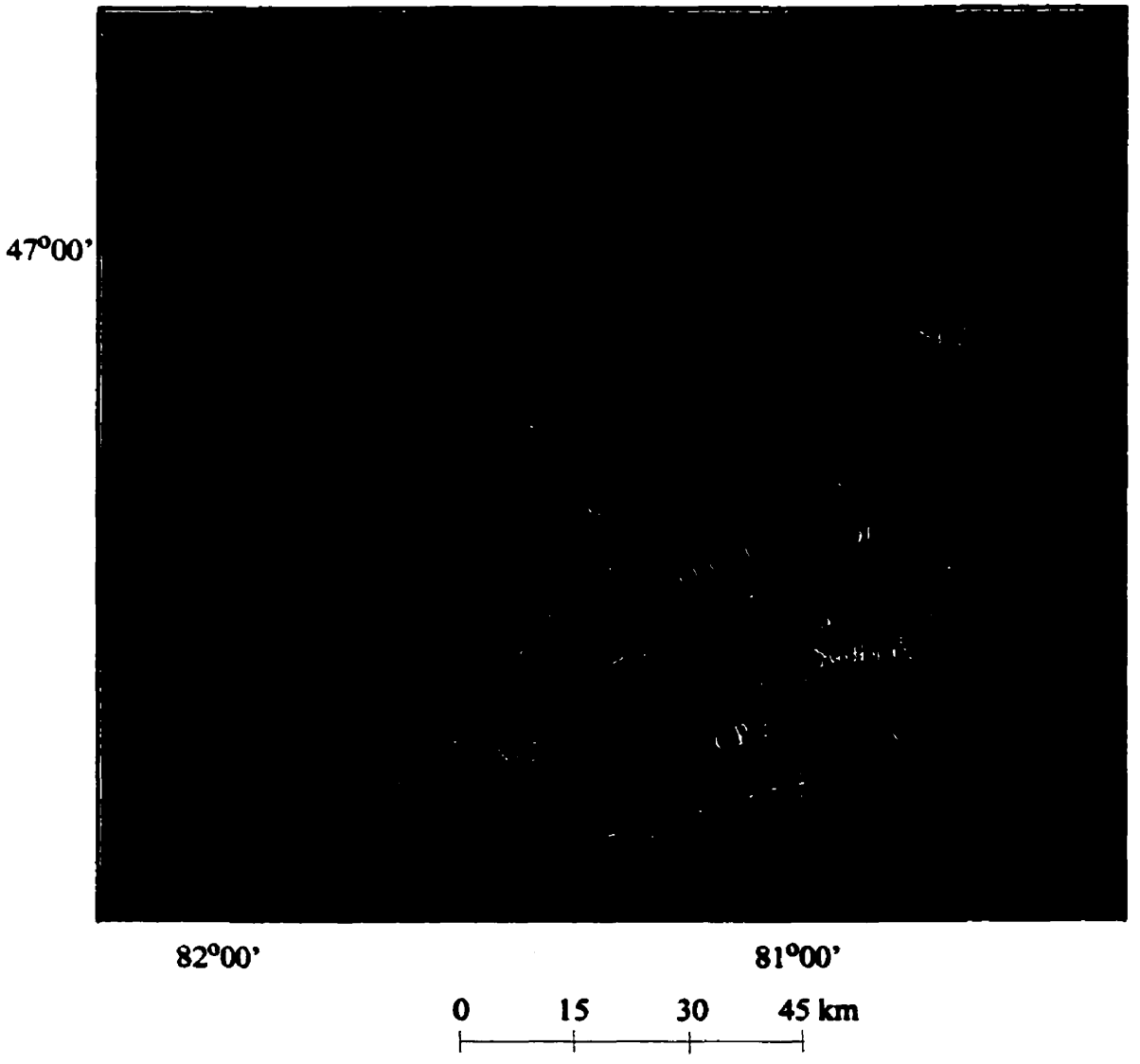

Figure D.5 The filtered radarsat image overlain by the geological boundaries and seismic survey locations marked by the red triangles. xy1 and ab1: shot locations; SIC: Sudbury Igneous Complex; OF: Onaping Formation; O-ChF: Onwatin and Chemsfilm Formations; LGC: Levack Gneiss Complex; CP: Creiton Pluton; SP1: Superior Province; SP2: Southern Province; GF: Grenville Front.